Spring 5-24-2022

Cysteine Metallochemistry and Metal Binding: Quantification of the Thermodynamic Foundations of Cellular Homeostasis

Matthew R. Mehlenbacher
Dartmouth College, matthew.r.mehlenbacher.gr@dartmouth.edu

Cysteine Metallochemistry and Metal Binding: Quantification of the Thermodynamic Foundations of Cellular Homeostasis

A Thesis
Submitted to the Faculty
In partial fulfillment of the requirements for the
Degree of

Doctor of Philosophy

In

Chemistry

By

Matthew Richard Mehlenbacher

Guarini School of Graduate and Advanced Studies
Dartmouth College
Hanover, New Hampshire
May 24th, 2022

Examining Committee:

_____
(chair) Professor Dean E. Wilcox

_____
Professor Ekaterina Pletneva

_____
Professor Robert S. Cantor

_____
Professor Fadi Bou-Abdallah

_____
F. Jon Kull, Ph.D.
Dean of the Guarini School of Graduate and Advanced Studies

Abstract

Metals are required for life. Many metalloproteins contain cysteine in their metal-binding site (MBS) and cysteines are unique in that they are reactive, and strongly bind certain metals, which aid in metal selectivity and specificity. Using isothermal titration calorimetry (ITC), the thermodynamic foundation for metal binding, cellular protection, and transcriptional regulation, which all utilize cysteines in their MBS, are quantified.

In bacteria there are metalloprotein pathways that actively uptake mercury, which are regulated by the metalloregulatory protein MerR. MerR de-represses the transcription of these *mer* proteins in a metal-dependent manner. Using ITC, the thermodynamic foundation of the negative allosteric coupling that regulates MerR is quantified. Within this regulated pathway is a metallochaperone in the periplasm of the cell, MerP, which functions as a mercury buffer, protecting the cell from the deleterious effects of the metal. The thermodynamic foundation of cellular protection and the mechanism of metal binding is characterized.

MerP is a part of a class of metallochaperones that all contain the same protein architecture and MBS. However, this class of metallochaperones binds a wide range of metals, including zinc, copper, and mercury. How one protein scaffold with the same MBS modulates metal binding is unknown. The fundamental thermodynamics suggest that second-sphere interactions are capable of modulating metal-binding properties of these ferredoxin-like folded proteins leading to metal selectivity and specificity.

Unlike bacterial *mer* protein, which generally bind one metal ion, other cysteine-rich proteins bind multiple metals simultaneously. In this work, the thermodynamics and mechanism of copper and zinc binding to human metallothionein (MT), a protein with many cellular functions in the regulation of metal toxicity and neuron growth inhibition, were quantified.

The binding of copper, zinc, and mercury to bacterial copper storage proteins (CSPs), which also utilize a large number of cysteine residues to bind and store copper, but unlike MT are conformationally stable. Metal binding in CSPs does not alter the global protein dynamics, thus a comparison between CSPs and MT provide valuable insight into how protein dynamics and the contribution of the protein scaffold can modulate the binding of different metals in solution.

Acknowledgements

To say that we pursue a Ph.D. alone feels like an understatement. Long, tireless days in the lab, and longer night sitting in a chair writing are not activities that are easily shared. But those around us experience these with us. They see the challenges. The excitement. And the setbacks. We are not really alone in this process. At the forefront of this is my wife, Victoria, whose support cannot be overstated. As we sit over a candle-lit dinner table, she listens patiently as I explain the difficulties in the experiments that are ongoing. Or when I criticize myself when they fail, seemingly missing one important step or another. She sits and listens. Without her support, my words fall on deaf ears. My own. Without her help in keeping me grounded and balanced, work overwhelms. And the joy of us bringing Eliza Lee Mehlenbacher into this world brings clarity.

Support at home is, however, only one aspect associated with the pursuit of knowledge. Confidence in the work we do is difficult to obtain, but with a mentor that stands beside us, supporting us when we need help, or teaching when we fail, this process becomes manageable. To that, I thank Dean Wilcox, who has patiently answered every knock on his door with his experience and knowledge. Dean gave me the freedom to pursue those research projects as I see fit. Partly because I forged ahead and asked permission later after I got results. Sorry, Dean! Patient and unwavering, Dean has been the key to my success, giving me the tools to continue my research journey.

Learning how to do experiments is one thing, but it is an entirely different to apply fundamental chemical knowledge to other areas that are outside our own work. Professor Kate Pletneva has, by far, expanding my general chemical knowledge than any reading that I could have done. Pushing me to question what is known and what are the governing principals. Pushing on the limits of our memories of chemistry learned years ago. Dusty. Torturous at times, knowing I lost knowledge of what I once had worked to gain. Learning to question every assumption and idea, leading us towards each conclusion. These are not easy skills to gain and require discipline and reading in research areas far beyond our own work. I could not have started these processes without Kate, and these skills and teaching techniques will propagate far beyond my time at Dartmouth. I couldn't be more thankful.

Others have supported me along the way, in many different ways. Professor Robert Cantor, who has gone out of his way to teach me many wonderful scientific topics. He also

served on my committee, provide inquisitive questions, and really made me think about all aspects of my thesis work. Professor Mike Ragusa who always tried to help with questions inside and outside the classroom, or his students Kelsie Leary, Katie Bauer, and Erin Reinhart who taught me everything I know about protein expression and purification. And Professor Dale Mierke, who I have taken many pivotal classes during my time at Dartmouth.

Some contributions did not start here at Dartmouth, but years prior. Professor Fadi Bou-Abdallah has been a fantastic mentor who has taught me how to be a scientist and to do good research. He worked tirelessly to ensure I knew physical chemistry as an undergraduate at SUNY Potsdam. And he supported me during challenging times as I made the choice to leave medicine. Now, as my outside examiner, Dr. Fadi has, yet again, continued to be supportive and encouraging. His experiences that he has shared with me will never be forgotten, and I look forward to continuing as his colleague in bioinorganic chemistry. I would not be here today without him.

Thank you to past and present members of the Wilcox lab: Kaitlyn Connelly, Michael Cukan, Theodore Press, Sunyo Park, and Elizabeth DeGaetano. All of you have taught me something new about chemistry and ITC. And several of you have given me ample opportunities to teach ITC and to thoroughly talk your ear off about pretty much everything!

As much as each of these people have helped with my research career, others in the department have made my life infinitely easier. Amer Akram, who has single-handedly saved me many grey hairs and frustrations, through purchasing. And to Michelle Swanson who has brought such joy to the department.

Finally, but not least, is my family. I couldn't be more grateful to have Elena, Denis, and Stefan in my life. You mean the world to me. To Mom and Karen, Grandma and Grandpa Cookies, Grandma Moo-Moo, Dad, Uncle Rusty and Aunt Yvonne, and all the rest of our endless family: I don't know where I would be without you. Thank you for the encouragement, and the part each of you have played in making me who I am today.

I did not do this alone. Each of you joined me on my journey, some big and some small, but every one of you played a part and I couldn't be more grateful.

Table of Contents

	Abstract	ii
	Acknowledgments	iii
	Table of Contents	v
	List of Common Abbreviations	xi
	List of Thermodynamic Terms	xii
	List of Figures	xiii
	List of Tables	xvii
	List of Schemes	xix
Chapter 1:	**Cysteines in Metallochemistry and Cellular Homeostasis**	**1**
	1.1. Metals in Biology	2
	1.2. Cysteine Chemistry in Metalloproteins	10
	1.3. Methods in the Study of Metalloproteins	12
	1.4. Thesis Summary and Organization	14
	1.5. References	17
Chapter 2:	**Metal Binding Thermodynamics and Protein Dynamics: Quantification and Characterization by Isothermal Titration Calorimetry and Molecular Dynamics**	**26**
	2.1. A Brief History of Calorimetry	27
	2.2. The Theoretical Foundation of Isothermal Titration Calorimetry	27
	2.2.1. Theory, Application, and Limitations of ITC	27
	2.3. The Ligand-Macromolecule Interaction	31
	2.3.1. Experimental and Calculated Binding Enthalpy	31
	2.3.2. *Post-hoc* Analysis to Establish Ligand Macromolecule Binding Affinity	33
	2.4. Molecular Dynamics: Exploring Protein Dynamics and Metal-Binding	41
	2.4.1. Foundational Molecular Dynamics: Theory, History, and Practice	42
	2.5. Conclusions for Instrumentations and Computational Techniques	53
	2.6. References	54
Chapter 3:	**Energetics of Heterotropic and Homotropic Allosteric Regulation in the Mercury Metalloregulatory Protein, *Bacillus megaterium* MerR**	**58**
	3.1. Introduction	59
	3.1.1. Metal-Responsive Protein Transcription in Bacteria	59
	3.1.2. Allosteric Regulation of Metal-Responsive Transcriptional Regulators	60

3.1.3. Metal-Response Transcriptional Regulation and the MerR Family 62
3.1.4 Allosteric Regulation of MerR and the Mercury Detoxification Proteins 64
3.2. Materials and Methods 68
3.2.1. Chemicals 68
3.2.2. MerR Operon, *merO*, Preparation 68
3.2.3. Transformation, Expression, and Purification of MerR 68
3.2.4. Isothermal Titration Calorimetry 70
3.3. Results 71
3.3.1. Coupled Equilibria Model for the Hg-MerR-*merO* Complex Formation 71
3.3.2. Selection of Mercury Competing Ligands 72
3.3.3. Thermodynamics of the Mercury-Penicillamine Interaction 74
3.3.4. Hg^{2+} Binding to apo-MerR 76
3.3.5. Mercury Binding to the MerR-*merO* Complex 81
3.3.6. Thermodynamics of the MerR-*merO* Complex Formation 86
3.3.7. Binding of Mercury-bound-MerR to *merO* 91
3.3.8. Coupling Energies 96
3.4. Discussion 100
3.4.1. Mercury Binding to MerR and the MerR-*merO* Complex 100
3.4.2. Homotropic Allostery in MerR and the MerR-*merO* Complex 103
3.4.3. Heterotropic Coupling Components 104
3.5. Summary 105
3.6. References 106
Chapter 4: Modulation of Metal Binding Thermodynamics by Second Sphere Interactions and Protein Dynamics in Mercury and Copper Metalloproteins with the Ferredoxin-Like Fold 112
4.1. Introduction 113
4.l.1. Interplay Between Protein Structures, Conformational Dynamics, and Ligand Binding 113
4.1.2. Second Coordination Sphere and its Role in Modulating Protein Function 115
4.1.3. Similar Structure, Similar Function, Yet Different Thermodynamic Contributions? 119

4.2. Materials and Methods 121
4.2.1. Materials 121
4.2.2. Protein Transformation, Expression, and Purification 122
4.2.3. Determination and Preparation of Protein, Metal, and Ligand Concentrations 123
4.2.4. Isothermal Titration Calorimetry Experimental Conditions 123
4.3. Results 124
4.3.1. Quantification of the Mercury-MerP Binding Thermodynamics 124
4.3.2. Copper(I)-MerP Binding Thermodynamics 137
4.3.3. Quantification of the Zinc-MerP Thermodynamics 139
4.3.4. Quantification of the Cadmium-MerP Thermodynamics 147
4.3.5. Thermodynamics of Hg^{2+} Binding to WND4 148
4.3.6. Thermodynamics Associated with the Cu^{+}-WND4 Complex 153
4.3.7. Thermodynamics of the Zn^{2+} Binding to WND4 157
4.3.8. Thermodynamics of the Cd^{2+} Binding to WND4 160
4.4. Discussion 160
4.4.1. Comparative Analysis of the Binding of Native and Non-Native Metals to MerP 160
4.4.2. Comparative Thermodynamics of Hg^{2+} and Cu^{+} Binding to WND4 171
4.4.3. Unusual Zn^{2+} and Cd^{2+} Coordination in WND4 177
4.4.4. Impacts of Ferredoxin-Like Protein Architecture on Metal Binding, Selectivity, and Specificity 178
4.4.5. Future Work and Conclusions 181
4.5. References 182
Chapter 5: Cellular Protection from Environmentally-Relevant Metals and Organomercurial Compounds by the Bacterial Periplasmic Mercury Protein, MerP 189
5.1. Introduction 190
5.1.1. Mercury and Organomercurial Compounds in the Environment 190
5.1.2. Mechanisms of Mercury Toxicity 190
5.1.3. Bacterial Defense Mechanisms for Mercury Protection 193
5.1.4. The Bacterial Mercury Detoxification Pathway 194
5.1.5. Protection from Environmental Mercury Toxicity

by MerP 196
5.2. Materials and Methods 199
5.2.1. Chemicals 199
5.2.2. Protein Preparation 200
5.2.3. Methylmercury Safe Handling Procedure for Solution Preparation 200
5.2.4. Isothermal Titration Calorimetry Experiments 201
5.2.5. Molecular Dynamics Experiments 202
5.3. Results 204
5.3.1. Anion Competition for Methylmercury in the Binding to MerP 205
5.3.2. Thermodynamics of the Methylmercury-Buffer Complex Formation 205
5.3.3. Condition-Independent Binding Thermodynamics of Methylmercury to MerP 211
5.3.4. Molecular Dynamics for the Methylmercury-Binding Mechanism 223
5.3.5. Binding of Organomercurial Compounds to MerP 223
5.4. Discussion 227
5.4.1. Alternative Physiological Function of MerP 227
5.4.2. Thermodynamics of the Methylmercury-MerP Interaction 228
5.4.3. Binding of Organomercurial Compounds to MerP 233
5.4.4. Thermodynamic and Structural Support for the Physiological Function of MerP 235
5.5. References 235
Chapter 6: Thermodynamic Contributions of Metal-Swapping and Interdomain Interactions in Neuronal Metallothionein 243
6.1. Introduction 244
6.1.1. An Introduction to Metallothionein 244
6.1.2. Physiological Function of MT-3 245
6.1.3. Metal-Swap Hypothesis: Function of MT-3 in Neuronal Copper Chemistry 247
6.1.4. Metal-Binding Properties of Metallothionein-3 248
6.1.5. Structural Dynamics and Folding of Apo- and Metalated-Metallothionein 250
6.1.6. Thermodynamic Foundation of Metal-Swapping and Interdomain Contributions to Metal Binding in Metallothionein-3 251
6.2. Materials and Methods 252

6.2.1. Chemicals and Materials 252
6.2.2. Isothermal Titration Calorimetry: Data Collection and Analysis 253
6.3. Results and Analysis 253
6.3.1. Thermodynamics of Zinc Binding to Metallothionein-3 254
6.3.2. Thermodynamics of the Cu^{+}–MT-3 and MT-2 Interaction 265
6.4 Discussion 273
6.4.1. Entropic and Enthalpic Contributions of Zinc Binding to MT-3 274
6.4.2. Decoupling Metal Binding Thermodynamics from the Protein Folding Thermodynamics 276
6.4.3. Quantifying Interdomain Contributions to Zinc Binding Thermodynamics in MT-3 279
6.4.4 Entropically Driven and Enthalpically Favorable Copper(I) Binding to MT-3 281
6.4.5. Implications of Cu^{+} and Zn^{2+} Binding Thermodynamics on the Physiological Function of MT-3 285
6.5. Summary 285
6.6. References 286
Chapter 7: Thermodynamic Foundation of Metal Selectivity and Specificity in Bacterial Copper Storage Proteins: A Comparative Analysis of the Binding of d^{10} Metals by Isothermal Titration Calorimetry 294
7.1. Introduction 295
7.1.1. Copper in Biology 295
7.1.2. Copper Homeostasis 295
7.1.3. Introduction to *Methylosinus trichosporium* Copper Storage Proteins 297
7.1.4. Specificity and Selectivity of Copper Over Competitive d^{10} Metal Ions 301
7.2. Materials and Methods 302
7.2.1. Chemicals 302
7.2.2. Copper Storage Protein (CSP1 and CSP3) Transformation, Expression, and Purification 302
7.2.3. Determination of Ligand and Metal Salt Concentrations 303
7.2.4. Determination of Copper(I) Concentrations 303

7.2.5. Isothermal Titration Calorimetry Experiments 303
7.3. Results and Analysis 304
7.3.1. Calorimetric Characterization of Copper(I) Binding to CSP1 304
7.3.2. Calorimetric Characterization of Copper(I) Binding to CSP3 315
7.3.3. Binding of Zinc to CSP1 326
7.3.4. Binding of Zinc to CSP3 330
7.3.5. Binding of Hg^{2+} to CSP1 and CSP3 337
7.4. Discussion 341
7.4.1. Quantification of the Thermodynamics of each Copper(I) Population Binding to CSP1 343
7.4.2. Binding of Three Distinct Cu^{+} Populations to CSP1 345
7.4.3. Thermodynamic Contributions of Copper(I) Binding in CSP1 346
7.4.4. CSP3 Binds Copper(I) in Three Distinct Thermodynamically Stable Populations 350
7.4.5. Thermodynamic Contributions to Copper(I) Binding in CSP3 352
7.4.6. Comparative Analysis of CSP1 and CSP3 and their Copper(I)-Binding Properties 354
7.4.7. Evaluating the Zinc(II)-CSP1 Interaction 354
7.4.8. Comparative Zinc(II)-Binding Thermodynamics in CSP1 and Metallothionein 355
7.4.9. CSP3 Binds Zinc(II) in Two Thermodynamically-Distinct Populations 357
7.4.10. Thermodynamic Contributions to Zn^{2+} Binding in CSP3 358
7.4.11. Comparative Zinc(II)-Binding Thermodynamics in CSP1 and CSP3 360
7.4.12. Binding of Mercury to CSP1 and CSP3 360
7.4.13. Metal Selectivity, Specificity, and Cooperativity in CSP1 and CSP3 362
7.5. Conclusions 362
7.6. References 363
Chapter 8: Reflections of Cysteine Metallobiochemistry Thermodynamics and the Implications in Biological Systems 367
8.1. References 371

List of Common Abbreviations

ACES	N-(2-acetamido)-2-aminoenthanesulfonic acid
βME	β-mercaptoethanol
BCA	Bicinchoninic acid
BCS	Bathcuproine disulfonic acid
BisTris	2-bis(2-hydroxyethyl)amino-2-(hydromethyl)-1,3-propanediol
Cys	Cysteine
DTDP	4,4'-dithiodipyridine
DTNB	Dithionitrobenzoic acid
DTPA	Diethylenetriaminepentaacetic acid
DTT	Dithiolthreitol
EDTA	Ethylenediaminetetraacetic acid
GSH	Glutathione
HAH1	Cuprous Copper Metallochaperone
HEPES	4-(2-hydroxyethyl)-1-piperazineethanesulfonic acid
IPTG	Isopropyl β-D-1thiogalactopyranoside
ITC	Isothermal Titration Calorimetry
MBD	Metal binding domain
MBS	Metal binding site
MeCN	Acetonitrile
MerA	Mercuric Reductase
MerB	Organomercurial Lyase
MerO	MerR Operon
MerP	Periplasmic Mercury Metallochaperone
MerR	Mercury Metalloregulatory Protein
MerT	Transmembrane Mercury Transport Protein
NAPA	N-acetyl-penicillamine
NmerA	N-terminal Domain of MerA
Pen	Penicillamine
PIPES	Piperazine-N,N'-bis(2ethanesulfonic acid)
Rg	Radius of Gyration
RMSD	Root Mean Square Deviation
RMSF	Root Mean Square Fluctuations
SASA	Solvent-Accessible Surface Area
TAPSO	3-[N-Tris(Hydroxymethyl)methylamino]-2-hydroxypropanesulfonic acid
TRIS	Tris(hydroxymethyl)aminomethane
WND4	Wilson's Domain 4 Metal-Binding Domain

List of Thermodynamic Terms

ΔH	Change in Enthalpy
ΔH_{ITC}	Apparent Enthalpy Determined by ITC
ΔH_{BH}	Buffer-Protonation Enthalpy
ΔH_{PH}	Protein-Protonation Enthalpy
ΔH_{MB}	Metal-Buffer Enthalpy
ΔH_{ML}	Metal-Ligand Enthalpy
ΔH_{MP}	Metal-Protein Enthalpy
ΔG	Change in Gibbs Free Energy
ΔG_{ITC}	Apparent Gibbs Free Energy
K	Binding constant
K_{ITC}	Apparent Binding Affinity Determined by ITC
K_{BH}	Buffer Protonation Equilibrium Constant
K_{PH}	Protein Protonation Equilibrium Constant
K_{MB}	Metal-Buffer Equilibrium Constant
K_{ML}	Metal-Ligand Equilibrium Constant
K_{MP}	Metal-Protein Equilibrium Constant
MD	Molecular Dynamics
n	Stoichiometry
QM	Quantum Mechanics
ΔS	Change in Entropy, Reported as: $-T\Delta S = \Delta G - \Delta H$ (kcal/mol)

List of Figures

Chapter 1:

Figure 1.1.1.	Biologically-Relevant Transition Metal Periodic Table	3
Figure 1.1.2.	Protein Primary, Secondary, Tertiary, and Quaternary Structures	5
Figure 1.1.3.	Structure of Ferric Iron-Bound Human Transferrin	8
Figure 1.1.4.	Structure of Cuprous Copper-Bound CueR	9

Chapter 2:

Figure 2.2.1.1.	Simple, Single-Site, Direct Metal-Binding Isotherm	29
Figure 2.3.2.1.	Fitting with One-Site and Two-Site Fitting Models	39
Figure 2.4.1.1.	Bonded and Non-Bonded Interactions for Molecular Dynamics	46
Figure 2.4.1.2.	Free Energy Landscape for Protein Conformations	51

Chapter 3:

Figure 3.1.2.1.	General Metalloregulatory Protein Mechanisms	61
Figure 3.1.3.1.	Structure of MerR, MerO Genes, and the MerO Sequence	63
Figure 3.1.4.1.	General Mercury Detoxification Pathway in *Bacillus megaterium*	66
Figure 3.1.4.2.	General Coupling Scheme for the Binding of Mercury to MerR	67
Figure 3.3.1.1.	Detailed Thermodynamics Cycle for Mercury Binding to MerR	73
Figure 3.3.2.1.	Isotherms for Hg into apo-MerR with Competing Ligands Present	75
Figure 3.3.4.1.	Representative Isotherms for Hg-Pen into apo-MerR	78
Figure 3.3.4.2.	Proton Plot for Hg-Pen into apo-MerR	80
Figure 3.3.5.1.	Representative Isotherms for Hg-Pen into the MerR-MerO	82
Figure 3.3.5.2.	Proton Plots for Hg-Pen into MerR-MerO	84
Figure 3.3.6.1.	Representative Isotherm of apo-MerR into MerO	88
Figure 3.3.6.2.	Proton Plot for apo-MerR into MerO	90
Figure 3.3.7.1.	Representative Isotherm for Hg-MerR into MerO	93
Figure 3.3.7.2.	Proton Plot for Hg-MerR into MerO	95

Chapter 4:

Figure 4.1.1.1.	Lock-and-Key Enzyme Mechanism Example	114
Figure 4.1.2.1.	Modulation of Metal Reduction Potentials at pH 7.0	116

Figure 4.1.2.2.	Ferredoxin-Like Folded Protein Structures and Sequence Comparison	117
Figure 4.1.2.3.	First and Second-Sphere Interactions within a Protein	118
Figure 4.1.3.4.	Proposed Mechanism for the Transfer of Cu(I) from HAH1 to WND4	120
Figure 4.3.1.1.	Representative Isotherm for Hg-EDTA into apo-MerP	126
Figure 4.3.1.2.	Proton Plot for the Titration of Hg-EDTA into apo-MerP	128
Figure 4.3.1.3.	Representative Isotherm of Mercury Chelation from MerP by NAPA	130
Figure 4.3.1.4.	Proton Plot for the Chelation of Mercury from MerP by NAPA	131
Figure 4.3.2.1.	Representative Isotherm of Cu(I)-GSH into apo-MerP	134
Figure 4.3.2.2.	Proton Plot for Cu(I)-GSH into apo-MerP	136
Figure 4.3.3.1.	Representative Isotherm for the Titration of Zinc into apo-MerP	140
Figure 4.3.3.2.	Proton Plot for Zinc into apo-MerP	142
Figure 4.3.4.1.	Representative Isotherm for Cadmium into apo-MerP	144
Figure 4.3.4.2.	Proton Plot for Cadmium into apo-MerP	146
Figure 4.3.5.1.	Representative Isotherms for Mercury into apo-WND4	150
Figure 4.3.5.2.	Proton Plot for Mercury into apo-WND4	151
Figure 4.3.6.1.	Representative Isotherm for the titration of Cu(I)-GSH into apo-WND4	154
Figure 4.3.6.2.	Proton Plot for Cu(I)-GSH into apo-WND4	155
Figure 4.3.7.1.	Representative Isotherm for the Titration of Zinc into WND4	158
Figure 4.3.8.1.	Representative Isotherm for Cadmium into WND4	159
Figure 4.4.1.1.	Graphical Representation of Enthalpic and Entropic Contributions	164

Chapter 5:

Figure 5.1.2.1.	Mercury Toxicity in Humans	192
Figure 5.1.4.1.	Bacterial Mercury Detoxification Pathway Proteins	195
Figure 5.1.5.1.	Structure and Metal-Binding Site of MerP	197
Figure 5.3.2.1.	Representative Isotherms of Methylmercury into Cysteine with NaCl	208
Figure 5.3.2.2.	Representative Isotherms of Methylmercury into Cysteine with NaBr	209
Figure 5.3.2.3.	Representative Isotherms of Methylmercury into Cysteine with NaI	210

Figure 5.3.3.1. Representative Isotherms of Methylmercury into apo-MerP with NaCl 214
Figure 5.3.3.2. Representative Isotherms of Methylmercury into apo-MerP with NaBr 215
Figure 5.3.3.3. Representative Isotherms of Methylmercury into apo-MerP with NaI 216
Figure 5.3.3.4. Proton Plot of Methylmercury into apo-MerP with NaCl 217
Figure 5.3.3.5. Proton Plot of Methylmercury into apo-MerP with NaBr 218
Figure 5.3.3.6. Proton Plot of Methylmercury into apo-MerP with NaI 219
Figure 5.3.4.1. Molecular Dynamics Solvent-Accessible Surface Area of Met12, Cys14, and Cys17 224
Figure 5.3.5.1. Structure of Merbromin and Thimerosal 225
Figure 5.3.5.2. Representative Isotherms for Thimerosal and Merbromin Binding to apo-MerP 226
Figure 5.4.2.1. Graphical Representation of Enthalpic and Entropic Contributions Associated with Metal Binding 232

Chapter 6:
Figure 6.3.1. Solution Structure of mouse α-MT3 and β-MT-3 bound with Cadmium 255
Figure 6.3.1.1. Representative Isotherms for the Titration of DTPA into Zinc 257
Figure 6.3.1.2. Representative Thermograms for the Chelation of Zinc from Zn_7-MT3 by DTPA 258
Figure 6.3.1.3. Representative Isotherms for the Chelation of Zinc by DTPA in αMT-3 and βMT-3 261
Figure 6.3.1.4. Proton Plots Associated with the Chelation of Zinc from MT-3, αMT-3, and βMT-3 263
Figure 6.3.2.1. Representative Isotherms of Cu(I)-GSH into MT-3 and MT-2. 267
Figure 6.3.2.2. Proton Plots Associated with Cu(I)-GSH into MT-3 and MT-2 271

Chapter 7:
Figure 7.1.3.1. Tetrameric and Monomeric Structures of CSP1 in *Methylosinus trichosporium* 298
Figure 7.1.3.2. Crystal Structure, and Cu(I) Binding Populations, of CSP3 in *Methylosinus trichosporium* 300
Figure 7.3.1.1. Representative Isotherms of the Titration of Cu(I)-MeCN into apo-CSP1 307

Figure 7.3.2.1. Representative Isotherms of the Titration of Cu(I)-MeCN into apo-CSP3 316
Figure 7.3.3.1. Representative Isotherms of Zinc into CSP1 324
Figure 7.3.4.1. Representative Isotherms of Zinc into CSP3 331
Figure 7.3.5.1. Representative Isotherms of Mercury into CSP1 338
Figure 7.3.5.2. Representative Isotherms of Mercury into CSP3 339
Figure 7.4.3.1. Graphical Representation of the Enthalpic and Entropic Contributions 348

List of Tables

Chapter 3:

Table 3.3.4.1.	Apparent and Condition-Independent Thermodynamics for Hg into apo-MerR	79
Table 3.3.5.1.	Apparent and Condition-Independent Thermodynamics for Hg into MerR-MerO	85
Table 3.3.6.1.	Apparent and Condition-Independent Thermodynamics for apo-MerR into MerO	89
Table 3.3.7.1.	Apparent and Condition-Independent Thermodynamics for Hg-MerR into MerO	94
Table 3.3.8.1.	Summary of Condition-Independent Thermodynamics for the Hg-MerR-MerO Thermodynamic Cycle	97
Table 3.3.8.2.	Summary of Homotropic and Heterotropic Coupling Energies	98

Chapter 4:

Table 4.3.1.1.	Apparent Binding Thermodynamics of Hg-EDTA into apo-MerP	127
Table 4.3.1.2.	Apparent Binding Thermodynamics of NAPA Chelation of Hg from apo-MerP	132
Table 4.3.2.1.	Apparent and Condition-Independent Binding Thermodynamics for Cu(I)-GSH into apo-MerP	135
Table 4.3.3.1.	Apparent and Condition-Independent Binding Thermodynamics of Zinc into apo-MerP	141
Table 4.3.4.1.	Apparent and Condition-Independent Binding Thermodynamics of Cadmium into apo-MerP	145
Table 4.3.5.1.	Apparent and Condition-Independent Binding Thermodynamics of Mercury-GSH into apo-WND4	152
Table 4.3.6.1.	Apparent and Condition-Independent Binding Thermodynamics of Cu(I)-GSH into apo-WND4	156
Table 4.4.1.1.	Summary of Apparent Metal Binding Thermodynamics for MerP, WND4, and HAH1	163

Chapter 5:

Table 5.3.2.1.	Average Apparent Thermodynamics of Methylmercury into cysteine in Various Buffers	212
Table 5.3.3.1.	Average Apparent Thermodynamics of Methylmercury into apo-MerP	220

Table 5.3.3.2. Average Condition-Independent Binding thermodynamics of Methylmercury into apo-MerP 222

Chapter 6:

Table 6.3.1.1. Apparent Binding Thermodynamics for the Chelation of Zinc by DTPA from MT-3, αMT-3, and βMT-3 259

Table 6.1.3.2. Condition-Independent Zinc-Binding Thermodynamics for MT3, αMT-3, and βMT-3 264

Table 6.1.3.3. Comparative Condition-Independent Binding Thermodynamics for Zinc Binding to MT-3, αMT-3, and βMT-3 266

Table 6.3.2.1. Apparent Thermodynamics for the Binding of Cu(I) to MT-3 and MT-2 270

Table 6.3.2.2. Condition-Independent Cu(I) Binding Thermodynamics to MT-3 and MT-2 272

Chapter 7:

Table 7.3.1.1. Apparent Thermodynamics of Cu(I)-MeCN into CSP1 308

Table 7.3.1.2. Condition-Independent Thermodynamics of Cu(I)-MeCN into CSP1 312

Table 7.3.2.1. Apparent Thermodynamics of Cu(I)-MeCN into CSP3 317

Table 7.3.2.2. Condition-Independent Thermodynamics of Cu(I)-MeCN into CSP3 320

Table 7.3.3.1. Average Apparent Thermodynamics Associated with the Binding of Zinc to CSP1 325

Table 7.3.3.2. Average Condition-Independent Binding Thermodynamics of Zinc to CSP1 327

Table 7.3.4.1. Average Apparent Thermodynamics Associated with the Binding of Zinc to CSP3 332

Table 7.3.4.2. Average Condition-Independent Binding Thermodynamics of Zinc to CSP3 335

Table 7.3.5.1. Average Apparent Thermodynamics for Mercury Binding to CSP1 and CSP3 340

List of Schemes

Chapter 2:

Scheme 2.2.1.1.	Mercury into EDTA Competing Equilibria	30
Scheme 2.3.2.1.	Hg-EDTA Competition Experiment Competing Equilibria	37

Chapter 3:

Scheme 3.3.3.1.	Competing Equilibria for the Titration for Hg-DTPA into Penicillamine	77
Scheme 3.3.6.1.	Competing Equilibria for apo-MerR into *merO*	87

Chapter 5:

Scheme 5.3.2.1.	Generalized Competing Equilibria for Methylmercury into apo-MerP	207

Chapter 6:

Scheme 6.3.1.4.	Competing Equilibria for the Chelation of Zinc from MT-3 with DTPA	262
Scheme 6.3.2.2.	Competing Equilibria for the Binding of Cu(I)-GSH to MT-3	269

Chapter 7:

Scheme 7.3.1.1.	Generalized Competing Equilibria First Metal-Binding Event in the Titration of Cu(I)-MeCN into CSP1	310
Scheme 7.3.1.2.	Generalized Competing Equilibria Second Metal-Binding Event in the Titration of Cu(I)-MeCN into CSP1	311
Scheme 7.3.2.1.	Generalized Competing Equilibria First Metal-Binding Event in the Titration of Cu(I)-MeCN into CSP3	319
Scheme 7.3.2.2.	Generalized Competing Equilibria Second Metal-Binding Event in the Titration of Cu(I)-MeCN into CSP3	321
Scheme 7.3.3.1.	Generalized Competing Equilibria First Metal-Binding Event in the Titration of Zinc into CSP1	323
Scheme 7.3.3.2.	Generalized Competing Equilibria Second Metal-Binding Event in the Titration of Zinc into CSP1	328
Scheme 7.3.4.1.	Generalized Competing Equilibria First Metal-Binding Event in the Titration of Zinc into CSP3	333
Scheme 7.3.4.2.	Generalized Competing Equilibria Second Metal-Binding Event in the Titration of Zinc into CSP3	334

Chapter 1:

Cysteines in Metallochemistry and Cellular Homeostasis

1. Introduction

1.1. Metals in Biology

Long before biological life as we know it emerged on earth, chemical reactions were occurring within the ancient oceans. In a groundbreaking paper, Miller (1953) demonstrated the creation of the simple amino acids alanine and glycine under primitive earth-like conditions by combining water (H_2O), methane (CH_4), ammonia (NH), and hydrogen (H_2).[1] Later studies by Parker (2011) expanded on this experiment through the inclusion of hydrogen sulfide and confirmed the presence of all amino acids necessary for the creation of proteins.[2] The early results by Miller sparked a surge in the following decades that describes the creation of biological components that are the precursors for life.[3,4] Of particular interest is the formation of precursor "organisms" that formed on surfaces, deemed surface metabolists, which formed within the anaerobic, reducing environment. Although barely considered an organism, as they are acellular and do not divide; they do grow and evolve.[5] These surfaces that support life are hypothesized to be positively charged with metabolists that are anionically bonded to the surface, forming a layer of organic, autocatalytic metabolites. Growth occurs by spreading across the vacant surface and they evolve toward higher complexity as the thermodynamic equilibria favor synthesis, not degradation. This cationic surface that allowed for the formation of these metabolists is composed of metals, ferrous iron in particular.[5] From this perspective, it can be seen that metals formed the basis of life. And, with time, life emerged, grew, and evolved to incorporate metals into numerous aspects of all living organisms.

Approximately 25-33%, with some estimates approaching 50%, of all proteins, in all forms of life require metals for their function.[6,7] Some metals are essential and are required for proper function of cells such as iron, zinc, copper, manganese, cobalt, and others. Some metals may be essential for other forms of life, but non-essential for humans, including tungsten, cadmium, and vanadium (**Figure 1.1.1**).[8] Lastly, several metals are detrimental to life; binding and displacing native metals, abolishing metalloprotein function, or binding to non-metalloproteins and causing general protein dysfunction. These metals include mercury, aluminum, lead, and arsenic, which have no known biological function.[9–13]

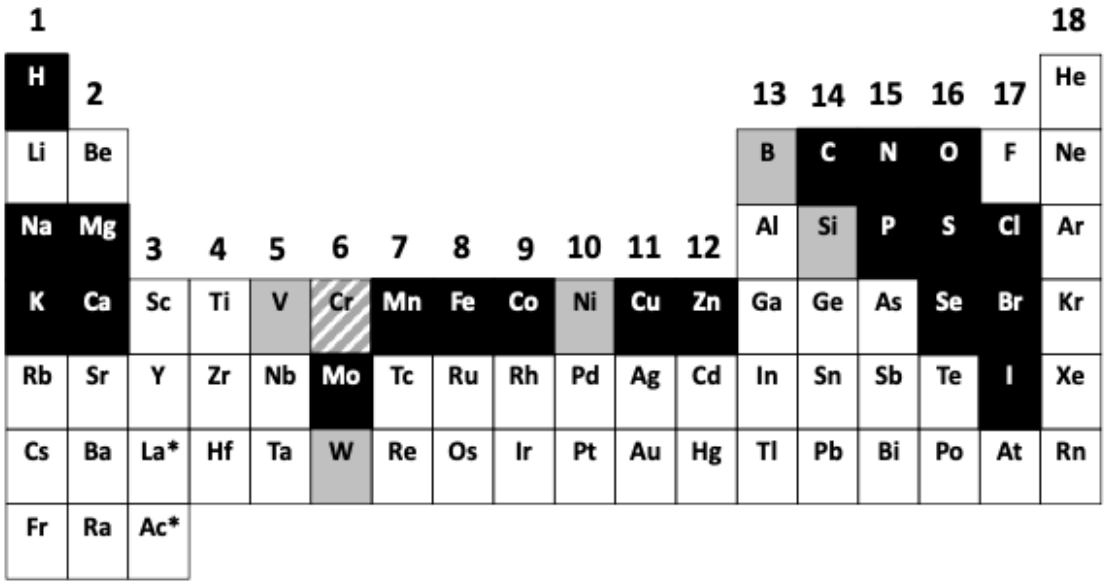

Figure 1.1.1. *Periodic table of elements describing essential, non-essential, and unused metals. F-block elements are not shown. Black boxes represent elements that are essential for life, grey boxes are elements that are essential for some organisms, and white boxes are not generally used in biological systems. Chromium is an exception as both its essentiality and biologically-relevant oxidation state is in question still and is shown with upward diagonals. Adapted from Maret (2015).*[8]

More specifically, metalloproteins are involved in numerous aspects of life including respiration, DNA replication, protein transcription, cellular protection, electron transfer, and oxygen metabolism, to name a few.[14–21] Several of these functions relate to work done within this thesis. The metals themselves also have specific roles. Zinc, for example, can be found to perform a structural role in proteins, such as DNA polymerase, or a catalytic role in enzymes such as glyoxalase, carbonic anhydrase, and carboxypeptidase.[22–25] Iron is often found in both catalytic proteins and in oxygen carrying proteins, such as hemoglobin and myoglobin in humans.[26–29] Both zinc and iron bind to circulating proteins, albumin and transferrin, respectively, allowing for the movement of metals from the digestive tract to cells that require the metals.[30,31] Similar to iron, copper is frequently found in metalloenzymes, such as Cu,Zn-superoxide dismutase and in proteins involved in electron transfer, such as azurin and plastocyanin; all of which contain a single copper ion.[32–36] Other di-copper proteins include the monooxygenase, tyrosinase, the invertebrate oxygen-carrier protein, hemocyanin, and the copper-dependent oxidase, ceruloplasmin. These zinc, iron, and copper proteins just scratch the surface of the sheer number of proteins that bind metals for their cellular processes. While each of these proteins bind different metals, they do have some similarities.

All proteins, in fact, share some similarities, whether they bind metals or not. They are composed of amino acids, linked into polypeptides that may fold into secondary structures in the form of an α-helix or a β-sheet. These secondary structures the can then form hydrogen-bonding networks leading to the formation of tertiary structures, this, in turn, results in a complex 3-dimensional structure composed of β-sheets and α-helices. Frequently, these tertiary structures bind to other tertiary protein structures to form quaternary structures, which may be necessary for biological activity (**Figure 1.1.2**). These tertiary structures can be proteins that are identical, as homo-oligomers, or as different tertiary structures, as hetero-oligomers.

Of particular interest to this thesis, however, are those proteins that bind and interact with metals for which they share some similarities as well. Prominent for metalloproteins

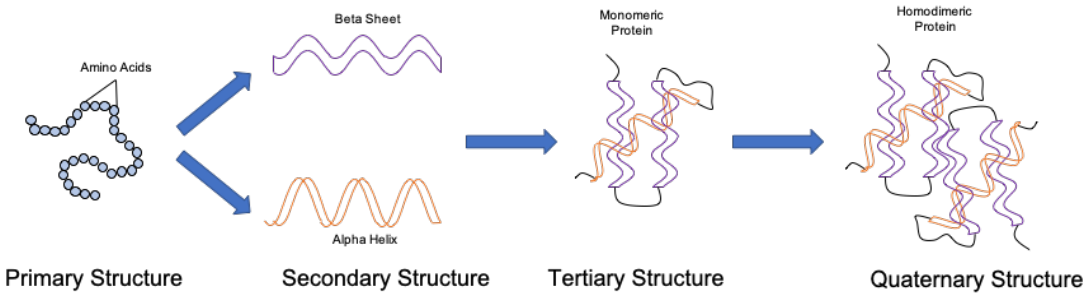

Figure 1.1.2. *Building blocks of a protein. Proteins are composed of connected amino acids that form a peptide. Peptide chains interact and form the secondary structure of the protein in the form of alpha helices or beta sheets. Alpha helices and beta sheets interact to form the tertiary structure of a protein, which is a single, 3-dimensional, monomeric structure. Lastly, tertiary structures are capable of interacting with other proteins with tertiary structure to form quaternary structures in the form of homo- or hetero-multimeric proteins.*

are the amino acids that are involved in metal binding, with the most common of which are histidine, cysteine, glutamic acid, aspartic acid, tyrosine, and methionine. As previously mentioned, metalloproteins bind specific metals for their biological function; this specificity is driven, at least partially, by the amino acids that are present in the metal binding site of the protein. Of particular relevance is hard-soft acid-base (HSAB) theory, which suggests that small, weakly polarizable metals with high oxidation states are hard acids (Fe^{3+}, Al^{3+}, Na^{+}, Co^{3+}, Cr^{3+}, Ti^{4+}, etc.) and large, highly polarizable, low oxidation state metals are soft acids (Hg^{2+}, Cu^{+}, Cd^{2+}, Ag^{+}, Au^{+}, etc.). These hard and soft acids have a most favorable interaction with their complimentary hard or soft base, respectively.[37] As an example, consider a metalloprotein that contains two cysteine residues in the metal-binding site. Because of the soft nature of the sulfur on cysteine, the predicted native metal is likely to be Hg^{2+} or Cu^{+}, depending on the function of the protein. It is unlikely that hard acids like Fe^{3+} would bind to this protein binding site. These physical properties of Lewis acids and Lewis bases lead to intrinsic metal ion specificity and selectivity.

HSAB theory is not the only property of metals that impacts metal specificity in proteins. The Irving William's series, which predicts that for a given metal binding site, the strength of binding is as follows; $Mn^{2+} < Fe^{2+} < Co^{2+} < Ni^{2+} < Cu^{2+} > Zn^{2+}$. Metal binding specificity is also dependent on the binding site geometry and metal coordination. Evidence of metal geometry preferences in the metal ion can be approximately described by the ligand field stabilization energy (LFSE). Consider the LFSE for a 6-coordinate, octahedral geometry (**Equation 1.1.1**), in which:

$$LFSE = \left[\left(\#elections\ in\ t_{2g}\right) * \left(-\frac{2}{5}\Delta_{oct}\right)\right] + \left[\left(\#elections\ in\ e_g\right) * \left(\frac{3}{5}\Delta_{oct}\right)\right] \quad \textbf{Equation 1.1.1}$$

For example, if we consider two transition metals; d^{10} Zn^{2+} and d^{3} V^{2+}. The calculated LFSE is $0\Delta_{oct}$ and $-1.2\Delta_{oct}$, respectively. This suggests that V^{2+} favors an octahedral geometry more than Zn^{2+}. This can further be shown by exploring the LFSE of these same metals in a tetrahedral geometry. The equation for the LFSE of a tetrahedral geometry (**Equation 1.1.2**) is as follows:

$$LFSE = \left[(\#elections\ in\ e) * \left(-\frac{3}{5}\Delta_{td}\right)\right] + \left[(\#elections\ in\ t_2) * \left(\frac{2}{5}\Delta_{td}\right)\right] \qquad \textbf{Equation 1.1.2}$$

The LFSE for Zn^{2+} in a tetrahedral geometry is $0D_{td}$, suggesting that the geometry that is determined by the valence 4S and 4P d-orbitals no longer have a dominant effect in the geometric preference of the metal. The LFSE for tetrahedral V^{2+}, which is likely high spin, is $-0.8D_{td}$. This would suggest that V^{2+} strongly favors the more energetically favorable octahedral geometry over the less energetically favorable tetrahedral geometry. Furthermore, in a similar metal binding site favoring tetrahedral coordination, V^{2+} would be more likely to bind that Zn^{2+}, all other aspects being equal. Similar foundational principles apply to metalloproteins, which modulate the geometry of the metal binding site, thus providing a means to enhance metal binding specificity. Direct evidence of preferred geometries can be seen in both metalloproteins and in small inorganic molecules.[38]

Although both the geometry provided by the protein at the metal binding site and the amino acids that are present in the binding site generally dictate the metal specificity, this is not always true. Consider the metal binding site of transferrin. Transferrin binds a ferric iron in a metal binding site that is composed of two tyrosines, one histidine, and one aspartic acid, along with a anion, like carbonate (**Figure 1.1.3**).[39–41] Although Fe^{3+} is the native metal, this metal binding site also readily binds other metals, like Zn^{2+}, Al^{3+}, Ga^{3+}, Cr^{3+}, actinides, and many other metals.[42–45] This example highlights one aspect of metal specificity, or the lack thereof.

In contrast to the broad metal binding characteristics of transferrin is the metalloregulatory protein, CueR, which is an example of highly specific metal binding. CueR is a Cu^{+}-binding protein within the MerR family of metalloregulatory proteins, and function as a homodimer with two identical Cu^{+} binding sites. Each site binds one Cu^{+} with two cysteine residues in a linear geometry (**Figure 1.1.4**).[46] This binding site, however, should have a high affinity for another metal, Hg^{2+}, which is generally found binding to two cysteines in a linear coordination as well.[47,48] Although, Hg^{2+} is able to bind to the metal-binding site of CueR, it is unable to activate it. This is proposed to be due to the much larger size of Hg^{2+} and its dipositive charge, disrupting the hydrogen bonding network propagating throughout the protein. Though this is describing Hg^{2+}, this also applies to other divalent cations as well, such that only monovalent cations like Cu^{+} are

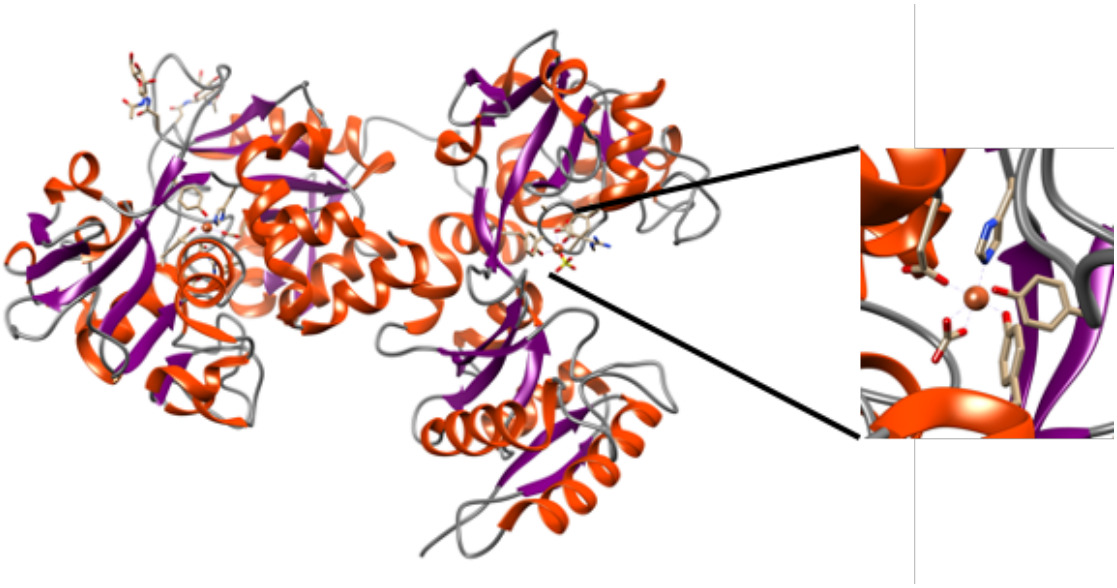

Figure 1.1.3. *The full structure of Fe^{3+}-bound human transferrin, showing both the N– and C–lobes of the protein (left). The metal binding site of a single Fe^{3+} bound to the N-lobe of the protein is shown in the insert. This metal binding site is composed of two tyrosine residues, one histidine, one aspartic acid, and one anion (carbonate in the insert).*[39-41]

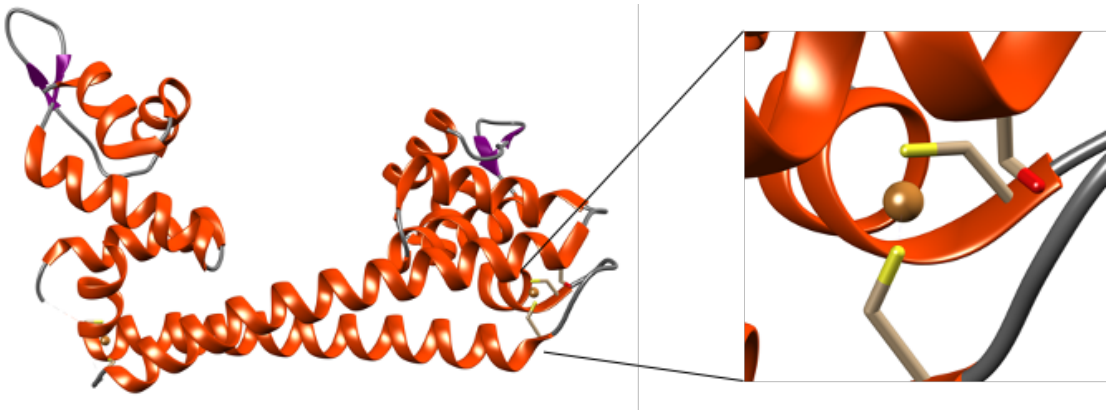

Figure 1.1.4. *CueR, a copper metalloregulatory protein which is a homodimer in solution, has two identical metal binding sites composed of two cysteine residues in each (Left). These two cysteines bind a single* Cu^{+} *in a two-coordinate, linear geometry (Insert).* [46]

able to bind and activate CueR.[49] Less specific to CueR, proteins are also able to enhance the metal binding specificity through modulating the solvation and charge of the binding site, changing the effective dielectric constant and hydrogen bonding interactions that accompany metal binding, as shown with CueR, and stabilizing different charges within the binding site; each of which can alter the specificity of the metal binding site.[50,51] Despite these factors to ensure that each metalloprotein has the required metal, this is not always possible as the mechanisms in place to enhance the overall metal specificity of the protein can be overridden, depending on the metal. This is most evident when considering the mechanism of mercury toxicity. Mercury does not have any one specific protein or cellular target but causes widespread cellular dysregulation. Mercury is able to displace native metals and bind to proteins that utilize cysteines for their function.[52,53] Another possibility for mercury, due to its affinity for thiols, is its binding and depletion of free glutathione as well as reducing the function of superoxide dismutase, glutathione peroxidase, and catalase, all of which are involved in minimizing oxidative stress within the cell.[54]

From an evolutionary perspective, the broad toxicity of mercury provided pressure for both prokaryotes and eukaryotes to develop mechanisms that provide some level of protection from mercury toxicity. For example, in humans, metallothionein-1 and metallothionein-2 biosynthesis is induced by the binding of mercury and directly modulates its excretion.[55] In bacteria, several protein-based mechanisms have also evolved. Of interest herein is the inorganic mercury reduction pathway, or mercury detoxification pathway, which systematically imports inorganic mercury into the cell for its reduction to elemental mercury. This elemental mercury is harmless to the cell and volatilizes out without causing cellular damage.[56,57] These processes that have evolved over time prevent aberrant metals from binding to proteins that are necessary for life.

1.2. Cysteine Chemistry in Metalloproteins

Several amino acids bind metals, each with their own metal-binding properties, as previously described. These residues can modulate the ability for the protein to bind and utilize the metal for their physiological function. Of particular interest to this work are cysteine residues, which are the metal-binding amino acids for each protein system described within this thesis.

Cysteines are an intriguing and unique amino acid due to their chemical reactivity of the thiol group (S–H). These cysteine residues are critically important to many biological functions including disulfide bond formation, redox catalysts, proton donors, and, of course, metal binding.[58–61] Thus, cysteine residues are typically found in oxidases, reductases, disulfide isomerases, peroxidases, phosphatases, and many other proteins involved in metal homeostasis. Although a free cysteine residue in aqueous conditions has a pK_a of approximately 8.6, the range of accessible pK_a's is massive.[62] In Papaya Protease Omega (ppΩ), for example, the pK_a of the cysteine in the active site is 2.88 ± 0.02, whereas in acetyl-coenzyme A binding protein (τ17c), the reactive cysteine has a pK_a of 9.8 ± 1.0.[63–65] This sulfur-proton bond of the cysteine thiol is very weak, allowing for ready access to the reactive thiolate (S^-). These pK_a values of cysteines within proteins is readily modulated by surrounding amino acids. Generally, stabilization of the thiolate or destabilization of the thiol will, lower the pK_a. Likewise, intermolecular interactions that are destabilizing the thiolate, or stabilizing the thiol will raise the pK_a. This thiol, however, is a mediocre hydrogen bond donor, due to the weak S–H bond, but the thiolate is a great hydrogen-bond acceptor, thus hydrogen-bonds will tend to lower the pK_a as well, as this will stabilize the thiol. Stabilization of the thiolate, thus lowering the pK_a of the cysteine, will also occur through electrostatic interactions, where surrounding positive charges will stabilize the thiolate.

Determination of the pK_a values for cysteine residues, although informative, can be challenging. Many spectroscopic methods can be used to follow the formation of the thiol group during a pH titration, or through chemical modification of the thiol, however other techniques are just as viable. Potentiometry, mass spectroscopy (MS), isothermal titration calorimetry (ITC) and numerous computational methods, have all been utilized in the determination of cysteine pK_a values.[59,63,64,66–70] This determination requires good yield and purity of the protein. However, this become more difficult when multiple cysteine residues are present on the protein, and near impossible for proteins with many cysteine residues, like metallothionein or bacterial copper storage proteins. If a few cysteine residues are present, systematic site-directed mutagenesis can be used to determine the pK_a values of each individual cysteine residues.[71] Computationally determining cysteine pK_a values, although simple in nature, is very difficult as well. The reactivity of the cysteine

residues and the ease in which these residues have their pK_a's modified by surrounding residues makes computationally determining the pK_a's challenging. Many different computational techniques have been developed to establish amino acid pK_a values including implicit solvent models (H++) and all-atom molecular dynamics (AMBER, Gromacs, and NAMD) that utilizes thermodynamic integration at different pH values.[63,64,72–78]

In metalloproteins that utilize cysteine within the metal-binding site will typically bind to soft acids, according to HSAB theory. Cysteines are soft bases that have large polarizability, which will favorably interact with soft acids like Cu^{+}, Hg^{2+}, and Cd^{2+}, although other borderline metals, like Zn^{2+} and Cu^{2+} will also bind to metal-binding sites with cysteines.

These metal-cysteine interactions are the crux of this work. Each system that is discussed herein will explore the binding of monovalent and divalent metals to metalloproteins that utilize cysteines within their metal-binding site. The function of these proteins are entirely dependent on these cysteine residues, which modulate metal specificity and selectivity. Quantitatively determining the thermodynamics of these native and non-native metals to metalloproteins aims to establish the foundation of the metal-cysteine interactions, which can be used for rational protein design and modifications for industrial or pharmaceutical purposes.

1.3. Methods in the Study of Metalloproteins

Studying the interaction between native and non-native metal ions with a metalloprotein requires multiple techniques and instruments. Spectroscopic techniques, which include UV-visible absorption, fluorescence, electron paramagnetic resonance (EPR), circular dichroism (CD), and X-Ray absorption spectroscopy (XAS), can provide valuable insight into the metal binding site. Measurements with these instruments can be utilized to characterize the metal coordination and geometry in the metal binding site, as well as the coordinating residues. They can also be used to better understand protein dynamics and the overall secondary structure of the protein. Both kinetics and thermodynamics of ligand or metal binding can also be probed using these techniques. There are important limitations, however. For example, metals with a full d-shell or those

without an unpaired electron are not detectable with EPR or other absorbance spectroscopy, preventing its use for the study of Zn^{2+}, Cu^{+}, and Hg^{2+} binding to metalloproteins.

Other techniques can be used to investigate the coordinating residues, and coordination geometry of the metal binding site, including X-Ray crystallography and Nuclear Magnetic Resonance (NMR) spectroscopy. These techniques are used to determine protein structures and are frequently used on metalloproteins. Similar to spectroscopic techniques, these have certain limitations that may diminish their use with metalloproteins, depending on the questions that are being addressed. Most importantly is the amount of protein necessary for either technique and the accuracy in the characterization of the metal binding site. The X-rays used in X-ray crystallography are capable of destroying Fe-S clusters and changing the oxidation state of metals that are bound. Understandably, this can result in different bond lengths or coordinating residues, thereby making the results less useful. This is also a primarily limitation of XAS, which can readily distort the metal in the metal binding site, even though XAS provides valuable insight into metal coordination. These limitations do not necessarily suggest that other techniques are better, but that multiple techniques should be used in conjunction to ensure the accuracy of the results.

Of particular interest to the study of protein and metal-protein interactions are different computational techniques including bioinformatics and molecular dynamics (MD. Bioinformatics is used to evaluate evolutionary protein function and gain insight into uncharacterized proteins, whereas MD can be used to directly study protein dynamics and the coordination of the metal binding site.

These computational techniques have a direct role in the comparison with experimental data to provide enhanced insight into the experimental technique. Consider a differential scanning calorimetry (DSC) experiment. These experiments are used to determine several thermodynamic parameters associated with the unfolding of a protein, including melting temperature (T_m), enthalpy of unfolding, and heat capacity (ΔC_p). Although this can be of interest, without other experimental data, this thermodynamic information, generally, has limited use. However, using MD, the unfolding pathway of the protein that occurs are high temperatures at which the protein unfolds can be characterized.[79,80] This temperature-based unfolding by MD can then be correlated with

the DSC data or experimental data from other techniques like atomic force microscopy (AFM).[81,82] The enthalpic information associated with the unfolding of a protein by DSC, or other techniques, can then be related to MD to provide molecular mechanisms into the unfolding of the protein.

Lastly, along with determining the coordination, geometry, and coordinating residues of the metal binding site, many of these techniques can establish the thermodynamics of metal binding. Sequential injections of the metal into the protein and observing the spectroscopic change, can be plotted as a function of metal concentration vs. the spectroscopic change and the equilibrium constant can be obtained at a given temperature. Thus the temperature-dependent equilibrium constant can be quantified.This can be further expanded by doing similar experiments at different temperatures and, using a van't Hoff equation (**Equation 1.3.1**).

$$\ln K_{ITC} = \frac{-H^o}{R}\left(\frac{1}{T}\right) + \frac{\Delta S^o}{R} \qquad \textbf{\textit{Equation}}\ \mathbf{1.3.1}.$$

By plotting experimental binding constants with respect to temperature, at constant pressure, the enthalpy and entropy of the metal-protein interaction can be determined. However, **Equation 1.3.1** assumes that there is an insignificant change in the hydrogen bonding network of the protein, thus the heat capacity (ΔC_p). This, however, is not necessarily valid in all proteins.[83] Understandably, this analysis, although effective, is both time and sample consuming.

The gold standard in the determination of these metal-protein interactions, as well as protein-protein, protein-DNA, and ligand-macromolecule interactions in general, is isothermal titration calorimetry (ITC), which is capable of quantifying the entire array of thermodynamics components associated with the ligand-macromolecule interaction (equilibrium constant, stoichiometry, enthalpy, and entropy) in a single experiment.[84] ITC directly quantifies both the enthalpy and equilibrium constant to determine ligand-macromolecule interactions, simplifying data analysis and minimizing both time and samples consumption. The foundational theory, limitations, and applications of ITC will be discussed in detail in the subsequent chapter.

1.4. Thesis Summary and Organization

Within this thesis, several aspects of metal homeostasis will be examined ranging from metal storage and transport to the impact of metals on protein function and regulation of metalloproteins. The thermodynamics of native and non-native metal ions binding to metalloproteins will be quantified using isothermal titration calorimetry (ITC). Thermodynamic characterization of metal binding, obtained by ITC, will be augmented through simulated experiments using computational techniques. This synergy aims to better understand protein dynamics and protein structural changes that occur upon metal binding. An initial discussion of the foundational principals of ITC and computational techniques will be address. Following the discussion on the primary instrumentation that is used throughout the thesis, characterization of the metal-binding properties of each metalloprotein system that is involved in cell homeostasis.

The first of these chapters aim to discuss several proteins involved in the mercury detoxification pathway that is found in the majority of both gram-positive and gram-negative bacteria: the *mer* proteins. The first chapter on the characterization of *mer* proteins will discuss the thermodynamics of Hg^{2+} binding to the mercury metalloregulatory protein, MerR, to establish the thermodynamic foundation of negative allosteric regulation of the metal-protein-DNA interaction. This will involve studying the Mercury-MerR interaction with and without the presence of the DNA, MerO, the *mer* operon, which aims to better understand the thermodynamic implications of inorganic mercury binding and to set the thermodynamic foundation in the regulation of the *mer* pathway. Thermodynamic comparisons allow for the determination of homotropic and heterotropic regulation, and the fundamental thermodynamics components that drive these interactions.

The next chapter will utilize MerP to probe the effect of the protein structure on metal binding by comparing MerP with other proteins, Wnd4 and HAH1; all of which have both the same metal binding site and overall protein architecture, yet their thermodynamics associated with metal-binding are vastly different. The source of these thermodynamic differences between these proteins is largely unknown, so an exploration into protein dynamics and second-sphere interactions that modulate these thermodynamics will be quantitatively determined by ITC. A comparison of these thermodynamics between these protein samples provides an approximation on the proteins scaffold contribution to metal

binding, with the goal of decoupling the metal-binding thermodynamics and the protein contribution.

The subsequent chapter relating to the *mer* proteins involve the physiological role of the periplasmic mercury metallochaperone, MerP, which seems to be involved in protecting the cell from the damaging effects of inorganic mercury, organomercurials, including merbromin and thimerosal, as well as other toxic metals. MerP is proposed to bind and buffer the incoming mercury species that enter the microenvironment of the cell. Furthermore, due to the nature of methylmercury, which has only one open coordination site, this work provides a thermodynamic and structural basis for the atomistic mechanism involved in the binding of methylmercury and inorganic mercury.

The following chapter will then quantitatively determine how metal binding impacts protein structure using the intrinsically disordered protein, metallothionein. In this system the thermodynamics of Zn^{2+} and Cu^{+} binding to metallothionein, the thermodynamics foundation in the physiological function of metallothionein in the brain, and the impact that these metals have on protein structure can be more thoroughly understood. Metal binding in metallothionein seems to have a dramatic impact on stabilizing the overall protein structure, inducing interdomain interactions which modulate the thermodynamic components involved in metal binding. The thermodynamic contributions that arise from these interdomain interactions and overall protein conformational stabilization are quantified.

Finally, the last chapter will aim to quantify the thermodynamics of copper, and other potentially relevant metals like Zn^{2+} and Hg^{2+}, binding to the copper storage proteins, CSP1 and CSP3 from *Methylosinus trichosporium* OB3b. Copper storage proteins are similar to metallothionein, in that they are composed of a large number of cysteine residues that are able to bind a large number of metals simultaneously. However, unlike the conformationally dynamic metallothionein, CSP1 and CSP3 have well-defined secondary and tertiary structures. This will provide a unique thermodynamic comparison in the binding of Cu^{+}, Hg^{2+}, and Zn^{2+} to CSP and metallothionein. Furthermore, this work shows thermodynamic differences that drive the formation of various metal-binding populations. These different populations have significantly different thermodynamic components, which can be quantified. Quantification of these thermodynamics contributions also

provide an understanding into metal selectivity and specificity and provide fundamental new insight into the protein binding and storage mechanism within the cell.

The work in this thesis aims to quantify the thermodynamic foundation that drives a small selection of metalloproteins involved in cellular homeostasis through the control of metals in both bacterial and mammalian metalloproteins. Understanding metal transport, transfer, storage, regulation of protein transcription, and metal-ion utilization from a thermodynamics perspective will provide valuable new knowledge into the function and mechanisms of these proteins in a cellular environment. Quantification of the thermodynamic foundation will be utilized for the future understanding of the role of metals in molecular physiology and can be used to understand the role of environmental factors in metallobiochemistry and biology.

1.5. References

(1) Miller, S. L. A Production of Amino Acids under Possible Primitive Earth Conditions. *Science (80-.).* **1953**, *117* (3046), 528–529. https://doi.org/10.1126/science.117.3046.528.

(2) Parker, E. T.; Cleaves, H. J.; Dworkin, J. P.; Glavin, D. P.; Callahan, M.; Aubrey, A.; Lazcano, A.; Bada, J. L. Primordial Synthesis of Amines and Amino Acids in a 1958 Miller H 2S-Rich Spark Discharge Experiment. *Proc. Natl. Acad. Sci. U. S. A.* **2011**, *108* (14), 5526–5531. https://doi.org/10.1073/pnas.1019191108.

(3) Wachtershauser, G. Evolution of the First Metabolic Cycles. *Proc. Natl. Acad. Sci.* **1990**, *87*, 200–204.

(4) Keller, M. A.; Turchyn, A. V.; Ralser, M. Non-Enzymatic Glycolysis and Pentose Phosphate Pathway-like Reactions in a Plausible Archean Ocean. *Mol. Syst. Biol.* **2014**, *10* (4). https://doi.org/10.1002/msb.20145228.

(5) Wächtershäuser, G. Before Enzymes and Templates: Theory of Surface Metabolism. *Microbiol. Rev.* **1988**, *52* (4), 452–484.

(6) Waldron, K. J.; Robinson, N. J. How Do Bacterial Cells Ensure That Metalloproteins Get the Correct Metal? *Nat. Rev. Microbiol.* **2009**, *7* (1), 25–35. https://doi.org/10.1038/nrmicro2057.

(7) Waldron, K. J.; Rutherford, J. C.; Ford, D.; Robinson, N. J. Metalloproteins and

Metal Sensing. *Nature* **2009**, *460* (7257), 823–830. https://doi.org/10.1038/nature08300.

(8) Maret, W. The Metals in the Biological Periodic System of the Elements: Concepts and Conjectures. *Int. J. Mol. Sci.* **2016**, *17* (1), 1–8. https://doi.org/10.3390/ijms17010066.

(9) Leal, S. S.; Botelho, H. M.; Gomes, C. M. Metal Ions as Modulators of Protein Conformation and Misfolding in Neurodegeneration. *Coordination Chemistry Reviews*. October 2012, pp 2253–2270. https://doi.org/10.1016/j.ccr.2012.04.004.

(10) Diamond, G. L.; Zalups, R. K. Understanding Renal Toxicity of Heavy Metals. *Toxicol. Pathol.* **1998**, *26* (1), 92–103. https://doi.org/10.1177/019262339802600111.

(11) Sterritt, R. M.; Lester, J. N. Interactions of Heavy Metals with Minerals. *Sci. Total Environ.* **1980**, *14*, 5–17.

(12) Roesijadi, G. *Metallothionein and Its Role in Toxic Metal Regulation*; 1996; Vol. 113. https://doi.org/10.1016/0742-8413(95)02077-2.

(13) Zahir, F.; Rizwi, S. J.; Haq, S. K.; Khan, R. H. Low Dose Mercury Toxicity and Human Health. *Environ. Toxicol. Pharmacol.* **2005**, *20* (2), 351–360. https://doi.org/10.1016/j.etap.2005.03.007.

(14) Wernimont, A. K.; Yatsunyk, L. A.; Rosenzweig, A. C. Binding of Copper(I) by the Wilson Disease Protein and Its Copper Chaperone. *J. Biol. Chem.* **2004**, *279* (13), 12269–12276. https://doi.org/10.1074/jbc.M311213200.

(15) Baksh, K. A.; Zamble, D. B. Allosteric Control of Metal-Responsive Transcriptional Regulators in Bacteria. *Journal of Biological Chemistry*. American Society for Biochemistry and Molecular Biology Inc. 2020, pp 1673–1684. https://doi.org/10.1074/jbc.REV119.011444.

(16) Wu, F.; Wu, C. Zinc in DNA Replicaiton and Transcription. *Ann. Rev. Nutr* **1987**, *7*, 251–272.

(17) Theil, E. C. Ferritin: Structure, Gene Regulation, And Cellular Function In Animals, Plants, And Microorganisms. *Annu. Rev. Biochem.* **1987**, *56* (1), 289–315. https://doi.org/10.1146/annurev.biochem.56.1.289.

(18) Summers, A. O. Damage Control: Regulating Defenses against Toxic Metals and

Metalloids. *Curr. Opin. Microbiol.* **2009**, *12* (2), 138–144. https://doi.org/10.1016/j.mib.2009.02.003.

(19) Rizzolo, K.; Cohen, S. E.; Weitz, A. C.; López Muñoz, M. M.; Hendrich, M. P.; Drennan, C. L.; Elliott, S. J. A Widely Distributed Diheme Enzyme from Burkholderia That Displays an Atypically Stable Bis-Fe(IV) State. *Nat. Commun.* **2019**, *10* (1). https://doi.org/10.1038/s41467-019-09020-4.

(20) Geng, J.; Davis, I.; Liu, F.; Liu, A. Bis-Fe(IV): Natures Sniper for Long-Range Oxidation. *J. Biol. Inorg. Chem.* **2014**, *19* (7), 1057–1067. https://doi.org/10.1007/s00775-014-1123-8.

(21) Pitcher, R. S.; Watmough, N. J. The Bacterial Cytochrome Cbb3 Oxidases. *Biochimica et Biophysica Acta - Bioenergetics*. April 12, 2004, pp 388–399. https://doi.org/10.1016/j.bbabio.2003.09.017.

(22) Garcia-Iniguez, L.; Powers, L.; Chance, B.; Sellin, S.; Mannervik, B.; Mildvan, A. S. X-Ray Absorption Studies of the Zn2+ Site of Glyoxalase I. *Biochemistry* **1984**, *23* (4), 685–689. https://doi.org/10.1021/bi00299a016.

(23) Suttisansanee, U.; Honek, J. F. Bacterial Glyoxalase Enzymes. *Seminars in Cell and Developmental Biology*. Elsevier Ltd 2011, pp 285–292. https://doi.org/10.1016/j.semcdb.2011.02.004.

(24) Christianson, D. W.; Lipscomb, W. N. Carboxypeptidase A. *Acc. Chem. Res.* **1989**, *6323* (13), 62–69. https://doi.org/10.1021/ar00158a003.

(25) Keilin, D. Carbonic Anhydrase, Purification Adn Nature of the Enzyme. *Pharmacol. Ther.* **1940**, *74* (1), 1–20.

(26) Champion, P. M.; Debrunner, P.; Gunsalus, I. C.; Lipscomb, J. D.; Münck, E. *Möessbauer Investigations of High-Spin Ferrous Heme Proteins. I. Cytochrome P-450*; 1975; Vol. 14. https://doi.org/10.1021/bi00690a001.

(27) Bak, D. W.; Elliott, S. J. Conserved Hydrogen Bonding Networks of MitoNEET Tune Fe-S Cluster Binding and Structural Stability. *Biochemistry* **2013**, *52* (27), 4687–4696. https://doi.org/10.1021/bi400540m.

(28) He, P.; Moran, G. R. Structural and Mechanistic Comparisons of the Metal-Binding Members of the Vicinal Oxygen Chelate (VOC) Superfamily. *J. Inorg. Biochem.* **2011**, *105* (10), 1259–1272. https://doi.org/10.1016/j.jinorgbio.2011.06.006.

(29) Chen, H.; Ikeda-saito, M.; Shaik, S. Nature of the Fe-O2 Bonding in Oxy-Myglobin: Effect of the Protein. *J. Am. Chem. Soc.* **2008**, *130* (4), 14778–14790. https://doi.org/10.1021/ja805434m.

(30) Chesters, J. K.; Will, M. Zinc Transport Proteins in Plasma. *Br. J. Nutr.* **1981**, *46* (1), 111–118. https://doi.org/10.1079/bjn19810014.

(31) Gkouvatsos, K.; Papanikolaou, G.; Pantopoulos, K. Regulation of Iron Transport and the Role of Transferrin. *Biochimica et Biophysica Acta - General Subjects*. March 2012, pp 188–202. https://doi.org/10.1016/j.bbagen.2011.10.013.

(32) Norris, G. E.; Anderson, B. F.; Baker, E. N. Blue Copper Proteins. The Copper Site in Azurin from Alcaligenes Denitrificans. *J. Am. Chem. Soc.* **1986**, *108* (11), 2784–2785. https://doi.org/10.1021/ja00270a064.

(33) North, M. L.; Wilcox, D. E. Shift from Entropic Cu2+ Binding to Enthalpic Cu+ Binding Determines the Reduction Thermodynamics of Blue Copper Proteins. *J. Am. Chem. Soc.* **2019**, *141* (36), 14329–14339. https://doi.org/10.1021/jacs.9b06836.

(34) Redinbo, M. R.; Yeates, T. O.; Merchant, S. *Plastocyanin: Structural and Functional Analysis*; 1994; Vol. 26. https://doi.org/10.1007/BF00763219.

(35) Gross, E. L. *Plastocyanin: Structure and Function*; KluwerAcademic Publishers, 1993; Vol. 37. https://doi.org/10.1007/BF02187469.

(36) Yim, M.; Chock, B.; Stadtman, E. Enzyme Function of Copper,Zinc Superoxide Dismutase as a Free Radical Generator. *J. Biol. Chem.* **1993**, *268* (6), 4099–4105.

(37) Pearson, R. G. Hard and Soft Acids and Bases. *J. Am. Chem. Soc.* **1963**, *85* (22), 3533–3539. https://doi.org/10.1021/ja00905a001.

(38) Ruíšek, L.; Vondrášek, J. Coordination Geometries of Selected Transition Metal Ions (Co2+, Ni2+, Cu2+, Zn2+, Cd2+, and Hg2+) in Metalloproteins. *J. Inorg. Biochem.* **1998**, *71*, 115–127.

(39) Martin, R. B.; Savory, J.; Brown, S.; Bertholf, R. L.; Wills, M. R. Transferrin Binding Al3+ and Fe3+. *Clin. Chem.* **1987**, *33* (3), 405–407. https://doi.org/10.1093/clinchem/33.3.405.

(40) Yang, N.; Zhang, H.; Wang, M.; Hao, Q.; Sun, H. Iron and Bismuth Bound Human Serum Transferrin Reveals a Partially-Opened Conformation in the N-Lobe. *Sci.*

Rep. **2012**, *2*, 1–7. https://doi.org/10.1038/srep00999.

(41) MacGillivray, R. T. A.; Moore, S. A.; Chen, J.; Anderson, B. F.; Baker, H.; Luo, Y.; Bewley, M.; Smith, C. A.; Murphy, M. E. P.; Wang, Y.; Mason, A. B.; Woodworth, R. C.; Brayer, G. D.; Baker, E. N. *Two High-Resolution Crytal Sructures of the Recombinant N-Lobe of Human Tranferrin Reveal a Structure Change Implicated in Iron Release*; 1998; Vol. 37. https://doi.org/10.1021/bi980355j.

(42) Vincent, J. B.; Love, S. The Binding and Transport of Alternative Metals by Transferrin. *Biochimica et Biophysica Acta - General Subjects*. March 2012, pp 362–378. https://doi.org/10.1016/j.bbagen.2011.07.003.

(43) Harris, W. R. Binding Constants for Neodymium (III) and Samarium (III) with Human Serum Transferrint. *Inorg. Chem.* **1986**, *25*, 2041–2045. https://doi.org/10.1021/ic00232a026.

(44) Terpstra, T.; McNally, J.; Han, T. H. L.; Ha-Duong, N. T.; El-Hage-Chahine, J. M.; Bou-Abdallah, F. Direct Thermodynamic and Kinetic Measurements of Fe2 + and Zn2 + Binding to Human Serum Transferrin. *J. Inorg. Biochem.* **2014**, *136*, 24–32. https://doi.org/10.1016/j.jinorgbio.2014.03.007.

(45) Lin, L. N.; Brandts, J. F.; Mason, A. B.; Woodworth, R. C. Calorimetric Studies of the Binding of Ferric Ions to Human Serum Transferrin. *Biochemistry* **1993**, *32* (36), 9398–9406. https://doi.org/10.1021/bi00087a019.

(46) Changela, A.; Chen, K.; Xue, Y.; Holschen, J.; Outten, C. E.; O'Halloran, T. V.; Mondragón, A. *Molecular Basis of Metal-Ion Selectivity and Zeptomolar Sensitivity by CueR*; 2003; Vol. 301. https://doi.org/10.1126/science.1085950.

(47) Manceau, A.; Lemouchi, C.; Rovezzi, M.; Lanson, M.; Glatzel, P.; Nagy, K. L.; Gautier-Luneau, I.; Joly, Y.; Enescu, M. Structure, Bonding, and Stability of Mercury Complexes with Thiolate and Thioether Ligands from High-Resolution XANES Spectroscopy and First-Principles Calculations. *Inorg. Chem.* **2015**, *54* (24), 11776–11791. https://doi.org/10.1021/acs.inorgchem.5b01932.

(48) Riccardi, D.; Guo, H. B.; Parks, J. M.; Gu, B.; Summers, A. O.; Miller, S. M.; Liang, L.; Smith, J. C. Why Mercury Prefers Soft Ligands. *J. Phys. Chem. Lett.* **2013**, *4* (14), 2317–2322. https://doi.org/10.1021/jz401075b.

(49) Ibáñez, M. M.; Checa, S. K.; Soncini, F. C. A Single Serine Residue Determines

Selectivity to Monovalent Metal Ions in Metalloregulators of the MerR Family. *J. Bacteriol.* **2015**, *197* (9), 1606–1613. https://doi.org/10.1128/JB.02565-14.

(50) Mazmanian, K.; Sargsyan, K.; Lim, C. How the Local Environment of Functional Sites Regulates Protein Function. *Journal of the American Chemical Society*. American Chemical Society June 3, 2020, pp 9861–9871. https://doi.org/10.1021/jacs.0c02430.

(51) Dudev, T.; Lim, C. Metal Binding Affinity and Selectivity in Metalloproteins: Insights from Computational Studies. *Annu. Rev. Biophys.* **2008**, *37* (1), 97–116. https://doi.org/10.1146/annurev.biophys.37.032807.125811.

(52) Lu, W.; Zelazowski, A. J.; Stillman, M. J. Mercury Binding to Metallothioneins: Formation of the Hg18-MT Species. *Inorg. Chem.* **1993**, *32* (6), 919–926. https://doi.org/10.1021/ic00058a028.

(53) Henkel, G.; Krebs, B. Metallothioneins: Zinc, Cadmium, Mercury, and Copper Thiolates and Selenolates Mimicking Protein Active Site Features - Structural Aspects and Biological Implications. *Chem. Rev.* **2004**, *104* (2), 801–824. https://doi.org/10.1021/cr020620d.

(54) Stohs, S. J.; Bagchi, D. Oxidative Mechanisms in the Toxicity of Metal Ions. *Free Radic. Biol. Med.* **1995**, *18* (2), 321–336. https://doi.org/10.1016/0891-5849(94)00159-H.

(55) Cherian, M. G.; Nordberg, M. Cellular Adaptations in Metal Toxicology and Metallothionein. *Toxicology* **1983**, *28*, 1–15.

(56) Summers, A. O. Organization, Expression, and Evolution of Genes for Mercury Resistance. *Annu. Rev. Microbiol.* **1986**, *40*, 607–634. https://doi.org/10.1146/annurev.mi.40.100186.003135.

(57) Barkay, T.; Miller, S. M.; Summers, A. O. Bacterial Mercury Resistance from Atoms to Ecosystems. *FEMS Microbiol. Rev.* **2003**, *27* (2–3), 355–384. https://doi.org/10.1016/S0168-6445(03)00046-9.

(58) Denoncin, K.; Collet, J. F. Disulfide Bond Formation in the Bacterial Periplasm: Major Achievements and Challenges Ahead. *Antioxidants Redox Signal.* **2013**, *19* (1), 63–71. https://doi.org/10.1089/ars.2012.4864.

(59) Dyson, H. J.; Jeng, M. F.; Tennant, L. L.; Slaby, I.; Lindell, M.; Cui, D. S.; Kuprin,

S.; Holmgren, A. *Effects of Buried Charged Groups on Cysteine Thiol Ionization and Reactivity in Escherichia Coli Thioredoxin: Structural and Functional Characterization of Mutants of Asp 26 and Lys 57*; 1997; Vol. 36. https://doi.org/10.1021/bi961801a.

(60) Lillig, C. H.; Berndt, C. Glutaredoxins in Thiol/Disulfide Exchange. *Antioxidants and Redox Signaling*. May 1, 2013, pp 1654–1665. https://doi.org/10.1089/ars.2012.5007.

(61) Barr, I.; Stich, T. A.; Gizzi, A. S.; Grove, T. L.; Bonanno, J. B.; Latham, J. A.; Chung, T.; Wilmot, C. M.; Britt, R. D.; Almo, S. C.; Klinman, J. P. X-Ray and EPR Characterization of the Auxiliary Fe-S Clusters in the Radical SAM Enzyme PqqE. *Biochemistry* **2018**, *57* (8), 1306–1315. https://doi.org/10.1021/acs.biochem.7b01097.

(62) Roos, G.; Foloppe, N.; Messens, J. Understanding the PKa of Redox Cysteines: The Key Role of Hydrogen Bonding. *Antioxid. Redox Signal.* **2013**, *18* (1), 94–127. https://doi.org/10.1089/ars.2012.4521.

(63) Awoonor-Williams, E.; Rowley, C. N. Evaluation of Methods for the Calculation of the PKa of Cysteine Residues in Proteins. *J. Chem. Theory Comput.* **2016**, *12* (9), 4662–4673. https://doi.org/10.1021/acs.jctc.6b00631.

(64) Jensen, K. S.; Pedersen, J. T.; Winther, J. R.; Teilum, K. The PKa Value and Accessibility of Cysteine Residues Are Key Determinants for Protein Substrate Discrimination by Glutaredoxin. *Biochemistry* **2014**, *53* (15), 2533–2540. https://doi.org/10.1021/bi4016633.

(65) Pinitglang, S.; Watts, A. B.; Patel, M.; Reid, J. D.; Noble, M. A.; Gul, S.; Bokth, A.; Naeem, A.; Patel, H.; Thomas, E. W.; Sreedharan, S. K.; Verma, C.; Brocklehurst, K. *A Classical Enzyme Active Center Motif Lacks Catalytic Competence until Modulated Electrostatically*; 1997; Vol. 36. https://doi.org/10.1021/bi9705974.

(66) Nelson, K. J.; Day, A. E.; Zeng, B. B.; King, S. B.; Poole, L. B. Isotope-Coded, Iodoacetamide-Based Reagent to Determine Individual Cysteine PKa Values by Matrix-Assisted Laser Desorption/Ionization Time-of-Flight Mass Spectrometry. *Anal. Biochem.* **2008**, *375* (2), 187–195. https://doi.org/10.1016/j.ab.2007.12.004.

(67) Thurlkill, R. L.; Grimsley, G. R.; Scholtz, J. M.; Pace, C. N. PK Values of the

Ionizable Groups of Proteins. *Protein Sci.* **2006**, *15* (5), 1214–1218. https://doi.org/10.1110/ps.051840806.

(68) Grauschopf, U.; Winther, J. R.; Korber, P.; Zander, T.; Dallinger, P.; Bardwell, J. C. A. Why Is DsbA Such an Oxidizing Disulfide Catalyst? *Cell* **1995**, *83* (6), 947–955. https://doi.org/10.1016/0092-8674(95)90210-4.

(69) Jacobi, A.; Huber-Wunderlich, M.; Hennecke, J.; Glockshuber, R. Elimination of All Charged Residues in the Vicinity of the Active-Site Helix of the Disulfide Oxidoreductase DsbA: Influence of Electrostatic Interactions on Stability and Redox Properties. *J. Biol. Chem.* **1997**, *272* (35), 21692–21699. https://doi.org/10.1074/jbc.272.35.21692.

(70) Tajc, S. G.; Tolbert, B. S.; Basavappa, R.; Miller, B. L. Direct Determination of Thiol PKa by Isothermal Titration Microcalorimetry. *J. Am. Chem. Soc.* **2004**, *126* (34), 10508–10509. https://doi.org/10.1021/ja047929u.

(71) Powlowski, J.; Sahlman, L. Reactivity of the Two Essential Cysteine Residues of the Periplasmic Mercuric Ion-Binding Protein, MerP. *J. Biol. Chem.* **1999**, *274* (47), 33320–33326. https://doi.org/10.1074/jbc.274.47.33320.

(72) Phillips, J. C.; Braun, R.; Wang, W.; Gumbart, J.; Tajkhorshid, E.; Villa, E.; Chipot, C.; Skeel, R. D.; Kalé, L.; Schulten, K. Scalable Molecular Dynamics with NAMD. *Journal of Computational Chemistry*. John Wiley and Sons Inc. 2005, pp 1781–1802. https://doi.org/10.1002/jcc.20289.

(73) Van Der Spoel, D.; Lindahl, E.; Hess, B.; Groenhof, G.; Mark, A. E.; Berendsen, H. J. C. GROMACS: Fast, Flexible, and Free. *J. Comput. Chem.* **2005**, *26* (16), 1701–1718. https://doi.org/10.1002/jcc.20291.

(74) Weiner, P. W.; Kollman, P. A. AMBER: Assisted Model Building with Energy Refinement . *J. Comput. Chem.* **1981**, *2*, 287–303.

(75) Alexov, E.; Mehler, E. L.; Baker, N.; M. Baptista, A.; Huang, Y.; Milletti, F.; Erik Nielsen, J.; Farrell, D.; Carstensen, T.; Olsson, M. H. M.; Shen, J. K.; Warwicker, J.; Williams, S.; Word, J. M. Progress in the Prediction of PK a Values in Proteins. *Proteins Struct. Funct. Bioinforma.* **2011**, *79* (12), 3260–3275. https://doi.org/10.1002/prot.23189.

(76) Mongan, J.; Case, D. A.; McCammon, J. A. Constant PH Molecular Dynamics in

Generalized Born Implicit Solvent. *J. Comput. Chem.* **2004**, *25* (16), 2038–2048. https://doi.org/10.1002/jcc.20139.

(77) Lee, J.; Miller, B. T.; Brooks, B. R. Computational Scheme for PH-Dependent Binding Free Energy Calculation with Explicit Solvent. *Protein Sci.* **2016**, *25* (1), 231–243. https://doi.org/10.1002/pro.2755.

(78) Jensen, J. H.; Li, H.; Robertson, A. D.; Molina, P. A. Prediction and Rationalization of Protein PK a Values Using QM and QM/MM Methods. *J. Phys. Chem. A* **2005**, *109* (30), 6634–6643. https://doi.org/10.1021/jp051922x.

(79) Yadav, A.; Paul, S.; Venkatramani, R.; Ainavarapu, S. R. K. Differences in the Mechanical Unfolding Pathways of Apo- and Copper-Bound Azurins. *Sci. Rep.* **2018**, *8* (1), 1–13. https://doi.org/10.1038/s41598-018-19755-7.

(80) Kundu, S.; Roy, D. Temperature-Induced Unfolding Pathway of a Type III Antifreeze Protein: Insight from Molecular Dynamics Simulation. *J. Mol. Graph. Model.* **2008**, *27* (1), 88–94. https://doi.org/10.1016/j.jmgm.2008.03.002.

(81) Schönfelder, J.; Perez-Jimenez, R.; Muñoz, V. A Simple Two-State Protein Unfolds Mechanically via Multiple Heterogeneous Pathways at Single-Molecule Resolution. *Nat. Commun.* **2016**, *7*. https://doi.org/10.1038/ncomms11777.

(82) Ho, B. K.; Agard, D. A. An Improved Strategy for Generating Forces in Steered Molecular Dynamics: The Mechanical Unfolding of Titin, E2lip3 and Ubiquitin. *PLoS One* **2010**, *5* (9). https://doi.org/10.1371/journal.pone.0013068.

(83) Grossoehme, N. E.; Spuches, A. M.; Wilcox, D. E. Application of Isothermal Titration Calorimetry in Bioinorganic Chemistry. *J. Biol. Inorg. Chem.* **2010**, *15* (8), 1183–1191. https://doi.org/10.1007/s00775-010-0693-3.

(84) Freire, E.; Mayorga, O. L.; Straume, M. Isothermal Titration. *Anal. Chem.* **1990**, *62* (18), 950A-959A. https://doi.org/10.1021/ac00217a002.

Chapter 2:

Metal Binding Thermodynamics and Protein Dynamics: Quantification and Characterization by Isothermal Titration Calorimetry and Molecular Dynamics.

2.1. A Brief History of Calorimetry

The art of calorimetry dates back to the 18th century under the work of the field's founding father, Joseph Black. Recognizing that the addition of heat to ice does not increase the temperature of the ice/water mixture yet increases the amount of water in the solution, he set the foundation for the concept of latent heat and the distinction between heat and temperature.[1] This discovery marked the beginning of thermodynamics as we know it today. Building on Black's work on latent heat, Antione Lavoisier and Pierre Laplace built the first indirect calorimeter to determine the heat associate with chemical changes.[2] These experiments set in motion the field of thermodynamics and thermochemistry as a whole. By the early 1800's, Sadi Carnot established the first thermodynamic principle, which would later be defined as entropy by Rudolf Clausius, and Lord Kelvin, developed the second law of thermodynamics.[3,4] By the end of the 19th Century, Josiah Willard Gibbs furthered the field of thermodynamics with the introduction of internal energy in terms of entropy, chemical potential and, alongside James Clerk Maxwell and Ludwig Boltzmann, founded the field of statistical mechanics.[5]

Our understanding of thermodynamics, which expanded over the 18th, 19th, and 20th century, ultimately led to the development of the isothermal titration calorimeter (ITC). Today's ITC is capable of measuring small heat changes associated with the interactions of two species.[6] These interactions include protein-protein, ligand-protein, micellization/demicellization, and, most importantly to this work, metal-protein interactions strong binding affinities ($\log K > 10$)[11], weak binding affinities ($\log K < 3$)[12], and protonation changes upon ligand binding[13–15]. The applications of ITC has grown significantly in the last two decades, resulting in its use in pK_a calculations of cysteines[7], exploring ligand-binding cooperativity[8,9], solvent reorganization contribution to binding[10], membrane protein ligand binding[16–18], metal-ion binding[19–23], enzyme kinetics[24], solvent surface tension[25], and many other applications.

2.2. The Theoretical Foundation of Isothermal Titration Calorimetry

2.2.1. Theory, Application, and Limitations of ITC

The underlying engineering of any isothermal titration calorimeter as a power-compensation device is effectively the same for instruments by the two manufacturers, Malvern Panalytical and TA Instruments. The ITC must maintain both an adiabatic and isothermal environment, as only the heat from two interacting species should be measured. As such, two ITC cells (sample and reference cell) are set deep inside a calorimeter, isolated from the atmosphere, and are connected by a temperature controller and a heater. During the course of a reaction, any heat exchanged in the sample cell is compared to the heat in the reference cell. Matching the heat generated or consumed quantifies the heat of the two species interaction. The power that is applied to the control heater to maintain constant temperature in the sample cell is recorded over time through the entire experiment. During the fitting process the area under each peak, from the baseline, is converted from the power compensation units, μcalorie/second, to the units, kilocalorie/injection or kilojoule/injection (mole titrant). A schematic of a simple, single binding site ITC experiment of Hg^{2+} into EDTA, and its interpretation, is shown in **Figure 2.2.1.1**.

Most intriguingly, in theory, all of the key thermodynamic properties of an interaction can be quantified in a single titration. That includes the how many ligands bind to the macromolecule (stoichiometry, n), the apparent binding affinity or equilibrium constant (K_{ITC}), the apparent binding enthalpy (ΔH_{ITC}), and, from these, the apparent binding entropy (ΔS_{ITC}), and the apparent Gibbs free energy (ΔG_{ITC}). The difference between the heats of the initial injections and the final injections defines ΔH_{ITC}, the slope of the titration curve defines K_{ITC}, and the molar ratio at the maximum slope defines the stoichiometry, n. The other parameters, ΔG_{ITC} and ΔS_{ITC}, can then be solved from these direct observations. It is important to note the use of the word “apparent” for the binding thermodynamics. Due to the non-specific nature of ITC, any interactions that contribute heat upon an injection will contribute to the observed signal, not just the desired ligand-macromolecule interaction. This includes, but is not limited to, protein (de)-protonation, ligand-buffer interaction, buffer (de)-protonation, and chelator (de)-protonation. An example of the competing and coupled equilibria in a simple ITC experiment involving Hg^{2+} titrated into EDTA is shown in **Scheme 2.2.1.1.**

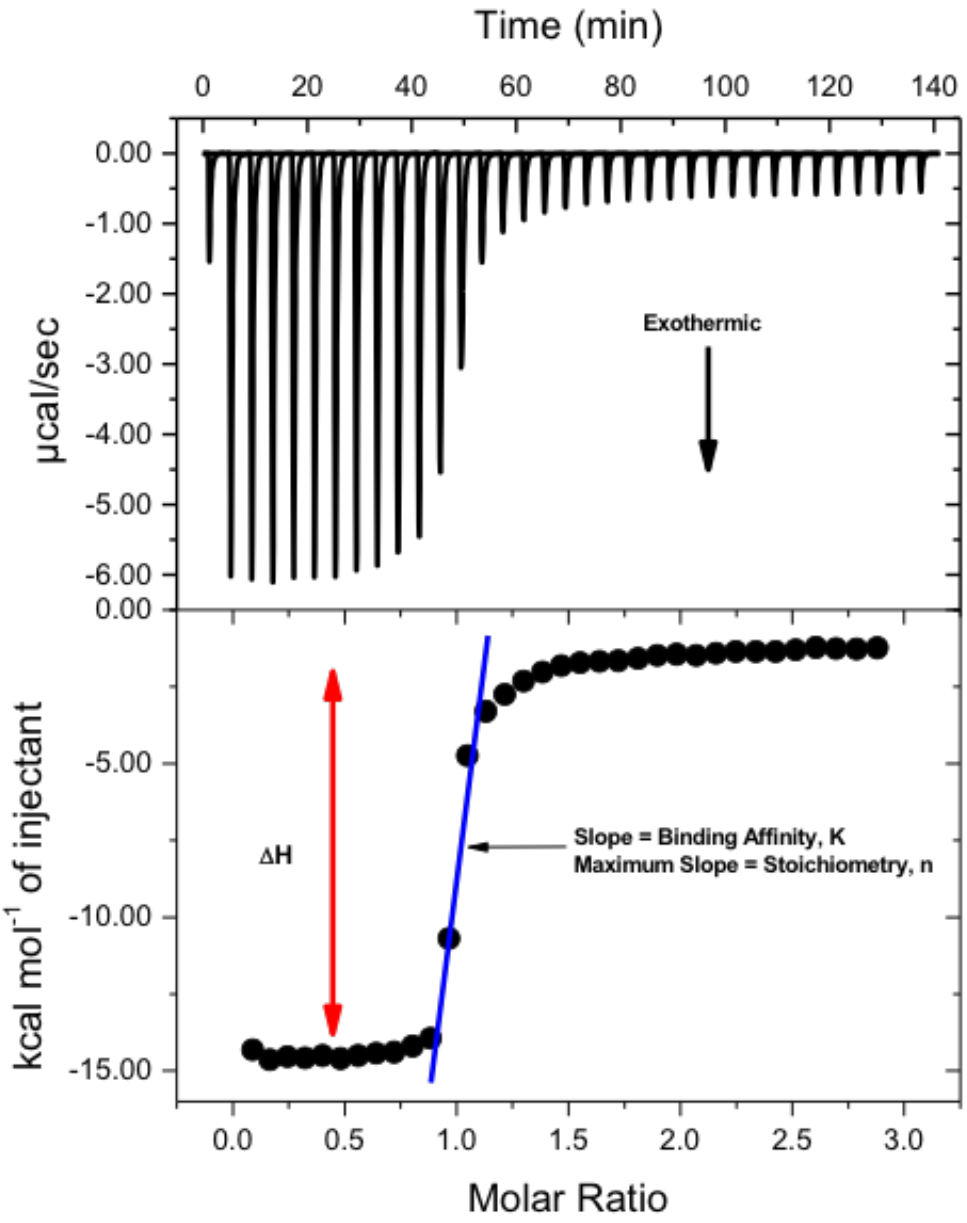

Figure 2.2.1.1. A typical example of a simple, single-site, direct metal binding experiment. (top panel) Downward peaks on the Microcal VP-ITC indicate an exothermic reaction and upward peaks as an endothermic reaction. (bottom panel) The difference between the initial heats and the final heats define the experimental enthalpy of the binding event, ΔH_{ITC} (red double arrow). Stoichiometries and binding affinities are found at the inflection point in which the slope of the inflection (blue line) is the binding affinity, K_{ITC}, and the point of maximum slope is the stoichiometry, n. From these experimental values, all other apparent thermodynamic parameters (ΔS_{ITC} and ΔG_{ITC}) can be calculated. The top panel represents the raw heats of injection with respect to time, whereas the bottom panel represents the integrated area under each peak with respect to the molar ratio of ligand-to-macromolecule.

Scheme 2.2.1.1. Competing equilibria in a simple ITC experiment of Hg^{2+} in buffer titrated into EDTA in buffer at approximately pH 7.4.

Hg–Buffer	$\rightleftharpoons$	Hg^{2+} + Buffer	$-\Delta H^o_{MB}$
Buffer + nH^+	$\rightleftharpoons$	Buffer–H	$n_{H^+}\Delta H^o_{BH}$
EDTA–H	$\rightleftharpoons$	EDTA + nH^+	$-n_{H^+}\Delta H^o_{LH}$
EDTA + Hg^{2+}	$\rightleftharpoons$	EDTA–Hg	ΔH^o_{ML}

Hess's Law: $\boldsymbol{\Delta H^o_{ITC} = n_{H^+}\Delta H^o_{BH} + \Delta H^o_{ML} - \Delta H^o_{MB} - n_{H^+}\Delta H^o_{LH}}$

Although the information gained from ITC measurement is valuable, there are physical limits on the data that can be collected. Ligand binding experiments that have very low heat of interaction are difficult or impossible to explore. Because the generation of an isotherm requires heat that evolves (exothermic) or absorbed (endothermic), binding without apparent heat cannot be observed. Increasing the concentration of both the ligand and macromolecule may overcome this, however it is generally impractical as proteins are difficult to obtain at very high concentrations and may aggregate or precipitate. Changes in buffers with differing buffer-protonation enthalpies can also aid in the determination. Further limitations on ITC revolve around the binding affinity as well, where log K < 3 and log K > 8 cannot be measured by a simple, one-site binding experiment. To delineate and accurate binding affinity, the c-value was established. This arbitrary and unitless value is defined as:

$$c = [cell]\ x\ K_{ITC}\ x\ n \qquad \textbf{Equation 2.2.1.1}$$

Where [cell] is the concentration of the macromolecule in the sample cell of the ITC, K_{ITC} is the apparent binding affinity of the ligand-macromolecule interaction, and n is the stoichiometry of the interaction. As a general guideline in simple, one-site, direct binding experiments, 5 < c < 1000 will provide binding data that is accurate. The c values that are > 1000 are only capable of defining the enthalpy of the interaction and c-Window values < 5 are difficult to accurately fit without additional chemical information such as stoichiometry or enthalpy of the interaction. Like the enthalpy of the interaction, the apparent binding affinity can be modulated through changes in the experimental design and the inclusion of competing or chelating ligands.

2.3. The Ligand–Macromolecule Interaction

2.3.1. Experimental and Calculated Binding Enthalpy

As previously mentioned, the heat evolved from each injection of an ITC experiment is a cumulation of the heat of all bonds that are made and broken within the cell, which is shown by the illustration of the competing equilibria in **Scheme 2.2.1.1**. Fortunately, assuming these interactions are in equilibrium and are reversible, Hess's law is applicable. This suggests, then, that as the enthalpies of all competing equilibria are

known, with the exception of the ligand-macromolecule interaction, the enthalpy associated with the desired interaction can be solved through a *post-hoc* analysis. The cumulative ΔH_{ITC}, as shown in **Scheme 2.2.1.1,** can be rearranged to solve for the buffer-independent, pH-dependent ΔH_{ML} interactions such that:

$$\Delta H^o_{ITC} = n_{H^+}\Delta H^o_{BH} + \Delta H^o_{ML} - \Delta H^o_{MB} - n_{H^+}\Delta H^o_{LH} \qquad \textbf{Equation 2.3.1.1}$$

where n_{H^+} is the number of protons, ΔH^o_{ITC} is the experimental enthalpy, ΔH^o_{BH} is the enthalpy associated with buffer protonation, ΔH^o_{MB} is the enthalpy associated with the metal-buffer interaction, ΔH^o_{LH} is the enthalpy associated with ligand protonation, and ΔH^o_{ML} is the desired enthalpy associated with the ligand-metal interaction. Because all enthalpies, except ΔH^o_{ML}, are known or can be readily quantified, the enthalpy of the desired metal-ligand interaction can be calculated by,

$$\Delta H^o_{ML} = \Delta H^o_{ITC} + \Delta H^o_{MB} + n_{H^+}\Delta H^o_{LH} - n_{H^+}\Delta H^o_{BH} \qquad \textbf{Equation 2.3.1.2}$$

It is an important distinction that the notation used above, ΔH^o, is considered to be the standard state enthalpy in which the solutes are at 1 M concentration. However, due to the nature of ITC, this is not the case for the vast majority of experiments. Historically, though, this is the notation that is used for thermodynamics found by ITC, as opposed to ΔH at non-standard state conditions. In any event, throughout this work, I will assume that $\Delta H^o \cong \Delta H$ and all other thermodynamic parameters will be denoted similarly.

Furthermore, ITC titrations at the same pH in buffers with different protonation enthalpies, allow the calculation of the displacement or uptake of protons upon the ligand binding to the macromolecule. This can be seen by rearranging **Equation 2.3.1.2** into a $y = mx + b$ format:

$$\Delta H^o_{ITC} + \Delta H^o_{MB} = n_{H^+}\Delta H^o_{BH} + (n_{H^+}\Delta H^o_{LH} - \Delta H^o_{ML}) \qquad \textbf{Equation 2.3.1.3}$$

which can be plotted as y-axis = $\Delta H^o_{ITC} + \Delta H^o_{MB}$, x-axis = ΔH^o_{BH}, y-intercept = $(n_{H^+}\Delta H^o_{LH} - \Delta H^o_{ML})$, and the slope, m = n_{H^+}. This slope quantifies the number of protons that bind to,

or are released from, the buffer upon ligand binding such that a positive slope indicates that there are protons leaving the ligand and/or macromolecule and binding to the buffer, and a negative slope indicates that the binding of a ligand to a macromolecule result in protons leaving the buffer to bind to the macromolecule.

2.3.2. Post-hoc Analysis to Establish Ligand-Macromolecule Binding Affinity

The binding affinity that is found experimentally by ITC is the apparent binding affinity that includes the binding and competition of all interacting species. These binding events must be understood in order to calculate the equilibrium constant of the ligand-macromolecule interaction. There are three distinct ITC experiments that are done, each with a different *post-hoc* analysis of the data: (1) direct metal titration (i.e. Hg^{2+} into EDTA), (2) competition experiments (i.e. Hg-EDTA into a protein), and (3) chelation experiments (i.e. EDTA into Hg-protein). The *post-hoc* analysis for each will be discussed in sequence.

The competing equilibria for the direct binding experiment of Hg^{2+} titrated into EDTA in buffer can be found in **Scheme 2.2.1.1**. The *post-hoc* analysis to calculate the affinity of EDTA, (L), for Hg^{2+}, (M), assuming as well that EDTA will be protonated by 1.04 protons (H_1 and H_2) at pH 7.4, begins by defining the total concentration of the metal and metal complexes and the total concentration of the macromolecule such that:

$$C_M = [M] + [MB] + [ML] \qquad \textbf{Equation 2.3.2.1}$$

$$C_L = [L] + [LH^+] + \left[LH_2{}^{2+}\right] + [ML] \qquad \textbf{Equation 2.3.2.2}$$

where C_M is the total concentration of the metal and metal complexes in solution, [M] is the concentration of the free Hg^{2+}, [MB] is the concentration of the Hg-buffer complex, and [ML] is the concentration of the Hg-EDTA complex in **Equation 2.3.2.1**. Similarly, in **Equation 2.3.2.2**, C_L is the total concentration of EDTA and EDTA species in solution, [L] is the concentration of the free EDTA, $[LH^+]$ is the concentration of EDTA protonated with its first protonation event, $[LH_2{}^+]$ is the concentration of EDTA protonated with its

second protonation event, and [ML] is the concentration of the Hg-EDTA complex. These equations allow us to pull out equilibrium constants for each of the binding events:

$$K_{MB} = \frac{[MB]}{[M][B]} \qquad \textbf{Equation 2.3.2.3}$$

$$K_{ML} = \frac{[ML]}{[M][L]} \qquad \textbf{Equation 2.3.2.4}$$

$$K_{LH^+} = \frac{[LH^+]}{[L][H^+]} = K_{a1} \qquad \textbf{Equation 2.3.2.5}$$

$$K_{LH_2^{2+}} = \frac{[LH_2^{2+}]}{[LH^+][H^+]} = K_{a2} \qquad \textbf{Equation 2.3.2.6}$$

With these equations in mind, let:

$$\beta_2 = (K_{LH^+})\,(K_{LH_2^{2+}}) = \frac{[LH_2^{2+}]}{[LH^+][H^+]^2} = (K_{a1})(K_{a2}) \qquad \textbf{Equation 2.3.2.7}$$

Now that the equilibrium constants for the various binding events have been defined, we can show how to determine the equilibrium constant of interest found by ITC in which:

$$K_{ITC} = \frac{[ML]}{[M]_{ITC}[L]_{ITC}} \qquad \textbf{Equation 2.3.2.8}$$

where K_{ITC} is the equilibrium constant found experimentally by ITC, [ML] is the concentration of the Hg^{2+}-EDTA complex, $[M]_{ITC}$ and $[L]_{ITC}$ are the concentrations of Hg^{2+} and EDTA not involved in the ML complex. Thus:

$$[M]_{ITC} = C_M - [ML] = [M] + [MB] \qquad \textbf{Equation 2.3.2.9}$$

$$[L]_{ITC} = C_L - [ML] = [L] + [LH^+] + \left[LH_2{}^{2+}\right] \qquad \textbf{Equation 2.3.2.10}$$

Rearranging and substituting the equilibrium constants within these equations gives:

$$[M]_{ITC} = [M] + [MB] = [M] + (1 + K_{MB}[B]) = [M]\alpha_{buffer} \quad \textbf{Equation 2.3.2.11}$$

$$[L]_{ITC} = [L] + [LH^+] + \left[LH_2{}^{2+}\right] = [L] + (1 + K_{LH^+}[H^+] + \beta_2[H^+]^2) = [L]\alpha_{proton} \quad \textbf{Equation 2.3.2.12}$$

Where $\alpha_{buffer} = (1 + K_{MB}[B])$ and $\alpha_{proton} = (1 + K_{LH^+}[H^+] + \beta_2[H^+]^2)$. Substituting **Equations 2.3.2.11** and **2.3.1.12** into **Equation 2.3.2.8** provides us with the general experimental equilibrium constant where:

$$K_{ITC} = \frac{[ML]}{[M][L]} x \frac{1}{\alpha_{proton}\alpha_{buffer}} = \frac{K_{ML}}{\alpha_{proton}\alpha_{buffer}} \quad \textbf{Equation 2.3.2.13}$$

Thus, the binding affinity of the ML complex is:

$$K_{ML} = K_{ITC}\ x\ \alpha_{proton}\ x\ \alpha_{buffer} \quad \textbf{Equation 2.3.2.14}$$

or, substituting in the equations for α_{proton} and α_{buffer}:

$$K_{ML} = K_{ITC}\ x\ (1 + K_{LH^+}[H^+] + \beta_2[H^+]^2)\ x\ (1 + K_{MB}[B]) \quad \textbf{Equation 2.3.2.15}$$

These equations, though based on the direct titration of Hg^{2+} into EDTA, can be modified for other macromolecules that have a different number of protons in the competing equilibrium and different metal-binding thermodynamic properties. However, this technique is limited to the narrow range of thermodynamic parameters that are directly accessible by ITC. Although Hg^{2+} into EDTA is a good example, the known binding affinity of EDTA for Hg^{2+} is far greater than what can be directly measured by ITC (log K ~21). Thus, other experiment design types must be applied.

The second type of ITC experiments involves the titration of a metal-bound chelator into the protein of interest. As discussed previously, one of the primary limitations of a direct titration ITC experiment is that the affinity of the macromolecule for the ligand must be 10^3 to 10^8. To measure larger binding affinities, competition experiments can be done

to bring the c-Window value within the range of that is accurate by ITC. An example of the competing equilibria associated with the titration of Hg-EDTA into a protein is found in **Scheme 2.3.2.1**. Similar to the simple direct metal-binding experiments, ΔH_{ITC} is the cumulative enthalpy of all competing equilibria such that

$$\Delta H^o_{ITC} = n_{H^+}\Delta H^o_{LH} + \Delta H^o_{MP} - \Delta H^o_{ML} - n_{H^+}\Delta H^o_{BH} - n_{H^+}\Delta H^o_{PH} \quad \textbf{Equation 2.3.2.16}$$

where ΔH^o_{ITC} is the experimental enthalpy found by ITC, $n_{H^+}$is the number of protons, ΔH^o_{LH} is the enthalpy of the protonation of EDTA, ΔH^o_{MP} is the enthalpy associated with the binding of Hg^{2+} to the protein, ΔH^o_{ML} is the enthalpy associated with the Hg^{2+}-EDTA interaction, ΔH^o_{BH} is the enthalpy of the buffer protonation, and ΔH^o_{PH} is the enthalpy associated with the protonation of the protein.

Again, rearrangement of this general equation allows us to calculate the enthalpy associated with the metal-protein interaction, where:

$$(\Delta H^o_{MP} - n_{H^+}\Delta H^o_{PH}) = \Delta H^o_{ITC} - n_{H^+}\Delta H^o_{LH} + \Delta H^o_{ML} + n_{H^+}\Delta H^o_{BH} \quad \textbf{Equation 2.3.2.17}$$

However, it is important to note that the enthalpy associated with the protonation of the protein is not generally known. As **Equation 2.3.2.17** suggests, the enthalpy of the metal-protein interaction is both the metal binding enthalpy as well as the protein protonation/deprotonation enthalpy, thus is pH-dependent. Furthermore, the change in the number of protons associated with EDTA, $n_{H^+}\Delta H^o_{LH}$, is known from the experimental pK_a values and the number of protons associated with the buffer, $n_{H^+}\Delta H^o_{BH}$, is found through the aforementioned proton plot.

The *post-hoc* analysis of a chelation experiment is similar to that of the direct metal titration. One important distinction, which can also be seen in the competing equilibria, is that the metal does not interact with the buffer and, as such, the metal–buffer interaction does not compete with the metal-protein or metal-ligand enthalpy or binding affinity in the *post-hoc* analysis. Nonetheless, this results in a slightly modified version of **Equation 2.3.2.15**, which reflects the lack of metal-buffer interaction:

Scheme 2.3.2.1 Competing equilibria in a competition ITC experiment of Hg-bound EDTA titrated into a protein in buffer at approximately pH 7.4.

Hg–EDTA	$\rightleftharpoons$	Hg^{2+} + EDTA	$-\Delta H^o_{ML}$
Buffer–H	$\rightleftharpoons$	Buffer + H^+	$-n_{H^+}\Delta H^o_{BH}$
EDTA + nH^+	$\rightleftharpoons$	EDTA–H	$n_{H^+}\Delta H^o_{LH}$
Protein–H	$\rightleftharpoons$	Protein + H^+	$-n_{H^+}\Delta H^o_{PH}$
Protein + Hg^{2+}	$\rightleftharpoons$	Protein–Hg	ΔH^o_{MP}
Hess's Law: $\boldsymbol{\Delta H^o_{ITC}} = n_{H^+}\Delta H^o_{LH} + \Delta H^o_{MP} - \Delta H^o_{ML} - n_{H^+}\Delta H^o_{BH} - n_{H^+}\Delta H^o_{PH}$			

$$K_{MP} = K_{ITC}\, x \left(1 + K_{ML}\, x\, \frac{[B]}{\alpha_{proton,L}}\right) \qquad \textbf{Equation 2.3.2.18}$$

where [B] is the concentration of the buffer, $\alpha_{proton,L}$ is the protonation of the chelator as seen in **Equation 2.3.2.12**, K_{ML} is the binding affinity of the metal to the chelator, K_{ITC} is the apparent, experimental binding affinity, and K_{MP} is the desired metal-protein binding affinity. Similar to the direct metal binding analysis, the equations involved in this *post-hoc* analysis are modified for the specific system in question, as it depends on the chelator protonation and the number of metals the chelator binds.

The third type of ITC experiment is the chelation experiment, in which a strong metal chelator is titrated into the protein-metal complex. The analysis here is based on the concept of microscopic reversibility, in which the binding in the forward direction is equal and opposite to the reverse direction. A caveat to this concept, however, is that metal titrated into a chelator and chelator titrated into a metal have the same equilibria competing overall, but the formation of the complex can be different. Consider a typical ITC experiment in which Hg^{2+} is titrated into EDTA at pH 7.4. In this experiment Hg^{2+} will bind to the strong binding site of EDTA resulting in a simple one-site binding event, as seen in **Figure 2.2.1.1**. Consider then the reverse titration, where EDTA is titrated into Hg^{2+}, and initially Hg^{2+} is in excess in the cell. EDTA will be saturated with Hg^{2+}, such that all possible binding sites will be occupied, as Hg^{2+} is in large excess, which is then followed by the well-defined and stable complex formation (**Figure 2.3.2.1**). This results in distinct differences between isotherms associated with the Hg^{2+} titration into EDTA and EDTA titrated into Hg^{2+}.

The *post-hoc* analysis for the chelation of a metal, Hg^{2+}, from a protein with a stronger chelator, EDTA, begins with the overall apparent binding affinity where:

$$K_{ITC} = \frac{[ML]}{[M]_{ITC}[L]_{ITC}} \qquad \textbf{Equation 2.3.2.19}$$

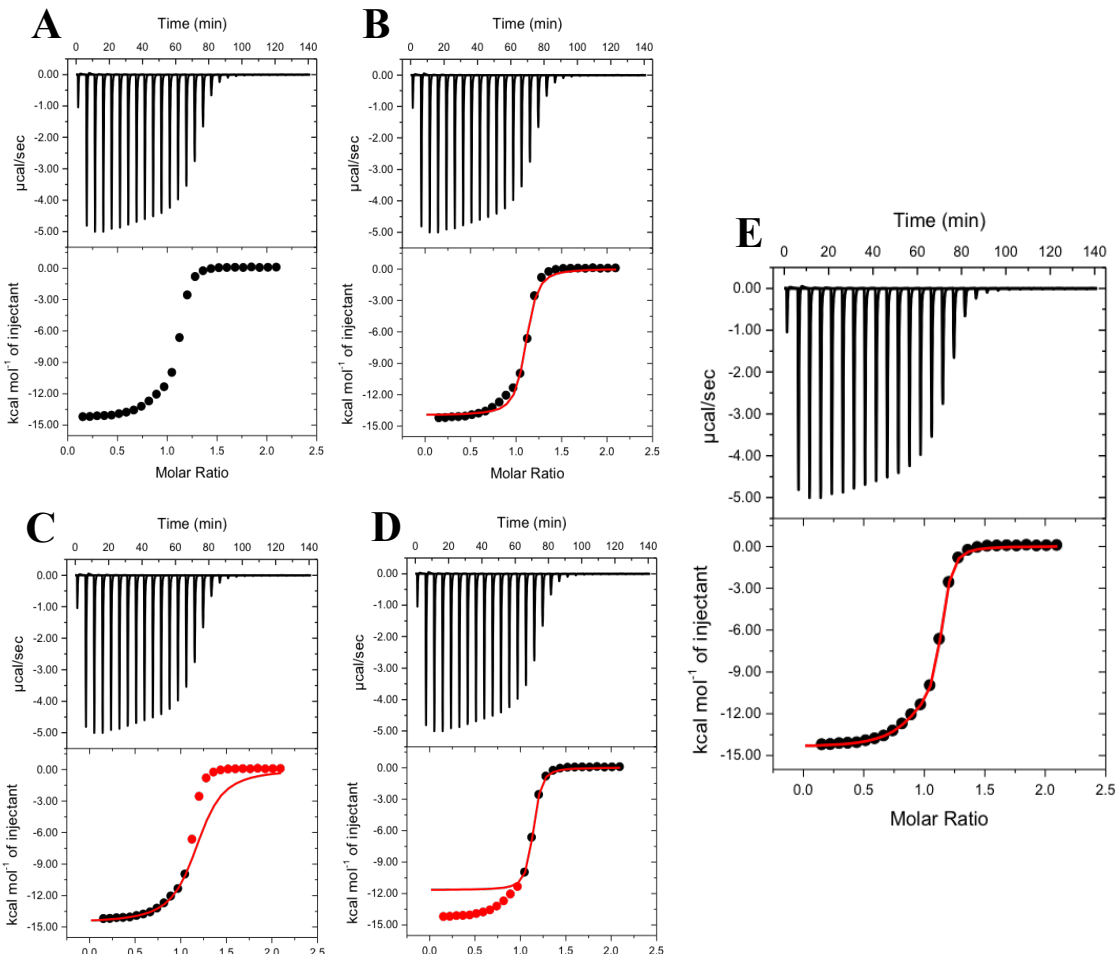

Figure 2.3.2.1. Titration of EDTA into Hg^{2+} in 50 mM Bis-Tris 50 mM NaCl, pH 7.4. Although the overall thermodynamics of the forward (metal into chelator) and reverse (chelator into metal) is the same through the principle of microscopic reversibility, the competing equilibria of the titration vary, leading to differences that are difficult to rationalize. Qualitatively, the unfitted data, A, seems to be slightly different than what is anticipated from a typical ITC experiment. Deconvolution of the differences are shown as evidence of these distinct differences. Although thermodynamic values can be obtained from the single-site fitting model, B, the fit is very poor, suggesting that more than one binding event is occurring. Dissecting the binding event into two single-sit binding events leads to a good fit of the first and second binding events (C & D, respectively). It is noted that the fit in C and D does not fit over the masked (red) out data points, providing evidence as to why the qualitative and single-site fitted data were not wholly accurate. Finally, the actual two-site fitting model, E, is utilized to establish the thermodynamics of the two binding events and is a qualitatively better fit than that of the single-site fit. The apparent enthalpy of binding of each of the two binding events in the two-site fit was equivalent to the apparent enthalpies in the deconvoluted, single-site fit of the first and second binding event.

The expression for the experimental concentration for all metal complexes in solution, is different, however, as the metal is already bound to the protein, thus there is no metal-buffer interaction, such that:

$$C_M = [M] + [ML] + [MP] \qquad \textbf{Equation 2.3.2.20}$$

Equation 2.3.2.20 can then be rearranged, similar to **Equation 2.3.2.11**, because the protein effectively takes the place of the buffer, such that:

$$[M]_{ITC} = C_M - [ML] = [M] + [MP] = [M] + (1 + K_{MP}[P]) \qquad \textbf{Equation 2.3.2.21}$$

The total concentration of the chelator, L, which at pH 7.4 has 1.04 H^+ bound at two protonation sites (H_1 and H_2), is denoted by C_L such that:

$$C_L = [L] + [LH_1] + [LH_2] + [ML] \qquad \textbf{Equation 2.3.2.22}$$

where $[L]_{ITC}$ can be found by the following equation:

$$[L]_{ITC} = C_L - [ML] = [L] + [LH_1] + [LH_2] \qquad \textbf{Equation 2.3.2.23}$$

For this experiment, EDTA protonation can be shown by:

$$K_{LH_1} = \frac{[LH^+]}{[L][H^+]} \qquad \textbf{Equation 2.3.2.24}$$

$$K_{LH_2} = \frac{[LH_2^{2+}]}{[LH^+][H^+]} \qquad \textbf{Equation 2.3.2.25}$$

$$\beta_{LH} = K_{LH1} \times K_{LH2} \qquad \textbf{Equation 2.3.2.26}$$

Now, **Equation 2.3.2.23** can be rewritten as the following:

$$[L]_{ITC} = [L] + [LH_1] + [LH_2] = [L]\, X\, \left(1 + \, K_{LH_1}[H^+] + \, \beta_{LH}[H^+]^2\right) \textbf{Equation 2.3.2.27}$$

and with **Equations 2.3.2.21** and **2.3.2.27** in mind, **Equation 2.3.19** can be rearranged such that:

$$K_{ITC} = \frac{[ML]}{[M][L]} X \frac{1}{(1 + K_{MP}[P])} X \frac{1}{(1 + K_{LH_1}[H^+] \, + \, \beta_{LH}[H^+]^2)} \quad \textbf{Equation 2.3.2.28}$$

Substituting K_{ML} for $\frac{[ML]}{[M][L]}$, this equation can be rearranged to solve for the buffer independent, pH-dependent metal-protein binding affinity:

$$K_{MP} = \frac{\left(\frac{K_{ML}}{K_{ITC}(1 + \, K_{LH_1}[H^+] + \beta_{LH}[H^+]^2)} - 1\right)}{[P]} \qquad \textbf{Equation 2.3.2.29}$$

It should be noted that this general equation is for the chelation of a metal with EDTA, or a similar chelating ligand, which has two relevant (de)protonation events. Utilization of different ligands with more or less protons competing with metal binding will require altering **Equation 2.3.2.29** accordingly.

2.4. Molecular Dynamics: Exploring Protein Binding and Dynamics

A complete appreciation of the function of proteins requires knowledge of both structure and dynamics, along with the understanding of how ligand binding impacts both of these. These conformational dynamics of a protein is essentially embedded within the structure of the protein and is frequently an important aspect of its overall function. Protein structures are relatively easy to obtain experimentally through NMR and/or X-ray crystallography, but protein dynamics are much more difficult to determine. This is particularly true if the observed property occurs in a timeframe of femtoseconds to nanoseconds, as with bond vibrations, sidechain motion, and mainchain motion, since few experimental techniques are able to quantify changes on these timescales. Gross

conformational changes and dynamics, those that occur in the microsecond range, are much easier to follow experimentally with NMR or stopped-flow spectroscopy but are fundamentally a bulk, or average, property for the ensemble of proteins in solution. One method to determine conformational changes in a protein and the impact of ligand binding on protein structure is through molecular dynamics.

Molecular dynamics (MD), in conjunction with quantum mechanics (QM) as necessary, is a valuable tool to probe the conformational and energetic landscapes of biomolecules. Of particular interest to this thesis is the utilization of QM to determine *ab initio* metal-residue bond lengths, bond angles, and dihedral angles, as well as bond strengths, for use in MD experiments. The MD experiments then aim to determine differences in the protein dynamics when different metals are bound, for example. Or molecular dynamics can be used to probe conformational differences between proteins from the same family of proteins bound with the same metal, but which show different binding thermodynamics. This allows the development of a hypothesis for why these differences exist and what they mean from a biochemical perspective. Changes in sidechain conformations in highly conserved residues can be described in both the holo and apo form of the protein, which provides insight on the role of certain amino acids. Lastly, at least relevant herein, is the use of MD to understand how the binding of a metal to a protein can impact the global architecture of the protein and how this can alter another distant ligand binding site on the protein. In order to fully appreciate the connection between protein structure and dynamics of a biomolecule through MD and QM, a brief history of the techniques is necessary.

2.4.1. Foundational Molecular Dynamics: Theory, History, and Practice

In 1998 the Nobel Prize was awarded to Walter Kohn and John Pople for their pioneering work applying quantum mechanical equations to determine problems in chemistry that are related to small molecules and simple reactions. The application of these equations, along with classical mechanics to biomolecular systems is, however, much more recent.[26] From small biomolecules, proteins with >20 amino acids, for example, are composed of far too many atoms to appropriately determine their dynamics through quantum mechanical equations. This necessitates the use of classical mechanics, which can

be broadly applied to much larger systems, limited, at least today, by the computational technology that is available. To fundamentally understand how molecular dynamics can be used to study conformational dynamics, among many other topics, an understanding of the foundational theory is necessary.

Molecular dynamics simulations are based on solving Newton's equation of motion for each *i* atom, such that:

$$\mathrm{F_i} = \mathrm{m_i a_i} \qquad \textbf{Equation 2.4.1.1}$$

where F_i is the force exerted on atom *i,* m_i is the mass of atom *i,* and a_i is the acceleration of atom *i.* Force can also be expressed through the potential energy of the system, where:

$$\mathrm{F_i} = -\nabla_i \mathrm{U} \qquad \textbf{Equation 2.4.1.2}$$

in which the force exerted on particle *i* is equal to the negative gradient of the potential energy, *U*. Thus, combining **Equations 2.4.1.1** and **2.4.1.2** gives a relationship between the potential energy of the system and the position of each atom, with respect to time, such that:

$$-\frac{dU}{dr_i} = m_i \frac{d^2 r_i}{dt^2} \qquad \textbf{Equation 2.4.1.3}$$

Now that the relationship between potential energy and position with respect to time has been established, it is useful to understand how changes in the position of an atom can change through Newton's Second Law of Motion. Similar to before, begin with the general force equation and solve for the second derivative of acceleration:

$$\mathrm{F} = \mathrm{ma} = \mathrm{m} \cdot \frac{dv}{dt} = \mathrm{m} \cdot \frac{d^2 x}{dt^2} \qquad \textbf{Equation 2.4.1.4}$$

Assuming a simple case, in which the acceleration is constant,

$$\mathrm{a} = \frac{dv}{dt} \qquad \textbf{Equation 2.4.1.5}$$

and taking the derivative provides us with an expression for the velocity where:

$$\mathrm{v} = \mathrm{at} + v_0 \qquad \textbf{Equation 2.4.1.6}$$

Since,

$$\mathrm{v} = \frac{dx}{dt} \qquad \textbf{Equation 2.4.1.7}$$

integrating again provides the equation for the new position with respect to the velocity and time where:

$$\mathrm{x} = \mathrm{v} \cdot \mathrm{t} + x_0 \qquad \textbf{Equation 2.4.1.8}$$

Combining **Equation 2.4.1.8** and **Equation 2.4.1.6**,

$$\mathrm{x} = \frac{1}{2}at^2 + v_0\mathrm{t} + x_0 \qquad \textbf{Equation 2.4.1.9}$$

which shows the value of x at time t as a function of the acceleration, a, initial velocity, v_0, and initial position, x_0. The acceleration is defined by the derivative of the potential energy with respect to the position r, where:

$$\mathrm{a} = -\frac{1}{m}\frac{dU}{dr} \qquad \textbf{Equation 2.4.1.10}$$

This shows that the trajectory of the system only requires the initial positions of the atoms, a distribution of the velocities, and the acceleration, which comes from the potential energy of the system. These equations, then, are deterministic, in which the initial positions and velocities at time zero determine the velocities and positions at all other times, t. These initial positions are obtained from protein structures though NMR or X-Ray crystallography and the initial velocities are distributed randomly following a Maxwell-Boltzmann or Gaussian distribution. This random distribution of initial velocities, determined by a random see, allows for repeat MD experiments.

Now that the foundational application of potential energy for a system, and its relationship to force, velocity, and position have been established, the foundational theory of molecular dynamics is considering with a general system composed of 7 arbitrary atoms, as show in **Figure 2.4.1.1**. Each of these atoms interact with each other through both bonded and non-bonded interactions. The potential energy of the system can be quantified by the summation of the potential energy of each of the bonded and non-bonded parameters. These sets of equations, described below, are included in each specialized forcefield. Bonded potential energies, in the simplest forcefields without cross terms, involve bond lengths (**Equation 2.4.1.11**), bond angles (**Equation 2.4.1.12**), and torsional/dihedral angles (**Equation 2.4.1.13**). Similarly, non-bonded potential energies are broadly defined as van der Waals interactions (**Equation 2.4.1.14**) and electrostatic interactions (**Equation 2.4.1.15**). Although more sophisticated models can be used to describe both the bonded and non-bonded interactions, these equations must be calculated for each atom of a biomolecule for each timestep over an extended, but reasonable, period of time, defining the need for simple approximations.

$$\mathrm{E}_{Bond} = \sum_{Bond} k_r\left(r - r_{eq}\right)^2 \qquad \textbf{Equation 2.4.1.11}$$

$$\mathrm{E}_{Angle} = \sum_{Angle} k_\theta\left(\theta - \theta_{eq}\right)^2 \qquad \textbf{Equation 2.4.1.12}$$

$$\mathrm{E}_{Dihedral} = \sum_{Dihedral} k_\phi(1 + \cos\left[n\phi - \gamma\right])^2 \qquad \textbf{Equation 2.4.1.13}$$

$$\mathrm{E}_{van\ der\ Waals} = \sum_{i<j}^{atoms} \varepsilon_{ij}\left[\left(\frac{r_m}{r_{ij}}\right)^{12} - 2\left(\frac{r_m}{r_{ij}}\right)^{6}\right] \qquad \textbf{Equation 2.4.1.14}$$

$$\mathrm{E}_{Electrostatics} = \sum_{i<j}^{atoms} \frac{q_i q_j}{4\pi\epsilon_0 r_{ij}} \qquad \textbf{Equation 2.4.1.15}$$

Thus, the total potential energy of the system is the sum of each of the potential energy terms:

$$\begin{aligned} U_{(r)} = & \sum_{Bond} k_r\left(r - r_{eq}\right)^2 \\ & + \sum_{Angle} k_\theta\left(\theta - \theta_{eq}\right)^2 \sum_{Dihedral} k_\phi(1 + \cos\left[n\phi - \gamma\right])^2 \\ & + \sum_{i<j}^{atoms} \varepsilon_{ij}\left[\left(\frac{r_m}{r_{ij}}\right)^{12} - 2\left(\frac{r_m}{r_{ij}}\right)^{6}\right] \\ & + \sum_{i<j}^{atoms} \frac{q_i q_j}{4\pi\epsilon_0 r_{ij}} \end{aligned} \qquad \textbf{Equation 2.4.1.16}$$

This calculated potential energy is input into the system as described above, and the new position of each atom is then defined, leading to a new structure at each timestep.

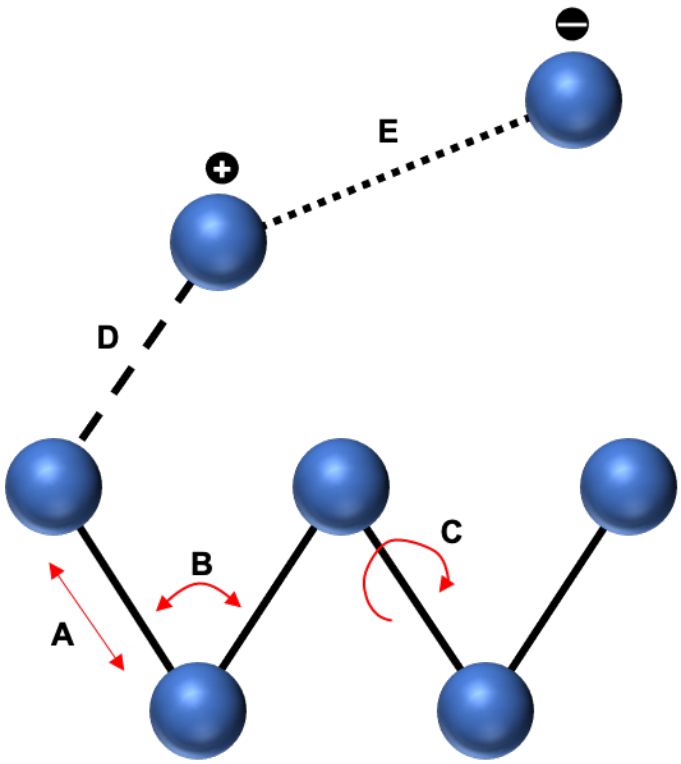

Figure 2.4.1.1. *General representation of interactions between arbitrary atoms. These are characterized by both bonded and non-bonded interactions such that: (A) bond length, (B) bond angles, (C) Torsion/Dihedral angles account for the fundamental bonded parameters and (D) van de Waals, and (E) Electrostatics account for the non-bonded parameters.*

With this potential energy calculation in mind, we turn to the total number of atoms in the system and the strategies that are employed to maximize MD experimental accuracy and minimize computational power. As mentioned previously, the primary limitation of the size and length of time for each MD experiment depends on the computational power that is accessible. Consider, for example, a small 70 amino acid protein, which contains approximately 1,000 atoms, in a vacuum. The potential energy calculation must be calculated for each of these atoms for each timestep over the course of the MD experiment. However, protein structures in a vacuum are rarely of interest. To obtain reasonable protein dynamics and structural changes, the protein needs to be solvated, either with implicit or explicit solvent. Implicit solvent, as the name suggests, is a solvent that resembles water and contains important elements, such as the dielectric constant of water, but no atoms are explicitly defined in the system. Likewise, explicit solvent utilizes thousands of water molecules to solvate the protein to better replicate a protein in water. Although explicit solvent will be inherently more accurate than implicit solvent, a fully solvated, 70 amino acid protein may contain 10,000 atoms from water alone. How can a MD experiment be run to microsecond timescales, and beyond, with tens of thousands of atoms?

This question is further complicated by non-bonded potentials, which track atom-atom interactions through space. Without any effective limitation to this distance parameter, calculations of one atom from one end of the protein to an atom on the other end will massively increase the need for computational power, even though there is negligible non-bonded interactions between these molecules. This distance is determined by the cut-off parameter, which is generally set to approximately 8-12 Å.

Ideally, a protein would be solvated within the explicit solvent that stretches far from the protein, so the protein is wholly solvated without the possibility of exposure to the vacuum outside the solvent. This, however, would dramatically increase the number of atoms that are required to solvate the protein. This is overcome through the use of periodic boundary conditions, in which the protein is placed in a box that sufficiently covers all surfaces of the protein (~12–15 Å from the protein's surface), and this box is repeated across all edges of the primary box, each of which is mirroring the original box. These periodic boundary conditions mirror the motion and conditions within the primary box but does not add to the total number of atoms. As such, this grossly diminishes the number of

atoms that are necessary to solvate a protein. It should be noted that molecular dynamics that involve gross structural changes that result in collisions with the periodic boundary boxes, as can be observed in protein unfolding experiments, can disrupt the system.

Directed changes to bond length calculations can also aid in improving computational performance. The vibration of a C–H or a O–H bond, for example, can be minimized in protein as these are not typically relevant to changes in protein conformations or conformational dynamics. Thus, these can be excluded unless they are explicitly being studied. Hydrogen-bond vibrations can effectively be eliminated the SHAKE algorithm which fixes hydrogen bond lengths, preventing the vibration from occurring. These types of bonded interactions add to computational power linearly, unlike non-bonded parameters which are quadratic. Thus, minimizing bonded parameters can be useful, but is unlikely to provide extensive differences compared to non-bonded parameter limitations.

Turning to the conditions for each MD experiment. The basis for temperature, pressure, and volume follow basic statistical mechanics. Each of these experiments involves the creation of a particular ensemble, which is a collection of all possible states that have different microscopic states, but the macroscopic or thermodynamics states are identical. Traditionally, these ensembles are defined by microscopic aspects that are constant. For example, the microcanonical ensemble (NVE) is a thermodynamic state that has a fixed number of atoms, N, volume, V, and energy, E, which is an isolated system. Canonical ensemble (NVT) is composed of a fixed number of atoms, volume, and temperature, T. The isobaric-isothermal ensemble (NPT) has fixed number of atoms, pressure, P, and temperature. Finally, the Grand Canonical ensemble (μVT) has a fixed chemical potential, volume, and temperature. Understandably, for proteins that are in solution, the two primary MD ensembles are NVT and NPT, as these follow experimental conditions that are most realistic and comparable to real experimental conditions.

These statistical ensembles require precise control to maintain the fixed microscopic state. A fixed number of atoms, for example, requires little extra input, as extra atoms will not be automatically added to the system throughout the course of the simulation. However, fixed temperature and pressure can be much more challenging. We consider each of these thermodynamic states individually. Maintaining a fixed temperature for these experiments generally utilizes a Berendsen thermostat, which places the entire

system within a heat bath. This bath is weakly coupled with the system and supplies or removes heat from the system as necessary to maintain a constant temperature in the system. This coupling to a thermostat exponentially scales the velocity within the system through λ, where[27]:

$$\lambda = \left[1 + \frac{\Delta T}{\tau_T}\left(\frac{T_{bath}}{T} - 1\right)\right]^{1/2} \qquad \textbf{Equation 2.4.1.17}$$

The coupling strength of the Berendsen thermostat to the system is modified by τ and T is defined as the kinetic temperature. Similarly, constant pressure is achieved through a Berendsen barostat, which utilizes a pressure bath instead. The pressure of the system is moderated by the weak coupling of this pressure bath through an exponential scaling through λ,

$$\lambda = 1 - \kappa \frac{\Delta t}{\tau_P}(P - P_{bath}) \qquad \textbf{Equation 2.4.1.18}$$

in which:

$$P = \frac{2}{3V}\left(E_{kin} + \sum_{i=1}^{N} x_i \cdot F_i\right) \qquad \textbf{Equation 2.4.1.19}$$

where κ is the isothermal compressibility, τ_P is the pressure coupling constant, V is the volume of the system, E_{kin} is the kinetic energy of the system, x_i is the position of particle i, F_i is the force on particle i, and N is the total number of atoms.

With each of these ensembles briefly explained, it is necessary to consider the purpose of molecular dynamics experiments and how insight into protein dynamics can be obtained. It should be noted that protein dynamics is just one of the many things that can be done by molecular dynamics experiments. More specifically, MD experiments can be set up as experiments on protein folding/unfolding pathways, solvation thermodynamics, amino acid pK_a calculations, ligand binding thermodynamics, redox potential calculations, and protein-protein, protein-ligand, and protein-DNA interactions, to name a few possibilities.[28–35] Generally, for a simple MD experiment on a small protein, the goal is to establish gross protein dynamics. This can be visualized through a 2-dimentional energetic landscape of a protein and further expanded for clarity by the 3-dimentional view (**Figure 2.4.1.2**). The transition between two conformational states is related to the energetic barrier

between them. The time for transition can be quick, but the waiting time for the protein in each conformation can take much longer. Average wait time of the transitions between the two states, A and B, can be expressed as:

$$\tau_{A\to B} = Ce^{\frac{\Delta G}{kT}} \qquad \textbf{Equation 2.4.1.20}$$

The wait time between conformational transitions, unfortunately, is difficult to predict. Thus, knowing how long to run a molecular dynamics experiment is challenging. Compounding this difficulty, each MD experiment is just describing the dynamics or conformations of a single protein, as opposed to an actual protein solution that has many orders of magnitude more proteins in the ensemble. To get around this issue, MD experiments are repeated multiple times for long periods of time. An average MD experiment, such as those in this thesis, which is trying to observe general protein conformations, may run up to ~50 nanoseconds and be repeated ~20 times. For some proteins this may be excessive, but for others this run may not be long enough or repeated enough. *Ad-hoc* changes can be done after initial MD experiments for optimization. These time frames and number of repeats can be viable for a fairly small protein of about 70 amino acids on a common desktop computer equip with a GPU. These estimated timeframes and number of experiments can be drastically diminished if the protein is larger, as the total number of atoms in these systems grows very quickly, as discussed previously.

Analysis of molecular dynamics experiments is necessary to pull out important information that aids in understanding. Initially, a simple analysis of the root mean square deviation (RMSD) (**Equation 2.4.1.21**) can be used to understand both protein conformational dynamics and conformational stability. This RMSD is effectively evaluating the overall structure of the protein at each timestep and compares the position of each atom to the initial, minimized protein structure.

$$RMSD_{weighted} = \sqrt{\frac{\sum_{i=0}^{N}[m_i \cdot (X_i - Y_i)^2]}{N}} \qquad \textbf{Equation 2.4.1.21}$$

where N is the number of atoms in the protein, m_i is the mass of atom i, X_i is the

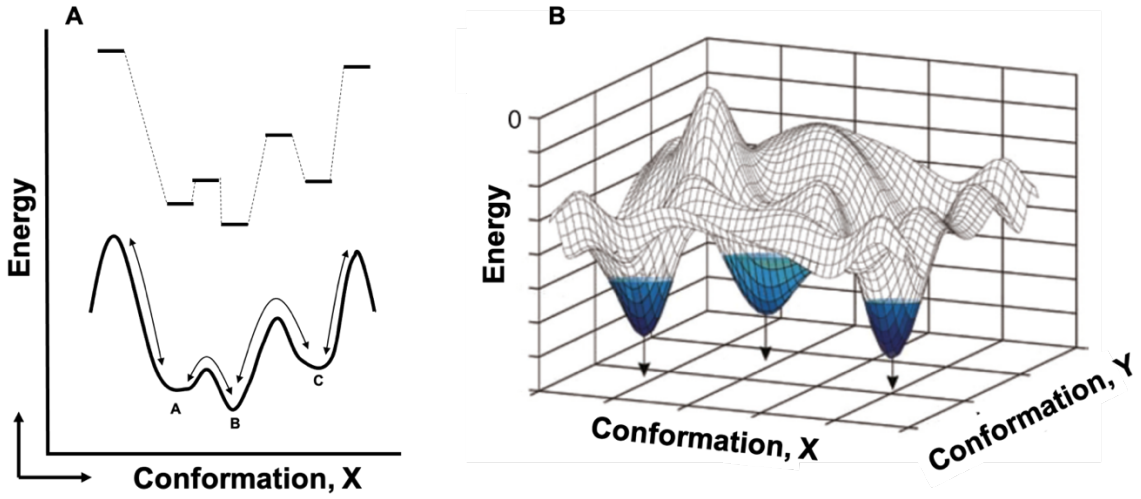

Figure 2.4.1.2. *Representation figures of free energy landscapes that correspond to changes in protein conformations with respect to the potential energy of the stable structure. Panel A represents the 2-dimentional changes in a protein. Each arrow suggests possible pathways and energetic barrier from one conformation to another conformation. Energetic barriers such as between A and B in panel A are more easily traversed than from B to C, for example. Panel B represents the 3-dimentional free energy landscape, which is much more reasonable for a protein which is changing conformations in space. A similar analysis as panel A can be done for the 3-dimentional landscape, in which larger energetic barriers are difficult to cross, whereas smaller energetic barriers are easier and less costly. In both free energy landscape diagrams, the lowest valley tends to be the most stable and likely to be the native protein conformation. In intrinsically disordered protein, which do not have well-defined protein structures, this free energy landscape is flattened, and the energetic cost between the valleys is much lower, leading to a protein with greater conformational dynamics. Panel B is modified.*[36]

coordinate vector of atom i, Y_i is the coordinate vector of atom i, and M is the total mass. If the RMSD is not mass-weighted, then $m_i = 0$ and $M = N$. Taking the RMSD of a particular section of the protein (backbone, side chains, total protein, etc.) at each timestep can show overall conformational stability and changes in the conformations. This can also be useful in knowing if a MD experiment is long enough. If the RMSD still has large fluctuations at the end of the experiment, then the timeframe of the experiment may need to be extended, particularly if this is repeatable. Extending the total experiment time enhances access to other potential energy wells, uncovering other protein conformations.

Radius of gyration (Rg) analysis can be performed in conjunction with the RMSD analysis to further explore conformational states that are sampled during the course of the MD experiment. The radius of gyration accounts for the compactness of a protein. Different conformational states may have different Rg values, where higher Rg values represent proteins that are less compact. The radius of gyration is calculated as the distribution of the molecular structure with respect to the center of mass or an axis of rotation such that

$$\text{Radius of Gyration} = r_{Rg} = \sqrt{\frac{\sum_{i=1}^{N} m_i \cdot (r_i - r_{CM})^2}{\sum_{i=1}^{N} m_i}} \qquad \textbf{Equation 2.4.1.22}$$

where m_i is the mass of the atom at each timestep, r_i is the position of the atom at timestep i, r_{CM} is center of mass of the system, and N is the total number of atoms in the system. Plotting the RMSD vs. Rg with respect to time can be useful in determining conformational states, as different conformations will result in distinct clusters.

Other types of analysis for molecular dynamics are also possible but tend to be more specific to the question that is being asked. For example, solvent accessible surface area (SASA) can be used to sample the ability of solvent to occupy space around a protein or in pockets and channels within the structure. The SASA has been expanded with the grid inhomogeneous solvation theory (GIST), which can be used to determine the solvation thermodynamics. This can be useful in extracting differences in ligand binding due to solvation.[35,37] SASA can also be used to characterize specific amino acid solvation. The SASA of amino acids can be used to determine small conformational differences upon ligand binding, which results in burying or exposure of highly conserved amino acids. More specific analyses, such as hydrogen bond characterization, root mean square fluctuations (RMSF), and principal component analysis (PCA), which can help to answer

important questions on protein folding, residue-specific dynamics, and different conformational states, respectively.[38,39]

Finally, the use of molecular dynamics to probe conformational dynamics in a protein can be augmented by conformational differences between the ligand-bound forms and free forms. However, the binding of a ligand to a protein can be fairly simple, when the ligand is a small molecules or peptide, because these tend to interact non-covalently. This becomes much more complicated for metal ions, which bind with strong bonding to proteins. Metal binding is challenging because of the stronger chemical bonds, and bond lengths, bond angles, bond strengths, and coordinating geometries that are not usually known for the more common 2nd row transition metals, let alone for 3rd and 4th row metals like Cd^{2+} or Hg^{2+}. As such, other methods to determine chemical bonds involving metals are necessary in order to do molecular dynamics on metalloproteins. *Ab-initio* chemical bond characterization for metal ions can be done using quantum mechanics combined with molecular mechanics (QM/MM). This is possible due to recent work from the lab of Kenneth Merz, who developed novel ways to accurately model metal-based non-bonded interactions. These models were shown to be accurate though characterization of metal hydration free energies for monovalent, divalent, trivalent, and some tetravalent metal ions.[40,41] Thus, the conformational changes of proteins when a metal is bound can be sampled by both bonded and non-bonded interactions.

2.5 Conclusion for Instrumentation and Computational Techniques

Determination of metal binding thermodynamics and protein conformational changes, with and without a bound metal is important for deeper understanding of metalloproteins. Isothermal titration calorimetry (ITC) is considered the "gold standard" for determining binding thermodynamics in a single experiment. Metal binding can often involve conformational changes of the protein, as well, which can be further probed with molecular dynamics. Molecular dynamics compliments the thermodynamics determined by ITC through the ability to establish protein dynamics, conformational changes, and solvation thermodynamics computationally. Although not specifically addressed within this thesis, a long-term goal of molecular dynamics is to be able to establish, computationally, the thermodynamic parameters of metal binding. This imparts a direct

and advantageous synergy between the experimental techniques and the computational experiments.

2.6 References

1. Emeis, S. The discovery of latent heat 250 years ago. *Meteorol. Zeitschrift* **13**, 329–333 (2004).
2. Buchholz, A. C. & Schoeller, D. A. Is a calorie a calorie? *Am. J. Clin. Nutr.* **79**, 899–906 (2004).
3. Carnot, S. Reflections on the Motive Power of Fire, and on Machines Fitted to Develop that Power. *Sadi Carnot*. (1825).
4. Clausius, R. On the Dynamical Theory of Heat, with numerical remits deduced from Mr Joule's Equivalent of a Thermal Unit. **xxiii**, 261–288 (1851).
5. Gibbs, J. W. a Method of Geometrical Representation of the Thermodynamic Properties of Substances By Means of Surfaces. *Trans. Connect. Acad.* **II**, 382–404 (1873).
6. Freyer, M. W. & Lewis, E. A. Isothermal Titration Calorimetry: Experimental Design, Data Analysis, and Probing Macromolecule/Ligand Binding and Kinetic Interactions. *Methods Cell Biol.* **84**, 79–113 (2008).
7. Tajc, S. G., Tolbert, B. S., Basavappa, R. & Miller, B. L. Direct determination of thiol pKa by isothermal titration microcalorimetry. *J. Am. Chem. Soc.* **126**, 10508–10509 (2004).
8. Freire, E., Schön, A. & Velazquez-Campoy, A. Chapter 5 Isothermal Titration Calorimetry. General Formalism Using Binding Polynomials. *Methods Enzymol.* **455**, 127–155 (2009).
9. Brown, A. Analysis of cooperativity by isothermal titration calorimetry. *Int. J. Mol. Sci.* **10**, 3457–3477 (2009).
10. Chervenak, M. C. & Toone, E. J. A Direct Measure of the Contribution of Solvent Reorganization to the Enthalpy of Binding. *J. Am. Chem. Soc.* **116**, 10533–10539 (1994).
11. Velazquez-Campoy, A. & Freire, E. Isothermal titration calorimetry to determine association constants for high-affinity ligands. *Nat. Protoc.* **1**, 186–191 (2006).

12. Zhang, Y. L. & Zhang, Z. Y. Low-affinity binding determined by titration calorimetry using a high- affinity coupling ligand: A thermodynamic study of ligand binding to protein tyrosine phosphatase 1B. *Anal. Biochem.* **261**, 139–148 (1998).
13. Quinn, C. F., Carpenter, M. C., Croteau, M. L. & Wilcox, D. E. Isothermal Titration Calorimetry Measurements of Metal Ions Binding to Proteins. *Methods Enzymol.* **567**, 3–21 (2016).
14. Grossoehme, N. E., Spuches, A. M. & Wilcox, D. E. Application of isothermal titration calorimetry in bioinorganic chemistry. *J. Biol. Inorg. Chem.* **15**, 1183–1191 (2010).
15. Jelesarov, I. & Bosshard, H. R. Isothermal titration calorimetry and differential scanning calorimetry as complementary tools to investigate the energetics of biomolecular recognition. *J. Mol. Recognit.* **12**, 3–18 (1999).
16. Chao, Y. & Fu, D. Thermodynamic Studies of the Mechanism of Metal Binding to the Escherichia coli Zinc Transporter YiiP. *J. Biol. Chem.* **279**, 17173–17180 (2004).
17. Draczkowski, P., Matosiuk, D. & Jozwiak, K. Isothermal titration calorimetry in membrane protein research. *J. Pharm. Biomed. Anal.* **87**, 313–325 (2014).
18. Situ, A. J., Schmidt, T., Mazumder, P. & Ulmer, T. S. Characterization of membrane protein interactions by isothermal titration calorimetry. *J. Mol. Biol.* **426**, 3670–3680 (2014).
19. Carpenter, M. C. & Wilcox, D. E. Thermodynamics of formation of the insulin hexamer: Metal-stabilized proton-coupled assembly of quaternary structure. *Biochemistry* **53**, 1296–1301 (2014).
20. Wahba, H. M. *et al.* Structural and Biochemical Characterization of a Copper-Binding Mutant of the Organomercurial Lyase MerB: Insight into the Key Role of the Active Site Aspartic Acid in Hg-Carbon Bond Cleavage and Metal Binding Specificity. *Biochemistry* **55**, 1070–1081 (2016).
21. Wahba, H. M. *et al.* Structural and biochemical characterization of organotin and organolead compounds binding to the organomercurial lyase MerB provide new insights into its mechanism of carbon-metal bond cleavage. *J. Am. Chem. Soc.* **139**, 910–921 (2017).

22. Bou-Abdallah, F., Woodhall, M. R., Velázquez-Campoy, A., Andrews, S. C. & Chasteen, N. D. Thermodynamic analysis of ferrous ion binding to Escherichia coli ferritin EcFtnA. *Biochemistry* **44**, 13837–13846 (2005).
23. Wilcox, D. E. Isothermal titration calorimetry of metal ions binding to proteins: An overview of recent studies. *Inorganica Chim. Acta* **361**, 857–867 (2008).
24. Wang, Y., Wang, G., Moitessier, N. & Mittermaier, A. K. Enzyme Kinetics by Isothermal Titration Calorimetry: Allostery, Inhibition, and Dynamics. *Front. Mol. Biosci.* **7**, 1–19 (2020).
25. Garrido, P. F. *et al.* Unsupervised bubble calorimetry analysis: Surface tension from isothermal titration calorimetry. *J. Colloid Interface Sci.* **606**, 1823–1832 (2022).
26. Karplus, M. Molecular dynamics simulations of biomolecules. *Acc. Chem. Res.* **35**, 321–323 (2002).
27. Berendsen, H. J. C., Postma, J. P. M., Van Gunsteren, W. F., Dinola, A. & Haak, J. R. Molecular dynamics with coupling to an external bath. *J. Chem. Phys.* **81**, 3684–3690 (1984).
28. Yadav, A., Paul, S., Venkatramani, R. & Ainavarapu, S. R. K. Differences in the mechanical unfolding pathways of apo- and copper-bound azurins. *Sci. Rep.* **8**, 1–13 (2018).
29. Henriksen, N. M., Fenley, A. T. & Gilson, M. K. Computational Calorimetry: High-Precision Calculation of Host-Guest Binding Thermodynamics. *J. Chem. Theory Comput.* **11**, 4377–4394 (2015).
30. Ramsey, S. *et al.* Solvation thermodynamic mapping of molecular surfaces in ambertools: GIST. *J. Comput. Chem.* **37**, 2029–2037 (2016).
31. Cruzeiro, V. W. D., Amaral, M. S. & Roitberg, A. E. Redox potential replica exchange molecular dynamics at constant pH in AMBER: Implementation and validation. *J. Chem. Phys.* **149**, (2018).
32. Mongan, J., Case, D. A. & McCammon, J. A. Constant pH molecular dynamics in generalized Born implicit solvent. *J. Comput. Chem.* **25**, 2038–2048 (2004).
33. Karplus, M., McCammon, J. A. & Gelin, B. R. *Dynamics of folded proteins*. *Nature* vol. 267 https://www.nature.com/articles/267585a0.pdf%0Ahttp://www.msg.ucsf.edu/BI20

4/Discussion/Q1/Jacobson/MacCammon_1977.pdf (1977).

34. Zheng, W. & Glenn, P. Probing the folded state and mechanical unfolding pathways of T4 lysozyme using all-atom and coarse-grained molecular simulation. *J. Chem. Phys.* **142**, (2015).
35. Nguyen, C. N., Kurtzman Young, T. & Gilson, M. K. Grid inhomogeneous solvation theory: Hydration structure and thermodynamics of the miniature receptor cucurbit[7]uril. *J. Chem. Phys.* **137**, 973–980 (2012).
36. Jansen, M. The energy landscape concept and its implications for synthesis planning. in *Pure and Applied Chemistry* vol. 86 883–898 (Walter de Gruyter GmbH, 2014).
37. Nguyen, C. N., Cruz, A., Gilson, M. K. & Kurtzman, T. Thermodynamics of water in an enzyme active site: Grid-based hydration analysis of coagulation factor xa. *J. Chem. Theory Comput.* **10**, 2769–2780 (2014).
38. Kundu, S. & Roy, D. Temperature-induced unfolding pathway of a type III antifreeze protein: Insight from molecular dynamics simulation. *J. Mol. Graph. Model.* **27**, 88–94 (2008).
39. Eubanks, C. S., Forte, J. E., Kapral, G. J. & Hargrove, A. E. Small molecule-based pattern recognition to classify RNA structure. *J. Am. Chem. Soc.* **139**, 409–416 (2017).
40. Li, P. & Merz, K. M. Metal Ion Modeling Using Classical Mechanics. *Chem. Rev.* **117**, 1564–1686 (2017).
41. Li, P. & Merz, K. M. Taking into account the ion-induced dipole interaction in the nonbonded model of ions. *J. Chem. Theory Comput.* **10**, 289–297 (2014).

Chapter 3:

Energetics of Heterotropic and Homotropic Allosteric Regulation in the Mercury Metalloregulatory Protein, *Bacillus megaterium* MerR

3.1. Introduction

3.1.1. Metal-Responsive Protein Transcription in Bacteria

Metals are ubiquitous within the environment, and many are absolutely required for life. In living organisms, these metals serve in components to structural or catalytic roles in biomolecules, many of which are fundamental to biological processes.[1] However, high concentrations of these metals in cells are toxic.[2] This presents a delicate balance in modulating necessary metal utilization and cellular damage, which is achieved through regulation of proteins involved in binding, transport, and delivery of the different metal ions.[3] Balancing of this regulation is dependent on the metal. Typically, essential first-row transition metals, including zinc (Zn), iron (Fe), or copper (Cu), play some role in physiological function and cell biochemistry.[4–9] Since these are used within the cell, proteins are required to import the metal into the cell, but also to export them as the concentration raises and thereby maintain an appropriate level, a process known as homeostasis.[10–14]

Unlike these essential transition metals, other metals have no known biological function, like mercury (Hg).[15] Intriguingly, however, some bacteria have a protein pathway designed to important toxic mercury into the cell. This uptake requires careful control through protein pathways that actively bind and transfer the metal from one protein to the other, which requires careful cellular regulation to prevent cell death due to mercury toxicity. Each of these metal systems, whether for import, transport, or export, of essential first-row transition metals or non-essential, biologically inactive and dangerous metals are regulated by metal-responsive transcriptional regulators in bacteria.[16–21]

These metal-responsive regulators, also called metalloregulatory proteins or metal-sensor proteins, are directly involved in regulating the transcription of these different metal-related protein pathways. The development of these metal-related protein pathways for the import and export of metals by bacteria require a significant investment of cellular resources.[22] However, energy expenditure for the transcription of proteins involved in the uptake of metals must be balanced with proteins to prevent the overaccumulation of these metals. Balancing these two features is particularly difficult in bacteria as these metals are not just utilized for physiological function, but also in host defense mechanisms by using

metals, like copper, to poison the microenvironment of the cell.[23] In bacteria, as well as cells of higher organisms, metalloregulatory proteins play a crucial role the overall homeostasis of each metal, coordinating the acquisition, uptake, transport, storage, delivery, and export proteins. This leads to the orchestration of entire protein pathways designated for each metal that are managed by metal-specific metal-responsive transcriptional regulators.[3]

3.1.2. Allosteric Regulation of Metal-Responsive Transcriptional Regulators

Metalloregulatory proteins respond to changes in metal concentrations in the cell through allosterically binding a metal ion to the protein, which alters the protein-DNA binding and thereby increases or decreases the transcription of the subsequent regulated proteins. Allosteric regulation is the generally-accepted model for these metalloproteins, as the binding of a metal to a distant site modulates the protein-DNA interface.[3] The molecular mechanism of this allosteric regulation, on the other hand, varies. Each metal homeostasis pathways may be modulated by positive or negative feedback mechanisms, leading to activation, repression, or de-repression of the transcription of proteins in the pathway (**Figure 3.1.2.1**). This control of transcription is further distinguished by the atomistic allosteric mechanism, that modulates protein conformational changes and interactions with the DNA. Metal-responsive transcriptional regulators can bind a metal ion that significantly alters the protein scaffold, as found with AdcR, a Zn^{2+} metalloregulatory protein, or minimally alters the protein scaffold, as found with CueR, the Cu^{+} metalloregulatory protein.[24–28]

How metal binding, and the subsequent allosteric changes, modulate protein structures and regulates transcription is a fundamental question in metallobiochemistry and bioinorganic chemistry. Loss of this control would be catastrophic to cellular homeostasis, both from the utilization of significant cellular resources, but also from the aberrant import or export of metals that can lead to cytotoxicity. Thus, the mechanism of metal binding and allosteric regulation of protein-DNA interactions is fundamental to understanding metal homeostasis in cells.

Allostery takes many forms but can generally be described as the binding of a ligand, or metal, resulting in a change in another ligand binding site at a distant point in the

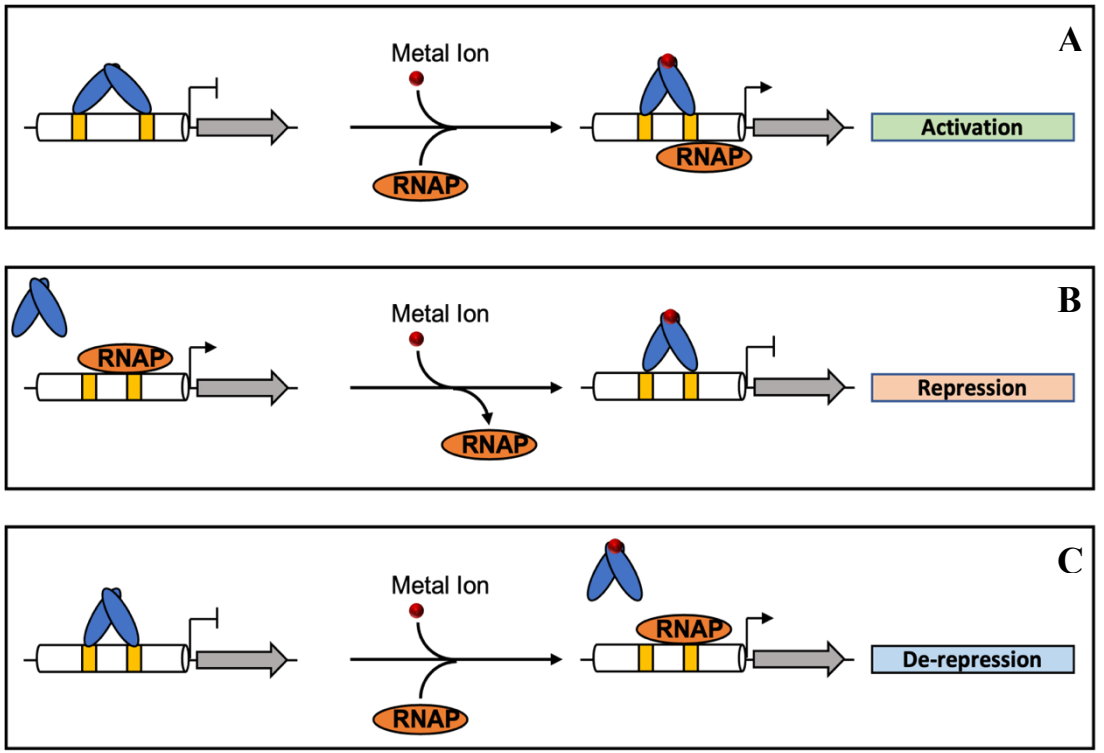

Figure 3.1.2.1. *Mechanisms associated with the allosteric metal binding to metalloregulatory proteins for their transcriptional regulation. Metalloregulatory proteins (blue), whether apo or metal-bound, bind to their metal-response elements (gold), which can lead to diminished or enhance activity of RNA polymerase (RNAP, orange) and the protein transcriptional machinery. (A) Activation: the metalloregulatory protein initially is bound to the DNA, which inhibits the binding of RNAP, until the metal ion binds, leading to the binding of the RNAP, allowing for transcription to occur. (B) Repression: RNAP is initially bound to the DNA sequence, enhancing protein transcription, but metal binding to the apo-metalloregulatory protein leads to the displacement of RNAP and binding to the DNA sequence, repressing transcription. (C) De-repression: the apo-metalloregulatory protein is bound to the DNA sequence, repressing transcription, however the binding of the metal to the metalloregulatory protein leads to its dissociation from the DNA, allowing for the binding of RNAP and subsequent activation. Adapted from Bakch and Zamblel, 2020.*[3]

protein. This modulation is not the result of a direct interaction, but through alteration in the protein scaffold through electrostatic changes, hydrogen-bonding networks, or conformational changes, for example.[29–32] The mechanism of allosteric regulation by metalloregulatory proteins can have significant variability, and only the MerR family of metalloregulatory proteins will be discussed here.

3.1.3. Metal-Response Transcriptional Regulation and the MerR Family

Each metalloregulatory protein family is named after the founding metalloregulatory protein. Although different metals are regulated, each protein within the family has very similar attributes, including a similar protein scaffold, protein oligomerization, DNA binding sequence and localization, but different signal-sensing motifs.[3] These molecular modifications modulate conformational changes and dynamics associated with allostery, expanding on the mechanisms associated with protein regulation.

One such family is the MerR family, named after the mercury metalloregulatory protein of the same name. MerR is of particular interest because mercury has no known biological function, yet both Zn^{2+} and Cu^{+}, which are required for life, have metalloregulatory proteins with similar properties to that of MerR and are members of the same metalloregulatory family. MerR and the MerR family all share a similar allosteric mechanism, in which the protein is bound to DNA in both the apo- and metal-bound form. Binding of the metal to the protein-DNA complex has been proposed to result in conformational changes in the DNA allowing RNA polymerase to bind and the subsequent transcription of specific proteins downstream (**Figure 3.1.2.1.A**).[26,33,34] Although there are no structures of the MerR-DNA complex, there is a structure of the CueR-DNA complex, which regulates the transcription of proteins involved in Cu^{+} homeostasis.[25,35] Furthermore, from the crystal structures of MerR in both gram positive and gram negative bacteria have been determined in the apo-form and mercury-bound form.[27,28]

Each member of the MerR family has three distinct components, two DNA binding domains (helix-2), two metal-binding sites (helix-5 and helix-6), and a helical dimerization region (helix-5) (**Figure 3.1.3.1, Top**).[27] MerR, like CueR and ZntR, the Cu^{+} and Zn^{2+} regulatory proteins, respectively, binds two metal ions in a homodimeric structure, where,

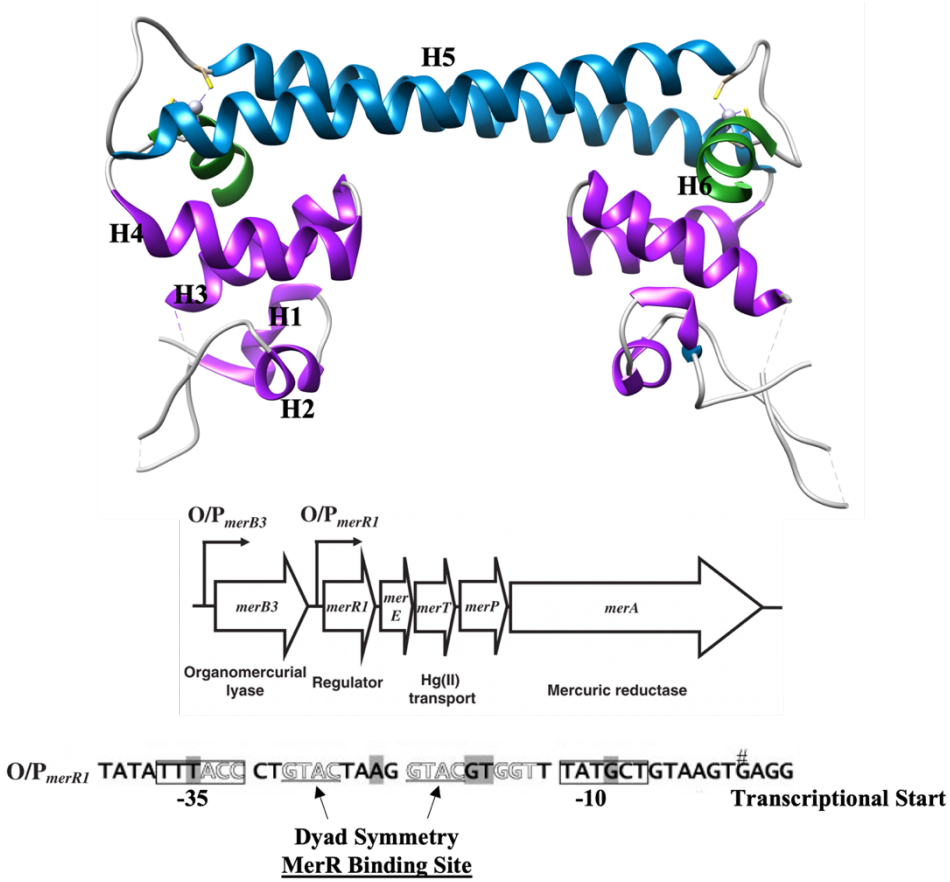

Figure 3.1.3.1. *Crystal structure of Hg-bound MerR homodimer, with labelled helices.(Top) Helix 2 (Purple) is the DNA-recognition site and winged helix-turn-helix motif, helix 5 (Blue) is the dimerization site and the metal binding site is found in helix 5 and helix 6 (Green) formed by both monomers. (Middle) Mercury detoxification proteins that are regulated by MerR. (Bottom) MerR operon,* merO*, that shows the –10 and –35 regions, which are the RNA polymerase binding sites, and the symmetrical GTACnnnnGTAC sequence as the MerR binding site. Finally, # denotes the transcriptional start site. Figure adapted from Yi and coworkers and mercury-bound MerR structure modified from Chang and coworkers (PDB: 4UA1).*[27,36]

as shown by crystal structures, the metal-binding site contains residues from each monomer. The DNA-binding domain consists of a winged helix-turn-helix fold, where helix 2 from both monomers interacts with the DNA recognition sequence, GTAC*nnnn*GTAC, where *n* is any nucleic acid (**Figure 3.1.3.1, Bottom**).[27,36] In MerR, Hg^{2+} binds to each site with a tri-coordinate geometry of three highly-conserved cysteine residues, in which two cysteines are from one monomer and the third cysteine is from the other monomer. However, the stoichiometry of Hg^{2+} binding to the dimer that was found in crystal structures has been debated, as solution-based biochemical studies have shown that, in the absence of DNA, MerR only binds one Hg^{2+} per dimer.[37] This solution-based stoichiometry has not been experimentally tested or observed for CueR, with the binding of Cu^{+}, or ZntR, with the binding of Zn^{2+}.

Although much has been done with structural and cell-based functional methods to characterize the protein properties of MerR, significantly less work has been done on the protein-DNA interaction, the allosteric mechanisms of metal binding, and the energetics of these interactions.

3.1.4. Allosteric Regulation of MerR and the Mercury Detoxification Proteins

Structure-based allosteric interactions have two primary mediating mechanisms: homotropic and heterotropic. Homotropic allosteric interactions involve the binding of a ligand that then modulates the binding of the same ligand to another ligand-binding site, which is typically observed for homo-oligomeric proteins. Heterotropic allostery, as the name suggests, involves a change at a binding site for a different ligand upon initial binding of a ligand. These structure-based allosteric mechanisms can be described by the thermodynamics of the site-site interaction. By comparing the free energy differences (ΔG), to the enthalpic (ΔH) and entropic (ΔS) components of binding, the driving force for the allosteric interactions can be quantified and elucidated. This leads to three types of allosteric effects: (1) entropically driven, (2) enthalpically driven, and (3) modulated by both entropy and enthalpy.[16] MerR, like other homo-oligomeric metalloregulatory proteins with multiple binding sites, has the possibility for both homotropic allostery, in that Hg^{2+} binding to one of MerR site may modulate Hg^{2+} binding to the other site, and heterotropic allostery, in that Hg^{2+} binding to MerR may modulate its binding to the DNA, *merO*.[16]

Linked equilibria, which define each aspect of the metal-protein-DNA interaction, are coupled through modulating structures, amino acid dynamics, and global energetics in MerR. Allosteric regulation of the protein-DNA complex upon Hg^{2+} binding would result in alterations within these coupled equilibria. In *Bacillus megaterium*, MerR is constitutively bound to the MerR operon (denoted *merO*), repressing the transcription of the downstream mercury detoxification proteins (**Figure 3.1.4.1**). When mercury enters the cell, it will readily bind to MerR, resulting in the binding of RNA polymerase and transcription of the mercury detoxification proteins, MerP, MerT, and MerA (See Chapter 4). From an allosteric perspective, the binding of Hg^{2+} to MerR results in a conformational change in the DNA, opening up the RNA polymerase binding site.[26] This observation is supported by the spacing of the RNA polymerase binding sites (–10 and –35). In *merO*, they are ~2 nucleotides further apart than is required for binding. It is proposed that this addition spacing is the mechanism to control RNA polymerase binding. When Hg^{2+} binds to MerR that is bound to *merO*, these –10 and –35 regions move closer together, allowing RNA polymerase to bind, as predicted from studies of CueR.[35] Although this would suggest that the binding Hg^{2+} to MerR results in structural changes, crystal structures of apo-MerR and holo-MerR show minimal structural differences.[27] It has been proposed that the binding of Hg^{2+} weakens the MerR-*merO* interaction.[36]

Isothermal titration calorimetry (ITC) has the potential to quantify the thermodynamics of the homotropic and heterotropic allostery associated with the regulation of MerR and the MerR-*merO* complex by inorganic mercury. In theory, ITC can measure the thermodynamics of each step of the formation of the metal-protein-DNA complex (**Figure 3.1.4.2**). The degree to which ligand binding induces an allosteric response can be quantified by the magnitude of acoupling free energy,

$$\Delta G^{t}_{Coupled} = -RTln\left(K^{t}_{Coupled}\right) \qquad \textbf{Equation 3.1.4.1.}$$

where, *t* is the total ligand exchange that occurs in the coupled equilibria. Binding of Hg^{2+} to the MerR-*merO* complex has been observed to weaken the MerR-*merO* complex, resulting in $\Delta G_C > 0$, shifting the **Figure 3.1.4.2** overall equation to the left.[36] Systematic measurements of each step of the formation of the Hg-MerR-*merO* complex will provide the thermodynamics of the allostery associated with the binding of Hg^{2+}. Through a series of ITC measurements (Hg^{2+} into apo-MerR, Hg^{2+} into

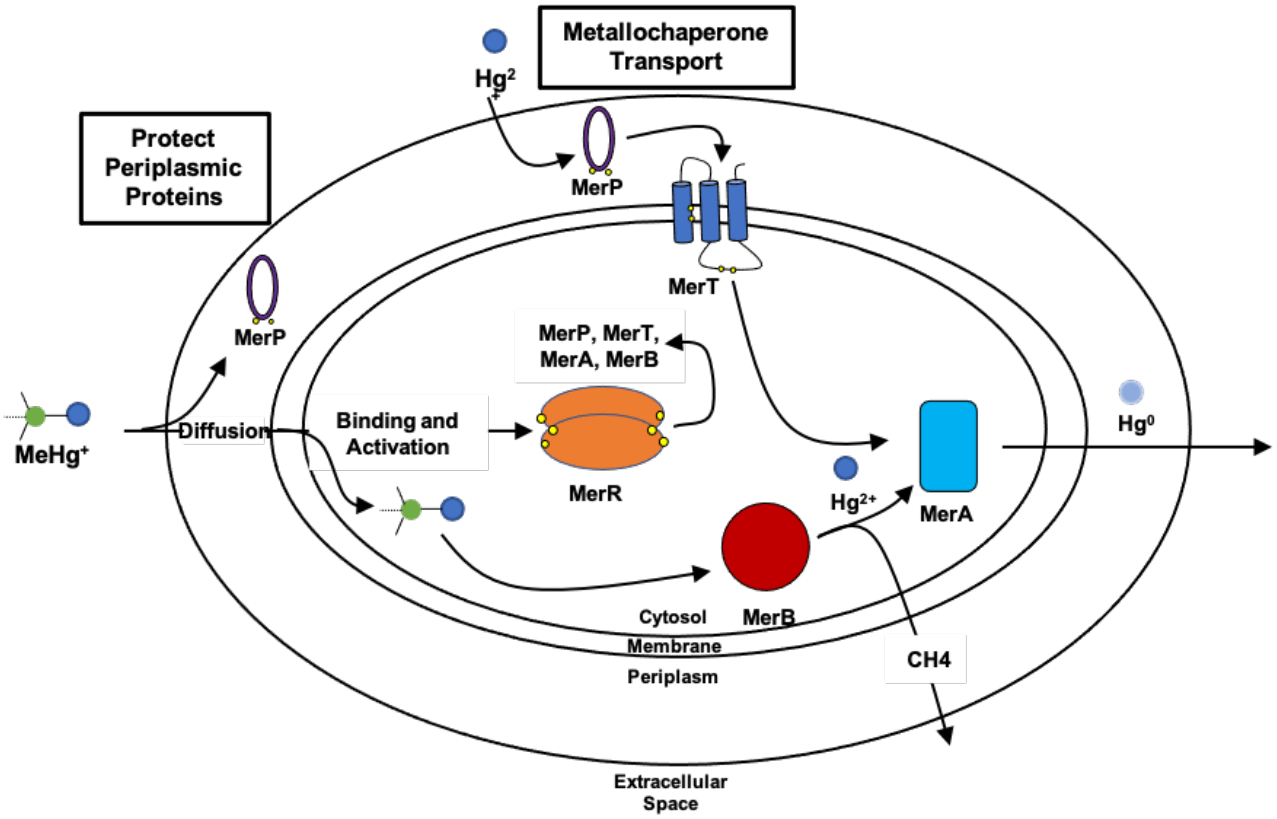

Figure 3.1.4.1. *Schematic of the mercury detoxification pathway in* Bacillus megaterium. *Regulation of the pathway is mediated through MerR and its interaction with its operon,* merO.

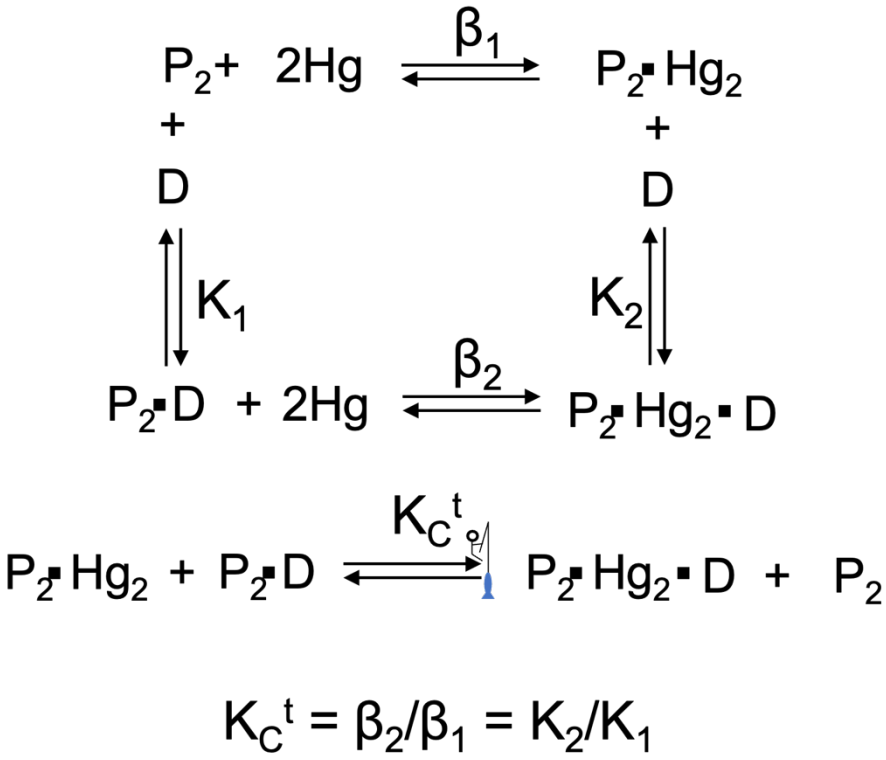

Figure 3.1.4.2. *General coupling scheme that for the binding of 2* Hg^{2+} *to* $MerR_{monomer}$ *(P) and* merO *(D) where β1and β2 are the total metal binding associated with the apo-MerR dimer* (P_2) *and* $(MerR)_2$–merO *complex, respectively. Allosteric coupling energies, denoted by* K_C^t*, describe the ligand exchange between* $(MerR)_2$–merO *and* Hg_2–$(MerR)_2$.

MerR-*merO*, apo-MerR into *merO*, and Hg-MerR into *merO*), the change in the free energy, entropy and enthalpy for the individual steps will be used to quantify the thermodynamic cycle of the homotropic and heterotropic regulation of the mercury detoxication pathway.

3.2 Materials and Methods

3.2.1. Chemicals

All materials utilized were purchased at the highest available purity and utilized without further modification. Buffers include PIPES (1,4-piperazinediethanesulfonic acid), HEPES (4-(2-hydroxyethyl)-1-piperazineethanesulfonic acid), BisTris (2-[bis(2-hydroxyethyl)amino]-2-(hydroxymethyl)propane-1,3-diol), and TAPSO (3-[[1,3-dihydroxy-2-(hydroxymethyl)propan-2-yl]amino]-2-hydroxypropane-1-sulfonic acid), all purchased from Sigma and VWR. Sodium chloride was purchased from VWR. Mercury dichloride (Baker Chemical), reduced D,L- glutathione (GSH) (VWR), diethylenetriaminepentaacetic acid (DTPA, Baker Chemical), N-acetyl-penicillamine (NAPA) and penicillamine (Pen, Sigma), were all utilized as received without modifications or further purification.

3.2.2. MerR Operon, merO, Preparation

The MerR operon, *merO*, was purchased from Integrated DNA Technologies (IDT) and utilized as received. The annealed duplex DNA oligonucleotide that was employed had a forward strand sequence of (3'-CCTCACTTACAGCATAAACCACGTACCTTAGTACAGGGTAAATATA-5') along with its reverse compliment strand. DNA oligonucleotide samples arrived in water at ~200 – 1000 μmole and have a molecular weight of 28,294 g/mol. DNA samples were diluted in nanopure (>18 MΩ) water to 1 mM. This was diluted to the appropriate concentration in metal-free buffer that was utilized in the ITC experiments.

3.2.3. Transformation, Expression, and Purification of MerR

The modified pET19-b plasmid was purchased from Genscript and utilized as received. Gel electrophoresis showed a purity of >95%. The construction of this expression plasmid produced the N-terminal *strep-tag* (WSHPQFEK) labelled MerR from the gram-positive bacterium *Bacillus megaterium* MB1. For transformation, *Escherichia coli* BL21(DE3) (New England Biolabs) cells were utilized. Addition of 2 µL of the MerR plasmid was gently mixed with 50 µL of the competent cells and incubated, on ice, for 30 minutes. The cell-plasmid mix was then heat shocked for 1 minute at 42 ºC, and returned to the ice bath for another 2 minutes. After the heat-shock, approximately 150 µL of SOC media (New England Biolabs) was added to the heat-shocked cells and shaken at 37 ºC for 1 hour. MerR-containing cells were then plated on agar with 100 µg/mL ampicillin and grown overnight at 37 ºC.

For expression, the plasmid-harboring BL21(DE3) cells were cultured in 1 L of LB (Sigma) medium at 37ºC with 100 µg/mL ampicillin to an OD600 = 1.0. Grown cells were then dispersed into 4 L of pre-warmed LB medium and grown to an OD_{600} = 0.6. IPTG was added to a final concentration of 0.5 mM in each 1 L of cells for induction. Expression of *strep-tag* MerR was induced at 37 ºC and grown for 4 hours. Bacteria were harvested by centrifugation and stored at -80 ºC for future utilization.

For the purification of *strep-tag* MerR, centrifuged cells were resuspended in 50 mM Tris, 500 mM NaCl, pH 8.1, 15 mM β-mercaptoethanol (βME, VWR), and 0.3 µM phenylmethylsulfonyl fluoride (PMSF, Sigma). Cells were lysed by French press at 4 ºC resulting in the crude cell lysate, which was centrifuged at 18,000 RPM for 1 hour at 4 ºC. Supernatant from the centrifuged cells was added to a Streptactin-XL column, which was pre-equilibrated with 50 mM Tris, 500 mM NaCl, 15 µM βME at pH 8.1, and equilibrated for 1 hour at 4 ºC to ensure complete binding. The column was washed with 1 column volume of 50 mM Tris, 500 mM NaCl, 15 mM βME at pH 8.1. Elution of the *strep-tag* MerR was achieved through the addition of 50 mM Tris, 500 mM NaCl, 15 mM βME, 50 mM biotin at pH 8.1. Protein samples were collected in 3 mL aliquots and aliquots with >95% purity, as determined by SDS-PAGE gel electrophoresis, were selected for experimentation. MerR in solution was previously found to be >95% dimerized.[37] Purified and reduced protein samples were brought into a Coy Laboratory glovebox that is constantly purged with N_2. Prior to use, *strep-tag* MerR was buffer exchanged into the

metal-free, deoxygenated ITC buffer using a Cytiva PD-10 buffer exchange column. Protein concentrations were determined by the absorbance of MerR at 280 nm (ε = 14,400 $M^{-1}cm^{-1}$) under anaerobic conditions.

3.2.4. Isothermal Titration Calorimetry

All sample preparation was completed in a Coy Laboratory glovebox, which is anaerobic through a constant purging of nitrogen. Daily, the glovebox is purged with 5% hydrogen, to reduce the platinum catalyst that maintains an anaerobic environment with a consistent oxygen concentration of <5 ppm. Prior to ITC experimentation, buffers were made metal-free through the addition of Chelex (Sigma) resin. These buffers were then filtered into acid-washed glassware and deoxygenated under vacuum. Mercury dichloride salt was weighed under aerobic conditions and brought into the glovebox for dissolution. Metal salts were dissolved in deoxygenated nanopure (> 18 MΩ) water at pH ~2 to a final concentration of 50 mM. Solutions of competing ligands were made similarly, except these were dissolved in the ITC buffer at 50 mM, when possible. Metal concentrations were confirmed through an ITC measurement of the prepared metal-buffer complex with a known concentration of a metal chelator, like EDTA, and confirmed with the known experimental binding enthalpies. Metal stock solutions were prepared and tested approximate biweekly.

To ensure anaerobic conditions, all ITC experiments were completed under a nitrogen-rich environment. Both the VP-ITC and PEAQ-ITC (Microcal, Malvern Panalytical) are housed in custom-built gloveboxes that are constantly purged with nitrogen prior to and during the ITC experiment. Titration of Hg^{2+} into apo-MerR and the MerR-*merO* complex were done with the VP-ITC, whereas titrations of apo-MerR and Hg-MerR into *merO* were done with the PEAQ-ITC. For the VP-ITC and PEAQ-ITC, injection volumes depend on the experimental system and range from 6 to10 μL for the VP-ITC and 2 to 3 μL for the PEAQ-ITC. Stirring speeds were 307 RPM (VP-ITC) and 750 RPM (PEAQ-ITC) and all ITC measurements, with both instruments, are completed at 25 ± 0.2 °C. The heat of dilution that is associated with the ligand titrated into the titrand, is determined by the heat that is measured at the end of the experiment after all binding is complete. This heat of dilution was subtracted from each data point, as this heat of dilution

occurs similarly throughout the duration of the experiment upon each injection. Each experiment was repeated in triplicate, at a minimum.

Isotherms collected on the VP-ITC were analyzed with one-binding site binding or two-binding sites fitting models included in Origin Pro data analysis software, whereas PEAQ-ITC isotherms were fit with a one-binding site fitting model provided with the Malvern Panalytical ITC data analysis software. For accurate experimental heats associated with each injection, the solutions in the cell and the syringe must be identical in the concentration and pH of the buffer.

3.3. Results and Analysis

3.3.1. Coupled Equilibria Model for the Hg-MerR-merO Complex Formation

The coupled thermodynamic analysis that describes how the binding of Hg^{2+} modulates the binding of MerR to the MerR operon, *merO*, is found in **Figure 3.3.1.1**. Previous studies had shown that MerR binds to *merO* with a high affinity in a 1:1 complex, which is modulated by the binding of Hg^{2+}.[36] Although MerR can exists in an equilibrium of monomeric, dimeric, and higher order species, under solution conditions utilized here, apo-MerR is >95% dimeric.[38] Using ITC, the buffer-independent equilibrium constant for each interaction associated with the formation of the Hg-MerR- *merO* complex at pH 7.4 was determined. This allows the free energy of all the linked equilibria within the system to be quantified. Overall, this coupled equilibrium constant, K_c^t, is found by the equilibria described in **Figure 3.1.4.2** (general scheme) and **Figure 3.3.1.1** (detailed scheme) where:

$$\Delta G_c^t = -RTlnK_c^t \qquad \textbf{Equation 3.3.1.1.}$$

This coupled equilibrium constant can describe the heterotropic coupled equilibrium thermodynamics, ΔG_c^t, ΔH_c^t, and $-T\Delta S_c^t$, which are state functions corresponding to **Figure 3.3.1.1**, defined by the **Equations 3.3.1.2 – 3.3.1.4**:

$$\Delta G_c^t = -RTln\frac{K_3K_5}{K_1K_6} = -RTln\frac{K_7}{K_2} \qquad \textbf{Equation 3.3.1.2.}$$

$$\Delta H_c^t = (\Delta H_3 + \Delta H_5) - (\Delta H_1 + \Delta H_6) = (\Delta H_7 - \Delta H_2) \qquad \textbf{Equation 3.3.1.3.}$$

$$\Delta S_c^t = (\Delta S_3 + \Delta S_5) - (\Delta S_1 + \Delta S_6) = (\Delta S_7 - \Delta S_2) \qquad \textbf{Equation 3.3.1.4.}$$

These overall coupled equilibria can be further divided into the two step-wise equilibrium constants that correspond to the successive binding of the first Hg^{2+} and the second Hg^{2+} to apo-MerR and the MerR-*merO* complex. These step-wise heterotropic coupling energies, where ΔG_c^i, ΔH_c^i, and $-T\Delta S_c^i$ are the energies for each step, i, for both the first and second binding events, can be described by:

$$\Delta G_c^1 = -RTln\frac{K_3}{K_1} = -RTln\frac{K_4}{K_2} \qquad \textbf{Equation 3.3.1.5.}$$

$$\Delta H_c^1 = (\Delta H_3 - \Delta H_1) = (\Delta H_4 - \Delta H_2) \qquad \textbf{Equation 3.3.1.6.}$$

$$-T\Delta S_c^1 = ([-T\Delta S_3] - [-T\Delta S_1]) = ([-T\Delta S_4] - [-T\Delta S_2]) \qquad \textbf{Equation 3.3.1.7.}$$

$$\Delta G_c^2 = -RTln\frac{K_5}{K_6} = -RTln\frac{K_7}{K_4} \qquad \textbf{Equation 3.3.1.8.}$$

$$\Delta H_c^2 = (\Delta H_5 - \Delta H_6) = (\Delta H_7 - \Delta H_4) \qquad \textbf{Equation 3.3.1.9.}$$

$$-T\Delta S_c^2 = ([-T\Delta S_5] - [-T\Delta S_6]) = ([-T\Delta S_7] - [-T\Delta S_4]) \qquad \textbf{Equation 3.3.1.10.}$$

Although these coupled equilibria are the theoretical equilibrium constants, K_6 is not directly observed by ITC, thus K_7 was not directly quantifiable by ITC. However, prior work, using gel shift assays, reported a value for K_7, of 3.4×10^7.[36] Utilizing ITC, all other step-wise pH-dependent, buffer-independent equilibrium constants were quantified. The thermodynamic data were then used to determine the total coupling energies of ΔG_c^t, ΔH_c^t, and $-T\Delta S_c^t$.

3.3.2. Selection of Mercury Competing Ligands

The metal-binding site on MerR is composed of 3 cysteine residues, which should result in strongly favorable mercury binding, as predicted from hard-soft acid-base theory. Thus, ITC titrations of Hg^{2+} into the binding affinities. A series of Hg-binding chelators with varying affinities for Hg^{2+} were selected and evaluated (weakest to strongest) and these include DTPA (log K = 24.6), reduced glutathione (log K = 30.9), N-acetyl-penicillamine (log K = 35.4), and penicillamine (log K = 38.3).[39–41] Of these competing ligands, only penicillamine was capable of binding Hg^{2+}

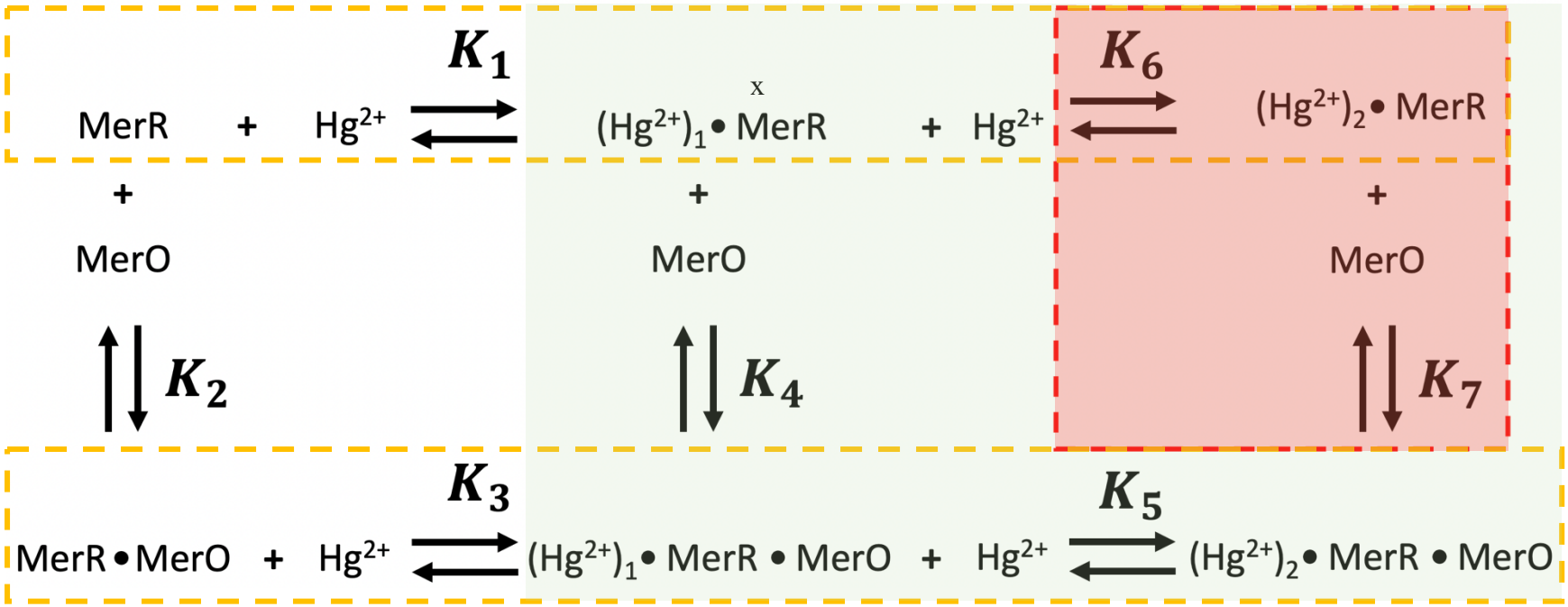

Figure 3.3.1.1. *Thermodynamic cycle that describes the formation of each metal-protein-DNA complex coupled equilibria considered herein. MerR refers to the dimer in aqueous solution. The red dashed box indicates complex formation that was not observed by ITC. The green box corresponds to heterotropic allostery, in which the binding of Hg^{2+} modulates the MerR-merO complex. The gold dashed box describes the homotropic coupling associated with Hg^{2+} binding in which the first Hg^{2+} modulates the binding of the second Hg^{2+} in both apo-MerR and in the MerR-merO complex. It is noted that the β2 from* ***Figure 3.1.4.2****. is equal to* $K_3 * K_5$.

strong enough to obtain an apparent binding affinity within the accuracy range of ITC (10^3 – 10^8). For all Hg-ligand combinations, only one binding event was observed, which corresponds to the formation of a 1:2 Hg:$MerR_{dimer}$ complex, consistent with solution-based experiments that reported only one Hg^{2+} binds to MerR when it is not bound to *merO* (**Figure 3.3.2.1**).[37,38] Systematically measuring Hg^{2+} binding to MerR with each ligand allowed the ITC results to be optimized for a detailed analysis with the Hg^{2+}-$(Pen)_2$ complex. A concentration of 500 μM penicillamine was selected over 5 mM penicillamine to prevent aberrant protein-ligand or higher-order metal-ligand complexes were forming.

3.3.3. Thermodynamics of the Mercury-Penicillamine Interaction

Unlike the case with many common ligands, such as glutathione or DTPA, the thermodynamics of formation of many metal-ligand complexes remain unknown. This is true for the Hg^{2+}-penicillamine interaction, although the relevant penicillamine pK_a's and the Hg-$(Pen)_2$ stability constants are known.[41–44] However, the enthalpy of both penicillamine deprotonation and the binding of mercury had not been reported. To determine the pH-dependent, buffer-independent binding thermodynamics for Hg-MerR with penicillamine as the competing ligand, these enthalpies must be determined.

Fortunately, by considering the competing equilibria for a titration of the Hg–DTPA complex into penicillamine in buffers with a known protonation enthalpy, the coupled Hg-penicillamine and penicillamine-deprotonation enthalpies can be quantified (**Scheme 3.3.3.1**). This coupled enthalpy, can then be used in place of the decoupled Hg-penicillamine formation and penicillamine protonation enthalpies in titrations of Hg-Pen into MerR, as long as the experimental conditions (pH, ionic strength, temperature, etc.) are identical. This was further simplified because the relevant pK_a's of both DTPA and penicillamine are known, so the number of protons that bind to the buffer at pH 7.4 in these titrations are also known. Titration of Hg-DTPA into penicillamine resulted in a stoichiometry of 0.58 ± 0.02 Hg:Pen, indicating that a Hg-$(Pen)_2$ complex forms in 50 mM Tris, 500 mM NaCl, pH 7.4. Taking the enthalpy associated with the competing equilibria into account through a *post-hoc* analysis, the buffer-independent change in enthalpy for the coupled Hg-$(Pen)_2$ formation and displacement of 1.6 H^+ from two Pen at pH 7.4 is found to be -29.7 ± 0.8 kcal/mol.

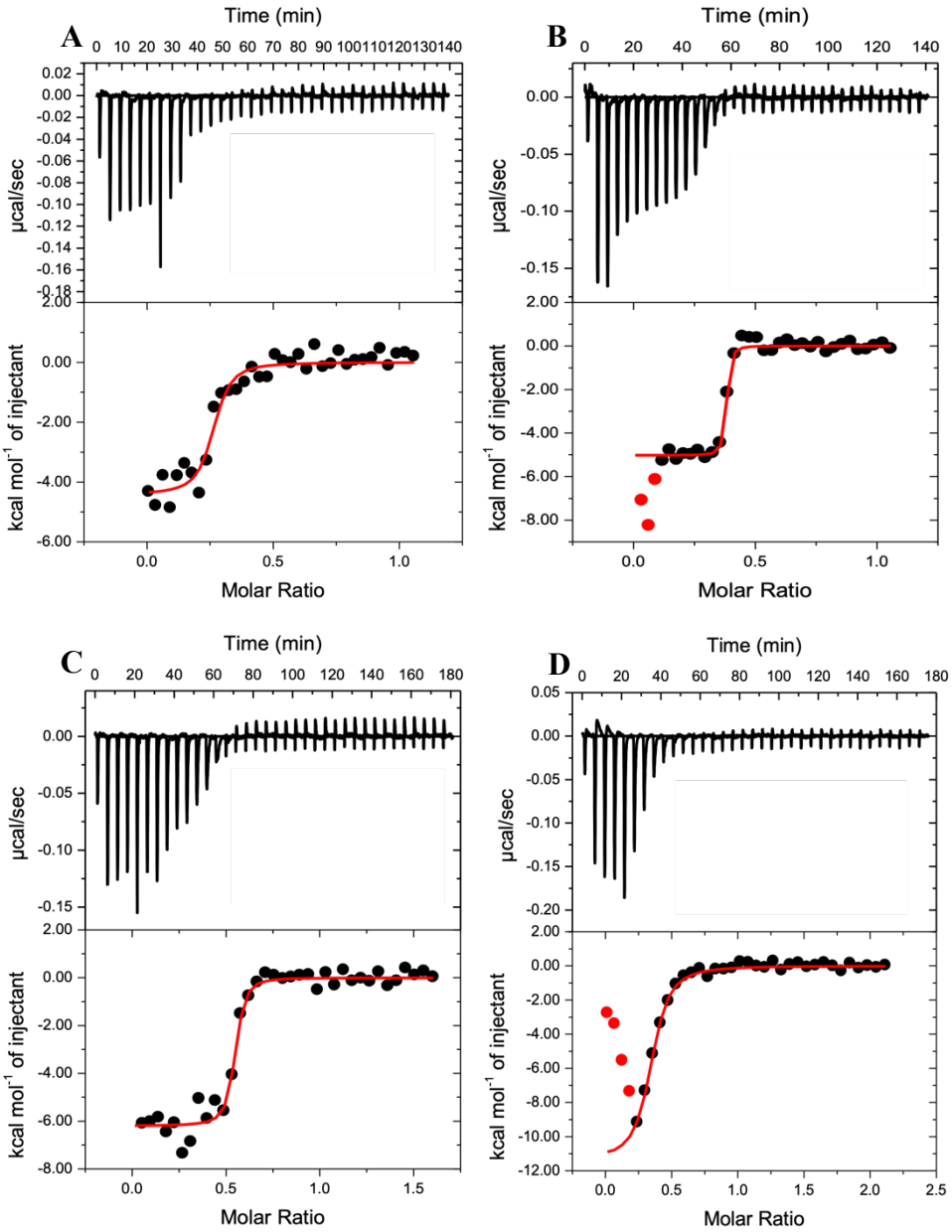

Figure 3.3.2.1. *Representative isotherms for the titration of Hg into apo-MerR in 50 mM BisTris, 500 mM NaCl, pH 7.4, and 500 µM TCEP.(A)Hg-DTPA (375 µM ligand): n = 0.255 ± 0.009, ΔH_{ITC} = -4.4 ± 0.2 kcal/mol, K_{ITC} = 1.4 (± 0.7)×10^7; (B) Hg-GSH (375 µM ligand): n = 0.370 ± 0.002, ΔH_{ITC} = -5.02 ± 0.08 kcal/mol, K_{ITC} = 4 (± 3)×10^8; (C)Hg-NAPA (375 µM): n = 0.529 ± 0.006, ΔH_{ITC} = -6.2 ± 0.1 kcal/mol, K_{ITC} = 8 (± 4)×10^7; (D) Hg-Pen (5 mM): n = 0.334 ± 0.007, ΔH_{ITC} = -11.4 ± 0.5 kcal/mol, K_{ITC} = 7 (± 1)×10^6.*

3.3.4. Hg^{2+} Binding to apo-MerR

With the thermodynamics of formation of the Hg-$(Pen)_2$ complex quantified, the buffer-independent thermodynamics of Hg^{2+} binding to MerR at pH 7.4 can now be determined. Titrations of Hg-$(Pen)_2$ into apo-MerR under anaerobic conditions, without the addition of reducing agents, were obtained in the buffers, PIPES, HEPES, BisTris, and Tris with 500 mM NaCl, at pH 7.4. A small excess of penicillamine was utilized to ensure complete metal-complex formation to prevent free metal ions from binding. These experiments are done under conditions that are far from ideal, since the high salt concentration was required to maintain apo-MerR in solution. Lower salt concentrations resulted in rapid precipitation, in agreement with prior work on MerR and MerR-family proteins.[16,37,38] These isotherms showed one inflection, which was preceded by a less exothermic binding event with a low stoichiometry (**Figure 3.3.4.1**). Low experimental heats were found for these conditions, but the peaks are well-defined and rapidly return to equilibrium. These initial peaks are possibly the binding of Hg^{2+} in other complexes when MerR is in large excess since as they show an approximate stoichiometry of ~0.25, or 1:4 Hg:$MerR_{monomer}$. This is possibly an Hg^{2+}-bridged dimer of MerR dimers. Given the lack of literature precedence for a Hg^{2+}-bridged dimer of dimers in both solution-based experiments and MerR crystal structures and may only be observed due to the unique ITC experimental conditions with large excess of MerR, these data points were masked (red data points) and not included in the analysis. The primary inflection gives in an average stoichiometry of 0.38 ± 0.06 Hg^{2+} per $MerR_{monomer}$, indicating the binding of ~1 Hg^{2+} per $MerR_{dimer}$ in solution, which is in agreement with prior findings.[37,38] Somewhat lower experimental stoichiometries than the expected 0.5 Hg^{2+} per $MerR_{monomer}$ are presumably due to protein oxidation. Average apparent thermodynamic data collected in multiple buffers, as well as condition-independent thermodynamics obtained from these experimental values, are collected in **Table 3.3.4.1**.

To accurately determine condition-independent thermodynamics, the number of protons released from or binding to the buffer must be accounted for. By plotting the buffer protonation enthalpy vs. the experimental enthalpy, the number going to or coming from the buffer can be quantified (**Figure 3.3.4.2**). As the each penicillamine

Scheme 3.3.3.1. Hess's law analysis of the enthalpy for the competing equilibria upon addition of the Hg-DTPA complex to penicillamine in 50 mM buffer (Tris), 500 mM NaCl, pH 7.4. ΔH_{ML} as the enthalpy of the Hg-DTPA formation, ΔH_{LH1} and ΔH_{LH2} are the enthalpies of the first and second DTPA protonation, respectively, ΔH_{PH} is the enthalpy of penicillamine deprotonation, ΔH_{BH} is the enthalpy of buffer-protonation, and ΔH_{MP} is the enthalpy of formation of Hg-penicillamine. The weighted sum of these enthalpies is equal to the experimental enthalpies found directly by ITC, ΔH_{ITC}, as defined by **Equation 3.3.3.1**. The coupled penicillamine deprotonation and Hg^{2+} formation enthalpies that are solved for are found in brackets in the equation.

Hg-DTPA	⇄	Hg^{2+} + DTPA	$-\Delta H_{ML}$
DTPA + H^+	⇄	DTPA–H	1.0 $n_{H+}\Delta H_{LH1}$
DTPA–H + H^+	⇄	$DTPA–H_2$	0.91 $n_{H+}\Delta H_{LH2}$
$2Pen–H_{1.6}$	⇄	$2Pen + H^+_{1.6}$	$-1.6\ n_{H+}\Delta H_{PH}$
$H^+_{0.31}$ + Buffer	⇄	$Buffer–H_{0.09}$	0.31 $n_{H+}\Delta H_{BH}$
Hg^{2+} + 2Pen	⇄	$Hg–(Pen)_2$	ΔH_{MP}

$$\Delta H_{ITC} = (-\Delta H_{ML}) + (1.0 \times \Delta H_{LH1}) + (0.91 \times \Delta H_{LH2}) + (0.31 \times \Delta H_{BH}) + [(-1.6 \times \Delta H_{PH}) + \Delta H_{MP}]$$

Equation. 3.3.3.1

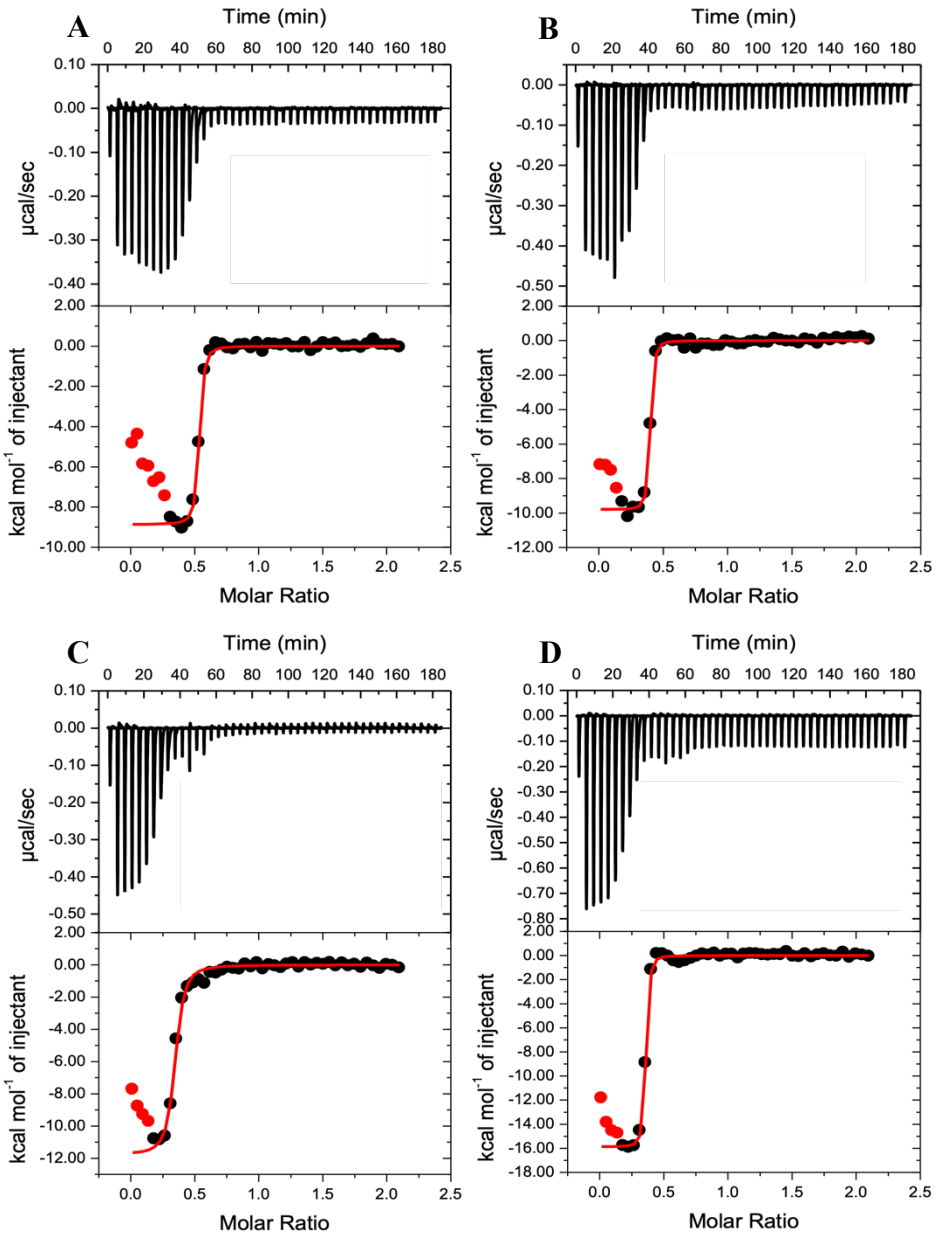

Figure 3.3.4.1. *Representative isotherms associated with the titration of 200 µM Hg-(Pen)$_2$ into 20 µM apo-MerR$_{monomer}$ in 50 mM Buffer, 500 mM NaCl, pH 7.4, and 500 µM Penicillamine. (A) PIPES: n = 0.516 ± 0.001, ΔH_{ITC} = -8.87 ± 0.09 kcal/mol, K_{ITC} = 9 (± 2) × 10^7; (B) HEPES: n = 0.380 ± 0.001, ΔH_{ITC} = -9.8 ± 0.1 kcal/mol, K_{ITC} = 1.2 (± 0.3) × 10^8; (C) BisTris: n = 0.330 ± 0.003, ΔH_{ITC} = -11.8 ± 0.3 kcal/mol, K_{ITC} = 1.4 (± 0.2) × 10^7; (D) Tris: n = 0.341 ± 0.001, ΔH_{ITC} = -15.9 ± 0.1 kcal/mol, K_{ITC} = 1.3 (± 0.2) × 10^8.*

Table 3.3.4.1. *Apparent and condition-independent thermodynamics associated with the titration of 200 μM Hg^{2+} into 20 μM apo-$MerR_{monomer}$ in 50 mM Buffer, 500 mM NaCl, pH 7.4 and 500 μM penicillamine. Condition-independent thermodynamics are buffer-independent values determined at pH 7.4 by taking all associated competing equilibria into account, including the Hg-$(Pen)_2$ and $(Pen)_2$-H_2 thermodynamics described in the text*.

Hg-$(Pen)_2$ into apo-$MerR_{Monomer}$	**Buffer**	**n**	**K_{ITC}**	**ΔH_{ITC} (kcal/mol)**	**$K_{(Hg)\text{-}MerR}$**	**$\Delta H_{Hg\text{-}MerR}$ (kcal/mol)**
Site 1	**PIPES**	0.47 ± 0.05	1.2 (± 0.6) × 10^8	-9.8 ± 0.8	1.4 (± 0.5) × 10^{49}	-35.1 (± 1.2)
	HEPES	0.36 ± 0.03	2 (± 3) × 10^8	-11.4 ± 1.6	2 (± 1) × 10^{49}	-35.1(± 1.8)
	BisTris	0.33 ± 0.01	3 (± 2) × 10^7	-12.4 ± 1.6	3 (± 1) × 10^{48}	-34.8 (± 1.0)
	TRIS	0.38 ± 0.05	3 (± 2) × 10^8	-15.7 ± 0.7	3 (± 1) × 10^{49}	-34.9 (± 1.0)
Average		**0.38 ± 0.06**			**2 (± 1) × 10^{49}**	**-34.9 ± 0.1**

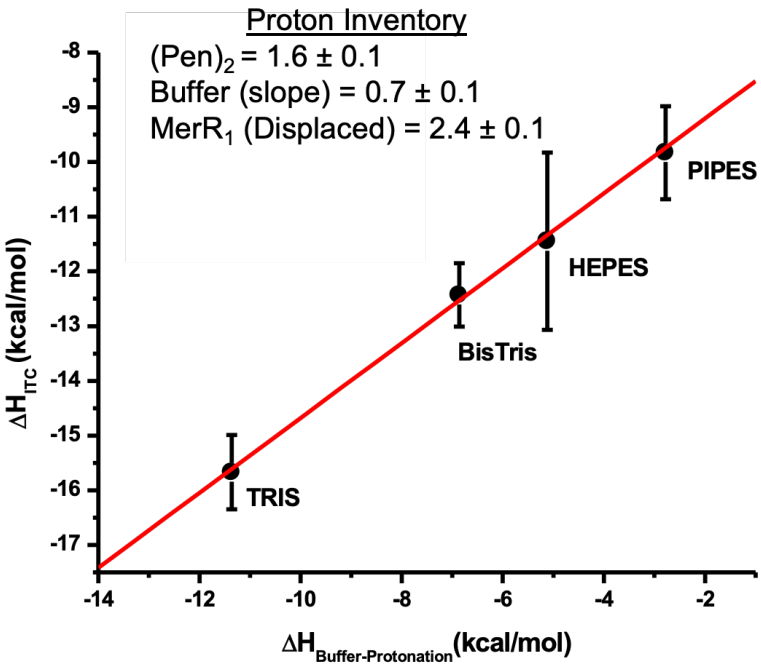

Figure 3.3.4.2. *Proton plot associated with the titration of Hg-(Pen)$_2$ into apo-MerR. The slope, calculated from the linear regression analysis, indicates the number of protons that associate with or dissociate from the buffer; thus 0.7 ± 0.1 protons bind to the buffer for this titration. When Hg^{2+} dissociates from the Hg-(Pen)$_2$ complex, each penicillamine is protonated by 0.8 protons, for a total of 1.6 protons. Finally, the number of protons to account for these (de)protonations reveal that Hg^{2+} displaces 2.4 ± 0.1 protons from apo-MerR when it binds to the metal binding site. Note that this is the number of protons per Hg^{2+} binding to the MerR dimer ,which includes the three cysteines in the metal-binding site.*

would bind 0.8 protons at pH 7.4 after the release of Hg^{2+}, a proton inventory can be determined. This reveals that 2.3 ± 0.1 protons are displaced from apo-$MerR_{dimer}$ when Hg^{2+} binds.

By rearranging **Equation 3.3.3.1**, the condition-independent Hg-$MerR_{dimer}$ enthalpy can be quantified. By taking the enthalpies of all competing equilibria into account, we can show that:

$$\Delta H_{Hg-MerR_{dimer}} = \Delta H_{ITC} + \Delta H_{Hg-(Pen)_2} - \left(n_{H^+} \times \Delta H_{Buffer-H}\right) \quad \textbf{Equation 3.3.4.1}$$

Where:

$$\Delta H_{Hg-(Pen)_2} = \Delta H_{Hg-(Pen)_2} - \Delta H_{(Pen)_2-H_{1.6}} \quad \textbf{Equation 3.3.4.2}$$

This results in a buffer-independent enthalpy for 1 Hg^{2+} binding to the MerR dimer of ΔH = -34.9 ± 0.1 kcal/mol at pH 7.4.

Similar to the quantification of the condition-independent binding enthalpy, an analysis for the buffer-independent formation constant of the 1 Hg^{2+}:$MerR_{dimer}$ (0.5 Hg:$MerR_{monomer}$) takes all competing equilibria into account at pH 7.4. The condition-independent binding constant is calculated with,

$$K_{Hg-MerR_{dimer}} = K_{ITC} \times (a_{proton}) \times \left(1 + K_{Hg-(Pen)_2}[Pen]\right) \quad \textbf{Equation 3.3.4.3}$$

where α_{proton} is the competition from the proton with Hg^{2+} for the binding to MerR. This *post-hoc* analysis to determine the condition-independent equilibrium constant for Hg^{2+} binding to $MerR_{dimer}$ gives an average value of $K_{Hg\text{-}MerR} = 2\ (\pm\ 1) \times 10^{49}$. This binding corresponds to K_1 in **Figure 3.3.1.1**.

3.3.5. Mercury Binding to the MerR-merO Complex

Similar to the binding of Hg^{2+} to apo-MerR, it may be expected that the binding of Hg^{2+} to MerR in the MerR-*merO* complex would also require a strong competing ligand. Therefore, the Hg-$(Pen)_2$ complex was titrated into the MerR-*merO* complex, in 50 mM Buffer, 500 mM NaCl, pH 7.4 and excess penicillamine and a molar ratio of 1:4 $MerR_{dimer}$:*merO* (1:2 $MerR_{monomer}$:*merO*). These conditions prevent aberrant metal binding to apo-MerR as excess *merO* ensures that Hg^{2+} binds to MerR in the MerR-*merO* complex, not free apo-MerR. **Figure 3.3.5.1** shows the representative isotherms of the titration of the Hg-$(Pen)_2$ complex into the MerR-*merO* complex in a series of buffers. These isotherms show two binding events and are fit with a two-site binding model with the first

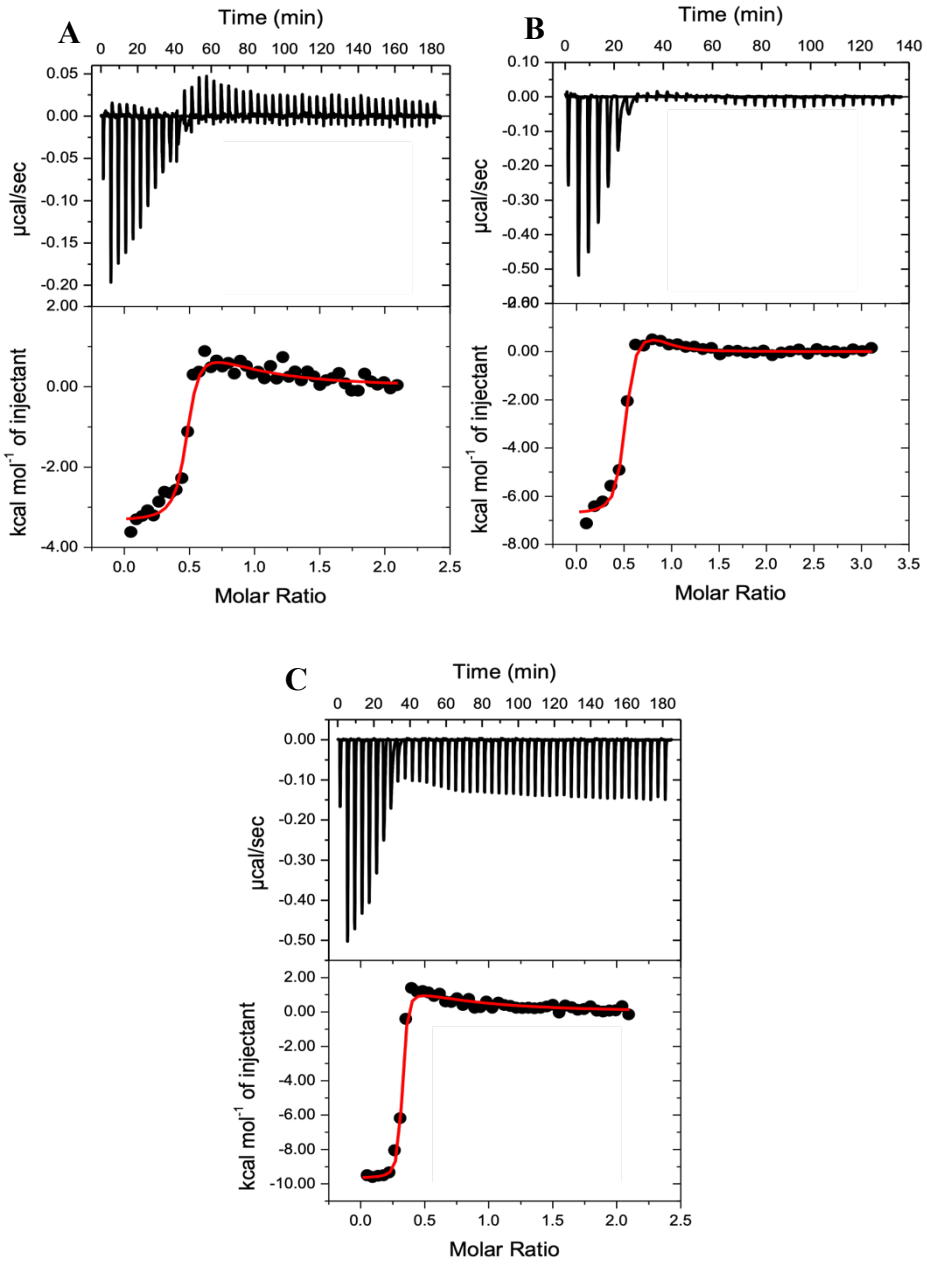

Figure 3.3.5.1. *Representative isotherms associated with the titration of 200 µM Hg^{2+} bound to penicillamine, forming the Hg-$(Pen)_2$ complex, into 20 µM $MerR_{monomer}$*-merO *(1:2) complex in 50 mM Buffer, 500 mM NaCl, pH 7.4, and 500 µM penicillamine. Isotherms were fit with a two-site fitting model. (A) PIPES (Site 1): n_1 = 0.46 ± 0.02, ΔH_1 = -3.3 ± 0.1 kcal/mol, $K_1 = 2 (\pm 3) \times 10^7$; (Site 2): n_2 = 0.39 ± 0.5, ΔH_2 = 2 ± 3 kcal/mol, $K_2 = 2 (\pm 2) \times 10^5$; (B) BisTris (Site 1): n_1 = 0.47 ± 0.01, ΔH_1 = -6.7 ± 0.1 kcal/mol, $K_1 = 1 (\pm 2) \times 10^8$; (Site 2): n_2 = 0.4 ± 0.1, ΔH_2 = 1.0 ± 0.4 kcal/mol, $K_2 = 1 (\pm 2) \times 10^6$. (C) TRIS (Site 1): n_1 = 0.306 ± 0.003, ΔH_1 = -9.7 ± 0.1 kcal/mol, $K_1 = 1 (\pm 1) \times 10^8$; (Site 2): n_2 = 0.5 ± 0.5, ΔH_2 = 3 ± 3 kcal/mol, $K_1 = 1 (\pm 1) \times 10^5$.*

binding event occurring at an average stoichiometry of 0.39 ± 0.06 and the second binding event has a stoichiometry of n = 0.36 ± 0.09. These stoichiometries are the binding of Hg^{2+} per monomer of MerR, which allows for comparisons to the apo-MerR experiments. These stoichiometries indicate that 1 Hg^{2+} binds to the first site on the $MerR_{dimer}$, followed by 1 Hg^{2+} binding to the second site on the dimer. This supports the proposed mechanism that the second mercury binding site on MerR is only accessible when MerR is bound to its operon. To determine the proton displacement from each binding site, the buffer protonation enthalpy is plotted against the experimental enthalpy, which show that 0.78 ± 0.07 protons bind to the buffer in the first binding event and -0.1 ± 0.1 protons are released from the buffer in the second binding event (**Figure 3.3.5.2**). These values, along with the 1.6 protons that bind to the two penicillamines upon the dissociation of Hg^{2+}, show that Hg^{2+} binding to the first site on MerR displaces 2.4 ± 0.1 protons, whereas the second Hg^{2+} displaces 1.5 ± 0.1 protons. The experimental thermodynamics for the first and second binding events can then be utilized to quantify the buffer-independent binding thermodynamics at pH 7.4. The average apparent thermodynamics, and a summary of the condition-independent binding affinities and enthalpies at pH 7.4 are shown in **Table 3.3.5.1**.

By taking the enthalpy associated with the competing equilibria into account, the condition-independent enthalpy for both the first and second Hg^{2+} binding to MerR in the MerR-*merO* complex can be quantified. These are the enthalpies associated with K_3 and K_5 in **Figure 3.3.1.1**. The condition-independent enthalpy of the first and second binding events can be described by:

$$\Delta H_{Hg-MerR} = \Delta H_{ITC} + \Delta H_{Hg-(Pen)_2} - (n_{H^+}\Delta H_{Buffer-H}) \qquad \textbf{Equation 3.3.5.1}$$

where ΔH_{ITC} is the buffer-dependent experimental enthalpy at pH 7.4, $\Delta H_{Hg\text{-}(Pen)2}$ is the coupled enthalpy associated with the formation of the Hg-$(Pen)_2$ binding and enthalpy of penicillamine deprotonation, n_{H+} is the number of protons that bind to the buffer after their displacement from MerR, and $\Delta H_{Buffer\text{-}H}$ is the buffer-specific protonation enthalpy. This reveals that the average buffer-independent enthalpies for the first and second Hg^{2+} binding to MerR in the MerR-*merO* complex are ΔH_1 = -28.2 ± 0.6 kcal/mol and ΔH_2 = -25.5 ± 1.1 kcal/mol, respectively. Average condition-independent thermodynamics for the first and second Hg^{2+} binding at pH 7.4 are shown in **Table 3.3.5.1**.

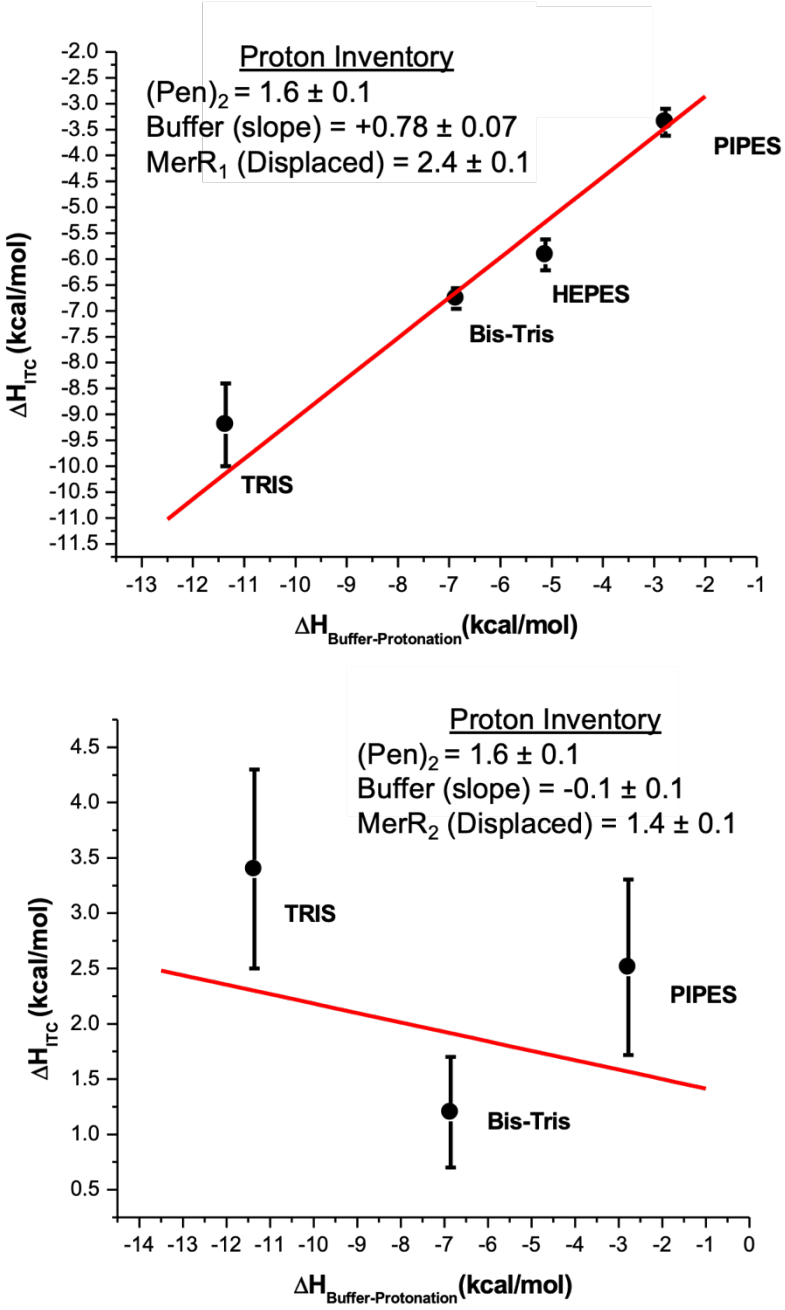

Figure 3.3.5.2. *Proton plots associated with the titration of Hg-(Pen)$_2$ into the MerR-*merO *(1:2) complex. The slope, calculated from a linear regression analysis, represents the number of protons that associate or dissociate from the buffer. When Hg^{2+} dissociates from the Hg-(Pen)$_2$ complex, each penicillamine is protonated by 0.8 protons, for a total of 1.6 protons, which is the same for both binding events. Finally, this proton inventory shows that Hg^{2+} displaces 2.4 protons from MerR in the first binding event and 1.4 protons in the second binding event.*

Table 3.3.5.1. *Average experimental binding affinity (K_{ITC}) and enthalpy (ΔH_{ITC}), along with calculated standard deviations from at least 3 independent experiments, are shown for titrations of the Hg-$(Pen)_2$ complex into the MerR-merO (1:4) complex. Condition-independent thermodynamics are buffer-independent values determined at pH 7.4 by taking all associated competing equilibria into account, including the Hg-$(Pen)_2$ and $(Pen)_2$-H_2 thermodynamics described in the text.*

Hg into MerR-*merO*	**Buffer**	**n**	**K_{ITC}**	**ΔH_{ITC} (kcal/mol)**	**$K_{Hg\text{-}MerR\text{-}merO}$**	**$\Delta H_{(Hg)\text{-}MerR\text{-}merO}$ (kcal/mol)**
Site 1	PIPES	0.44 ± 0.03	5 (± 2)×10^7	-3.4 ± 0.3	5 (± 2)×10^{48}	-27.2 (± 0.8)
	BisTris	0.39 ± 0.06	2 (± 2) X10^8	-6.8 ± 0.2	1.7 (± 0.9)×10^{49}	-28.6 (± 0.8)
	TRIS	0.33 ± 0.05	1.1 (± 0.5)×10^8	-9.2 ± 0.8	1.3 (± 0.4)×10^{49}	-27.2 (± 1.1)
Average		**0.39 ± 0.06**			**1 (± 0.6)×10^{49}**	**-28.2 ± 0.6**
Site 2	PIPES	0.37 ± 0.05	2.0 (± 0.8)×10^5	+2.5 ± 0.8	2.2(± 0.4)×10^{46}	-24.9 (± 1.1)
	BisTris	0.35 ± 0.10	2 (± 2) X10^6	+1.2 ± 0.5	1.8 (± 1.0)×10^{47}	-26.7 (± 0.9)
	TRIS	0.38 ± 0.12	1.0 (± 0.2)×10^5	+3.4 ± 0.9	1 (± 0.2)×10^{46}	-24.9 (± 1.2)
Average		**0.36 ± 0.09**			**7 (± 9)×10^{46}**	**-25.5 ± 1.0**

Quantification of the condition-independent affinity of the MerR-*merO* complex for Hg^{2+}, using penicillamine as a competing ligand, follows a similar analysis as used for Hg^{2+} binding to MerR. The equilibrium constants for each of the competing equilibria are included to establish the buffer-independent binding affinity, which is shown with,

$$K_{Hg-MerR-MerO} = K_{ITC} \times (a_{proton}) \times \left(1 + K_{Hg-(Pen)_2}[Pen]\right) \quad \textbf{Equation 3.3.5.2}$$

where α_{proton} is the competition from the proton associated with Hg^{2+} binding to MerR in the MerR-*merO* complex. This *post-hoc* analysis to determine the condition-independent affinity of the MerR-*merO* complex for Hg^{2+} shows an average value of $K_{(Hg)1\text{-MerR-}merO} = 1 (\pm 0.6)\times10^{49}$ for the first binding event, and $K_{(Hg)2\text{-MerR-}merO} = 7 (\pm 9)\times10^{46}$ for the second binding event. These correspond to K_3 and K_5 in **Figure 3.3.1.1**.

3.3.6. Thermodynamics of the MerR-merO Complex Formation

Unlike the binding of metals to proteins, the thermodynamics of a protein binding to a protein or DNA are typically less complicated. This comes from the fewer competing equilibria that contribute to the experimental thermodynamics, which appears to be true for MerR binding to *merO*. The proposed competing equilibria are shown in **Scheme 3.3.6.1**, which include the deprotonation of MerR, buffer protonation, and the formation of the MerR-*merO* complex. Other competing equilibria that are not explicitly defined may also contribute and this includes the Na^+-DNA interaction. However, in a comparison with the titration of the $(Hg)_1$-MerR complex titrated into *merO* (*vide infra*), the salt-DNA interactions would be similar and this thermodynamic contribution would be comparable.

Titrations of apo-MerR into *merO* show low experimental heats that are exothermic with a binding stoichiometry of 1.0 ± 0.3 $MerR_{monomer}$ binding per *merO*, as depicted by the single binding event, which was obtained with a one-site fitting model (**Figure 3.3.6.1**). This stoichiometry suggests that each $MerR_{monomer}$ would bind to *merO,* which has two $MerR_{monomer}$ binding sites with dyad symmetry (GTACnnnnGTAC, **Figure 3.1.3.1**). The stoichiometry indicates that each $MerR_{monomer}$ binds to one MerR site on *merO*, which is equivalent to the $MerR_{dimer}$ binding to both identical MerR binding sites on *merO*. A summary of the experimental binding thermodynamics, as well as the condition-independent thermodynamics at pH 7.4, is shown in **Table 3.3.6.1**.

Scheme 3.3.6.1. Hess's law analysis of the enthalpies of competing equilibria for the titration of apo-MerR into *merO* in 50 mM buffer and 500 mM NaCl, pH 7.4. ΔH_{PH} is the enthalpy for the deprotonation of apo-MerR, ΔH_{BH} is the enthalpy of buffer-protonation, and ΔH_{PD} is the enthalpy of formation of the MerR-*merO* complex. The sum of these enthalpies is equal to the experimental enthalpy found directly by ITC, ΔH_{ITC}, as defined by **Equation 3.3.6.1**.

$MerR + H_x$	$\rightleftarrows$	$MerR–H^+_x$	$(n_{H^+}\Delta H_{PH})$
$H^+_x–Buffer$	$\rightleftarrows$	$Buffer + H_x$	$–(n_{Hx}\Delta H_{BH})$
$MerR + merO$	$\rightleftarrows$	$MerR–merO$	ΔH_{PD}

$$\Delta H_{ITC} = (n_{H^+}\Delta H_{PH}) – (n_{Hx}\Delta H_{BH}) + \Delta H_{PD} \quad \textbf{Equation. 3.3.6.1}$$

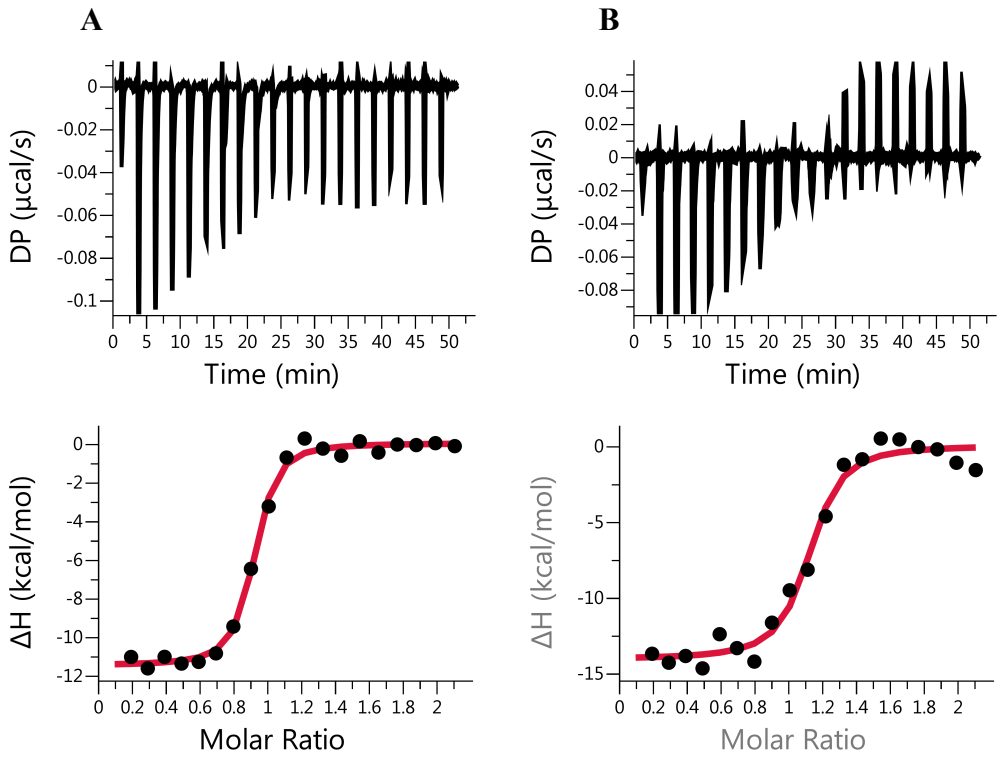

Figure 3.3.6.1. *Representative isotherms associated with the titration of 40 µM apo-MerR$_{monomer}$ into 4 µM* merO *in 50 mM Buffer, 500 mM NaCl, pH 7.4.(A) BisTris: n = 0.869 ± 0.008, ΔH_{ITC} = -11.50 ± 0.2 kcal/mol, K_{ITC} = 5.6 (± 0.1)×10^7; (B) PIPES: n = 1.07 ± 0.02, ΔH_{ITC} = -14.10 ± 0.7 kcal/mol, K_{ITC} =3 (± 1)×10^7.*

Table 3.3.6.1. *Summary of thermodynamic data from the titration of apo-MerR into* merO*. Both the apparent binding affinity (K_{ITC}) and apparent binding enthalpy (ΔH_{ITC}) and the buffer-independent binding affinities ($K_{apoMerR\text{-}merO}$) and enthalpies ($\Delta H_{apoMerR}$merO) at pH 7.4 are the average of at least 3 independent experiments and the error is the standard deviation from these sets of experiments.*

Apo-MerR into *merO*	**Buffer**	**n**	**K_{ITC}**	**ΔH_{ITC} (kcal/mol)**	**$K_{apoMerR\text{-}merO}$**	**$\Delta H_{apoMerR\text{-}merO}$ (kcal/mol)**
Site 1	PIPES	1.3 ± 0.1	5 (± 2)×10^7	-15.1 ± 0.8	5 (± 2)×10^7	-17.4 (± 0.9)
	BisTris	0.80 ± 0.08	6 (± 5)×10^7	-11.7 ± 1.2	6 (± 5)×10^7	-17.2 (± 1.3)
Average		**1.0 ± 0.3**			**5.7 (± 0.7)×10^7**	**-17.3 ± 0.1**

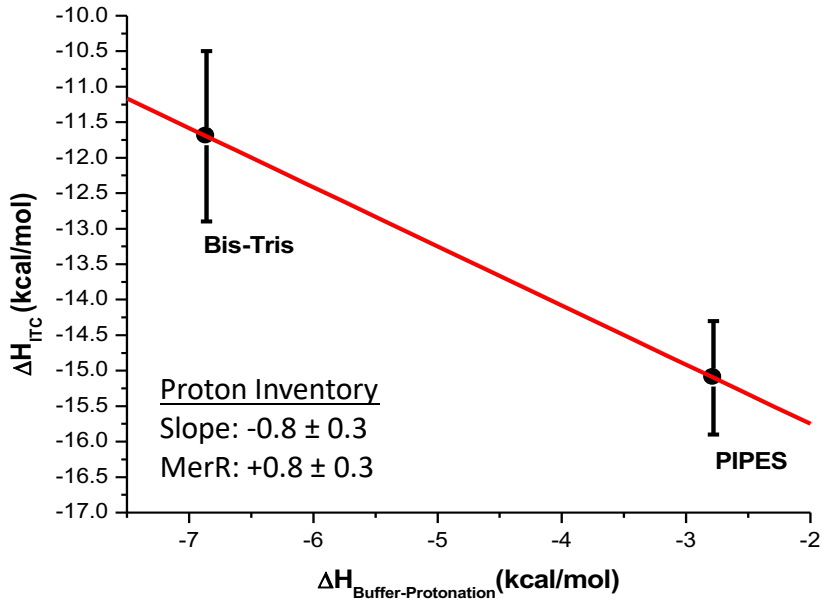

Figure 3.3.6.2. *Quantification of the number of protons that dissociate from the buffer when 40 μM apo-MerR binds to 4 μM* merO *in 50 mM buffer, 500 mM NaCl, pH 7.4. The slope from the linear regression analysis shows that -0.8 ± 0.3 protons leave the buffer to bind to the apo-MerR-*merO *complex. Error was determined by taking the average of the maximum and minimum slope.*

To quantify any protons that are displaced or bind when apo-MerR binds to *merO*, buffer protonation enthalpy ($\Delta H_{Buffer\text{-}protonation}$) is plotted against the

To quantify any protons that are displaced or bind when apo-MerR binds to *merO*, buffer protonation enthalpy ($\Delta H_{Buffer\text{-}protonation}$) is plotted against the experimental enthalpy (ΔH_{ITC}) (**Figure 3.3.6.2**). A linear regression analysis gives the slope of this plot, which shows that 0.8 protons dissociate from buffer and bind to the apo-MerR-*merO* complex when it forms.

With the number of protons that dissociate from buffer quantified the buffer-independent binding thermodynamics at pH 7.4 can be determined. By rearranging **Equation 3.3.6.1**, the enthalpy associated with the formation of the MerR-*merO* complex and its protonation can be solved,

$\Delta H_{MerR-MerO-H} = (\Delta H_{PD} + [n_{H^+}\Delta H_{PH}]) = \Delta H_{ITC} + (n_{H_x^+}\Delta H_{BH})$ ***Equation* 3.3.6.2.**

The average condition-independent binding enthalpy is –17.3 ± 0.1 kcal/mol.

Similarly, using these same competing equilibria, the buffer-independent equilibrium constant for the formation of the MerR-*merO* complex at pH 7.4 is described by:

$$K_{apoMerR-MerO} = K_{ITC} \qquad \textbf{\textit{Equation}}\ \textbf{3.3.6.3.}$$

with the experimental binding affinity equal to the buffer-independent binding affinity at pH 7.4. With this analysis, the affinity of *merO* for apo-MerR is equal to $K_{MerR\text{-}merO} = 5.7\ (\pm\ 0.7)\times10^7$, which is in agreement with results from previous gel shift assays that had determined an equilibrium constant of $K_{MerR\text{-}merO} = 3.42\times10^7$.[36] These binding thermodynamics are summarized in **Table 3.3.6.1**. and correspond to K_2 in **Figure 3.3.1.1**.

3.3.7. Binding of Mercury-bound-MerR to merO

It was previously shown that titration of Hg^{2+} into apo-MerR resulted in the binding of 1 Hg^{2+} per MerR dimer, with no evidence of Hg^{2+} binding to the second metal binding site when MerR is not bound to *merO*. Examining **Figure 3.3.1.1**, this indicates that K_6 is too small to be determined by ITC. This makes the quantification of K_7 in the same figure difficult by ITC. Titrations of MerR into *merO* under conditions of large Hg^{2+} excess may favor the formation, and subsequent binding of $(Hg)_2$-MerR to *merO*, but this is difficult to show experimentally. However, prior work that utilized gel-shift assays to quantify formation of the Hg-MerR-*merO* complex reported $K = 8.55\times10^6$, which corresponds to K_7 in **Figure 3.3.1.1**. [36] This suggests that if the linked equilibrium constant, K_4, can be

determined, then it can be used to solve for K_6. Thus, ITC experiments were undertaken to measure the binding of the Hg–MerR complex to *merO*.

Solutions of 40 μM Hg-MerR (1:1) were titrated into 4 μM *merO* in 50 mM buffer, 500 mM NaCl, pH 7.4 (**Figure 3.3.7.1**). These isotherms show a single weakly exothermic binding event, which was fit to a one-site fitting model. Note that this binding is done with in a slight excess of Hg^{2+}, yet no evidence of a second Hg^{2+} binding was observed, as this should result in large exothermic heats, given the thermodynamics associated with the titration of Hg^{2+} into the MerR-*merO* complex (*vide supra*). Furthermore, if any buffer-bound mercury was binding in these experiments, a stronger binding would be observed, as Hg^{2+} binds with K ~10^{46}, which was not observed in these titrations. The experimental and condition-independent thermodynamics for Hg-MerR binding to *merO* are shown in **Table 3.3.7.1**.

The *post-hoc* analysis associated with the binding of Hg-MerR to *merO* is identical to that of apo-MerR binding to *merO*, including the general competing equilibria in **Scheme 3.3.6.1**. First, buffer protonation must be determined for a proton inventory. Plotting the buffer protonation enthalpy vs. the experimental enthalpy, and determining the slope through a linear regression analysis, shows that 1.9 ± 0.4 protons dissociate from the buffer and bind to the Hg-MerR-*merO* complex (**Figure 3.3.7.2**).

With the number of protons that bind upon Hg-MerR-*merO* complex formation, the buffer-independent binding enthalpy at pH 7.4 can be determined by accounting for the enthalpies of all competing equilibria. This is described by:

$$\Delta H_{Hg-MerR-MerO-H} = (\Delta H_{MPD} + [n_{H^+}\Delta H_{MPH}]) = \Delta H_{ITC} + (n_{H_x^+}\Delta H_{BH}) \quad \textbf{Equation 3.3.7.1.}$$

The average condition-independent enthalpy associated with the formation of the Hg-MerR-*merO* complex is ΔH = -23.29 ± 0.09 kcal/mol at pH 7.4, as shown in **Table 3.3.7.1**. Likewise, the quantification of the binding affinity, like the binding of apo-MerR to *merO*, is equal to the experimental K_{ITC},

$$K_{Hg-MerR-MerO} = K_{ITC} \quad \textbf{Equation 3.3.7.2.}$$

The average equilibrium constant for the formation of the Hg-MerR-*merO* complex, K4 in

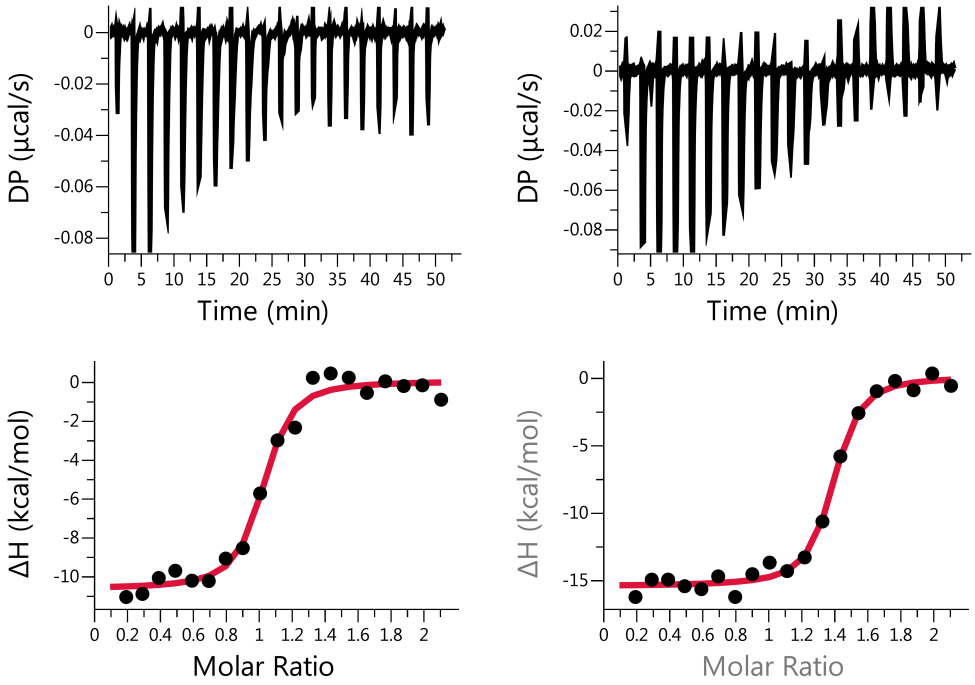

Figure 3.3.7.1. *Representative isotherms associated with the titration of 40 µM Hg-MerR into 4 µM* merO *in 50 mM Buffer, 500 mM NaCl, pH 7.4.(A) BisTris: n = 0.975 ± 0.02, ΔH_{ITC} = -10.7 ± 0.4 kcal/mol, K_{ITC} = 3.4 (± 0.9)×10^7; (B) PIPES: n = 1.34 ± 0.01, ΔH_{ITC} = -15.5 ± 0.4 kcal/mol, K_{ITC} =5.7 (± 0.1)×10^7.*

Table 3.3.7.1. *Summary of experimental binding thermodynamics for the titration of Hg-MerR$_{monomer}$ (1:1) into* merO *in 50 mM Buffer, 500 mM NaCl, pH 7.4. Buffer-independent binding thermodynamics at pH 7.4 are shown for the formation of the Hg-MerR-merO complex.*.

Hg-MerR into *merO*	**Buffer**	**n**	**K_{ITC}**	**ΔH_{ITC} (kcal/mol)**	**$K_{Hg\text{-}MerR\text{-}merO}$**	**$\Delta H_{Hg\text{-}MerR\text{-}merO}$ (kcal/mol)**
Site 1	PIPES	1.3 ± 0.2	2 (± 2)×10^7	-18.0 ± 2.1	2 (± 2)×10^7	-23.2 (± 2.2)
	BisTris	0.9 ± 0.1	1.2 (± 0.9)×10^8	-10.3 ± 1.2	1.2 (± 0.9)×10^8	-23.4 (± 1.2)
Average		**1.1 ± 0.3**			**8 (± 7)×10^7**	**-23.29 ± 0.09**

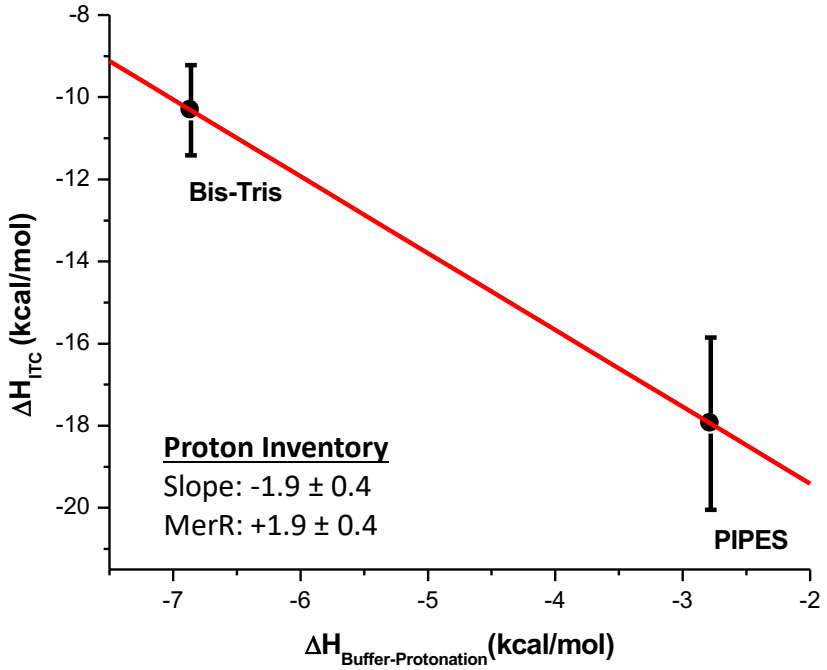

Figure 3.3.7.2. *Quantification of the number of protons that dissociate from the buffer when 40 μM Hg-MerR is titrated into 4 μM* merO *in 50 mM buffer, 500 mM NaCl, pH 7.4. The slope of the linear regression analysis shows that 1.9 ± 0.4 protons leave the buffer and bind to the Hg-MerR-*merO *complex upon its formation. Error was determined by taking the average of the maximum and minimum slope.*

Figure 3.3.1.1, is $K_{Hg\text{-}MerR\text{-}merO} = 8\ (\pm\ 7)\times10^7$. A summary of the condition-independent binding thermodynamics at pH 7.4 are shown in **Table 3.3.7.1**.

3.3.8. Coupling Energies

Control of the linked equilibria (**Figure 3.1.4.2** and **Figure 3.3.1.1**) is readily described by the heterotropic coupling energies, ΔG_c^t, ΔH_c^t, and $-T\Delta S_c^t$ as defined by **Equations 3.3.1.2** to **3.3.1.4**. These are the thermodynamics of the equilibrium:

$$(Hg^{2+})_2MerR + MerR{\bullet}MerO \rightleftharpoons (Hg^{2+})_2MerR{\bullet}MerO + MerR \quad \textbf{Equation 3.3.8.1.}$$

Thermodynamic cycles, and their subsequent coupled free energies, can be used to determine the homotropic and heterotropic thermodynamics for Hg^{2+} binding to apo-MerR and Hg^{2+} binding to the MerR-*merO* complex. **Table 3.3.8.1** summarizes all *vertical* (K_2, K_4, and K_7) and *horizontal* (K_1, K_6, K_3, and K_5) equilibrium constants and thermodynamics in **Figure 3.3.1.1** that are known. Differences between these values can quantify the thermodynamics of the heterotropic and homotropic allostery that modulate the binding that controls *mer* transcription.

The thermodynamics of the homotropic and heterotropic allosteric coupling are summarized in **Table 3.3.8.2**. The overall heterotopic coupling energy, ΔG_c^t, is -0.9 kcal/mol, indicating weakly positive allosteric regulation of *merO* mediated by the binding of Hg^{2+}. This assumes that K_7, measured previously by a gel shift assay accurately quantifies that binding of $(Hg)_2$-MerR to *merO*. Literature values for the equilibrium constant associated with the formation of the $(Hg)_2$-MerR-*merO* complex allow the quantification of K_6, the equilibrium constant for Hg^{2+} filling the second metal binding site of apo-MerR, which was not observed experimentally with ITC. Two possibilities exist for this unobserved binding: (1) the binding of Hg^{2+} to fill the second metal binding site of apo-MerR is not occurring, due to strong negative cooperativity of the first Hg^{2+} or (2) the calculated K_6 would be the observed equilibrium constant if the metal binding site was accessible for binding.

Table 3.3.8.1. *Summary of the average buffer-independent thermodynamics for the binding equilibria observed by ITC or by gel-shift assay at pH 7.4, 25.0 °C in 50 mM buffer, 500 mM NaCl.*

Site 1				Site 2			
K_1[a]	**ΔG_1**	**ΔH_1**	**$-T\Delta S_1$**	**K_2[a]**	**ΔG_2**	**ΔH_2**	**$-T\Delta S_2$**
Hg ⟶ apoMerR (Pen)							
K_1	ΔG_1	ΔH_1	$-T\Delta S_1$	K_6	ΔG_6	ΔH_6	$-T\Delta S_6$
$2 (\pm 1)\times 10^{49}$	–67.0 ± 0.6	–34.9 ± 0.1	–32.1 ± 0.5	6×10^{47}	–65	—	—
Hg ⟶ MerR●merO (Pen)							
K_3	ΔG_3	ΔH_3	$-T\Delta S_3$	K_5	ΔG_5	ΔH_5	$-T\Delta S_5$
$1 (\pm 0.6)\times 10^{49}$	–66.8 ± 0.4	–28.2 ± 0.6	–38.6 ± 0.7	$7 (\pm 9)\times 10^{46}$	–63.4 ± 0.8	–25.5 ± 1.1	–37.9 ± 0.6
MerR ⟶ *merO*							
K_2	ΔG_2	ΔH_2	$-T\Delta S_2$				
$5.7 (\pm 0.7)\times 10^{7}$	–10.57 ± 0.07	–17.3 ± 1.3	+6.7 ± 0.2				
(Hg)1●MerR ⟶ *merO*							
K_4	ΔG_4	ΔH_4	$-T\Delta S_4$				
$8 (\pm 7)\times 10^{7}$	–10.6 ± 0.7	–23.29 ± 0.09	+12.7 ± 0.6				
(Hg)2●MerR ⟶ *merO*							
K_7	ΔG_7	ΔH_7	$-T\Delta S_7$				
9.11×10^{6}	-9.46 ± 0.07	—	—				

[a]K1 and K2 describe the general equilibria for each reaction that is occurring. Individual reactions are described by K_i, ΔG_i, ΔH_i and $-T\Delta S_i$, as shown in **Figure 3.3.1.1**. Errors reflect the propagation of error for multiple ITC experiments and protonation, as described by each proton plot. K_7 is the equilibrium constant observed in gel-shift assays.[36] The K_6 value was calculated by taking the difference in free energies such that $\Delta G_6 = \Delta G5 - \Delta G_7 + \Delta G_4$.

	Δ(ΔG)[a]	**Δ(ΔH)**	**Δ(–TΔS)**
Homotropic[b]			
$MerR_{Calc}$*	*2.0 ± 0.6*	—	—
MerR●*merO*	3.4 ± 0.9	2.7 ± 1.3	0.7 ± 0.9
Heterotropic[c]			
	ΔG_c^1	**ΔH_c^1**	**$-T\Delta S_c^1$**
Hg_1	0.2 ± 0.7	6.7 ± 0.6	-6.5 ± 0.9
	ΔG_c^2	**ΔH_c^2**	**$-T\Delta S_c^2$**
$Hg_{2,Cal}$	*1.6 ± 0.8*	—	—
	ΔG_c^t	**ΔH_c^t**	**$-T\Delta S_c^t$**
$Total_{calc}$	*-1.1 ± 1.0*	—	—

[a] $\Delta(\Delta G) = \Delta(\Delta H) + \Delta(-T\Delta S)$

[b] Homotropic coupling energies indicating the negative cooperativity occurring when Hg_1 binds to apoMerR ($K_6 - K_1$ in **Table 3.3.8.1**) and the MerR●*merO* complex ($K_5 - K_3$ in **Table 3.3.8.1**).

[c] Heterotropic coupling describing the effect of Hg-binding on the MerR-*merO* interaction when Hg^{2+} fills the first metal binding site (**Equations 3.3.1.5.** to **3.3.1.7**), when Hg^{2+} fills the second metal binding site (**Equations 3.3.1.8.** to **3.3.1.10**), and the total effect on the filling of both sites (**Equations 3.3.1.2.** to **3.3.1.4**).

Calc* are calculated by literature gel-shift assays that describe K7 in **Table 3.3.8.1.[36] *Italics* utilize the free energy calculated from the gel-shift assay.

Table 3.3.8.2. *Homotropic and heterotropic coupling energies are described by ITC and gel-shift assay.*

Mercury binding to the first metal-binding site of MerR and MerR in the MerR-*merO* complex was quantifiable by ITC. Heterotropic coupling analysis shows that there is very little difference in the binding affinity, where $\Delta(\Delta G_c^t) = 0.2 \pm 0.7$ kcal/mol, but the thermodynamic components are significantly different. From an enthalpic perspective, the binding of Hg_1 to the MerR-*merO* complex is 6.7 ± 0.6 kcal/mol more disfavorable than Hg^{2+} binding to MerR. Since the binding affinities are similar, this enthalpic difference is cancelled by the favorable entropic contribution of Hg^{2+} binding to the MerR-*merO* complex where $\Delta(-T\Delta S_c^t) = -6.5 \pm 0.9$ kcal/mol. For the second mercury, if the reported K_7 value, and thus K_6 value, is accurate, then Hg_2 also binds less favorably to the MerR-*merO* complex with $\Delta(\Delta G_c^2) = 1.6$ kcal/mol. Since the binding enthalpy and entropy are not available for both K_6 and K_7, individual thermodynamics components are not currently quantifiable. However, the trend that Hg_2 would bind more favorably to the MerR-*merO* complex is also supported if the second mercury-binding event is not occurring in the apo-protein. This, however, is a trivial analysis.

A similar issue is faced with the determination of the homotropic allosteric interactions, as the second metal-binding site on MerR, K_6, may not be accessible after the first metal-binding site is filled. However, by assuming that K_7, from the literature, is accurate, the equilibrium constant for K_6 can be determined. Using this analysis, the filling of the first metal-binding site results in negative cooperativity, as indicated by $\Delta(\Delta G) = 2.0 \pm 0.6$ kcal/mol ($K_6 - K_1$). Alternatively, as there was no observable binding at the second metal-binding site of MerR, the binding of mercury to the first metal-binding site may completely suppresses the second metal-binding site, which would also be described as negative homotropic cooperativity. Thermodynamic components that determine this difference in binding affinity cannot be quantified under known conditions.

As both metal-binding sites are available in the MerR-*merO* complex, a more detailed analysis of the homotropic coupling can be described. The binding of the first Hg^{2+} is 3.4 ± 0.9 kcal/mol more favorable than the binding of the second Hg^{2+} to MerR in the MerR-*merO* complex. This is largely due to both an enthalpic ($\Delta(\Delta H) = 2.7$ kcal/mol) and an entropic ($\Delta(-T\Delta S) = 0.7$ kcal/mol) disfavorability. These two analyses to determine the homotropic allostery reveal that binding of Hg^{2+} to the first metal-binding site, whether to MerR or to MerR in the MerR-*merO* complex, results in negative homotropic allostery.

3.4. Discussion

This study aimed to utilized isothermal titration calorimetry to measure the thermodynamics of the allostery in the Hg^{2+}-binding metalloregulatory protein, MerR, and its binding to *merO*. This mechanism is readily described by **Figure 3.1.2.1.A**, in which MerR is bound to *merO*, and metal binding results in a conformational change in the DNA structure, allowing for the binding of RNA polymerase and subsequent transcription. Global thermodynamics are described for the interconversion of six independent states, MerR (P), MerR●*merO* (PD), $(Hg)_1$-MerR (M_1P), $(Hg)_2$-MerR (M_2P), $(Hg)_1$-MerR●*merO* (M_1PD), and $(Hg)_2$-MerR●*merO* (M_2PD). Discussions will focus on Hg^{2+}-binding thermodynamics associated with the homotropic (*horizontal* equilibria, K_1, K_6, K_3, and K_5 **Figure 3.3.1.1**) and heterotropic (*vertical* equilibria, K_2, K_4, and K_7, **Figure 3.3.1.1)** allostery and the coupled equilibria that modulate protein structure and overall function.

3.4.1. Mercury Binding to MerR and the MerR-merO Complex

Mercury binding to MerR for all quantified equilibria (K_1, K_3, and K_5) are strongly enthalpically and entropically favored, with a moderate shift in enthalpic and entropic contributions in the complex with *merO* (**Table 3.3.8.1**). This is the first time that the thermodynamic components of mercury binding to MerR have been quantified. For a better understanding of these global thermodynamics, and the thermodynamic components, it is useful to deconvolute the enthalpic and entropic components into their fundamental interactions. Broadly speaking, this includes metal desolvation, protein desolvation, metal-bond formation, or conformational changes and dynamics, to name a few. This is particularly relevant in describing the binding of the same metal to the same protein that has been perturbed, as in the binding of Hg^{2+} to MerR compared to the MerR-*merO* complex.

Briefly, the three primary contributions to the change in enthalpy for metal binding are: (1) metal-bond formation, (2) protein (de)-protonation, and (3) electrostatic changes within the protein structure. Both metal binding sites on MerR are identical, as this is a homodimer in solution, and provides tris-thiolate coordination for mercury; two cysteines from one monomer and a third cysteine from the other monomer. This remains the same

for Hg^{2+} binding to MerR or to MerR in the MerR-*merO* complex. However, when Hg^{2+} binds to the first metal-binding site on MerR at pH 7.4, whether or not part of the MerR-*merO* complex, 2.4 total protons are displaced, which would contribute to the overall change in enthalpic and entropic components. This would suggest that the enthalpic contribution to metal binding and the formation of metal-thiolate bonds would be similar as well. This leaves changes in the electrostatic interactions within the protein scaffold as the primary modulating component of the enthalpy of metal binding.

Hg^{2+} binding to the first metal-binding site of MerR results in a condition-independent change in enthalpy of $\Delta H = -34.9 \pm 0.1$ kcal/mol. Subtracting the enthalpy that would be associated with cysteine deprotonation (approximately –8.6 kcal/mol cysteine) gives the enthalpy of Hg^{2+}-binding to three Cys thiolates in the first metal-binding site, $\Delta H = -55.5$ kcal/mol. For MerR in the MerR-*merO* complex, the thiolate-binding enthalpy is $\Delta H = -48.8$ kcal/mol. The difference of ~6.7 kcal/mol is due to complexation of MerR to *merO*. *merO*, which is highly negatively charged, is proposed to stabilize the conformational dynamics of MerR, as the formation of the MerR-*merO* complex permits mercury to bind to the second metal binding site, which does not seem to occur in free MerR. The large negative charge of *merO* may weaken mercury-thiolate bonds, however, thereby lowering the enthalpy of the interaction, which is compensated by a more favorable entropic contribution to binding. As the overall equilibrium constants are similar, this appears to be another case of enthalpy-entropy compensation.

A similar analysis can be done with the second Hg^{2+} binding site on the MerR-*merO* complex. This metal binds with a ~2.5 order of magnitude weaker affinity, compared to the first metal binding site, but the magnitudes of the enthalpic and entropic contributions are similar. Although the metal-thiolate bond formation enthalpies would be similar, the second binding event only displaces ~1.4 protons. This results in a thiolate-binding enthalpy $\Delta H = -37.5$ kcal/mol, significantly lower value than that of the first binding site, after proton displacement is accounted for. This suggests that the presence of Hg^{2+} in the first binding site directly modulates the enthalpy of Hg^{2+} binding to the second site. The origination of this modulation of a distant metal-binding site is not known. However, in CueR, a Cu^{+} metalloregulatory protein within the MerR family, experimental and computational work has aimed to understand the conformational changes that occur when

metals bind and how this impacts binding to DNA. Using molecular dynamics and double electron-electron resonance (DEER), Ruthstein and coworkers found that there are some distinct changes in the protein structure both in the metal-protein-DNA complex and the metal-protein complex, which would support the finding herein that there is a significant enthalpic driving force that propagates throughout the protein scaffold.[34,35] It is noted that these studies assumed that two Cu^{+} ions are bound to CueR, whether the protein is bound to DNA or not, which has only been shown experimentally using crystal structures. Solution-based biochemical characterization of CueR and its metalation-state, has yet to be determined.

From an entropic perspective, five fundamental contributions are proposed: (1) metal desolvation, (2) protein desolvation, (3) protein dynamics, (4) protein (de)-protonation, and (5) cratic, or translational entropy. Similar to the enthalpic analysis, certain components are identical in the binding of Hg^{2+} to MerR or to MerR in the MerR-*merO* complex, including metal desolvation. Likewise, given the similarity in metal binding sites (amino acids) and the similarities in protein deprotonation, for the first metal-binding site at least, this would suggest that protein desolvation may be similar as well. No differences in the cratic entropy are expected, where:

$$Hg(II) + apoMerR - H_{2.4} \longrightarrow HgMerR + 2.4\,H^{+}$$
$$\Delta_{species} = 3.4 - 2.0 = +1.4 \qquad \textbf{Equation 3.4.1.1}$$

$$Hg(II) + MerR \bullet MerO - H_{2.4} \longrightarrow Hg \bullet MerR \bullet MerO + 2.4\,H^{+}$$
$$\Delta_{species} = 3.4 - 2.0 = +1.4 \qquad \textbf{Equation 3.4.1.2}$$

in which **Equation 3.4.1.1** and **Equation 3.4.1.2**, show that Hg^{2+} binding to the first metal-binding site on MerR would be identical.[45–47] However, the cratic entropy for the second binding of the second Hg^{2+} binding to the MerR-*merO* complex would be:

$$Hg(II) + Hg \bullet MerR \bullet MerO - H_{1.4} \longrightarrow (Hg)_2 \bullet MerR \bullet MerO + 1.4\,H^{+}$$
$$\Delta_{species} = 2.4 - 2.0 = +0.4 \qquad \textbf{Equation 3.4.1.3}$$

As such, a small contribution to the entropy of metal binding would likely be observed for the binding of the second Hg^{2+} to the MerR-*merO* complex.

This leaves protein conformational changes and conformational dynamics that modulate the binding. The binding of Hg^{2+} to the MerR-*merO* complex is ~6 kcal/mol more entropically favorable, suggesting that this binding results in greater conformational dynamics, where the system is going from ordered to more disordered. The initial structure

may be stabilized by *merO*, more so than free MerR, which would then result in a conformational change in both MerR and *merO* to allow for the binding of RNA polymerase. When the second Hg^{2+} binds to the MerR-*merO* complex, there is a ~2 kcal/mol entropic penalty, which may come from differences in protein deprotonation or stabilization of the second binding site. This leads to a less dynamic protein structure, which is observed in a comparison in the apoMerR and $(Hg)_2$-bound MerR, although *merO* is not present in these crystal structures.[27]

3.4.2. Homotropic Allostery in MerR and the MerR-merO Complex

It is curious that the second metal-binding site on free MerR is not readily available to bind Hg^{2+} after the first metal-binding site has been filled, yet it is available when MerR is bound to *merO*. This suggests that binding of the first Hg^{2+} results in negative homotropic cooperativity, as the first Hg^{2+} binding seems to inhibit Hg^{2+} binding at this second site. The abrogation of Hg^{2+} binding to solvent-accessible cysteines is unusual and unexpected. Even using a relatively weak mercury chelator, DTPA, the binding of the second Hg^{2+} to MerR is not observed when *merO* is not present. It has been proposed previously that binding of this first Hg^{2+} results in a coiled-coil conformation of the dimerization helix that pushes the cysteines at the second metal binding site further apart. Unfortunately, this has not been shown experimentally, but it supports the strong homotropic allostery that regulates the binding of Hg^{2+} to MerR, as the binding of Hg^{2+} directly, and significantly, suppresses the metal-binding properties of this second binding site.[48]

Although the second metal-binding site does not appear to be available for metal binding in the apo-protein after the first site is occupied, the binding affinity for the second binding site on apoMerR can still be quantified through the linked equilibria shown in **Figure 3.3.1.1**. This linked equilibrium analysis would suggest that this binding site, if it were available for metal binding, would have a binding energy of ΔG = -65 kcal/mol or $K = 6\times10^{47}$. This discrepancy between the ITC results and the linked equilibrium analysis would support the explanation that the first metal-binding site modulates the second site through negative homotropic allostery, leading to the abrogation of binding.

Unlike the binding of Hg^{2+} to MerR, Hg^{2+} binding to the MerR-*merO* complex shows two distinct binding events with the second one ~2.5 orders of magnitude weaker. Factors that contribute to this difference provide the thermodynamics of homotropic allostery. Comparing these two binding events reveals a negative homotropic allosteric interaction, which results in a second binding site that is both enthalpically and entropically less favorable by ~2 kcal/mol. Although the Hg_1–MerR–*merO* intermediate has not been studied previously, examining the differences at the start- and end-points of the thermodynamic cycle can provide some insight into the source of these thermodynamic differences. As previously discussed, many factors can modulate the metal binding thermodynamics. The bulk of the thermodynamic differences at the second binding site are likely to come from structural changes that occur after the first site is occupied.

In summary, stabilization of a dynamic protein-DNA complex would result in a more disfavorable entropic interaction through a decrease in conformational dynamics. Likewise, stabilization of a protein conformation would likely originate from changes in the hydrogen-bonding network that propagate throughout the protein scaffold, leading to a net increase in bond formation, and an overall decrease in the enthalpic favorability associated with the second binding event.[49]

3.4.3. Heterotropic Coupling Components

Given the mechanism associated with MerR regulation by inorganic mercury, in which MerR is bound to *merO* in both the apo- and metal-bound form, it is not surprising that the overall equilibrium constant for MerR binding to *merO* shows minimal differences with and without mercury bound. This small ΔG_c^t = -1.1 kcal/mol suggests that there is a very small positive heterotropic coupling energy that enhances the binding of MerR to *merO*. However, the thermodynamic components of this heterotropic interactions are challenging to determine, given the inability of MerR to bind two Hg^{2+} until MerR binds to *merO*.

However, titration of intermediate $(Hg)_1$–MerR into *merO* can be compared to the titration of free MerR into *merO* (K_2 and K_4, **Figure 3.3.1.1,** respectively). The difference between the equilibrium constants show ΔG_c^1 = 0.2 kcal/mol, indicating that formation of the MerR-*merO* complex is not modulated by Hg^{2+} bound at the first metal binding site.

However, the individual thermodynamics suggest there are changes in the overall structure that occur when that first site is occupied. The MerR-*merO* interaction becomes ~6.7 kcal/mol more enthalpically disfavored, yet ~6.5 kcal/mol more entropically favored with one Hg^{2+} bound.. Consider the different sources of protein-DNA interactions, particularly under conditions of high salt concentrations. It may be expected that this interaction would be entropically favorable, driven by the displacement of water molecules when MerR binds to *merO*. This may extend to the large number of positively charged residues that would be in close proximity to the negatively charged DNA.

While these may be important, the buffer-independent binding thermodynamics at pH 7.4 reveal there is a large enthalpically favorable contribution that drives this interaction. Some of this enthalpic favorability likely comes from the protonation of MerR, where the binding of MerR to *merO* results in protonation of the complex by 0.8 protons, whereas 1.9 protons bind to the complex when $(Hg)_1$-MerR binds to *merO*. Differences in protein protonation would certainly add to the enthalpic favorability, but other sources are likely present, largely from the formation of electrostatic interactions and hydrogen-bonding networks that result in a net increase in bonds being formed. This is supported by the mercury binding thermodynamics and evidence that MerR in solution is much more conformationally dynamic than when it is bound to DNA. This would contribute to the net entropic disfavorability. However, the binding of mercury to the first metal binding site results in an enhancement of the entropic interaction, which supports, as previously discussed, the idea that this first mercury binding event leads to dramatic changes at the other metal binding site.

3.5. Summary

For homotropic and heterotropic allosteric interactions to occur, structural changes must be modulated by the interaction of MerR with mercury and with *merO*. Allostery is present at all levels of the metal-protein-DNA interaction, where the binding of Hg^{2+} to one site suppresses the metal-binding capabilities of the other metal binding site, the binding of Hg^{2+} to both the apo-protein and DNA-bound protein show dramatic differences in the entropic contribution to binding, and the thermodynamics of the second Hg^{2+} binding

site on the MerR-*merO* complex are modulated by occupation of the first metal-binding site.

This thermodynamic analysis provides foundational experimentally validated knowledge about the regulation of the mercury detoxification pathway by MerR through the binding of inorganic mercury. Fundamentally, this interaction is driven and regulated by large entropic and enthalpic driving forces, which are the basis for the heterotropic and homotropic coupling. This results in modulation of protein function. The large homotropic regulation associated with each metal binding site is consistent with the traditional definition of allostery, in which the binding of a ligand on one site modulates ligand binding at another distant site. However, the heterotropic allostery is much more subtle and modulated by enthalpy-entropy compensation, in which the overall binding affinity is similar, but the thermodynamic components shift dramatically. This is suggestive of more subtle changes in the protein scaffold, electrostatics, and hydrogen-bonding networks that propagate throughout the structure.

3.6. References

(1) Waldron, K. J.; Rutherford, J. C.; Ford, D.; Robinson, N. J. Metalloproteins and Metal Sensing. *Nature* **2009**, *460* (7257), 823–830. https://doi.org/10.1038/nature08300.

(2) Finney, L. A.; O'Halloran, T. V. Transition Metal Speciation in the Cell: Insights from the Chemistry of Metal Ion Receptors. *Science (80-.).* **2003**, *300* (5621), 931–936. https://doi.org/10.1126/science.1085049.

(3) Baksh, K. A.; Zamble, D. B. Allosteric Control of Metal-Responsive Transcriptional Regulators in Bacteria. *Journal of Biological Chemistry*. American Society for Biochemistry and Molecular Biology Inc. 2020, pp 1673–1684. https://doi.org/10.1074/jbc.REV119.011444.

(4) Bou-Abdallah, F.; Woodhall, M. R.; Velázquez-Campoy, A.; Andrews, S. C.; Chasteen, N. D. Thermodynamic Analysis of Ferrous Ion Binding to Escherichia Coli Ferritin EcFtnA. *Biochemistry* **2005**, *44* (42), 13837–13846. https://doi.org/10.1021/bi0514212.

(5) Suttisansanee, U.; Honek, J. F. Bacterial Glyoxalase Enzymes. *Seminars in Cell and Developmental Biology*. Elsevier Ltd 2011, pp 285–292. https://doi.org/10.1016/j.semcdb.2011.02.004.

(6) Ekici, S.; Pawlik, G.; Lohmeyer, E.; Koch, H. G.; Daldal, F. Biogenesis of Cbb3-Type Cytochrome c Oxidase in Rhodobacter Capsulatus. *Biochim. Biophys. Acta - Bioenerg.* **2012**, *1817* (6), 898–910. https://doi.org/10.1016/j.bbabio.2011.10.011.

(7) Andrews, N. C. Metal Transporters and Disease. *Curr. Opin. Chem. Biol.* **2002**, *6* (2), 181–186. https://doi.org/10.1016/S1367-5931(02)00307-1.

(8) Dennison, C.; David, S.; Lee, J. Bacterial Copper Storage Proteins. *J. Biol. Chem.* **2018**, *293* (13), 4616–4627. https://doi.org/10.1074/jbc.TM117.000180.

(9) Wilcox, D. E. Isothermal Titration Calorimetry of Metal Ions Binding to Proteins: An Overview of Recent Studies. *Inorganica Chim. Acta* **2008**, *361* (4), 857–867. https://doi.org/10.1016/j.ica.2007.10.032.

(10) Pi, H.; Helmann, J. D. Ferrous Iron Efflux Systems in Bacteria. *Metallomics* **2017**, *9* (7), 840–851. https://doi.org/10.1039/c7mt00112f.

(11) Donovan, A.; Lima, C. A.; Pinkus, J. L.; Pinkus, G. S.; Zon, L. I.; Robine, S.; Andrews, N. C. The Iron Exporter Ferroportin/Slc40a1 Is Essential for Iron Homeostasis. *Cell Metab.* **2005**, *1* (3), 191–200. https://doi.org/10.1016/j.cmet.2005.01.003.

(12) Utz, M.; Andrei, A.; Milanov, M.; Trasnea, P. I.; Marckmann, D.; Daldal, F.; Koch, H. G. The Cu Chaperone CopZ Is Required for Cu Homeostasis in Rhodobacter Capsulatus and Influences Cytochrome Cbb 3 Oxidase Assembly. *Mol. Microbiol.* **2019**, *111* (3), 764–783. https://doi.org/10.1111/mmi.14190.

(13) Velayudhan, J.; Hughes, N. J.; McColm, A. A.; Bagshaw, J.; Clayton, C. L.; Andrews, S. C.; Kelly, D. J. Iron Acquisition and Virulence in Helicobacter Pylori: A Major Role for FeoB, a High-Affinity Ferrous Iron Transporter. *Mol. Microbiol.* **2000**, *37* (2), 274–286. https://doi.org/10.1046/j.1365-2958.2000.01987.x.

(14) Miller, C. E.; Williams, P. H.; Ketley, J. M. Pumping Iron: Mechanisms for Iron Uptake by Campylobacter. *Microbiology*. 2009, pp 3157–3165. https://doi.org/10.1099/mic.0.032425-0.

(15) Morby, A. P.; Parkhill, J.; Lee, B. T. O.; Brown, N. L.; Rouch, D. A.; Camakaris,

J.; Williams, T. *Bacterial Resistances to Mercury and Copper*; 1991; Vol. 46. https://doi.org/10.1002/jcb.240460204.

(16) Grossoehme, N. E.; Giedroc, D. P. Energetics of Allosteric Negative Coupling in the Zinc Sensor S. Aureus CzrA. *J. Am. Chem. Soc.* **2009**, *131* (49), 17860–17870. https://doi.org/10.1021/ja906131b.

(17) Shewchuk, L. M.; Helmann, J. D.; Ross, W.; Park, S. J.; Summers, A. O.; Walsh, C. T. Transcriptional Swtching by the MerR Protein: Activation and Repression Mutants Implicate Distinct DNA and Mercury(II) Binding Domains. *Biochemistry* **1989**, *28* (5), 2340–2344. https://doi.org/10.1021/bi00431a053.

(18) Reyes-Caballero, H.; Campanello, G. C.; Giedroc, D. P. Metalloregulatory Proteins: Metal Selectivity and Allosteric Switching. *Biophysical Chemistry*. July 2011, pp 103–114. https://doi.org/10.1016/j.bpc.2011.03.010.

(19) Dosanjh, N. S.; Michel, S. L. J. Microbial Nickel Metalloregulation: NikRs for Nickel Ions. *Curr. Opin. Chem. Biol.* **2006**, *10* (2), 123–130. https://doi.org/10.1016/j.cbpa.2006.02.011.

(20) Prabaharan, C.; Kandavelu, P.; Packianathan, C.; Rosen, B. P.; Thiyagarajan, S. Structures of Two ArsR As(III)-Responsive Transcriptional Repressors: Implications for the Mechanism of Derepression. *J. Struct. Biol.* **2019**, *207* (2), 209–217. https://doi.org/10.1016/j.jsb.2019.05.009.

(21) Chen, P. R.; He, C. Selective Recognition of Metal Ions by Metalloregulatory Proteins. *Current Opinion in Chemical Biology*. April 2008, pp 214–221. https://doi.org/10.1016/j.cbpa.2007.12.010.

(22) Merchant, S. S.; Helmann, J. D. *Elemental Economy. Microbial Strategies for Optimizing Growth in the Face of Nutrient Limitation*; 2012; Vol. 60. https://doi.org/10.1016/B978-0-12-398264-3.00002-4.

(23) Palmer, L. D.; Skaar, E. P. Transition Metals and Virulence in Bacteria. *Annu. Rev. Genet.* **2016**, *50*, 67–91. https://doi.org/10.1146/annurev-genet-120215-035146.

(24) Makthal, N.; Do, H.; Wendel, B. M.; Olsen, R. J.; Helmann, J. D.; Musser, J. M.; Kumaraswami, M. Group a Streptococcus AdcR Regulon Participates in Bacterial Defense against Host-Mediated Zinc Sequestration and Contributes to Virulence. *Infect. Immun.* **2020**, *88* (8), 1–16. https://doi.org/10.1128/IAI.00097-20.

(25) Changela, A.; Chen, K.; Xue, Y.; Holschen, J.; Outten, C. E.; O'Halloran, T. V.; Mondragón, A. *Molecular Basis of Metal-Ion Selectivity and Zeptomolar Sensitivity by CueR*; 2003; Vol. 301. https://doi.org/10.1126/science.1085950.

(26) Philips, S. J.; Canalizo-Hernandez, M.; Yildirim, I.; Schatz, G. C.; Mondragón, A.; O'Halloran, T. V. Allosteric Transcriptional Regulation via Changes in the Overall Topology of the Core Promoter. *Science (80-.).* **2015**, *349* (6250), 877–881. https://doi.org/10.1126/science.aaa9809.

(27) Chang, C. C.; Lin, L. Y.; Zou, X. W.; Huang, C. C.; Chan, N. L. Structural Basis of the Mercury(II)-Mediated Conformational Switching of the Dual-Function Transcriptional Regulator MerR. *Nucleic Acids Res.* **2015**, *43* (15), 7612–7623. https://doi.org/10.1093/nar/gkv681.

(28) Wang, D.; Huang, S.; Liu, P.; Liu, X.; He, Y.; Chen, W.; Hu, Q.; Wei, T.; Gan, J.; Ma, J.; Chen, H. Structural Analysis of the Hg(II)-Regulatory Protein Tn501 MerR from Pseudomonas Aeruginosa. *Sci. Rep.* **2016**, *6*. https://doi.org/10.1038/srep33391.

(29) Kern, D.; Zuiderweg, E. R. P. The Role of Dynamics in Allosteric Regulation. *Curr. Opin. Struct. Biol.* **2003**, *13* (6), 748–757. https://doi.org/10.1016/j.sbi.2003.10.008.

(30) Popovych, N.; Sun, S.; Ebright, R. H.; Kalodimos, C. G. Dynamically Driven Protein Allostery. *Nat. Struct. Mol. Biol.* **2006**, *13* (9), 831–838. https://doi.org/10.1038/nsmb1132.

(31) Cooper, A.; Dryden, D. T. F. Allostery without Conformational Change - A Plausible Model. *Eur. Biophys. J.* **1984**, *11* (2), 103–109. https://doi.org/10.1007/BF00276625.

(32) Jardetzky, O. Protein Dynamics and Conformational Transitions in Allosteric Proteins. *Prog. Biophys. Mol. Biol.* **1996**, *65* (3), 171–219. https://doi.org/10.1016/S0079-6107(96)00010-7.

(33) Newberry, K. J.; Brennan, R. G. The Structural Mechanism for Transcription Activation by MerR Family Member Multidrug Transporter Activation, N Terminus. *J. Biol. Chem.* **2004**, *279* (19), 20356–20362. https://doi.org/10.1074/jbc.M400960200.

(34) Schwartz, R.; Ruthstein, S.; Major, D. T. Molecular Dynamics Simulations of the Apo and Holo States of the Copper Binding Protein CueR Reveal Principal Bending and Twisting Motions. *J. Phys. Chem. B* **2021**, *125* (33), 9417–9425. https://doi.org/10.1021/acs.jpcb.1c02553.

(35) Sameach, H.; Narunsky, A.; Azoulay-Ginsburg, S.; Gevorkyan-Aiapetov, L.; Zehavi, Y.; Moskovitz, Y.; Juven-Gershon, T.; Ben-Tal, N.; Ruthstein, S. Structural and Dynamics Characterization of the MerR Family Metalloregulator CueR in Its Repression and Activation States. *Structure* **2017**, *25* (7), 988-996.e3. https://doi.org/10.1016/j.str.2017.05.004.

(36) Chen, C. Y.; Hsieh, J. L.; Silver, S.; Endo, G.; Huang, C. C. Interactions between Two MerR Regulators and Three Operator/Promoter Regions in the Mercury Resistance Module of Bacillus Megaterium. *Biosci. Biotechnol. Biochem.* **2008**, *72* (9), 2403–2410. https://doi.org/10.1271/bbb.80294.

(37) Zeng, Q.; Stålhandske, C.; Anderson, M. C.; Scott, R. A.; Summers, A. O. The Core Metal-Recognition Domain of MerR. *Biochemistry* **1998**, *37* (45), 15885–15895. https://doi.org/10.1021/bi9817562.

(38) Song, L.; Caguiat, J.; Li, Z.; Shokes, J.; Scott, R. A.; Olliff, L.; Summers, A. O. Engineered Single-Chain, Antiparallel, Coiled Coil Mimics the MerR Metal Binding Site. *J. Bacteriol.* **2004**, *186* (6), 1861–1868. https://doi.org/10.1128/JB.186.6.1861-1868.2004.

(39) Stevenson, M. J. Thermodynamic Studies of Cu(I) and Other d 10 Metal Ions Binding to Proteins in the Copper Homeostasis Pathway and the Organomercurial Detoxification Pathway, 2016.

(40) Anderegg, V. G.; Nageli, P.; Miiller, F.; Schwarzenbach, G.; Prof, H.; Karrer, P. *90. Komplexone XXX. Diathylentriamin-Pentaessigsaure (DTPA)*.

(41) Casas, J. S.; Jones, M. M. Mercury(II) Complexes with Sulfhydryl Containing Chelating Agents: Stability Constant Inconsistencies and Their Resolution. *J. Inorg. Nucl. Chem.* **1980**, *42* (1), 99–102. https://doi.org/10.1016/0022-1902(80)80052-2.

(42) Kõszegi-Szalai, H.; Paál, T. L. *Equilibrium Studies of Mercury(II) Complexes with Penicillamine*; 1999; Vol. 48. https://doi.org/10.1016/S0039-9140(98)00258-6.

(43) Cardiano, P.; Falcone, G.; Foti, C.; Sammartano, S. Sequestration of Hg 2+ by Some Biologically Important Thiols. *J. Chem. Eng. Data* **2011**, *56* (12), 4741–4750. https://doi.org/10.1021/je200735r.

(44) Liem-Nguyen, V.; Skyllberg, U.; Nam, K.; Björn, E. Thermodynamic Stability of Mercury(II) Complexes Formed with Environmentally Relevant Low-Molecular-Mass Thiols Studied by Competing Ligand Exchange and Density Functional Theory. *Environ. Chem.* **2017**, *14* (4), 243–253. https://doi.org/10.1071/EN17062.

(45) Gilson, M. K.; Given, J. A.; Bush, B. L.; McCammon, J. A. The Statistical-Thermodynamic Basis for Computation of Binding Affinities: A Critical Review. *Biophys. J.* **1997**, *72* (3), 1047–1069. https://doi.org/10.1016/S0006-3495(97)78756-3.

(46) Tamura, A.; Privalov, P. L. *The Entropy Cost of Protein Association*; 1997; Vol. 273. https://doi.org/10.1006/jmbi.1997.1368.

(47) Holtzer, A. The "Cratic Correction" and Related Fa. *BiopolymersBiopolymers* **1995**, *35*, 595–602.

(48) Guo, H. B.; Johs, A.; Parks, J. M.; Olliff, L.; Miller, S. M.; Summers, A. O.; Liang, L.; Smith, J. C. Structure and Conformational Dynamics of the Metalloregulator MerR upon Binding of Hg(II). *J. Mol. Biol.* **2010**, *398* (4), 555–568. https://doi.org/10.1016/j.jmb.2010.03.020.

(49) Yao, X.-Q.; Hamelberg, D. From Distinct to Differential Conformational Dynamics to Map Allosteric Communication Pathways in Proteins. *J. Phys. Chem. B* **2022**, *126* (14), 2612–2620. https://doi.org/10.1021/acs.jpcb.2c00199.

Chapter 4:

Modulation of Metal Binding Thermodynamics by Second Sphere Interactions and Protein Dynamics in Mercury and Copper Metalloproteins with the Ferredoxin-like Fold

4.1. Introduction

4.1.1. Interplay Between Protein Structures, Conformational Dynamics, and Ligand Binding

Protein structures are able to modulate ligand binding capabilities, allowing for ligand specificity, selectivity, and aiding in enzyme mechanisms.[1] Consider the classical lock-and-key model for enzyme function and the binding of a native substrate to an enzyme (**Figure 4.1.1.1.**).[2] The binding results in a change in global and local protein structures, enzymatic function, and subsequent release of the product. Within this model are several aspects that are necessary for enzyme function: (1) Native substrate binding requires specific interactions of the ligand with the amino acids in the substrate binding pocket (2) Non-native substrate may not have these contacts, which allow for some level of substrate specificity and selectivity. (3) Binding of the native substrate may result in a change in the protein conformation, thus ligand binding can directly shape and alter both the local and global protein structure. (4) Global and local protein conformational changes upon substrate binding drive enzyme function. (5) Enzymatic modification of the substrate results in changes with the amino acids in the ligand binding pocket, allowing release of the product from the enzyme.[3,4]

Although the classical lock-and-key mechanism is useful for visualization purposes of enzyme mechanisms, it lacks the nuance that is required to fully appreciate the interplay between the protein and the ligand.[5] This is further complicated by allosteric binding, in which protein function can be regulated through the binding of a ligand to a remote, non-active site.[6–8] This regulation holds true for small monomeric protein structures to large and intricate multiprotein complexes.[9] At the heart of these conformational changes from ligand binding, or vice versa, is physics, which is the cornerstone of protein dynamics, ligand binding, structural modifications, and the overall energetics of such systems.

Many metal-protein interactions are modulated by the surrounding protein scaffold, just like the classic lock-and-key enzyme mechanism, leading to changes in metal binding thermodynamics, kinetics, or reduction potential of the metal.[10–12] This

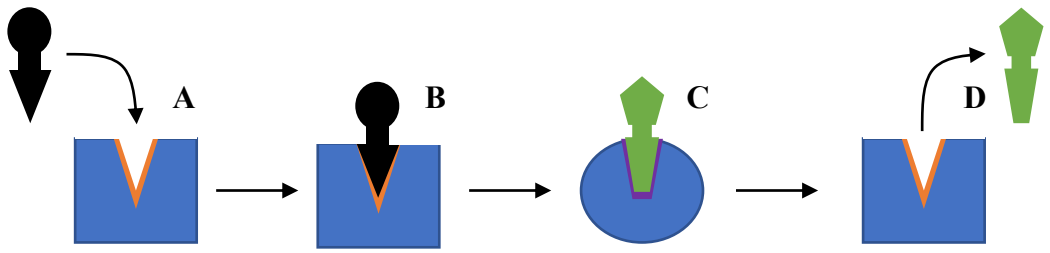

Figure 4.1.1.1. *Classic example of the Lock-and-Key enzyme mechanism. (A) Prior to the binding of the native substrate, the ligand binding site of the enzyme is empty resulting in the apo-enzyme with the ligand in proximity to the protein. (B) The native ligand is able to bind to the substrate binding site, which is the correct fit resulting in the substrate bound enzyme or holo-enzyme. (C) Global and local changes in the enzyme result in the enzymatic modification of the substrate to form the product. (D) Product release from the enzyme results in a conformational change back to the apo-enzyme, primed for the next enzymatic binding and modification.*

modulation can also directly impact enzyme function and mechanisms, and substrate specificity and selectivity.[13] Consider the reduction potential of iron, copper, and iron-sulfur clusters in proteins (**Figure 4.1.2.1.**).[14] Modulation of this property, even within an identical protein structure, can be achieved through altering the nearby amino acids, which, in turn, impacts the overall protein function.[15]

4.1.2. Second Coordination Sphere and its Role in Modulating Protein Function

Metal binding to proteins is not unlike the binding of a substrate to an enzyme. Metal binding is driven by distinct molecular interactions that can modulate metal selectivity, specificity, and overall protein function. And the formation of these metal-residue bonds within the metal-binding site of the protein can also modulate the protein structure and conformational dynamics.[16–18] These interactions can work in both directions, however, and the source of the factors that drive this modulation are not always known. One approach iron uncover these factors is through thermodynamic analysis, particularly the enthalpic and entropic contributions to the overall binding free energy.[19] Although the binding thermodynamics are useful in characterizing these contributions, the enthalpic and entropic contributions to metal binding are the sum of all contributing factors, including metal-bond formation, (de)-protonation of the protein, protein conformational dynamic, protein-coupled electrostatic interactions, and metal and protein (de)-solvation, for example.[20–24] The absolute thermodynamics associated with metal binding must be isolated from competing and coupled interactions to better understand the sources of enthalpic and entropic thermodynamics.[1] One way to focus on specific thermodynamic contributions is through relative thermodynamics, via ΔΔ-values. These can provide valuable insight into metal binding when comparing two similar systems, in which the similarities, like metal solvation, would be the same, thus magnifying and focusing on other differences. Furthermore, other synergistic techniques can aid in decoupling or elucidating distinct protein-driven metal interactions and these include computational techniques like molecular dynamics.[5]

Understanding these so-called second sphere interactions can provide important insight about homologous protein structures that have different function.[25] This is evident in a series

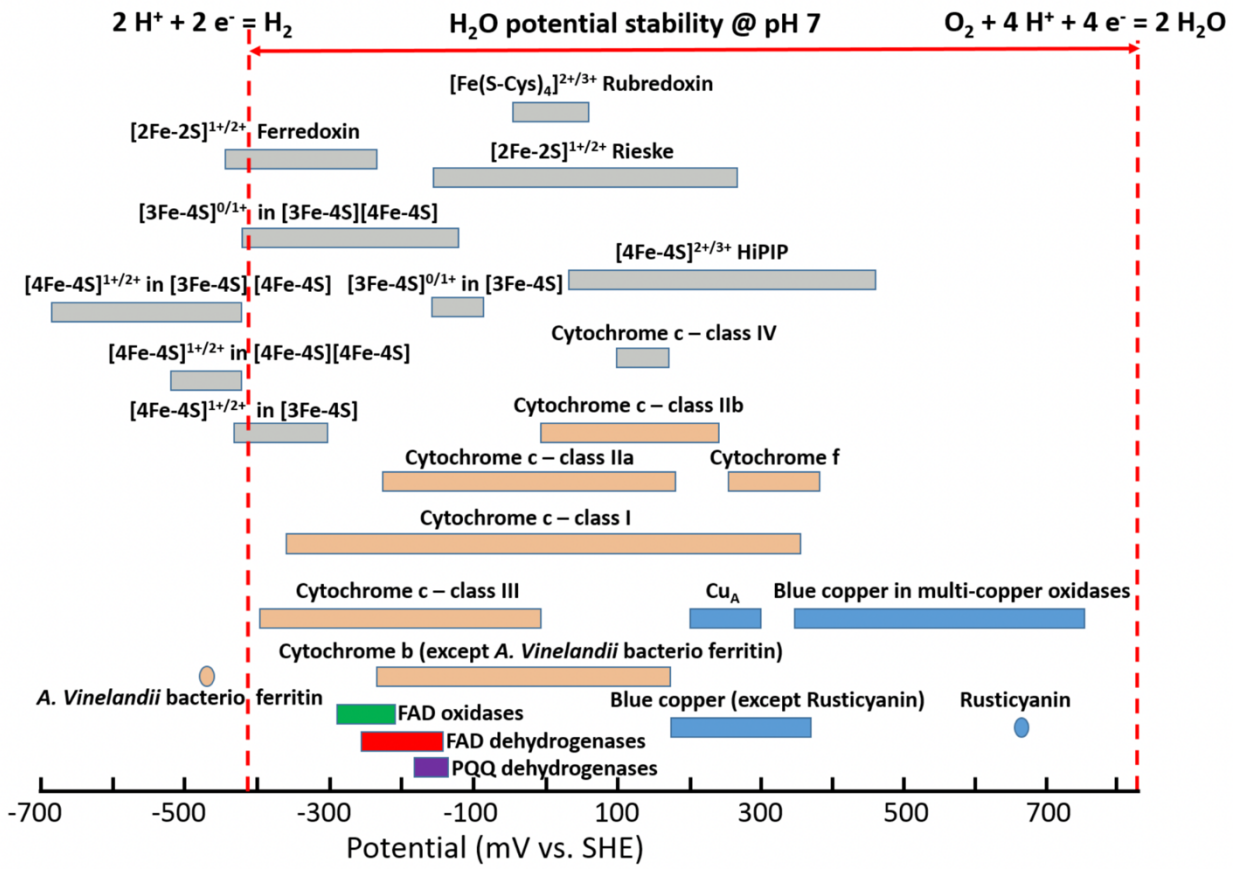

Figure 4.1.2.1. *Protein modulation of reduction potentials at pH 7.0. The range of reduction potential come from different biological sources for each protein species.*

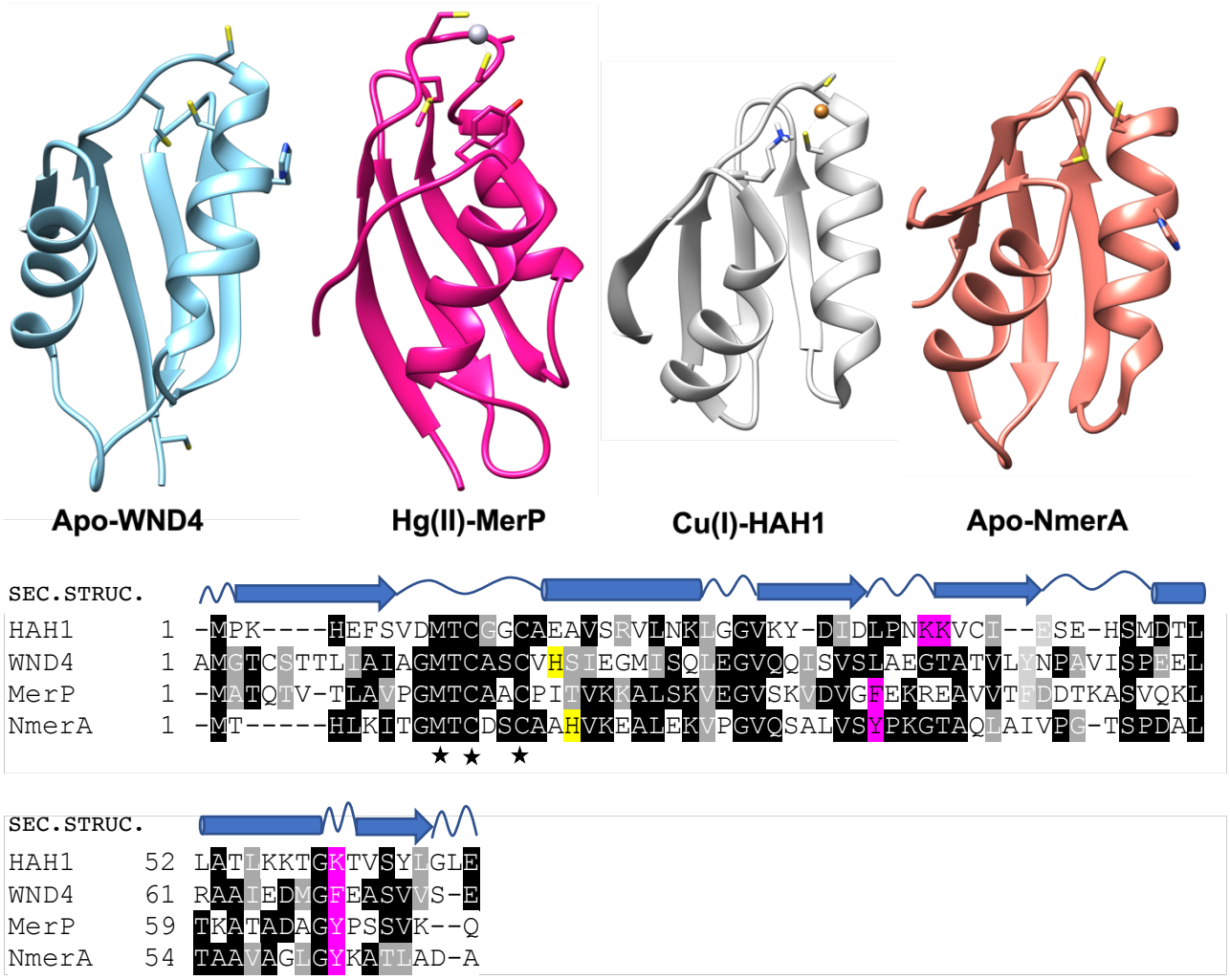

Figure 4.1.2.2. *(Top) Comparable solution structures of Apo-WND4, Hg^{2+}-bound MerP, Cu^{+}-bound HAH1, and Apo-NmerA with residues within the first and second coordination spheres shown. (Bottom) Multiple sequence alignment of the relevant ferredoxin-like fold proteins, HAH1, WND4, MerP , and NmerA, which bind Cu^{+} and Hg^{2+} through as soluble, monomeric metalloproteins (MerP and HAH1), or metal-binding domains, (WND4 and NmerA). Conserved residues within the $MX_1CX_2X_3C$ sequence is highlighted by black stars. The proposed second-sphere modulating residues are marked as the second-sphere loop residues. Black highlighting is indicative of highly conserved residues, gray highlighting are less conserved residues or residues that share similar properties, and no highlighting are residues that are not similar or related. Highlighted in yellow are histidine residues which are located at the dimerization interface of WND4 and NmerA. Highlighted in pink are the residues that modulate metal binding and cystine pK_as through second-sphere interactions.*

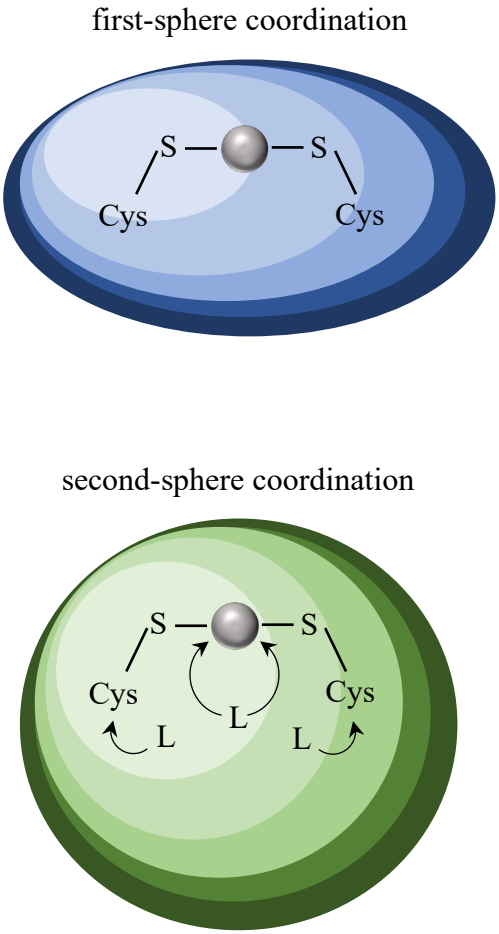

Figure 4.1.2.3. *Schematic representation of first- and second-sphere interactions within a protein. Top, blue: first-sphere coordination is the direct metal-bond which is found within the metal-binding site of the protein. Bottom, green: second-sphere coordination is the indirect interaction with both the metal and metal-binding residues which can modulate the properties of the metal-binding site (silver-sphere = metal ion).*

of metallochaperones that bind and transport a wide range of monovalent and divalent metal ions, using the same metal-binding site residues and the same general protein architecture.[26–28] Ferredoxin-like folded metallochaperones all share the αβ-sandwich motif from a sequence of βαββαβ secondary structures.[29–34] Binding of their native metal ion, which includes Cu^{+}, Zn^{2+}, Cd^{2+}, and Hg^{2+}, is achieved through a highly conserved metal-binding sequence, $MX_1CX_2X_3C$, in which X_1 is typically H, T, D, or S and X_2 and X_3 are small, hydrophobic amino acids like A, G, or S (**Figure 4.1.2.2.**).[27,35] Although the metal-binding sites of these proteins are identical, other amino acids, which do not directly form bonds to the metal create the second-sphere coordination, that has been proposed to modulate metal-binding properties (**Figure 4.1.2.3.**).[29,33]

Second-sphere interactions are able to modulate ligand binding properties of proteins through their interactions with the first-sphere coordinating ligands. These interactions are generally non-covalent in nature, and include hydrogen-bonding, electrostatic interactions, van der Waals forces, and hydrophobic interactions.[11] Although it is well-known that second-sphere coordination can modify protein function, the role they play is difficult to elucidate within the complex protein scaffold and non-covalent nature of the interactions.

4.1.3. Similar Structure, Similar Function, Yet Different Thermodynamic Contributions?

In these ferredoxin-like proteins, the pK_as of the two cysteine residues in the $MX_1C_nX_2X_3C_c$ (C_n or Cys_N = N-terminal cysteine; C_c or Cys_C = C-terminal cysteine) metal-binding site are modified by electrostatic interactions within the second coordination sphere. Located within loop 5 of these proteins of lysine (HAH1), phenylalanine (WND4), or tyrosine (MerP and NmerA) residues that have been shown, or hypothesized, to stabilize the thiolate of C_c in these proteins, leading to a dramatic decrease in the C_c pK_a to ~5.5 in MerP and HAH1 and ~7.7 in WND4 and, presumably, NmerA.[17,29,33] The K60A mutation in HAH1 was shown to decrease Cu^{+} binding affinity by 3-fold, in a pH-dependent manner.[17] Unlike C_c, the C_n of these proteins is exposed to the solvent, leading to an increase in the pK_a to ~8.5–9.1 (HAH1 and MerP, respectively) from the electrostatic interactions between the cysteine and the solvent, which stabilizes the thiol, instead of the thiolate.[17,26,33] This differential cysteine pK_a has been

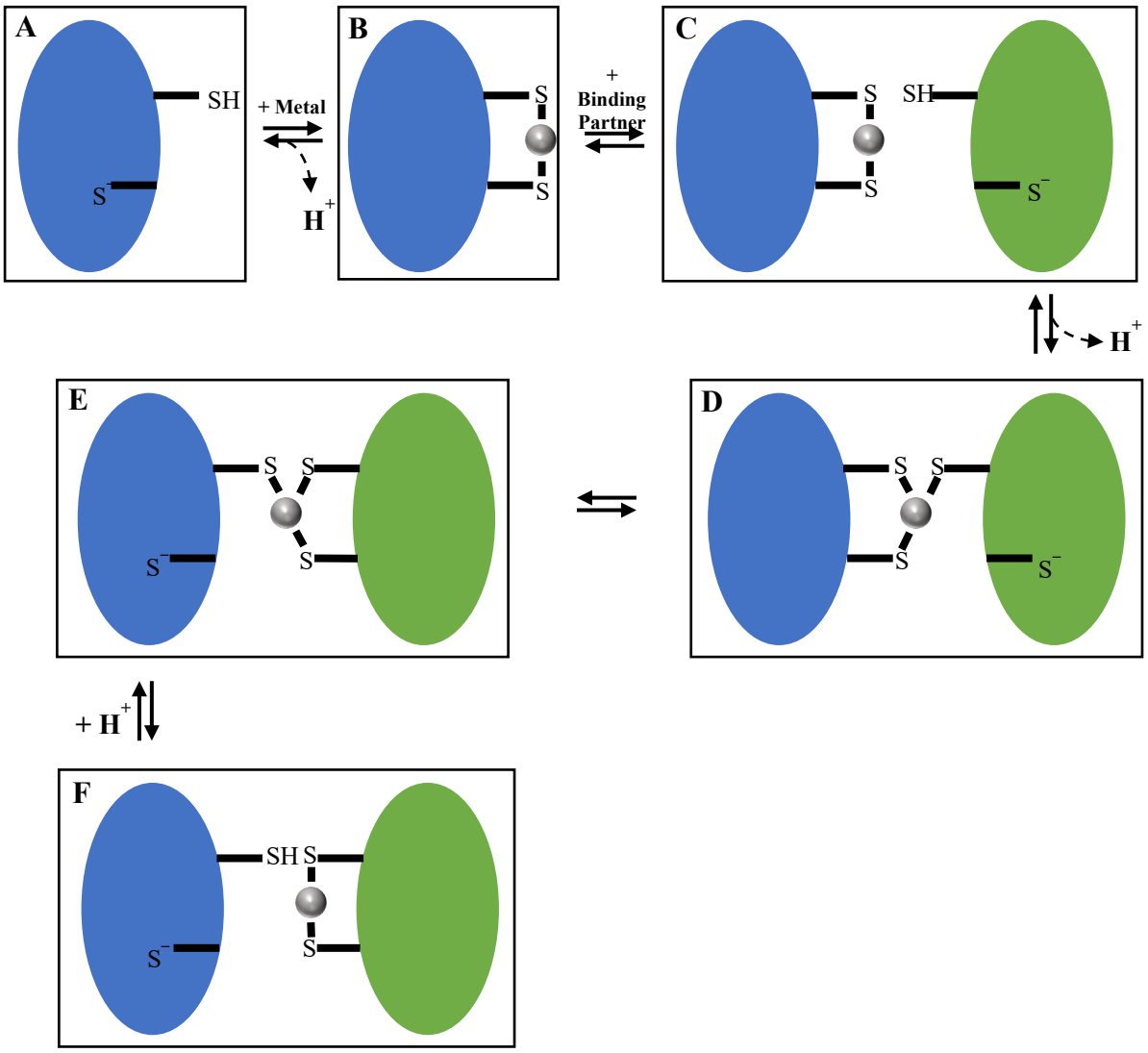

Figure 4.1.3.4. *Proposed mechanism for the transfer of monovalent or divalent metals from one ferredoxin-like folded protein to its ferredoxin-like fold binding partner. (A) Initially, Cys_N is solvent exposed with a pK_a of ~9.1 and Cys_C is buried within the protein core with a pK_a of ~5.5, resulting in a thiol and thiolate at pH 7.4, respectively. (B) Addition of a monovalent or divalent metal results in the linear, 2-coordinate binding to Cys_N and Cys_C which occurs through the deprotonation of Cys_N, and conformational change resulting in Cys_C moving towards the protein surface for metal binding. (C) The addition of the ferredoxin-like fold binding partner begins similarly to that in (A), with Cys_N being protonated and Cys_C being deprotonated and buried. (D) The tri-coordinate metal binding occurs, which results in the deprotonation of CysN in the binding partner. (E) The weaker Cys_C-metal bond is broken and the Cys_C-metal bond in the binding partner is formed, maintaining a tri-coordinate metal complex. (F) Metal transfer is completed, in which CysN is protonated and the metal forms a linear, 2-cooridnate complex in the metal-binding partner between Cys_N and Cys_C.*

implicated in the mechanism of metal transfer (**Figure 4.1.3.4.**). Mechanistically, the second-sphere interactions lead to modulation of the metal transfer mechanism.

Given the non-covalent nature of the second-sphere interactions in ferredoxin-like folded proteins, the enthalpic and entropic contributions to metal binding come into question. As previously described, a K60A mutation resulted in a 3-fold decrease in binding affinity, but the thermodynamic origin of this diminished binding affinity is unknown.

This chapter aims to address the source of thermodynamics differences among MerP, WND4, and HAH1 in the binding of native and non-native metal ions. Binding of Cu^{+}, Zn^{2+}, Cd^{2+}, and Hg^{2+} to each of these proteins system will provide insight the into metal binding thermodynamic foundation for differences within the second coordination sphere that can directly impact the enthalpic and entropic contributions to metal binding.

4.2. Materials and Methods

4.2.1. Materials

All materials were purchased at highest grade available and utilized as received. PIPES (1,4-piperazinediethanesulfonic acid), BisTris (2-[bis(2-hydroxyethyl)amino]-2-(hydroxymethyl)propane-1,3-diol), TAPSO (3-[[1,3-dihydroxy-2-(hydroxymethyl)propan-2-yl]amino]-2-hydroxypropane-1-sulfonic acid), ACES (2-[(2-amino-2-oxoethyl)amino]ethane-1-sulfonic acid), TRIS (1-amino-2-(hydroxymethyl_propate-1,3-diol), and MOPS (3-(morpholin-4-yl)propane-1-sulfonic acid) were purchased from VWR or Sigma. Buffer solutions were prepared in acid-washed Pyrex containers using Milli-Q deionized water (>18 MΩ) and treated with Chelex 100® (Sigma) to remove trace metals from solution. EDTA (ethylenediaminetetraacetic acid), DTPA (diethylenetriaminepentaacetic acid), DTT (dithiothreitol), reduced glutathione (GSH), cysteine, BCS (bathocuproinedisulfonic acid), BCA (bicinchoninic acid), DTNB (5-(3-carboxy-4-nitrophenyl)disulfanyl-2-nitrobenzoic acid), and DTDP (4,4'-dithiodipyridine) were purchased from Sigma, Alfa Aesar, or VWR and utilized directly as received without further purification. Metal salts of $HgCl_2$, $ZnCl_2$, $CdCl_2$, and CuCl were

purchased from Baker Chemical or Sigma at their highest purity. PD-10 buffer exchange columns were purchased from GE Healthcare and Cytiva Life Sciences.

4.2.2. Protein Transformation, Expression, and Purification

Purified, metal-free, and reduced MerP was provided by James Omichinski from the Université de Montréal and utilized as received.

Expression and purification of Wilson's Disease protein domain 4 (WND4) was adapted from Anastassopoulou et al.[36] Briefly, WND4, provided in a pET30a(+) vector with an enterokinase cleavage site between 6X-His and WND4 sequence, was transformed into BL21(DE3) cells (New England Biolabs). Transformed cells were grown at 37°C until OD600 is 0.6-0.8 when they are induced with 0.5 mM Isopropyl β-d-1-thiogalactopyranoside (IPTG). Induced cells were then grown for another 4 hours, centrifuged, decanted, and frozen for future use.

Thawed pellets were lysed by French press at 1,500 PSI and centrifuged. The supernatant was collected and equilibrated with Ni-NTA resin (VWR) at 4°C. Collected His-Tagged WND4 was incubated with light-chain enterokinase (96 units/mL WND4, Genscript) for 48 hours at 4°C. Phenylmethylsulfonyl fluoride (PMSF) was added to the cleaved WND4 to inhibit enterokinase cleavage and equilibrated with Ni-NTA at 4°C for separation of the 6X-His tag. The solution of WND4 and enterokinase is further separated by size-exclusion chromatography by FPLC on a Superdex 75 HL column. Purity was confirmed by SDS-PAGE, which showed >95% pure WND4. WND4 fractions were collected, concentrated, and stored in an anaerobic glovebox for further preparation for isothermal titration calorimetry (ITC) experiments.

Prior to the ITC experiments, WND4 was reduced and made metal-free by dialysis with ethylenediaminetetraacetic acid (EDTA) and then with dithiothreitol (DTT) in an anaerobic (Coy labs) glovebox with 95% N_2 and 5% H_2 atmosphere and a Pd catalyst to ensure ≤ 2 ppm oxygen. Reduced and metal-free WND4 was further dialyzed into the metal-free ITC buffer with 5 mM DTT. Metal-free ITC buffers were incubated with Chelex overnight, prior to utilization, to remove free metals from solution. Immediately prior to utilization, prepared on a daily basis, WND4 was buffer-exchanged into the metal-free ITC buffer without DTT using a GE Healthcare PD-10 desalting column.

4.2.3. Determination and Preparation of Protein, Metal, and Ligand Concentrations

Both MerP and WND4 concentrations were measured using either 5,5'-dithio-bis-[2-nitrobenzoic acid] (DTNB: ε_{412} = 14,150 M^{-1} cm^{-1}) or 4,4'-dithiodipyridine (DTDP: ε_{324} = 21,400 M^{-1} cm^{-1}).[37]

Cu^{+} solutions were prepared from $Cu^{+}Cl$ in deionized water at pH ~2 under anaerobic conditions. Stock Cu^{+} concentrations were measured spectrophotometrically with bathocuproinedisulfonic acid ($Cu^{I}(BCS)_2^{3-}$: ε_{483} = 13,000 M^{-1} cm^{-1}) or bicinchoninic acid ($Cu^{I}(BCA)_2^{3-}$: ε_{563} = 7,900 M^{-1} cm^{-1}).[38] Glutathione (GSH) and N-acetyl-penicillamine (NAPA) used in the ITC experiments were prepared fresh for each individual experiment. Stock concentrations of $HgCl_2$ and $ZnCl_2$ were dissolved in deionized water at pH ~2 and working solutions for ITC measurements were prepared daily as necessary. Stock concentrations of NAPA were prepared in deionized water at pH ~11 and diluted prior to the ITC experiments. ITC working solutions of Cu^{+}-GSH, Hg-GSH, and Hg-EDTA were also prepared fresh for each ITC experiment. Competition experiments had excess ligand (10:1 GSH:Cu^{+}/Hg^{2+} or 2:1 EDTA:Hg), in both the ITC cell and syringe. Chelation experiments with NAPA were prepared such that NAPA was titrated into the Hg-MerP complex (1:1).

4.2.4. Isothermal Titration Calorimetry Experimental Conditions

ITC experiments were done using a Malvern Panalytical MicroCal VP-ITC with an active cell volume of 1.4197 mL and a 300 μL syringe. Each ITC experiment used an injection volume of 6-10 μL, stirring at 307 rpm, at 25°C. Both the cell and syringe solutions were prepared in the same buffer and the reference cell was filled with water. Anaerobic ITC measurements were maintained through the use of a custom Plexiglass housing, which is constantly purged with N_2 gas. ITC experiments are shown with the raw (power vs. time) output in the top panel. Downward and upward peaks indicate exothermic and endothermic heats, respectively. Subsequent concentration-normalized integrations of each peak are shown in the bottom panel and the enthalpy is plotted against the molar ratio of the syringe (ligand) to the cell (protein). Fitting of the data was done using the provided VP-ITC Origin 7.0 software with a one-sit fitting model. A minimum of three experiments

were obtained and analyzed. Errors, unless otherwise indicated, are the standard deviation between the experimental data collected from these titrations.

4.3. Results and Analysis

Measurements involving metal ions to metalloproteins that utilize cysteine residues for their metal binding site are challenging due, in large part, to the susceptibility of cysteine oxidation and redox activity of the metal ions in aqueous solution. However, under anaerobic conditions, many of these challenges are mitigated, with the sole exception of Cu^{+}, which also requires a Cu^{+}-stabilizing ligand. The addition of a stabilizing ligand also serves as a competing ligand for the metal, dramatically increasing the typical binding affinity range that is quantifiable by ITC. In these series of titrations, the thermodynamics of Zn^{2+}, Cd^{2+}, Cu^{+}, and Hg^{2+} were determined for both MerP and WND4, which can be compared to thermodynamic data already obtained for HAH1 by ITC by Michael Stevenson.[39]

4.3.1. Quantification of the Mercury-MerP Binding Thermodynamics

The thiophilic nature of Hg^{2+} leads to binding affinities with cysteine that are far outside the typical range accessible by ITC (typical range: $K = 10^{3} – 10^{8}$, Hg^{2+}–Cys: $>10^{16}$). Thus, a Hg^{2+} chelator, which binds Hg^{2+} strongly, but weak enough that the metal can be displaced from the protein, must be included. Although the binding affinity is important, other thermodynamics values must also be known, such as the enthalpies associated with the Hg^{2+}-chelate interaction and chelate protonation. These chelators must also be available at reasonable cost and maintain adequate solubility in aqueous solution. Understandably, these conditions limit the number of chelators that are available to determine the binding thermodynamics associated with the Hg^{2+}-MerP interaction. Thus, two separate experimental designs were utilized to establish the thermodynamic parameters.

Titration of Hg^{2+}-EDTA into MerP allowed the Hg-MerP binding enthalpy to be determined, as both the Hg^{2+}-EDTA and EDTA protonation thermodynamics are well-characterized. However, the apparent binding affinity for these experiments was $>10^{7}$, outside the range of ITC. Confirmation of this high binding affinity was achieved using

DTPA, which binds Hg^{2+} ~2 orders of magnitude greater as the chelator, but this also shows an apparent binding affinity $>10^7$. Reduced glutathione, which fulfilled each of these limitations, was limited by the very low experimental heats, which would require far greater concentrations of MerP than were acceptable. Overcoming these challenges came not from a competing ligand but from a chelation experiment, in which a chelator that binds Hg^{2+} stronger than MerP was utilized. Thus, the titration of N-Acetyl-D-penicillamine (NAPA) into Hg-bound MerP (1:1 complex) showed chelation of Hg^{2+} from the protein within the range of ITC, with experimental heats that were quantifiable and reproducible. However, the NAPA protonation enthalpy and enthalpy of the Hg^{2+}-$(NAPA)_2$ complex were unknown, but their equilibrium constants had been quantified.

Two sets of experiments were utilized to establish the thermodynamics of Hg^{2+} to MerP. Hg-EDTA titrations were used to establish the condition-independent Hg^{2+}-MerP binding enthalpy and the chelation of Hg^{2+} from MerP by NAPA was used to determine the condition-independent binding affinities. These values can then be utilized to quantify both the Gibbs free energy and the entropic contribution to metal binding.

Mercury(II) was titrated into apo-MerP, where both solutions contained 50 mM buffer (TAPSO, BisTris, and PIPES), 50 mM NaCl, pH 7,4 and excess EDTA (**Figure 4.3.1.1.**). These experiments were strongly exothermic, with well-defined peaks, and a step-function at the inflection. This provides very well-defined initial and final heats, with the final injections defining the heat of dilution. The stoichiometry was found to be consistent with the literature.[40,41] In each isotherm, immediately before the inflection, one or two data points were observed to be more exothermic. These data points were not masked and were included in the fit as the binding enthalpy, not the binding affinity, is the desired observable. These isotherms were fit with a one-site binding model. The best-fit for at least two independent experiments in each buffer were collected, and the average experimental thermodynamics are summarized in Table **4.3.1.1**.

Although the pK_a of both the Cys_N and Cys_C residues of MerP were previously determined (Cys_N = 9.1 and Cys_C = 5.5), further confidence in these ITC

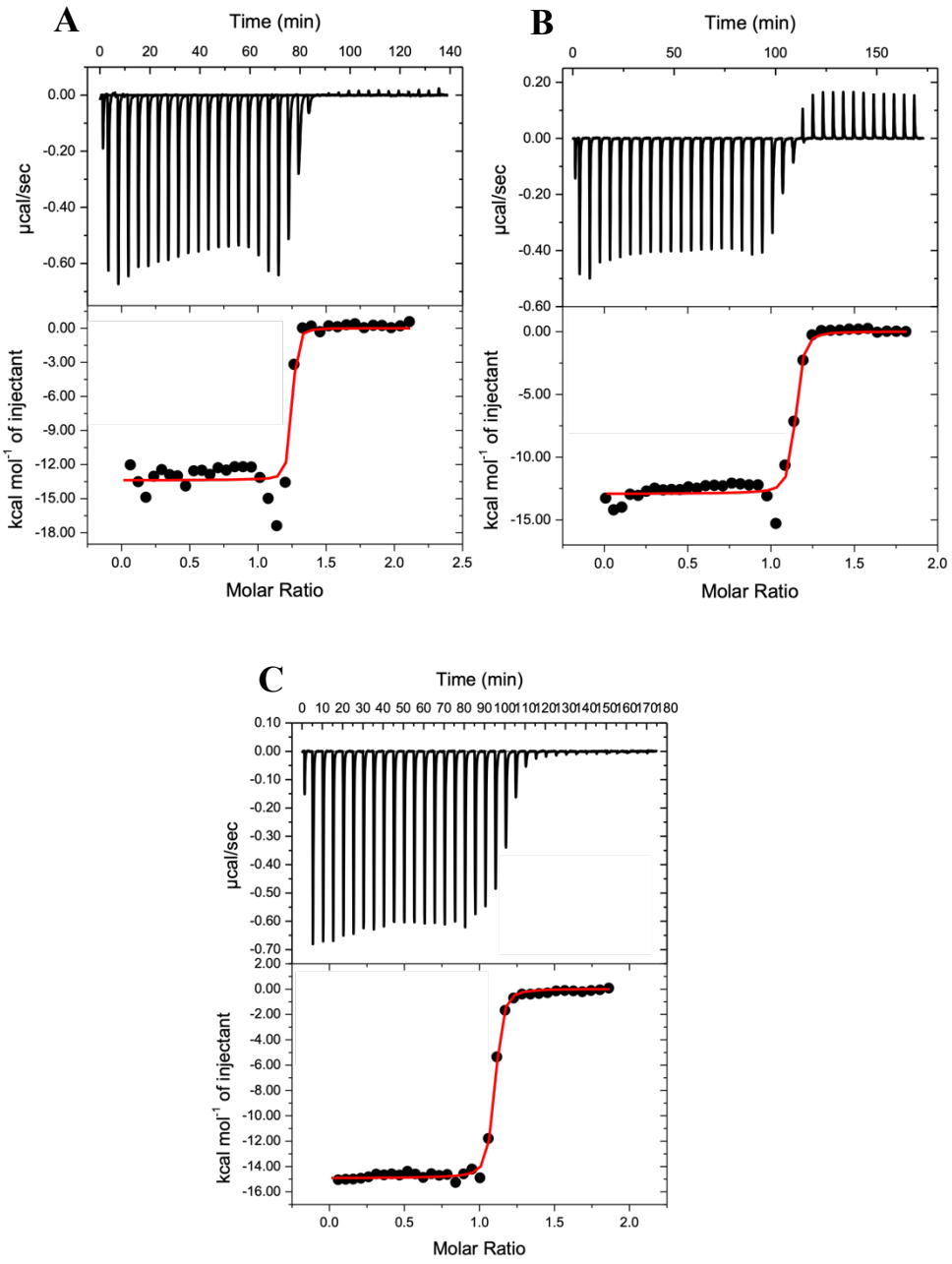

Figure 4.3.1.1. *Representative isotherms in the titration of Hg-EDTA into apo-MerP in 50 mM Buffer, 50 mM NaCl, pH 7.4, and 2-fold excess EDTA-to-Hg. (A) TAPSO: n = 1.22 ± 0.01, ΔH = -13.37 + 0.3 kcal/mol; (B) BisTris: n = 1.12 ± 0.01, ΔH = -12.9 + 0.2 kcal/mol; and (C) PIPES: n = 1.08 ± 0.01, ΔH = -14.9 + 0.1 kcal/mol.* K_{ITC} *values are not reported as these are not reflective of the actual experimental binding affinity, only a lower-limit to the binding affinity.*

Table 4.3.1.1 *Average experimental binding stoichiometry and enthalpy associated with the titration of Hg-EDTA into apo-MerR in 50 mM buffer, 50 mM NaCl, pH 7.4, and stabilized by 2-fold excess EDTA to* Hg^{2+} *and the corresponding condition-independent binding enthalpy of the Hg-MerP interaction. Average pH-dependent, buffer-dependent enthalpy and experimental stoichiometry is also shown.*

Buffer	**n**	**ΔH_{ITC} (kcal/mol)**	**$\Delta H_{Hg\text{-}MerP}$ (kcal/mol)**
PIPES	1.08 ± 0.08	-14.1 ± 0.9	-28.0 ± 1.0
BisTris	1.1 ± 0.1	-13.6 ± 0.8	-28 ± 1
TAPSO	1.22 ± 0.02	-13.6 ± 0.8	-27.6 ± 0.2
Average	**1.1 ± 0.1**		**-27.8 ± 1.4**

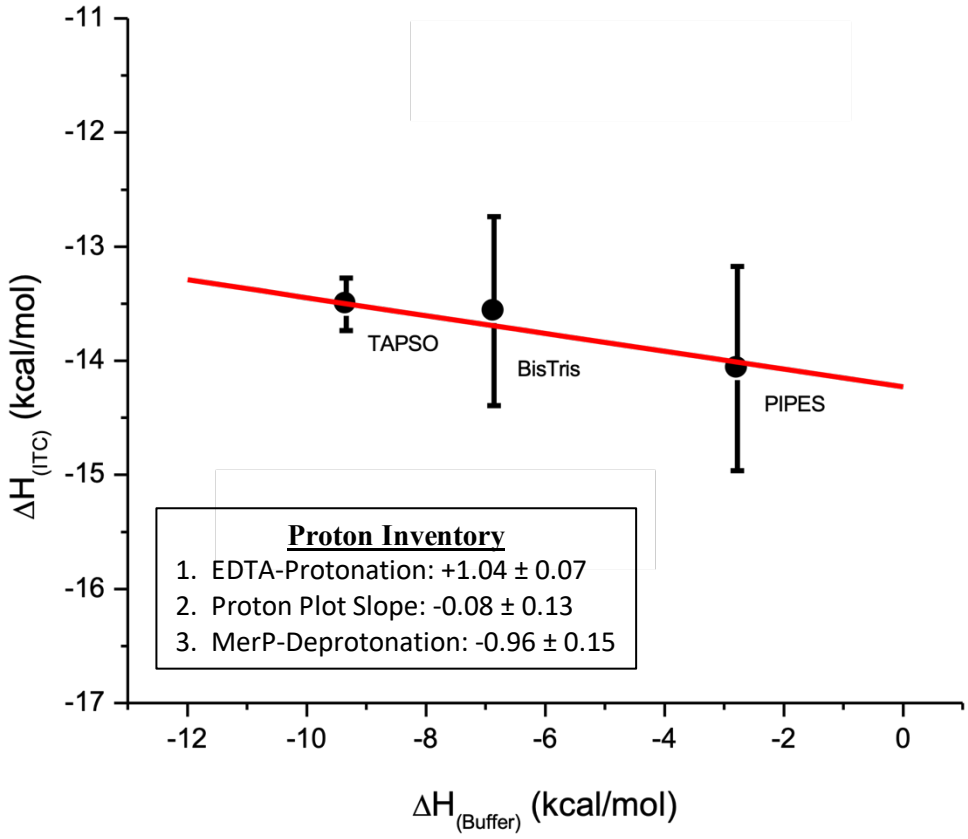

Figure 4.3.1.2. *Proton plot indicating the number of protons that dissociate from buffer upon the binding of* Hg^{2+} *to MerP in 2-fold excess EDTA-to-*Hg^{2+}*. Insert: Proton inventory that delineates the number of protons that bind to EDTA after* Hg^{2+} *is chelated out, which is +1.04 ± 0.07 protons according the relevant* pK_a*s of EDTA, the slope of the proton plot that suggests that -0.08 ± 0.13 proton leave buffer upon* Hg^{2+} *binding to MerP, thus the number of protons that dissociate from MerP when* Hg^{2+} *binds is equal to 0.96 ± 0.15 protons.*

isotherms can be gained through quantification of the number of protons released from MerP upon the Hg^{2+} binding. Based on the pK_as of the cysteines it is predicted that one proton would be released from MerP at the experimental pH of 7.4.[33] The number of protons can also be determined experimentally because these measurements were done in multiple buffer that have different buffer- protonation enthalpies (Chapter 2). By plotting the buffer-protonation enthalpy in the X-axis vs. the experimental enthalpy in the Y-axis and obtaining the slope of the data by a linear regression analysis, the number of protons that bind to buffer can be determined (**Figure 4.3.1.2.**). This proton plot has a slope of -0.08 ± 0.13, indicating that 0.08 ± 0.13 protons are leaving the buffer upon the Hg^{2+} binding to MerP. Considering that these experiments involved MerP removing Hg^{2+} from EDTA, the EDTA would become protonated. At pH 7.4, EDTA would gain 1.04 ± 0.07 protons after it releases Hg^{2+}. Thus, this proton inventory indicates that, indeed, MerP is deprotonated by 0.96 ± 0.15 protons, consistent with the expected protons that would be released from the two cysteine residues based on their pK_as. This consistency suggests that all competing equilibria are considered, and that the determination of the buffer-independent binding enthalpy of Hg^{2+} binding to MerP at pH 7.4 can be appropriately quantified.

After the number of protons that are protonating EDTA, dissociating from the buffer, and dissociating from MerP have been determined, the condition-independent binding enthalpy can be established at pH 7.4. This enthalpic contribution is quantified,

$$\Delta H_{Hg-MerP} = (\Delta H_{MP} - \Delta H_{PH}) = \Delta H_{ITC} + [\Delta H_{ML}] - \left[(0.99) * \Delta H_{LH_1}\right] - \left[(0.05) * \Delta H_{LH_2}\right] \quad \textbf{Equation 4.3.1.1}$$

where $\Delta H_{Hg\text{-}MerP}$ is the coupled Hg-MerP binding enthalpy and the MerP-deprotonation enthalpy (ΔH_{MP} and ΔH_{PH}, respectively), ΔH_{ITC} is the average buffer-dependent experimental enthalpy, ΔH_{ML} is the enthalpy of the Hg-EDTA interaction, and ΔH_{LH1} and ΔH_{LH2} are the enthalpies associated with the two relevant pK_as of EDTA, multiplied by the number of protons that bind at pH 7.4. This pH-independent binding enthalpy was determined for each buffer individually and the average enthalpy is equal to -28 ± 1 kcal/mol (**Table 4.3.1.1**).

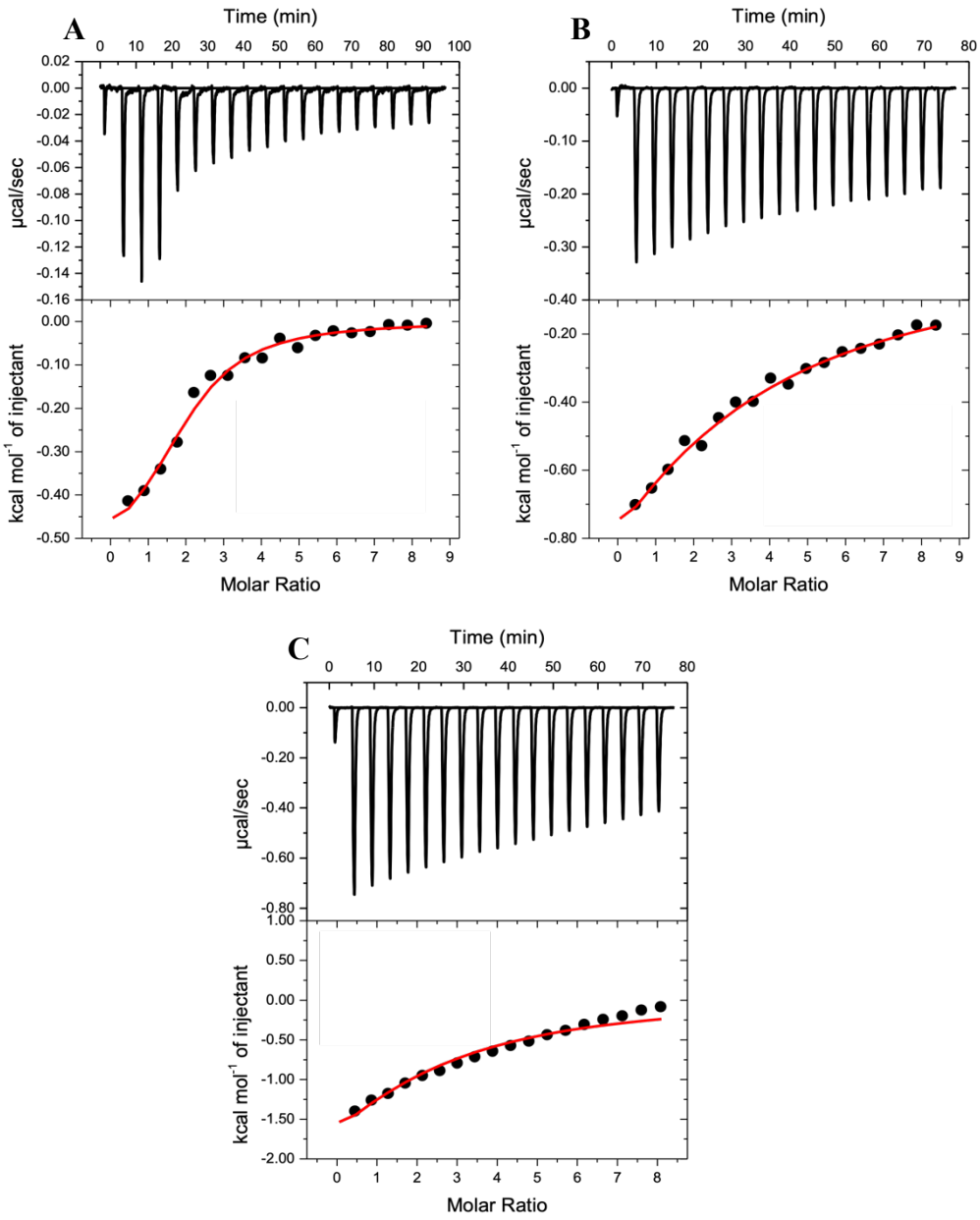

Figure 4.3.1.3. *Representative isotherms of the chelation of Hg^{2+} from a 1:1 Hg-MerP complex by NAPA in 50 mM buffer, 50 mM NaCl, pH 7.4. (A) BisTris: n = 1.93 ± 0.13, ΔH = -0.57 ± 0.05 kcal/mol, K_{ITC} = 1.34 (± 0.3)×10^5 M^{-1}; (B) ACES: n = 2.3 ± 1.0, ΔH = -2.8 ± 1.6 kcal/mol, K_{ITC} = 1.0 (± 0.3)×10^4 M^{-1}; and (C) TRIS: n = 2 ± 1, ΔH = -4.2 ± 2.5 kcal/mol, K_{ITC} = 1.91 (± 0.8)×10^4 M^{-1}.*

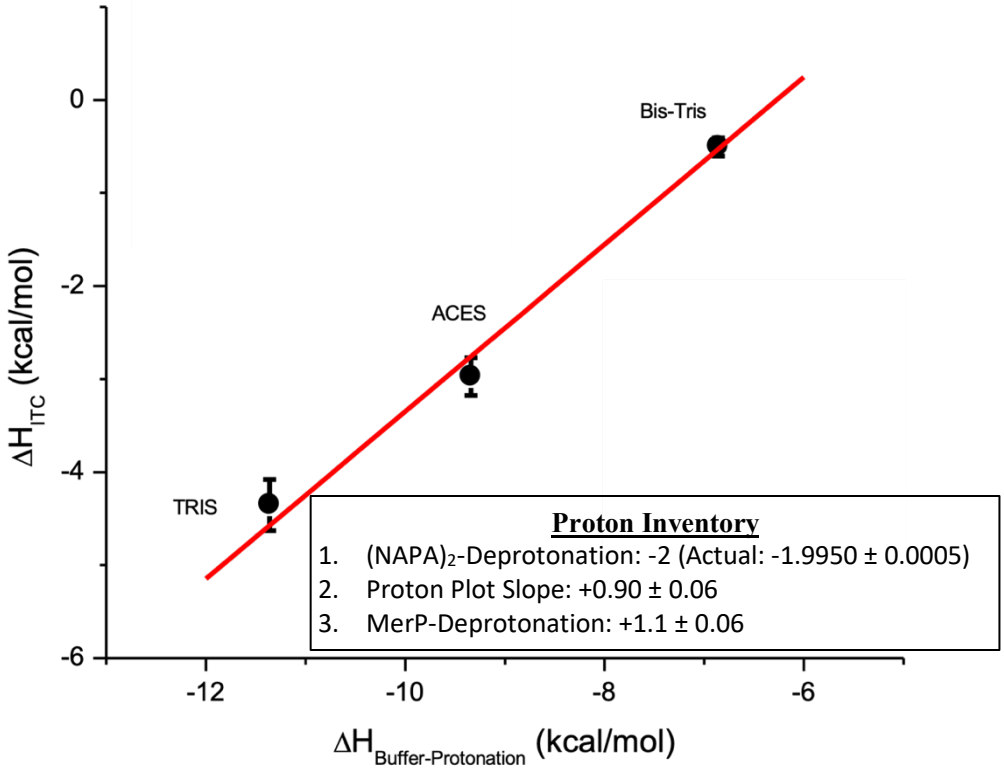

Figure 4.3.1.4. *Proton plot associated with the chelation of* Hg^{2+} *from the Hg-MerP (1:1) complex by NAPA, which forms a Hg-(NAPA)*$_2$ *complex upon chelation. Insert: proton inventory to establish the number of protons that leave MerP upon the chelation of* Hg^{2+}*. Experimental stoichiometries suggest that the chelation of* Hg^{2+} *by NAPA results in the Hg-(NAPA)*$_2$ *complex, which would result in the dissociation of ~2 protons from (NAPA)*$_2$*. The slope of the proton plot indicates that 0.90 ± 0.06 protons are binding to the buffer upon* Hg^{2+} *chelation. Thus, 1.10 ± 0.06 protons are binding to MerP when* Hg^{2+} *is chelated out.*

Table 4.3.1.2. *Average experimental binding stoichiometry, enthalpy, and apparent binding affinity associated with the chelation of Hg from the Hg-MerP (1:1) complex by NAPA in 50 mM buffer, 50 mM NaCl, pH 7.4, and the corresponding condition-independent binding affinity of the Hg-MerP interaction. Experimental stoichiometry indicates that the chelation of* Hg^{2+} *by NAPA results in the Hg-(NAPA)*$_2$ *complex.*

Buffer	**n**	**ΔH_{ITC} (kcal/mol)**	**K_{ITC}**	**$K_{Hg\text{-}MerP}$**
BisTris	1.9 ± 0.1	-0.5 ± 0.1	1.0 (± 0.3)×10^5	1.6 (± 0.3)×10^{33}
ACES	2.1 ± 0.2	-3.0 ± 0.2	1.2 (± 0.3)×10^4	1.2 (± 0.3)×10^{34}
TRIS	2.2 ± 0.1	-4.4 ± 0.3	1.8 (± 0.1)×10^4	8.9 (± 0.1)×10^{33}
Average	**2.0 ± 0.2**			**8 (± 6)×10^{33}**

Determination of the condition-independent affinity of MerP for Hg^{2+}, as discussed previously, requires an additional set of experiments, although a similar analysis to that of the binding enthalpy. In these experiments, immediately prior to the ITC measurement, 1 molar equivalent of Hg^{2+} was added to apo-MerP to form the Hg-MerP complex (1:1). Then N-Acetyl-D-penicillamine was titrated into this Hg-MerP complex, resulted in the chelation of Hg^{2+} from MerP to form the Hg-$(NAPA)_2$ complex.[40,42] The Hg-$(NAPA)_2$ was confirmed by the experimental stoichiometry, whereby two NAPA chelate the Hg^{2+} from MerP.

These chelation experiments result in weak exothermic binding with an apparent binding affinity that is within the range of ITC (**Figure 4.3.1.3**). As noted above, the enthalpy of this binding cannot be utilized to determine the Hg-MerP interaction as the NAPA protonation and Hg-$(NAPA)_2$ formation enthalpies are unknown. However, prior to quantification of the condition-independent binding constant of the Hg-MerP complex, confidence can be gained by a similar proton analysis. Since the pK_as of NAPA are known, the number of protons that would dissociate from NAPA upon formation of the Hg-$(NAPA)_2$ complex is quantifiable. As such, repeating the chelation of Hg^{2+} from MerP in multiple buffers can establish the number of protons that bind to buffer through plotting the buffer-protonation enthalpy in the X-axis vs. the experimental binding enthalpy in the Y-axis (**Figure 4.3.1.4**). This proton plot reveals a slope of +0.90 ± 0.06. Thus, the chelation of Hg^{2+} from MerP by $NAPA_2$ results in 0.90 ± 0.06 protons binding to the buffer. Each NAPA has one relevant pK_a (10.01 ± 0.1), which, at pH 7.4, suggests that ~2 (0.9975 ± 0.0005 per NAPA; 1.9950 ± 0.0005 per $NAPA_2$) protons would be released upon the formation of the Hg-$(NAPA)_2$ complex. This proton inventory reveals that 1.1 ± 0.06 protons would to MerP upon the chelation of Hg^{2+} by NAPA, which is in agreement with the previous Hg-EDTA competition experiments, above.

Quantification of the MerP affinity for Hg^{2+} via the chelation of Hg^{2+} by $(NAPA)_2$ utilizes the average apparent binding affinities (**Table 4.3.1.2**). A detailed derivation of metal chelation experiments to determine the condition-independent binding affinity is described in Chapter 2. For the chelation of Hg^{2+} by NAPA, the following describes the equilibrium constant where (**Equation 4.2.1.2**),

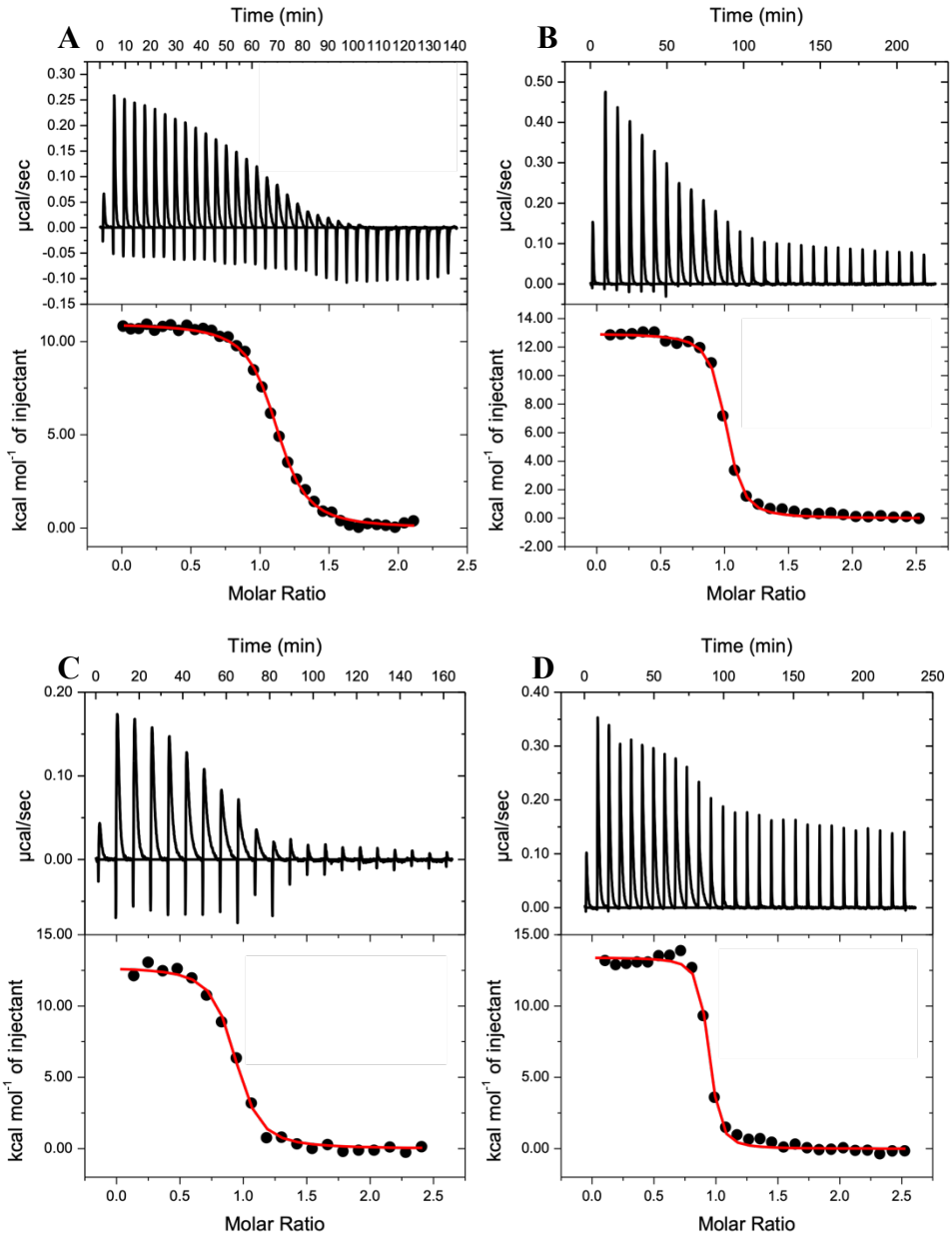

Figure 4.3.2.1. *Representative isotherms of the titration of Cu^{+}, stabilized by excess reduced GSH, titrated into 15 µM apo-MerP in 50 mM buffer, 50 mM NaCl, pH 7.4, and 10-fold excess glutathione in 10-fold excess to Cu^{+}. (A) PIPES: n = 1.10 ± 0.01, K_{ITC} = 6.2 (± 0.4)×10^{6} M^{-1}, ΔH_{ITC} = 10.96 ± 0.05 kcal/mol; (B) BisTris: n = 0.97 ± 0.01, K_{ITC} = 1.6 (± 0.1)×10^{7} M^{-1}, ΔH_{ITC} = 12.93 ± 0.07 kcal/mol;(C) ACES: n = 0.89 ± 0.01, K_{ITC} = 1.3 (± 0.2)×10^{7} M^{-1}, ΔH_{ITC} = 12.73 ± 0.2 kcal/mol; (D) TRIS: n = 0.90 ± 0.01, K_{ITC} = 3.6 (± 0.7)×10^{7} M^{-1}, ΔH_{ITC} = 13.4 ± 0.1 kcal/mol.*

Table 4.3.2.1. *Apparent (K_{ITC} and ΔH_{ITC}) and condition-independent (KCu^{+}_{-MerP} and ΔHCu^{+}_{-MerP}) binding thermodynamics for the interaction between Cu^{+} and MerP in 50 mM buffer, 50 mM NaCl, pH 7.4, and 10-fold excess to Cu^{+} of reduced glutathione.*

Buffer	**n**	**K_{ITC}**	**ΔH_{ITC} (kcal/mol)**	**$K_{Cu+-MerP}$**	**$\Delta H_{Hg-MerP}$ (kcal/mol)**
PIPES	1.10 ± 0.03	1.0 (± 0.5)×10^{7}	10.3 ± 0.8	1.0 (± 0.9)×10^{16}	-6.5 (± 0.8)
BisTris	0.90 ± 0.08	1 (± 1)×10^{7}	12.4 ± 0.8	2 (± 2)×10^{16}	-6.0 (± 0.8)
ACES	0.7 ± 0.2	1.0 (± 0.4) X10^{7}	12.8 ± 0.1	1.9 (± 0.8)×10^{16}	-6.6 (± 0.1)
TRIS	0.89 ± 0.02	3.3 (± 0.3)×10^{7}	13.4 ± 0.6	6.3 (± 0.6)×10^{16}	-6.8 (± 0.6)
Average	**0.94 ± 0.15**			**3 (± 2)×10^{16}**	**-6.5 ± 0.3**

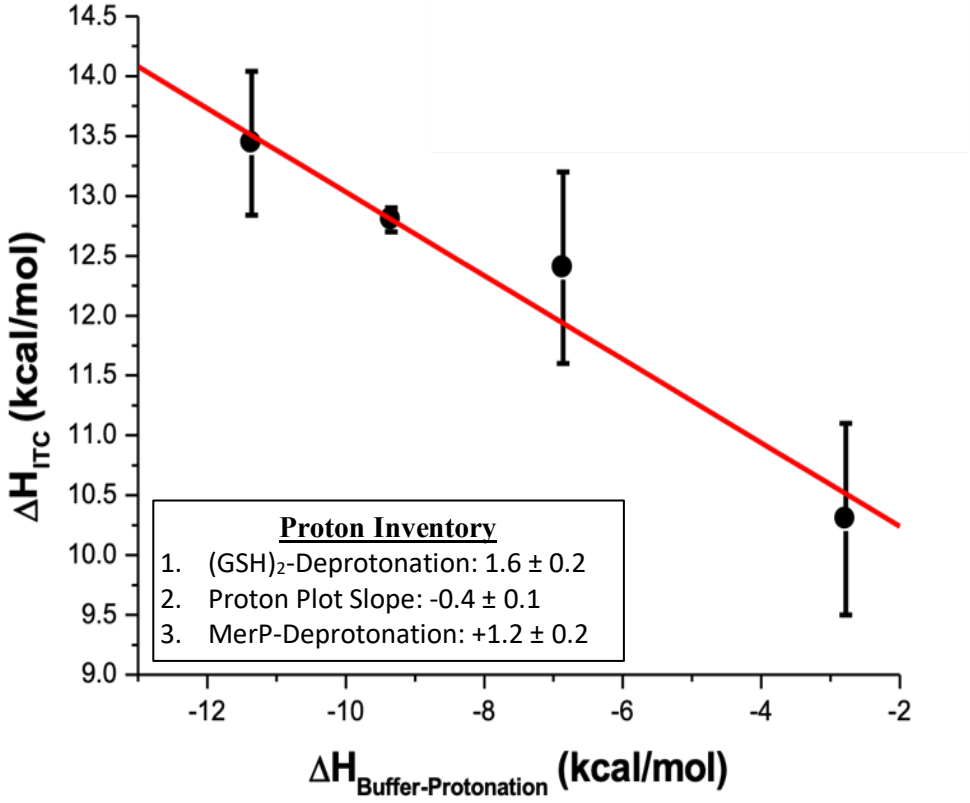

Figure 4.3.2.2. *Proton plot associated with the titration of Cu^{+} into apo-MerP to form the Cu^{+}-MerP (1:1) complex in excess reduced glutathione. Insert: proton inventory to establish the number of protons that leave MerP upon the binding of Cu^{+}. The slope of the proton plot indicates that 0.4 ± 0.1 protons dissociate from the buffer when Cu^{+} binds to apo-MerP, with 1.6 ± 0.2 protons binding to reduced glutathione after forming the Cu^{+}-MerP complex. Thus, 1,2 ± 0.2 protons dissociate from MerP when Cu^{+} binds.*

$$K_{Hg-MerP} = \left(\frac{K_{Hg-(NAPA)_2}}{K_{ITC}\left(1 + K_{NAPA-H_1}[H^+] + \beta_{NAPA-H_2}[H^+]^2\right)} - 1 \right) \Big/ [Protein] \quad \textbf{Equation 4.3.1.2}$$

Using **Equation 4.3.1.2**, the buffer-independent equilibrium constant for the formation of the Hg-MerP complex at pH 7.4 is 8 (± 6)×10^{33} M^{-1} (**Table 4.3.1.2**).

Combining the condition-independent enthalpy that was found with the EDTA-competition experiment and the condition-independent equilibrium constant that was quantified by the NAPA chelation of Hg^{2+} allows the entropic contribution to Hg^{2+} binding to be determined. **Table 4.4.1** summarizes the average buffer-independent thermodynamic values at pH 7.4 for Hg^{2+}, and other monovalent and divalent metals binding to MerP.

4.3.2. Copper(I)-MerP Binding Thermodynamics

Quantitation of the thermodynamics of Cu^+ binding to MerP is challenging due to do aerobic oxidation of Cu^+ and the thiophilic nature of Cu^+, which leads to binding affinities outside the accessible range of ITC and the propensity of Cu^+ to disproportionate, as shown in the equilibrium:

$$2Cu^+_{(aq)} \rightleftharpoons Cu^{2+}_{(aq)} + Cu^0_{(s)} \qquad Equation\ 4.3.2.1$$

which has a K ~10^6 of these challenges, however, can be overcome through anaerobic conditions and the addition of a Cu^+ stabilizing ligand such as acetonitrile (log β_3 = 4.23), hexamethyltrien (Me_6trien: logK = 12.7), glutathione (GSH: log β_2 = 14.5), bichinchoninic acid (BCA: log β_2 = 17.5), or bathocuproinedisulfonic acid (BCS: log β_2 = ~20.6). Careful consideration of the competition for Cu^+ must be balanced and optimized for ITC experimental design.

The Cu^+ was stabilized by reduced glutathione under anaerobic conditions for its binding to MerP because previous experimental work on Cu^+ binding to HAH1 suggested that the MerP affinity for Cu^+ would be greater than that of GSH, but less than that of BCA or BCS.

Copper(I), stabilized by 10-fold excess GSH, was titrated into apo-MerP in 50 mM buffer (PIPES, BisTris, ACES, and TRIS), 50 mM NaCl, pH 7.4, and excess GSH in both the cell and syringe (**Figure 4.3.2.1**). These isotherms show moderate heat from a net endothermic binding. The inflection of these isotherms is within the c-window of ITC and

includes multiple datapoints within the inflection itself, indicating that the apparent binding affinity can be utilized to determine the condition-independent equilibrium constant for Cu^+ binding to MerP. The experimental binding thermodynamics are summarized in **Table 4.3.2.1** and are the result of at least 2 independent experiments.

The apparent binding parameters are the sum of all thermodynamic contributions the titration (i.e. buffer (de)-protonation, protein (de)-protonation, GSH protonation, etc.). Taking the thermodynamics of each of these events into account via a *post-hoc* analysis allows the buffer-independent binding thermodynamics at pH 7.4 to be quantified to determine the number of protons that dissociate from the protein when Cu^+ binds. A proton inventory can be used. Previously, the thermodynamics and protonation of GSH upon dissociation of the Cu^+-$(GSH)_2$ complex, were determined by ITC, which showed that Cu^+ binding two GSH results in the deprotonation of 1.6 ± 0.2 protons. By plotting the buffer protonation enthalpy for each buffer (TRIS, ACES, BisTris, and PIPES) vs. the experimental enthalpy (ΔH_{ITC}), the slope determines the number of protons that associate or dissociate from the buffer (Figure 4.3.2.2). The proton plot shows a slope of -0.4 ± 0.1 H^+, which indicates that 0.4 protons are dissociating from buffer. Thus, the proton inventory shows that 1.6 ± 0.2 protons must bind to $(GSH)_2$, and 0.4 ± 0.1protons leave buffer, requiring that, 1.2 ± 0.2 protons leave MerP when Cu^+ binds, which is consistent with literature values as well as other metal-binding experiments discussed herein.

Now that the proton inventory has been established, the condition-independent enthalpy for Cu^+ binding to MerP interaction can be determined. By defining each of the competing equilibria that occurs in the titration of Cu^+-$(GSH)_2$ into MerP and establishing the enthalpy of each of these association or dissociation events, the coupled metal-binding and protein deprotonation enthalpy can be quantified. The sum of each of these events is equal to the experimental enthalpy. So, accounting for each of these contributing thermodynamics, the buffer-independent enthalpy of formation of the Cu^+-MerP complex at pH 7.4 can be determined, as shown by,

$$\Delta H_{Cu(I)-MerP} = \Delta H_{MP} - \Delta H_{PH} = \Delta H_{ITC} + \Delta H_{LH} \times \left(nH^+{}_{(GSH)_2} - nH^+{}_{PH}\right) \times \Delta H_{BH} \qquad \textbf{Equation 4.3.2.2.}$$

This equation is slightly different from the typical calculation of the condition-independent enthalpy, as the formation enthalpy of the Cu^{+}-$(GSH)_2$ was determined experimentally, leading to a coupled metal-ligand enthalpy and ligand deprotonation enthalpy. Thus, the enthalpy of the GSH complex is already considered, and careful attention is required to prevent counting this enthalpy twice. The average condition-independent Cu^{+}-MerP binding enthalpy at pH 7.4 is -6.8 ± 0.3 kcal/mol. The associated pH-dependent, buffer-independent equilibrium constant is calculated by:

$$K_{Cu(I)-MerP} = K_{ITC} \times (1 + K_{Cu(I)-(GSH)_2} \times [GSH] \times \alpha_{proton-GSH} \quad \textbf{Equation 4.3.2.3.}$$

Similar to the condition-independent enthalpy, this equation utilizes the coupled thermodynamics for the Cu^{+}-$(GSH)_2$ complex, which originates from the $\alpha_{proton\text{-}GSH}$ in which,

$$\alpha_{proton-GSH} = \left(\frac{\alpha_{proton-GSH-apparent}}{\alpha_{proton-GSH-real}}\right)^2 = 4.19\ X\ 10^{-3} \qquad \textbf{Equation 4.3.2.4}$$

The buffer-independent equilibrium constant for Cu^{+} binding to MerP at pH 7.4 is 3 (± 2)×10^{16}. **Table 4.3.2.1** summarizes the condition-independent thermodynamic values at pH 7.4 for each buffer utilized.

4.3.3. Quantification of the Zinc-MerP Thermodynamics

Although metal binding thermodynamics of the Zn^{2+} metallochaperone, ZntA, which also has a ferredoxin-like fold and metal binding site, are not known and suggest an interesting comparison with other monovalent and divalent metal ion metallochaperones. Typically Zn^{2+} concentrations in the cell are far larger than those of Cu^{+} or Hg^{2+}, yet the same protein architecture is utilized to bind each of these metals, as well as Cd^{2+} (*vide infra*). The thermodynamic foundation of this metal selectivity and specificity in these proteins may provide some insight into the cellular function of these metallochaperones. Thus, the thermodynamics of Zn^{2+} binding to MerP, and other metallochaperones, although they are not expected to bind Zn^{2+}, is explored.

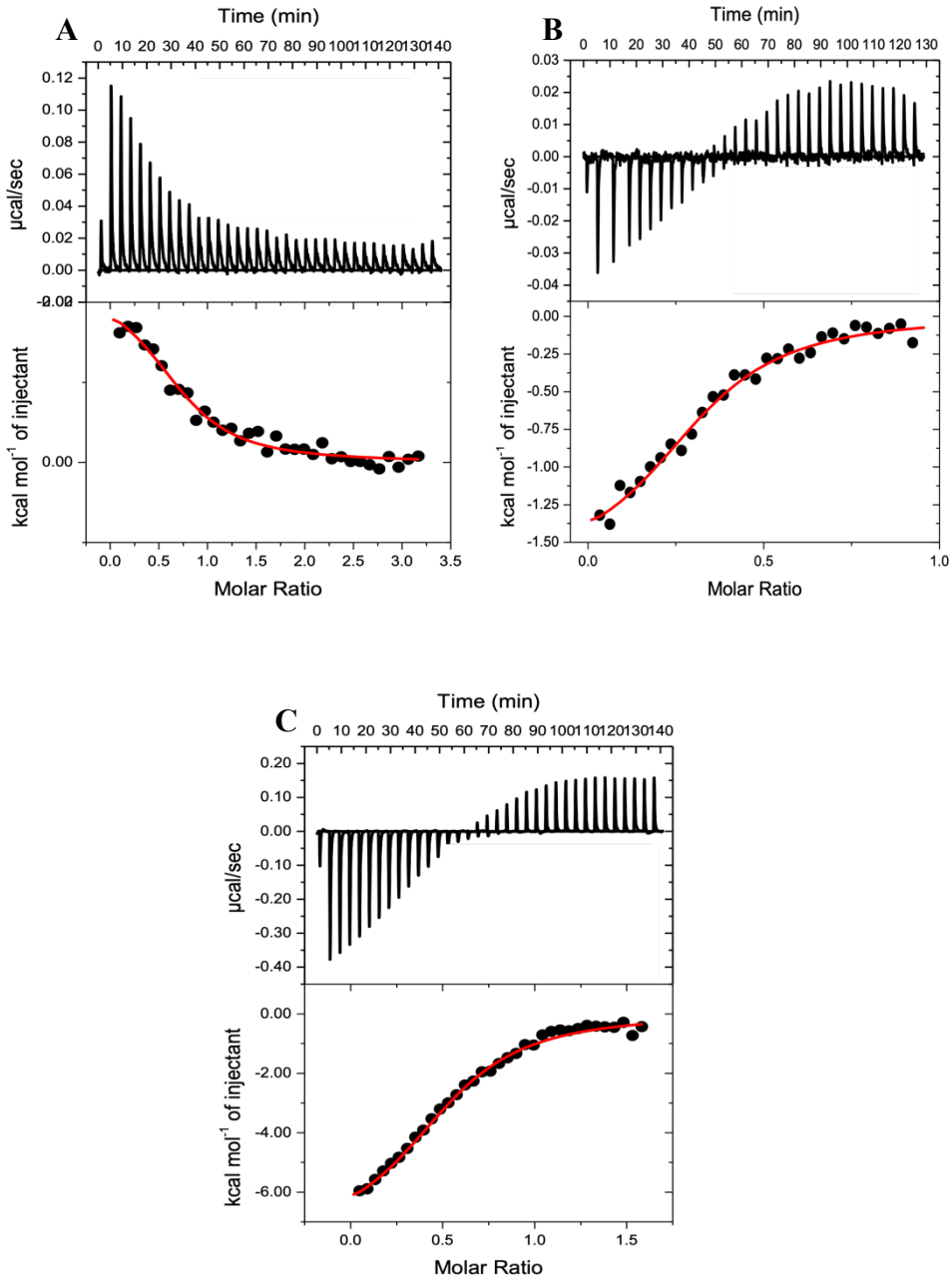

Figure 4.3.3.1. *Representative isotherms of the titration of 150-225 uM Zn^{2+} titrated into 15 µM apo-MerP in 50 mM buffer, 50 mM NaCl, pH 7.4. (A) HEPES: n = 0.73 ± 0.04, K_{ITC} = 3.72 (± 0.7)×10^5 M^{-1}, ΔH_{ITC} = 2.2 ± 0.2 kcal/mol; (B) BisTris: n = 0.33 ± 0.01, K_{ITC} = 4.33 (± 0.7)×10^5 M^{-1}, ΔH_{ITC} = -1.68 ± 0.09 kcal/mol;(C) TRIS: n = 0.55 ± 0.01, K_{ITC} = 1.7 (± 0.1)×10^5 M^{-1}, ΔH_{ITC} = -7.6 ± 0.2 kcal/mol.*

Table 4.3.3.1. *Apparent (K_{ITC} and ΔH_{ITC}) and condition-independent ($K_{Zn2+\text{-}MerP}$ and $\Delta H_{Zn2+\text{-}MerP}$) binding thermodynamics for the interaction between Zn^{2+} and MerP in 50 mM buffer, 50 mM NaCl, pH 7.4.*

Buffer	**n**	**K_{ITC}**	**ΔH_{ITC} (kcal/mol)**	**$K_{Zn2+\text{-}MerP}$**	**$\Delta H_{Zn2+\text{-}MerP}$ (kcal/mol)**
HEPES	0.7 ± 0.03	4 (± 0.9)×10^5	2.21 ± 0.05	2.3 (± 0.5)×10^7	12.3 (± 0.1)
BisTris	0.33 ± 0.01	7 (± 4)×10^5	-2.5 ± 1.2	8 (± 4)×10^6	10.2 (± 1.3)
TRIS	0.64 ± 0.03	2 (± 0.7)×10^5	-7.1 ± 0.7	5 (± 2)×10^5	12.4 (± 0.7)
Average	**0.57 ± 0.18**			**1.0 (± 0.6)×10^7**	**11.6 ± 1.5**

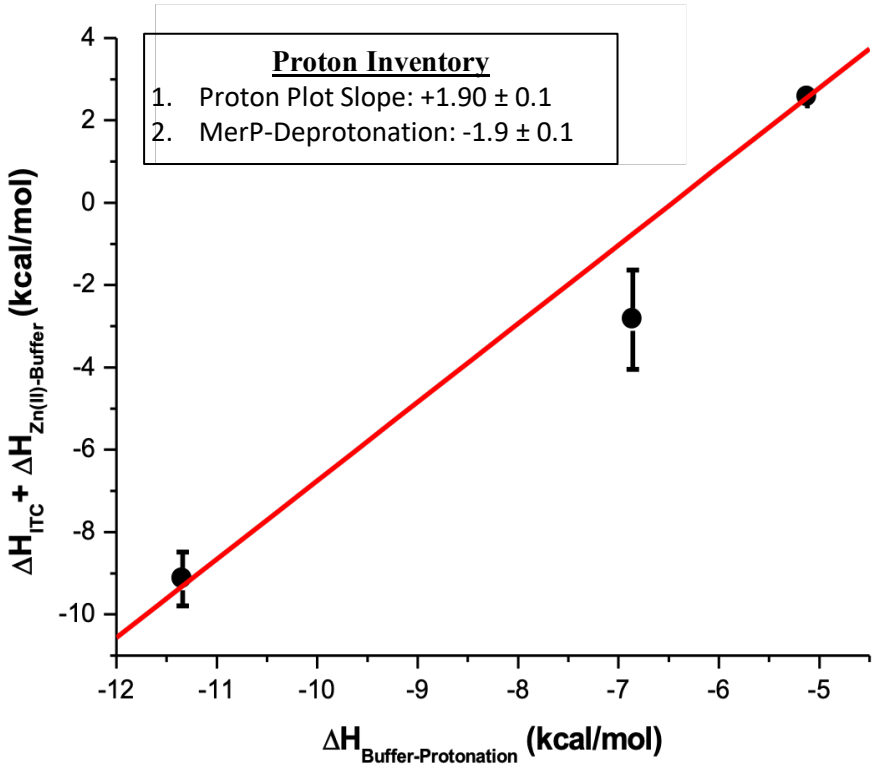

Figure 4.3.3.2. *Proton plot associated with the titration of Zn^{2+} into apo-MerP to form the Zn^{2+}-MerP (1:2) complex. Insert: proton inventory to establish the number of protons that leave MerP upon the binding of Zn^{2+}. The slope of the proton plot indicates that 1.9 ± 0.1 protons bind to the buffer when Zn^{2+} binds to apo-MerP, which forms the Zn-$(MerP)_2$ complex. Thus, 1.9 ± 0.1 protons dissociate from 2MerP when Zn^{2+} binds to form the metal-bridged protein dimer complex.*

Unlike Cu^{+} and Hg^{2+}, titrations of Zn^{2+} into a protein can typically be completed without the use of a competing ligand. The Zn^{2+}-buffer interaction is generally strong enough to compete with the Zn^{2+}-protein interactions. However, the inclusion of a competing ligand can be utilized if the Zn^{2+}-protein experimental binding affinity falls outside the range accessible by ITC.

Calorimetric measurements of Zn^{2+} binding to MerP were completed through titrations of Zn^{2+} in a series of buffers (TRIS, BisTris, and HEPES), as shown in **Figure 4.3.3.1**. These isotherms show well-defined peaks with low experimental enthalpies, which were fit with a one-site binding model to show a binding stoichiometry of 0.57 ± 0.18. To quantify the condition-independent thermodynamics, the deprotonation of MerP must be determined. As with other metals, construction of a proton plot shows a slope of +1.9 ± 0.1, indicating that 1.9 ± 0.1 protons are displaced from MerP when Zn^{2+} binds. Average buffer-dependent experimental thermodynamics are shown in **Table 4.3.3.1**.

Quantification of the proton-coupled condition-independent metal-binding enthalpy is achieved by:

$$\Delta H_{Zn(II)-MerP} = \Delta H_{MP} - (n_{H^+} \times \Delta H_{PH}) = \Delta H_{ITC} + \Delta H_{MB} - (n_{H^+} \times \Delta H_{BH}) \quad \textbf{Equation 4.3.3.1}$$

where n_{H+} is equal to 1.9 ± 0.1.

Similarly, determination of the condition-independent equilibrium constant is:

$$K_{Zn(II)-MerP} = K_{ITC} \times (1 + K_{MB} \times [Buffer]_{basic}) \quad \textbf{Equation 4.3.3.2.}$$

where $[Buffer]_{basic}$ is the concentration of the deprotonated form of each buffer. Thus, at pH 7.4, the average buffer-independent enthalpy and equilibrium constant at pH 7.4 are $\Delta H_{Zn2+-MerP}$ = 11.6 ± 1.5 kcal/mol and $K_{Zn-MerP}$ = 1 (± 0.6)×10^7 M^{-1}. These condition-independent thermodynamics are shown in **Table 4.3.3.1**. A comparative thermodynamic summary of Zn^{2+} and other metals binding to MerP is found in **Table 4.4.1**.

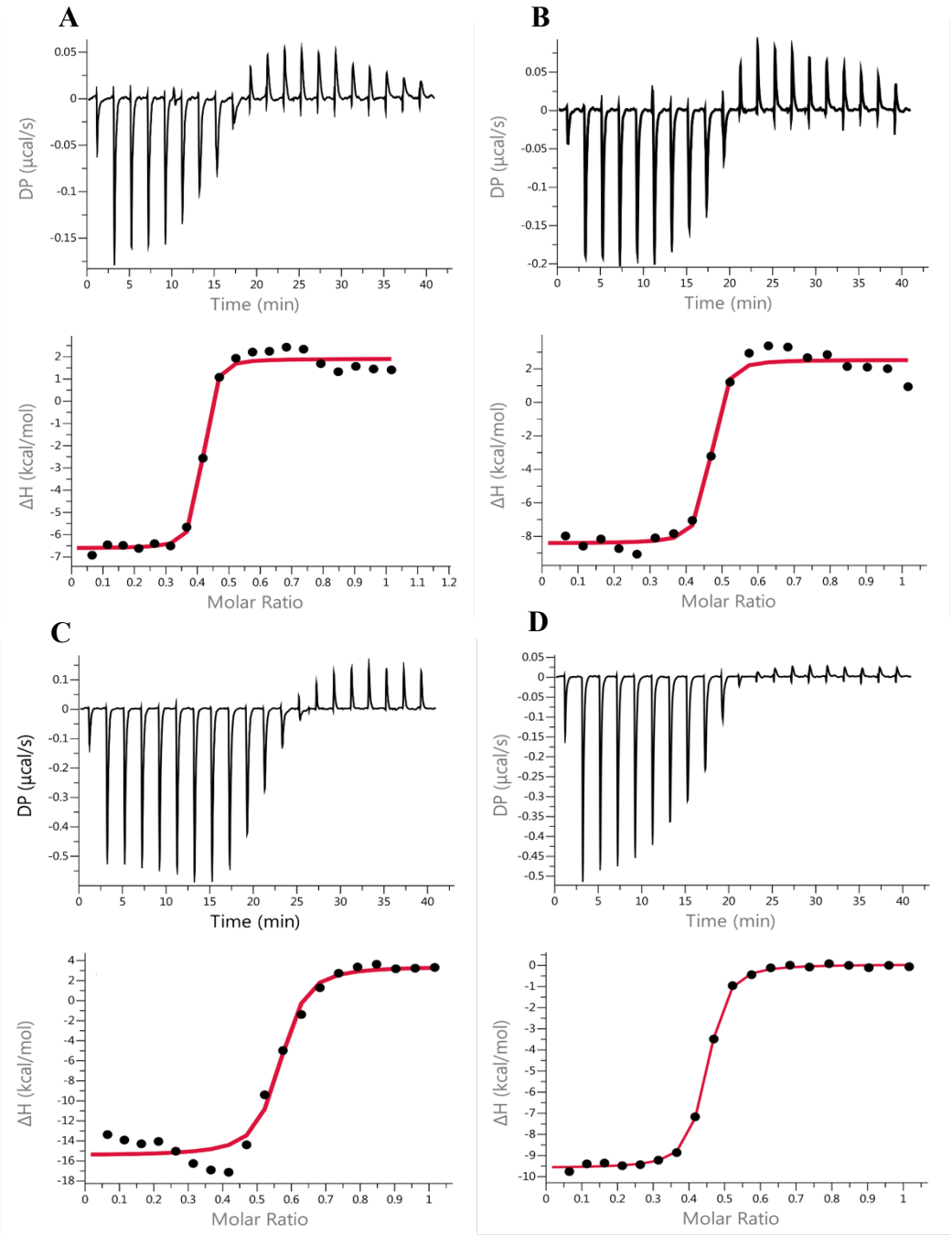

Figure 4.3.4.1. *Representative isotherms for the titration of Cd^{2+}, in buffer, into 30-45 uM apo-MerP under anaerobic conditions in 50 mM buffer, 50 mM NaCl, pH 7.4. (A) HEPES: n = 0.392 ± 0.004, K_{ITC} = 5.3 (± 0.3)×10^7 M^{-1}, ΔH_{ITC} = -8.5 ± 0.2 kcal/mol; (B) BisTris: n = 0.444 ± 0.005, K_{ITC} = 5 (± 2)×10^5 M^{-1}, ΔH_{ITC} = -10.9 ± 0.4 kcal/mol;(C) ACES: n = 0.426 ± 0.001, K_{ITC} = 1 (± 2)×10^7 M^{-1}, ΔH_{ITC} = -9.62 ± 0.06 kcal/mol. (D) TRIS: n = 0.54 ± 0.01, K_{ITC} = 9.6 (± 0.3)×10^6 M^{-1}, ΔH_{ITC} = -18.8 ± 0.9 kcal/mol.*

Table 4.3.4.1. *Buffer-dependent apparent (K_{ITC} and ΔH_{ITC}) and pH-dependent, buffer-independent ($K_{Cd2+\text{-}MerP}$ and $\Delta H_{Cd2+\text{-}MerP}$) binding thermodynamics for the interaction between Cd^{2+} and MerP in 50 mM buffer, 50 mM NaCl, pH 7.4.*

Buffer	**n**	**K_{ITC}**	**ΔH_{ITC} (kcal/mol)**	**$K_{Cd2+\text{-}MerP}$**	**$\Delta H_{Cd2+\text{-}MerP}$ (kcal/mol)**
HEPES	0.44 ± 0.09	3 (± 2)×10^7	-8.5 ± 0.4	1.1 (± 0.5)×10^{10}	2.0 (± 0.4)
BisTris	0.40 ± 0.03	5 (± 5)×10^7	-11.2 ± 0.3	6.5 (± X)×10^8	1.2 (± 0.3)
ACES	0.40 ± 0.05	6 (± 4)×10^6	-9.4 ± 0.3	2.4 (± X)×10^8	1.9 (± 0.3)
TRIS	0.48 ± 0.06	9 (± 2)×10^6	-20 ± 1	1.7 (± X)×10^7	1 (± 1)
Average	**0.43 ± 0.07**			**3 (± 5)×10^9**	**1.5 ± 0.6**

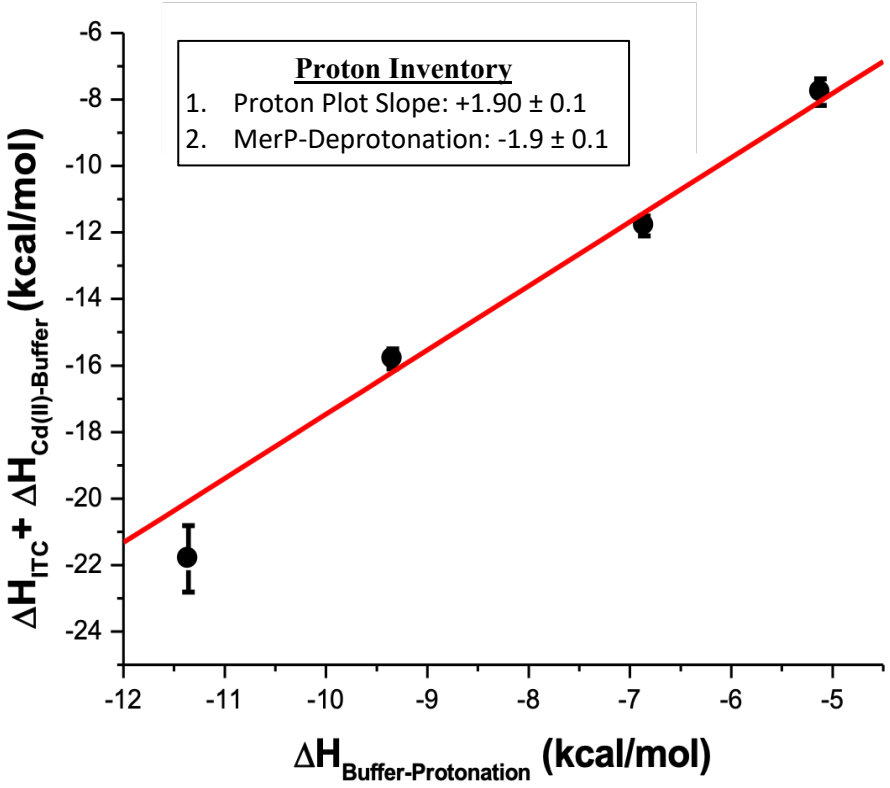

Figure 4.3.4.2. *Proton plot associated with the titration of Cd^{2+} into apo-MerP to form the Cd^{2+}-MerP (1:2) complex. Insert: proton inventory to establish the number of protons that leave MerP upon the binding of Cd^{2+}. The slope of the proton plot indicates that 1.9 ± 0.1 protons bind to the buffer when Cd^{2+} binds to apo-MerP, which forms the Cd-$(MerP)_2$ complex. Thus, 1.9 ± 0.1 protons dissociate from 2MerP when Cd^{2+} binds to form the metal-bridged protein dimer complex.*

4.3.4. Quantification of the Cadmium-MerP Thermodynamics

The rational to include Cd^{2+} in this series of metals binding to MerP, and WND4 (*vide infra*), is similar to that for Zn^{2+}. CadA, like ZntA for Zn^{2+}, MerP for Hg^{2+}, and HAH1 for Cu^{+}, is a ferredoxin-like fold metallochaperone that binds Cd^{2+} via the conserved $MX_1C_nX_2X_3C_c$ sequence. Thermodynamics associated with Cd^{2+} binding to MerP is probed to explore the metal selectivity and metal specificity within this ferredoxin-like protein architecture.

Like the binding of Zn^{2+} to MerP, the binding of Cd^{2+} is done without the use of a competing ligand. Buffer, in large excess, is utilized as a competing ligand for Cd^{2+}, which requires the thermodynamics of the Cd^{2+}-buffer interaction to be included in the *post-hoc* analysis. Use of a complexing ligand can also be used, if the Cd^{2+}-buffer interaction is too weak, compared to the protein.

Quantification of the Cd^{2+}-MerP binding thermodynamics requires MerP deprotonation. This analysis was done using four buffers, HEPES, BisTris, ACES, and TRIS, each with their own set of Cd^{2+}-buffer thermodynamics. These isotherms show well-defined exothermic peaks with a primary inflection at a stoichiometry of 0.43 ± 0.07 Cd^{2+} binding per MerP (**Figure 4.3.4.1**).

Although the number of protons that are displaced from MerP when metals bind has been thoroughly discussed, both in the literature and within this thesis, the number of protons that dissociate from MerP when Cd^{2+} binds should be determined to ensure this is consistent for this metal ion. By plotting buffer-protonation enthalpy vs the sum of the experimental enthalpy and the Cd^{2+}-buffer enthalpy, and applying a linear regression to these data points, the slope of the line indicates the number of protons that bind to or dissociate from the buffer. This proton plot shows that 1.9 ± 0.1 protons bind to buffer, from their dissociation from MerP, upon Cd^{2+} binding to the protein (**Figure 4.3.4.2**).

Using this protein and buffer (de)-protonation, the condition-independent enthalpy could be quantified by:

$$\Delta H_{Cd(II)-MerP} = \Delta H_{MP} - (n_{H^+} \times \Delta H_{PH}) = \Delta H_{ITC} + \Delta H_{MB} - (n_{H^+} \times \Delta H_{BH}) \quad \textbf{Equation 4.3.4.1}$$

where n_{H+} is equal to the number of protons are bind to the buffer, or dissociate from MerP, when Cd^{2+} binds to the protein. This condition-independent binding enthalpy is equal to $\Delta H_{Cd2+\text{-}MerP} = 1.5 \pm 0.6$ kcal/mol, on a *per-metal* basis.

Likewise, the determination of the Cd^{2+}-MerP equilibrium constant must also take into account the equilibrium constants for each of the competing equilibria. This is achieved by:

$$K_{Zn(II)-MerP} = K_{ITC} \times (1 + K_{MB} \times [Buffer]_{basic}) \qquad \textbf{Equation 4.3.4.2.}$$

The condition-independent binding affinity is equal to $3 (\pm 5) \times 10^9$. Summarization of both the experimental and condition-independent thermodynamics are shown in **Table 4.3.4.1**.

4.3.5. Thermodynamics of Hg^{2+} Binding to WND4

Unlike the characterization of the Hg^{2+} binding to MerP, the measurements to establish the enthalpy and affinity for Hg^{2+} binding to WND4 used a single competing ligand, reduced glutathione (GSH) in large excess to Hg^{2+}. At least 3 independent ITC experiments were completed in three buffers (TRIS, TAPSO, and BisTris). These isotherms show low experimental heat that is endothermic (**Figure 4.3.5.1**). The peaks are well-defined, indicating that Hg^{2+} binds to WND4 rapidly and readily returns to equilibrium. These experiments show a distinct inflection at a stoichiometry of 0.5 ± 0.1, suggesting that these form a metal-bridged dimer in solution. This inflection is typical of binding affinities and within the accuracy range of ITC: $K = \sim 10^6$.

To determine of the number of protons that are released Hg^{2+} binding to WND4 requires a proton plot and subsequent proton inventory. This proton plot has a slope of -0.41 ± 0.09. Since 1.4 ± 0.2 protons bind to GSH, upon dissociation of the Hg-$(GSH)_2$ complex, after WND4 binds Hg^{2+}, this indicates that 1.0 ± 0.2 protons must be released to form the Hg-$(WND4)_2$ complex, from which 0.5 ± 0.1 protons are released per WND4 monomer (**Figure 4.3.5.2**). With the number of protons that are released when Hg^{2+} binds to WND4 in excess GSH quantified the buffer-independent thermodynamics at pH 7.4 can be established.

By taking the enthalpies of the competing equilibria into account, the condition-independent binding enthalpy can be calculated, as shown by,

$$\Delta H_{Hg(II)-Wnd4} = \Delta H_{MP} - \Delta H_{PH} = \Delta H_{ITC} + \Delta H_{ML_2} + \left[\left(n_{H_{L_2}^+} - n_{H_P^+}\right) \times \Delta H_{BH}\right] \quad \textbf{Equation 4.3.5.1}$$

Quantifying the Hg-$(WND4)_2$ thermodynamics requires the thermodynamics of the Hg-$(GSH)_2$ complex, which had been determined previously within the Wilcox lab. This enthalpy, however, is the coupled metal-ligand enthalpy and ligand-deprotonation enthalpy. So, the enthalpy associated with GSH deprotonation was already included in the analysis. Subtracting the heat associated with this deprotonation, the remainder of the protons that interact with the buffer are included in the calculation. The average condition-independent binding enthalpy associated with the formation of the Hg^{2+}-WND4 complex at pH 7.4 after the chelation of Hg^{2+} from excess GSH is -30.0 ± 0.1 kcal/mol on a *per-metal* basis.

Likewise, quantification of the condition-independent binding affinities is shown by:

$$K_{Hg(II)-Wnd4} = K_{ITC} \times (1 + K_{Hg(II)-(GSH)_2} \times [GSH] \times \alpha_{proton-GSH} \quad \textbf{Equation 4.3.5.2}$$

Similar to the condition-independent enthalpy, this equation utilizes the coupled thermodynamics from the coupled Hg^{2+}-$(GSH)_2$ complex, which originates, in part, from the $\alpha_{proton\text{-}GSH}$, in which:

$$\alpha_{proton-GSH} = \left(\frac{\alpha_{proton-GSH-apparent}}{\alpha_{proton-GSH-real}}\right)^2 = 4.19\ X\ 10^{-3} \qquad \textbf{Equation 4.3.5.3}$$

This *post-hoc* analysis indicates that WND4 binds Hg^{2+} with an affinity of 3 (± 1)×10^{32}. Average experimental and condition-independent thermodynamics associated with the formation of the Hg-$(WND4)_2$ complex at pH 7.4 are shown in **Table 4.3.5.1**.

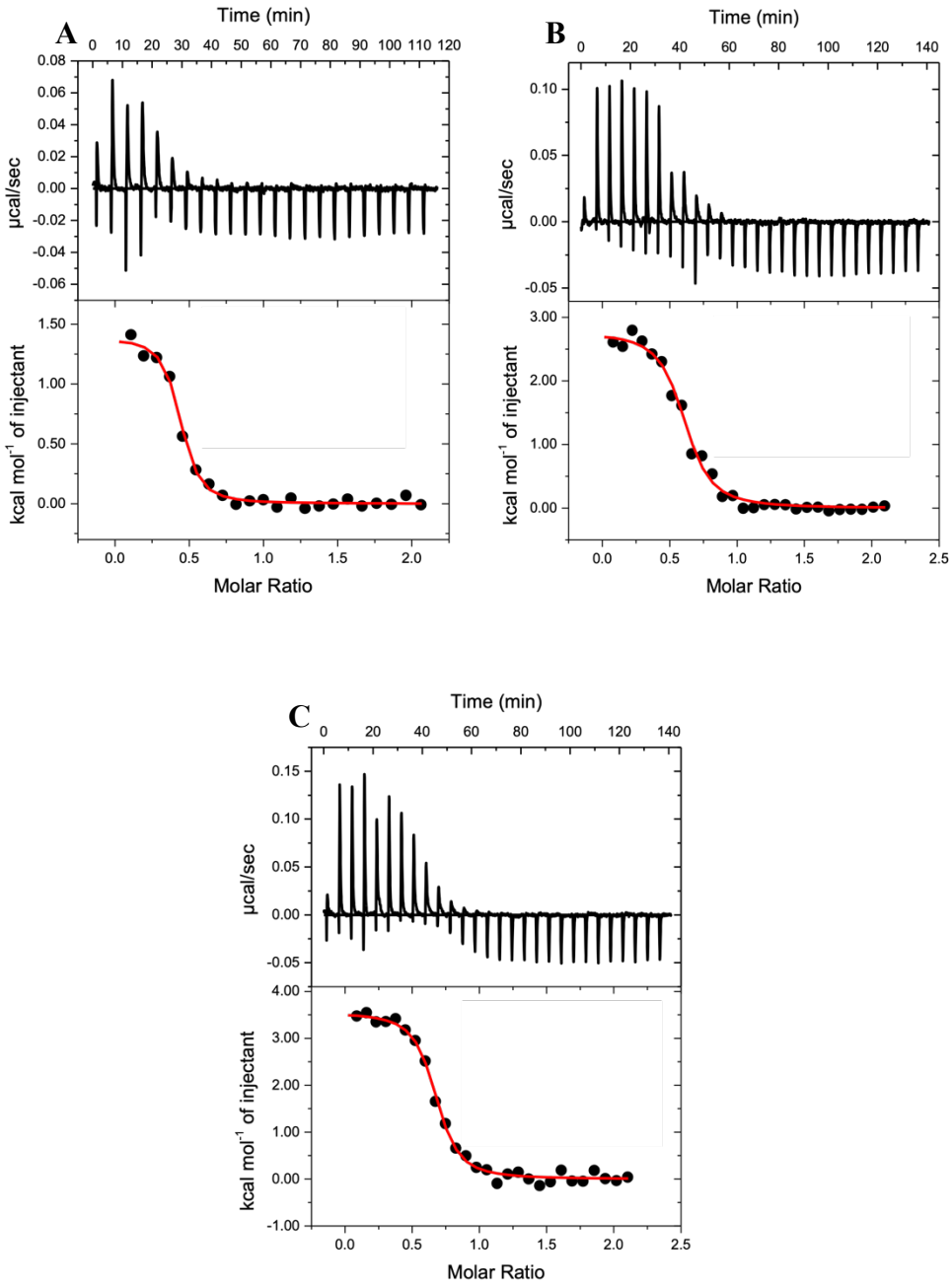

Figure 4.3.5.1. *Representative isotherms for the titration of 150 µM Hg^{2+} into 15 µM apo-WND4 in 50 mM Buffer, 50 mM NaCl, pH 7.4 and 10-fold excess of reduced glutathione to Hg^{2+}. (A) BisTris: n = 0.41 ± 0.01, K_{ITC} = 7 (± 1)×10^6 M^{-1}, ΔH_{ITC} = 1.39 ± 0.04 kcal/mol; (B) TAPSO: n = 0.60 ± 0.01, K_{ITC} = 3.9 (± 0.7)×10^6 M^{-1}, ΔH_{ITC} = 2.77 ± 0.07 kcal/mol;(C) TRIS: n = 0.652 ± 0.007, K_{ITC} = 6 (± 0.9)×10^6 M^{-1}, ΔH_{ITC} = 3.55 ± 0.05 kcal/mol.*

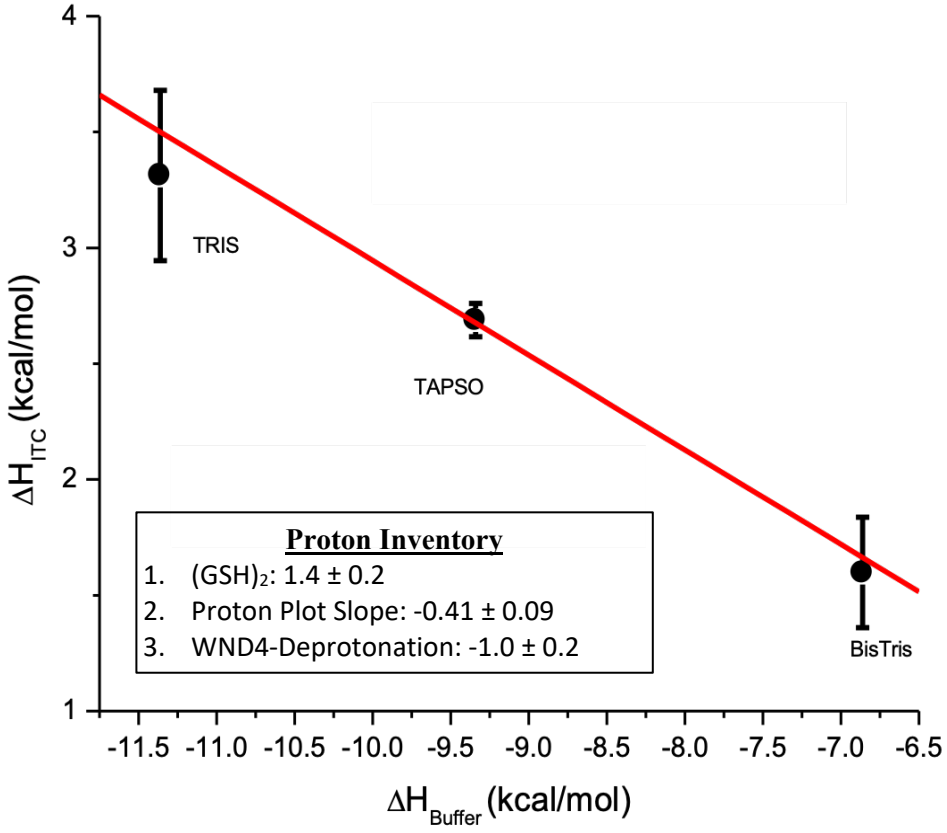

Figure 4.3.5.2. *Proton plot associated with the titration of Hg^{2+}, in 10-fold excess GSH into apo-WND4 to form the Hg^{2+}-WND4 (1:2) complex. Insert: proton inventory to establish the number of protons that leave MerP upon the binding of Hg^{2+}. The slope of the proton plot, along with the number of protons that bind to $(GSH)_2$, indicates that 1.0 ± 0.2 protons dissociate from the Hg^{2+}-$(WND4)_2$ complex to form the metal-bridged protein dimer complex.*

Table 4.3.5.1. *Average apparent and condition-independent binding thermodynamics associated with the titration of Hg^{2+} into apo-WND4 in 50 mM buffer, 50 mM NaCl, pH 7.4 with 10-fold excess GSH to Hg^{2+}.*

Buffer	**n**	**K_{ITC}**	**ΔH_{ITC} (kcal/mol)**	**$K_{Hg2+\text{-}WND4}$**	**$\Delta H_{Hg2+\text{-}WND4}$ (kcal/mol)**
BisTris	0.34 ± 0.06	7 (± 1)×10^{6}	1.6 ± 0.2	3.7 (± 0.6)×10^{32}	-30.0 (± 0.2)
TAPSO	0.60 ± 0.03	7 (± 6)×10^{6}	2.7 ± 0.7	4 (± 3)×10^{32}	-29.85 (± 0.07)
TRIS	0.62 ± 0.03	3 (± 2)×10^{6}	-20 ± 1	1.2 (± 0.3)×10^{32}	-30.0 (± 0.4)
Average	**0.5 ± 0.1**			**3 (± 1)×10^{32}**	**-30.0 ± 0.1**

4.3.6. Thermodynamics Associated with the Cu^+*-WND4 Complex*

The stabilization of Cu^+ to determine the thermodynamics of its binding to WND4 was achieved through the addition of reduced glutathione. These titrations show sharp, well-defined bi-phasic peaks with rapid binding and slow return to equilibrium. Initial injections show an immediate exothermic feature followed by a slower endothermic feature, possibly a rearrangement before returning to equilibrium. Isotherms in each buffer show a distinct inflection with an average stoichiometry of 0.41 ± 0.07 Cu^+ binding to WND4 in excess GSH (**Figure 4.3.6.1**). This stoichiometry corresponds to the formation of the Cu^+-$(WND4)_2$ complex. At the inflection, the calculated binding affinities are within the accuracy range of ITC, with c-window values of ~500.

Determination of the number of protons released from the protein when Cu^+ binds is achieved through a proton plot and proton inventory. This plot indicates that -0.7 ± 0.2 protons dissociate from buffer when the Cu^+-$WND4)_2$ complex is formed. Likewise, after the Cu^+ dissociates from GSH, 1.6 ± 0.2 protons will bind to the 2 GSH molecules. With these two protonation values, the formation of the Cu^+-$(WND4)_2$ complex releases 0.9 ± 0.2 protons, or 0.5 ± 0.1 protons per-monomer (**Figure 4.3.6.2**).

Using this protons inventory, the buffer-independent binding thermodynamics at pH 7.4 can be elucidated. By taking into account the enthalpy of each competing equilibrium, the condition-independent enthalpy can be found by:

$$\Delta H_{Cu(I)-Wnd4} = \Delta H_{MP} - \Delta H_{PH} = \Delta H_{ITC} + \Delta H_{ML_2} + \left[\left(n_{H_{L_2}^+} - n_{H_P^+}\right) \times \Delta H_{BH}\right] \quad \textbf{Equation 4.3.6.1}$$

The condition-independent formation enthalpy for the Cu^+-$(WND4)_2$ complex has an average value of -12.7 ± 0.5 kcal/mol.

Similarly, quantification of the condition-independent equilibrium formation constant of the Cu^+-$(WND4)_2$ complex with the competition from excess GSH can be shown by:

$$K_{Cu(I)-Wnd4} = K_{ITC} \times (1 + K_{Cu(I)-(GSH)_2} \times [GSH] \times \alpha_{proton-GSH} \quad \textbf{Equation 4.3.6.2}$$

Similar to the condition-independent enthalpy, this equation utilizes the coupled

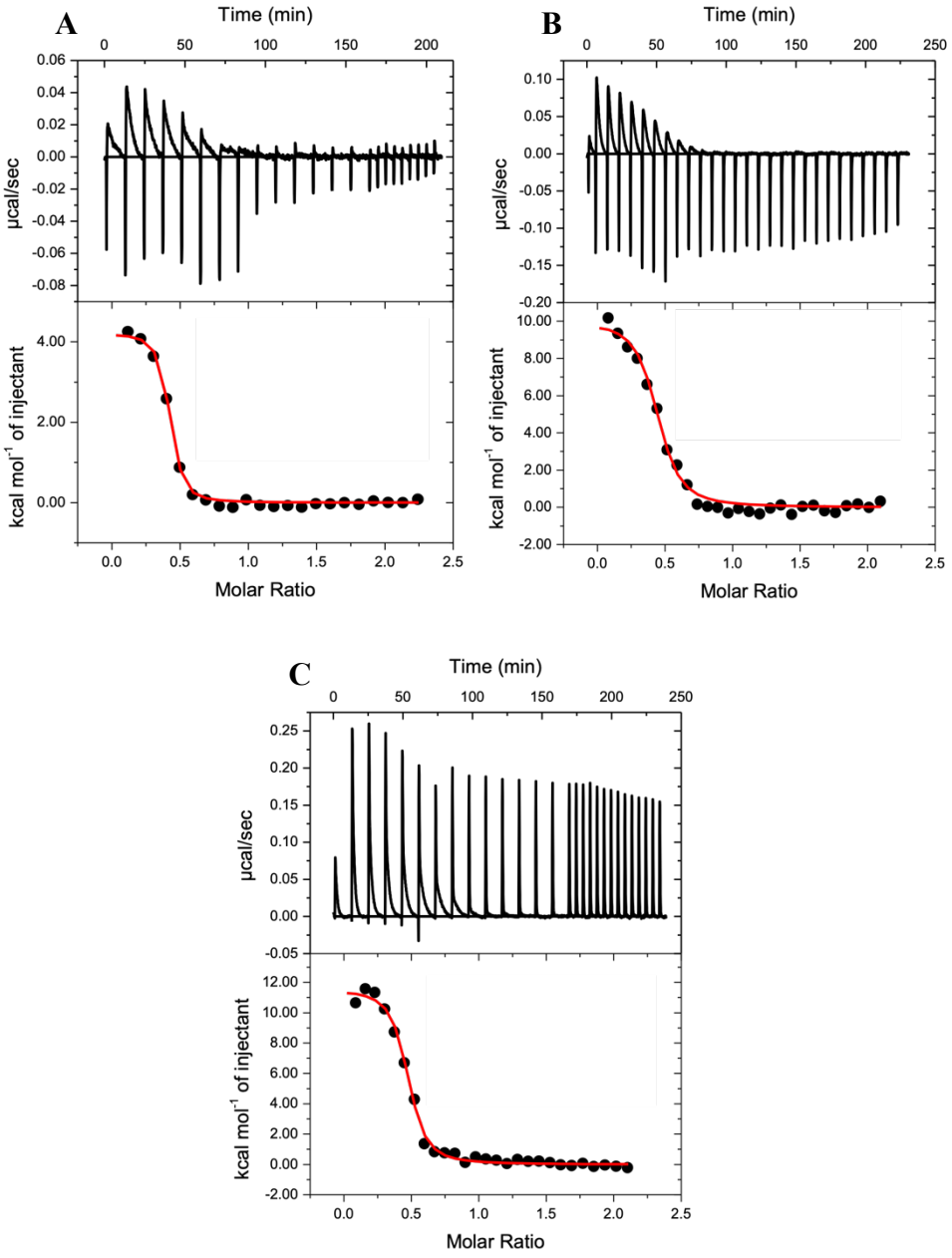

Figure 4.3.6.1. *Representative isotherms for the titration of 150 µM Cu^{+} into 15 µM apo-WND4 in 50 mM Buffer, 50 mM NaCl, pH 7.4 and 10-fold excess of reduced glutathione to Cu^{+}. (A) BisTris: n = 0.384 ± 0.005, K_{ITC} = 1.5 (± 0.3)×10^{6} M^{-1}, ΔH_{ITC} = 4.22 ± 0.08 kcal/mol; (B) TAPSO: n = 0.43 ± 0.01, K_{ITC} = 3.9 (± 0.8)×10^{6} M^{-1}, ΔH_{ITC} = 10.0 ± 0.3 kcal/mol;(C) TRIS: n = 0.459 ± 0.005, K_{ITC} = 7 (± 1)×10^{6} M^{-1}, ΔH_{ITC} = 11.6 ± 0.2 kcal/mol.*

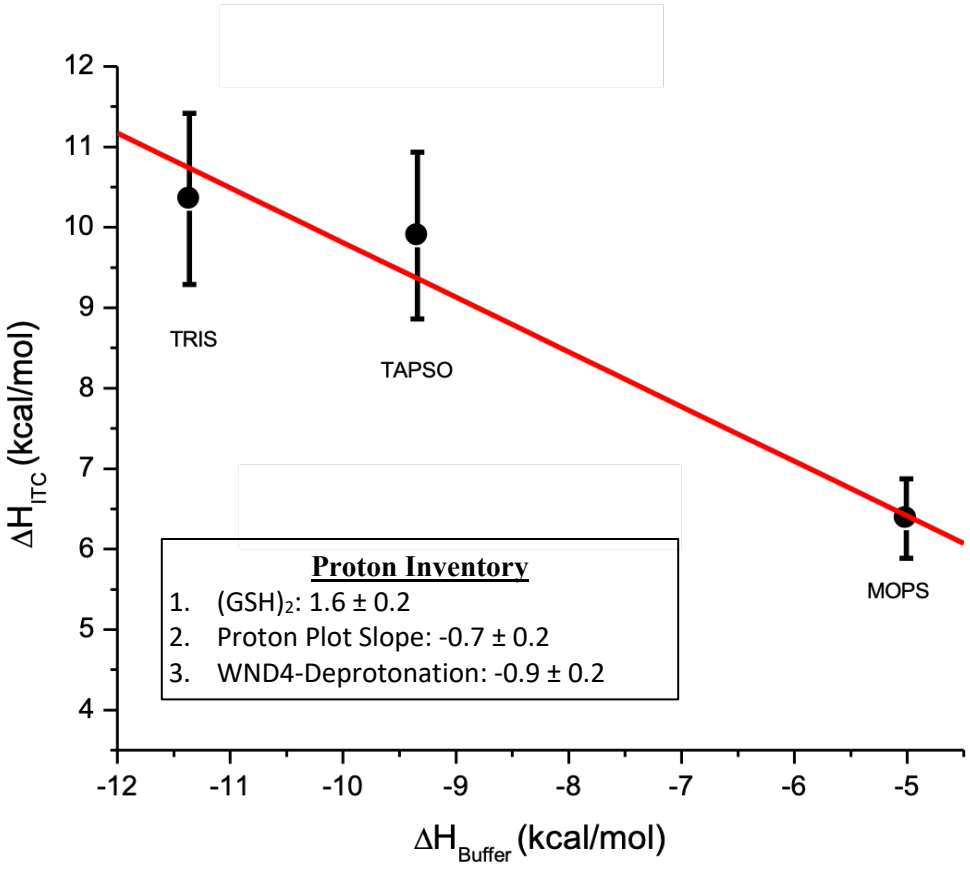

Figure 4.3.6.2. *Proton plot associated with the titration of Cu^{+}, in 10-fold excess GSH into apo-WND4 to form the Cu^{2+}-$(WND4)_2$ complex. Insert: proton inventory to establish the number of protons that leave MerP upon the binding of Hg^{2+}. The slope of the proton plot, along with the number of protons that bind to $(GSH)_2$, indicates that 0.9 ± 0.2 protons dissociate from the Cu^{+}-$(WND4)_2$ complex to form the metal-bridged protein dimer complex in which 0.45 ± 0.1 protons are released per WND4 monomer.*

Table 4.3.6.1. *Average apparent (ΔH_{ITC} and K_{ITC}) and condition-independent ($\Delta H_{Cu+\text{-}WND4}$ and $K_{Cu+\text{-}WND4}$) thermodynamics associated with the formation of the Cu^{+}-$(WND4)_2$ complex from the titration of the Cu^{+}-$(GSH)_2$ complex in 50 mM buffer, 50 mM NaCl, pH 7.4 and excess glutathione in 10-fold excess to Cu^{+}.*

Buffer	**n**	**K_{ITC}**	**ΔH_{ITC} (kcal/mol)**	**$K_{Cu+\text{-}WND4}$**	**$\Delta H_{Cu+\text{-}WND4}$ (kcal/mol)**
MOPS	0.45 ± 0.05	5 (± 3)×10^{6}	6 ± 0.5	8 (± 5)×10^{15}	-12.8 (± 0.5)
TAPSO	0.46 ± 0.03	8 (± 3)×10^{6}	10 ± 1	1.3 (± 0.8)×10^{16}	-12.9 (± 0.9)
TRIS	0.45 ± 0.04	1 (± 1)×10^{7}	10 ± 1	2 (± 2)×10^{16}	-13 (± 1)
Average	**0.45 ± 0.04**			**1.4 (± 0.8)×10^{16}**	**-12.7 ± 0.5**

thermodynamics from the Cu(I)-$(GSH)_2$ complex, which originates, in part, from the $\alpha_{proton-GSH}$, in which:

$$\alpha_{proton-GSH} = \left(\frac{\alpha_{proton-GSH-apparent}}{\alpha_{proton-GSH-real}}\right)^2 = 4.19\ X\ 10^{-3} \qquad \textbf{Equation 4.3.6.3}$$

This *post-hoc* analysis indicates that WND4 binds Cu^+ with an affinity of 1.4 (± 0.8)×10^{16}. Experimental and condition-independent thermodynamics for the formation of the Cu^+-$(WND4)_2$ complex at pH 7.4 are shown in **Table 4.3.6.1**.

4.3.7. Thermodynamics of Zn^{2+} *Binding to WND4*

Like the ITC experiments to determine the thermodynamics of Zn^{2+} binding to MerP, the measurements of Zn^{2+} binding to WND4 were completed by the titration of Zn^{2+} in buffer solutions into WND4 with different buffers, including BisTris and TRIS (**Figure 4.3.7.1**). Like other Zn^{2+} binding experiments, they were completed in 50 mM buffer, 50 mM NaCl, pH 7.4. However, these isotherms are much more complicated, showing two or three inflections depending on the buffer. Although two-site fitting is possible for those with two inflections, these binding events were not consistent between buffers; thus, the determination of buffer-protonation and the subsequent proton plot is difficult. The metal-binding site is similar to MerP but near the metal-bridged dimer interface of WND4 is a histidine (His18). This additional metal-binding amino acid also makes a chelation experiment difficult as well, as the expected metal-protein complex may not be occurring in solution. An additional histidine may lead to unusual metal-protein interactions and the chelation experiments may lead to thermodynamics that incorrectly described the WND4 metal-binding site. Thus, although Zn^{2+} binding to WND4 was attempted, these were too complicated for analysis and interpretation.

4.3.8. Thermodynamics of Cd^{2+} *Binding to WND4*

Like Zn^{2+}, Cd^{2+} generally prefers to bind to amino acids in a tetrahedral geometry, with a greater preference for soft cysteines. Linear coordination of Cd^{2+} is less likely to form. Unfortunately, isotherms to measure Cd^{2+} binding to WND4 were complicated although different from those of the Zn^{2+}-binding experiments. Two buffers, TAPSO and TRIS show a single inflection at a stoichiometry of ~0.5, whereas BisTris and MOPS show

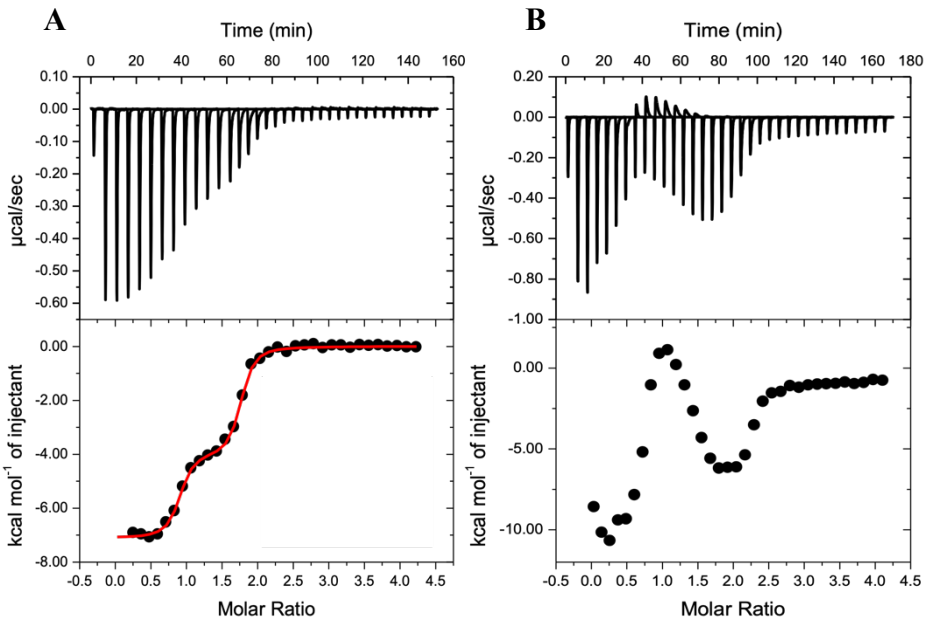

Figure 4.3.7.1. *Representative isotherms of Zn^{2+} in buffer, titrated into 15 µM WND4 in 50 mM buffer, 50 mM NaCl, pH 7.4. (A) Titration of Zn^{2+} into apo-WND4 in BisTris; (B) Titration of Zn(II0 into apo-WND4 in TRIS.*

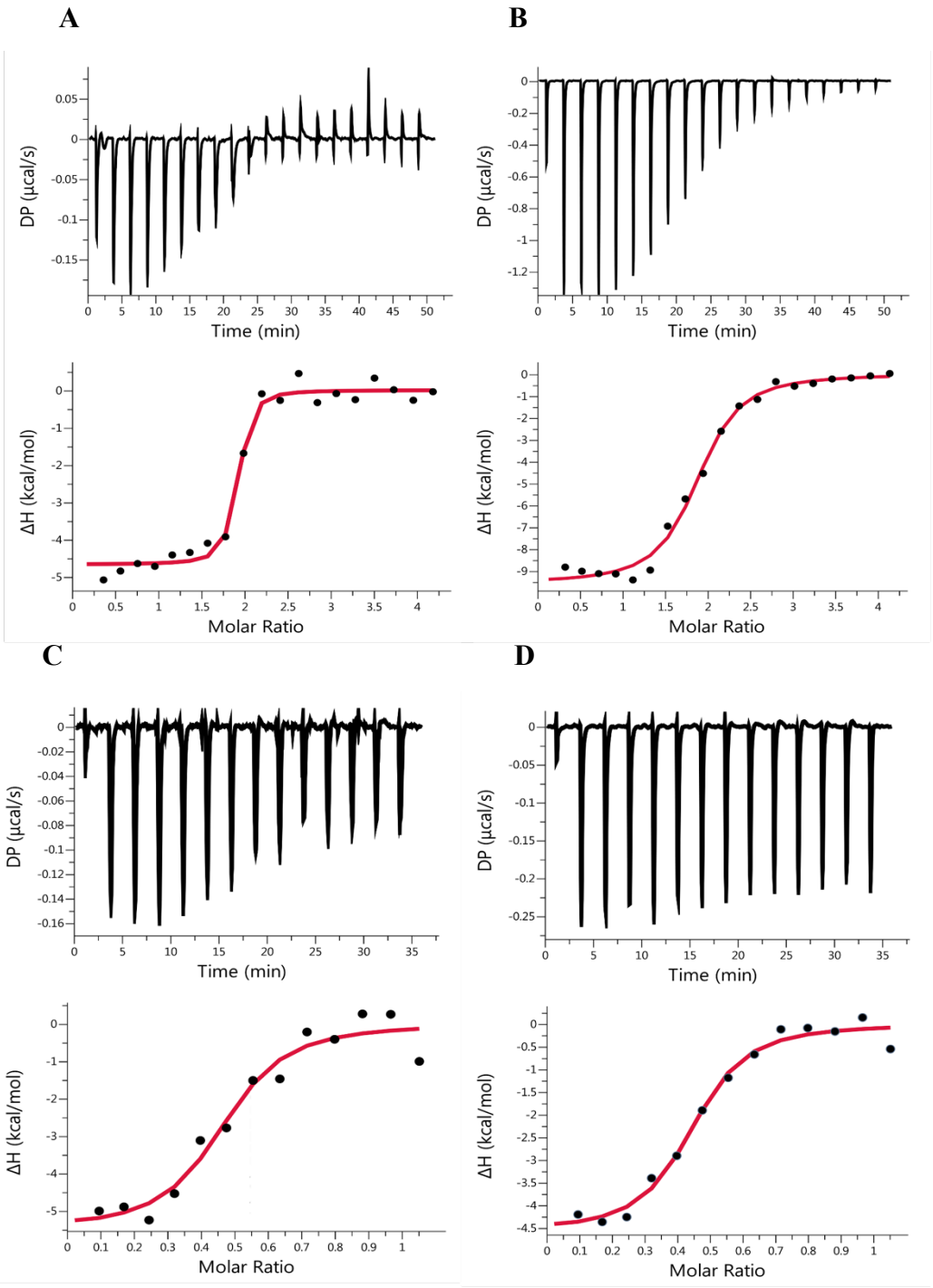

Figure 4.3.8.1. *Representative isotherms of Cd^{2+} in buffer, titrated into 15 µM WND4 in 50 mM buffer, 50 mM NaCl, pH 7.4. Titration of Cd^{2+} into apo-WND4 in: (A) MOPS, (B) BisTris, (C) TAPSO, and (D) TRIS.*

a single inflection at a stoichiometry of ~2 (**Figure 4.3.9.1** and **4.3.9.2**, respectively). Although these isotherms can be fit and the condition-independent binding thermodynamics may be quantified, the difference between these buffers leads to questionable conclusions. The stoichiometry of ~0.5 would be expected, yet a stoichiometry of ~2 is unusual and difficult to understand as WND4 is a small protein with very few metal-binding residues. Furthermore, these two sets of data show different numbers of protons that are released from WND4 when Cd^{2+} binds, ~0.6 for TAPSO and TRIS and ~2.6 for BisTris and MOPS. Like the binding of Zn^{2+}, the binding of Cd^{2+} is difficult to understand and determine the condition-independent binding thermodynamics.

4.4. Discussion

4.4.1. Comparative Analysis of the Binding of Native and Non-Native Metals to MerP

Ferredoxin-like folded metallochaperones and metal-binding domains in both humans and bacteria that bind, and transfer or transport metals share many structural characteristics. Although these metallochaperones and metal-binding domains have been found to bind and transfer many monovalent and divalent metals, their metal-binding site on the protein is identical. This $MX_1C_CX_2X_3C_N$ sequence has been found to bind metals with high affinity. These metal-binding thermodynamics, in some cases, have been quantified, but very few have elucidated the enthalpic and entropic contributions of binding. Thermodynamic contributions provide valuable insight into the molecular basis for the affinity of the protein for the metal, including metal desolvation, bond formation, protein desolvation, conformational dynamics and structural changes. Each of these contribute to the overall thermodynamics quantified by ITC. However, accessing these contributions can be challenging. One way to elucidate this is through the use of differences in the thermodynamics, ΔΔ-values. Thermodynamic differences that occur upon changes to the experimental design provide insight, even quantify, these different contributions. For example, consider the titration of Hg^{2+} into MerP and WND4. Metal desolvation would be identical between these two experiments, the metal-binding site is the same, and protein desolvation is likely similar due to the similarity in the metal-binding site. But, the protein sequence is not exactly the same, although many residues are conserved between the two

structures. Comparative thermodynamics, then, will provide fundamental insight into the differences in the protein structure, that contribute to the metal-binding thermodynamics.

Initial quantification of the buffer-independent thermodynamics associated with the binding of Hg^{2+}, Cu^{+}, Zn^{2+}, and Cd^{2+} to MerP and WND4 at pH 7.4 was necessary to understand fundamental differences in the ferredoxin-like fold. As shown in **Figure 4.1.2.2**, many amino acids are conserved, with a few amino acids that are significantly different. Key variations in these structures can directly impact the metal-binding site, modulating metal-protein thermodynamics. This work aims to quantify the contribution of the protein scaffold to metal-binding within these ferredoxin-like folded proteins with the goal to better understand, from an inorganic perspective, metal selectivity and metal-specificity for these proteins. Comparative condition-independent thermodynamics for the binding of these metals to MerP and WND4 are shown in **Table 4.4.1.1**.

Studies on the binding of Hg^{2+} to MerP were done in two stages. The first stage was a titration of Hg^{2+}-EDTA into apo-MerP to determine the Hg^{2+}-MerP binding affinity. The second stage was the chelation of Hg^{2+} through the titration of N-acetyl-penicillamine (NAPA) into the Hg-MerP (1:1) complex. These two sets of experiments allow quantification of the binding enthalpy and binding affinity, which were determined to be -27.8 ± 1.4 kcal/mol and 8 (± 6)×10^{33}. This binding affinity is far larger than that reported previously by Opella and coworkers, 3×10^{5} M^{-1}.[43] Also reported were the binding affinities of other monovalent and divalent metals, including Zn^{2+}, Cd^{2+}, and Ag^{+}, all of which are far smaller than the binding affinities determined herein, but also the range of typical metal-protein binding affinities. This dissonance between the results found in these NMR experiments and the majority of other metal-protein interactions places significant doubt on these results. Thus, the quantification of the thermodynamics associated with the Hg^{2+} binding to MerP determined in this chapter is, I believe, the first accurate value for the metal-protein affinity.

Both the direct titration of Hg^{2+} and the chelation of Hg^{2+} from MerP show a consistent number of protons released from MerP when Hg^{2+} binds, which is in agreement with the calculated pK_a values of Cys_C and Cys_N, 5.5 and 9.1, respectively, previously reported by Sahlman and coworkers.[33] By using a pH-titration, the formation of the thiolate (ε = 4,000 M^{-1} cm^{-1} at 240 nm) can be observed by UV-Vis. Native MerP showed two

inflections, and site-directed mutagenesis of each of these cysteines individually allowed for the quantification of their respective pK_a. The authors proposed that the unusually low pK_a of Cys_C may be useful in Hg^{2+}-transfer from MerP to MerT, which has a proposed Hg-$(Cys)_3$ intermediate, as this would favor Cys_C for the preferred leaving group, facilitating Hg^{2+} transfer. Although this mechanism has not been tested for MerP, a similar mechanism has been proposed for the transfer of Cu^+ from ATX1/HAH1 to WND4 by Rosenzweig[44] and Dennison.[17] This mechanism, however, is supported by computational work on the binding of methylmercury to CysN, which leads to a shift in Cys_C to be solvent exposed (See Chapter 5). These pK_as suggest that Hg^{2+} binding to MerP would displace 1 proton at pH 7.4, which was found by these ITC experiments, supporting this thermodynamics analysis.

These thermodynamic results provide insight into the structure-function relationship in MerP, and its relation to metal specificity, selectivity, and contribution of the protein structure to metal binding. Dissection of the enthalpic and entropic components associated with the large and favorable free energy reveals that the binding of Hg^{2+} to MerP is both enthalpically and entropically favored, with the enthalpic contribution as the driving force of the interaction. These components can be further divided into molecular components that directly and significantly impact both the enthalpy and entropy of ligand binding (**Figure 4.4.1.1**). Mercury(II) binding to MerP is enthalpically driven, which is expected, given the favorable soft-soft interaction between Hg^{2+} and the sulfur on the cysteines. This metal-bond formation, however, is offset by the deprotonation of Cys_N, which would diminish the enthalpy by 8-9 kcal/mol. Lastly, electrostatic interactions within a protein can significantly impact the enthalpy. Although MerP is small, the electrostatic interaction between Cys_C and two tyrosine residues would be disrupted, leading to differences in the enthalpy. In order for Hg^{2+} to bind to Cys_C, it must move to the surface of the protein to become more exposed to the solvent and available for metal-bond formation. This suggests that metal coordination results in small conformational changes in the protein, which would also lead to a more favorable entropic contribution to metal binding. Lastly is cratic, or mixing, entropy, which is the entropy associated with the

Table 4.4.1.1. *Average pH-dependent, buffer-independent thermodynamics associated with the protein-metal complex.*

Protein	Metal Ion	Competing or Chelating Ligand	H+ Displaced	Stoichiometry	$K_{Metal-Protein}$	$\Delta G_{Metal-Protein}$ (kcal/mol)	$\Delta H_{Metal-Protein}$ (kcal/mol)	$-T\Delta S_{Metal-Protein}$ (kcal/mol)
MerP	Hg^{2+}	EDTA	0.96 ± 0.15	1 ± 0.1	—	—	–27.8 ± 1.4	–18.5 ± 1.7
		NAPA	1.1 ± 0.06	2.0 ± 0.2 (NAPA:Hg)	$8 (\pm 6)\times10^{33}$	–46.3 ± 1.0	—	
	Cu^{+}	GSH	1.2 ± 0.2	0.94 ± 0.15	$3 (\pm 2)\times10^{16}$	–22.5 ± 0.3	–6.5 ± 0.3	–16.0 ± 0.4
	Zn^{2+}	Buffer	1.9 ± 0.1	0.57 ± 0.18	$1.0 (\pm 0.6) X10^{7}$	–9.8 ± 0.3	11.6 ± 1.5	–21.4 ± 1.5
	Cd^{2+}	Buffer	1.9 ± 0.1	0.43 ± 0.07	$3 (\pm 5)\times10^{9}$	–13.5 ± 0.6	1.5 ± 0.6	–15 ± 0.8
WND4	Hg^{2+}	GSH	1.0 ± 0.2	0.5 ± 0.1	$3 (\pm 1)\times10^{32}$	–44.3 ± 0.2	–30.0 ± 0.1	–14.3 ± 0.2
	Cu^{+}	GSH	0.9 ± 0.2	0.45 ± 0.04	$1.4 (\pm 0.8)\times10^{16}$	–22.0 ± 0.3	–12.7 ± 0.5	–9.3 ± 0.6
	Zn^{2+}	Buffer	—	—	—	—	—	—
	Cd^{2+}	Buffer	—	—	—	—	—	—
[a]HAH1	Hg^{2+}	GSH	1.1 ± 0.2	0.87 ± 0.06	$1.1 (\pm 0.6)\times10^{28}$	–38.3 ± 0.6	–18 ± 1	–20 ± 1
	Cu^{+}	GSH	0.5 ± 0.2	0.8 ± 0.1	$2.0 (\pm 0.8)\times10^{17}$	–23.5 ± 0.3	–9 ± 1	–16.6 ± 0.4
	Zn^{2+}	Buffer	0.7 ± 0.4	1.1 ± 0.1	$6.1 (\pm 0.8)\times10^{7}$	–10.3 ± 0.1	–1.1 ± 0.9	–9.3 ± 0.9

a) Data collected and analyzed previously by Michael Stevenson.[39]

Binding Enthalpy	Binding Entropy
1. (De)–Protonation 2. Changes in Hydrogen Bonding 3. Metal Bond Formation	1. Metal Desolvation 2. Conformational Restraints 3. Metal Coordination 4. Water Displacement 5. Cratic Entropy

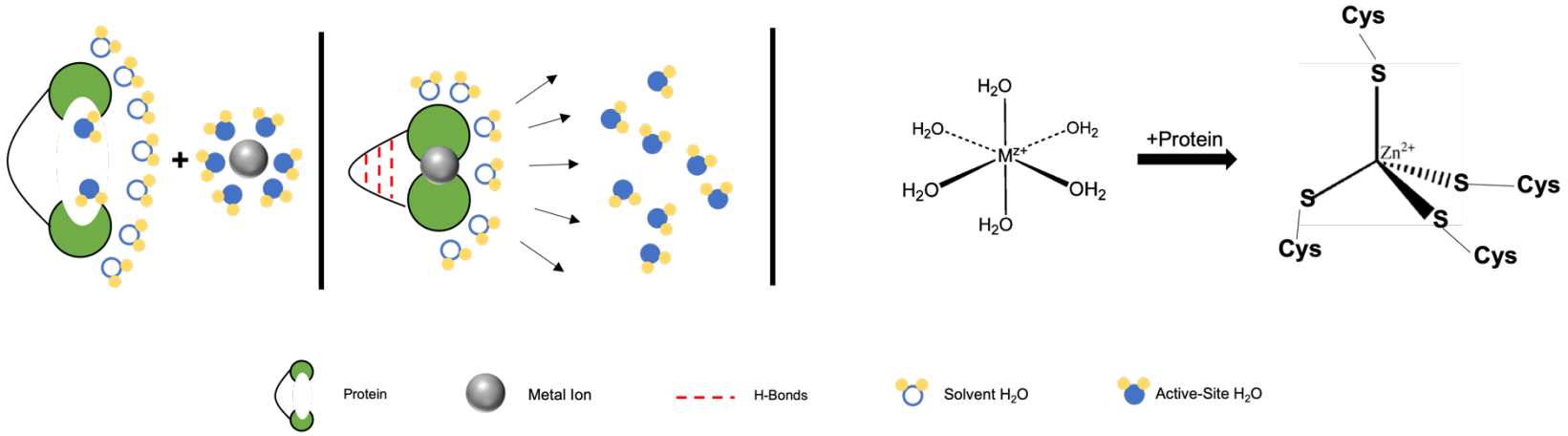

Figure 4.4.1.1. *Graphical representation of major components that make up the enthalpic and entropic contributions to metal binding in a protein in aqueous conditions.*

translational entropy. This entropic contribution is estimated by:

$$MerPH + 1\,Hg^{2+} \rightarrow HgMerP + 1\,H^{+} \qquad \Delta_{species} = 2 - 2 = 0 \quad \textbf{Equation 4.4.1.1}$$

Generally, contributions from translation entropy are small, so differences between the protonated apo-MerP and deprotonated Hg^{2+}-MerP are minimal.[45,46]

In isolation, the breakdown of the enthalpic and entropic contributions associated with metal binding are less useful. However, these thermodynamic components can be compared to other systems to provide insight into the differences that occur with small perturbations of the metal-protein system. To gain additional insight into the structural contributions associated with metal-binding to MerP, the thermodynamics of native Hg^{2+} binding to MerP will be compared to the binding of non-native Cu^{+}, Zn^{2+}, and Cd^{2+}.

Unlike the challenges of Hg^{2+}, the binding of Cu^{+} was less complex because the stabilization of Cu^{+} by a 10-fold excess of GSH was effective in the competition with MerP. This allowed for the determination of the Cu^{+}-MerP binding thermodynamics, which had not been studied previously. The relevant binding affinity that had been reported was the equilibrium constant for Cu^{+} binding to a small, unstructured peptide that modelled the MerP binding site. The value reported by Opella and coworker is far lower than the binding affinity found here, in part because of the utilization of the peptide, not the full-length protein, but also because of the lack of adequate competition for the strong Cu^{+}-MerP binding interaction. They found a binding affinity of 8×10^{3}, which is unreasonable for Cu^{+}-cysteine interactions.[47,48] However, the MerP affinity for Cu^{+} can be compared to the binding affinities that were determined by ITC and spectrophotometry for Cu^{+} binding to ATX1/HAH1. Because of the similarities in the metal binding site, the approximate order of magnitude in the Cu^{+} binding affinity should be similar. The ATX1/HAH1 affinity for Cu^{+} was found to be 2.0 ($\pm$ 0.8)$\times10^{17}$ from ITC experiments in the Wilcox lab and 1.4 ($\pm$ 0.2)$\times10^{17}$ from spectrophotometry by Dennison and coworkers.[17,39] Thus, the equilibrium constant for the formation of the Cu^{+}-MerP complex is 3 ($\pm$ 2)$\times10^{16}$ and in reasonable agreement with the literature. Furthermore, like the binding of Hg^{2+} to MerP, the binding of Cu^{+} resulted in the release of 1.2 $\pm$ 0.2 protons, which is also in good agreement with the predicted deprotonation of MerP determined cysteine pK_a values.

While Cu^+ is not the native metal that binds to MerP, both the metal-binding site and global protein scaffold is similar to the Cu^+ metallochaperone and metal-binding domains HAH1/ATX1 and WND4. This raises an interesting question about the source of metal specificity or selectivity. Why does MerP prefer Hg^{2+}, and not Cu^+, and ATX1/HAH1 prefer Cu^+, and not Hg^{2+}? Differences in the fundamental metal-binding thermodynamics can provide insight into the source of this specificity and selectivity that may be modulated by the protein architecture. Thus, the thermodynamics of MerP binding Cu^+, Zn^{2+}, and Cd^{2+}, all of which have metallochaperones and metal-binding domains with the same protein architecture, will compared to the thermodynamics of MerP binding Hg^{2+}.

With the knowledge that the affinity of MerP for Cu^+ agrees with that of relevant Cu^+-binding proteins, the enthalpic and entropic components can be considered. The binding of Cu^+ to MerP is both enthalpically and entropically favorable, with the entropic contribution driving the interaction, in which $\Delta H_{Cu+\text{-}MerP}$ = -6.5 ± 0.3 kcal/mol and $-T\Delta S_{Cu+\text{-}MerP}$ = -16.0 ± 0.4 kcal/mol at pH 7.4. Consider the various contributions to both enthalpy and entropy (**Figure 4.4.1.1**): Cu^+, like Hg^{2+}, is a soft acid, and an enthalpically favorable soft-soft interaction would be expected. However, compared to Hg^{2+}, the Cu^+ would have a smaller desolvation enthalpy and less protein desolvation due to the size and charge differences between the two metal ions. Deprotonation of MerP upon binding Hg^{2+} or Cu^+ is not significantly different, so this should not affect the enthalpy of Cu^+ compared to Hg^{2+}. Nevertheless, the difference in enthalpy between these two ions, $\Delta\Delta H_{[Hg2+\text{-}Cu+]\text{-}MerP}$ = -21.3 kcal/mol is significant, which is likely the result of differences in the Hg–S and Cu–S bond enthalpy.

From an entropic perspective, the contributions are much more nuanced. The difference between the entropic contribution is quantified by $-T\Delta\Delta S_{[Hg2+\text{-}Cu+]\text{-}MerP}$ = -2.5 kcal/mol. We can be fairly certain that the cratic entropy between Cu^+ and Hg^{2+} is not contributing. But, as mentioned, metal desolvation and protein desolvation would likely be less significant for Cu^+ than Hg^{2+}, leading to a less favorable entropic contribution in the binding of Cu^+ to MerP. Although we know that the buried Cys_C must move to the surface of the protein for metal binding, this entropic contribution would likely cancel as this would be similar for both Hg^{2+} and Cu^+. By ITC, we can obtain a qualitative dissection of the

contributions, but to determine these difference quantitatively, other techniques are required.

Distinct from the binding of Cu^{+} and Hg^{2+} to MerP, Zn^{2+} binds to MerP not in a 1:1 complex, but in a 1:2 complex forming a Zn^{2+}-bridged protein dimer. Although there are no structures of the MerP-Zn complex, other ferredoxin-like metallochaperones have shown this metal-bridged dimer, providing precedence for this complex formation. This is also supported from a fundamental inorganic perspective, in which the preferred geometry for Zn^{2+} is tetrahedral, not linear. A 1:1 complex is very unlikely. The thermodynamics that are described herein are quantified on the *per-metal* basis, which allows for the direct comparison to the binding of Hg^{2+} and Cu^{+}, which bind in a 1:1 complex. However, thermodynamics compared on a *per-protein* basis can also be utilized for comparison as well.

Titrations of Zn^{2+} into MerP shows a stoichiometry of 0.57 ± 0.18. This results in a total of 1.9 ± 0.1 protons released, corresponding to 0.95 ± 0.05 protons per MerP monomer. This is in good agreement with the number of protons that are released when Hg^{2+} and Cu^{+} bind in a 1:1 complex, but also in good agreement with the number of protons that are predicted to dissociate according to the cysteine pK_a values. Condition-independent equilibrium constants Zn^{2+} binding to MerP are 1.0 (± 0.6)×10^{7}. Like the binding of Hg^{2+} to MerP, Opella and coworker quantified the MerP binding to Zn^{2+}. They found, by NMR measurements, that the equilibrium constant was 2×10^{5} M^{-1}, which is 2 orders of magnitude lower than quantified here by ITC. This is far lower than expected for Zn^{2+}-cysteine binding interactions as well. Thus, this is not a good representative binding affinity for comparison. However, previous ITC measurements of the binding of Zn^{2+} to HAH1 by Stevenson found 6.1 (± 0.8)×10^{7}.[39] Although the protein is not the same, the metal binding site is identical, and the binding affinity of Zn^{2+} to MerP is in good agreement, as the affinity was quantified for a comparable *per-monomer* basis.

The enthalpic and entropic contributions can be used to evaluate the binding of Zn^{2+} and formation of the metal-bridged Zn^{2+}-$(MerP)_2$ dimer complex. The buffer-independent binding enthalpy at pH 7.4, on a *per-metal* basis, was found to be $\Delta H_{Zn2+-(MerP)2}$ = 11.6 ± 1.5 kcal/mol, or 5.8 ± 0.75 kcal/mol *per-monomer*, with the entropic contribution being both

favorable and the driving force in the Zn^{2+}-protein interaction where $-T\Delta\Delta S_{Zn2+-(MerP)2}$ = -21.4 ± 1.5 kcal/mol and on a *per-protein* basis, $-T\Delta\Delta S_{Zn2+-MerP}$ = -10.7 ± 0.75 kcal/mol.

Comparing the enthalpy of formation of the Zn^{2+}-$(MerP)_2$ complex to the binding of Hg^{2+} a $\Delta\Delta H_{[Hg-Zn]}$ = -39.4 kcal/mol on a *per-metal* basis, and –33.6 kcal/mol on a *per-protein* basis. The binding of Hg^{2+} to $MerP_{monomer}$ is far more enthalpically favored than the binding of Zn^{2+} to $MerP_{monomer}$. Much of this difference is the much more favorable Hg^{2+}-thiolate bond enthalpy.

The disfavorable Zn^{2+} binding enthalpy is not surprising, when compared to other tetrahedral, tetrathiolate Zn^{2+} interactions, such as with an unstructured glycine-rich, Cys4 peptide.[1] This peptide models a 4-cysteine coordination and shows $\Delta H_{Cys-Pep}$ = 6.4 kcal/mol and $-T\Delta S_{Cys-Pep}$ = -23.0 kcal/mol for the condition-independent thermodynamics, in which Zn^{2+} binding to the peptide results in the release of 3.6 protons. If we assume that each cysteine is protonated by ~0.9 protons, and each cysteine has a deprotonation enthalpy of –8.6 kcal/mol, then the enthalpy of the Zn^{2+}-tetrathiolate coordination is equal to $\Delta H_{Zn-Thiolate}$ = –25.4 kcal/mol. In order to compare MerP with the binding of Zn^{2+} to this peptide, a similar analysis assumes that each cysteine on MerP has a deprotonation enthalpy of –8.6 kcal/mol. When a similar subtraction is made for Cys thiols that are deprotonated upon Zn^{2+} binding to MerP $\Delta H_{Zn-(MerP)-thiolate}$ = -4.7 kcal/mol. However, the Zn^{2+}-thiolate bond enthalpy is ≅ -4 kcal/mol. The predicted binding enthalpy for the formation of the Zn^{2+}-$(MerP)_2$ would be approximately -19 kcal/mol, which is far more enthalpically favored than the experimental enthalpy for Zn^{2+} binding to MerP. These differences reveal a significant endothermic contribution to Zn^{2+} binding from the protein scaffold.

The high buffer-independent affinity of MerP for Zn^{2+} is due to a large favorable change in entropy, which is much more favorable than the entropic contribution to Zn^{2+} binding to an unstructured glycine-rich tetrathiolate peptide. These two systems have similar metal desolvation, but different cratic entropies. Considering deprotonation would suggest a less favorable entropic contribution for MerP than the peptide as well. This suggests that the differences in the conformational changes of MerP would result in the greater entropic favorability. There is balance between the cratic entropy that favors the peptide and protein conformational changes that favor MerP.

Like the binding of Zn^{2+} to MerP, the binding of Cd^{2+} to MerP results in the formation of a proposed metal-bridged protein dimer. Titrations of Cd^{2+} in buffer into MerP resulted a binding stoichiometry of 0.43 ± 0.07 Cd^{2+}:MerP which release a total of 1.9 ± 0.1 protons upon metal binding. This deprotonation is in agreement with the literature precedence. Although there are no Cd^{2+}-MerP structures, this coordination complex would be anticipated, given the propensity for Cd^{2+} to favor tetrahedral tetrathiolate coordination and only 2 cysteines available per monomer.

The formation of the Cd-$(MerP)_2$ complex is entropically driven, and slight enthalpically disfavorable with a stability constant of 3 (± 5)×10^9. Opella and coworkers report a Cd^{2+}-MerP binding constant of 2×10^3, which, like the other metal binding affinities, is far lower than the expected affinity Cys-containing peptides and proteins for Cd^{2+}. Another concern with the previously reported result is binding of Zn^{2+}, a borderline acid, is stronger than Cd^{2+}, a soft acid, which has little precedence from a fundamental inorganic perspective. Because there are no reported thermodynamics for Cd^{2+} binding to MerP or other metallochaperones, this works utilizes the Hg-MerP thermodynamics to gain insight into the protein structure when Cd^{2+} binds. Like Cu^{+} and Zn^{2+}, a comparison with Hg^{2+} is preferential as understanding how the thermodynamic components of Cd^{2+} binding to MerP compared to the native Hg^{2+} provide insight into metal specificity and selectivity. As MerP does not natively bind Zn^{2+}, this does not provide valuable insight, although a comparison is possible.

As the binding of Cd^{2+} results in the formation of the Cd^{2+}-$(MerP)_2$ complex, thermodynamics on a *per-metal* and *per-protein* basis must be considered. This complex has a formation enthalpy of ΔH = 1.5 ± 0.6 kcal/mol, and a formation entropy of $-T\Delta\Delta S$ = -15 ± 0.8 kcal/mol *per-metal* at pH 7.4. On a *per-protein* basis, Cd^{2+} binds with an enthalpy of 0.7 ± 0.3 kcal/mol and an entropy ($-T\Delta S$) of -7.5 ± 0.4 kcal/mol.

Comparative analysis with the Hg-MerP complex reveals a differential binding enthalpy of $\Delta\Delta H_{[Hg\text{-}Cd]\text{-}(MerP)2}$ = -29.3 kcal/mol and a binding entropy of $-T\Delta\Delta S$ = -3.5 kcal/mol on a *per-metal* basis. However, when considering this on per-monomer, $\Delta\Delta H_{[Hg\text{-}Cd]\text{-}MerP}$ = -28.5 kcal/mol and a binding entropy of $-T\Delta\Delta S$ = -11 kcal/mol. In both of these situations, the binding of Hg^{2+} to MerP is far more favorable, which is largely from the

enthalpic contribution of metal binding. However, the binding of Cd^{2+} to MerP is nearly equivalent to the binding of Hg^{2+}.

Consider the contributions of enthalpy and entropy summarized in **Figure 4.4.1.1**. From an enthalpic perspective, Hg^{2+} is anticipated to have a more favorable enthalpy due to the strong thiophilicity of Hg^{2+}, as compared to Cd^{2+}. Although both Cd^{2+} and Hg^{2+} are both soft acids, Hg^{2+} is much more polarizable than Cd^{2+}, leading to more enthalpically favorable interactions. This enthalpic penalty in the binding of Cd^{2+} is further augmented by the deprotonation of $(MerP)_2$, in which ~2 protons dissociate when Cd^{2+} binds. Metal-bridged dimerization, as suggested by other metal-induced metallochaperone structures, may be further stabilized by electrostatic interactions on the protein-protein interface, leading to further differences in the enthalpic contribution of Cd^{2+} binding and the formation of the Cd^{2+}-$(MerP)_2$ complex.

Likewise, a comparative analysis of Cd^{2+} to Hg^{2+} can aid in understanding the entropic contribution of Cd^{2+} binding. The difference in entropy likely comes from a wide range of differences. Hg^{2+} and Cd^{2+}, though more similar in size, have different solvation, thus the desolvation entropy would be greater in Hg^{2+} than Cd^{2+}. Metal-induced dimerization by Cd^{2+} would also likely result in dramatic differences in protein desolvation, as desolvation would occur at both the metal binding site and at the interface of the protein-protein interaction. Building on this Cd^{2+}-induced dimer formation, this would likely result in a significant difference in the entropy relating to protein conformational changes, as each monomer would have fewer degrees of freedom in the dimerization complex, leading to a less-favorable binding entropy, as compared to Hg^{2+}. Lastly, cratic entropy would be estimated to contribute to the greater Cd^{2+} entropic penalty, though small.

From a fundamental inorganic perspective, it is unlikely that any monovalent or divalent transition metal could effectively outcompete Hg^{2+} for binding to MerP, and little crosstalk between metal transport proteins is expected to occur for the mercury detoxification pathway. However, this cannot be said for the ferredoxin-like fold proteins that transport transition metals, all of which contain two cysteine residues in the metal-binding site, mimicking that of MerP. The results here suggest that mercury could hijack Cu^{+} and Zn^{2+} transport mechanisms. Actively binding and importing Hg^{2+} through other pathways would be a viable mechanism of toxicity, leading to cell death. This is further

amplified by the displacement of Cu^+ by Hg^{2+}, which these results show to be possible and which would result in the formation of reactive oxygen species through Cu^+-based Fenton chemistry.

4.4.2. Comparative Thermodynamics of Hg^{2+} *and* Cu^+ *Binding to WND4*

Unlike MerP and HAH1, which are soluble metallochaperones for Hg^{2+} and Cu^+, respectively, WND4 is one of six Cu^+ binding domains of the Wilson disease protein (ATP7PB) and is proposed to be one of the primary binding partners of HAH1.[49,50] Although the mechanism of metal transfer from HAH1 to WND4 has been proposed to involve a thiolate leaving group in HAH1, the thermodynamics of this transfer remain perplexing as Cu^+ binds HAH1 with high affinity. How does a strongly bound metal readily transfer from one binding site to another? Similarly, given the identical metal-binding site of WND4 to HAH1 and MerP, what prevents Hg^{2+} from binding to either the former two and interrupting the transport of Cu^+? Utilizing ITC, a thermodynamic foundation for the binding of native Cu^+ and non-native Hg^{2+} are quantified. Furthermore, this thermodynamic analysis is broadened to include the binding of non-native Cd^{2+} and Zn^{2+}. Thermodynamics of both native and non-native metals binding to WND4 are then compared to the soluble metallochaperones. This will provide valuable insight into the thermodynamics that drives metal-selectivity and specificity, but also an understanding of how differences in the ferredoxin-like fold protein scaffold modulates the metal binding.

Unlike MerP, Hg^{2+} binding to WND4 was successfully measured using reduced glutathione as the competing ligand, allowing the buffer-independent binding affinities and enthalpies to be determined at PH 7.4. The titration of Hg-GSH into WND4 in a series of buffers (BisTris, TAPSO, and Tris), showed a binding stoichiometry of 0.5 ± 0.1, suggesting that, unlike MerP and HAH1, the binding of Hg^{2+} results in the formation of a metal-bridged dimer. Curiously, this binding resulted in the release of 1.0 ± 0.2 protons. Unlike MerP and HAH1, the pK_as of Cys_N and Cys_C in Menkes disease metal-binding domains, which are similar to Wilson disease metal-binding domains, like WND4, have less thiol and thiolate characteristics, respectively, through changes in their cysteine pK_as.[17]

Visualization of this metal-bridged dimer has suggested that the Hg^{2+} is four-coordinate, but tetrahedral mercury complex, although known, are not common. It may be

that this metal-bridged dimer still results in a linear coordination, in which Cys_N of WND4 is the coordinating ligand. However, the pK_a of Cys_N for WND4 is likely to be ~9, which would suggest that ~1 proton per-WND4 would be released. This seems unlikely, as the metal stoichiometry suggests a 1:2, Hg^{2+}:WND4 complex, in which 2 protons would be expected to be released. Although the binding of a metal to a Cys thiol would result in its deprotonation, and it is assumed that the net release of protons is equal to the number of protons that are released upon metal binding, this is not necessarily the case in every protein system. Consider a scenario in which a metal binds to a Cys thiol, displacing 1 proton, but a large conformational change brings a buried cysteine with a pK_a of ~5.5 to the surface, thereby raising its pK_a to ~9. The proton from the Cys thiol would not be released into buffer, but would bind to this now-solvent-exposed cysteine. The number of protons that bind to buffer would be 0. A similar situation may be occurring here. Herein, I propose that the binding of Hg^{2+} to form a metal-bridged dimer is still primarily coordinating in a 2-coordinate linear geometry through Cys_N, which has a pK_a of ~9. Hg^{2+} binding to these cysteine would result in the *gross* displacement of 2 protons. However, the binding of Hg^{2+} to these cysteines also results in a conformational change that shift Cys_C closer to the surface, thereby raising its pK_a. This upward shift in pK_a for Cys_C to ~7.4 would then be protonated by ~0.5 protons per WND4. Thereby a *net* displacement of 1 proton would occur in the formation of this metal-bridged dimer. Previous work has proposed a related mechanism transfer of Hg^{2+} from HAH1 to WND4 (**Figure 4.1.3.4**). However, this case involves is a metal-bridged homodimer, where both proteins would be predicted to have identical metal-binding characteristics.

An alternative hypothesis utilizes a similar principle, but relies on three-coordinate Hg^{2+}, in which two cysteine residues on one monomer bind Hg^{2+}, and the solvent-exposed cysteine in the other monomer also is binding to this Hg^{2+} complex. This would result in the *gross* displacement of 2 protons. The monomer that is coordinating only through the one cysteine residue would result in a conformational change in the buried cysteine residue, thereby raising its pK_a such that it would then bind 1 proton. Subsequently, this mechanism would result in the *net* displacement of 1 proton. Given that these two monomers are identical, it seems unlikely that one monomer would refer the two-coordinate Hg^{2+} over another monomer.

Unfortunately, differentiation between these two mechanisms, with current experimental results, is difficult. A comparison of the thermodynamics of Hg^{2+} binding to WND4, as compared to MerP, show very similar thermodynamics on a *per-metal* basis. This may be more supportive of the alternative hypothesis, in which each WND4 monomer binds Hg^{2+} in the linear, two-coordinate geometry, with the other monomer coordinating with the solvent-exposed cysteine.

Now that a metal-bridged dimer mechanism seems most likely, the metal-binding thermodynamics can be understood from a *per-metal* perspective. This allows a comparison Hg^{2+} binding to both MerP and HAH1. As such the titration of Hg^{2+} into WND4 shows a buffer-independent binding affinity of 3 (± 1)×10^{32} at pH 7.4. By taking the enthalpy associated with competing equilibria into account then allows for the quantification of the condition-independent enthalpy in which ΔH = -30.0 ± 0.1 kcal/mol Hg^{2+}. Finally, by utilizing these two directly measured thermodynamic values, the free energy and entropic contribution can be quantified resulting in ΔG = -44.3 ± 0.2 kcal/mol Hg^{2+} and $-T\Delta S$ = -14.3 ± 0.2 kcal/mol Hg^{2+} at pH 7.4 (**Table 4.4.1**). These results show that the binding of Hg^{2+} to WND4 is both enthalpically and entropically favorable, and enthalpically driven.

With the condition-independent thermodynamics of Hg^{2+} binding to WND4 in hand, they can then be directly compared to the thermodynamics associated with the binding of Hg^{2+} to MerP, HAH1. By comparing the thermodynamics on a *per-metal* basis, the difference and similarities between these systems become evident. First, to understand that origin of the enthalpic and entropic components of Hg^{2+} binding, a breakdown of the expected components of the enthalpic and entropic contributions are summarized in **Figure 4.4.1.1**.

Condition-independent binding enthalpies indicate that WND4 binds Hg^{2+} ~2.2 kcal/mol Hg^{2+} more favorable that MerP. Since these experiments utilize the same metal ion and the metal-coordination would be similar, it is unlike that metal-thiolate bond formation enthalpies are much different. Protein deprotonation differences may result in some enthalpic differences, as I propose that Cys_N will be deprotonated, but Cys_C moves towards the surface to be partially protonated. However, metal-binding may also result in

changes of the electrostatic interactions within the protein scaffold, which could lead to more enthalpic favorability over MerP.

From an entropic perspective, we should consider the sequence alignment (**Figure 4.1.2.2**). Several residues that are within the second-coordination sphere of the metal-binding site could contribute to differences in entropy. The binding of Hg^{2+} to WND4 is 4.2 kcal/mol more entropically disfavorable than the binding of MerP. Unlike enthalpy, the entropic contributions can suggest modulations of the protein dynamics and differences in solvation. However, in a comparison with MerP, some entropic contributions are unlike to contribute much. For example, metal and protein desolvation for both protein systems should be nearly identical, when considering like protein oligomers (i.e. monomers vs. dimers). Likewise with metal coordination, which could modulate protein conformation. However, protein scaffold dynamics are likely very different. The binding of Hg^{2+} to MerP seems to result in greater conformational dynamics, particularly in the qualitative comparison of the free MerP and Hg-bound MerP structures, in which F38 moves from buried within the core of the protein to solvent exposed.[51] However, in WND4, there is no equivalent amino acid. This may indicate that Hg^{2+} binding to WND4 does not result in such dramatic changes in protein dynamics. Furthermore, since WND4 appears to bind Hg^{2+} through a metal-bridged dimer, this would seemingly result in few degrees of freedom, thus a more disfavorable entropic contribution of metal binding. Also, as expected, cratic entropy would be different for these two systems.

Overall, given these distinct thermodynamic differences between Hg^{2+} binding to WND4 and MerP, the equilibrium constants are only ~ 1 order of magnitude different, in which MerP binds Hg^{2+} at 8 (± 6)×10^{33} and WND4 binds Hg^{2+} at 3 (± 1)×10^{32}. Given the dramatic differences in metal-protein structure through 1:1 and 1:2 binding, differences in protonation upon metal-binding and the second-coordination sphere are expected. Given these significant differences, the fact that the binding affinities are nearly similar suggests that this is another example of enthalpy-entropy compensation. Although these differences have minimal impact on the overall affinity, the thermodynamic components modulate the Hg^{2+} binding enthalpy (favoring) and entropy (disfavoring) of WND4.

Unlike Hg^{2+}, Cu^{+} is the native metal for WND4 binds, after its delivery from the metallochaperone HAH1. This provides a valuable comparison to understand how the

protein scaffold modulates metal binding to enhance metal specificity and selectivity through thermodynamics. Like the binding of Hg^{2+}, WND4 has an experimental binding stoichiometry of 0.45 ± 0.04 Cu^{+} that bind per WND4, indicating that WND4 binds Cu^{+} in a metal-bridged dimer, similar to the binding of Hg^{2+}. This is supported by the number of protons that are displaced upon Cu^{+} binding. By using a series of buffers, the number of protons that are displaced can be quantified, 0.9 ± 0.2, which is in agreement with the binding of Hg^{2+}. This suggests a similar binding of these two metal ions. Although Cu^{+} tends to have more flexibility in its coordination preferences, I propose that this metal-bridged dimer results in a linear coordination of the solvent-exposed Cys_N, which allows for greater conformational changes in Cys_C. The binding of Cu^{+} to Cys_N would be predicted to release 2 protons, but the augmented flexibility of Cys_C would lead to a moderate increase in its pK_a such that each Cys_C binds ~0.5 protons. Thus, the net displacement of 1 proton binds to the buffer.

Alternatively, WND4 may be binding Cu^{+} in a tri-coordinate geometry, in which each monomer binds with both cysteines, but another monomer binds to Cu^{+} with only one cysteine. Support for this argument comes from the fact that the binding affinities on a *per-metal* basis are very similar to the binding of Cu^{+} to MerP, which does bind Cu^{+} in a linear, two-coordinate geometry. The buried Cys_C in WND4 as been proposed to have a higher pK_a than that of HAH1, which would give this cysteine greater thiol characteristics, but this would also weaken the metal-thiolate bond. Weakening this bond would lead to a higher propensity for the exchange between the adjacent WND4 metal-bridged dimers, leading to the asymmetry. This is a similar argument as to how Cu^{+} is delivered to WND4 by HAH1.

Since Cu^{+} binding to WND4 seems to form the metal-bridged dimer, the thermodynamics are described on a *per-metal* basis to ensure accurate comparisons with MerP and, later, HAH1. WND4 binds Cu^{+} with a condition-independent binding affinity of 1.4 (± 0.8)×10^{16}. This is not significantly different than the binding affinity of Cu^{+} to MerP, which has an equilibrium constant of 3 (± 2)×10^{16}.

Although the equilibrium constants associated with the Cu^{+} binding to WND4 is very similar to that of MerP, the thermodynamic contributions are not the same. Binding to WND4 is both enthalpically and entropically favorable and enthalpically driven, which

is in contrast to the binding of Cu^+ to MerP, which is also enthalpically and entropically favorable, but is entropically driven. This is particularly surprising given that Cu^+ binding to WND4 displaces more protons that Cu^+ binding to MerP. This is further confounding because Cu^+ binding to WND4 is more enthalpically favorable than the Cu^+-MerP interaction. Similarly, the greater number of protons that are displaced from WND4 when Cu^+ binds would likely have been more enthalpically disfavorable, as cysteine deprotonation is disfavorable.

These differences in Cu^+ binding to WND4 and MerP can be further explored through a breakdown of the enthalpic and entropic components (**Figure 4.4.1.1**). Enthalpic contributions are the sum of the metal-thiolate bond, cysteine deprotonation, and changes in the protein scaffold electrostatic interactions. Compared to MerP, the metal-thiolate enthalpies should be equivalent, and the greater deprotonation of WND4 would suggest that binding is less exothermically favorable than it is for MerP. However, this is not the case, which suggests that the binding of Cu^+ results in significant changes in the electrostatic interactions within the protein scaffold. This may originate from changes within the hydrogen-bonding network that stabilizes the protein.

A similar trend is observed with the entropic contribution to Cu^+ binding to WND4. The entropy that originates from metal desolvation is likely to be nearly identical between WND4 and MerP, but other entropic components are not. The cratic entropy is likely to be less significant, with the translational motion of the metal-bridged dimer of WND4 being less entropically favorable that MerP, as shown by,

$$Cu(I) + MerP - H_1 \longrightarrow CuMerP + 1\,H^+$$
$$\Delta_{species} = 2.0 - 2.0 = 0 \qquad \textbf{Equation 4.4.2.1}$$

$$Cu(I) + 2\,WND4 - H_{0.45} \longrightarrow Cu - (WND4)_2 + 0.9\,H^+$$
$$\Delta_{species} = 1.9 - 3.0 = +1.1 \qquad \textbf{Equation 4.4.2.2}$$

Displacement of protons from WND4, however, is predicted to be more entropically favorable, as a larger number of protons are displaced, compared to MerP. Although both proteins bind Cu^+ to a similar metal-binding site, the differences in the 1:1 complex with MerP and the 1:2 complex with WND4 suggest that desolvation would be different. Differences in protein desolvation may be augmented by desolvation of the protein-protein

interface, if this is present. Lastly are differences in the conformational dynamics of WND4 and MerP. The binding entropy of Cu^{+} to WND4 is $-T\Delta S = 6.7$ kcal/mol less favorable than the binding of Cu^{+} to MerP, which, similar to the enthalpic contribution, likely originates from protein conformational differences. These conformational differences overcome the entropic favorability and suggests that Cu^{+} binding may not stabilize the conformations but result in greater conformational dynamics than the apo-protein.

4.4.3. Unusual Zn^{2+} *and* Cd^{2+} *Coordination to WND4*

The binding of Hg^{2+} and Cu^{+} to WND4 show well-defined, and well-characterized binding isotherms, which leads to accurate condition-independent binding thermodynamics. However, this is not true for the binding of Zn^{2+} and Cd^{2+}. Like the binding of these metals to MerP, the goal is to understand the fundamental thermodynamics associated with metal selectivity and specificity within a series of proteins that utilize the same metal-binding site and same protein architecture. Both Zn^{2+} and Cd^{2+}, though unable to compete with Cu^{+} or Hg^{2+}, are readily present within the environment and both utilize the same protein architecture for their transport with the ferredoxin-like fold proteins ZntA and CadA.

The binding of both Cd^{2+} and Zn^{2+} to WND4 was unusual in that multiple binding events are observed, and these do not correspond to the stoichiometry of the metal-binding site. Zn^{2+} showed distinct buffer-dependent coordination, in which Bis-Tris has two binding events, and three binding events are found in TRIS. The final stoichiometries of both of these metals was equal to the binding of 2 Zn^{2+} per WND4 monomer, which is unlikely given the small size of the protein. It is observed, however, that WND4 does have two additional metal-binding residues that could explain these unusual binding characteristics. Near the MXCXXC metal binding site is a histidine (His18) and an additional cysteine (Cys2). Neither are particularly close to the primary metal-binding site, but their presence may dramatically alter the coordination of these metals. Both Zn^{2+} and Cd^{2+} generally prefer tetrahedral coordination, so some combination of these metal-binding residues may be resulting in the usual isotherms. Neither of these additional amino acids are present in MerP, so this type of interaction is not expected.

Like the binding of Zn^{2+} to WND4, the binding of Cd^{2+} results in similar unusual isotherms that are buffer-dependent, with TAPSO and TRIS showing the expected stoichiometry of 0.5 Cd^{2+} per WND4, suggesting a metal-bridged dimer, but MOPS and BisTris showing a stoichiometry of 2 Cd^{2+} per WND4 monomer. Again, two distinct metal-binding sites are not expected for WND4, thus the rationalization of these is not possible.

To accurately determine the Zn^{2+} and Cd^{2+} thermodynamics, I suggest that these additional histidine and cysteine residues should be mutated into non-metal binding amino acids which should eliminate aberrant metal-binding activity. Thus, a titration of Zn^{2+} and Cd^{2+} into the apo-WND4 with these mutations should result in only binding to desired metal-binding site.

4.4.4. Impacts of Ferredoxin-Like Protein Architecture on Metal Binding, Selectivity, and Specificity.

Understanding how the same metal-binding site in identical protein architecture modulates the metal-binding thermodynamics to ensure the correct metal is bound and delivered is challenging. Modulation of metal binding by second-sphere interactions was investigated through measurements of the binding of a set of metals to metallochaperones and metal-binding domains that all share a similar architecture. The binding of Hg^{2+} and Cu^{+} to the Cu^{+} metallochaperone, HAH1, was previously described by Michael Stevenson.[39]

Overall, similar trends are observed, in which the binding affinities of a given metal ion to these proteins are generally equivalent, but the thermodynamic contributions can be significantly different. The thermodynamic contributions do not seem to modulate the equilibrium constant, but rather, the components (i.e. enthalpy and entropy) of this binding.

I start with a comparison of binding of Hg^{2+} binding to MerP (native), HAH1 (non-native), and WND4 (non-native). The binding of Hg^{2+} is enthalpically driven in MerP and WND4. Hg^{2+} binding in HAH1, given the comparison with MerP and WND4, may be slightly underestimated, as the affinity of HAH1 for Hg^{2+} was ~4 orders of magnitude smaller. This enthalpic favorability for all 3 proteins in spite of a 1:2 complex for WND4 is not surprising given the very favorable soft-soft interactions between Hg^{2+} and cysteines. However, WND4, even though more protons are displaced, binds Hg^{2+} more enthalpically

favorable than MerP, which is unusual. I propose that this difference likely originates from changes to the overall protein scaffold upon Hg^{2+} binding, which would favor the formation of hydrogen-bonds, or the binding of Hg^{2+} to MerP is more enthalpically disfavored due to a disruption in these electrostatic interactions. Examining two loops of the proteins that flank either side of the primary metal-binding site, MerP has a tyrosine (Y67) that is likely involved in stabilizing the thiolate of Cys_C. However, in WND4 this is a phenylalanine (F69), which is hydrophobic. In WND4, F69 would be proposed to destabilize the thiolate, unlike the thiolate stabilization that happens in MerP. Binding of Hg^{2+} to MerP would disrupt that thiolate-tyrosine interaction, leading to more enthalpically disfavorable interactions. Curiously, in HAH1, neither a tyrosine or a phenylalanine are observed, but a lysine (K60). This positive charge would likely stabilize this thiolate differently than either WND4 or MerP. On the other flanking loop of these systems, however, is F38 in MerP, which would destabilize the thiolate, yet in HAH1, is K38 and K39, which would stabilize the thiolate. Curiously, there is no similar residue in WND4.

Considering MerP and Hg-MerP, Phe38 is very dynamic, in which in free MerP, this residue is buried destabilizing the thiolate, but this phenylalanine becomes solvent exposed. This conformational change is likely one of the sources of entropic favorability, in which Hg^{2+}-binding result in MerP to become more conformationally dynamic. Although we do not have a metal-bound WND4 structure, if we observe the sequence analysis (**Figure 4.1.2.2**), there are no residues that would provide an equivalent entropic contribution. Thus, the binding of Hg^{2+} to WND4 would be predicted to not be as dynamic of a structure, as compared to MerP. In HAH1, where there are structures for both free HAH1 and metal-bound HAH1, two lysine residues (K38 and K39) have been proposed to stabilize the thiolate, but the dynamics of this are not as pronounced. Unlike in MerP, this lysine does not have as much conformational difference between the apo and metal-bound structure.

Why, then, does Hg^{2+} preferentially bind to MerP and not HAH1 or WND4? The likely answer does not involve thermodynamics at all, but through their separation. MerP is found solely within the periplasm of the cell, whereas HAH1 and WND4 would primarily be found within the cytosol of the cell. It is recognized that HAH1 and WND4 are human Cu^{+} proteins and that MerP is only found in bacterial cells, but similar Cu^{+}

metallochaperones and metal-binding domains are also observed in bacteria. A better question is, would Hg^{2+} preferentially bind to MerP, over HAH1 or WND4, if these were the only components within the solution? Given the similar equilibrium constants, it is unlikely that Hg^{2+} would bind to MerP over the other proteins, but the relative thermodynamics contributions could modulate this binding. Second-sphere interactions of these proteins may not necessarily play a role in the metal binding, but in the physiological function of the protein: metal transport and transfer. Transfer from one protein to another that have equivalent binding affinities require thermodynamics or kinetic differences to drive the transfer. The binding and transfer can be transient, but entropic and enthalpic differences could modulate this behavior to preferentially release the metal to its binding partner.

Like the binding of Hg^{2+}, Cu^{+} binding thermodynamics show many of the same trends. Similar binding affinities, but different enthalpic and entropic contributions indicate enthalpy-entropy compensation, but these thermodynamics differences may drive the transfer of the metal from one protein to the next.

Finally, there is WND4, which forms unusual metal-protein complexes. The propensity for WND4 to form metal-bridged dimers makes good chemical sense. WND4 acquires Cu^{+} from HAH1, through a process that, at least temporarily, forms a metal-bridged heterodimer. The presence of a histidine that seems to be immediately between a homodimer interface, may indicate that this residue is required for the formation of these dimers in solution. Modulation of this histidine may result in more metallochaperone characteristics, as opposed to metal-binding domain characteristics. This distinction between characteristics is driven by the propensity for a protein to be a soluble metallochaperone or a domain that would have higher protein-protein contacts for metal transfer. Furthermore, this could be readily probed through site-direct mutagenesis of HAH1 or MerP, that mutate a histidine residue into a solvent-facing component, which could lead to the formation of this dimer.

Overall, this work highlights how protein architecture, even in protein samples that are be expected to have identical thermodynamics, can modulate the enthalpic and entropic contributions associated with metal binding. Although not explored herein, this work could

be used to modify these metallochaperones to enhance metal selectivity and specificity through the second-sphere interactions.

4.4.5. Future Work and Conclusions

Future experiments using ITC could provide insight on the thermodynamics of this same series of metals binding to the N-terminal metal-binding domain of mercuric reductase, NmerA. This Hg^{2+}-binding domain is nearly identical to MerP but contains a few differences in its protein architecture that would, given our results with WND4, preclude it to have more metal-binding domain characteristics, over metallochaperone characteristics, leading to the formation of metal-bridged dimers, as opposed to 1:1 metal:protein complexes. For example, NmerA, like WND4, has a histidine that is solvent exposed near the metal-binding site, which may be located at the dimerization interface (**Figure 4.1.2.2**).

Several of the hypotheses that were developed here rely on solution structures of the apo and holo proteins. However, mutagenesis of these residues, like the phenylalanine and tyrosine that flank the metal-binding site on MerP, to other residues could provide insight on thiolate stabilization and the difference in the entropic contributions to metal binding. This could be taken as far as mutating key residues in MerP to mirror those in HAH1 or WND4 and observing the thermodynamic differences. Thermodynamic differences could indicate the entropic and enthalpic contribution of each individual proteins to metal binding in a much more quantitative way.

A better understanding of how the protein scaffold modulates metal binding will also provide valuable insight. Two techniques are immediately applicable: molecular dynamics and model systems. Utilization of molecular dynamics simulations can provide atomistic information on protein dynamics and fluctuations in the protein structure when the metal is bound as compared to the apo form. This also allows for simple mutagenesis to provide a better understanding of enthalpy-entropy compensation. Likewise, utilization of an unstructured peptide that models the linear cysteine binding site would be useful in subtracting the metal-binding thermodynamics from the thermodynamics that originate from the protein structure itself. By subtracting the thermodynamics of Hg^{2+} binding to such a peptide with an identical metal-binding site from the thermodynamics of Hg^{2+}

binding to the ferredoxin-like metallochaperones, the contribution from the protein scaffold could then be quantified. This difference would approximate the thermodynamics that come from the protein, but not the metal-binding site, providing further insight into how protein structures modulate metal-binding.

Overall, this work highlights the modulation of enthalpic, and entropic contributions to metal binding that occur through the protein scaffold and second-sphere interactions. With this knowledge, a better understanding of enthalpy-entropy compensation has been achieved. This work also clarifies previous efforts to quantify metal-binding thermodynamics. Lastly, this work provides experimental evidence for metal-bridged dimer formation as a primary mechanism of metal transfer from metallochaperones to metal-binding domains. This transfer mechanism is also likely used in the transfer of a metal from a metal-binding domain to another metal-binding site on the protein, as is the case with MerA.[34,52] Further work is required to define the exact molecular mechanism, but this work provides the thermodynamic foundation for the characterization.

4.5. References

(1) Reddi, A. R.; Guzman, T. R.; Breece, R. M.; Tierney, D. L.; Gibney, B. R. Deducing the Energetic Cost of Protein Folding in Zinc Finger Proteins Using Designed Metallopeptides. *J. Am. Chem. Soc.* **2007**, *129* (42), 12815–12827. https://doi.org/10.1021/ja073902+.

(2) Du, X.; Li, Y.; Xia, Y. L.; Ai, S. M.; Liang, J.; Sang, P.; Ji, X. L.; Liu, S. Q. Insights into Protein–Ligand Interactions: Mechanisms, Models, and Methods. *Int. J. Mol. Sci.* **2016**, *17* (2), 144. https://doi.org/10.3390/ijms17020144.

(3) Jelesarov, I.; Bosshard, H. R. Isothermal Titration Calorimetry and Differential Scanning Calorimetry as Complementary Tools to Investigate the Energetics of Biomolecular Recognition. *J. Mol. Recognit.* **1999**, *12* (1), 3–18. https://doi.org/10.1002/(SICI)1099-1352(199901/02)12:1<3::AID-JMR441>3.0.CO;2-6.

(4) Koshland, D. E. The Key–Lock Theory and the Induced Fit Theory. *Angew. Chemie Int. Ed. English* **1995**, *33* (23–24), 2375–2378. https://doi.org/10.1002/anie.199423751.

(5) Verteramo, M. L.; Stenström, O.; Ignjatović, M. M.; Caldararu, O.; Olsson, M. A.; Manzoni, F.; Leffler, H.; Oksanen, E.; Logan, D. T.; Nilsson, U. J.; Ryde, U.; Akke, M. Interplay between Conformational Entropy and Solvation Entropy in Protein-Ligand Binding. *J. Am. Chem. Soc.* **2019**, *141* (5), 2012–2026. https://doi.org/10.1021/jacs.8b11099.

(6) Sparks, R. P.; Arango, A. S.; Jenkins, J. L.; Guida, W. C.; Tajkhorshid, E.; Sparks, C. E.; Sparks, J. D.; Fratti, R. A. An Allosteric Binding Site on Sortilin Regulates the Trafficking of VLDL, PCSK9, and LDLR in Hepatocytes. *Biochemistry* **2020**, *59* (45), 4321–4335. https://doi.org/10.1021/acs.biochem.0c00741.

(7) Popovych, N.; Sun, S.; Ebright, R. H.; Kalodimos, C. G. Dynamically Driven Protein Allostery. *Nat. Struct. Mol. Biol.* **2006**, *13* (9), 831–838. https://doi.org/10.1038/nsmb1132.

(8) Motlagh, H. N.; Wrabl, J. O.; Li, J.; Hilser, V. J. The Ensemble Nature of Allostery. *Nature* **2014**, *508* (7496), 331–339. https://doi.org/10.1038/nature13001.

(9) Guarnera, E.; Berezovsky, I. N. Allosteric Sites: Remote Control in Regulation of Protein Activity. *Curr. Opin. Struct. Biol.* **2016**, *37*, 1–8. https://doi.org/10.1016/j.sbi.2015.10.004.

(10) Amacher, J. F.; Zhong, F.; Lisi, G. P.; Zhu, M. Q.; Alden, S. L.; Hoke, K. R.; Madden, D. R.; Pletneva, E. V. A Compact Structure of Cytochrome c Trapped in a Lysine-Ligated State: Loop Refolding and Functional Implications of a Conformational Switch. *J. Am. Chem. Soc.* **2015**, *137* (26), 8435–8449. https://doi.org/10.1021/jacs.5b01493.

(11) Zhao, M.; Wang, H. B.; Ji, L. N.; Mao, Z. W. Insights into Metalloenzyme Microenvironments: Biomimetic Metal Complexes with a Functional Second Coordination Sphere. *Chem. Soc. Rev.* **2013**, *42* (21), 8360–8375. https://doi.org/10.1039/c3cs60162e.

(12) Keskin, O.; Nussinov, R. Favorable Scaffolds: Proteins with Different Sequence, Structure and Function May Associate in Similar Ways. *Protein Eng. Des. Sel.* **2005**, *18* (1), 11–24. https://doi.org/10.1093/protein/gzh095.

(13) Valasatava, Y.; Rosato, A.; Furnham, N.; Thornton, J. M.; Andreini, C. To What Extent Do Structural Changes in Catalytic Metal Sites Affect Enzyme Function? *J.*

Inorg. Biochem. **2018**, *179*, 40–53. https://doi.org/10.1016/j.jinorgbio.2017.11.002.

(14) Bollella, P.; Katz, E. Enzyme-Based Biosensors: Tackling Electron Transfer Issues. *Sensors (Switzerland)* **2020**, *20* (12), 1–32. https://doi.org/10.3390/s20123517.

(15) Vallee, B. L.; Williams, R. J. Metalloenzymes: The Entatic Nature of Their Active Sites. *Proc. Natl. Acad. Sci. U. S. A.* **1968**, *59* (2), 498–505. https://doi.org/10.1073/pnas.59.2.498.

(16) Das, A.; Chakrabarti, J.; Ghosh, M. Conformational Thermodynamics of Metal-Ion Binding to a Protein. *Chem. Phys. Lett.* **2013**, *581*, 91–95. https://doi.org/10.1016/j.cplett.2013.07.022.

(17) Badarau, A.; Dennison, C. Copper Trafficking Mechanism of CXXC-Containing Domains: Insight from the PH-Dependence of Their Cu(I) Affinities. *J. Am. Chem. Soc.* **2011**, *133* (9), 2983–2988. https://doi.org/10.1021/ja1091547.

(18) Chen, S. H.; Chen, L.; Russell, D. H. Metal-Induced Conformational Changes of Human Metallothionein-2A: A Combined Theoretical and Experimental Study of Metal-Free and Partially Metalated Intermediates. *J. Am. Chem. Soc.* **2014**, *136* (26), 9499–9508. https://doi.org/10.1021/ja5047878.

(19) Huang, Y.; Ackers, G. K. Enthalpic and Entropic Components of Cooperativity for the Partially Ligated Intermediates of Hemoglobin Support a “Symmetry Rule” Mechanism. *Biochemistry* **1995**, *34* (19), 6316–6327. https://doi.org/10.1021/bi00019a009.

(20) North, M. L.; Wilcox, D. E. Shift from Entropic Cu2+ Binding to Enthalpic Cu+ Binding Determines the Reduction Thermodynamics of Blue Copper Proteins. *J. Am. Chem. Soc.* **2019**, *141* (36), 14329–14339. https://doi.org/10.1021/jacs.9b06836.

(21) Grossoehme, N. E.; Spuches, A. M.; Wilcox, D. E. Application of Isothermal Titration Calorimetry in Bioinorganic Chemistry. *J. Biol. Inorg. Chem.* **2010**, *15* (8), 1183–1191. https://doi.org/10.1007/s00775-010-0693-3.

(22) Quinn, C. F.; Carpenter, M. C.; Croteau, M. L.; Wilcox, D. E. Isothermal Titration Calorimetry Measurements of Metal Ions Binding to Proteins. *Methods Enzymol.* **2016**, *567*, 3–21. https://doi.org/10.1016/bs.mie.2015.08.021.

(23) Carpenter, M. C.; Shami Shah, A.; Desilva, S.; Gleaton, A.; Su, A.; Goundie, B.;

Croteau, M. L.; Stevenson, M. J.; Wilcox, D. E.; Austin, R. N. Thermodynamics of Pb(II) and Zn(II) Binding to MT-3, a Neurologically Important Metallothionein. *Metallomics* **2016**, *8* (6), 605–617. https://doi.org/10.1039/c5mt00209e.

(24) Carpenter, M. C.; Wilcox, D. E. Thermodynamics of Formation of the Insulin Hexamer: Metal-Stabilized Proton-Coupled Assembly of Quaternary Structure. *Biochemistry* **2014**, *53* (8), 1296–1301. https://doi.org/10.1021/bi4016567.

(25) Baksh, K. A.; Zamble, D. B. Allosteric Control of Metal-Responsive Transcriptional Regulators in Bacteria. *Journal of Biological Chemistry*. American Society for Biochemistry and Molecular Biology Inc. 2020, pp 1673–1684. https://doi.org/10.1074/jbc.REV119.011444.

(26) Rosenzweig, A. C. Metallochaperones: Bind and Deliver. *Chem. Biol.* **2002**, *9* (6), 673–677. https://doi.org/10.1016/S1074-5521(02)00156-4.

(27) Shoshan, M. S.; Tshuva, E. Y. The MXCXXC Class of Metallochaperone Proteins: Model Studies. *Chem. Soc. Rev.* **2011**, *40* (11), 5282–5292. https://doi.org/10.1039/c1cs15086c.

(28) Arnesano, F.; Banci, L.; Bertini, I.; Ciofi-Baffoni, S.; Molteni, E.; Huffman, D. L.; O'Halloran, T. V. Metallochaperones and Metal-Transporting ATPases: A Comparative Analysis of Sequences and Structures. *Genome Res.* **2002**, *12* (2), 255–271. https://doi.org/10.1101/gr.196802.

(29) Badarau, A.; Firbank, S. J.; McCarthy, A. A.; Banfield, M. J.; Dennison, C. Visualizing the Metal-Binding Versatility of Copper Trafficking Sites. *Biochemistry* **2010**, *49* (36), 7798–7810. https://doi.org/10.1021/bi101064w.

(30) Rodriguez-Granillo, A.; Wittung-Stafshede, P. Structure and Dynamics of Cu(I) Binding in Copper Chaperones Atox1 and CopZ: A Computer Simulation Study. *J. Phys. Chem. B* **2008**, *112* (15), 4583–4593. https://doi.org/10.1021/jp711787x.

(31) Banci, L.; Bertini, I.; Ciofi-Baffoni, S.; Huffman, D. L.; O'Halloran, T. V. Solution Structure of the Yeast Copper Transporter Domain Ccc2a in the Apo and Cu(I)-Loaded States. *J. Biol. Chem.* **2001**, *276* (11), 8415–8426. https://doi.org/10.1074/jbc.M008389200.

(32) Banci, L.; Bertini, I.; Ciofi-Baffoni, S.; Su, X. C.; Miras, R.; Bal, N.; Mintz, E.; Catty, P.; Shokes, J. E.; Scott, R. A. Structural Basis for Metal Binding Specificity:

The N-Terminal Cadmium Binding Domain of the P1-Type ATPase CadA. *J. Mol. Biol.* **2006**, *356* (3), 638–650. https://doi.org/10.1016/j.jmb.2005.11.055.

(33) Powlowski, J.; Sahlman, L. Reactivity of the Two Essential Cysteine Residues of the Periplasmic Mercuric Ion-Binding Protein, MerP. *J. Biol. Chem.* **1999**, *274* (47), 33320–33326. https://doi.org/10.1074/jbc.274.47.33320.

(34) Ledwidge, R.; Patel, B.; Dong, A.; Fiedler, D.; Falkowski, M.; Zelikova, J.; Summers, A. O.; Pai, E. F.; Miller, S. M. NmerA, the Metal Binding Domain of Mercuric Ion Reductase, Removes Hg 2+ from Proteins, Delivers It to the Catalytic Core, and Protects Cells under Glutathione-Depleted Conditions. *Biochemistry* **2005**, *44* (34), 11402–11416. https://doi.org/10.1021/bi050519d.

(35) Rodriguez-Granillo, A.; Crespo, A.; Wittung-Stafshede, P. Conformational Dynamics of Metal-Binding Domains in Wilson Disease Protein: Molecular Insights into Selective Copper Transfer. *Biochemistry* **2009**, *48* (25), 5849–5863. https://doi.org/10.1021/bi900235g.

(36) Anastassopoulou, I.; Banci, L.; Bertini, I.; Cantini, F.; Katsari, E.; Rosato, A. Solution Structure of the Apo and Copper(I)-Loaded Human Metallochaperone HAH1. *Biochemistry* **2004**, *43* (41), 13046–13053. https://doi.org/10.1021/bi0487591.

(37) Riener, C. K.; Kada, G.; Gruber, H. J. Quick Measurement of Protein Sulfhydryls with Ellman's Reagent and with 4,4′-Dithiodipyridine. *Anal. Bioanal. Chem.* **2002**, *373* (4–5), 266–276. https://doi.org/10.1007/s00216-002-1347-2.

(38) Blair, D.; Diehl, H. Bathophenanthrolinedisulphonic Acid and Bathocuproinedisulphonic Acid, Water Soluble Reagents for Iron and Copper. *Talanta* **1961**, *7* (3–4), 163–174. https://doi.org/10.1016/0039-9140(61)80006-4.

(39) Stevenson, M. J. Thermodynamic Studies of Cu(I) and Other d 10 Metal Ions Binding to Proteins in the Copper Homeostasis Pathway and the Organomercurial Detoxification Pathway, 2016.

(40) Casas, J. S.; Jones, M. M. Mercury(II) Complexes with Sulfhydryl Containing Chelating Agents: Stability Constant Inconsistencies and Their Resolution. *J. Inorg. Nucl. Chem.* **1980**, *42* (1), 99–102. https://doi.org/10.1016/0022-1902(80)80052-2.

(41) Liem-Nguyen, V.; Skyllberg, U.; Nam, K.; Björn, E. Thermodynamic Stability of

Mercury(II) Complexes Formed with Environmentally Relevant Low-Molecular-Mass Thiols Studied by Competing Ligand Exchange and Density Functional Theory. *Environ. Chem.* **2017**, *14* (4), 243–253. https://doi.org/10.1071/EN17062.

(42) Basinger, M. A.; Casas, J. S.; Jones, M. M.; Weaver, A. D.; Weinstein, N. H. *Structural Requirements for Hg(II) Antidotes*; 1981; Vol. 43. https://doi.org/10.1016/0022-1902(81)80058-9.

(43) Veglia, G.; Porcelli, F.; DeSilva, T.; Prantner, A.; Opella, S. J. The Structure of the Metal-Binding Motif GMTCAAC Is Similar in an 18- Residue Linear Peptide and the Mercury Binding Protein MerP [10]. *J. Am. Chem. Soc.* **2000**, *122* (10), 2389–2390. https://doi.org/10.1021/ja992908z.

(44) Rosenzweig, A. C.; Huffman, D. L.; Hou, M. Y.; Wernimont, A. K.; Pufahl, R. A.; O'Halloran, T. V. Crystal Structure of the Atx1 Metallochaperone Protein at 1.02 Å Resolution. *Structure* **1999**, *7* (6), 605–617. https://doi.org/10.1016/S0969-2126(99)80082-3.

(45) Tamura, A.; Privalov, P. L. *The Entropy Cost of Protein Association*; 1997; Vol. 273. https://doi.org/10.1006/jmbi.1997.1368.

(46) Gilson, M. K.; Given, J. A.; Bush, B. L.; McCammon, J. A. The Statistical-Thermodynamic Basis for Computation of Binding Affinities: A Critical Review. *Biophys. J.* **1997**, *72* (3), 1047–1069. https://doi.org/10.1016/S0006-3495(97)78756-3.

(47) DeSilva, T. M.; Veglia, G.; Porcelli, F.; Prantner, A. M.; Opella, S. J. Selectivity in Heavy Metal-Binding to Peptides and Proteins. *Biopolymers* **2002**, *64* (4), 189–197. https://doi.org/10.1002/bip.10149.

(48) Banci, L.; Bertini, I.; Ciofi-Baffoni, S.; Kozyreva, T.; Zovo, K.; Palumaa, P. Affinity Gradients Drive Copper to Cellular Destinations. *Nature* **2010**, *465* (7298), 645–648. https://doi.org/10.1038/nature09018.

(49) Banci, L.; Bertini, I.; Cantini, F.; Rosenzweig, A. C.; Yatsunyk, L. A. Metal Binding Domains 3 and 4 of the Wilson Disease Protein: Solution Structure and Interaction with the Copper(I) Chaperone HAH1. *Biochemistry* **2008**, *47* (28), 7423–7429. https://doi.org/10.1021/bi8004736.

(50) Wernimont, A. K.; Yatsunyk, L. A.; Rosenzweig, A. C. Binding of Copper(I) by the

Wilson Disease Protein and Its Copper Chaperone. *J. Biol. Chem.* **2004**, *279* (13), 12269–12276. https://doi.org/10.1074/jbc.M311213200.

(51) Steele, R. A.; Opella, S. J. Structures of the Reduced and Mercury-Bound Forms of MerP, the Periplasmic Protein from the Bacterial Mercury Detoxification System. *Biochemistry* **1997**, *36* (23), 6885–6895. https://doi.org/10.1021/bi9631632.

(52) Ledwidge, R.; Hong, B.; Dötsch, V.; Miller, S. M. NmerA of Tn 501 Mercuric Ion Reductase: Structural Modulation of the p K a Values of the Metal Binding Cysteine Thiols. *Biochemistry* **2010**, *49* (41), 8988–8998. https://doi.org/10.1021/bi100537f.

Chapter 5:

Cellular Protection from Environmentally-Relevant Metals and Organomercurial Compounds by the Bacterial Periplasmic Protein, MerP

5.1. Introduction

5.1.1. Mercury and Organomercurial Compounds in the Environment

Mercury is a particularly toxic element that is ubiquitous in Nature without any known biological function. It enters the environment through both natural and anthropogenic means, including volcanoes, pulp and paper manufacturing, and mercury-based gold extraction.[1–4] Mercury is a constituent of various medical applications such as antiseptics and antifungals, like merbromin and thimerosal. Approximately 5,000 – 8,000 metric tons of mercury are deposited into the environment each year leading to massive worldwide contamination of our soils and waterways.[5]

The mercury problem is augmented on a global scale by the volatility of elemental mercury, which is easily oxidized, reduced, or methylated in the environment. Furthermore, mercury has a tendency to bioaccumulate and biomagnify within marine plants and animals, poisoning the predators that prey on them.[6] Human consumption of these marine species like albacore tuna, for example, have been the primary mechanism of mercury toxicity in humans. As such, the level of mercury toxicity positively correlates with increased fish consumption.[7] However, mercury is not always added to the environment accidentally. This includes the use of mercury as a fungicide for certain agricultural plants, leading to contamination of farmland.[8] Mercury pollution is pervasive within the environment, and effects all forms of life, from bacteria to humans.

5.1.2. Mechanisms of Mercury Toxicity

The primary mechanism of mercury toxicity through binding to thiol groups on proteins, particularly those in mitochondria, and to DNA, resulting in extensive cellular disruption. It is suggested that the neurological damage caused by methylmercury is related to extensive oxidative damage within neuronal cells and is correlated with a significant decrease in reduced glutathione.[9] It was shown that the strong oxidant, H_2O_2, causes similar damage in cerebellar neuronal preparations as that found with methylmercury. Other mechanisms involve the binding of methylmercury to the thiol-rich Purkinje cells which, when damaged, can lead to neurological symptoms such as ataxia.[10] Other studies have found specific proteins within yeast, GFAT and Ubc3, that are thought to be the primary

target of methylmercury damage.[11] It was suggested that there are homologous proteins in the human body that can be considered the primary target for methylmercury toxicity. The overall damage caused by mercury, and methylmercury in particular, is extensive to most biological organisms. As such, efforts to effectively control and eliminate mercury is at the forefront of environmental protection.

In humans, the chemical and molecular effects of mercury are extensive. However, the majority of the damage and terminating events are related to its effect on the brain and kidney, depending on the form of mercury intoxication. Both ionic forms of mercury, Hg^{+}, found as Hg_2^{2+} and Hg^{2+}, primarily damage the kidneys, while Hg^0 and organomercurials, like $MeHg^{+}$, are capable of crossing the blood-brain barrier (BBB) due to their lipophilicity, and damaging the central nervous system. It is suggested that organomercurials, particularly methylmercury, are able to passively diffuse through the BBB through small, water-soluble cationic channels.[12] Similarly, Hg^0 is able to cross the BBB via passive diffusion; however, some of the Hg^0 that enters the brain will subsequently be oxidized to Hg^{2+}, which is then unable to cross the BBB, and accumulates in the brain (***Figure 5.1.2.1***). Furthermore, evidence suggests that methylmercury, which is the predominant organomercurial in the environment, will also slowly degrade into inorganic mercury over time through demethylases in various organisms in the environment, leading to further contamination.[13]

This formation and accumulation of inorganic mercury within the central nervous system (CNS) leads to significant damage that appears to be related to the primary excitatory neurotransmitter, glutamate. Inorganic mercury is proposed to cause neurological damage by inhibition of the clearance of extracellular glutamate and accumulates within astrocytes, inhibiting glutamate uptake which leads to neuronal dysfunction.[14,15] Inorganic mercury compounds like mercuric chloride, which are generally unable to cross the BBB in significant amounts, tend to accumulate in the kidney, causing extensive damage, due to Hg^{2+} binding to sulfhydryl groups on components necessary for kidney function, including proteins and glutathione (GSH).[16] Mercury's ability to bind these thiol groups is the basis of mercury damage on a molecular level, which directly translates to overall system effects in humans.

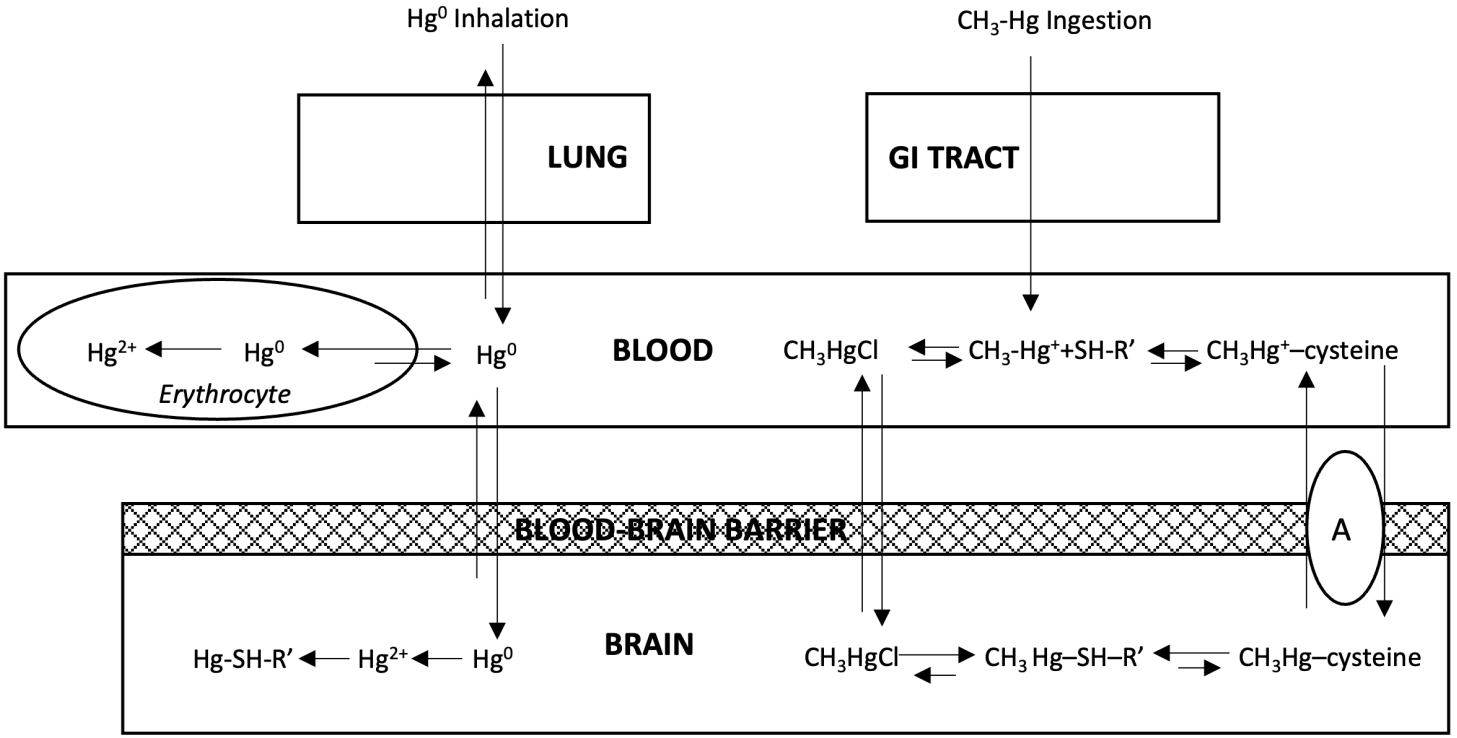

Figure 5.1.2.1. *The mechanism of elemental and methylmercury intoxication. Hg^0 enters the blood through the lungs during inhalation, where it can then diffuse into erythrocytes and be oxidized to Hg^{2+}, or Hg^0 can diffuse across the BBB, and again, becoming oxidized to Hg^{2+}, which subsequently binds to thiol groups within the central nervous system. Methylmercury tends to enter the circulatory system through ingestion and absorption in the gastrointestinal (GI) tract, where it then follows two main routes into the brain. It can bind to cysteine groups on proteins within the blood, and cross the BBB through a Na^+ independent carrier (A). Methylmercury can also bind to Cl^- groups within the blood, and again, cross the BBB. While in brain, the cysteine and Cl^- bound methylmercury then binds to thiol groups within the central nervous system. Arrows represent approximate rate constants of the reactions and are not to scale. Figure adapted from Aschner and Aschner, 1990.*

The damage from mercury begins on a molecular level and leads to gross changes in the overall health of humans. Mercury in the human body affects the respiratory system, central nervous system, peripheral nervous system, and genitourinary system primarily, with secondary damage to the cardiovascular and immunological systems [17–20]. Each form of mercury (elemental, ionic, and organometallic) tends to affect the human body in different ways due to the chemical properties of each form. Hg^0 is readily absorbed and distributed in the body through inhalation and acts on the body by causing renal failure and severe neurological damage, including tremors and memory loss on an acute basis and depression and memory impairment chronically.[21] Inorganic Hg^{2+}, due to its charged nature, is unable to cross the BBB, and accumulated within the kidneys, causing tubular necrosis and proteinuria, which is the principle cause of death after inorganic mercury exposure.[22] Furthermore, inorganic mercury salts are associated with general widespread damage leading to acrodynia in children and the proliferation of adult T-cells, which are involved in cell mediated immunity.[23,24] Organomercurials are distinctly different, as they effortlessly cross the BBB, causing rapid and severe neurological damage including paresthesia (tingling, numbness, and loss of feeling in the extremities), ataxia, insomnia, and diminished sensory capabilities (sight, smell, hearing, etc.).[25] Each form of mercury is similar in its function on a molecular level, yet each causes a discrete constellation of systematic damage.

Historically, mercury compounds were used as antibacterials and antifungals. Their mechanism of action is through mercury's strong affinity for soft bases, such as the thiol group of cysteine residues, which has a direct negative impact on protein function. Through the disruption of Fe-S clusters, mercury induces the release of iron, which generates reactive oxygen species (ROS). This appears to be the mechanism by which mercury can produce ROS, even though it is incapable of Fenton chemistry.[26] Due to its high affinity for thiol groups, a key mode of toxicity is through its binding to catalytically active centers that contain sulfhydryl and thioether groups.[27] In mercury-sensitive bacteria, the bactericidal effect of mercury is due, primarily, to binding to these thiol groups, leading to the inactivation of key enzymes and protein pathways.

5.1.3. Bacterial Defense Mechanisms for Mercury Protection

Bacterial species have developed different cellular mechanisms for resistance to mercury in the environment. Some anaerobic bacteria, like the sulfur-reducing bacteria *Desulfovibrio desulfuricans,* for example, utilize an active transport mechanism for the uptake of Hg^{2+}, which is suggested to be a consequence of the active uptake of other necessary trace metals.[28,29] These *deltaproteobacteria* species then methylate the mercury and are considered the primary source of methylmercury in aquatic environments. These methylmercury-producing bacterial species utilize a two-gene cluster that encodes for a cobalamin-dependent corrinoid protein and a 2[4Fe-4S] ferredoxin-like protein, HgcA and HgcB, respectively. HgcA binds Co(III) for methylcobalamin and facilitates transfer of the methyl-carbanion to Hg^{2+} while, HgcB serves as an electron donor for HgcA.[30,31] The proposed mechanism of mercury methylation appears to be directly connected to the folate pathway branch in the production of acetyl-CoA.[32] This mechanism seems counterintuitive, as the bacteria are actively importing the, seemingly, less toxic ionic mercury, and transforming it to the seemingly more toxic methylmercury. However, it has been proposed that methylmercury is less toxic to bacteria than ionic mercury. Mercury resistance is maintained for these bacteria because of the active export of methylmercury out of the cell. This mechanism of uptake, methylation, and export is very tightly coupled to prevent cellular damage.[28]

Other mechanisms have been characterized in other bacterial species, including one that reduces mercury uptake into the cell, which has been found in *Enterobacter aerogenes*.[33] Mercury resistance can also be conveyed by the demethylation of methylated mercury compounds, and the subsequent addition of sulfide to form insoluble mercuric sulfides, which has been found in *Clostridium cochlearium*, thereby removing soluble mercury from the microenvironment of the cell.[34]

5.1.4. The Bacterial Mercury Detoxification Pathway

Many species of bacteria achieve resistance to mercury through either a narrow-spectrum or broad-spectrum mechanism. These involve: (1) uptake and enzymatic reduction of Hg^{2+} or (2) cleavage of the C-Hg bond of organomercurials and subsequent

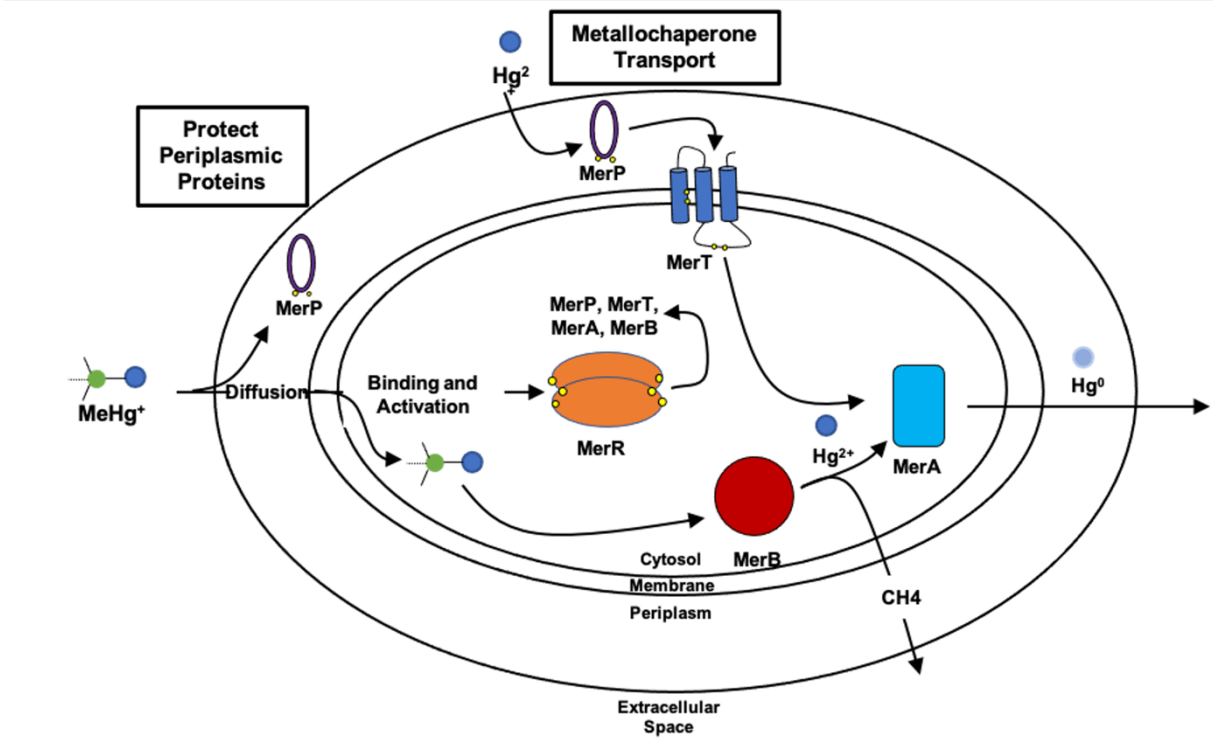

Figure 5.1.4.1. *Representation of the bacterial mercury detoxification pathway (*mer *pathway). Both narrow-spectrum and broad-spectrum pathways are depicted, although both are not always found together within a given cell. Other related* mer *proteins that are less commonly found, including MerC, MerE MerF, and MerG are not included.*

enzymatic reduction of Hg^{2+}, respectively. In both pathways, Hg^{2+} is reduced to Hg^0 which then volatilizes out of the cell without causing cellular damage.[35] This pathway involves a series of cysteine-containing proteins that bind and transport the metal (**Figure 5.1.4.1**).

This pathway has been described as follows. As Hg^{2+} enters the microenvironment of the cell, it diffuses into the periplasm through large porins in the outer cell membrane, where it binds to the periplasmic mercury metallochaperone, MerP. This metal-protein complex subsequently interacts with the transmembrane protein, MerT, where Hg^{2+} is transferred to a pair of cysteines on the periplasmic site. Hg^{2+} then moves through MerT to another pair of cysteines located on the cytosolic side of the protein. Mercuric reductase (MerA), accepts Hg^{2+} from MerT via its MerP-like N-terminal domain (NmerA), finally transferring it to the catalytic core of MerA where Hg^{2+} is reduced to Hg^0. Metallic mercury, unlike Hg^{2+}, is relatively inert, so it dissociates from MerA and volatilizes out of the cell. This pathway is enhanced in broad-spectrum resistance, by the addition of MerB. Methylmercury diffuses directly through the cell membrane, without the assistance of MerP or MerT, and binds to the organomercurial lyase, MerB that catalyzes the cleavage of the C-Hg bond, leading to a bound Hg^{2+} and methane that volatilizes out of the cell. Finally, like the narrow-spectrum pathway, NmerA chelates Hg^{2+} from MerB and transfers it to the catalytic core of MerA where Hg^{2+} is reduced to Hg^0.[36] Biosynthesis of all of these proteins is regulated, primarily, by the mercury metalloregulatory protein, MerR and its variants.[37,38]

5.1.5. Protection from Environmental Mercury Toxicity by MerP

The classical mechanism of Hg^{2+} uptake, transfer, and enzymatic reduction suggests that MerP is a metallochaperone that binds and transports Hg^{2+} to, MerT. In this mechanism, it is suggested that Hg^{2+} is accepted by MerT from MerP, which implies that MerP is required for this transfer. However, Hg^{2+} tolerance is still observed for MerP knockout cell lines.[39] If MerP was required for the transfer of Hg^{2+} to MerT, then Hg^{2+} tolerance of these cells should be approximately equal to that of cells without the *mer* pathway. This, however, is not the case, indicating that MerP

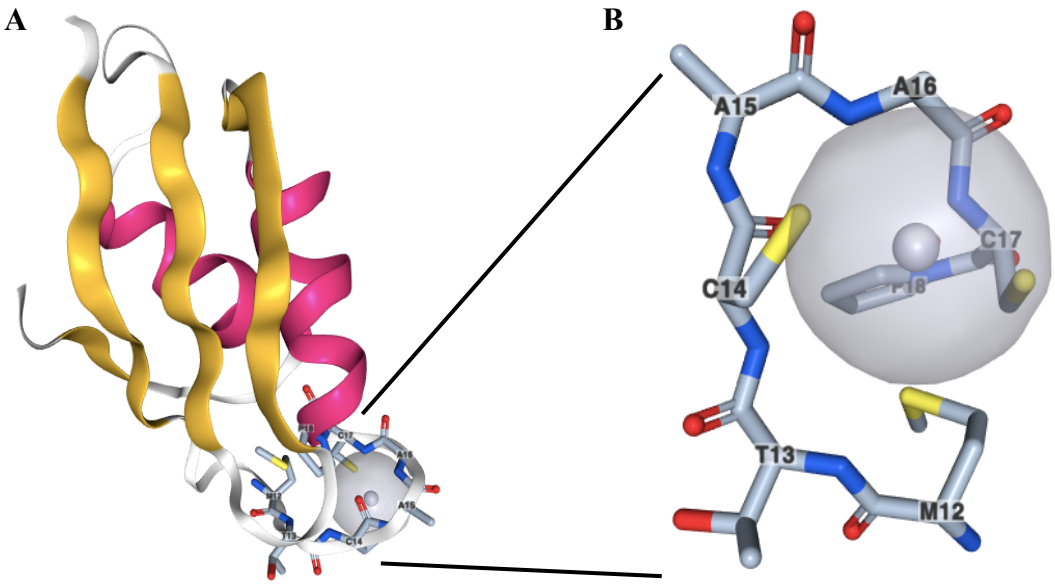

Figure 5.1.5.1. *Overall MerP structure with bound* Hg^{2+} *from* Shigella flexneri.[41] (A) *The βαββαβ ferredoxin-like structure is shown with the binding site of* Hg^{2+}. *(B) Shows the soft-metal binding motif, MXCXXC, in which* Cys^{14} *and* Cys^{17} *bind* Hg^{2+}. *PDB:1AFJ*

is not required for the uptake of Hg^{2+}. Why, then, is MerP found in nearly all *mer* operons if it is not strictly required for the pathway to function? This is further confounded by the broad-spectrum pathway. As methylmercury diffuses through the cell membrane into the cytosol, this must be preceded by diffusion through the periplasmic space. The propensity of methylmercury for cysteine residues suggest that it would bind to proteins in the periplasmic space, to the detriment of the health of the cell. How do cells cope with the potentially damaging effects of methylmercury, and organomercurial compounds in general, before it reaches MerB?

In order to better understand how MerP in the periplasm could be functioning to protect the cell from the toxic effects of mercury and methylmercury, it is important to examine its protein structure. MerP is a small, 76-residue (~7,600 Da, ε = 1,490 M^{-1} for *Pseudomonas aeruginosa*) globular protein, which contains the highly conserved metal-binding motif, MXCXXC, which binds Hg^{2+}, as well as numerous other metals, including Cu^{+}, Cd^{2+}, Zn^{2+}, and Pb^{2+} (**Figure 5.1.5.1**).[40] The overall structure of MerP is similar to that of other soluble metal-binding proteins and domains, with the $\beta\alpha\beta\beta\alpha\beta$ ferredoxin-like structure, where the 4 β-strands are connect to the two α-helices by various loops, that contain the metal-binding motif.[41]

This soft metal-binding motif is highly conserved across all known MerP's structures, where metals bind to the N-terminal cysteine (Cys_N) and the C-terminal cysteine (Cys_C). It was determined that both Cys_N and Cys_C are necessary for binding Hg^{2+}, and it was also reported that MerP binds other metal ions, including Cu^{2+}, Ni^{2+}, Zn^{2+}, Cd^{2+}, and Ag^{+} with an affinity similar to that of Hg^{2+}, although this has been disputed in this work (See Chapter 4).[42,43] Nonetheless, this MXCXXC metal-binding sequence was found to coordinate soft metals primarily with a linear bi-coordinate geometry. However, when the sequence of cysteines was changed to, MXCXCX, and MXCCXX, there were significant differences in the binding of Hg^{2+} and other metals. It was found that the MXCCXX sequence had a comparable affinity for Hg^{2+} as the original MXCXXC sequence in MerP. However, it was highly specific for Hg^{2+} and unable to bind Cu^{+}, Zn^{2+}, Cd^{2+}, Ni^{2+}, or Ag^{+}, where each can bind to the original MXCXXC sequence (See Chapter 4).[44]

The periplasm of a cell, unlike the cytosol, is an oxidizing environment with many different proteins to ensure proper cellular function. Understandably, this type of

environment is favorable for reduced cysteines, particularly those that are close enough to a form disulfide bond. Augmenting this oxidative environment is achieved through the disulfide bond protein A (DsbA), which is an oxidoreductase that catalyzes disulfide bond formation.[45–47] It is unusual that MerP, unlike most proteins in the periplasm, has two cysteine in close proximity that do not form disulfide bonds even in this disulfide-favoring environment. It has been proposed that this is due to the buried thiolate, Cys_C, which is not readily available for disulfide bond formation with Cys_N. I propose that this is a key mechanism associated with the function of MerP in protecting the cell from Hg^{2+} and methylmercury, in which these reduced cysteines are available for binding these metal ions and organometallic compound.

I hypothesize that the transfer of Hg^{2+} to MerT is not the primary function of MerP, but an ancillary function, with its primary function to bind toxic metals and organomercurial compounds, and serve as a metal-sink. This chapter focuses on the thermodynamics and structural changes that occur upon methylmercury binding to MerP, and aims to inform the function of MerP within the cell. The mechanism of methylmercury binding is bolstered by known inorganic mercury binding studies and evaluated in conjunction with structural characterization. Although methylmercury is the most environmentally-relevant organomercurial compound, synthetic organomercurials may also be found in the environment, including merbromin and thimerosal studied here.

5.2. Materials and Methods

5.2.1. Chemicals

Buffers of the highest purity were purchased and utilized without further purification or modifications. These include: HEPES (4-(2-hydroxyethyl)-1-piperazineethanesulfonic acid) PIPES (1,4-piperazinediethanesulfonic acid), BisTris (2-[bis(2-hydroxyethyl)amino]-2-(hydroxymethyl)propane-1,3-diol), and TAPSO (3-[[1,3-dihydroxy-2-(hydroxymethyl)propan-2-yl]amino]-2-hydroxypropane-1-sulfonic acid), all of which were purchased from VWR or Sigma. Sodium chloride (NaCl), sodium bromide (NaBr), and sodium iodide (NaI) were all purchased from Sigma and utilized as received. Methylmercury chloride (MeHgCl) was purchased from BeanTown Chemical, dissolved

in water at 1000 ppm, and used as received. Thimerosal was purchased at >97% purity from Spectrum Chemical Manufacturing Group. Merbromin (Mercurochrome) was purchased from Thermo Scientific Chemicals. D,L-cysteine was purchased from Sigma.

Buffer solutions were prepared in acid-washed Pyrex bottles using Milli-Q deionized water (>18MΩ) and subsequently treated with Chelex®, purchased from Sigma, which removed any trace metals. Protein concentrations were confirmed by an assay with Ellmans reagent (5,5-dithio-bis-(2nitrobenzoic acid); DTNB) assay, purchased from Sigma. Finally, buffer exchange was achieved using GE Healthcare or Cytiva Life Sciences PD-10 columns.

5.2.2. Protein Preparation

MerP was generously provided by Professor James Omichinski from the Universite de Montreal. These samples were flash frozen and shipped in solutions containing ~7 mg/mL in 20 mM phosphate buffer, 10 mM NaCl, 5 mM DTT, at pH 7.5. Upon arrival, these samples were stored in a –80 ºC freezer for future use. Individual samples were thawed and divided into ~60-80 μM aliquots in Eppendorf tubes, with additional DTT, and frozen as the working sample. All protein handling was completed under anaerobic conditions in a Coy Laboratory glovebox that maintains anaerobicity through constant purging of nitrogen. A platinum catalyst regenerated daily by the addition of 5% hydrogen removed any residual oxygen, such that the oxygen concentration remained <5 ppm. Prior to each set of ITC experiments, an aliquot of the working protein sample was buffer exchanged into the desired ITC buffer that was previously demetallated and deoxygenated within the anaerobic glovebox. Using a PD-10 column, the protein was exchanged into the desired buffer, and the concentration was measured either directly ($\varepsilon = 2980$ at 280 nm) or by a DTNB assay. The resulting protein sample was then diluted to the concentration required for each ITC experiment.

5.2.3. Methylmercury Safe Handling Procedure for Solution Preparation

Safe handling of methylmercury is of utmost importance, given the danger it poses for both those who handle it and those who may come in contact with sample residue. Every possible precaution was utilized.

Methylmercury chloride was received in water at 1000 ppm and was subsequently stored at 4 ºC within a dark glass bottle. This bottle was wrapped in the spill-absorbing fabric that it was sent in and stored within a secondary container. During use, safety goggles were utilized the entire time. Solutions were prepared aerobically in the hood with constant airflow to prevent contamination. Two pairs of Kimberly Clarke purple nitrile gloves were used while preparing samples, providing protection through 12 mm total glove thickness at the hand. Two sets of gloves were utilizing for skin protect near the wrist area. Solutions were prepared in 11 mL screwcap glass tubes, and transported to the anaerobic glovebox. Movement of methylmercury solutions were announced to lab members in the vicinity to prevent spilling. Within the glovebox, methylmercury was diluted to the appropriate concentration for the ITC experiments for the day. All experimental waste was collected at the end of each day and all solutions and containers that came in contact with methylmercury were handled with two pairs of gloves. This safety protocol was approved by Environmental Health and Safety (EHS) at Dartmouth College, initially before experimentation, and again later to ensure these safety protocols were maintained and updated accordingly. To ensure that methylmercury was bound to the appropriate anion, each buffer was composed of 50 mM buffer, 50 mM salt, pH 7.4. This large excess of Cl^-, Br^-, or I^- ensured a majority of methylmercury salt complex, although Cl^- is present in all solutions from the original MeHgCl sample.

5.2.4. Isothermal Titration Calorimetry Experiments

All ITC experiments were completed under anaerobic conditions in a custom-made plexiglass glovebox. This glovebox is constantly purged with nitrogen to maintain anaerobicity. ITC experiments were completed using the Malvern Panalytical Microcal VP-ITC, which has an active cell volume of 1.4197 mL and a syringe volume of 274 µL. Each experiment was done using 15 µM MerP and a ligand concentration of 300 µM. Throughout the experiment, the syringe was constantly stirred at 317 RPM and each injection had a total volume of 8 µL, all at 25.0 ± 0.2 ºC. Isotherms are shown in two panels. The top panel shows a power vs. time output, where upward peaks indicate an endothermic binding event and downward peaks indicate an exothermic binding event. The bottom panel shows the concentration-normalized integrations of each peak in the top panel. This

enthalpy is plotted against the molar ratio of the syringe (ligand) to the cell (protein). Fitting of the integrated data was completed using VP-ITC Origin 7.0 data analysis software. The isotherms were fit using a one or two-site binding model. A minimum of 3 independent experiments were completed in each of the four buffers. Experimental data is averaged and the error is the standard deviation among the collected data.

5.2.5. Molecular Dynamics Experiments

All MD simulations were run utilized the Amber 16 software suite using a Nvidia GTX 1080TI GPU and Intel i7-7800X Skylake-X 6-core CPU.[48] The solution structure of MerP (PDB:1AFI) was used as the starting point for all MD experiments. Structures of $MeHg^+$ bound to MerP are not known, but were made in Chimera using $MeHg^+$ obtained from PDB: 4CT3.[49] This was saved as an independent PDB file and subsequently added to the apo-MerP PDB file. Finally, the $MeHg^+$ was moved to within ~2 Å of the solvent-exposed cysteine, Cys14 for analysis of the MeHg-MerP complex.

The protein was described by the Amber ff19SB forcefield, the water by TIP3P, and parameterization of the bound metal-ion was done through the Metal Center Parameter Builder (MCPB) software in which the bonded parameters were characterized by the QM software, Gamess.[50–52] Metal binding geometry optimization of a Hessian matrix of a small and large model was done through *ab initio* DFT calculations at the M06/MIDI level. Finally, the ParmEd program in Amber16 was used to check the parameters of the metal center, including equilibrium bond lengths, bond and angle force constants, dihedral potential barriers, RESP charge of the metal, and non-bonded parameters.

All water molecules and hydrogen atoms were initially removed in Chimera. Protein protonation was determined using *tleap* software in Amber20 or with H++ web server[53] with modifications to cysteine residues when their protonation state was based upon experimental pK_a values, and confirmed visually by Chimera.[46,49] All structures were solvated with 5169-7438 water molecules in a rectangular box that was 15 Å away from the edge of the protein and Cl^- or Na^+ ions were added as counterions for neutralization using *tleap*.

Conformational sampling of MeHg-bound MerP was done to observe structural changes upon ligand binding. Initial minimization of 1,000 steps was used to eliminate

poor contacts, followed by a 2 ns constant-volume equilibration, in which the temperature is raised from 0 K to 300 K. A 2 ns constant-pressure equilibration at 300 K was then utilized, in which all heavy, non-water atoms were restrained with a force constant of 2.0 kcal/molÅ^2, preparing the system for the final equilibration. Finally, a 200 ns equilibration at constant pressure and 300 K was run without any restraints. Hydrogen bonds throughout the minimization and equilibration were maintained at equilibrium by the SHAKE algorithm[54], allowing for a 2 ps timestep to be used. Solvation temperature was maintained by Langevin dynamics with a collision frequency of 2 ps^{-1}. Pressure was controlled by the Barensted barostat with a relaxation time of 1 ps during equilibration and 2 ps during the production equilibration. Periodic boundary conditions were used with a cutoff distance for the Lennard-Jones parameters of 8.0 Å. Snapshots of the MD experiments were analyzed by *cpptraj*, Visual Molecular Dynamics (VMD), Origin 7.0 data analysis software, and XMGRACE.[55–57]

Data analysis was completed using the *cpptraj* data analysis program included in the Amber20 software and Visual Molecular Dynamics (VMD).[55,57] Calculating the Root Mean Square Deviation (RMSD; **Equation 5.2.4.1**) of the structure, on a per-atom basis, as compared to the initial solution structure, provides both the ability to evaluate the experimental timescale as well as insight into the stability of the protein. The mass-weighted RMSD, when compared to a reference structure, is calculated by:

$$RMSD_{(t1,t2)} = \sqrt{\frac{\sum_{i=0}^{N} m_i \times \left[\left(r_{i,t1} - r_{i,t2}\right)\right]^2}{N}} \qquad \textbf{Equation 5.2.4.1}$$

where N is the total number of atoms, m_i is the mass of atom i, $r_{i,t}$ is the position of atom i at time t, in which the change in coordination is with respect to a reference structure. This RMSD is calculated for each snapshot or frame that is taken ever 100 ps. Stabilization of the RMSD suggests that an energy-well has been located and the energetically favorable structure has been found.

Taking this further, the compactness of a structure is, quantified by the Radius of Gyration (Rg), which can be used in conjunction with the RMSD to understand gross

conformational changes of the protein. The Rg calculation is similar to the RMSD calculation,

$$Rg_t = \sqrt{\frac{\sum_{i=1}^{N} m_i \times (r_i - r_{CM})^2}{\sum_{i=1}^{N} m_i}} \qquad \textbf{Equation 5.2.4.2}$$

where Rg_t is the radius of gyration calculated at a given time point, t, N is the number of atoms in the system, m_i is the mass of atom i, and r_i is the position of atom i at a given time, and r_{CM} is the center of mass of the calculated system. Like the RMSD, the Rg is calculated for each frame of the molecular dynamics experiment.

Quantification of the solvent-accessible surface area for specific amino acids utilizes the Connolly surface area to evaluate the solvation of selected amino acids.[58] In this analysis, each solvent molecule is depicted as a sphere. This sphere is then, effectively, rolled over the surface of the selected protein structure to form a smooth outer surface. The entirety of this surface forms the initial solvent sphere, and thus all pieces can be quantified. The analytical expression of this surface is defined by the Van der Waals radii, atomic coordinates, and probe radius, which establish the area of a particular amino acid (or atom, protein, protein-protein interface, etc.) that is solvated.[59]

5.3. Results

Measurements to obtain the thermodynamics of the formation of the MeHg-MerP complex are complicated by the risk of disulfide bond formation in MerP. Since the metal binding site consists of two nearby cysteine residues, appropriate measures were taken to prevent their oxidation to cysteine. All samples were prepared within an anaerobic glovebox and the ITC experiments were run within an anaerobic glovebox to maintain reduced cysteines. Confirmation of success is obtained through the titration of Hg^{2+} into MerP, which showed the expected 1:1 complex formation (See Chapter 4). With confidence in the techniques, the binding of $MeHg^{+}$ was undertaken.

5.3.1. Anion Competition for Methylmercury in the Binding to MerP

The binding of $MeHg^+$ to MerP was initially completed in 50 mM buffer, 50 mM NaCl, pH 7.4, which is the standard buffer composition that is used in metal-binding experiments. This binding shows two distinct inflections for $MeHg^+$ binding to MerP (*vide infra*). However, the apparent binding constants for both binding events under these conditions are far above the range that is accessible by ITC. The binding constants for a two-site fit were $K_{a1} = \sim 10^9$ and $K_{a2} = \sim 10^7$, giving c = ~30,000. As previously discussed, a one-site fitting model is only accurate in the range $5 < c < 1000$. Unfortunately, the thermodynamics associated with most competing ligands for $MeHg^+$ are not know, so the method of using a stronger metal chelator was not feasible. However, since these conditions utilized a high concentration of NaCl, the solution should contain the MeHgCl complex. So, if the Cl^- was replaced with another anion that binds more tightly to $MeHg^+$, this might shift the competing equilibrium such that the apparent binding affinities could be determined by ITC. Considering hard-soft acid-base theory, mercury is soft, yet Cl^- is not. Thus the replacement of Cl^- with Br^- or I^-, both of which are softer than Cl^-, may provide sufficient competition as the MeHgBr and MeHgI would be more stable. Therefore, three sets of experiments were completed: (1) MeHgCl into MerP, (2) MeHgBr into MerP, and (3) MeHgI into MerP, each in 4 separate buffers. Since the goal of these experiments was to quantify the MeHg-MerP interaction, determination of this binding association under multiple conditions allowed the buffer-independent binding thermodynamics to be obtained.

5.3.2. Thermodynamics of the Methylmercury-Buffer Complex Formation

As described in Chapter 2, to establish the buffer-independent binding thermodynamics of a metal ion binding to a protein requires in-depth knowledge of the thermodynamics of all interactions that occur in solution. These competing equilibria are usually known and a typical experiment will involve titration of the desired metal ion into the protein. In the case of $MeHg^+$, however, the thermodynamics of several of these competing equilibria are unknown. This is particularly true for the MeHg-buffer and $MeHg^+$-anion thermodynamics. The competing equilibria are shown in **Scheme 5.3.1.1,** which assumes that the MerP cysteines are deprotonated upon $MeHg^+$ binding. Of these binding events, the only enthalpy that was known *a priori* was the buffer protonation

enthalpy. So, the enthalpy of each of these interactions that were not found within the literature had to be determined. It is noted that the $MeHg^+$-halide thermodynamics have been quantified, but here the anion and buffer are present in equal concentrations; thus MeHg-buffer thermodynamics must still be characterized.

Reported thermodynamics for the interaction of $MeHg^+$ with other ligands is sparse. Many equilibrium constants have been reported, but not the enthalpy of the interaction, which is required for the MeHg-MerP analysis. Previous studies have, however, determined the enthalpy and the equilibrium constant for $MeHg^+$ binding to cysteine, where $K_{MeHg\text{-}Cys} = 1.51\times10^{15}$ and $\Delta H_{MeHg\text{-}Cys} = -20.6$ kcal/mol, which are the thermodynamics of the interaction between $MeHg^+$ and the thiol of the cysteine.[60,61] Therefore, control experiments in the different buffers\ (PIPES, HEPES, TAPSO, and TRIS) with excess salt (NaCl, NaBr, and NaI) were necessary. Because the thermodynamics of cysteine deprotonation, buffer protonation, and the $MeHg^+$-cysteine association are known, the thermodynamic contribution from the MeHg-buffer and/or anion interaction could be solved.

The titrations of $MeHg^+$ into cysteine under anaerobic conditions show sharp, well-defined peaks, which could be fit with a one-site or two-site fitting model for each salt (NaCl: **Figure 5.3.2.1**, NaBr: **Figure 5.3.2.2**, and NaI: **Figure 5.3.2.3**). The binding of $MeHg^+$ to cysteine in TAPSO seems to be unusual, in that this binding requires a two-site fitting model, where the first, strong binding event is $MeHg^+$ binding to cysteine and the second event is attributed to aberrant buffer interactions.

From the apparent thermodynamics obtained by ITC, and taking the competing equilibria

Scheme 5.3.2.1. Generalized relevant competing equilibria for the binding of $MeHg^+$ to MerP in 50 mM buffer, 50 mM salt, pH 7.4 under anaerobic conditions. ΔH_{MB} is the enthalpy of the MeHg-buffer interaction, ΔH_{MA} is the enthalpy of the $MeHg^+$-anion interaction, ΔH_{PH} is the enthalpy of MerP deprotonation, ΔH_{BH} is the enthalpy of buffer-protonation, and ΔH_{MP} is the enthalpy of the $MeHg^+$–MerP interaction. The sum of these enthalpies is equal to the apparent enthalpy found directly by ITC, as defined by **Equation 5.3.2.1**.

$MeHg^+$–Buffer	⇄	$MeHg^+$ + Buffer	$-\Delta H_{MB}$
$MeHg^+$–Anion	⇄	$MeHg^+$ + $Anion^-$	$-\Delta H_{MA}$
MerP–H_x	⇄	MerP + H_x^+	$-(n_{Hx}\Delta H_{PH})$
H^+_x + Buffer	⇄	Buffer–H_x	$(n_{H+}\Delta H_{BH})$
$MeHg^+$ + MerP	⇄	$MeHg^+$–MerP	ΔH_{MP}

$$\Delta H_{ITC} = -\Delta H_{MB} - \Delta H_{MA} - (n_{H+}\Delta HB_H) + (n_{H+}\Delta H_{PH}) + \Delta H_{MP} \qquad \textbf{Equation. 5.3.2.1}$$

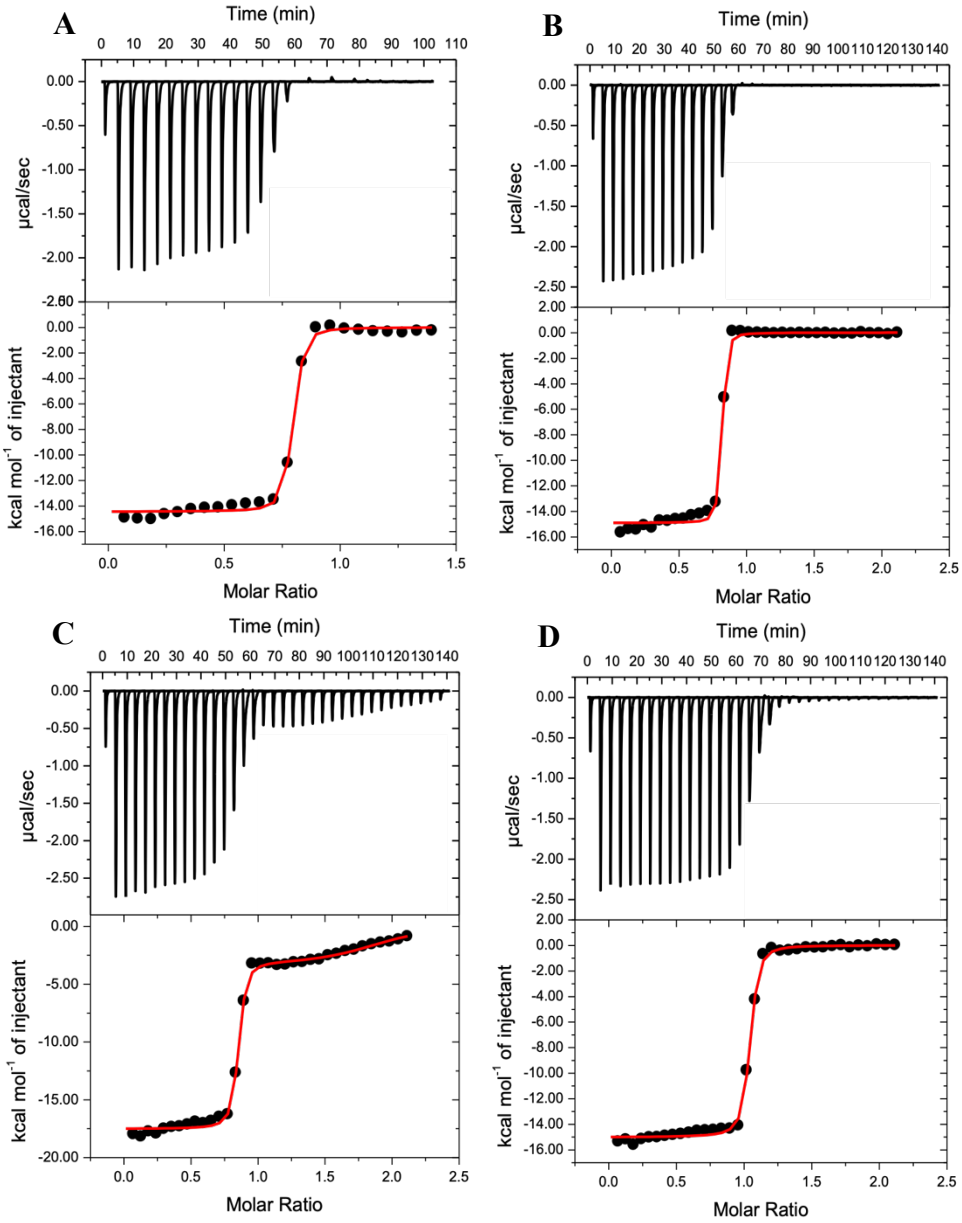

Figure 5.3.2.1. *Representative isotherms for the titration of 50 µM $MeHg^+$ into 500 µM cysteine in 50 mM buffer, 50 mM NaCl, pH 7.4. Experiments were repeated at least in triplicate. (A) PIPES, n = 0.770 ± 0.003, ΔH = -14.4 ± 0.1 kcal/mol, and K_{ITC} = 4 (± 1)×10^7; (B) HEPES, n = 0.791 ± 0.002, ΔH = -14.91 ± 0.09 kcal/mol, and K_{ITC} = 8 (± 2)×10^7; (C) TAPSO (site 1), n = 0.826 ± 0.003, ΔH = -17.50 ± 0.10 kcal/mol, and K_{ITC} = 6 (± 3)×10^8; (site 2), n = 1.06 ± 0.05, ΔH = -3.3 ± 0.3 kcal/mol, and K_{ITC} = 4 (± 3)×10^5; (D) TRIS, n = 1.020 ± 0.002, ΔH = -15.00 ± 0.07 kcal/mol, and K_{ITC} = 2 (± 0.3)×10^7. Only TAPSO required fitting via the two-site binding model, in which the first binding event is the primary interaction between $MeHg^+$ and cysteine.*

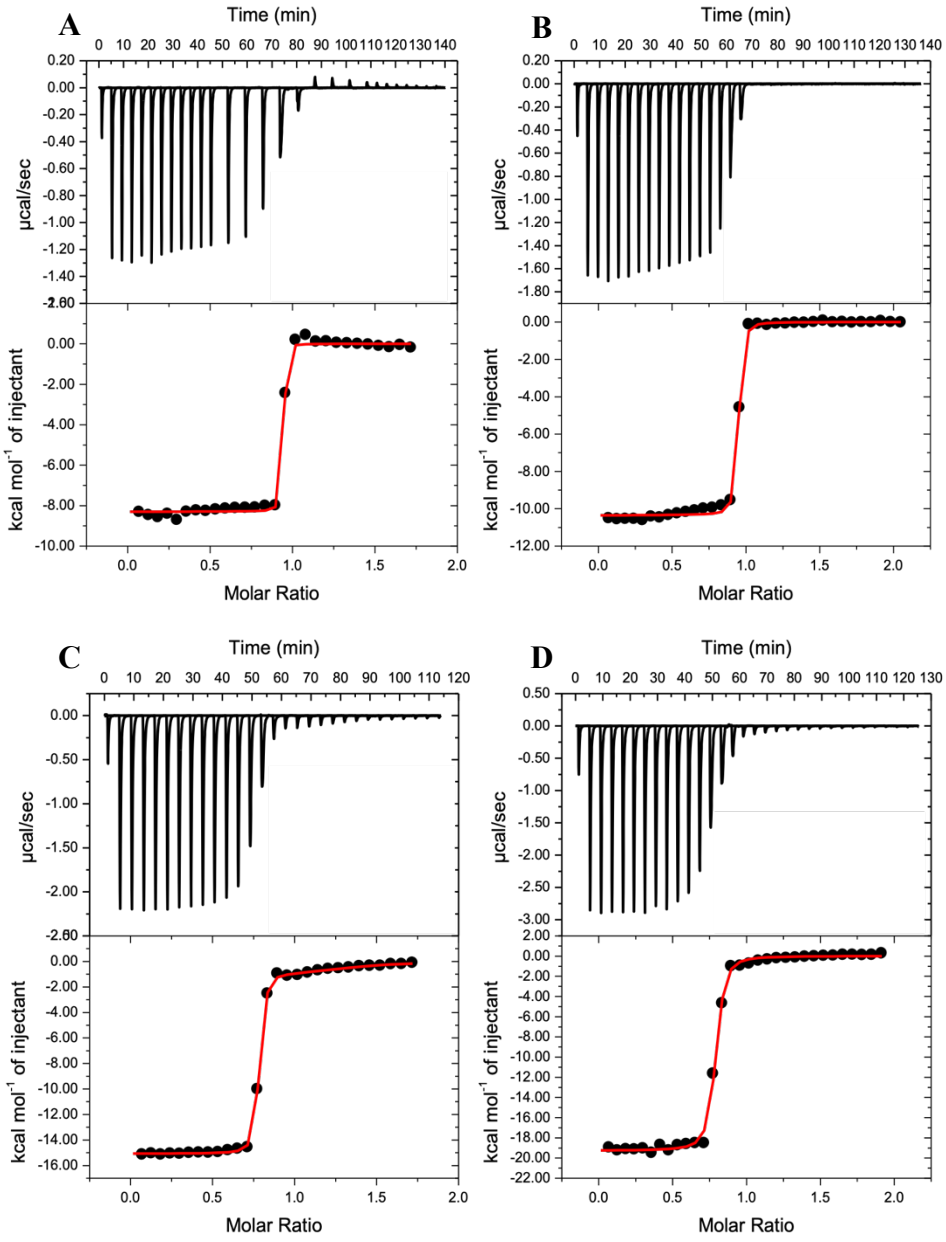

Figure 5.3.2.2. *Representative isotherms for the titration of 50 µM $MeHg^+$ into 500 µM cysteine in 50 mM buffer, 50 mM NaBr, pH 7.4. Experiments were repeated at least in triplicate. (A) PIPES, n = 0.913 ± 0.002, ΔH = -8.30 ± 0.05 kcal/mol, and K_{ITC} = 5 (± 5)×10^8; (B) HEPES, n = 0.922 ± 0.001, ΔH = -10.35 ± 0.04 kcal/mol, and K_{ITC} = 1 (± 0.2)×10^8; (C) TAPSO (site 1), n = 0.757 ± 0.001, ΔH = -15.08 ± 0.03 kcal/mol, and K_{ITC} = 5 (± 3)×10^8; (site 2), n = 0.57 ± 0.07, ΔH = -1.2 ± 0.2 kcal/mol, and K_{ITC} = 3 (± 2)×10^5; (D) TRIS, n = 0.764 ± 0.002, ΔH = -19.3 ± 0.1 kcal/mol, and K_{ITC} = 2 (± 0.2)×10^7. Only TAPSO required fitting via the two-site binding model, in which the first binding event is the primary interaction between $MeHg^+$ and cysteine, consistent with $MeHg^+$ binding to cysteine in excess NaBr.*

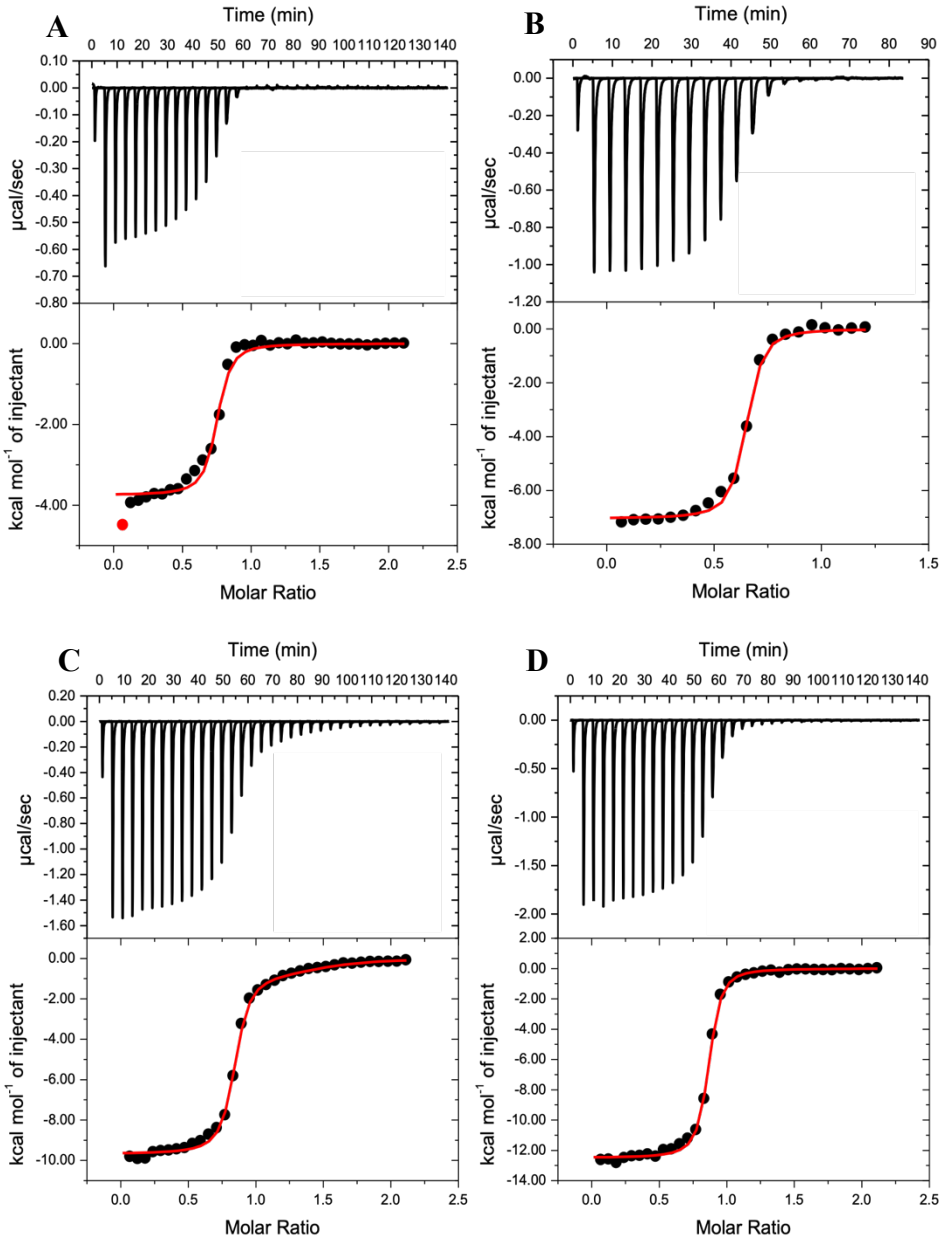

Figure 5.3.2.3. *Representative isotherms for the titration of 50 µM methylmercury into 500 µM cysteine in 50 mM buffer, 50 mM NaI, pH 7.4. Experiments were repeated at least in triplicate. (A) PIPES, n = 0.728 ± 0.005, ΔH = -3.75 ± 0.05 kcal/mol, and K_{ITC} = 6 (± 1)×10^6; (B) HEPES, n = 0.625 ± 0.003, ΔH = -7.04 ± 0.06 kcal/mol, and K_{ITC} = 9 (± 1)×10^6; (C) TAPSO, n = 0.815 ± 0.005, ΔH = -9.68 ± 0.06 kcal/mol, and K_{ITC} = 5 (± 4)×10^7; (D) TRIS, n = 0.841 ± 0.002, ΔH = -12.49 ± 0.06 kcal/mol, and K_{ITC} = 9 (± 0.7)×10^6. Only TAPSO required fitting via the two-site binding model, in which the first binding event is the primary interaction between MeHg$^+$ and cysteine, consistent with MeHg$^+$ binding to cysteine in excess NaI.*

into account, MeHg-buffer thermodynamics at pH 7.4 can be determined. However, decoupling of the enthalpy associated with the MeHg-buffer and MeHg-anion interaction is not possible under these experimental conditions. Thus, these measurements determine a coupled enthalpy, which is appropriate for the MeHg-MerP binding experiments (*vide infra*). This coupled enthalpy is obtained by:

$$\Delta H_{MB} = \Delta H_{MeHg-buffer} + \Delta H_{MeHg-anion} = -\Delta H_{ITC} - 0.85\Delta H_{Cys-H} + 0.85\Delta H_{buffer-H} + \Delta H_{MeHg-Cys} \qquad \textbf{Equation 5.3.2.1}$$

where cysteine would be deprotonated by 0.85 protons upon binding $MeHg^+$ at pH 7.4 with the enthalpy of both cysteine deprotonation and buffer protonation included in the analysis. Similarly, the equilibrium constants associated with the MeHg-buffer interaction, the coupled MeHg-buffer and $MeHg^+$-anion interaction is quantified by:

$$K_{MeHg-Buffer} = \left(\frac{K_{MeHg-Cys}}{K_{ITC}\alpha_{Cys-proton}} - 1\right) \times \frac{1}{[Buffer]_{basic}} \qquad \textbf{Equation 5.3.2.2}$$

where $\alpha_{Cys\text{-}proton}$ is the equilibrium constant associated with deprotonation of cysteine thiol, as this is the group that binds $MeHg^+$, and $[Buffer]_{basic}$ is the concentration of the basic form of the buffer. Summary of the averaged experimental thermodynamics and the condition-independent binding thermodynamics associated with the coupled MeHg-buffer and $MeHg^+$-anion interaction is found in **Table 5.3.2.1**.

5.3.3. Condition-Independent Binding Thermodynamics of Methylmercury to MerP

With the thermodynamics for the coupled MeHg-buffer and $MeHg^+$-anion interaction quantified, the buffer-independent MeHg-MerP binding at pH 7.4 can be determined. Although the buffer and anions vary, this does not modulate the general $MeHg^+$ binding trends. When $MeHg^+$ is titrated into MerP, two binding events are observed. The first, which is the stronger of the two, is more exothermic, while the second, weaker binding event is less exothermic. Peaks associated with each injection are sharp, well-defined, and return to equilibrium rapidly. These two binding events were fit using a two-site binding model to determine the apparent thermodynamics for each binding event, assuming they are independent of each other. Each of these experiments were repeated

Table 5.3.2.1. *Average experimental binding thermodynamics for the titration of 500 μM $MeHg^+$ into 50 μM cysteine in 50 mM buffer, 50 mM salt, pH 7.4. Condition-independent binding enthalpies and equilibrium constants are for the coupled MeHg-buffer and MeHg-salt interaction, which were quantified using the MeHg-Cysteine binding thermodynamics.*

Buffer	Salt	n_{ITC}	K_{ITC}	ΔH_{ITC} (kcal/mol)	$K_{MeHg\text{-}buffer}$	$\Delta H_{MeHg\text{-}buffer}$ (Kcal/mol)
PIPES	NaCl	0.76 ± 0.01	7 (± 3)×10^7	-14.3 ± 0.2	8 (± 2)×10^7	-1.4 ± 0.2
	NaBr	0.85 ± 0.08	3 (± 2)×10^8	-8.3 ± 0.2	2 (± 0.7) X10^7	-7.5 ± 0.2
	NaI	0.74 ± 0.02	5.0 (± 0.8)×10^6	-3.9 ± 0.1	1.1 (± 0.2)×10^9	-11.9 ± 0.1
HEPES	NaCl	0.74 ± 0.05	3 (± 4)×10^8	-15.0 ± 0.2	2 (± 1)×10^7	-2.8 ± 0.2
	NaBr	0.89 ± 0.08	2.0 (± 0.7)×10^8	-10.3 ± 0.3	5 (± 1)×10^7	-7.4 ± 0.3
	NaI	0.64 ± 0.02	8 (± 1) x 10^6	-7.2 ± 0.1	1 (± 0.1)×10^9	-10.6 ± 0.1
TAPSO	NaCl	0.83 ± 0.02	9 (± 5)×10^8	-17.3 ± 0.2	1 (± 0.4)×10^7	-4.2 ± 0.2
	NaBr	0.80 ± 0.03	2 (± 2)×10^9	-15.5 ± 0.5	6 (± 3)×10^6	-5.8 ± 0.5
	NaI	0.77 ± 0.04	4 (± 1)×10^7	-9.8 ± 0.2	2.9 (± 0.6)×10^8	-11.5 ± 0.2
TRIS	NaCl	1.01 ± 0.02	5 (± 4)×10^7	-14.8 ± 0.2	6 (± 3)×10^8	-5.4 ± 0.2
	NaBr	0.75 ± 0.01	5 (± 2)×10^7	-19.17 ± 0.09	6 (± 2)×10^8	-3.9 ± 0.1
	NaI	0.80 ± 0.08	1.0 (± 0.2)×10^7	-12.54 ± 0.06	2.6 (± 0.4)×10^9	-10.5 ± 0.1

in triplicate for a complete series of four buffers, each in three different anion salts, which are the competing ligand for $MeHg^+$ (NaCl: **Figure 5.3.3.1**, NaBr: **Figure 5.3.3.2**, and NaI: **Figure 5.3.3.3**). A summary of the apparent thermodynamics is found in **Table 5.3.3.1**. It is important to note that the binding affinity for the first event, when fit with the two-site binding model, is above the range that is accessible by ITC, particularly in excess NaCl. However, this range, and qualitative evaluation by the c-window, are based on the one-site binding model, not the two-site binding models. It was observed qualitatively that this range is extend to ~10^9 with a two-site binding model, in which a step-function for the first event is not observed until ~10^{10}. Nonetheless, to ensure confidence in these experiments in excess NaCl, I expanded this series to include NaBr and NaI, which bind $MeHg^+$ more favorably. These salts shifted the binding affinity for this first site to ~10^6–10^7, well within the c-window.

With the apparent thermodynamics for $MeHg^+$ binding to MerP quantified, the thermodynamics of the competing equilibria that are occurring in solution can be accounted for. This *post-hoc* analysis results in the quantification of the buffer-independent binding thermodynamics for two $MeHg^+$ binding to MerP at pH 7.4 in solution.

In order to determine the buffer protonation contribution to the $MeHg^+$ binding enthalpy, the number of protons for each binding event must be quantified. By plotting the buffer protonation enthalpy for PIPES, HEPES, TAPSO, and TRIS vs. the apparent enthalpy (MeHg-buffer enthalpy and $MeHg^+$-anion enthalpy) the number of protons that are released upon $MeHg^+$ binding to MerP can be quantified. The slope of this plot for NaI indicates that ~1 proton is released when $MeHg^+$ binds in the first binding event, and ~0 protons are displaced when the second $MeHg^+$ binds (NaCl: **Figure 5.3.3.4**, NaBr: **Figure 5.3.3.5**, and NaI: **Figure 5.3.3.6**). In light of the pK_a of the two MerP cysteines (pK_a of Cys_N = 9.1 and Cys_C = 5.5), this proton displacement indicates that the first $MeHg^+$ binds to the solvent exposed Cys_N, displacing the ~1 proton that is bound. The second, weaker binding event, has no proton displacement and correlates with the binding of $MeHg^+$ to Cys_C. Unlike in NaI, $MeHg^+$ binding to MerP in NaBr and NaCl show slight deviations in

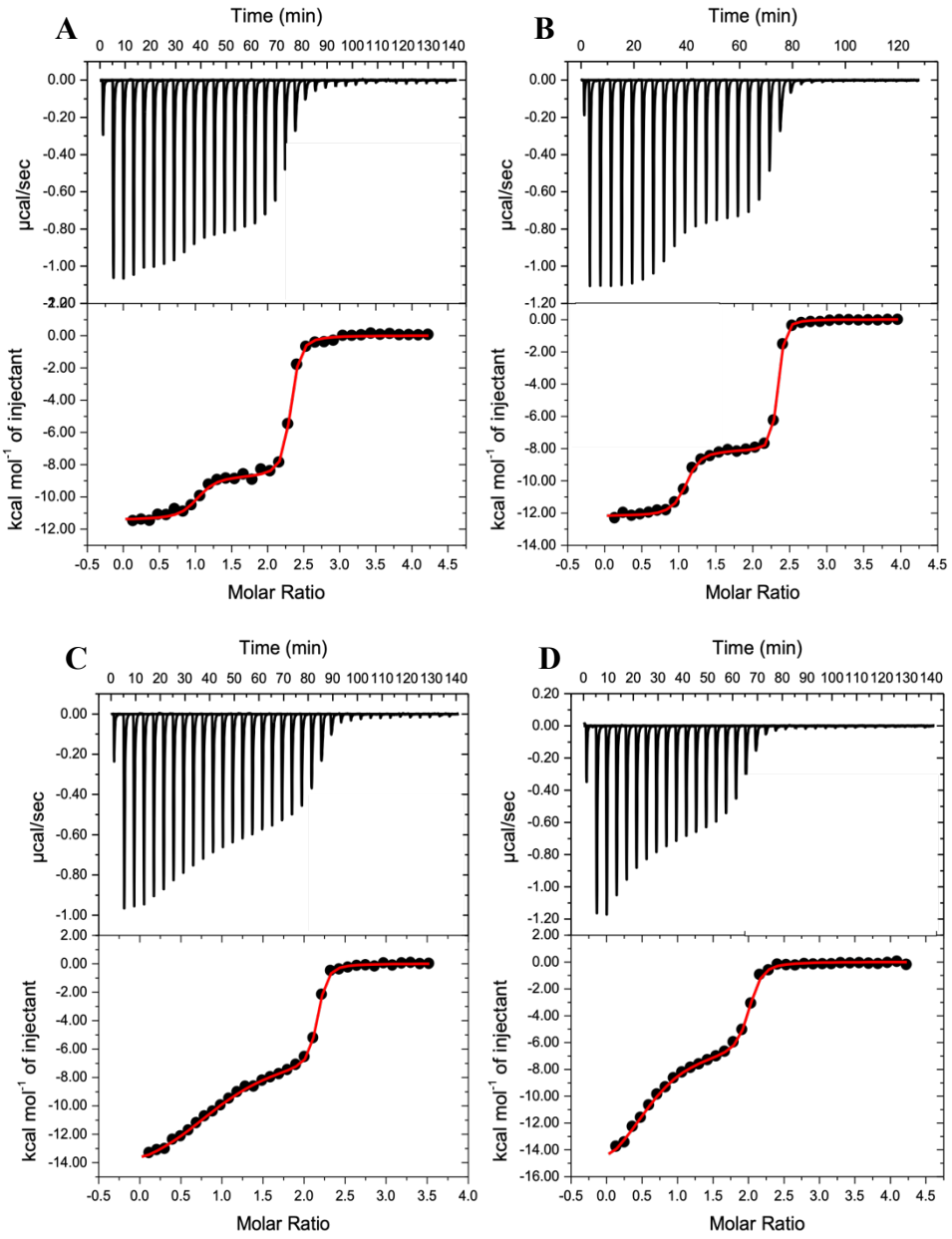

Figure 5.3.3.1. *Representative isotherms associated with the titration of 300 µM $MeHg^+$ into 15 µM MerP under anaerobic conditions in 50 mM buffer, 50 mM NaCl, pH 7.4 These titrations were fit with a two-site binding model. (A) PIPES, Site 1, n = 0.98 ± 0.02, ΔH = -11.42 ± 0.09 kcal/mol, K_{ITC} = 1.9 (± 0.7)×10^9; site 2: n = 1.29 ± 0.02, ΔH = -8.74 ± 0.09 kcal/mol, K_{ITC} = 2.6 (± 0.3)×10^7; (B) HEPES, Site 1, n = 1.05 ± 0.01, ΔH = -12.19 ± 0.04 kcal/mol, K_{ITC} = 9.6 (± 1.7)×10^9; site 2: n = 1.24 ± 0.008, ΔH = -8.13 ± 0.05 kcal/mol, K_{ITC} = 6.7 (± 0.7)×10^7; (C) TAPSO, Site 1, n = 0.82 ± 0.02, ΔH = -15.5 ± 0.5 kcal/mol, K_{ITC} = 2.3 (± 0.3)×10^8; site 2: n = 1.30 ± 0.02, ΔH = -6.4 ± 0.3 kcal/mol, K_{ITC} = 3.7 (± 0.5)×10^7; (D) TRIS, Site 1, n = 0.54 ± 0.03, ΔH = -17.3 ± 0.1 kcal/mol, K_{ITC} = 1.0 (± 0.1)×10^8; site 2: n = 1.42 ± 0.03, ΔH = -6.3 ± 0.3 kcal/mol, K_{ITC} = 1.4 (± 0.2)×10^7.*

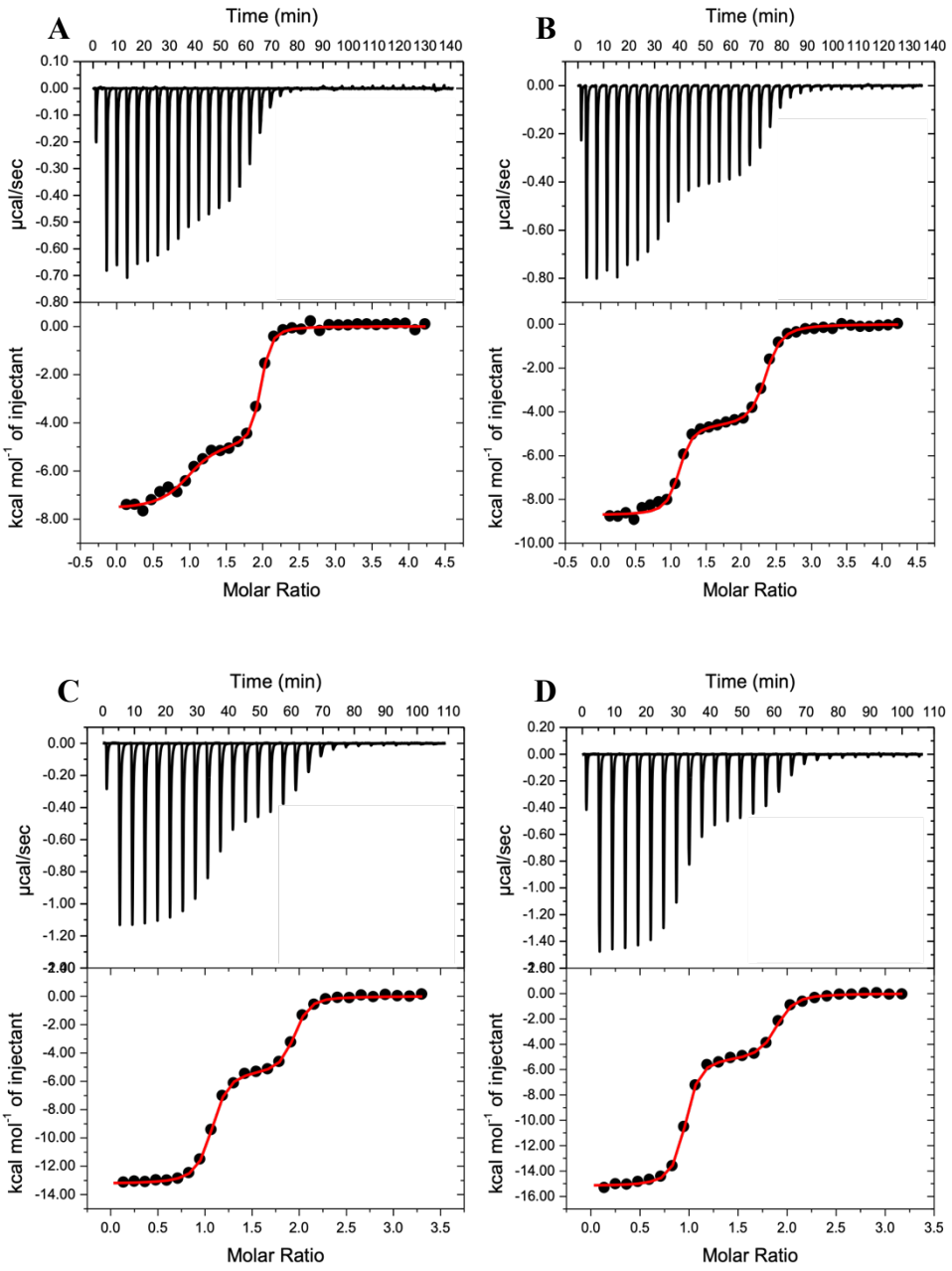

Figure 5.3.3.2. *Representative isotherms associated with the titration of 300 µM $MeHg^+$into 15 µM MerP under anaerobic conditions in 50 mM buffer, 50 mM NaBr, pH 7.4 These titrations were fit with a two-site binding model. (A) PIPES, Site 1, n = 0.93 ± 0.04, ΔH = -7.6 ± 0.1 kcal/mol, K_{ITC} = 4 (± 1)×10^8; site 2: n = 0.99 ± 0.03, ΔH = -4.8 ± 0.2 kcal/mol, K_{ITC} = 1.7 (± 0.4)×10^7; (B) HEPES, Site 1, n = 1.06 ± 0.01, ΔH = -8.72 ± 0.06 kcal/mol, K_{ITC} = 1.1 (± 0.3)×10^9; site 2: n = 1.24 ± 0.01, ΔH = -4.64 ± 0.08 kcal/mol, K_{ITC} = 7 (± 1)×10^6; (C) TAPSO, Site 1, n = 1.02 ± 0.01, ΔH = -13.32 ± 0.03 kcal/mol, K_{ITC} = 1.5 (± 0.1)×10^9; site 2: n = 0.880 ± 0.004, ΔH = -5.34 ± 0.06 kcal/mol, K_{ITC} = 1.1 (± 0.1)×10^7; (D) TRIS, Site 1, n = 0.906 ± 0.003, ΔH = -15.19 ± 0.01 kcal/mol, K_{ITC} = 1.5 (± 0.3)×10^9; site 2: n = 0.935 ± 0.007, ΔH = -5.17 ± 0.09 kcal/mol, K_{ITC} = 8 (± 1)×10^6.*

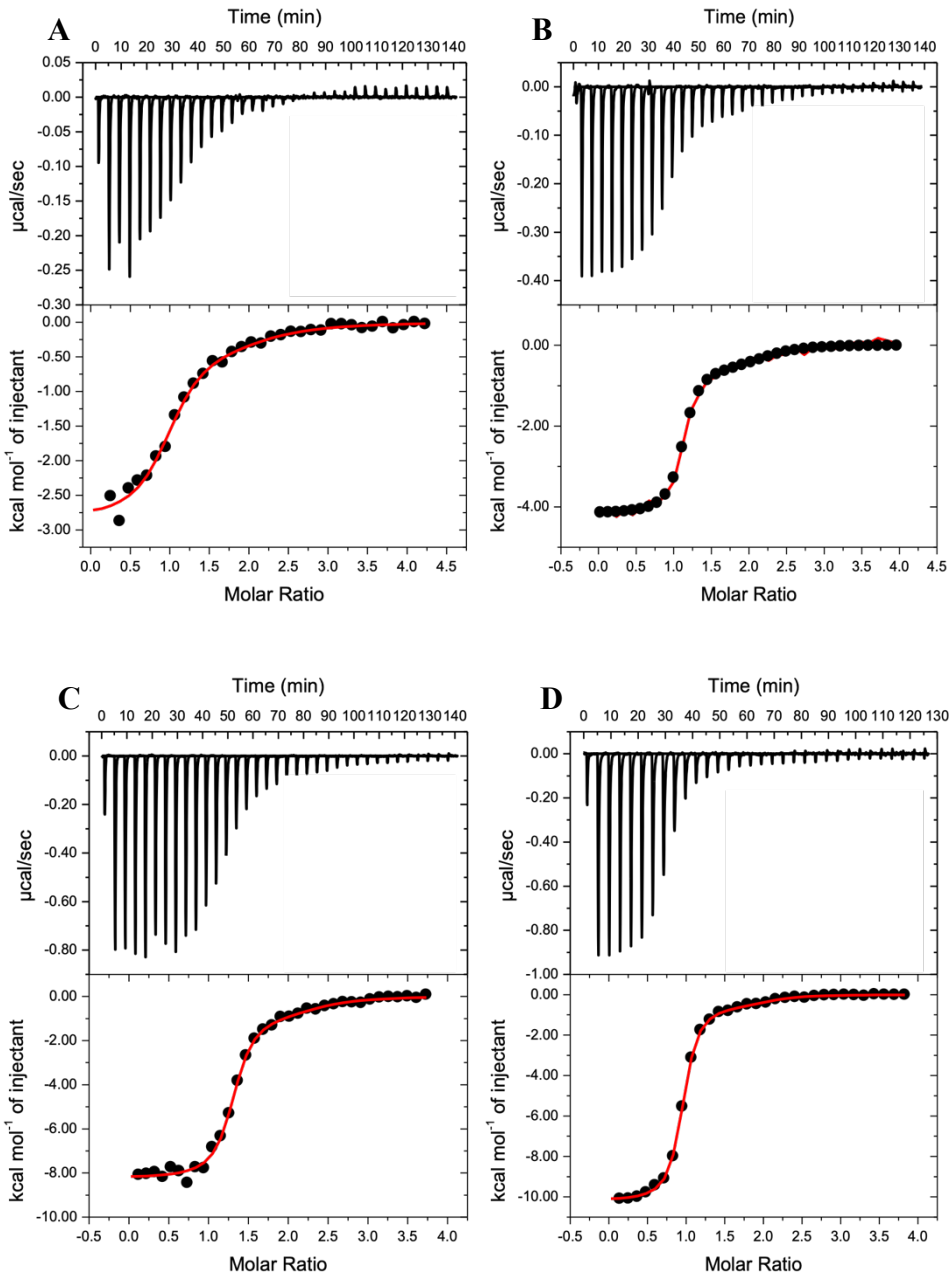

Figure 5.3.3.3. *Representative isotherms associated with the titration of 300 µM $MeHg^+$ into 15 µM MerP under anaerobic conditions in 50 mM buffer, 50 mM NaI, pH 7.4 These titrations were fit with a two-site binding model. (A) PIPES, Site 1, n = 0.95 ± 0.05, ΔH = -2.9 ± 0.1 kcal/mol, K_{ITC} = 9 (± 9)×10^6; site 2: n = 1.3 ± 0.5, ΔH = -0.4 ± 0.4 kcal/mol, K_{ITC} = 4 (± 3)×10^5; (B) HEPES, Site 1, n = 1.08 ± 0.01, ΔH = -4.19 ± 0.04 kcal/mol, K_{ITC} = 1.1 (± 0.8)×10^8; site 2: n= 1.1 ± 0.1, ΔH = -0.6 ± 0.1 kcal/mol, K_{ITC} = 1.0 (± 0.7)×10^6; (C) TAPSO, Site 1, n = 1.26 ± 0.01, ΔH = -8.24 ± 0.08 kcal/mol, K_{ITC} = 5 (± 4)×10^7; site 2: 1.1 ± 0.2, ΔH = -1.0 ± 0.4 kcal/mol, K_{ITC} = 6 (± 5)×10^5; (D) TRIS, Site 1, n = 0.904 ± 0.002, ΔH = -10.21 ± 0.03 kcal/mol, K_{ITC} = 1.3 (± 0.5)×10^7; site 2: 1.12 ± 0.06, ΔH = -0.62 ± 0.07 kcal/mol, K_{ITC} = 1.2 (± 0.5)×10^6.*

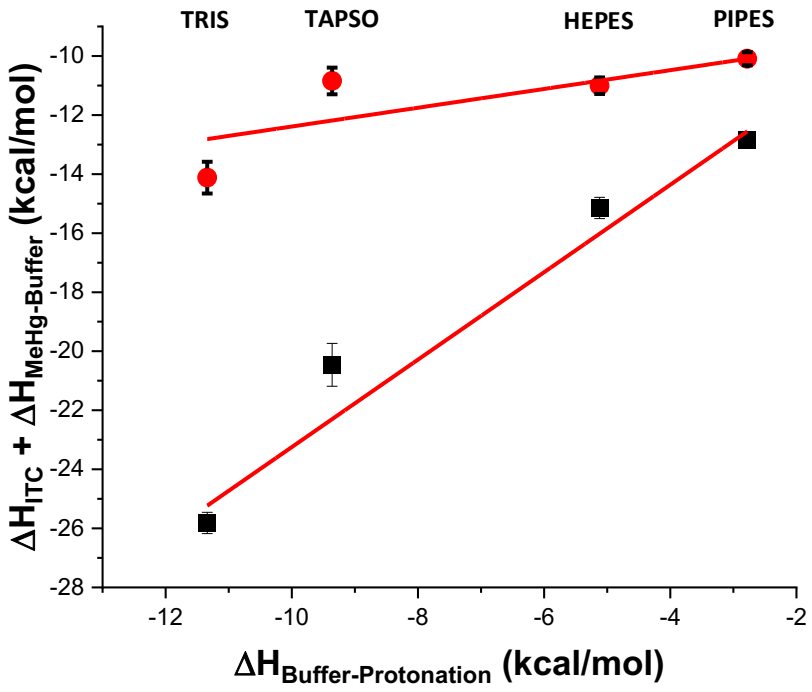

Figure 5.3.3.4. *Proton plots associated with the titration of 300 μM $MeHg^+$ into 15 μM MerP in 50 mM Buffer, 50 mM NaCl, pH 7.4. This shows a slope of 1.48 ± 0.14 for the first binding event (black datapoints) and 0.32 ± 0.15 for the second binding event (red datapoints).*

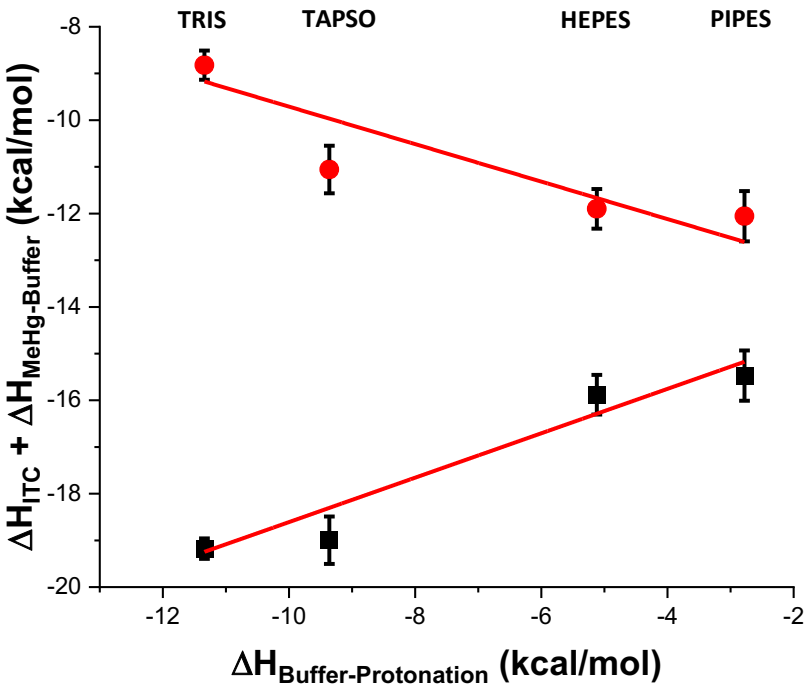

Figure 5.3.3.5. *Proton plots associated with the titration of 300 μM $MeHg^+$ into 15 μM MerP in 50 mM Buffer, 50 mM NaBr, pH 7.4. This shows a slope of 0.48 ± 0.07 for the first binding event (black datapoints) and -0.4 ± 0.12 for the second binding event (red datapoints).*

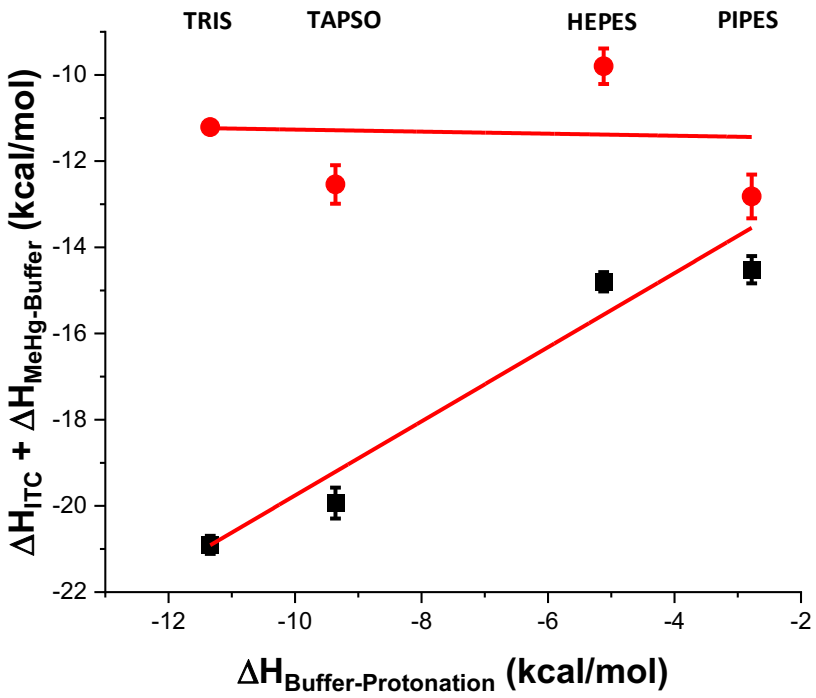

Figure 5.3.3.6. *Proton plots associated with the titration of 300 μM $MeHg^+$ into 15 μM MerP in 50 mM Buffer, 50 mM NaI, pH 7.4. This shows a slope of 0.86 ± 0.13 for the first binding event (black datapoints) and -0.02 ± 0.18 for the second binding event (red datapoints).*

Table 5.3.3.1. *Average apparent thermodynamics associate with the titration of $MeHg^+$ into MerP in 50 mM buffer, 50 mM salt, pH 7.4.*

Buffer	Salt	Binding Site	n_{ITC}	K_{ITC}	ΔH_{ITC} (kcal/mol)
PIPES	NaCl	1	0.98 ± 0.05	2.4 (± 0.6)×10^9	-11.4 ± 0.1
		2	1.24 ± 0.07	2.5 (± 0.3) X10^7	-8.7 ± 0.1
	NaBr	1	0.95 ± 0.02	2.9 (± 0.9)×10^8	-8.0 ± 0.5
		2	1.00 ± 0.01	2.0 (± 0.9)×10^7	-4.6 ± 0.5
	NaI	1	1.0 ± 0.1	2 (± 1)×10^7	-2.6 ± 0.3
		2	1.1 ± 0.3	4 (± 1)×10^5	-0.9 ± 0.5
HEPES	NaCl	1	1.02 ± 0.09	7 (± 3)×10^9	-12.4 ± 0.3
		2	1.1 ± 0.1	6 (± 1)×10^7	-8.2 ± 0.2
	NaBr	1	1.07 ± 0.05	1.4 (± 0.6)×10^9	-8.5 ± 0.3
		2	1.22 ± 0.08	9 (± 1) X10^6	-4.5 ± 0.3
	NaI	1	0.99 ± 0.07	1.0 (± 0.9)×10^8	-4.2 ± 0.2
		2	1.1 ± 0.2	1.1 (± 0.9)×10^6	-0.8 ± 0.4
TAPSO	NaCl	1	0.78 ± 0.04	2.3 (± 1.0)×10^8	-16.3 ± 0.7
		2	1.37 ± 0.09	3.3 (± 0.6)×10^7	-6.6 ± 0.4
	NaBr	1	1.01 ± 0.01	1.7 (± 0.5)×10^9	-13.2 ± 0.1
		2	0.88 ± 0.02	1.2 (± 0.3)×10^7	-5.3 ± 0.1
	NaI	1	1.26 ± 0.08	6 (± 3)×10^7	-8.4 ± 0.3
		2	1.2 ± 0.2	7 (± 4)×10^5	-1.0 ± 0.4
TRIS	NaCl	1	0.55 ± 0.05	1.2 (± 0.1)×10^8	-17.6 ± 0.3
		2	1.32 ± 0.07	1.8 (± 0.4)×10^7	-5.9 ± 0.5
	NaBr	1	0.95 ± 0.04	1.8 (± 0.3)×10^9	-15.3 ± 0.2
		2	0.98 ± 0.04	1.0 (± 0.2)×10^7	-5.0 ± 0.3
	NaI	1	0.90 ± 0.02	1.1 (± 0.4)×10^8	-10.4 ± 0.2
		2	1.09 ± 0.07	1.0 (± 0.4)×10^6	-0.74 ± 0.09

these slopes. In NaBr, the first binding event displaces 0.48 protons from MerP and binds 0.4 protons in the second event. Finally, NaCl shows a displacement of 1.48 protons from the first event and 0.32. in the second event. This deviation may result from discrepancies in anion-dependent $MeHg^+$ binding to cysteine, which would introduce errors that propagate throughout these experiments.

With a proton inventory, the enthalpy of the first and second binding events can now be determined. Because the apparent enthalpy determined by ITC is the sum of all enthalpies that occur in solution, we can solve for the MeHg-MerP enthalpy for both binding events,

$$\Delta H_{MeHg-MerP} = \Delta H_{ITC} + \Delta H_{MeHg-Buffer} - \left(n_{H^+} \times \Delta H_{Buffer-H}\right) \quad \textbf{Equation 5.3.3.1}$$

It is noted that $\Delta H_{MeHg\text{-}buffer}$ is the coupled enthalpy of both the MeHg-buffer interaction and $MeHg^+$-salt interaction. **Equation 5.3.3.1** is solved for each buffer-salt series, which accounts for this coupled enthalpy. Analysis of the MeHg-MerP results give the buffer-independent and salt-independent binding enthalpy for each buffer and salt combination, and, these enthalpies can then be averaged to determine the MeHg-MerP enthalpy for both the first and second binding event. This *post-hoc* analysis indicates that the binding of the first $MeHg^+$ to MerP has an enthalpy value of $\Delta H_{MeHg+\text{-}CysN}$ = -11.1 ± 0.8 kcal/mol and the binding enthalpy of second $MeHg^+$ to MerP has an enthalpy value of $\Delta H_{MeHg+\text{-}CysC}$ = -11.6 ± 1.1 kcal/mol. A summarization of the buffer-independent, salt-independent binding thermodynamics at pH 7.4 are shown in **Table 5.3.3.2**.

With the condition-independent binding enthalpy determined, the condition-independent binding affinity for both $MeHg^+$ binding events can be quantified. Similar to the enthalpy, this considers the competing equilibrium and their corresponding equilibrium constants. The stability constant for the MeHg-buffer complex, which is the coupled MeHg-buffer and $MeHg^+$-salt interactions, is included in this analysis. By taking these competing equilibria into account, the buffer-independent, salt-independent binding constant for both $MeHg^+$ at pH 7.4 is determined by:

$$K_{MeHg-MerP} = K_{ITC} \times (1 + K_{MeHg-Buffer} \times [Buffer]_{basic} \quad \textbf{Equation 5.3.3.2}$$

Again, identical to the *post-hoc* analysis for the binding enthalpy, $K_{MeHg\text{-}buffer}$ is the coupled equilibrium constant for the $K_{MeHg\text{-}buffer}$ and $K_{MeHg\text{-}salt}$. These coupled equilibria was found by quantifying the MeHg-cysteine interaction, and is unique for each buffer-salt series.

Table 5.3.3.2. *Average condition-independent thermodynamic data for the binding of 300 μM $MeHg^+$ to the first and second binding site on MerP (15 μM) in 50 mM Buffer, 50 mM salt, pH 7.4. Each set of thermodynamics has the average thermodynamic data that corresponds to the excess anion in solution. The overall average represents the total average and standard deviation from all buffer-independent MeHg-MerP binding at pH 7.4. Overall average includes ~50 independent ITC experiments.*

Salt	Site	Protons Released	n_{ITC}	$Ka_{MeHg\text{-}MerP}$	$\Delta G_{MeHg\text{-}MerP}$ (kcal/mol)	$\Delta H_{MeHg\text{-}MerP}$ (kcal/mol)	$-T\Delta S_{MeHg\text{-}MerP}$ (kcal/mol)
NaCl	1	1.5 ± 0.1	0.9 ± 0.2	$3 (\pm 3)\times10^{15}$	-20.4 ± 1.3	-8.0 ± 1.1	-12 .5 ± 1.1
	2	0.3 ± 0.2	1.3 ± 0.1	$5 (\pm 4)\times10^{13}$	-18.5 ± 0.7	-9.2 ± 1.1	-9.2 ± 0.6
NaBr	1	0.48 ± 0.07	1.00 ± 0.06	$3 (\pm 4)\times10^{15}$	-20.4 ± 1.1	-14.0 ± 0.5	-6.4 ± 1.5
	2	-0.4 ± 0.1	1.0 ± 0.1	$2 (\pm 2)\times10^{13}$	-17.7 ± 0.8	-13.8 ± 0.7	-3.9 ± 1.5
NaI	1	0.9 ± 0.1	1.1 ± 0.2	$2 (\pm 1)\times10^{15}$	-20.5 ± 0.6	-11.4 ± 0.8	-9.1 ± 1.3
	2	-0.0 ± 0.2	1.1 ± 0.2	$2 (\pm 1)\times10^{13}$	-17.9 ± 0.5	-11.7 ± 1.4	-6.2 ± 1.8
Overall Average	1	0.9 ± 0.2	1.0 ± 0.1	$2 (\pm 3)\times10^{15}$	-20.4 ± 1.0	-11.1 ± 0.8	-9.3 ± 1.3
	2	0.0 ± 0.2	1.2 ± 0.2	$3 (\pm 2)\times10^{13}$	-18.0 ± 0.7	-11.6 ± 1.1	-6.4 ± 1.3

However, this equation is the same for both the first and second $MeHg^+$ binding events. For the first binding event, which displaces ~1 proton, $K_{MeHg\text{-}MerP\text{-}CysN} = 2\ (\pm 3)\ X10^{15}$, and for the second binding event, in which ~0 protons are released, show a binding affinity equal to $K_{MeHg\text{-}MerP\text{-}CysC} = 3\ (\pm 2)\ X10^{13}$. These binding affinities, and the associated binding free energy as well as the binding enthalpy and entropy, are summarized in **Table 5.3.3.2**.

5.3.4. Molecular Dynamics for the Methylmercury-Binding Mechanism

The binding of $MeHg^+$ to MerP, which includes two distinct binding events, calls into question the cooperativity and mechanism of binding. ITC experiments suggest that $MeHg^+$ binds to the solvent exposed cysteine, Cys_N, first, which results in the displacement of ~1 proton. Then $MeHg^+$ binds to the buried cysteine, Cys_C. How does $MeHg^+$ bind to a buried thiolate, and why would it preferentially bind to solvent-exposed, protonated thiol, which would have greater competition from the proton than the thiolate? I hypothesize that $MeHg^+$ binding to Cys_N results in conformational changes at the buried Cys_C, leading to Cys_C becoming accessible for binding. This mechanism would be consistent with the mechanism of metal transfer described in Chapter 4. An intriguing observation is changes at the highly conserved methionine, Met12 between free MerP and Hg^{2+}-bound MerP. In the apo-MerP structure, this methionine is solvent-exposed, but this seems to become buried when Hg^{2+} binds.

Using molecular dynamics, where one $MeHg^+$ was bonded to the solvent-exposed Cys_N, the ligand-bound protein is equilibrated for 200 ns. This allowed the solvent-accessible surface area (SASA) of both the buried Cys_C and the solvent-exposed methionine to be quantified (**Figure 5.3.4.1**). These MD experiments show an amino acid flip, in which the solvent-exposed methionine becomes buried, and the buried C-terminal cysteine becomes more solvated. Shifting of the cysteine towards the surface allows $MeHg^+$ to bind. This residue swap seems to be mediated by the $MeHg^+$-Cys_N interaction.

5.3.5. Binding of Organomercurial Compounds to MerP

Although $MeHg^+$ is the most environmentally-relevant organomercurial, other mercury-based molecules have been broadly used for medical purpose. This includes thimerosal and merbromin, which have anti-septic and anti-fungal properties (**Figure**

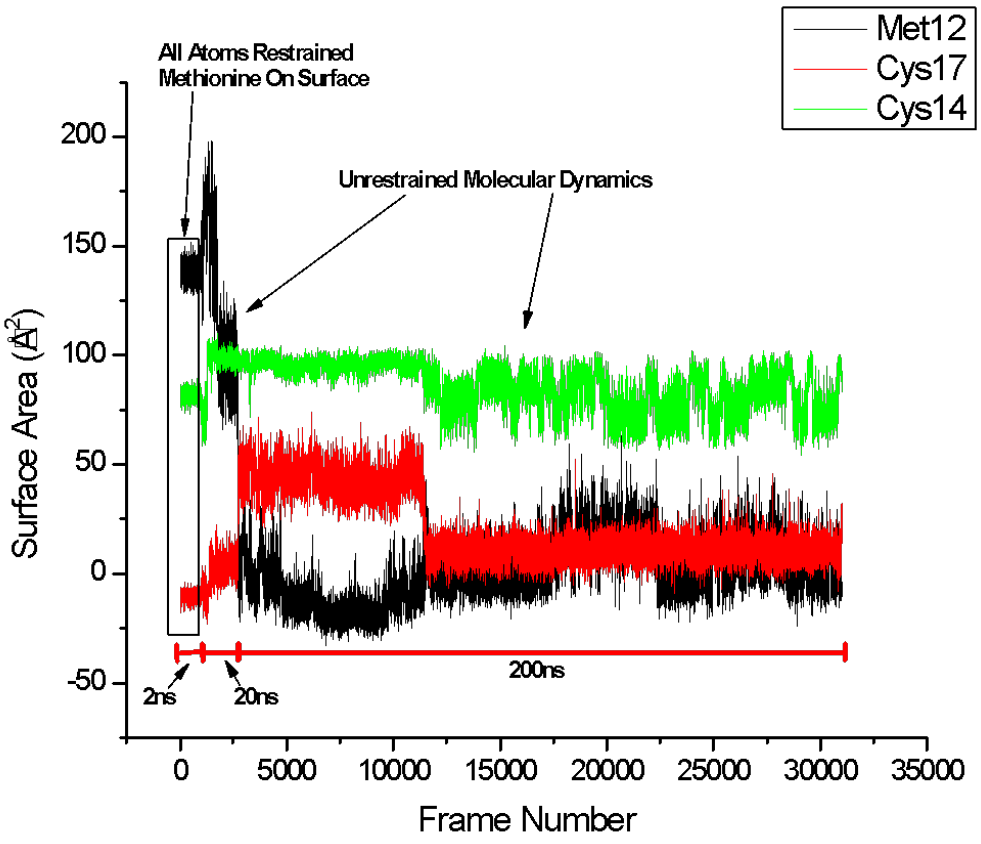

Figure 5.3.4.1. *Quantification of the solvent-accessible surface area (SASA) for Met12, Cys14 (Cys_N), and Cys17 (Cys_C) upon the binding of $MeHg^+$ to Cys_N. The first 2 ns represent the prepared structure that has been heated to 300 K. The next 20 ns represents the structure during the equilibration of density of the system. Finally, the last stage is the 200 ns final equilibration. Met12 is initially solvent-exposed and becomes buried within the core of the protein, whereas the buried cysteine, Cys17, becomes more solvent-exposed, allowing $MeHg^+$ to bind. Cys14 is bound to $MeHg^+$ and solvent-exposed throughout the entirety of the experiment.*

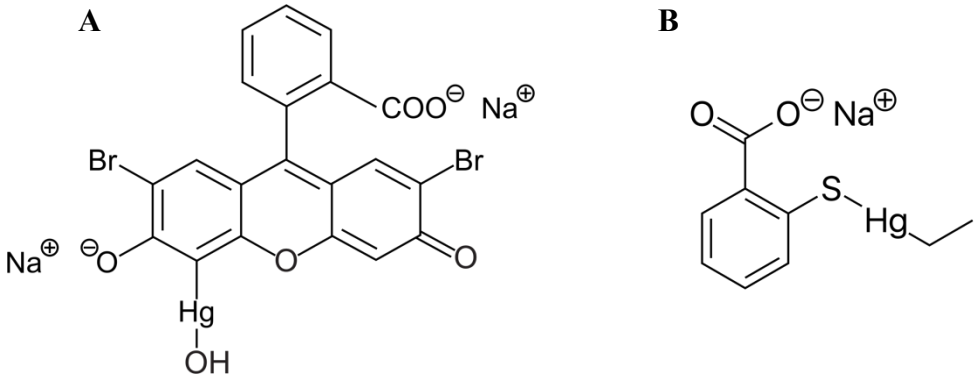

Figure 5.3.5.1. *Structures of (A) merbromin (Mercurochrome) and (B) thimerosal. In merbromin, the mercury is bound to an OH^-, where as in thimerosal, mercury is bound to ortho-mercaptobenzoic acid. In Merbormin, the thiols on MerP readily outcompete a OH^- leaving group on merbromin, but cannot outcompete the ortho-mercaptobenzoic acid group of thimerosal.*

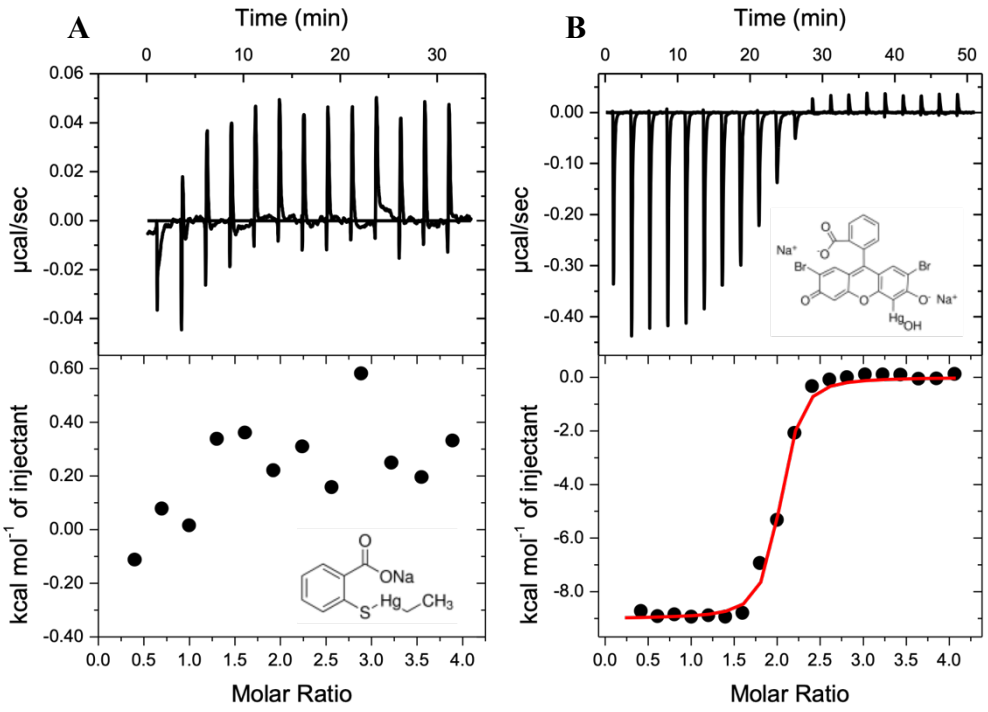

Figure 5.3.5.2. *Representative isotherms associated with the titration of 300 µM thimerosal (A) or Merbromin (B) into 15 µM MerP in 50 mM ACES, 50 mM NaCl, pH 7.4. (A) No binding is observed in the titration of thimerosal into MerP. (B) Merbromin titration to MerP: n = 1.95 ± 0.01, ΔH = -9.0 ± 0.1 kcal/mol, and K = 1.0 (± 0.2)×10^7.*

Unlike the binding of $MeHg^+$ to MerP, in which the titration of $MeHg^+$ into cysteine allowed the MeHg-buffer interaction to be quantified, there are no known thermodynamics for the binding of thimerosal and merbromin. This precludes the ability to determine the organomercurial-buffer interaction. Thus, these ITC experiments are used to observe apparent binding thermodynamics and gain insight on the possibility of MerP binding these organomercurial compounds (**Figure 5.3.5.2**).

Although thimerosal is an organomercurial compound, it does not have available mercury coordination, thus binding to MerP would be unlikely. Furthermore, without this open coordination, it would be unlikely that thimerosal would bind to organomercurial lyase (MerB) either. This hypothesis was supported by these ITC experiments in which the titration of thimerosal into MerP did not show any apparent binding.

Merbromin, with its exchangeable hydroxide ion that is bound to the Hg^{2+} shows significant binding to MerP. Merbromin, like $MeHg^+$, binds MerP in a 2:1 stoichiometry, likely through mercury-thiolate bonds to the N-terminal and C-terminal cysteines. Differentiating these two binding events is not possible, as the enthalpy of each interaction is similar. The binding of merbromin to MerP is strongly exothermic, with an experimental enthalpy of $\Delta H = -9.0 \pm 0.1$ kcal/mol. Although merbromin is much larger than methylmercury, MerP is still able to bind this organomercurial compound to both of its cysteine residues. This apparent binding affinity of $1.0 (\pm 0.2) \times 10^7$ is likely to be a lower limit of binding, since merbromin-buffer interactions are not known. Without more thermodynamic data, deconvolution of the condition-independent merbromin-MerP binding thermodynamics is not possible

5.4. Discussion

5.4.1. Alternative Physiological Function of MerP

Unlike Hg^{2+} binding to MerP, the interaction between $MeHg^+$ and MerP has not been well studied. It was hypothesized that the function of MerP could be more than a metallochaperone, as it is not strictly required Hg^{2+} transport by MerT.[62] If the function of MerP was only to serve as a metallochaperone and it was required for the transfer of Hg^{2+} to MerT, then deletion of this protein from a cell would result in greater Hg^{2+} sensitivity,

which is not the case. This leads to the question: if MerP is not necessary for the import of mercury, why is it found in nearly all mercury-resistant plasmids? This is compared to mercuric reductase (MerA), which is absolutely necessary for mercury resistance.

I hypothesize that this discrepancy between its function and abundance could originate from another function for MerP beyond that of a metallochaperone. Consider the purpose of MerP as a mercury-sink, aiming to protect the cell from excess mercury within the microenvironment of the cell. As mercury is bound and transported by MerT into the cytosol, the concentration in the microenvironment would decrease. Eventually, the mercury-bound MerP would transfer its bound metal to MerT. Effectively, MerP creates a buffer to enhance mercury tolerance through its metallochaperone function. Further support for this hypothesis comes from the mechanism of mercury toxicity in cells. Mercury, with its propensity to bind thiols, readily displaces native metals, which can lead to aberrant protein and cellular function. This hypothesis has only been tested through cell-based systems, however, and a biochemical and inorganic approach has not yet been evaluated.

This hypothesis can be taken a step further through the inclusion of organomercurial compounds like methylmercury. Just like inorganic mercury, methylmercury must enter the periplasm of the cell for it to cross into the cytoplasm, even if the mechanism of transport into the cell is through diffusion. If the function of MerP is to protect the cell as a metal-sink, then this should also apply to organomercurial compounds as well. This is a natural extension of the hypothesis, as MerP has cysteine residues that are readily available for binding organomercurials.

Testing these hypotheses from an inorganic and biochemical perspective can be achieved through an understanding of the thermodynamics of mercury and methylmercury binding to MerP. The binding of inorganic mercury to MerP was quantified in Chapter 4. Herein, the thermodynamics of $MeHg^+$ binding to MerP has been determined by ITC to understand both the physiological function of MerP, as well as the mechanism of $MeHg^+$ binding along with the associated structural changes that occur upon binding as probed by molecular dynamics calculations.

5.4.2. Thermodynamics of the Methylmercury-MerP Interaction

The thermodynamics of $MeHg^+$ binding to MerP have been measured by isothermal titration calorimetry. However, for accurate quantification of the MeHg-MerP interaction, in which $MeHg^+$ is titrated into the protein in buffer, the thermodynamics of the MeHg-buffer interaction must first be determined. This is required buffer binding to $MeHg^+$ is an equilibrium that competes with the binding of $MeHg^+$ to MerP.

For accurate quantification of the MeHg-buffer interaction, a titration of $MeHg^+$ into cysteine, which has a known binding equilibrium constant and enthalpy in excess buffer is used to quantify the MeHg-buffer thermodynamics. Previous studies had shown that $MeHg^+$ binds to cysteine with an affinity of $\log K_{MeHg+-Cys} = 15.18$ and an enthalpy of $\Delta H = -20.6$ kcal/mol when $MeHg^+$ binds to the thiol.[60,61] Competition with the buffer fives experimental values that are reduced by the magnitude of the MeHg+ binding to the buffer. However, $MeHg^+$ binding to MerP requires a stronger competing ligand than buffer. The halides NaCl, NaBr, and NaI were used along with the buffer as competing ligands to ensure accurate characterization.

With the quantification of the thermodynamics of methylmercury binding to each unique buffer-salt combination, the buffer-independent and halide-independent thermodynamics of $MeHg^+$ binding to MerP was determined. Regardless of the buffer-salt series, two distinct binding events are observed. When quantifying the proton inventory for each binding event, it is observed that ~1 proton is released from MerP in the first binding event and ~0 protons are released in the second binding event. This agrees with the pK_a's of the two cysteines, in which the N-terminal cysteine has a pK_a of 9.1 and the C-terminal cysteine has a pK_a of 5.5. Thus, at pH 7.4, this supports the hypothesis that the first $MeHg^+$ binds to the N-terminal cysteine, releasing 1 proton, followed by $MeHg^+$ binding to the C-terminal cysteine. It is noted that this proton on the N-terminal cysteine should provide some competition to the binding of $MeHg^+$, compared to the thiolate of the C-terminal cysteine. Why, then, does the first $MeHg^+$ bind to the N-terminal cysteine and the not the C-terminal cysteine? This binding and proton release suggests that the buried C-terminal cysteine is not accessible to ligand binding until the N-terminal cysteine is ligated.

This binding and protonation provide insight into the mechanism of $MeHg^+$ binding, and thus the mechanism of inorganic mercury binding. This may also be broadly applicable to other monovalent and divalent metallochaperones, like HAH1, that are

involved in the transfer of a metal to its binding partner. It is observed that the metal binding sequence in MerP, along with all ferredoxin-like metallochaperones, has a highly conserved methionine (MXCXXC motif). In the solution structure of MerP, this methionine is exposed to solvent, but this residue becomes buried in Hg^{2+}-bound structures. I hypothesize that this methionine switch is linked to the C-terminal cysteine moving to the surface for metal binding. For $MeHg^{+}$ binding to MerP, I propose the following mechanism. $MeHg^{+}$ binds to the N-terminal cysteine, displacing ~ 1 proton. This binding triggers a ligand switch that pushes the C-terminal cysteine towards the surface and shifts the solvent-exposed methionine into the core of the protein. To test this mechanism, molecular dynamics experiments of the MeHg-MerP (1:1) interaction was used to quantify the solvent-accessible surface area (SASA). Indeed, ligation of $MeHg^{+}$ to the deprotonated N-terminal cysteine results in a dramatic decrease in the SASA of the methionine. Likewise, there is an increase in the SASA of the buried C-terminal cysteine, indicating that this residue moves towards the surface. Finally, the SASA for the N-terminal, $MeHg^{+}$-bound cysteine shows no change its SASA. This residue switch may be driven by changes in the electrostatics within the metal binding site when $MeHg^{+}$ binds to the solvent-exposed cysteine.

This mechanism likely applies to the binding of inorganic mercury, in which binding of Hg^{2+} to the protonated N-terminal cysteine would result in similar structural changes for the C-terminal cysteine and conserved methionine. Likewise, this may be similar to the mechanism involved in the transfer of Cu(I) from HAH1 to Wnd4 (See Chapter 4). The residue switch between the buried C-terminal cysteine and the solvent-exposed methionine may aid in the transfer of Cu(I) from HAH1 to Wnd4, where this switch facilitates the breaking of the thiolate-metal bond, driving the transfer forward.

With the mechanism for the binding of $MeHg^{+}$ to MerP determined, the condition-independent thermodynamics can provide additional insight into this overall interaction. Of particular note, the binding of $MeHg^{+}$ in excess NaCl was concerning, as the apparent binding constant for the first binding event was greater than could be quantifiable by ITC. The chloride anion is a ligand that competes with MerP for the less favorable $MeHg^{+}$ and the interaction with Cl^{-} was replaced by a more favorable interaction with Br^{-} and I^{-}. Titrations of $MeHg^{+}$ into MerP in excess NaBr and NaI show apparent binding affinities

that are within the quantifiable range of ITC. The condition-independent binding affinity that was determined for the first $MeHg^+$ binding in competition with each halide was nearly identical, with an average $K_{MeHg\text{-}MerP\text{-}CysN} = 2 (\pm 3)\times10^{15}$. This was also found for the second $MeHg^+$ binding, which shows an average binding affinity of $3 (\pm 2)\times10^{13}$. These similar halide-independent binding affinities for both the first and second binding events also highlight an unusual situation in which the c-window and the quantifiable range that is found by ITC is expanded for two-site binding models.

With the buffer-independent and halide-independent equilibrium constants determined at pH 7.4 for both binding events, fundamental inorganic and biochemical principles can be used to understand the condition-independent enthalpies and entropies for both binding events. First, to understand these contributions, it is necessary to understand the different molecular contributions to these thermodynamics (**Figure 5.4.2.1**).

For both binding events, the enthalpy of $MeHg^+$-thiolate bond formation should be similar. The first binding event involves the displacement of ~1 proton has a binding enthalpy of –11.1 ± 0.8 kcal/mol. Curiously, the enthalpy for the second binding event, which has no proton displacement, is similar, where the enthalpy is –11.6 ± 1.1 kcal/mol. Taking into account the cysteine deprotonation enthalpy which is -8.6 kcal/mol, event into account, which is equal to –8.6 kcal/mol, indicates that this $MeHg^+$-thiolate bond enthalpy is –19.7 ± 0.8 kcal/mol. After accounting for the differences in deprotonation enthalpy, the metal-thiolate bond enthalpies are not identical. Changes in the electrostatics within the protein scaffold are predicted to be the source of the additional binding enthalpy for the first $MeHg^+$. Binding of $MeHg^+$ to the solvent-exposed cysteine, results in the ligand-switch of the methionine and C-terminal cysteine, would result in changes to the bonding network, that are more enthalpically favorable for the first binding event, relative to the second binding event.

From an entropic perspective, several aspects are nearly identical between the first

Binding Enthalpy	Binding Entropy
1. (De)–Protonation 2. Changes in Hydrogen Bonding 3. Metal Bond Formation	1. Metal Desolvation 2. Conformational Restraints 3. Metal Coordination 4. Water Displacement 5. Cratic Entropy

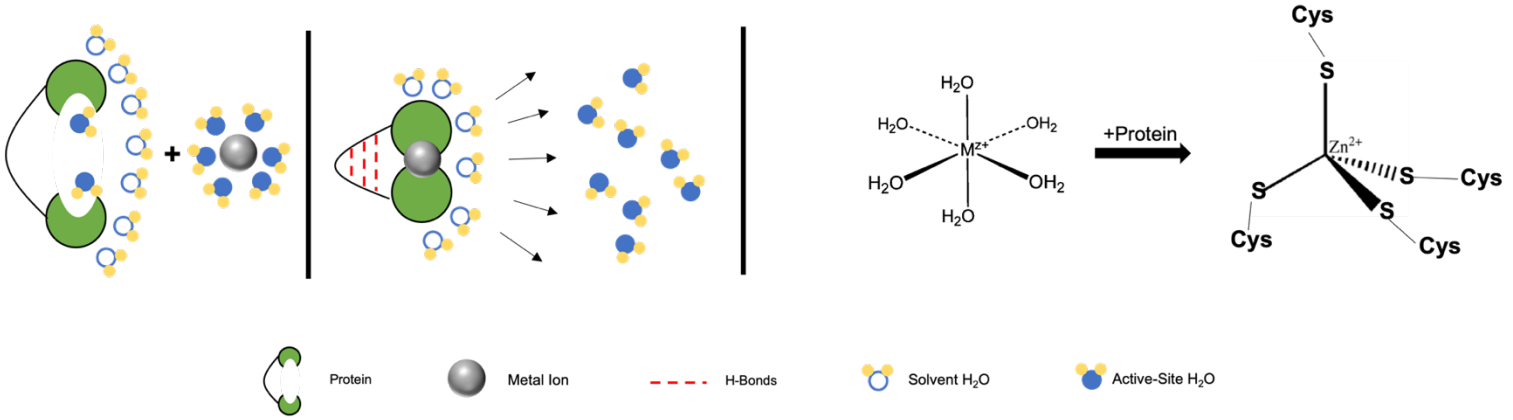

Figure 5.4.2.1. *Graphical representation of major components that make up the enthalpic and entropic contributions to metal binding in a protein in aqueous conditions.*

different between these two binding events but is unlike to be significantly different. Because of these similarities, we can predict the source of the entropic differences. The primary difference would come from the deprotonation in the first binding event, which would be predicted to be more favorable. Likewise, the binding of this $MeHg^+$ in the first binding site results in changes in the protein conformation. These conformational differences may lead to greater conformational dynamics, leading to more favorable entropic contributions. Indeed, the binding of the first $MeHg^+$ to the protonated cysteine shows an entropic contribution of–9.3 ± 1.3 kcal/mol, as compared to the second $MeHg^+$ binding event which shows an entropy of –6.4 ± 1.3 kcal/mol. These entropic contributions are significantly different, in which the first binding event is more entropically favorable.

Overall, the binding thermodynamics for these two binding events are nearly identical, where both are both enthalpically and entropically favorable, and moderately enthalpically driven.

5.4.3. Binding of Organomercurial Compounds to MerP

Unlike $MeHg^+$, which is the most environmentally-relevant organomercurial compound, other organomercurial compounds have also been synthesized. This includes merbromin and thimerosal, which were used for their anti-septic and anti-fungal properties. Unfortunately, there are no known binding thermodynamics for either of these molecules, with cysteine or other ligands, as there was for in $MeHg^+$. Thus, only the apparent thermodynamics can be quantified.

Thimerosal, which does not have an exchangeable mercury-bound ligand. Displacement of this hydroxide would result in the aryl-mercury molecules with a Given that the mercury is already coordinated to the sulfur and an ethyl group on thimerosal, and that mercury tends to favor two-coordinate interactions, the inability of MerP to bind the compound is not surprising. Titrations of thimerosal support this hypothesis, as no binding was observed. It is also observed that mercury coordination in thimerosal and merbromin are different. Thimerosal has a mercury bound with an ortho-nitrobenzoic, which is a poor leaving group for the cysteine on MerP. Merbromin, however, contains a hydroxide bound to the hydroxide ion, leading to rapid ligand-exchange. It is also observed that mercury

coordination in thimerosal and merbromin are different. Thimerosal has a mercury bound with an ortho-nitrobenzoic, which is a poor leaving group for the cysteine on MerP.

Merbromin, on the other hand, has an exchangeable hydroxide ion that is readily displaced by the cysteine thiolates on MerP. Displacement of this hydroxide would result in the mercury with a +1 charge and an open coordination site on the Hg^{2+}. Titrations of merbromin into MerP support this hypothesis as well, as significant binding is observed. These titrations show a binding stoichiometry of 2:1, in which 2 merbromin bind to 1 MerP, which is similar to the observed titrations of $MeHg^{+}$ into MerP. Given the size of merbromin, which is much larger than methylmercury, it was unexpected to find a 2:1 stoichiometry. Steric hinderance for this binding would have been expected, which may have limited binding stoichiometries, as the two cysteines on MerP are only separated by 2 amino acids. This was not the case, however. It is curious to note that these two binding events are equivalent and non-differentiable. This may suggest that the enthalpy associated with merbromin binding to each cysteine is similar, unlike methylmercury. Furthermore, this binding event binds with an apparent binding affinity of $\sim 10^{7}$, which may only represent a lower limit of binding. As no merbromin-buffer thermodynamics or merbromin-ligand thermodynamics are known, determining the pH-dependent, buffer-independent thermodynamics is not currently possible. Given the similarity of mercury coordination in methylmercury and merbromin, it may be expected that the binding thermodynamics are similar, only modulated by the merbromin structure.

Although there are no previous reports of merbromin binding to MerP, the organomercurial compound phenylmercury ($PhHg^{+}$) has been found to bind to MerP in a bacterial cell. MerP knockout cells that still contains MerT, MerB, and MerA had shown a decrease in $PhHg^{+}$ uptake into the cell, suggesting a need for MerP to cross the cell membrane into the cytosol.[63,64] This is surprising as it is expected that phenylmercury would be similar to methylmercury, in that it is able to diffuse across the cell membrane into the cytosol of the cell. This was not the case, as MerP aided in the transport of phenylmercury into the cytosol of the cell. An attempt to determining the binding thermodynamics of phenylmercury to MerP. Phenylmercury is very insoluble in aqueous solutions, and there are no known stabilizing ligand that could be utilized to keep it in solution throughout the ITC experiment. Characterization of this interaction using other

techniques, or more extensive utilization of organic solvents may aid in the biophysical characterization of the PhHg-MerP interaction.

5.4.4. Thermodynamic and Structural Support for the Physiological Function of MerP

Using ITC to determine the thermodynamics associated with the binding of inorganic mercury and methylmercury binding to MerP, I propose that MerP is involved in protecting periplasmic proteins from the toxic effects of mercury. As these mercury compounds enter the microenvironment of the cell, they will readily bind to the two cysteine residues on MerP, which would be more thermodynamically favorable then binding to in other proteins. For Hg^{2+}, this would result in a buffering capacity, lowering the freely available mercury, while MerT is able to bind and transport the ions across the cell membrane. A similar mechanism is proposed by $MeHg^{+}$, where the MerP would buffer the $MeHg^{+}$ that enters the periplasm of the cell, which, in turn, aims to keep a lower concentration of $MeHg^{+}$ that is freely binding. $MeHg^{+}$, however, will readily diffuse across the cell membrane into the cytosol. As the concentration in the periplasm diminishes over time, these $MeHg^{+}$ would dissociate from MerP and diffuse across the membrane. There is evidence suggesting that other transmembrane mercury proteins, like MerE, may also be involved in the transport of $MeHg^{+}$, which could be another mechanism for its movement of $MeHg^{+}$ into the cytosol.

This works defines the thermodynamics for this interaction, in which $MeHg^{+}$ and Hg^{2+} would be able to bind to the reduced cysteine residues of MerP. Binding these mercury compounds would be a buffering role for MerP and provide greater tolerance of mercury. Because MerP is found in nearly all plasmids that contains MerT and MerA, but is not required for the transport of Hg^{2+} and $MeHg^{+}$. I predict that the function of the protein may not be directly tied to the transport role but also a protection role.

5.5. References

(1) Fimreite, N. Mercury Uses in Canada and Their Possible Hazards as Sources of Mercury Contamination. *Environ. Pollut.* **1970**, *1* (2), 119–131. https://doi.org/10.1016/0013-9327(70)90012-1.

(2) Pyle, D. M.; Mather, T. A. The Importance of Volcanic Emissions for the Global

Atmospheric Mercury Cycle. *Atmos. Environ.* **2003**, *37* (36), 5115–5124. https://doi.org/10.1016/j.atmosenv.2003.07.011.

(3) Li, P.; Yang, Y.; Xiong, W. Impacts of Mercury Pollution Controls on Atmospheric Mercury Concentration and Occupational Mercury Exposure in a Hospital. *Biol. Trace Elem. Res.* **2015**, *168* (2), 330–334. https://doi.org/10.1007/s12011-015-0391-7.

(4) Rytuba, J. J. Mercury from Mineral Deposits and Potential Environmental Impact. *Environ. Geol.* **2003**, *43* (3), 326–338. https://doi.org/10.1007/s00254-002-0629-5.

(5) *The Global Mercury Assessment*; 2013. https://doi.org/DTI/1636/GE.

(6) Selin, N. E. Global Biogeochemical Cycling of Mercury: A Review. *Annu. Rev. Environ. Resour.* **2009**, *34*, 43–63. https://doi.org/10.1146/annurev.environ.051308.084314.

(7) Mergler, D.; Anderson, H. A.; Hing, L.; Chan, M.; Mahaffey, K. R.; Murray, M.; Sakamoto, M.; Stern, A. H. Royal Swedish Academy of Sciences Methylmercury Exposure and Health Effects in Humans: A Worldwide Concern. *Source: Ambio* **2007**, *36* (1), 3–11.

(8) Patra, M.; Sharma, A. Mercury Toxicity in Plants. *Bot. Rev.* **2000**, *66* (3), 379–422. https://doi.org/10.1007/BF02868923.

(9) Sarafian, T.; Anthony Verity, M. Oxidative Mechanisms Underlying Methyl Mercury Neurotoxicity. *Int. J. Dev. Neurosci.* **1991**, *9* (2), 147–153. https://doi.org/10.1016/0736-5748(91)90005-7.

(10) Jarius, S.; Wildemann, B. "Medusa-Head Ataxia": The Expanding Spectrum of Purkinje Cell Antibodies in Autoimmune Cerebellar Ataxia. Part 1: Anti-MGluR1, Anti-Homer-3, Anti-Sj/ITPR1 and Anti-CARP VIII. *J. Neuroinflammation* **2015**, *12* (1), 166. https://doi.org/10.1186/s12974-015-0356-y.

(11) Naganuma, A.; Furuchi, T.; Miura, N.; Hwang, G. W.; Kuge, S. Investigation of Intracellular Factors Involved in Methylmercury Toxicity. *Tohoku Journal of Experimental Medicine*. 2002, pp 65–70. https://doi.org/10.1620/tjem.196.65.

(12) Aschner, M.; Aschner, J. L. *Mercury Neurotoxicity: Mechanisms of Blood-Brain Barrier Transport*; 1990; Vol. 14. https://doi.org/10.1016/S0149-7634(05)80217-9.

(13) Suda, I.; Totoki, S.; Takahashi, H. Degradation of Methyl and Ethyl Mercury into

Inorganic Mercury by Oxygen Free Radical-Producing Systems: Involvement of Hydroxyl Radical. *Arch. Toxicol.* **1991**, *65* (2), 129–134. https://doi.org/10.1007/BF02034939.

(14) Brookes, N. In Vitro Evidence for the Hole of Glutamate in the CNS Toxicity of Mercury. *Toxicology* **1992**, *76* (3), 245–256. https://doi.org/10.1016/0300-483X(92)90193-I.

(15) Aschner, M.; Yao, C. P.; Allen, J. W.; Tan, K. H. Methylmercury Alters Glutamate Transport in Astrocytes. *Neurochem. Int.* **2000**, *37* (2–3), 199–206. https://doi.org/10.1016/S0197-0186(00)00023-1.

(16) Berndt, W. O. The Role of Transport in Chemical Nephrotoxicity. *Toxicol. Pathol.* **1998**, *26* (1), 52–57.

(17) Diamond, G. L.; Zalups, R. K. Understanding Renal Toxicity of Heavy Metals. *Toxicol. Pathol.* **1998**, *26* (1), 92–103. https://doi.org/10.1177/019262339802600111.

(18) Rice, K. M.; Walker, E. M.; Wu, M.; Gillette, C.; Blough, E. R. Environmental Mercury and Its Toxic Effects. *J. Prev. Med. Public Heal.* **2014**, *47* (2), 74–83. https://doi.org/10.3961/jpmph.2014.47.2.74.

(19) Graeme, K. A.; Pollack, C. V. Heavy Metal Toxicity, Part I: Arsenic and Mercury. *J. Emerg. Med.* **1998**, *16* (1), 45–56. https://doi.org/10.1016/S0736-4679(97)00241-2.

(20) Zahir, F.; Rizwi, S. J.; Haq, S. K.; Khan, R. H. Low Dose Mercury Toxicity and Human Health. *Environ. Toxicol. Pharmacol.* **2005**, *20* (2), 351–360. https://doi.org/10.1016/j.etap.2005.03.007.

(21) Park, J.-D.; Zheng, W. Human Exposure and Health Effects of Inorganic and Elemental Mercury. *J. Prev. Med. Public Heal. Prev Med Public Heal.* **2012**, *34445*, 344–352. https://doi.org/10.3961/jpmph.2012.45.6.344.

(22) Clarkson, T. W.; Magos, L.; Myers, G. J. The Toxicology of Mercury — Current Exposures and Clinical Manifestations. *N. Engl. J. Med.* **2003**, *349* (18), 1731–1737. https://doi.org/10.1056/nejmra022471.

(23) Havarinasab, S.; Hultman, P. Organic Mercury Compounds and Autoimmunity. *Autoimmunity Reviews*. June 2005, pp 270–275.

https://doi.org/10.1016/j.autrev.2004.12.001.

(24) Boyd, A. S.; Seger, D.; Vannucci, S.; Langley, M.; Abraham, J. L.; King, L. E. Mercury Exposure and Cutaneous Disease. *J. Am. Acad. Dermatol.* **2000**, *43* (1 I), 81–90. https://doi.org/10.1067/mjd.2000.106360.

(25) Risher, J. F.; Murray, H. E.; Prince, G. R. Organic Mercury Compounds: Human Exposure and Its Relevance to Public Health. *Toxicol. Ind. Health* **2002**, *18* (3), 109–160. https://doi.org/10.1191/0748233702th138oa.

(26) Lemire, J. A.; Harrison, J. J.; Turner, R. J. Antimicrobial Activity of Metals: Mechanisms, Molecular Targets and Applications. *Nature Reviews Microbiology*. June 2013, pp 371–384. https://doi.org/10.1038/nrmicro3028.

(27) Farrell, R. E.; Germida, J. J.; Huang, P. M. Biotoxicity of Mercury as Influenced by Mercury(II) Speciation. *Appl. Environ. Microbiol.* **1990**, *56* (10), 3006–3016. https://doi.org/10.1128/aem.56.10.3006-3016.1990.

(28) Schaefer, J. K.; Rocks, S. S.; Zheng, W.; Liang, L.; Gu, B.; Morel, F. M. M. Active Transport, Substrate Specificity, and Methylation of Hg^{2+} in Anaerobic Bacteria. *Proc. Natl. Acad. Sci. U. S. A.* **2011**, *108* (21), 8714–8719. https://doi.org/10.1073/pnas.1105781108.

(29) Parks, J. M.; Johs, A.; Podar, M.; Bridou, R.; Hurt, R. A.; Smith, S. D.; Tomanicek, S. J.; Qian, Y.; Brown, S. D.; Brandt, C. C.; Palumbo, A. V.; Smith, J. C.; Wall, J. D.; Elias, D. A.; Liang, L. The Genetic Basis for Bacterial Mercury Methylation. *Science (80-.).* **2013**, *339* (6125), 1332–1335. https://doi.org/10.1126/science.1230667.

(30) Smith, S. D.; Bridou, R.; Johs, A.; Parks, J. M.; Elias, D. A.; Hurt, R. A.; Brown, S. D.; Podar, M.; Wall, J. D. Site-Directed Mutagenesis of HgcA and HgcB Reveals Amino Acid Residues Important for Mercury Methylation. *Appl. Environ. Microbiol.* **2015**, *81* (9), 3205–3217. https://doi.org/10.1128/AEM.00217-15.

(31) Zhou, J.; Riccardi, D.; Beste, A.; Smith, J. C.; Parks, J. M. Mercury Methylation by HgcA: Theory Supports Carbanion Transfer to Hg^{2+}. *Inorg. Chem.* **2014**, *53* (2), 772–777. https://doi.org/10.1021/ic401992y.

(32) Qian, C.; Johs, A.; Chen, H.; Mann, B. F.; Lu, X.; Abraham, P. E.; Hettich, R. L.; Gu, B. Global Proteome Response to Deletion of Genes Related to Mercury

Methylation and Dissimilatory Metal Reduction Reveals Changes in Respiratory Metabolism in Geobacter Sulfurreducens PCA. *J. Proteome Res.* **2016**, *15* (10), 3540–3549. https://doi.org/10.1021/acs.jproteome.6b00263.

(33) Pan-Hou, H. S.; Nishimoto, M.; Imura, N. Possible Role of Membrane Proteins in Mercury Resistance of Enterobacter Aerogenes. *Arch. Microbiol.* **1981**, *130* (2), 93–95. https://doi.org/10.1007/BF00411057.

(34) Pan-Hou, H. S. K.; Imura, N. *Role of Hydrogen Sulfide in Mercury Resistance Determined by Plasmid of Clostridium Cochlearium T-2*; 1981; Vol. 129. https://doi.org/10.1007/BF00417179.

(35) Summers, A. O. Organization, Expression, and Evolution of Genes for Mercury Resistance. *Annu. Rev. Microbiol.* **1986**, *40*, 607–634. https://doi.org/10.1146/annurev.mi.40.100186.003135.

(36) Barkay, T.; Miller, S. M.; Summers, A. O. Bacterial Mercury Resistance from Atoms to Ecosystems. *FEMS Microbiology Reviews*. Elsevier 2003, pp 355–384. https://doi.org/10.1016/S0168-6445(03)00046-9.

(37) Parkhill, J.; Ansari, A. Z.; Wright, J. G.; Brown, N. L.; O'Halloran, T. V. Construction and Characterization of a Mercury-Independent MerR Activator (MerR(AC)): Transcriptional Activation in the Absence of Hg^{2+} Is Accompanied by DNA Distortion. *EMBO J.* **1993**, *12* (2), 413–421. https://doi.org/10.1002/j.1460-2075.1993.tb05673.x.

(38) Chen, C. Y.; Hsieh, J. L.; Silver, S.; Endo, G.; Huang, C. C. Interactions between Two MerR Regulators and Three Operator/Promoter Regions in the Mercury Resistance Module of Bacillus Megaterium. *Biosci. Biotechnol. Biochem.* **2008**, *72* (9), 2403–2410. https://doi.org/10.1271/bbb.80294.

(39) Hamlett, N. V.; Landale, E. C.; Davis, B. H.; Summers, A. O. *Roles of the Tn21 MerT, MerP, and MerC Gene Products in Mercury Resistance and Mercury Binding*; 1992; Vol. 174. https://doi.org/10.1128/jb.174.20.6377-6385.1992.

(40) Rousselot-Pailley, P.; Sénèque, O.; Lebrun, C.; Crouzy, S.; Boturyn, D.; Dumy, P.; Ferrand, M.; Delangle, P. Model Peptides Based on the Binding Loop of the Copper Metallochaperone Atx1: Selectivity of the Consensus Sequence MxCxxC for Metal Ions Hg^{2+}, Cu(I), Cd(II), Pb(II), and Zn(II). *Inorg. Chem.* **2006**, *45* (14), 5510–5520.

https://doi.org/10.1021/ic060430b.

(41) Steele, R. A.; Opella, S. J. Structures of the Reduced and Mercury-Bound Forms of MerP, the Periplasmic Protein from the Bacterial Mercury Detoxification System. *Biochemistry* **1997**, *36* (23), 6885–6895. https://doi.org/10.1021/bi9631632.

(42) Sahlman, L.; Skärfstad, E. G. Mercuric Ion Binding Abilities of Merp Variants Containing Only One Cysteine. *Biochem. Biophys. Res. Commun.* **1993**, *196* (2), 583–588. https://doi.org/10.1006/bbrc.1993.2289.

(43) Veglia, G.; Porcelli, F.; DeSilva, T.; Prantner, A.; Opella, S. J. The Structure of the Metal-Binding Motif GMTCAAC Is Similar in an 18- Residue Linear Peptide and the Mercury Binding Protein MerP [10]. *J. Am. Chem. Soc.* **2000**, *122* (10), 2389–2390. https://doi.org/10.1021/ja992908z.

(44) DeSilva, T. M.; Veglia, G.; Porcelli, F.; Prantner, A. M.; Opella, S. J. Selectivity in Heavy Metal-Binding to Peptides and Proteins. *Biopolymers* **2002**, *64* (4), 189–197. https://doi.org/10.1002/bip.10149.

(45) Grauschopf, U.; Winther, J. R.; Korber, P.; Zander, T.; Dallinger, P.; Bardwell, J. C. A. Why Is DsbA Such an Oxidizing Disulfide Catalyst? *Cell* **1995**, *83* (6), 947–955. https://doi.org/10.1016/0092-8674(95)90210-4.

(46) Powlowski, J.; Sahlman, L. Reactivity of the Two Essential Cysteine Residues of the Periplasmic Mercuric Ion-Binding Protein, MerP. *J. Biol. Chem.* **1999**, *274* (47), 33320–33326. https://doi.org/10.1074/jbc.274.47.33320.

(47) Denoncin, K.; Collet, J. F. Disulfide Bond Formation in the Bacterial Periplasm: Major Achievements and Challenges Ahead. *Antioxidants Redox Signal.* **2013**, *19* (1), 63–71. https://doi.org/10.1089/ars.2012.4864.

(48) D.A. Case, D.S. Cerutti, T.E. Cheatham, III, T.A. Darden, R.E. Duke, T.J. Giese, H. Gohlke, A.W. Goetz, D.; Greene, N. Homeyer, S. Izadi, A. Kovalenko, T.S. Lee, S. LeGrand, P. Li, C. Lin, J. Liu, T. Luchko, R. L.; D. Mermelstein, K.M. Merz, G. Monard, H. Nguyen, I. Omelyan, A. Onufriev, F. Pan, R. Qi, D.R. Roe, A.; Roitberg, C. Sagui, C.L. Simmerling, W.M. Botello-Smith, J. Swails, R.C. Walker, J. Wang, R.M. Wolf, X.; Wu, L. Xiao, D. M. Y. and P. A. K. *Amber 2016 Reference Man*; 2016.

(49) Pettersen, E. F.; Goddard, T. D.; Huang, C. C.; Couch, G. S.; Greenblatt, D. M.;

Meng, E. C.; Ferrin, T. E. UCSF Chimera - A Visualization System for Exploratory Research and Analysis. *J. Comput. Chem.* **2004**, *25* (13), 1605–1612. https://doi.org/10.1002/jcc.20084.

(50) Brauner, D. J. Later than Sooner: A Proposal for Ending the Stigma of Premature Do-Not-Resuscitate Orders. *J. Am. Geriatr. Soc.* **2011**, *59* (12), 2366–2368. https://doi.org/10.1111/j.1532-5415.2011.03701.x.

(51) Peters, M. B.; Yang, Y.; Wang, B.; Füsti-Molnár, L.; Weaver, M. N.; Merz, K. M. Structural Survey of Zinc-Containing Proteins and Development of the Zinc AMBER Force Field (ZAFF). *J. Chem. Theory Comput.* **2010**, *6* (9), 2935–2947. https://doi.org/10.1021/ct1002626.

(52) Nagothu, R. S.; Rajagopalan, A.; Indla, Y. R.; Paluru, R. Beneficial Effects of Yogasanas and Pranayama in Limiting the Cognitive Decline in Type 2 Diabetes. *Natl. J. Physiol. Pharm. Pharmacol.* **2017**, *7* (3), 232–235. https://doi.org/10.5455/njppp.2017.7.0825508092016.

(53) Anandakrishnan, R.; Aguilar, B.; Onufriev, A. V. H++ 3.0: Automating PK Prediction and the Preparation of Biomolecular Structures for Atomistic Molecular Modeling and Simulations. *Nucleic Acids Res.* **2012**, *40* (W1). https://doi.org/10.1093/nar/gks375.

(54) Ryckaert, J. P.; Ciccotti, G.; Berendsen, H. J. C. *Numerical Integration of the Cartesian Equations of Motion of a System with Constraints: Molecular Dynamics of n-Alkanes*; 1977; Vol. 23. https://doi.org/10.1016/0021-9991(77)90098-5.

(55) Humphrey, W.; Dalke, A.; Schulten, K. VMD: Visual Molecular Dynamics. *Journal of Molecular Graphics*. 1996, pp 33–38. https://doi.org/10.1016/0263-7855(96)00018-5.

(56) Edwards, P. M. *Origin 7.0: Scientific Graphing and Data Analysis Software*; 2002; Vol. 42. https://doi.org/10.1021/ci0255432.

(57) Roe, D. R.; Cheatham, T. E. PTRAJ and CPPTRAJ: Software for Processing and Analysis of Molecular Dynamics Trajectory Data. *J. Chem. Theory Comput.* **2013**, *9* (7), 3084–3095. https://doi.org/10.1021/ct400341p.

(58) Connolly, M. L. *Solvent-Accessible Surfaces of Proteins and Nucleic Acids*; 1983; Vol. 221. https://doi.org/10.1126/science.6879170.

(59) Connolly, M. L. Analytical Molecular Surface Calculation. *J. Appl. Crystallogr.* **1983**, *16* (5), 548–558. https://doi.org/10.1107/s0021889883010985.

(60) Alderighi, L.; Gans, P.; Midollini, S.; Vacca, A. Co-Ordination Chemistry of the Methylmercury(II) Ion in Aqueous Solution: A Thermodynamic Investigation. *Inorganica Chim. Acta* **2003**, *356*, 8–18. https://doi.org/10.1016/S0020-1693(03)00317-7.

(61) Jawaid, M.; Ingman, F. Potentiometric Studies on the Complex Formation between Methylmercury(II) and Some Keto- and Amino-Carboxylic Acids. *Talanta* **1981**, *28* (3), 137–143. https://doi.org/10.1016/0039-9140(81)80001-X.

(62) Morby, A. P.; Hobman, J. L.; Brown, N. L. The Role of Cysteine Residues in the Transport of Mercuric Ions by the Tn501 MerT and MerP Mercury-resistance Proteins. *Mol. Microbiol.* **1995**, *17* (1), 25–35. https://doi.org/10.1111/j.1365-2958.1995.mmi_17010025.x.

(63) Sone, Y.; Uraguchi, S.; Takanezawa, Y.; Nakamura, R.; Pan-Hou, H.; Kiyono, M. A Novel Role of MerC in Methylmercury Transport and Phytoremediation of Methylmercury Contamination. *Biol. Pharm. Bull.* **2017**, *40* (7), 1125–1128. https://doi.org/10.1248/bpb.b17-00213.

(64) Kiyono, M.; Pan-Hou, H. The MerG Gene Product Is Involved in Phenylmercury Resistance in Pseudomonas Strain K-62. *J. Bacteriol.* **1999**, *181* (3), 726–730. https://doi.org/10.1128/jb.181.3.726-730.1999.

Chapter 6:

Thermodynamic Contributions of Metal-Swapping and Interdomain Interactions in Neuronal Metallothionein.

Published in Chemical Science, 2022: Mehlenbacher, M. R., Elsiesy, R., Lakha, R., Villones, R. L. E., Orman, M., Vizcarra, C. L., Meloni, G., Wilcox, D., & Austin, R. N. (2022). Metal Binding and Interdomain Thermodynamics of Mammalian Metallothionein-3: Enthalpically Favoured Cu^{+} Supplants Entropically Favoured Zn^{2+} to form Cu_4^{+} Clusters Under Physiological Conditions . *Chemical Science*. https://doi.org/10.1039/d2sc00676f

6.1. Introduction

6.1.1. An Introduction to Metallothionein.

Metallothionein (MT), discovered in horse renal (kidney) cortex in 1957 in a search for physiologically-relevant cadmium proteins, is a cysteine-rich protein that has been found in a wide-range of organisms with many different isoforms.[1,2] Metallothionein is a small (~60-75 amino acids), conformationally-dynamic protein that is composed of approximately 30-35% cysteine residues.[3,4] Although many different isoforms of MT have been characterized from different organisms, some with proposed physiological functions that are far different than those found in mammals, the general purpose of metallothionein is to bind metals ions. This metal-binding property drives varying function from metal storage and detoxification, to metal-swapping and cellular protection from the formation of reactive oxygen species (ROS).[5]

Mammals have 4 isoforms of MT: MT-1, MT-2, MT-3, and MT-4.[6] MT-1 and MT-2 have been implicated in zinc homeostasis and in the protection from toxic metals, like cadmium and mercury.[7,8] These are the metallothionein isoforms that were originally discovered by Bert Vallee in 1960. They are found in nearly all tissue types in mammals and are up-regulated in response to toxic metal exposure.[9] Unlike MT-1 and MT-2, MT-3 is only found in the brain.[10] Although the location of MT-3 is known, the function of MT-3 has been widely disputed, with numerous studies claiming neuron-growth inhibition, Cu^{+} or Zn^{2+} storage, Zn^{2+}-Cu^{+} homeostasis, ROS protection, metal-swapping, modulation of metal lead neurochemistry, and combinations of these functions.[5,10–12] Lastly, in mammals, the MT-4 isoform is primarily found in squamous epithelial (skin) cells, and is believed to be involved in Zn^{2+} homeostasis.[13]

Mammalian metallothioneins are composed of 2 distinct domains, the N-terminal β-domain and C-terminal α-domain, which have been found to bind three and four Zn^{2+}, respectively.[6,14,15] Binding of these metals results in the conformationally dynamic apo-protein to become less dynamic and have well defined metal-binding domains, through the formation of metal-thiolate clusters.[16,17] The dynamic nature of metallothionein, coupled with its abundance of metal-binding cysteine residues, allow the protein to bind a wide range of metal ions, forming metal-thiolate clusters. These clusters in the separate domains

are formed through a combination of terminal and bridging cysteine residues, leading to one- or two-coordinate cysteines. This is particularly evident with divalent metal ions, like Zn^{2+} and Cd^{2+}, which prefer tetrahedral geometries.[3,18] The preference for these metals to bind in a 4-coordinate tetrahedral tetrathiolate geometry drives the formation of the metal-thiolate clusters in the two domains, and define the metal:protein stoichiometry of Zn^{2+} and Cd^{2+} that can bind to metallothionein as 7 total, with 3 in the β-domain and 4 in the α-domain.[19] However, this well-defined metal-thiolate cluster formation that dictates how many metals will bind to metallothionein is much less effective in describing the interaction of metallothioneins with other metals, such as Hg^{2+} and Cu^{+}, that have greater flexibility in their coordination preference. Further complicating the binding of metal ions to metallothionein is the ability of different isoforms to bind in a homometallic or heterometallic structure, in which each domain bind the same metal or different metal, respectively. This heterometallic property is most notable for MT-3, than MT-1, MT-2, or MT-4.[20]

The two MT domains are linked, in mammals, by a short, 3 amino acid linker, lysine-lysine-serine (KKS), which provides a small separation between the two domains.[21] The length of this linker, however, is not consistent in other organisms, where its length can be upwards of 40 amino acids in length, separating these two domains. Although the purpose of this linker, beyond the fact that it tethers the two domains together, has not been determined, it is hypothesized that the separation between the domains with varying-linker lengths may modulate the interaction between the two domains. Closely tethered domains may influence inter-domain chemistry of the domains, whereas longer linkers may lead to more independent properties.

6.1.2. Physiological Function of MT-3.

As noted above, the physiological function of MT-3 is controversial and somewhat ambiguous. This is partially due to unusual features of the protein itself, segregating it from MT-1, MT-2, and MT-4, although they share ~70% sequence homology. When MT-3 was discovered, it was initially thought to belong to an entirely different class of proteins, and given the name neuronal growth-inhibitory factor (GIF), as its' expression is notably diminished in patients with Alzheimer's disease (AD) and it was found to inhibit neuron

growth and survival.[22] It is unsurprising that MT-3 has both metal-binding and ROS scavenging properties, as these functions are found with other metallothionein isoforms as well. However, MT-3 is particularly unique in that it contains two distinct amino acid regions that do not exist in other isoforms: a proline-rich region in the β-domain and an acidic hexapeptide insertion in the α-domain.[14,23] This proline-rich region (P7 and P9) has been shown to be required for its inhibitory function, since single- and double-mutants (P7S and P9A) of these proline residues are completely inactive.[23] These mutations show that the repeated cysteine-proline sequence (CPCPS) did not impacting metal-binding, but the structural features of the protein. The amino acid sequence (X-Pro; where×is any amino acid) is known to function as stiff "sticky-arms", mediating protein interactions, suggesting that this proline-rich region is involved with protein-protein interactions that are necessary for the inhibitory function of MT-3.[24] Unlike the proline-rich region, the hexapeptide acidic insert (EAAEAE) that is found in the α-domain appears to be important for the structural dynamics of MT-3. This acidic region increases the conformational stability of the α-domain, lowering the stability of the metal-cluster, and enhancing the overall solvent accessibility of the domain.[25]

Although this neuronal growth inhibitory function is well-documented, the metal-binding function of MT-3 and metal-related protein function is uncertain. Initially, due to its overall similarity to MT-1 and MT-2, it was proposed that the function of MT-3 was metal storage and the protection from toxic metals. However, this hypothesis has been disputed, primarily based on the evidence that MT-3 is not regulated by the exposure to toxic metals, like cadmium. Instead, MT-3 is up-regulated by hypoxia, a decrease in cellular oxygen.[2,5] Other studies have concluded that, due to MT-3's unique metal binding capabilities, it is a protein for control metal ions through their binding and delivery, effectively a metal buffer within the cell.[11] Although this may be a role of MT-3 in the brain, other metal-based functions may also be interconnected. For example, MT-3 is able to bind lead through its displacement of zinc.[10,26] Further complicating the proposed metal-binding function is the native metals of MT-3. As mentioned previously, MT-3 is generally found to be heterometallic, in that it is able to bind both Zn^{2+} and Cu^{+}. Indeed, when MT-3 is purified from the brain of mammals, it is found with 4 Zn^{2+} bound to the α-domain and 3-4 Cu^{+} bound to the β-domain.[27–29] This heterometallic character of MT-3 would suggest

that the metal binding properties of the α- and β-domains are distinctly different, due to preferential binding of Zn^{2+} and Cu^{+} to their respective domains. This has led to an intriguing hypothesis that one of the functions of MT-3 involves metal-swapping, in which it binds a redox-active metal, like copper, and replaces it with a redox-inactive zinc to eliminate the formation of ROS that arise from neuronal copper-protein interactions.[5]

6.1.3. Metal-Swap Hypothesis: Function of MT-3 in Neuronal Copper Chemistry.

Beyond the neuronal growth inhibitory function of MT-3, a wide range of roles relating to the metal-binding properties of the protein have been proposed. One such proposal directly correlates the finding that MT-3 expression is significantly diminished in patients with neurological degeneration from Alzheimer's disease (AD) and the ability of MT-3 to reduce ROS formation.[4,29–31] A prominent outcome of AD is the formation of neurofibrillary tangles and amyloid plaques, which are found outside of the neuron and are protein aggregates, composed of a small peptide called Aβ.[32]

This peptide, under normal conditions, can be found in many different oligomeric states (monomer, fibrils, aggregates, etc.), and the kinetics of the formation of these oligomeric states favors the less detrimental monomeric and fibrillary oligomers with very slow aggregation.[33,34] However, the amino acid composition of this peptide, along with its conformationally-dynamic nature, also favors the binding of metal ions, including Zn^{2+}, Cu^{2+}, Fe^{2+}, and other borderline Lewis acids via aspartic acid and histidine residues. Binding of these metals alters the kinetic favorability of the oligomeric states such that the peptide will favor aggregates, leading to the formation of amyloid plaques. Aggregation of these peptides is further complicated by the addition of redox-active metal ions such as Cu^{2+} and Fe^{2+}, which enhance ROS formation. [35–38] Under normal conditions, in which the expression of MT-3 is not diminished, it has been proposed that MT-3, due to its heterometallic nature, will chelate the redox-active metal, Cu^{2+}, and replace it with the redox-inactive Zn^{2+}.[5] Subsequently, this Cu^{2+} is then reduced to Cu^{+} and a pair of cysteines are oxidized to form disulfide bonds. Evidence suggests that the replacement of Cu^{2+} with Zn^{2+} does not alter the favored oligomeric states, it does eliminate the formation of damaging ROS.

At the intersection of neuronal metallothionein, amyloid plaques, and neurodegenerative diseases, is the fact that MT-3 expression levels are significantly reduced in patients that have AD. Thus, a decrease in MT-3 leads to a decrease in this metal-swapping mechanism, diminishing the replacement of Cu^{2+} by Zn^{2+}, and, inevitably, enhancing the formation of ROS, resulting in greater cellular damage and progressive neurodegeneration. Although this is discussed through the lens of Alzheimer's disease, other aggregation-prone neurological peptides exhibit a similar phenomenon including α-synuclein (α–syn), associated with Parkinson's disease, and Prion proteins (PrP), associated with Creutzfeldt-Jacob syndrome.[35–38]

6.1.4. Metal-Binding Properties of Metallothionein-3.

Given that the bulk of metallothionein, including MT-3, is composed of cysteine residues, it is not surprising that this protein is capable of binding a wide range of borderline and soft Lewis acid metals. Although it appears as if Zn^{2+} and Cu^{+}/Cu^{2+} are physiologically relevant to MT-3, other metals may also bind. To better understand the physiological role of MT-3, it is useful to initially discuss the bioinorganic chemistry of the interaction between native and non-native metals with MT-3.

As previously mentioned, apo-MT-3 is very conformationally dynamic, and occasionally included within a group of proteins known as intrinsically disordered proteins (IDPs). Being a conformationally-dynamic protein provides some hints as to the type of interactions that MT-3 would have with different metal ions. This dynamic nature of the structure of MT-3 in solution has far-reaching implications in metal binding, both from a coordination and thermodynamic perspective. MT-3 has 20 total cysteine residues, 9 in the β-domain and 11 in the α-domain. Zinc tends to form a 4-coordinate tetrahedral geometry, so the dynamic nature of the protein would not necessarily be playing a role, as Zn^{2+} will bind until all bridging and terminal cysteine bonds are occupied. However, Cu^{+} is much more flexible, in which 2-, 3-, and 4-coordinate complexes are routinely found in nature. Thus, the dynamic nature of metallothionein does not restrict Cu^{+} coordination, *in-vitro*. These metal-bonding differences of Zn^{2+} and Cu^{+} lead to metal:protein stoichiometries of 7–Zn^{2+}, and 6–, 8–, 10–, 12–, 14–, and/or 20–Cu^{+}. Although these metal stoichiometries are accessible under *in-vitro* conditions, *in-vivo* metalation tends to be much more

restricted.[39] This is due, in part, to cellular metal concentrations and competing ligands like glutathione, but also to the nature of metal binding. For example, the binding of Cu^{2+} to MT-3 results in the oxidation of two cysteine residues and the subsequent reduction of Cu^{2+} to Cu^{+}, thus limiting the number of Cu^{+} that are able to bind to the protein.

Unsurprisingly, given the metal-binding properties of cysteine residues, other metals, both native and non-native, are able to bind to metallothionein. The binding of Cd^{2+} to metallothionein, with a similar coordination preference as Zn^{2+}, results in 7 bound Cd^{2+}, 4 in the α-domain and 3 in the β-domain, although the overall protein conformational dynamics have been proposed to be different.[1,7,40,41] The binding of Hg^{2+}, however, tends to be more similar to the binding of Cu^{+}. The preferred coordination of Hg^{2+} also tends to be more flexible, with 2-coordinate, 3-coordinate, and 4-coordinate geometries. As such, up to 18 Hg^{2+} are able to bind to human metallothionein, with structures containing 7 Hg^{2+}, 12 Hg^{2+}, then the 18 Hg^{2+} complex.[8] Most similar to Cu^{+}, although not likely to be a native metal of metallothionein, is Ag^{+}, which show varied metal:protein stoichiometries ranging from 3 to 9.[42,43] Beyond these metals, many others have been shown to bind as well including Au^{+}, As^{3+}, Bi^{3+}, and Pt^{2+}.[43,44]

Since the discovery of metallothionein in 1957, many attempts have been made to quantify the binding affinities of various metals. As such, many different association constants, under varying experimental conditions and using a wide range of techniques, have been reported. These binding affinities provide insight into the physiological function of the protein, particularly when they are compared to those of other cellular metalloproteins. A summary of these results is found elsewhere.[10] Of particular importance to this work is the association constants of Zn^{2+} and Cu^{+}. Although measurements of the MT affinity for Zn^{2+} have suggested domain-dependent binding or sequential metal binding, the general consensus is that the binding constant for the most tightly bound Zn^{2+} is approximately $10^{11\text{-}12}$, at physiological pH. Each subsequent Zn^{2+} is bound equal to or less tightly to the protein. The MT binding constants for Cu^{+} have been equally challenging, mostly due to Cu^{+} air sensitivity and flexible bond coordination, resulting in a broad range of binding constants from 10^{14} to 10^{21}, under physiological pH.[45] Although binding constants of these various metals have been reported, the enthalpic and entropic

contributions to metal binding have yet to be determined, with the sole exception of the thermodynamics of Pb^{2+} and Zn^{2+} binding to MT-3 under acidic conditions.[10]

6.1.5. Structural Dynamics and Folding of Apo- and Metalated-Metallothionein

The conformational dynamics of metallothionein are complex, due to its disordered nature in the absence of metals and interdomain interactions that are not entirely understood. Apo-Metallothionein, in particular, has no secondary structure, resulting in large degrees of freedom in the dynamics of the protein. Historically, this demetallated form of metallothionein, called thionein, was thought to be unstable, as it has high rates of degradation in rat liver samples.[46] Utilizing computational techniques, thionein has been found to have hydrogen bond stabilization of the whole structure, although it maintains a high-degree of flexibility. These computational results have suggested that the overall structure is more compact than that of the metallated-form.[16,47,48] Although these results suggest that thionein is more compact, it has been shown, computationally, that the overall volume is similar to the less-compact metalated-metallothionein.

Metalation of thionein to metallothionein has been shown to occur via metal-dependent protein folding. Initial binding of a metal to exposed cysteine residues results in buried cysteines moving towards the solvent, allowing for more metals bind. This metal-bound structure, however, has been shown to be less compact than that of thionein, although this has not, to the best of my knowledge, been probed experimentally under physiologically conditions. Under very acidic conditions, in the gas-phase, experimental evidence supports the proposed hypothesis of the computational data. Binding of metal ions to metallothionein, seems to stabilize the structure of the protein, resulting in the two well-defined α- and β-domains.

Curiously, the formation of these metal-thiolate clusters in the separate domains is much more convoluted, as spectroscopic studies of metallothionein are very difficult. Furthermore, other techniques, such as mass spectrometry, provide results that are in the gas-phase and may not be applicable to solution-based chemistry. The metal-thiolate cluster formation is also metal-dependent, due to the coordination preferences of each metal. Furthermore, this metal binding, and metal-dependent protein folding has been controversial. Condition-dependent metal binding and metal-protein interactions have

suggested both cooperative and non-cooperative metal binding in a pH-dependent manner. This is more complex due to the nature of these metal-stabilized domains, in which some studies have suggested that each domain is filled independently, while others have suggested a sequential binding that is not domain-dependent.

Connecting both metal-dependent folding and the overall compactness of the apo and metalated structures of metallothionein, along with condition-dependent metal-thiolate cluster formation, is the inter-domain interactions that may govern some of these condition-dependent changes. The two domains, which are connected by a three-residue linker (KKS), may play a role in altering metal-binding and metal-dependent function. These interdomain interactions, however, have been studied very little, so not much is known about the importance of this linker or how the two domains interact to impact the physiological function of MT-1/2 or MT-3. One study that aimed at understanding the function of this linker on MT function systematically expanded the 3-residue linker of MT-2 and observed changes to metal resistance. It was hypothesized that an increase in linker length would increase the overall flexibility of the two domains, leading to the two domains acting independently of each other. Metal-resistance markedly decreased with increasing linker length, although increasing the linker-length resulted in protein instability.[49] Another study utilized kinetic data on the seaweed *Fucus vesiculosus* MT with a long, ~40 residue linker, compared to the mammalian MT with the short, 3 residue linker. This study suggested that the shorter linker led to more rapid metalation, in which the two domains function as a unit, whereas the longer linker more effectively separated the two domains, resulting in slower, independent metalation of the two domains.[44] These results, taken together, suggest that this linker-region can directly impact the metalation and physiological function of the protein, although the extent of this impact on cellular function remains unknown.[50]

6.1.6. Thermodynamic Foundation of Metal-Swapping and Interdomain Contributions to Metal Binding in Metallothionein-3.

This work has three primary objectives: (1) to establish the binding thermodynamics of the physiologically relevant metals, Zn^{2+} and Cu^{+} to neuronal MT-3 and make a comparison to MT-2, (2) to quantify the thermodynamics associated with the

interdomain interactions and the contribution of this interaction to metal-binding, and (3) to deconvolute the metal binding thermodynamics from the protein-contribution to metal binding. Using isothermal titration calorimetry (ITC), the entire thermodynamics for Zn^{2+} and Cu^{+} binding to full-length MT-3, and the separated α- and β-domains were determined. The binding of Cu^{+} to MT-2 was also quantified in order to better understand differences between MT isoforms. These thermodynamic data set the inorganic foundation for the metal-swap hypothesis of the function of MT-3 and provides, for the first time, the thermodynamics of Zn^{2+} and Cu^{+} binding to MT-3 under physiological conditions of pH 7.4. The thermodynamics of the interdomain interaction were determined through Zn^{2+} binding to the separate domains, compared to the full-length protein. Lastly, utilizing known thermodynamic values for similarly-coordinated Zn^{2+} found with a tetrathiolate, glycine-rich peptide, the thermodynamics of metal binding to MT-3 was separated into the protein-folding contribution and the metal coordination contribution, providing valuable insight into the thermodynamics of metal-dependent protein folding.

6.2. Materials and Methods

6.2.1 Chemicals and Materials

Full-length MT-2, MT-3, and the α- and β-domains of MT-3 were generously gifted by our collaborators and utilized as received. All buffers were purchased and used at the highest purity without further treatment as were metal salts, reduced L-glutathione (GSH), ethylenediaminetetraacetic acid (EDTA), and diethylenetriaminepentaacetic acid (DTPA). Buffers were prepared with nanopore (18 MΩ) water in acid-washed glassware and subsequently treated with Chelex 100® cation exchange resin overnight to ensure that buffers were metal-free. Buffers were then filtered and subsequently degassed under vacuum with stirring for at least 1 hour, or until no bubbles were formed, and moved into an anaerobic glovebox with a N_2 and H_2 environment. Chelator and metal stock solutions were prepared in oxygen-free buffers and stored in the glovebox for use. These solutions were made and stored in the glovebox for several weeks. Their concentrations were confirmed by isothermal titration calorimetry (ITC) by titrating the metal into a known concentration of EDTA and verifying that the stoichiometry and enthalpy matched those

in the literature. Similarly, chelator stock solution concentrations were confirmed by titrating a metal of known concentration into the chelator by ITC and, again, determining the chelator concentration with the binding stoichiometry and verifying that the experimental thermodynamics matched the thermodynamics previously reported. Stock solutions of GSH were made fresh for each experiment.

6.2.2 Isothermal Titration Calorimetry: Data Collection and Analysis

For isothermal titration calorimetry (ITC) experiments, protein concentrations were used as received. Zn^{2+} chelation experiments were done by titrating the chelator at a concentration of 120-140 times the concentration of the protein (~600-700 μM), into Zn_7MT-3 (~5 μM). In the Cu^+ binding experiments, GSH is present at concentrations of 10:1 GSH:Cu^+ (equivalent to 2000:1 GSH:MT-3), and the Cu^+ concentration is approximately 200 times the concentration of the protein (~500 μM Cu^+ and 2.5 μM MT-3). All ITC experiments used the same buffer in both the cell and syringe to minimize heat from buffer mismatch. Experiments were performed on a Malvern Panalytical MicroCal VP-ITC within a custom-made plexiglass glovebox under a N_2 environment,which was maintained before and throughout the ITC experiments through constant purging. ITC experiments were done at 25 ± 0.2 ºC and stirred at a constant rate of 307 or 437 RPM. Typical experiments added a volume of 4-12 μL per injection of titratnt with a spacing between each injection of 240 – 600 seconds. Heat generated from the final injections defined the heat of dilution, which is subtracted from each injection. ITC data is presented such that the baseline adjusted heat flow vs. time raw data is in the upper panel and the integrated, concentration-normalized, heat of injections vs. molar ratio of ligand-to-protein (syringe-to-cell) is presented in the lower panel. Downward and upward peaks in the upper panel represent exothermic and endothermic binding, respectively. All data were analyzed using the appropriate binding model (one-site or two-site) provided by Origin 7.0 data analysis software. The reported thermodynamic values represent the average and standard deviations of at least three independent measurements, unless otherwise stated. Explanation and derivation of the general *post-hoc* analysis can be found in Chapter 2.

6.3. Results and Analysis

In-vitro metal binding measurements provide valuable insight into metal-protein interactions. Isothermal titration calorimetry (ITC) is a valuable tool to determine metal-binding thermodynamics in a single experiment: stoichiometry (n_{ITC}), apparent binding enthalpy (ΔH_{ITC}), and the apparent equilibrium constant (K_{ITC}). The accuracy of these values depends on known ligand and protein concentrations for the experimental stoichiometries and binding thermodynamics. However, thermodynamic values obtained by ITC are the sum of all events that occur in the. Cell and include protonation, deprotonation, metal-buffer interactions, etc.[51,52] These additional competing and coupled events must be accounted for in the apparent thermodynamics. Subtracting the thermodynamics of these events allows for the calculation of the buffer-independent metal-protein thermodynamics at pH 7.4.

The direct binding of metals to apo or demetallated metallothionein is challenging due to the large number of cysteine residues and their propensity to oxidation. To ensure protein stability, metallothionein samples were prepared with seven Zn^{2+} bound (Zn_7MT-3). A solution structure of mouse MT-1 with seven Cd^{2+}, which is an approximation of Zn-bound human MT-3, is shown in **Figure 6.3.1**. To overcome the inability to do direct metal binding and determine the metal-binding thermodynamics of a protein sample that is already bound with a stabilizing metal, two methods to detect the binding of Zn^{2+} and Cu^{+} to MT were developed: (1) chelation of Zn^{2+} with a metal chelator and (2) the direct titration of Cu^{+} after displacement of the bound Zn^{2+} by a large excess of GSH. The former of these two methods utilizes the concept of microscopic reversibility, such that the thermodynamics of the forward and backward reaction should be equivalent, but opposite sign.[52,53] The latter of these two methods utilizes reduced glutathione to stabilize Cu^{+} and also to chelate the Zn^{2+} from metallothionein, such that Cu^{+} binds to the demetallated protein. Metal-free metallothionein is stable for short durations (i.e., the duration of the sample preparation and ITC experiments), and no evidence of protein precipitation was noted in the collected ITC isotherms (excessive heats, large signal-to-noise ratios, excessive baseline drift, etc.).

6.3.1 Thermodynamics of Zinc Binding to Metallothionein-3

The DTPA chelation experiments that were used to determine the Zn^{2+} binding

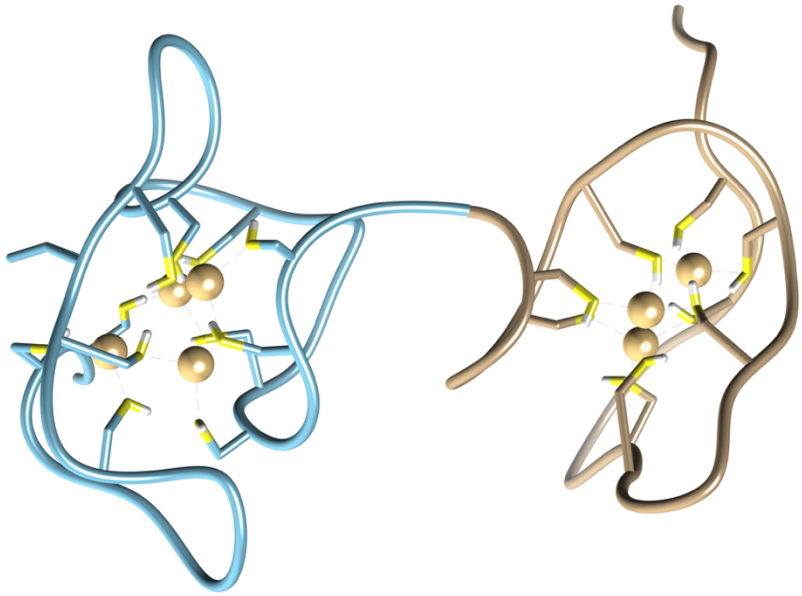

Figure 6.3.1*.Combined NMR structures of the α- and β-domains of mouse metallothionein-1 (MT-1) bound with* Cd^{2+}*. The α-domain, in blue, is composed, primarily, of 11 cysteine residues that bind 4* Cd^{2+} *ions in a tetrahedral geometry. The β-domain, in tan, is composed of 9 cysteine residues that are able to bind 3* Cd^{2+} *ions in a tetrahedral geometry. These two domains are linked by a short, lysine-lysine-serine (KKS) linker. Domains were solved separately, and modified in Chimera to show an approximation of the full-length protein.*[15,68] *(PDB: 1DFS, 1DFT)*

thermodynamics, are unusual in that there are two binding events (**Figure 6.3.1.2**). The stoichiometry of the first inflection is equivalent to the number of Zn^{2+} that are bound to the protein. The second binding event indicates a higher order complex forms when excess DTPA is added and is unrelated to the chelation of Zn^{2+} from the protein. Control experiments where DTPA is titrated into Zn^{2+} without the protein show similar sequential binding events (**Figure 6.3.1.1**).

Complexation of divalent metals by DTPA was characterized by Chaberek and coworkers who determined the structure of Cu^{2+} bound to DTPA (1:1) and suggested that a similar complex would be formed with Zn^{2+}. A complex where two Cu^{2+} were bound to one DTPA (2:1 complex) was also proposed at pH 7.4[54] Our thermodynamic analysis of the Zn^{2+}–MT-3 interaction only includes the first binding event, which is DTPA chelating Zn^{2+} (1:1 stoichiometry) from the protein. The second binding event is not included, as this is not related to the Zn-protein interaction, and corresponds to a 3:2 complex of Zn^{2+}:DTPA. This 3:2 complex was not described by Chaberek and coworkers, though their proposed 2:1 complex shows an open coordination site on the second metal, filled by a water molecule, that would be able to bind to a second metal-bound DTPA.

Quantification of the thermodynamics of the Zn–MT-3 interaction used the metal chelator DTPA, which chelates Zn^{2+} from the protein, as shown in the equilibrium **Equation 6.3.1.1 – 6.3.1.3**.

$$Zn_7MT3 + (DTPA)_7 \; + \; H_X^+ \rightleftharpoons \; MT3 - \; H_X + (Zn - DTPA)_7 \qquad \boldsymbol{Equation\ 6.3.1.1}$$

$$Zn_4\alpha MT3 + (DTPA)_4 \; + \; H_X^+ \rightleftharpoons \; \alpha MT3 - \; H_X + (Zn - DTPA)_4 \qquad \boldsymbol{Equation\ 6.3.1.2}$$

$$Zn_3\beta MT3 + (DTPA)_3 \; + \; H_X^+ \rightleftharpoons \; \beta MT3 - \; H_X + (Zn - DTPA)_3 \qquad \boldsymbol{Equation\ 6.3.1.3}$$

The representative thermogram that resulted from the titration of DTPA into full-length Zn_7–MT-3 has two distinct binding events, as shown in **Figure 6.3.1.2**. The binding event has been fit with a one-site binding model, as this is the binding event in which DTPA chelates Zn^{2+} from MT-3. The average experimental values for the first binding event in three separate buffers (HEPES, BisTris, and TAPSO) are shown in **Table 6.3.1.1**. Thermodynamic values were determined using known concentrations of protein, metal, and chelator, which confirms the anticipated metal stoichiometry of 7 Zn^{2+} bound to metallothionein-3.

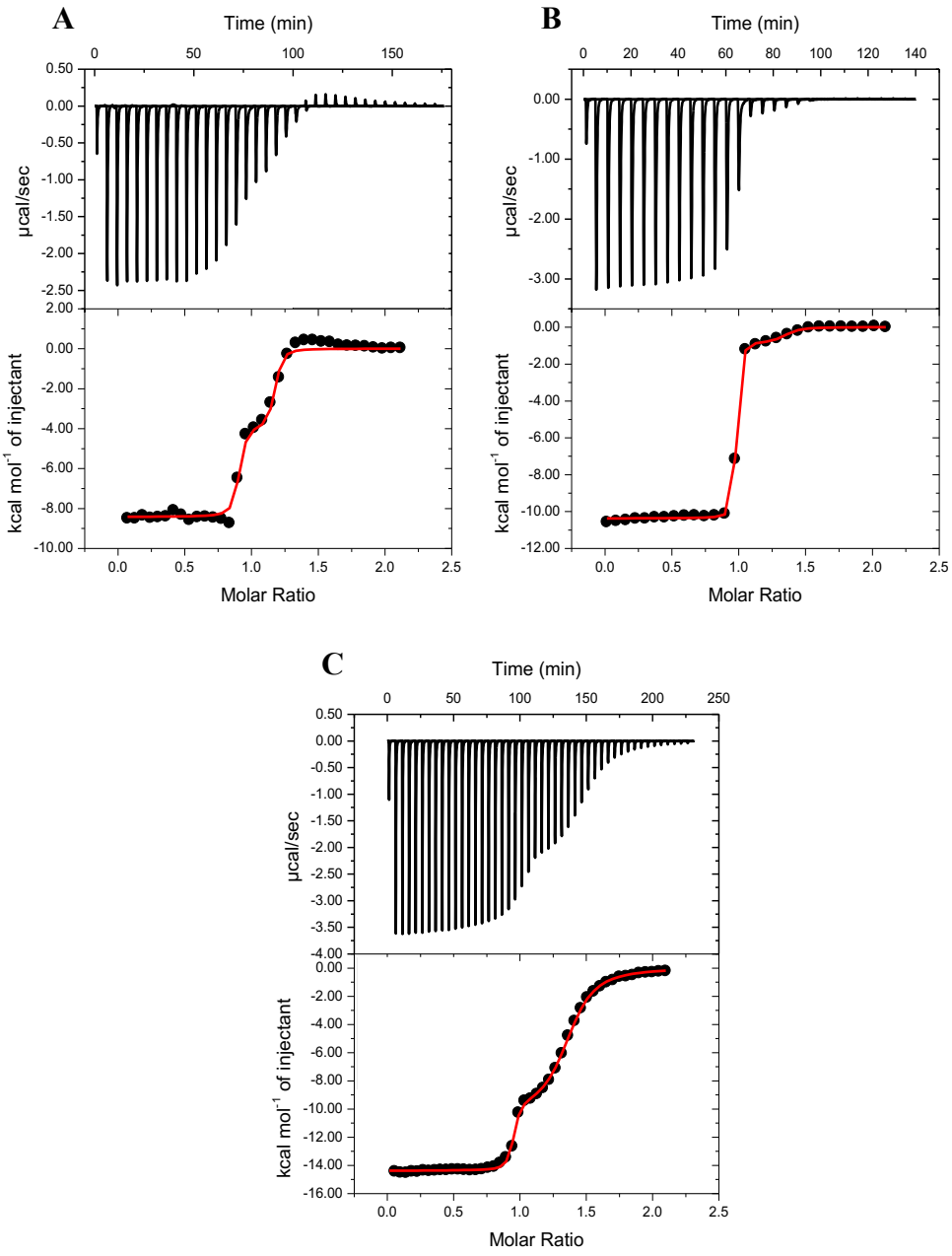

Figure 6.3.1.1. Binding isotherms for DTPA titrated into Zn^{2+} in (A) HEPES, (B) Bis-Tris, and (C) TAPSO buffers, with a fit to a 2-sites binding model. The first event (n = ~1) is the formation of the 1:1 DTPA-Zn^{2+} species, followed by an event (n ~ 0.5) that is subsequent formation of a 3:2 DTPA:Zn^{2+} species. Titrations are in 100 mM buffer and 150 mM NaCl at pH 7.4

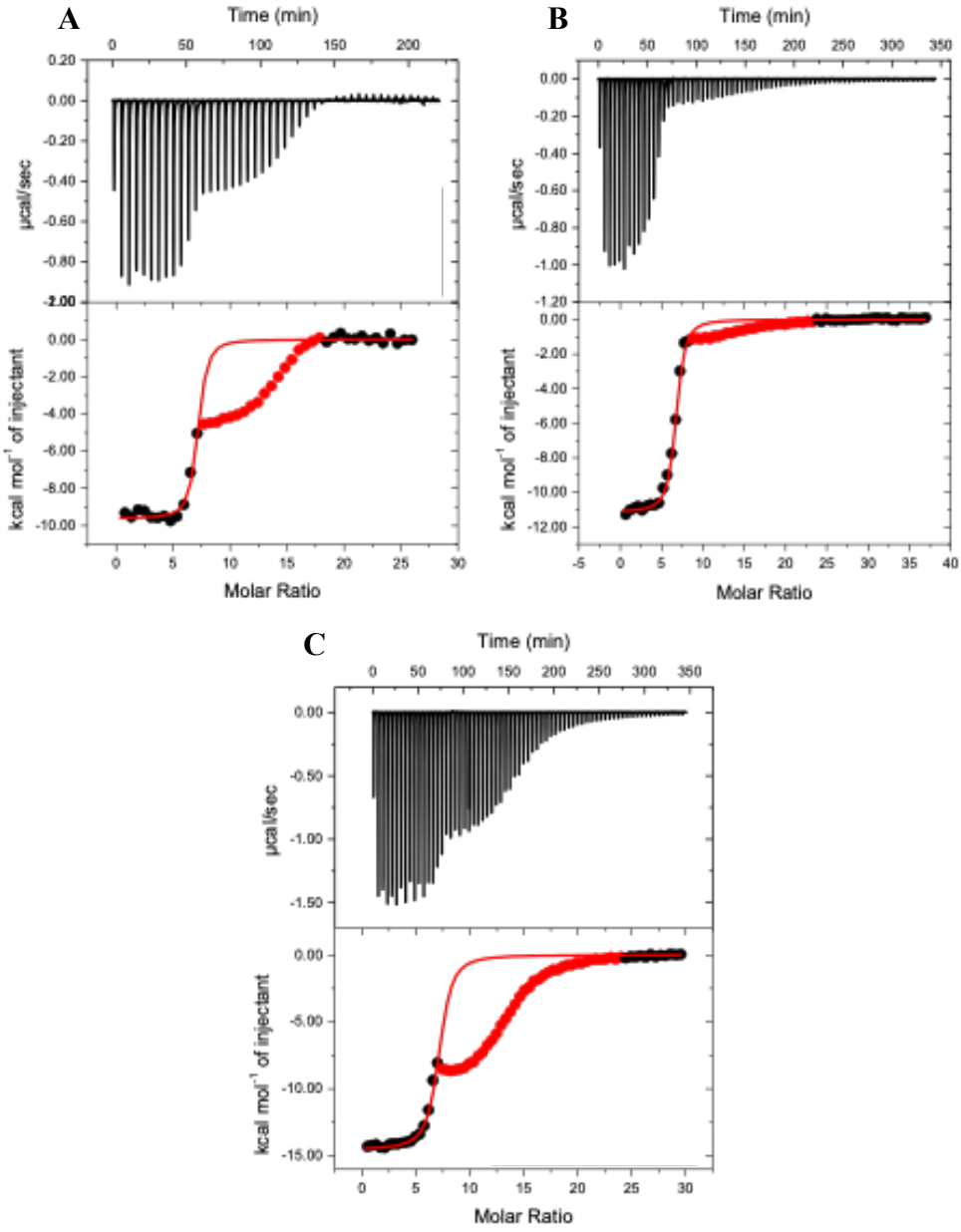

Figure 6.3.1.2. *Representative thermograms of the chelation of Zn^{2+} from Zn_7MT-3 with DTPA in 100 mM buffer, 150 mM NaCl pH 7.4, each fit with a one-site binding model. (A) HEPES: n_{ITC} = 6.90 ± 0.05, K_{ITC} = 1.27 (± 0.09)×10^7, ΔH^o_{ITC} = -9.5 ± 0.2 kcal/mol; (B) BisTris: n_{ITC} = 6.5 ± 0.1, K_{ITC} = 1.1 (± 0.3)×10^6, ΔH^o_{ITC} = -11.0 ± 0.2 kcal/mol; and (C) T APSO: n_{ITC} = 7.08 ± 0.06, K_{ITC} = 4.5 (± 0.6)×10^6, ΔH^o_{ITC} = -14.1 ± 0.7 kcal/mol*

Table 6.3.1.1. *Averaged apparent thermodynamic values for the chelation of Zn^{2+} from Full-length MT3-Zn_7,* α-MT3–Zn_4, and β-MT3Zn_4 *with DTPA. Values are average thermodynamics values for at least 2 independent experiments. Experimental data shown is the data collected from the first binding event, which is the chelation of Zn^{2+} from the protein.*

Protein	**Buffer**	**n_{ITC} Stoichiometry**	**K_{ITC}**	**ΔH_{ITC} (kcal/mol)**
Full-Length MT3–Zn_7	**HEPES**	6.90 ± 0.05	1.27 (± 0.09)×10^7	-9.5 ± 0.2
	BisTris	6.5 ± 0.1	1.1 (± 0.9)×10^7	-11.0 ± 0.2
	TAPSO	7.08 ± 0.06	4.5 (± 0.6)×10^6	-14.1 ± 0.7
α-MT3–Zn_4	**BisTris**	4.4 ± 0.3	9 (± 5)×10^7	-10.1 ± 0.6
	TAPSO	4.2 ± 0.2	6.5 (± 0.3)×10^6	-14.1 ± 0.1
β-MT3–Zn_3	**BisTris**	2.6 ± 0.1	2.8 (± 0.6)×10^7	-10.9 ± 0.5
	TAPSO	2.8 ± 0.2	4 (± 1)×10^6	-14.1 ± 0.4

Chelation experiments with the separated α– and β–domains of MT-3 (αMT-3 and βMT-3, respectively) were done with a similar experimental design as the full-length protein. The competing equilibria of the chelation of Zn^{2+} from αMT-3 and βMT-3 are shown in **Equation 6.3.1.2** and **6.3.1.3**, respectively. The representative thermograms that result from the chelation of Zn^{2+} from the individual domains of MT-3 also show two distinct binding events (**Figure 6.3.1.3**). Similar to the full-length MT-3 chelation experiments, the isotherm has been fit with a one-site binding model, where the first binding event is analyzed as this is due to the chelation of Zn^{2+} from MT-3. The second binding event, corresponding to further DTPA-Zn^{2+} complexation is not included in the analysis, in TAPSO, or not quantifiable, in BisTris. Apparent thermodynamic values for the αMT3 and βMT-3 in two buffers, BisTris and TAPSO, are shown in **Table 6.3.1.1**.

The apparent thermodynamic values that are obtained from the ITC experiments require additional analysis due to the competing equilibria, which are taken into account in a *post-hoc* analysis. Specifically, the competing equilibria for DTPA into Zn_7–MT-3 include the deprotonation of DTPA (ΔH_{LH1} and ΔH_{LH2}), buffer protonation (ΔH_{BH}), binding of Zn^{2+} to DTPA (ΔH_{ML}), protonation of MT-3 (ΔH_{PH}), and dissociation of Zn^{2+} from MT-3 (ΔH_{MP}) (**Scheme 6.3.1.1**). The sum of the enthalpies of each of these events, due to Hess's Law, equates to the apparent heat (ΔH_{ITC}) observed in the ITC experiment. Each of these events is replicated for each metal ion that is bound to the protein. The breakdown of the competing equilibria for αMT-3 and βMT-3 are similar to that of the full-length protein, with the exception of the number of Zn^{2+} that are chelated from the protein upon the addition of DTPA (**Table 6.3.1.1**). Quantification of the number of protons bound to the protein is essential for this analysis. By rearranging the **Equation 6.3.1.4.** for the experimental enthalpy (ΔH_{ITC}), the enthalpy associated with buffer protonation can be plotted against the experimental enthalpy, where the slope of the plot is equal to the number of protons binding to or leaving the buffer (**Figure 6.1.3.4**).

To determine the buffer-independent equilibrium constant at pH 7.4, the equilibrium constants of the competing equilibria must be considered, just as they were in the determination of the binding enthalpy (See *Post-hoc* Analysis in Chapter 2). The results of the buffer-independent, proton-corrected thermodynamic analysis of Zn^{2+} binding to Full-length, αMT-3, and βMT-3 at pH 7.4 are shown in **Table 6.1.3.2**. As a means of

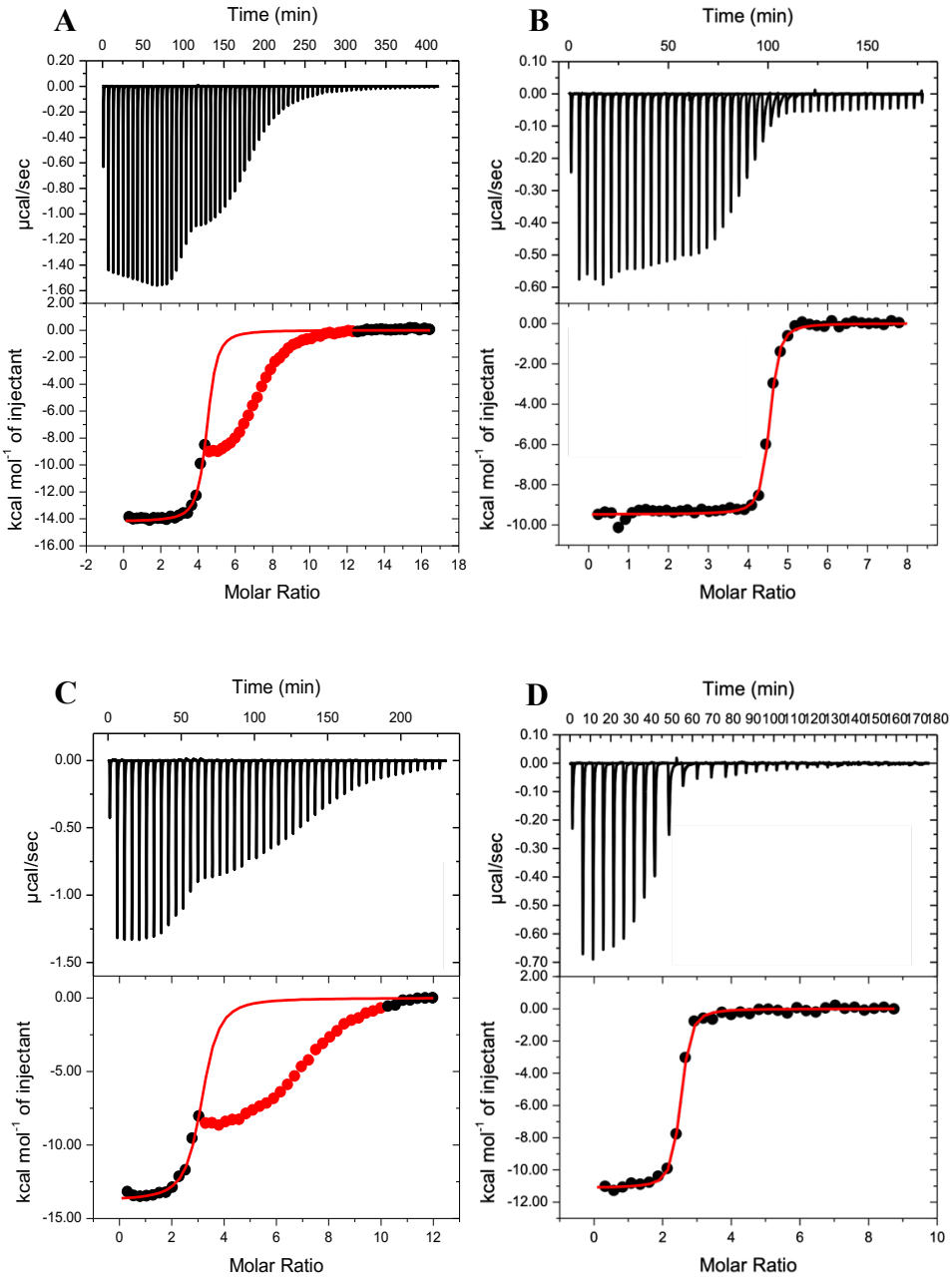

Figure 6.3.1.3. Representative isotherms for the DTPA chelation of Zn^{2+} in 100 mM TAPSO buffer and 150 mM NaCl at pH 7.4; data for the second event are masked (red) and data for the first event were fitted (solid line) to a one-site binding model with the best-fit values and fit errors: **A.** Zn_4αMT-3 (TAPSO): $n_{ITC} = 4.39 \pm 0.02$, $K_{ITC} = 6.7 (\pm 0.9) \times 10^6$ and $\Delta H_{ITC} = -14.19 \pm 0.06$ kcal/mol; **B.** Zn_4αMT-3 (BisTris): $n_{ITC} = 4.46 \pm 0.007$, $K_{ITC} = 7.1 (\pm 0.8) \times 10^6$ and $\Delta H_{ITC} = -9.47 \pm 0.04$ kcal/mol; **C.** Zn_3βMT-3 (TAPSO): $n_{ITC} = 3.07 \pm 0.04$, $K_{ITC} = 4.1 (\pm 0.9) \times 10^6$ and $\Delta H_{ITC} = -13.8 \pm 0.1$ kcal/mol; **D.** Zn_4βMT-3 (BisTris): $n_{ITC} = 2.41 \pm 0.009$, $K_{ITC} = 2.6 (\pm 0.3) \times 10^7$ and $\Delta H_{ITC} = -11.11 \pm 0.007$ kcal/mol.

Scheme 6.3.1.1. Relevant equilibria for DTPA chelation of Zn^{2+} from Zn_7MT-3 at pH 7.4. DTPA has two relevant pK_a's: 8.60, which provides 0.91 H^+, and 10.55, which provides 1.0 H^+. ΔH_{ML} is the enthalpy of the metal (M) – ligand (L) interaction, ΔH_{LH1} and ΔH_{LH2} are the enthalpies of deprotonation of the ligand (H_1 and H_2), ΔH_{PH} is the enthalpy of the protonation of the protein (P), ΔH_{BH} is the enthalpy of buffer (B) protonation, and ΔH_{MP} is the enthalpy of the desired metal-protein interaction.

$$7\ DTPAH^{+}_{1.91} + Zn^{2+}{}_7MT\text{-}3 + (13.4\text{-}X)\ Buffer \leftrightarrows 7\ Zn^{2+}DTPA + MT\text{-}3H^{+}_X + (13.4\text{-}X)\ BufferH^{+}$$

$DTPA + Zn^{2+} \leftrightarrows Zn^{2+}DTPA$	$7 \times \Delta H_{ML}$
$DTPAH^{+}_2 \leftrightarrows DTPAH^{+} + H^{+}$	$-7 \times \Delta H_{LH1}$
$DTPAH^{+} \leftrightarrows DTPA + H^{+}$	$-6.37 \times \Delta H_{LH2}$
$MT\text{-}3 + H^{+} \leftrightarrows MT\text{-}3H^{+}$	$X \times \Delta H_{PH}$
$B + H^{+} \leftrightarrows BH^{+}$	$(13.4 - X) \times \Delta H_{BH}$
$Zn^{2+}MT\text{-}3 \leftrightarrows MT\text{-}3 + Zn^{2+}$	$-7 \times \Delta H_{MP}$

$$\Delta H_{ITC} = 7\Delta H_{ML} - 7(\Delta H_{LH1}) - 6.37(\Delta H_{LH2}) + (13.4 - X)\,\Delta H_{BH} + X(\Delta H_{PH}) - 7\Delta H_{MP} \qquad \textbf{\textit{Equation}}\ \mathbf{6.3.1.4.}$$

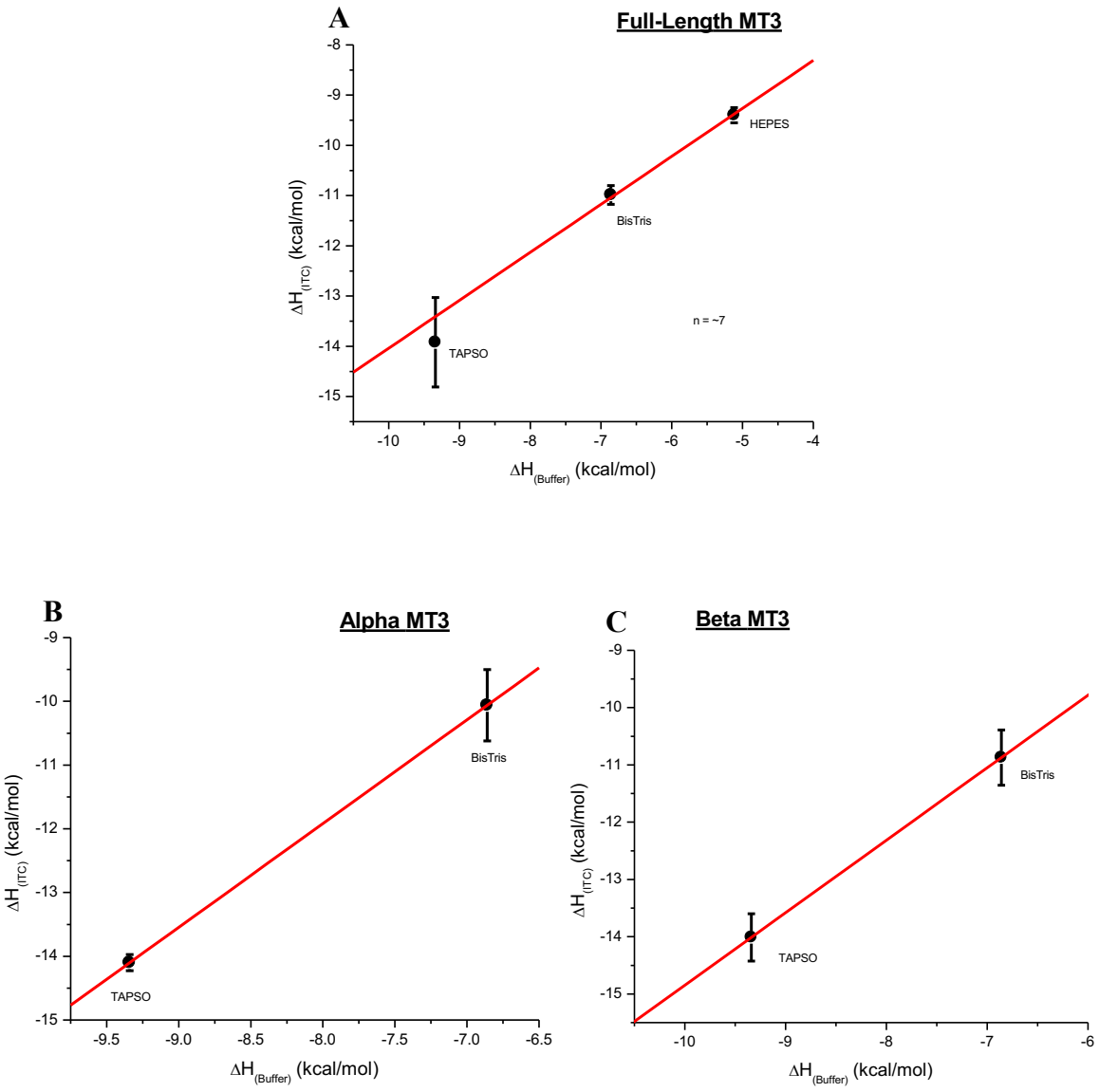

Figure 6.3.1.4. *Proton plots for the chelation of Zn^{2+} from (A) Full-Length MT-3, slope = +1.0 ± 0.1, (B) α-MT-3, slope = +1.6, and (C) β-MT-3, slope = +1.3 with DTPA. By plotting the enthalpy of buffer protonation vs. the experimental enthalpy obtained by the ITC experiments, the slope defines the change in protons with respect to the buffer. Proton inventories are found in the insert of each proton plot and determine the number of protons that bind to the protein upon Zn^{2+}dissociation.*

Table 6.1.3.2. *Average thermodynamic values for the Zn-MT-3 interaction determined by the chelation of Zn^{2+} from Zn_7MT-3 by DTPA. Buffer-independent, proton-corrected thermodynamic values obtained through the* post-hoc *analysis at pH 7.4, taking into account all relevant competing equilibria. These values are the thermodynamics on a per-metal basis which includes the proton competition for each metal ion. ΔΔ-Values are obtained by the subtraction of the corresponding value for the Full-Length MT-3 from each of the separate domains. Additive a- and β–domain thermodynamics provide a comparison of the combined domains with the full-length protein.*

Post-hoc Analysis Zn-MT-3	**N Stoichiometry**	**K**	**ΔH (kcal/mol)**	**-TΔS (kcal/mol)**	**ΔG (kcal/mol)**
Full-Length	6.8 ± 0.3	4 (± 2)×10^{11}	13.4 ± 0.2	-29 ± 0.5	-15.7 ± 0.3
α–domain	4.3 ± 0.3	4 (± 4)×10^{11}	4.26 ± 0.05	-20 ± 1	-15 ± 1
ΔΔ-Values	–	–	*-9.14 ± 0.21*	*9 ± 1.1*	–
β–Domain	2.7 ± 0.2	9 (± 9)×10^{11}	5.76 ± 0.06	-21.8 ± 0.8	-16.0 ± 0.8
ΔΔ-Values	–	–	*-7.64 ± 0.21*	*7.2 ± 0.9*	–
Additive α– + b-Domains	7.0 ± 0.4	–	10.02 ± 0.08	-41.8 ± 1.3	–
Additive ΔΔ-Values	–	–	*–3.38 ± 0.22*	*+12.8 ± 1.4*	–

comparison between the full-length protein and the separate domains, the difference in the enthalpic (ΔΔH) and entropic (–TΔΔS) contribution are included in the analysis. The additive enthalpic and entropic contributions of the α- and β-domains, along with the associated ΔΔ-values are also included for comparison. These additive thermodynamic values of the enthalpic and entropic contributions from αMT-3 and βMT-3 represent an approximate thermodynamic contribution of interdomain interactions.

Lastly, a comparison of the thermodynamics of Zn^{2+} binding to MT-3 to known thermodynamic values from the literature of tetrathiolate Zn^{2+} from an unstructured, glycine-rich, tetrathiolate peptide which allows for an approximation of the metal binding thermodynamics (**Table 6.1.3.3**). Assuming the thermodynamic values for a tetrathiolate Zn^{2+} under similar experimental conditions to be consistent between systems, these literature values can be subtracted from the Zn^{2+}-MT-3 values. By subtracting these thermodynamic values, the approximate thermodynamic contribution of MT-3 folding to the metal binding thermodynamics can be determined. This decouples metal binding thermodynamics from the protein contribution to metal binding, providing valuable insight into how the protein itself can impact metal binding. binding thermodynamics gives an approximation of the protein folding thermodynamics (**Table 6.1.3.3**). These ΔΔ-values for the separated α- and β-domains, compared to the unstructured, glycine-rich tetrathiolate peptide, shows there is very little protein contribution to metal binding, in which the enthalpic and entropic contributions is very similar to that of the peptide. Protein contributions to Zn^{2+} binding to the α–domain are ΔΔH = -1.34 ± 0.05 kcal/mol and –TΔΔS = 3 ± 1 kcal/mol and for the β–domain are ΔΔH = 0.16 ± 0.06 kcal/mol and –TΔΔS = 1.2 ± 0.8. However, for the full-length protein, the protein contribution is ΔΔH = 7.8 ± 0.2 kcal/mol and –TΔΔS = -6 ± 0.3 kcal/mol at pH 7.4.

6.3.2 Thermodynamics of the Cu^{+}–MT-3 and MT-2 Interaction

Isothermal titration calorimetry measurements of Cu^{+} in aqueous solution are challenging due to its oxidation to Cu^{2+} by O_2 and the disproportionation reaction of Cu^{+} that also converts it to Cu^{2+} and Cu^{0} (**Equation 6.3.2.1**).

$$2Cu^{+}_{(aq)} \rightarrow Cu_{(s)} + Cu^{2+}_{(aq)} \qquad (\boldsymbol{Equation\ 6.3.2.1})$$

These competing reactions can be minimized by the addition of a ligand that favors Cu^{+}

Table 6.1.3.3. *Average thermodynamics values for the Zn-MT-3 (full-length, α– and β–domains) interaction determined by the chelation of Zn^{2+} by DTPA. Buffer-independent, pH-dependent, proton-corrected thermodynamic values obtained through the* post-hoc *analysis, considering all relevant competing equilibria. These values are the thermodynamics on a per-metal basis which includes the proton competition for each metal ion. Enthalpic and Entropic contributions from the binding of Zn^{2+} to both the unstructured, glycine-rich tetrathiolate peptide (Cys_4–peptide) and the glucocorticoid receptor (GR-2) at pH 7.4.* ΔΔ-Values (Metallothionein – unstructured peptide) for full-length protein and the separated domains decouples the metal binding thermodynamics from the protein contribution to metal binding.

Post-hoc Analysis Zn-MT-3	**Stoichiometry N**	**K**	**ΔG (kcal/mol)**	**ΔH (kcal/mol)**	**-TΔS (kcal/mol)**
Full-Length	6.8 ± 0.3	4 (± 2)×10^{11}	-15.7 ± 0.3	13.4 ± 0.2	-29 ± 0.5
α–Domain	4.3 ± 0.3	4 (± 4)×10^{11}	-15 ± 1	4.26 ± 0.05	-20 ± 1
β–Domain	2.7 ± 0.2	9 (± 9)×10^{11}	-16.0 ± 0.8	5.76 ± 0.06	-21.8 ± 0.8
Glycine-Rich Cys_4 Peptide	–	–	–	5.6	-23.0
ΔΔ (FL-MT-3 – Cys_4)	–	–		7.8 ± 0.2	-6 ± 0.5
ΔΔ (αMT-3 – Cys_4)	–	–		-1.34 ± 0.05	3 ± 1
ΔΔ (βMT-3 – Cys_4)	–	–		0.16 ± 0.06	1.2 ± 0.8

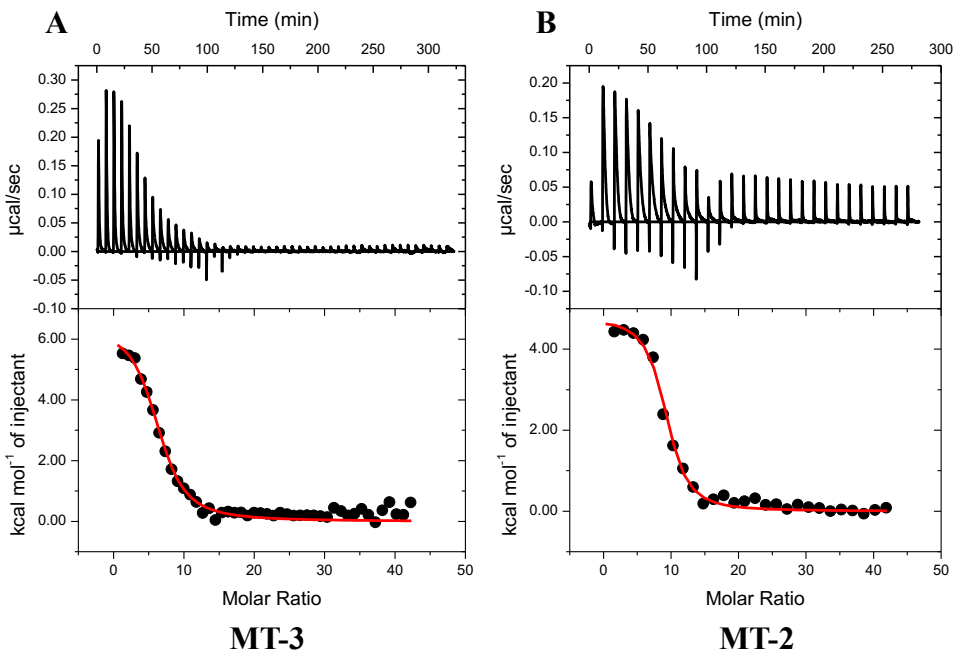

Figure 6.3.2.1. *(A) The representative isotherms of Cu^{+} in excess glutathione (GSH) titrated into (A) Zn_7–MT-3 and (B) Zn_7–MT-2 with in 100 mM buffer, 150 mM NaCl, pH 7.4. Average apparent thermodynamics with a one-site binding model of: (A) MT3-Zn_7 in BisTris, $n_{ITC} = 6 \pm 1$, $K_{ITC} = 4 (\pm 2) \times 10^5$, $\Delta H^o_{ITC} = 6.6 \pm 1.5$ kcal/mol; (B) MT2-Zn_7 in MOPS, $n_{ITC} = 8.5 \pm 1.5$, $K_{ITC} = 6 (\pm 1) \times 10^5$, $\Delta H^o_{ITC} = 3.6 \pm 0.2$ kcal/mol. Excess GSH, added immediately prior to each experiment, is proposed to chelate the Zn^{2+} from the MT-3 such that the Cu^{+} is binding to the protonated apo-protein.*

over Cu^{2+}, such as reduced L-glutathione (GSH), 1,1,4,7,10,10-hexamethyltriethylenetetramine (Me_6Trien), bicinchoninic acid (BCA) or bathocuproine disulfonate (BCS) and performing the ITC experiments under anaerobic conditions. Cu^+ binding to MT-3 was measured by titrating Cu^+ into Zn_7MT-3 in 3 buffers at pH 7.4 and 25 ^oC with ~10-fold excess GSH over the concentration of Cu^+. The presence of GSH in the syringe and the cell serves two purposes: (1) to stabilize Cu^+ and (2) to chelate Zn^{2+} from MT-3. Since the concentration of GSH was the same in the syringe and in the cell, this equates to a ~2,000-fold excess of GSH over the concentration of MT-3 in the cell. Given the stability of the Zn-$(GSH)_2$ complex, β_2 ~12, and the affinity of MT-3 for Zn^{2+} log K = ~10–12, the large excess of GSH competes with MT-3 for Zn^{2+}.[55] This was later confirmed through low temperature luminescence experiments completed by our collaborators, Meloni and coworkers, providing evidence that GSH does chelate Zn^{2+} from MT-3, leaving demetallated thionein (Submitted, Chemical Science, 2022). Thus, this ITC titration method allows for the direct titration of Cu^+ into metal-free, protonated MT-3. As such, Cu^+ titrations with excess GSH are, herein, analyzed as titrations into apo-MT-3. Representative data for Cu^+ titrated into apo-MT-3 and MT-2 is reported in **Figure 6.3.2.1** with both the titrant and the titrand in a 100 mM Bis-Tris, 150 mM NaCl, and 5 mM GSH buffered solution.

The apparent binding isotherm reflects the competition between the protein and excess GSH for the Cu^+ (**Scheme 6.3.2.2**). Average values for the experimental thermodynamic values from the best fits of a one-site binding model are found in **Table 6.3.2.1**.

Further analysis, considering the competing equilibria, requires the quantification of protons associated with metal binding. The enthalpy of buffer protonation and the experimental enthalpy of Cu^+ binding in each buffer were used in this analysis (**Figure 6.3.2.2**). These plots show that –0.5 ± 0.2 protons dissociate from the buffer upon Cu^+ binding to apo-MT-3 and -0.37 protons dissociate from apo-MT-2 at pH 7.4. Upon dissociation of the Cu^+–$(GSH)_2$ complex, the two GSH would then bind 1.6 ± 0.2 protons after the Cu^+ has been released. A proton inventory can then determine the number of protons that are displaced from the protein when Cu^+ binds. This proton analysis indicates

Scheme 6.3.2.2. Relevant equilibria for Cu^+ binding to MT-3 in the presence of excess GSH at pH 7.4. Each GSH picks up 0.8 H^+ when released from the $Cu^+(GSH)_2$ complex. ΔH_{ML} is the enthalpy of the metal (M) – ligand (L) interaction, ΔH_{LH} is the enthalpy of protonation of the ligand, ΔH_{PH} is the enthalpy of the protonation of the protein (P), ΔH_{BH} is the enthalpy of buffer (B) protonation, and ΔH_{MP} is the enthalpy of the desired metal-protein interaction.

$$6\ Cu^+(GSH)_2 + MT\text{-}3H^+_X + (9.6\text{-}X)\ BufferH^+ \leftrightarrows Cu^+_6MT\text{-}3 + 12\ GSH^+_{0.8} + (9.6\text{-}X)\ Buffer$$

$Cu^+(GSH)_2 \leftrightarrows Cu^+ + 2\ GSH$	$-6 \times \Delta H_{ML}$
$GSH + H^+ \leftrightarrows GSH^+$	$9.6 \times \Delta H_{LH}$
$MT\text{-}3H^+ \leftrightarrows MT\text{-}3 + H^+$	$-X \times \Delta H_{PH}$
$BH^+ \leftrightarrows B + H^+$	$-(9.6 - X) \times \Delta H_{BH}$
$Cu^+ + MT\text{-}3 \leftrightarrows Cu^+MT\text{-}3$	$6 \times \Delta H_{MP}$

$$\Delta H_{ITC} = -6\Delta H_{ML} + 9.6(\Delta H_{LH}) - (9.6 - X)\,\Delta H_{BH} - X(\Delta H_{PH}) + 6\Delta H_{MP} \quad \textbf{Equation 6.3.2.2}$$

Table 6.3.2.1. *Averaged apparent thermodynamic values for the binding of Cu^{+} to Full-length MT-3 and MT-2 in 100 mM buffer, 150 mM NaCl, pH 7.4, with 5mM excess gluthathione. Values are average thermodynamics for at least 2 independent experiments. Experimental fit data was obtained by a one-site fitting model.*

Protein	**Buffer**	**n_{ITC}**	**K_{ITC}**	**ΔH_{ITC} (kcal/mol)**
MT-3	**MOPS**	6.3 ± 0.7	5 (± 1)×10^7	4.5 ± 0.7
	BisTris	6 ± 1	4 (± 2)×10^5	6.6 ± 1.5
	TAPSO	4.7 ± 0.2	2.1 (± 0.2)×10^6	6.9 ± 0.5
MT-2	**MOPS**	8.5 ± 1.5	6 (± 1)×10^5	3.6 ± 0.2
	TAPSO	8.1 ± 0.9	1.5 (± 0.4)×10^6	5.2 ± 0.4

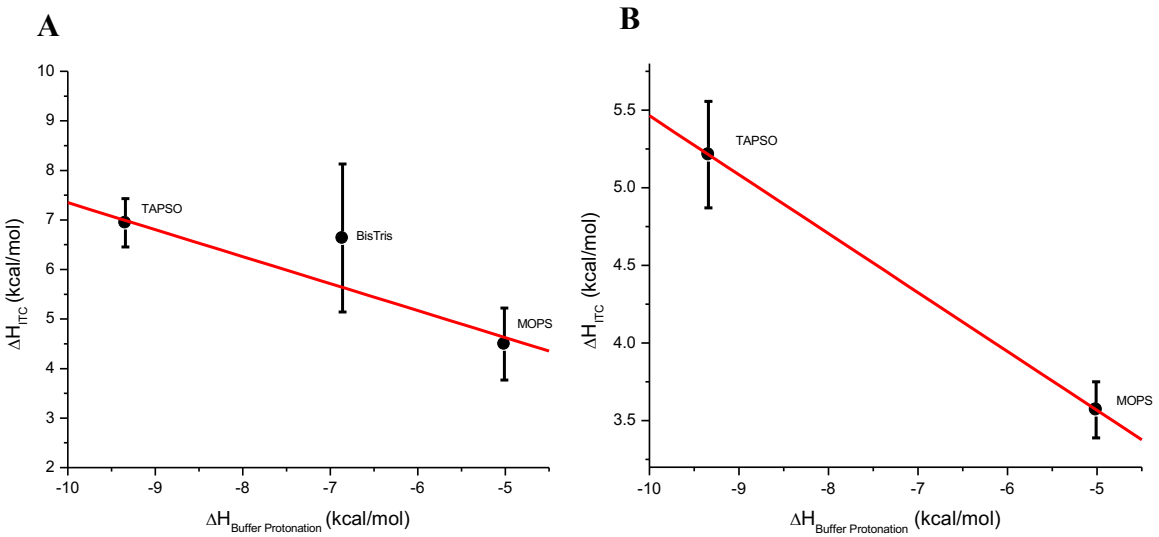

Cu^+-GSH Titration into apo-MT-3
6 $(GSH)_2$: 9.6 H^+
Proton Plot: -0.5 ± 0.2 H^+
Apo-MT-3 Protonation: 9.1 ± 0.2 H^+

Cu^+-GSH Titration into Apo-MT-2
8 $(GSH)_2$: 12.8 H^+
Proton Plot: -0.37 ± NA H^+
Apo-MT2 Protonation: 12.43 H^+

Figure 6.3.2.2*. Plotting the buffer protonation enthalpy vs. the experimental enthalpy allows for the calculation in the change in protonation upon Cu^+ binding. (A) For the binding of Cu^+ to apo-MT-3, these data establish an average total proton inventory, where a total of 9.6 protons would bind to ~12 GSH, 0.5 protons dissociate from the buffer (slope = -0.5), leaving a total of 9.1 protons that are released from apo-MT-3 when Cu^+ binds. (B) Similarly, for the binding of Cu^+ to apo-MT-2, these data establish an average total proton inventory, where a total of 12.8 protons would bind to ~16 GSH, 0.37 protons dissociate from the buffer (slope = -0.37), leaving a total of 12.43 protons that are released from apo-MT-2 when Cu^+ binds.*

Table 6.3.2.2. *Average thermodynamics values for the binding of Cu^+ to apo-MT-3, determined by direct titration of Cu^+ complexed with excess glutathione. Buffer-independent, pH-dependent thermodynamic values obtained through the* post-hoc *analysis, considering all relevant competing equilibria. These values are the thermodynamics on a per-metal basis which includes the proton competition for each metal ion that binds to the protein. ΔΔ-Values are obtained by subtracting the Cu^+ binding thermodynamics of MT-2 from MT-3.*

Post-hoc Analysis Cu^+ Binding	**Stoichiometry n**	**K**	**ΔG (kcal/mol)**	**ΔH (kcal/mol)**	**–TΔS (kcal/mol)**
MT-3	6 ± 1	4 (± 4)×10^{19}	-26.9 ± 0.5	-10 ± 1	-17 ± 1.5
MT-2	8 ± 1	8 (± 5)×10^{19}	-27.1 ± 0.4	-12 ± 1	-15 ± 1
ΔΔ-Values	–	–	–	*2 ± 1.4*	*–2 ± 1.8*

that 9.1 H^+ are displaced from MT-3 and 12.43 H^+ are displaced from MT-2, at pH 7.4 (**Figure 6.3.2.2**).

To determine the Cu^+ binding constant and the free energy of the interaction, the competition of GSH for Cu^+ at pH 7.4 was included in the *post-hoc* analysis. Under conditions of excess GSH, each Cu^+ ion is bound to two GSH, which displaces 1.6 H^+ at the experimental pH. The buffer-independent binding constants of each Cu^+ binding to MT-2 and MT-3 on a *per-metal* and proton-corrected basis are shown in **Table 6.3.2.1**.

Differences in the Cu^+ binding thermodynamics between MT-2 and MT-3 are compared using $\Delta\Delta H$ and $-T\Delta\Delta S$ values (**Table 6.3.2.2**). No significant quantitative differences in the thermodynamics of Cu^+ binding to MT-3 and MT-2 are observed. However, qualitative kinetic differences in Cu^+ binding to MT-2 and MT-3 are notable in the injection peak shapes, although difficult to quantify.

6.4. Discussion

Due to the difficulty in measuring the metal-binding thermodynamics of MT-3 directly, because of redox instability of apo-metallothionein, an alternative experimental design was employed to quantifying the thermodynamics of Zn^{2+} binding. Chelation of Zn^{2+} from the stable Zn_7MT-3 using a metal chelator DTPA was used to quantify the condition-independent binding thermodynamics. Recent studies have had success in determining the metal binding thermodynamics using isothermal titration calorimetry.[10,53] Chelation of Zn^{2+} from the cysteine-rich MT-3 enables the quantification of the metal binding thermodynamics without complications introduced by protein oxidation or excess metal ions in solution.

The binding of Cu^+ was studied by a direct titration of Cu^+ into the Zn_7-MT-3 with large excess of reduced glutathione (GSH). GSH has two primary functions in these ITC experiments: (1) GSH stabilizes Cu^+ throughout the ITC experiments and (2) GSH chelates the Zn^{2+} from MT-3, allowing Cu^+ to bind to apo-MT-3. The equilibrium constants of Zn^{2+} binding to MT-3 and GSH are similar ($K = 10^{10} – 10^{12}$ for MT-3 and $10^{12} – 10^{14}$ for GSH) but the large excess of GSH to MT-3 (2000:1) results in the chelation of Zn^{2+} from MT-3.[45,56] Our collaborators confirmed this through luminescence experiments that showed no evidence of Zn^{2+} bound to the metallothionein samples in excess GSH.[57]

In this study, isothermal titration calorimetry (ITC) was utilized to quantify the thermodynamics of the interdomain interactions and the metal-swapping mechanism of metallothionein-3 (MT-3) and its comparison with metallothionein-2 (MT-2). This is the first study, to my knowledge, that quantifies the condition-independent enthalpic and entropic contributions of Cu^{+} and Zn^{2+} binding to MT-3 under physiological conditions. First, I focus on the thermodynamics of Zn^{2+} binding to full-length MT-3 and the separate α– and β–domains, and then discuss the binding of Cu^{+} to MT-3 in light of a comparison with MT-2, and finally how the metal-binding thermodynamics relate to the physiological function of MT-3.

6.4.1. Entropic and Enthalpic Contributions of Zinc Binding to MT-3.

All Zn^{2+} binding constants for MT-3 and the separated α– and β–domains are dominated by a favorable entropic contribution, which is opposed by a smaller disfavorable enthalpic contribution. These observations are consistent with previously reported investigations of Zn^{2+} binding to biological macromolecules. For example, the binding of Zn^{2+} to the Zn-finger of the DNA-binding domain of the glucocorticoid receptor (GR-2), which binds Zn^{2+} with 4 cysteines in a tetrahedral geometry, is characterized by $\Delta H = +10 \pm 2$ kcal/mol and $-T\Delta S = -20 \pm 2$ kcal/mol at pH 7.4.[58] Zn^{2+} binding to the unstructured, glycine-rich peptide, NH_2–KLCEGGCGGCGGCGGW–$CONH_2$ (Cys_4-peptide), in which 4-cysteines binds Zn^{2+} in a tetrahedral geometry, is characterized by $-T\Delta S = -23.0$ kcal mol^{-1} and $\Delta H = +5.6$ kcal mol^{-1} at pH 7.4.[59]

Typical contributions to the entropic component of metal binding are (1) desolvation of the metal upon binding to the macromolecule, (2) conformational restraints from metal binding that diminish global protein dynamics, (3) formation of a coordinated metal complex, (4) displacement of water molecules from the metal binding site of the macromolecule, and (5) cratic, or mixing, entropy, which is the change in the translational entropy upon ligand binding with respect to a change in the mole fraction upon binding (i.e. 2 particles $\rightarrow$ 1 particle).[60–62]

Since the desolvation of Zn^{2+} upon binding to the macromolecule is similar in both the Cys_4-peptide and MT-3, the net contribution to the overall binding thermodynamics in (1) listed above should be reasonably similar in both systems. The Cys_4-peptide is an

unstructured peptide in which each cysteine can form a single bond with a bound Zn^{2+} and, in this regard, differs from the binding of Zn^{2+} to MT-3. Although MT-3 is considered to be generally unstructured, the formation of metal-thiolate clusters imposes some constraints on the conformational dynamics.[48] The binding of Zn^{2+} to the Cys_4-peptide causes a greater decrease in conformational flexibility relative to MT-3 because the metal-binding sites are comparatively preformed in MT-3. Computational modelling suggests that the global structure of MT-3 upon metal binding is stabilized compared to the apo-protein, which contributes to (2) described above, although this metalated structure is less compact than apo-MT-3. [16]

Though both systems form four-coordinate, tetrahedral Zn^{2+}, MT-3 forms metal-bridged thiolate clusters, in which the number of protons released upon Zn^{2+} binding on a *per-metal* basis is different than that of Cys_4-peptide (3.6 H^+/Zn^{2+} in Cys_4-peptide and ~1.4 H^+/Zn^{2+} in MT-3). This results in vastly different entropic contributions from (3) above. This is further emphasized by the difference in the total number of protons released on a *per-cysteine* basis (0.9 for the Cys_4-peptide and ~0.6 for the MT-3), suggesting that the apparent pK_a value of each individual cysteine is different in MT-3, relative to the unstructured peptide. Clearly, greater structural stability and differences in cysteine protonation likely result in differences in solvation of the macromolecule in solution, which would result in differences in the entropic contribution upon Zn^{2+} binding, as shown by (4). Lastly is the cratic entropy contribution, in which the Cys_4-peptide would be more favorable as the initial entropy of the system as compared to the final state is more similar (ligand + peptide $\rightarrow$ ligand-peptide complex). This is compared to the less favorable cratic entropy contribution for MT-3, in which the initial entropy is much greater than the final state ($7Zn^{2+}$ + MT-3 $\rightarrow$ Zn_7MT-3 complex), as shown in (5).

Although the contribution of each individual component to the total entropic driving force is difficult to establish experimentally, the net entropy term, $-T\Delta S$, for Cys_4-peptide would be less negative than MT-3, which is exactly what we find. Therefore, the likely origin of the entropic driving force in the binding of Zn^{2+} to MT-3, relative to the unstructured Cys_4-peptide, derives from both the difference in the conformational restraints that are imposed upon the structure of MT-3 upon metal binding and differences in the overall deprotonation and desolvation of the protein vs the unstructured peptide. Although

the contribution from the cratic entropy is likely different, previous statistical and experimental works suggests that the magnitude of the cratic entropy is relatively small.[60,61]

The enthalpic component of Zn^{2+} binding to MT-3 is much less favorable than it is for binding to the Cys_4-peptide. Similar to the entropic contribution, the enthalpic component of binding is described by (1) breaking S–H bonds upon metal binding (2) making the metal-thiolate bond, and (3) changes in both local and global hydrogen bonding. Although the binding of Zn^{2+} to both MT-3 and Cys_4-peptide result in the breakage of S–H bonds, not all of the Zn^{2+} that bind to MT-3 would result in S–H bond breakage due to the zinc-bridged cysteine coordination. This suggests, from (1), that MT-3 would be more enthalpically favorable, which is not the case, signifying that changes in the hydrogen bonding network within the protein may be playing a larger role, as shown in (3). However, MT-3 forms both terminal and bridging metal-thiolate clusters. Unlike the Cys_4 peptide, which only forms terminal metal-thiolate clusters, resulting in enthalpic differences, as shown in (2). In these regards, MT-3 and the Cys_4-peptide are distinctly different. This disfavorable enthalpic contribution from the breakage of S–H bonds is compounded by the breaking of intra– and interdomain hydrogen bonds upon Zn^{2+} binding through a decrease in the conformational flexibility and stabilization of the protein structure.[16,48,63]

6.4.2. Decoupling Metal Binding Thermodynamics from the Protein Folding Thermodynamics.

The typical *post-hoc* analysis associated with metal binding experiments, which considers all competing equilibria that are occurring throughout the ITC experiment, provides pivotal insight into metal-binding and into metal-protein interactions. However, these *post-hoc* analysis thermodynamics are the net thermodynamics, which are the sum of the individual interactions that are occurring. Many of these quantities are difficult to define, unfortunately. Others are insignificant when comparing two systems, as they may not be different, for example, Zn^{2+} hydration in the Zn^{2+} binding to MT-3 vs the domains. Lastly, some of these thermodynamic approximations are not coming from metal binding to protein, but the protein contribution to metal binding. These are very difficult to

decouple. However, fundamental bioinorganic properties can provide an avenue to decoupling these contributions.

For the binding of Zn^{2+} to full-length MT-3 and the separated domains, it is known that Zn^{2+} binds 4 cystine residues in a tetrahedral geometry at pH 7.4. This results in $\Delta H = 13.4 \pm 0.2$ kcal/mol and $-T\Delta S = -29 \pm 0.5$ kcal/mol for the full-length protein, $\Delta H = 4.26 \pm 0.05$ kcal/mol and $-T\Delta S = -20 \pm 1$ kcal/mol for the α-domain, and $\Delta H = 5.76 \pm 0.06$ kcal/mol and $-T\Delta S = -21.8 \pm 0.8$ kcal/mol for the β-domain, on a *per-metal* basis. Contributing to this binding is both the innate metal-binding properties, but also the effect of protein folding on binding. Using known thermodynamics for the binding of Zn^{2+} to 4 cysteine residues in a tetrahedral geometry with a system where the protein has negligible impact on the structure at pH 7.4, provides an approximation of the Zn^{2+} binding thermodynamics in MT-3.

Subtracting this approximation of metal-binding thermodynamics from each of the metallothionein samples (full-length, α- and β-domain) provides an estimate of this protein contribution to metal binding. Starting with the separated domains, the protein contribution to metal binding is minimal in which $\Delta\Delta H = -1.34 \pm 0.05$ kcal/mol and $-T\Delta\Delta S = 3 \pm 1$ kcal/mol for the α-domain and $\Delta H = 0.16 \pm 0.06$ kcal/mol and $-T\Delta\Delta S = 1.2 \pm 0.8$ kcal/mol for the β-domain. Individually, this suggests that the protein structure itself contributes very little to the binding of Zn^{2+}, and that these two domains are not significantly different from each other. This also suggests that the individual domains are very similar to the unstructured peptide, and likely to be unstructured before Zn^{2+} binds, which is not surprising, but also have very little structure after Zn^{2+} binds. Considering this thermodynamics insight suggests that Zn^{2+} binding results in a more structured protein and may provide indirect evidence of interdomain interactions that stabilize the metalloprotein, an are not present when in the two separated domains. This hypothesis can be further strengthened by determining the thermodynamic difference between the unstructured peptide and full-length MT-3.

Similar to the separated domains, subtracting the Zn^{2+} thermodynamics associated with the unstructured peptide from the full-length MT-3 thermodynamics provides an approximation of the protein contribution to metal-binding. This results in $\Delta\Delta H = 7.8 \pm 0.2$ kcal/mol and $-T\Delta\Delta S = -6 \pm 0.5$ kcal/mol. The protein contribution to the binding of Zn^{2+},

on a *per-metal* basis, is significantly different than either the unstructured peptide or the separated domains. Qualitatively, this shows that the two domains, connected by the short 3-residue (KKS) linker, have an interaction that affects the metal-binding properties of the protein. Quantitatively, the protein is providing a enthalpic penalty to metal binding and an entropic benefit. As previously shown, there are slight differences in the protonation of the unstructured peptide, separated domains, and full-length protein, which would contribute to the entropic differences. However, also contributing is the change in the compactness of the protein. Computational experiments on apo- and metalated-MT had shown that the binding of Zn^{2+} results in a less-compact structure. Changes in the compact-ness of MT would indicate changes in the entropic contribution of binding. Thus, Zn^{2+} binding to full-length MT-3, which is conformationally dynamic, results in less compact, metal-stabilized structure, which may not be seen in the separated domains. These are further supported by the enthalpic penalty for Zn^{2+} binding. Again, there are small protonation differences, which would contribute to this penalty, but the electrostatic interactions and the formation of interdomain hydrogen bonds also would support this enthalpic disfavorability.

Overall, the contribution of the structure of metallothionein on metal binding thermodynamics is particularly important for such a conformationally dynamic protein. Much of the structural impact of metal binding and the metal-protein interaction has been explored computationally, but very little has been probed experimentally. Furthermore, decoupling metal-binding thermodynamics from the protein contribution to metal binding further enhances our ability to understand the thermodynamic origins of these interactions.

It should be noted that this analysis was done solely for the binding of Zn^{2+}, although the thermodynamics of Cu^{+} binding to full-length MT-3 were also determined. Unfortunately, no known model systems that characterize the binding of Cu^{+} with similar coordination and geometries have been reported. This is more difficult by the flexible coordination in the binding of Cu^{+} to MT-3, which may be 2-, 3-, or 4-coordinate. As useful as the determination of the protein contribution to the binding of Cu^{+} would be, this is not feasible at this time. However, a similar thermodynamic control may be achieved using a similar method to the unstructured, glycine-rich peptide. A peptide that two cysteines on opposite termini of the peptide may be used to quantify the thermodynamics of linear, 2-coordinate Cu^{+} binding under similar experimental conditions.

Although for metallothionein it is useful to decouple metal coordination from the protein contribution to metal binding to better understand the experimental thermodynamics, this can be even more impactful with other protein systems. For example, understanding these protein contributions to metal binding with disease-associated mutations, as compared to native protein structures, can provide insight into the nature of the defects that may be occurring. This may aid in drug development or drug-target selection, allowing for thermodynamically-directed drug design for these targeted systems.

6.4.3. Quantifying Interdomain Contributions to Zinc Binding Thermodynamics in MT-3

To quantify interdomain interactions in full-length MT-3, the thermodynamics of Zn^{2+} binding to the separate α– and β–domains were quantified individually. The net enthalpic and entropic contributions to Zn^{2+} binding to the domains are consistent with Zn^{2+} binding to the full-length protein, such that the binding is entropically driven and enthalpically disfavorable. Although the overall trend is similar, binding to the separate domains is both more entropically favorable and less enthalpically disfavorable than the full-length protein. However, it is noted that two primary aspects of Zn^{2+} binding may limit the direct comparison: the number of protons that are displaced by Zn^{2+} are different, which can contribute to both the enthalpic disfavorability and the entropically favorability, and the cratic entropy would be different as the mole fractions before binding are different.

In order to compare the Zn^{2+} binding thermodynamics of the separate domains to the full-length MT-3, the additive thermodynamics of both the α– and β–domains eliminate the significant differences described above. The number of protons in the additive thermodynamics and the cratic entropy are similar to that of the full-length protein, providing a better comparison. It is hypothesized that if the domains are independent of each other, then the enthalpic and entropic contributions to the thermodynamics of Zn^{2+} binding to the full-length protein and to the additive values for both domains should be equivalent (**Table 6.1.3.2**). Calculating the ΔΔ-values (i.e., $\Delta\Delta H$, $-T\Delta\Delta S$, and $\Delta\Delta G$) should provide a quantitative comparison of the sum of the separate domains and the full-length protein.

The binding affinities of each binding event are equivalent, within the bounds of the ITC's accuracy, but the overall contributions to this binding are not. The additive

enthalpic contribution to Zn^{2+} binding is more favorable than the binding of Zn^{2+} to the full-length protein. Applying a similar analysis to the enthalpic contributions of metal binding (*supra vide*) suggests that the more disfavorable enthalpy in the full-length protein, compared to the additive values suggests that there are more S–H bonds that are broken when Zn^{2+} binds or there is greater disruption of the interdomain hydrogen bonding network. It is likely that this network is relatively similar between the full-length protein and the additive domains, but disruption of interdomain hydrogen bonding in the full-length protein would provide a greater enthalpic penalty upon Zn^{2+} binding.

The differences in the entropic contribution between the full-length protein and the additive α– and β–domains can be evaluated by a similar analysis as above. Entropic contributions from (1) metal desolvation, (2) metal-induced protein stabilization of the protein scaffold, (3) metal-binding site desolvation, and (4) cratic entropy should be relatively similar for Zn^{2+} binding to either system. As such, differences in the conformational flexibility (2) are proposed to be the main difference for the less favorable entropic contribution of Zn^{2+} binding to the full-length protein, compared to the additive α– and β–domains. The conformational flexibility of full-length MT-3 in the absence of Zn^{2+} is proposed to be more flexible, with the α– and β–domains metal binding sites being less defined or preformed due to the interdomain interactions. Then, when Zn^{2+} binds to the full-length protein, the overall structure becomes more compact and the conformationally stable, leading to an entropic penalty. The interdomain interaction may act to destabilize the overall structure in the absence of Zn^{2+}. Similarly, in the absence of Zn^{2+} in the separated domains, the overall structures and metal binding sites are more well-defined such that when Zn^{2+} binds there is less loss of entropy in the system leading to a more favorable entropic contribution to metal binding.

Overall, the additive thermodynamic values represent an approximation of the thermodynamics in the absence of the interdomain interactions and allows their overall contribution to Zn^{2+} binding to be determined. This interdomain interaction is augmented by the short three-residue (KKS) linker that connects the α– and β–domains, such that when the two domains are connected in the full-length protein, they are within close proximity to one another. Increasing the length of the linker in hamster MT-2 was proposed to not have an impact on the detoxification of Cd^{2+}, which led to the proposal that this hinge

region did not impact metallothionein functionality. However, it was noted that linker lengths greater than 16 residues were instable.[49] It was also proposed that the much longer linker of seaweed *Fucus vesiculosus* metallothionein (14 residues) allow the domains to act independently, suggesting that shorter linkers would have less independent domains. [44] Lastly are single-domain metallothioneins from yeast, which are proposed to be Cu^{+} storage proteins that also play a role in the deliver Cu^{+} to metallochaperones.[21] Each of these examples aim to highlight the proposed interdomain interactions that may impact physiological function. Although the physiological need for a short, highly conserved linker in mammalian MT-3 is not wholly understood, my results suggest that this interdomain interaction may be important, not just in mammalian metallothionein, but other families as well. In particular for MT-3, in which protein dynamics and metal-swapping likely are at the forefront of proposed functions, the interaction between the α– and β–domains could augment metal-swapping or metal transfer kinetics, thereby modulating the function of the protein.

6.4.4. Entropically Driven and Enthalpically Favorable Copper(I) Binding to MT-3

Unlike the binding of Zn^{2+} to metallothionein, the total number of Cu^{+}, and their subsequent geometries, that are able to bind to metallothionein varies. *In-vitro* experiments have demonstrated 8-Cu^{+}, 10-Cu^{+}, 12-Cu^{+}, and up to 20-Cu^{+} MT species under reducing conditions.[64,65] This suggests that the binding of Cu^{+}, and the associated binding geometry, is very dynamic. Due to this dynamic nature of MT-3, a comparison of Cu^{+} binding thermodynamics to a known reference, similar to that of Zn^{2+} above, is much more difficult. Thus, it is proposed that a comparison with MT-2, which has been studied significantly more than MT-3, along with a comparison to Zn^{2+} binding to MT-3, would be reasonable (**Table 6.4.4.1**). This comparison aims to provide thermodynamic insight into the structure-function relationship of both the proline-rich sequence and acidic hexapeptide region of MT-3 on the binding of Cu^{+}.

The binding of Cu^{+} to MT-3 is both enthalpically and entropically favorable, but entropically driven. Given the analysis of the entropic contribution to Zn^{2+} binding to MT-3, the entropic driving force is not unexpected. The release of protons would be entropically favorable, but enthalpically disfavorable. Comparing the number of protons that are

Table 6.4.4.1. Average thermodynamic values for Zn^{2+} and Cu^{+} ions binding to MT-3 at pH 7.4 and 25°C, and the difference between these thermodynamic values.

Metal Ion	**n**	**K**	**ΔG° (kcal/mol)**	**ΔH° (kcal/mol)**	**-TΔS° (kcal/mol)**
Zn^{2+}	6.8 ± 0.3	4 (± 2)×10^{11}	-15.7 ± 0.3	13.4 ± 0.2	-29 ± 0.5
Cu^{+}	6 ± 1	4 (± 4)×10^{19}	-27.1 ± 0.4	-10 ± 1	-17 ± 1
Difference: Cu^{+} - Zn^{2+}	–	–	*-11.4 ± 0.4*	*-23 ± 1*	*+12 ± 1*

released when Cu^+ binds to MT-3 with the number when Zn^{2+} binds to MT-3 reveals that fewer protons per metal are released for Cu^+ (~1.5 H^+/Cu^+) than for Zn^{2+} (~1.7 H^+/Zn^{2+}). This difference correlates with the entropic driving force, which is less favorable for the binding of Cu^+. Difference in the hydration of Cu^+ and Zn^{2+} would also reduce the entropic favorability for the binding of Cu^+. Lastly, the less entropically favorable Cu^+ binding, compared to Zn^{2+}, could also be an indication of differences in the overall global structure of MT-3. If we make the natural assumption that the demetallated MT-3 structure before either Cu^+ or Zn^{2+} bind is similar, and that the binding of either of these metals would result in a decrease in conformational flexibility, then the less favorable entropic contribution of Cu^+ binding may be from a significant difference in the conformational disorder of the overall structure of MT-3. Comparing the entropic contribution of Cu^+ to Zn^{2+}, it is observed that the binding of Cu^+

is ~12 kcal/mol less entropically favorable than the binding of Zn^{2+}. Although the relative amount of each entropic contribution to metal binding is difficult to establish, these entropic differences are suggestive of distinct structural ensembles of metallothionein when either Zn^{2+} or Cu^+ is bound.

The difference in the enthalpic contribution to Cu^+ binding, as compared to the binding of Zn^{2+}, is much more favorable ($\Delta\Delta H_{Cu(I)–Zn(II)}$ = -23.4 ± 1.0 kcal/mol). It has already been shown that fewer protons are released when Cu^+ binds, which would result in a smaller enthalpic penalty. Contributing to the favorable enthalpy of Cu^+ binding relates to the Lewis acidity of Cu^+ compared to Zn^{2+}. Cu^+ has much greater thiophilicity and lower Lewis acidity than Zn^{2+}, making the binding to cysteines more enthalpically favorable. Lastly, the structural ensemble of MT-3 when Cu^+ is bound might also involve the formation of more hydrogen bonds, which would also lead to a more favorable enthalpy of binding.

A comparison of Cu^+ binding to MT-2 and MT-3 aims to understand thermodynamic differences that exist due to differences in their structures – e.g. proline-rich sequence and the acidic hexapeptide insert in MT-3. It was previously shown in measurements of the binding of Zn^{2+} and Cu^+ to MT-2, MT-3, and MT-3 variants that mutations in these residues result in distinctly different kinetics of binding and binding constants.[6] This, however, was not observed in the ITC experiments. The thermodynamics

of Cu^+ binding to MT-3 and MT-2 were within experimental error for all thermodynamic parameters (**Table 6.3.2.2**). However, this is taken in stride, as two primary differences could be the cause of this. The previous work on the kinetics and affinity Cu^+ was examined in the mixed-metal species (i.e. Cu_4Zn_4-MT), whereas ITC measured the binding of Cu^+ to the demetallated protein. The difference in metalation would influence differences in metal binding thermodynamics, particularly if the domains are not independent of each other, as described above. Furthermore, there may be differences in the equilibrium constants from sensitive kinetics measurements, but isothermal titration calorimetry may not be sensitive enough to observe relatively small differences.

Although the binding of Cu^+ to MT-2 and MT-3 may not be quantitatively different, several aspects of the ITC isotherms suggest there may be underlying differences. Close inspection of the isotherms for Cu^+ binding to MT-2, reveal that each titration peak shows two kinetic phases, an initial exothermic phase followed by a slow endothermic phase (**Figure 6.3.2.1**). These two phases are generally attributed to an initial exothermic contact binding followed by a slow, endothermic rearrangement.[66,67] After MT-2 is saturated, and no more Cu^+ are binding, only the endothermic heat of dilution is present. This two-phase binding and rearrangement is also present in the MT-3 data, with a much more rapid exothermic contact binding that is quickly overtaken by the slow endothermic rearrangement (**Figure 6.3.2.1**). The small exothermic binding event may be too rapid for detection by ITC, such that the observed Cu^+ binding is primarily from the rearrangement into the Cu^+-thiolate clusters. The kinetic differences in binding may not be readily quantifiable by ITC but they do suggest differences in Cu^+ binding to MT-3 vs MT-2, possibly from differences in domain-specific binding or differences in interdomain interactions. The lack of observed thermodynamic differences for Cu^+ binding in MT-2 and MT-3, but differences in the kinetics of binding, suggest that the kinetics of metal binding and transfer play a large role in the function of metallothionein.[5]

The binding of Cu^+ to MT-2 and MT-3 does show differences in the deprotonation upon metal binding. MT-3 releases ~9.1 protons when Cu^+ binds, compared to the 12.4 protons when Cu^+ binds to MT-2, as determined by a proton plot analysis (**Figure 6.3.2.2**). However, as MT-3 only binds ~6 Cu^+, whereas MT-2 binds ~8 Cu^+, by ITC, both proteins displace ~1.5 H^+/Cu^+. This disparity likely arises from protein oxidation in MT-3. It has

been shown previously that 8 Cu^+ binding to metallothionein may not fully saturate all the cysteines in the protein, and there may still be protonated cysteines after the Cu^+ is bound.[64,65] Small changes in the Cu^+-thiolate clusters between MT-2 and MT-3 would explain the differences in both the qualitative kinetics and protein deprotonation.

6.4.5. Implications of Cu^+ and Zn^{2+} Binding Thermodynamics on the Physiological Function of MT-3

Taken together, the thermodynamics of Cu^+ and Zn^{2+} binding to MT-3 provides insight on how metal binding may impact protein structure and how protein structure modulates metal coordination and function. Recent studies have provided evidence for the metal-swapping capabilities of MT-3, and how this may be applied in neurophysiology and diseased neurophysiology.[5] The metal-swapping hypothesis would, intrinsically, rely on both strong metal binding, such that MT-3 could chelate metals from other proteins, and differential binding kinetics, allowing for the rapid exchange of metals. The metal-binding thermodynamics from ITC measurements contribute to our understanding of the interconnectedness of protein structure, binding thermodynamics, and binding kinetics.

I have quantified the thermodynamics of interdomain interaction and the contribution of the protein structure to metal binding. I propose that interdomain interactions in mammalian metallothionein help to drive metal-ion binding, enhancing the favorable metal-protein interaction, stabilizing the conformational flexibility of MT-3. This would assist in the proposed metal-swapping capabilities of MT-3 as more favorable binding thermodynamic, along with rapid metal binding kinetics, create an efficient system, preventing aberrant metal binding to other neurological proteins.[5] This is aided by protein structure contributions to metal binding, which provide a moderate entropic favorability to Zn^{2+} binding that is enhanced by the interdomain interactions. A thermodynamically favorable and rapid response to pathological metal binding would be neuroprotective and this neuroprotective nature of MT-3 is augmented by the interdomain interactions and the structural changes that occur upon metal binding.

6.5. Summary

The thermodynamic approach that is described here provides a means to quantify the energetics of Cu^{+} and Zn^{2+} binding to metallothionein thereby elucidating the physiological function of the protein from a thermodynamic perspective. Measurements of full-length and separate domains of MT-3 quantify the thermodynamics of the interdomain interactions, which may alter metal binding thermodynamics through changes to the protein structural ensemble. Comparing the thermodynamics of Zn^{2+} binding to MT-3 with the thermodynamics of an unstructured model peptide helped to elucidate the contribution of protein folding to metal binding, decoupling metal binding thermodynamics from the protein contribution. These structural changes upon metal binding are entropically driven, with the enthalpic contribution largely dependent on the bonding of the metal ion. Further, the binding of Cu^{+} to MT-3 and MT-2, provides a thermodynamic comparison for physiological differences between the two metallothionein isoforms. Quantitative differences in Cu^{+} binding show evidence for the metal-swapping capabilities of metallothionein and provide a thermodynamic foundation for this physiological phenomenon.

6.6. References

(1) KAGI, J. H.; VALEE, B. L. *Metallothionein: A Cadmium- and Zinc-Containing Protein from Equine Renal Cortex.*; 1960; Vol. 235. https://doi.org/10.1016/s0021-9258(18)64490-4.

(2) Coyle, P.; Philcox, J. C.; Carey, L. C.; Rofe, A. M. Metallothionein: The Multipurpose Protein. *Cell. Mol. Life Sci.* **2002**, *59* (4), 627–647. https://doi.org/10.1007/s00018-002-8454-2.

(3) Stillman, M. J. Metallothioneins. *Coord. Chem. Rev.* **1995**, *144* (C), 461–511. https://doi.org/10.1016/0010-8545(95)01173-M.

(4) Palumaa, P.; Tammiste, I.; Kruusel, K.; Kangur, L.; Jörnvall, H.; Sillard, R. Metal Binding of Metallothionein-3 versus Metallothionein-2: Lower Affinity and Higher Plasticity. *Biochim. Biophys. Acta - Proteins Proteomics* **2005**, *1747* (2), 205–211. https://doi.org/10.1016/j.bbapap.2004.11.007.

(5) Vašák, M.; Meloni, G. Mammalian Metallothionein-3: New Functional and Structural Insights. *Int. J. Mol. Sci.* **2017**, *18* (6).

https://doi.org/10.3390/ijms18061117.

(6) Calvo, J. S.; Lopez, V. M.; Meloni, G. Non-Coordinative Metal Selectivity Bias in Human Metallothioneins Metal-Thiolate Clusters. *Metallomics* **2018**, *10* (12), 1777–1791. https://doi.org/10.1039/c8mt00264a.

(7) Klaassen, C. D.; Liu, J.; Diwan, B. A. Metallothionein Protection of Cadmium Toxicity. *Toxicol. Appl. Pharmacol.* **2009**, *238* (3), 215–220. https://doi.org/10.1016/j.taap.2009.03.026.

(8) Lu, W.; Zelazowski, A. J.; Stillman, M. J. Mercury Binding to Metallothioneins: Formation of the Hg18-MT Species. *Inorg. Chem.* **1993**, *32* (6), 919–926. https://doi.org/10.1021/ic00058a028.

(9) Klaassen, C. D.; Liu, J.; Choudhuri, S. Metallothionein: An Intracellular Protein to Protect against Cadmium Toxicity. *Annu. Rev. Pharmacol. Toxicol.* **1999**, *39* (1), 267–294. https://doi.org/10.1146/annurev.pharmtox.39.1.267.

(10) Carpenter, M. C.; Shami Shah, A.; Desilva, S.; Gleaton, A.; Su, A.; Goundie, B.; Croteau, M. L.; Stevenson, M. J.; Wilcox, D. E.; Austin, R. N. Thermodynamics of Pb(II) and Zn(II) Binding to MT-3, a Neurologically Important Metallothionein. *Metallomics* **2016**, *8* (6), 605–617. https://doi.org/10.1039/c5mt00209e.

(11) Krężel, A.; Maret, W. The Functions of Metamorphic Metallothioneins in Zinc and Copper Metabolism. *International Journal of Molecular Sciences*. MDPI AG June 9, 2017. https://doi.org/10.3390/ijms18061237.

(12) Lee, S. J.; Seo, B. R.; Koh, J. Y. Metallothionein-3 Modulates the Amyloid β Endocytosis of Astrocytes through Its Effects on Actin Polymerization. *Mol. Brain* **2015**, *8* (1). https://doi.org/10.1186/s13041-015-0173-3.

(13) Meloni, G.; Zovo, K.; Kazantseva, J.; Palumaa, P.; Vašák, M. Organization and Assembly of Metal-Thiolate Clusters in Epithelium-Specific Metallothionein-4. *J. Biol. Chem.* **2006**, *281* (21), 14588–14595. https://doi.org/10.1074/jbc.M601724200.

(14) Wang, H.; Zhang, Q.; Cai, B.; Li, H.; Sze, K. H.; Huang, Z. X.; Wu, H. M.; Sun, H. Solution Structure and Dynamics of Human Metallothionein-3 (MT-3). *FEBS Lett.* **2006**, *580* (3), 795–800. https://doi.org/10.1016/j.febslet.2005.12.099.

(15) Zangger, K.; ÖZ, G.; Armitage, I. M.; Otvos, J. D. Three-Dimensional Solution

Structure of Mouse [Cd7]-Metallothionein-l by Homonuclear and Heteronuclear NMR Spectroscopy. *Protein Sci.* **2008**, *8* (12), 2630–2638. https://doi.org/10.1110/ps.8.12.2630.

(16) Rigby Duncan, K. E.; Stillman, M. J. Metal-Dependent Protein Folding: Metallation of Metallothionein. *J. Inorg. Biochem.* **2006**, *100* (12), 2101–2107. https://doi.org/10.1016/j.jinorgbio.2006.09.005.

(17) Ni, F.; Cai, B.; Ding, Z.; Zheng, F.; Zhang, M.; Wu, H.; Sun, H.; Huang, Z. Structural Predition of the Beta-Domain of Metallothionein-3 by Molecular Dynamics Simulation. *Proteins Struct. Funct. Bioinforma.* **2007**, *68*, 255–266. https://doi.org/10.1002/prot.

(18) Greisen, P.; Jespersen, J. B.; Kepp, K. P. Metallothionein Zn 2+- and Cu 2+-Clusters from First-Principles Calculations. *Dalt. Trans.* **2012**, *41* (8), 2247–2256. https://doi.org/10.1039/c1dt11785h.

(19) Presta, A.; Green, A. R.; Zelazowski, A.; Stillman, M. J. *Copper Binding to Rabbit Liver Metallothionein: Formation of a Continuum of Copper(I)-Thiolate Stoichiometric Species*; 1995; Vol. 227. https://doi.org/10.1111/j.1432-1033.1995.tb20380.x.

(20) Calvo, J. S.; Lopez, V. M.; Meloni, G. Non-Coordinative Metal Selectivity Bias in Human Metallothioneins Metal-Thiolate Clusters. *Metallomics* **2018**, *10* (12), 1777–1791. https://doi.org/10.1039/c8mt00264a.

(21) Sutherland, D. E. K.; Stillman, M. J. Challenging Conventional Wisdom: Single Domain Metallothioneins. *Metallomics*. Royal Society of Chemistry 2014, pp 702–728. https://doi.org/10.1039/c3mt00216k.

(22) Howells, C.; West, A. K.; Chung, R. S. Neuronal Growth-Inhibitory Factor (Metallothionein-3): Evaluation of the Biological Function of Growth-Inhibitory Factor in the Injured and Neurodegenerative Brain. *FEBS Journal*. July 2010, pp 2931–2939. https://doi.org/10.1111/j.1742-4658.2010.07718.x.

(23) Hasler, D. W.; Jensen, L. T.; Zerbe, O.; Winge, D. R.; Vasak, M. Effect of the Two Conserved Prolines of Human Growth Inhibitory Factor (Metallothionein-3) on Its Biological Activity and Structure Fluctuation: Comparison with a Mutant Protein. *Biochemistry* **2000**, *39* (47), 14567–14575. https://doi.org/10.1021/bi001569f.

(24) Williamson, M. P. *The Structure and Function of Proline-Rich Regions in Proteins*; 1994; Vol. 297. https://doi.org/10.1042/bj2970249.

(25) Zheng, Q.; Yang, W. M.; Yu, W. H.; Cai, B.; Teng, X. C.; Xie, Y.; Sun, H. Z.; Zhang, M. J.; Huang, Z. X. The Effect of the EAAEAE Insert on the Property of Human Metallothionein-3. *Protein Eng.* **2003**, *16* (12), 865–870. https://doi.org/10.1093/protein/gzg127.

(26) Waalkes, M. P.; Harvey, M. J.; Klaassen, C. D. Relative in Vitro Affinity of Hepatic Metallothionein for Metals. *Toxicol. Lett.* **1984**, *20* (1), 33–39. https://doi.org/10.1016/0378-4274(84)90179-6.

(27) Faller, P. Neuronal Growth-Inhibitory Factor (Metallothionein-3): Reactivity and Structure of Metal-Thiolate Clusters. *FEBS Journal*. July 2010, pp 2921–2930. https://doi.org/10.1111/j.1742-4658.2010.07717.x.

(28) Pountney, D. L.; Fundel, S. M.; Faller, P.; Birchler, N. E.; Hunziker, P.; Vašák, M. *Isolation, Primary Structures and Metal Binding Properties of Neuronal Growth Inhibitory Factor (GIF) from Bovine and Equine Brain*; 1994; Vol. 345. https://doi.org/10.1016/0014-5793(94)00452-8.

(29) Uchida, Y.; Takio, K.; Titani, K.; Ihara, Y.; Tomonaga, M. The Growth Inhibitory Factor That Is Deficient in the Alzheimer's Disease Brain Is a 68 Amino Acid Metallothionein-like Protein. *Neuron* **1991**, *7* (2), 337–347. https://doi.org/10.1016/0896-6273(91)90272-2.

(30) El Ghazi, I.; Martin, B. L.; Armitage, I. M. *Experimental Biology and Medicine Metallothionein-3 Is a Component of a Multiprotein Complex in the Mouse Brain*.

(31) Manso, Y.; Carrasco, J.; Comes, G.; Meloni, G.; Adlard, P. A.; Bush, A. I.; Vašák, M.; Hidalgo, J. Characterization of the Role of Metallothionein-3 in an Animal Model of Alzheimer's Disease. *Cell. Mol. Life Sci.* **2012**, *69* (21), 3683–3700. https://doi.org/10.1007/s00018-012-1047-9.

(32) Valko, M.; Morris, H.; Cronin, M. T. D. Metals, Toxicity and Oxidative Stress. *Curr. Med. Chem.* **2005**, *12*, 1161–1208.

(33) Klein, W. L.; Krafft, G. A.; Finch, C. E. *Targeting Small A β Oligomers: The Solution to an Alzheimer's Disease Conundrum?*; 2001; Vol. 24. https://doi.org/10.1016/S0166-2236(00)01749-5.

(34) Benilova, I.; Karran, E.; De Strooper, B. The Toxic Aβ Oligomer and Alzheimer's Disease: An Emperor in Need of Clothes. *Nat. Neurosci.* **2012**, *15* (3), 349–357. https://doi.org/10.1038/nn.3028.

(35) Meloni, G.; Vašák, M. Redox Activity of α-Synuclein-Cu Is Silenced by Zn 7-Metallothionein-3. *Free Radic. Biol. Med.* **2011**, *50* (11), 1471–1479. https://doi.org/10.1016/j.freeradbiomed.2011.02.003.

(36) Faller, P.; Hureau, C.; La Penna, G. Metal Ions and Intrinsically Disordered Proteins and Peptides: From Cu/Zn Amyloid-β to General Principles. *Acc. Chem. Res.* **2014**, *47* (8), 2252–2259. https://doi.org/10.1021/ar400293h.

(37) Meloni, G.; Sonois, V.; Delaine, T.; Guilloreau, L.; Gillet, A.; Teissié, J.; Faller, P.; Vašák, M. Metal Swap between Zn7-Metallothionein-3 and Amyloid-β-Cu Protects against Amyloid-β Toxicity. *Nat. Chem. Biol.* **2008**, *4* (6), 366–372. https://doi.org/10.1038/nchembio.89.

(38) Meloni, G.; Crameri, A.; Fritz, G.; Davies, P.; Brown, D. R.; Kroneck, P. M. H.; Vašák, M. The Catalytic Redox Activity of Prion Protein-Cu II Is Controlled by Metal Exchange with the Zn II-Thiolate Clusters of Zn 7Metallothionein-3. *ChemBioChem* **2012**, *13* (9), 1261–1265. https://doi.org/10.1002/cbic.201200198.

(39) Scheller, J. S.; Irvine, G. W.; Wong, D. L.; Hartwig, A.; Stillman, M. J. Stepwise Copper(i) Binding to Metallothionein a Mixed Cooperative and Non-Cooperative Mechanism for All 20 Copper Ions. *Metallomics* **2017**, *9* (5), 447–462. https://doi.org/10.1039/c7mt00041c.

(40) Nies, D. H. *Resistance to Cadmium, Cobalt, Zinc, and Nickel in Microbes*; 1992; Vol. 27. https://doi.org/10.1016/0147-619X(92)90003-S.

(41) Roesijadi, G. *Metallothionein and Its Role in Toxic Metal Regulation*; 1996; Vol. 113. https://doi.org/10.1016/0742-8413(95)02077-2.

(42) Bofill, R.; Palacios, Ò.; Capdevila, M.; Cols, N.; González-Duarte, R.; Atrian, S.; González-Duarte, P. A New Insight into the Ag+ and Cu+ Binding Sites in the Metallothionein β Domain. *J. Inorg. Biochem.* **1999**, *73* (1–2), 57–64. https://doi.org/10.1016/S0162-0134(98)10091-0.

(43) Salgado, M. T.; Bacher, K. L.; Stillman, M. J. Probing Structural Changes in the α and β Domains of Copper- and Silver-Substituted Metallothionein by Emission

Spectroscopy and Electrospray Ionization Mass Spectrometry. *J. Biol. Inorg. Chem.* **2007**, *12* (3), 294–312. https://doi.org/10.1007/s00775-006-0187-5.

(44) Ngu, T. T.; Lee, J. A.; Rushton, M. K.; Stillman, M. J. Arsenic Metalation of Seaweed Fucus Vesiculosus Metallothionein: The Importance of the Interdomain Linker in Metallothionein. *Biochemistry* **2009**, *48* (37), 8806–8816. https://doi.org/10.1021/bi9007462.

(45) Banci, L.; Bertini, I.; Ciofi-Baffoni, S.; Kozyreva, T.; Zovo, K.; Palumaa, P. Affinity Gradients Drive Copper to Cellular Destinations. *Nature* **2010**, *465* (7298), 645–648. https://doi.org/10.1038/nature09018.

(46) Feldman, S. L.; Failla, M. L.; Cousins, R. J. *Degradation of Rat Liver Metallothioneins in Vitro*; 1978; Vol. 544. https://doi.org/10.1016/0304-4165(78)90338-0.

(47) Summers, K. L.; Mahrok, A. K.; Dryden, M. D. M.; Stillman, M. J. Structural Properties of Metal-Free Apometallothioneins. *Biochem. Biophys. Res. Commun.* **2012**, *425* (2), 485–492. https://doi.org/10.1016/j.bbrc.2012.07.141.

(48) Rigby, K. E.; Stillman, M. J. Structural Studies of Metal-Free Metallothionein. *Biochem. Biophys. Res. Commun.* **2004**, *325* (4), 1271–1278. https://doi.org/10.1016/j.bbrc.2004.10.144.

(49) Rhee, I. K.; Lee, K. S.; Huang, P. C. *Metallothioniens with Interdomain Hinges Expanded by Insertion Mutagenesis*; 1990; Vol. 3. https://doi.org/10.1093/protein/3.3.205.

(50) Zangger, K.; Armitage, I. M. *Dynamics of Interdomain and Intermolecular Interactions in Mammalian Metallothioneins*; 2002; Vol. 88. https://doi.org/10.1016/S0162-0134(01)00379-8.

(51) Grossoehme, N. E.; Spuches, A. M.; Wilcox, D. E. Application of Isothermal Titration Calorimetry in Bioinorganic Chemistry. *J. Biol. Inorg. Chem.* **2010**, *15* (8), 1183–1191. https://doi.org/10.1007/s00775-010-0693-3.

(52) Quinn, C. F.; Carpenter, M. C.; Croteau, M. L.; Wilcox, D. E. Isothermal Titration Calorimetry Measurements of Metal Ions Binding to Proteins. *Methods Enzymol.* **2016**, *567*, 3–21. https://doi.org/10.1016/bs.mie.2015.08.021.

(53) Carpenter, M. C.; Wilcox, D. E. Thermodynamics of Formation of the Insulin

Hexamer: Metal-Stabilized Proton-Coupled Assembly of Quaternary Structure. *Biochemistry* **2014**, *53* (8), 1296–1301. https://doi.org/10.1021/bi4016567.

(54) Chaberek, S.; Frost, A. E.; Doran, M. A.; Bicknell, N. J. *Interaction of Some Divalent Metal Ions with Diethylenetriaminepentaacetic Acid*; American Chemical Society, 1959; Vol. 11. https://doi.org/10.1016/0022-1902(59)80245-1.

(55) Johnson, D. K.; Stevenson, M. J.; Almadidy, Z. A.; Jenkins, S. E.; Wilcox, D. E.; Grossoehme, N. E. Stabilization of Cu(i) for Binding and Calorimetric Measurements in Aqueous Solution. *Dalt. Trans.* **2015**, *44* (37), 16494–16505. https://doi.org/10.1039/c5dt02689j.

(56) Xiao, Z.; Brose, J.; Schimo, S.; Ackland, S. M.; La Fontaine, S.; Wedd, A. G. Unification of the Copper(I) Binding Affinities of the Metallo-Chaperones Atx1, Atox1, and Related Proteins: Detection Probes and Affinity Standards. *J. Biol. Chem.* **2011**, *286* (13), 11047–11055. https://doi.org/10.1074/jbc.M110.213074.

(57) Mehlenbacher, M. R.; Elsiesy, R.; Lakha, R.; Villones, R. L. E.; Orman, M.; Vizcarra, C. L.; Meloni, G.; Wilcox, D.; Austin, R. N. Metal Binding and Interdomain Thermodynamics of Mammalian Metallothionein-3: Enthalpically Favoured Cu + Supplants Entropically Favoured Zn 2+ to Form Cu + 4 Clusters Under Physiological Conditions . *Chem. Sci.* **2022**. https://doi.org/10.1039/d2sc00676f.

(58) Rich, A. M.; Bombarda, E.; Schenk, A. D.; Lee, P. E.; Cox, E. H.; Spuches, A. M.; Hudson, L. D.; Kieffer, B.; Wilcox, D. E. Thermodynamics of Zn 2+ Binding to Cys 2His 2 and Cys 2HisCys Zinc Fingers and a Cys 4 Transcription Factor Site. *J. Am. Chem. Soc.* **2012**, *134* (25), 10405–10418. https://doi.org/10.1021/ja211417g.

(59) Reddi, A. R.; Guzman, T. R.; Breece, R. M.; Tierney, D. L.; Gibney, B. R. Deducing the Energetic Cost of Protein Folding in Zinc Finger Proteins Using Designed Metallopeptides. *J. Am. Chem. Soc.* **2007**, *129* (42), 12815–12827. https://doi.org/10.1021/ja073902+.

(60) Tamura, A.; Privalov, P. L. *The Entropy Cost of Protein Association*; 1997; Vol. 273. https://doi.org/10.1006/jmbi.1997.1368.

(61) Gilson, M. K.; Given, J. A.; Bush, B. L.; McCammon, J. A. The Statistical-Thermodynamic Basis for Computation of Binding Affinities: A Critical Review.

Biophys. J. **1997**, *72* (3), 1047–1069. https://doi.org/10.1016/S0006-3495(97)78756-3.

(62) Holtzer, A. The "Cratic Correction" and Related Fallacies. *Biopolymers* **1995**, *35* (6), 595–602. https://doi.org/10.1002/bip.360350605.

(63) Rigby, K. E.; Chan, J.; Mackie, J.; Stillman, M. J. Molecular Dynamics Study on the Folding and Metallation of the Individual Domains of Metallothionein. *Proteins Struct. Funct. Genet.* **2006**, *62* (1), 159–172. https://doi.org/10.1002/prot.20663.

(64) Calvo, J.; Jung, H.; Meloni, G. Copper Metallothioneins. *IUBMB Life* **2017**, *69* (4), 236–245. https://doi.org/10.1002/iub.1618.

(65) Pountney, D. L.; Schauwecker, I.; Zarn, J.; Vašák, M. Formation of Mammalian Cu8-Metallothionein in Vitro: Evidence for the Existence of Two Cu(I)4-Thiolate Clusters. *Biochemistry* **1994**, *33* (32), 9699–9705. https://doi.org/10.1021/bi00198a040.

(66) Lin, L. N.; Brandts, J. F.; Mason, A. B.; Woodworth, R. C. Calorimetric Studies of the Binding of Ferric Ions to Ovotransferrin and Interactions between Binding Sites. *Biochemistry* **1991**, *30* (50), 11660–11669. https://doi.org/10.1021/bi00114a008.

(67) Lin, L. N.; Brandts, J. F.; Mason, A. B.; Woodworth, R. C. Calorimetric Studies of the Binding of Ferric Ions to Human Serum Transferrin. *Biochemistry* **1993**, *32* (36), 9398–9406. https://doi.org/10.1021/bi00087a019.

(68) Pettersen, E. F.; Goddard, T. D.; Huang, C. C.; Couch, G. S.; Greenblatt, D. M.; Meng, E. C.; Ferrin, T. E. UCSF Chimera - A Visualization System for Exploratory Research and Analysis. *J. Comput. Chem.* **2004**, *25* (13), 1605–1612. https://doi.org/10.1002/jcc.20084.

Chapter 7:

Thermodynamic Foundation of Metal Selectivity and Specificity in Bacterial Copper Storage Proteins: A Comparative Analysis of the Binding of d^{10} Metals by Isothermal Titration Calorimetry

7.1. Introduction

7.1.1 Copper in Biology

The utilization of copper by living organisms seems paradoxical. Accessibility to chemistry that would be unlikely under physiological conditions is made possible through copper bound to proteins, yet copper is highly toxic to cells. Inclusion of copper into cellular biology and biochemistry has allowed important processes, including oxygen transport and electron transfer.[1,2] Copper, however, is not essential for all forms of life and is damaging to cells at high concentrations.[3] Curiously, the same redox-activity and chemistry that permits biological function of copper also make copper damaging to cells if it is unregulated. Copper, at levels that overwhelm cellular protection mechanisms, can bind inappropriately to sulfur, oxygen, and imidazole ligands within a cell.[4] This can lead to aberrant displacement of native metals, like zinc (Zn) or iron (Fe).[5] Balancing these contradictory chemical functions requires large amounts of energy-consuming cellular resources to regulate, uptake, transport, and distribute copper from the microenvironment of the cell to specific Cu-requiring proteins inside the cytoplasm of the cell.[6] Defects in this cellular copper homeostasis in humans can result in copper overload disorders (Wilson's disease), copper deficiency (Menkes disease and Occipital Horn Syndrome), and defects in copper transport (alloalbuminemia).[7–9] Strict control of copper within a cell requires carefully orchestrated mechanisms for inclusion of the metal into the appropriate metalloproteins for utilization or storage.

7.1.2. Copper Homeostasis

Copper homeostasis, which is regulated by metalloregulatory proteins and mediated by metallochaperones, protect cells from the toxic effects of copper. Generally, metallothionein (MT) is a small, cysteine-rich protein that has two domains; α and β, which are able to bind up to 20 Cu^{+} in solution with dynamic coordination, including 2-, 3- and 4-coordinate binding.[10–12] Further exploration into the physiological and biochemical function of metallothionein and the binding of Cu^{+} and Zn^{2+} can be found in Chapter 6. Beyond MT, which has been proposed to store copper, very few dedicated copper storage proteins have been discovered. Recently, a small cysteine-rich protein that binds up to 6

Cu^{+}, and whose expression was induced by both copper and cadmium, was discovered in the gram-positive *Mycobacterium tuberculosis*.[13] Beyond these examples of copper storage proteins, the only other example is the bacterial copper storage protein in *Methylosinus trichosporium* OB3b.

The discovery of copper storage proteins (CSPs: CSP1, CSP2, & CSP3) in methane-oxidizing bacteria may not be particularly surprising, as these bacteria need large amounts of copper, which is required for membrane-bound methane monooxygenase (pMMO) that catalyzes the oxidation of methane to methanol.[15,16] Our understanding of the active site of pMMO has been controversial; pMMO was believed previously to contain a multinuclear copper site, but recently found to have only monocopper sites.[17] This lack of clarity has made the determination of a catalytic mechanism difficult, limiting our biochemical understanding of biological methane oxidation.[18] Controversy aside, pMMO contributes such an important activity in these cells that a large portion of the total cellular protein content is pMMO, suggesting that large amounts of copper are required for its function and it plays a vital role in the biology of *M trichosporium*.[19] Under conditions of low copper, the organism will switch over to a less efficient iron-utilizing soluble methane monooxygenase (sMMO), as low cellular copper downregulates pMMO and upregulates sMMO.[19] Understandably, due to extensive copper utilization in the cell, the copper-management system should be of considerable efficiency because, as discussed earlier, increased concentrations of copper are toxic but copper is required for cellular function.

Of initial interest for copper homeostasis in *M. trichosporium* was methanobactin and a suspected methanobactin-related transport protein. Methanobactin is a small peptide-derived molecule, similar to iron-binding siderophores, that binds Cu^{+} with an affinity of $\sim 10^{21}$.[20] Original characterization suggested that, because of its lower Cu^{2+}-binding affinity, oxidation of methanobactin-bound Cu^{+} to Cu^{2+} was required for the release of Cu^{+} to its binding partner.[20] This has since been contested, with more recent work suggesting that conformational changes in the N-terminus releases the Cu^{+}.[21] Unexpectedly, while work was underway on the role of methanobactin in Cu^{+} biology of *M. trichosporium*, CSPs were discovered and have since been of great interest as the site of copper storage for physiological utilization in these cells, which require large amounts of copper.[22]

7.1.3. Introduction to Methylosinus trichosporium Copper Storage Proteins

Copper storage proteins (CSPs), like metallothionein, are composed of a large percentage of cysteine residues. Unlike metallothionein, however, CSPs are structured proteins. Initial characterization by CD had suggested the CSPs have considerable helical structure, which was later confirmed by X-ray crystallography.[23] Subsequent structural characterization showed that CSPs are composed of a tetramer of four-helix bundles, in which the many cysteines are facing the central core of each four-helix monomer.[23] Each of these monomers in CSP1 and CSP2 contain 13 cysteine residues, which are the primary ligands for Cu^{+}. CSP1 and CSP2 are targeted by the twin-arginine translocation pathway for transport outside of the cytosol of the cell, and the four-helix bundle of each monomer binds up to 13 Cu^{+} by the 13 cysteine residues for a total of 52 Cu^{+} per tetramer (**Figure 7.1.3.1**).[23] Unlike CSP1 and CSP2, CSP3 is not targeted for export out of the cytosol. It is believed to remain in the cytosol, binding up to 19 Cu^{+} by 18 cysteine residues that line the core of the four-helix bundle for a total of 76 Cu^{+} ions bound to the tetramer.[24]

It is useful to consider other metal-storage proteins, for comparison. Although metallothionein has some metal-storage capabilities, its interaction with metals is much more labile, since the protein structure is conformationally dynamic and the metal ions can be readily displaced. Similarly, the iron-storage protein ferritin binds Fe^{2+}, where it is oxidized to Fe^{3+} upon incorporation into a core of the protein as an insoluble Fe^{3+} hydroxide or phosphate cluster.[25] Neither ferritin nor metallothionein bind and store metals like CSPs, which is the first and only known example, thus far, of a well-structured protein that binds and stores multiple metals within a folded protein motif.

Visual inspection of CSP structures show that the channel where the Cu^{+} binds is open only at one end. This opening is lined with histidine residues and a methionine.

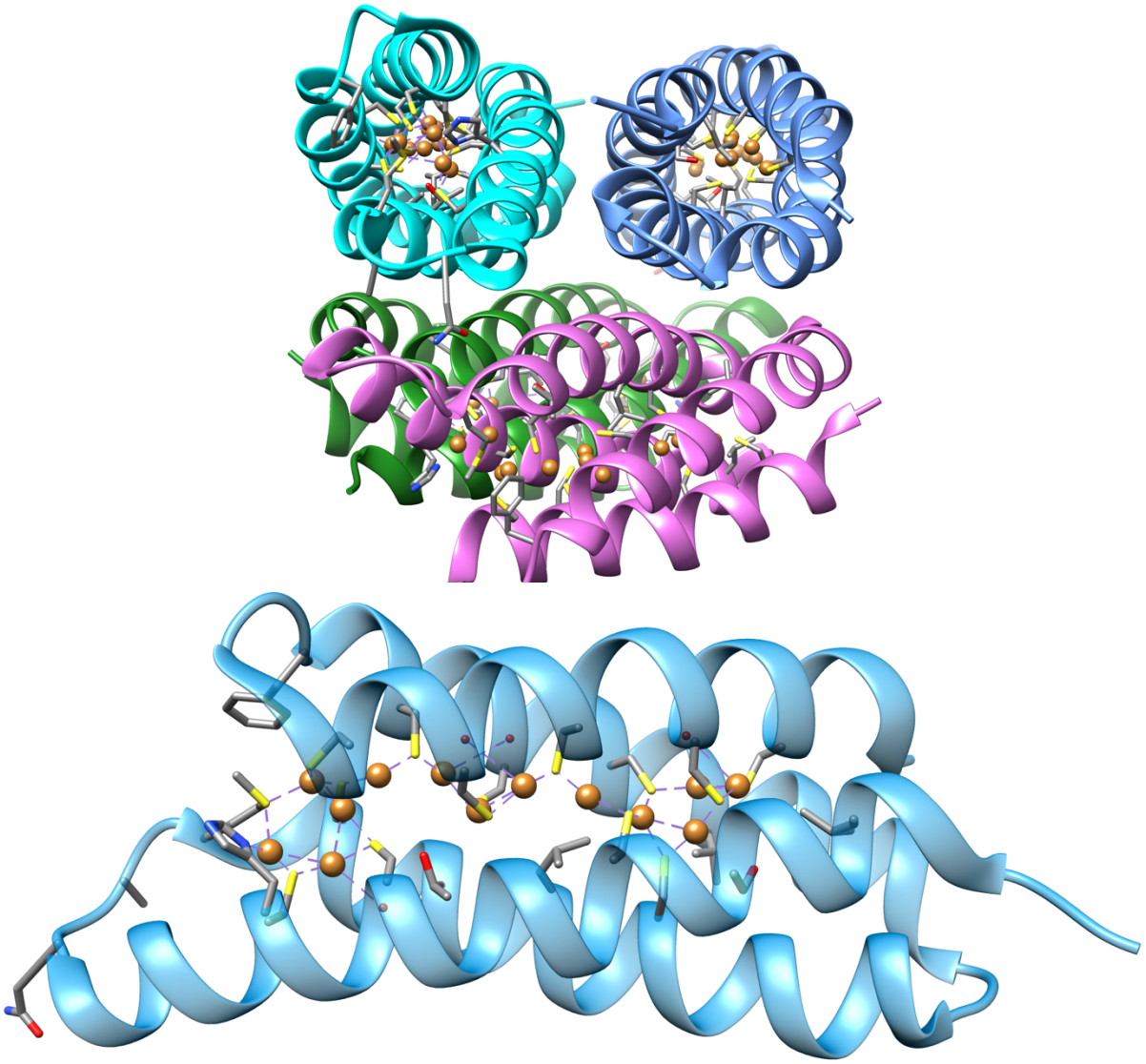

Figure 7.1.3.1. *(top) Tetrameric crystal structure of CSP1 from* Methysinus trichosporium OB3b *in which each individual monomer is colorized. (bottom) Individual monomer of CSP1 from* M. trichosporium OB3b*, depicting the structured, alpha-helical protein. 13* Cu^{+} *are show in each monomer. The opening of the metal channel is lined with 2 histidine residues and a methionine. (PDB: 5FJE)*

Initial proposals for Cu^+ binding to CSPs suggested that binding of the second Cu^+ requires, the first Cu^+ to bind at the far end of the channel. This mechanism, however, is confounded by the proposal of step-wise copper-thiolate cluster formation that occurs through the sequential addition of Cu^+.[26] Crystallization of CSP3 with partial loading of Cu^+ provides insight into copper-thiolate cluster formation. Addition of 4 Cu^+ to CSP3 results in partial occupation of the copper-binding sites. Curiously, these first 4 Cu^+ ions do not bind and move towards the closed end of the Cys-lined channel, as they maintain a position relatively close to the entrance of the channel instead (**Figure 7.1.3.2**). This results in the formation of an approximately symmetrical tetrathiolate cluster with C97, C101, C114, C118, and weakly-bound N58. The binding of additional Cu^+ results in a copper-bridged thiolate coordination, designated as μ_2-S-Cys, which is proposed to be further stabilized by Cu^+–Cu^+ interactions. Similar coordination and Cu^+ stabilization is observed upon the addition of 9 Cu^+ equivalents, with some slight rearranging, which results in the formation of 3 tetrathiolate clusters. Further addition of Cu^+, to approximately 17 molar equivalents, diminishes the symmetry of the tetrathiolate clusters that form, resulting in both major and minor species. Differences in the occupation of each metal site suggests that the incorporation of Cu^+ within the core requires dynamic coordination and labile Cu^+ binding. The final two Cu^+ ions (Cu_{18} and Cu_{19}) bind to the protein outside of the Cys-lined core. Of these two, Cu_{18} binds to both a single cysteine and a histidine, resulting in a linear geometry, which is mirrored in Cu_{19}, although the distance between Cu_{19} and the histidine residue is slightly larger.

Formation of tetrathiolate Cu^+ clusters are relatively rare in biological systems. Although Cu^+-thiolate clusters might allow for interesting and useful coordination chemistry, thiolate clusters enhance the risk of Cu^{2+}-catalyzed disulfide bond formation. This risk remains with the binding and storage of Cu^+ in CSPs of *M. trichosporium* but is suggested to be limited by the rigid and well-folded nature of these copper storage proteins. However, for CSP3, it is unlikely that Cu^{2+} would be present in the reducing intracellular environment, and binding of Cu^{2+} to CSP1 or CSP2 in the periplasm may result in disulfide oxidation and subsequent copper reduction, aiding in the binding and storage of Cu^+ over Cu^{2+}.

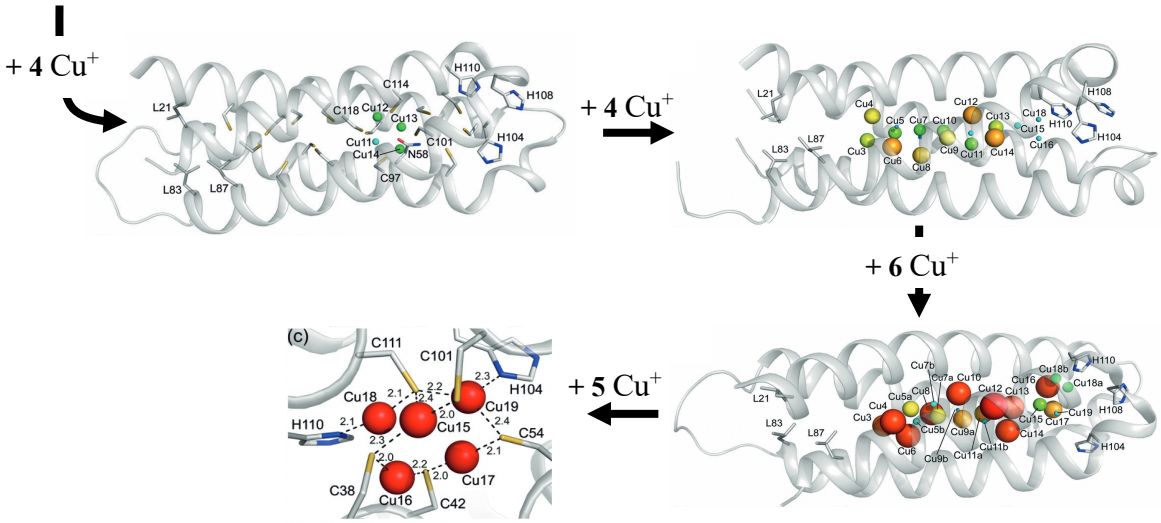

Figure 7.1.3.2 *Crystal structures of CSP3 with successive equivalents of Cu^+ bound to the protein are shown. The initial addition of 4 Cu^+ to apo-CSP3 show that these 4 metal ions bind and remain near the opening of the channel entrance, forming a near-symmetrical tetrathiolate copper cluster. Further addition of 4 Cu^+ (~8 total equivalents) results in these copper clusters binding towards the middle of the channel, forming similar tetrathiolate copper clusters. Each of these copper ions that are bound up to 8-9 equivalents are only partially occupied. 6 additional Cu^+ (14 total eq.) results in more compressed copper-thiolate clusters that are fully occupied. These Cu^+ continue to bind in the core of the protein, leaving the outer histidine-rich pocket empty. Lastly, addition of 5 more Cu^+ (19 total eq.) fills this histidine-rich pocket. After complete addition of Cu^+, each of the copper-binding sites are fully occupied. Modified from Baslé* et al.[34]

7.1.4. Specificity and Selectivity of Copper Over Competitive d^{10} Metal Ions

The affinities of CSP1 and CSP3 for Cu^+ were determined by using the colorimetric chelation of Cu^+ by bicinchoninic acid (BCA).[24] These experiments showed that Cu^+ binds to CSP3 with log K ~17, which is on the lower end of Cu^+ affinities of protein sites with cysteine residues. These experiments, however, are not specific to the copper-thiolate clusters that form within the copper storage proteins as each subsequent Cu^+ is added. Furthermore, cysteine protonation was neglected, and these experiments were unable to differentiate the enthalpic and entropic contributions to binding. Knowledge of these contributions would enhance our understanding of metal selectivity and specificity, which can be further expanded by the contribution of protein structural dynamics and second sphere interactions on metal binding. The selectivity and specificity for Cu^+, over other metals, could be probed by colorimetric chelation, but this has not yet been studied. Consider, for example, Zn^{2+}, which could compete with Cu^+ for the cysteine residues, depending on the coordinating geometry of the target protein and the overall cellular concentration. Zinc is ubiquitous in the environment and is also required for the survival of cells, yet Zn^{2+} is not found bound to CSPs under native conditions.[23,27] One metal, in particular, is expected to outcompete Cu^+ for binding to cysteine residues, Hg^{2+}. Inorganic mercury is ubiquitous in the environment and is extraordinarily toxic to cells. Furthermore, the more thiophilic nature of Hg^{2+} would predispose the much more favorable binding of Hg^{2+} over Cu^+ at a cysteine binding site. With this in mind, how do CSPs select for the binding and storage of Cu^+ over other competitive d^{10} metal ions? What fundamental bioinorganic principles drive the storage of Cu^+ over other metal ions?

Quantifying the binding thermodynamics of Cu^+ and competing d^{10} metals would reveal the metal specificity and selectivity of the CSPs. As described in the previous chapters, the thermodynamics of Cu^+, Zn^{2+}, and Hg^{2+} binding to CSP1 and CSP3 have been determined by isothermal titration calorimetry (ITC), which provides several thermodynamic values. These binding thermodynamics include contributions from proton exchange, protein conformational dynamics, and the thermodynamics associated with protein and metal (de)-solvation. As described in Chapter 2, measuring the binding of metals to a protein by ITC in multiple buffers provides the number of protons that are released from or bind to the protein upon metal binding. This, however, was not feasible

for these CSPs, due to limited samples from our collaboration with Chris Dennison at Newcastle University in Newcastle-on-Tyne, UK. However, prior characterization of the copper-thiolate clusters in CSPs allows an approximation of the release of protons from the metal-binding residues. Although Zn^{2+} and Hg^{2+} binding to CSPs has not been studied by Dennison or others, reference to previous literature data for metal coordination and binding geometries, along with experimental stoichiometries, provides insight into the metal binding thermodynamics for these other d^{10} metal ions. This chapter aims to provide the thermodynamics of the selectivity and specificity of CSP1 and CSP3 for the binding and storage of Cu^{+} over other competitive d^{10} metal ions.

7.2. Materials and Methods

7.2.1. Chemicals

The highest purity of, HEPES (4-(2-hydroxyethyl)-1-piperazineethanesulfonic acid) buffer was purchased from Akron Biotech and utilized without further modification. The metal salts CuCl (Aldrich), $ZnCl_2$ (Sigma), and $HgCl_2$ (Baker Chemical) were obtained in the highest purity available and utilized as received without further modification or purification. Chelex, for the removal of aberrant metals from buffer solutions, was purchased and utilized as received from Sigma-Aldrich.

7.2.2. Copper Storage Protein (CSP1 and CSP3) Transformation, Expression, and Purification

Purified CSP1 and CSP3 samples were generously provided by our collaborator, Chris Dennison, at Newcastle University, Newcastle-on-Tyne UK. Because these protein samples were not transformed, expressed, or purified here at Dartmouth College, a brief summary of the procedure can be found elsewhere.[23,24] Protein samples were received in their apo-form in 20 mM HEPES, 200 mM NaCl, pH 7.5, which was demetallated prior to the addition of the protein. These protein samples were kept in the –80 ^{o}C freezer until utilization. After thawing within the anaerobic glovebox, proteins samples were used as provided for ITC experiments with metal solutions in the same buffer that had been previously demetallated and made anaerobic under vacuum.

7.2.3. Determination of Ligand and Metal Salt Concentrations

Metal salts and competing ligands were weighed and brought into the Coy Labs anaerobic glovebox for dissolution in Milli-Q deionized water (>18 MΩ) at approximately pH 2 for metal salts, or in the experimental buffer for ligands. Confirmation of the concentration of the metal stock solution was done by a simple ITC titration of each metal solution into a known concentration of EDTA (ethylenediaminetetraacetic acid). Both the experimental stoichiometry and binding enthalpy was compared to known and expected values. If these values fell outside the range of expected values, stock concentrations were remade, and ITC experiments are repeated. Metal stock solutions were remade bi-weekly to ensure correct concentrations, whereas ligand solutions (EDTA, DPTA, reduced glutathione, etc.) were remade daily to ensure accuracy and stability. All buffer solutions that were used in the dissolution of ligands or metals were made metal-free with Chelex treatment in acid-washed glassware for at least one hour and filtered for later use. Buffers were pH-adjusted after filtration.

7.2.4. Determination of Copper(I) Concentration

Due to the difficulty in the handling of Cu^+, the determination of the concentration of Cu^+ is detailed for clarity, as it requires strict anaerobicity to prevent oxidation in aqueous solutions. An unspecified amount of CuCl is added to a pre-weighed 11 mL glass vial within the glovebox. Approximately 5 mL of deionized H_2O at pH 2 is added to the glass vial, and vigorously shaken to aid in dissolution. Additional aliquots of ~100 μL of 6 M HCl are added and further shaken until all the CuCl is dissolved. Determination of the Cu^+ concentration is done colorimetrically with bicinchoninic acid (BCA: $Cu^I(BCA)_2^{3-}$; ε_{563} = 7,900 M^{-1}) or bathocuproinedisulfonic acid (BCS: $Cu^I(BCS)_2^{3-}$; ε_{483} = 13,000 M^{-1}). Using UV-vis spectroscopy, a baseline is achieved with a buffered solution of BCA or BCS, 2-10 μL of the Cu^+ solution is added to the BCA- or BCS-containing cuvette and the absorbance at their specific wavelength is determined. This ensures an accurate Cu^+ is concentration determined without exposure of CuCl to environmental oxygen.

7.2.5. Isothermal Titration Calorimetry Experiments

Anaerobic samples were prepared in a Coy Labs glovebox that is continuously purged with N_2. Periodic addition of 5% H_2 to the glovebox regenerates a platinum catalyst that removes residual O_2 from within the environment of the glovebox. The VP-ITC (Microcal, Malvern Panalytical) is housed in its own custom-built anaerobic glovebox which is continuously purged with N_2 during measurements. All ITC experiments were completed using this anaerobic VP-ITC. Generally, injection volumes are dependent on the experimental system and range from 6 to 10 μL on the VP-ITC. Stirring speeds are 307 RPM and all ITC experiments are done at 25 ± 0.2 °C. Heat of dilution, associated with the ligand being titrated into the titrand, is determined by the heat of injections at the end of the experiment. This heat of dilution was subtracted from each data point as it contributes to each injection. Each experiment is repeated in triplicate, at a minimum.

The resulting isotherm is fit using a one-site or two-site binding model with the Origin fitting software provided for the VP. For accurate experimental heats associated with each injection, the solutions in the cell and the syringe must be as identical as possible in pH and concentration of the buffer. Mismatching the buffer compositions between the syringe and cell results in large experimental heats that mask the ligand-macromolecule binding, deemed a buffer-mismatch.

The binding of Cu^+ to CSP1 and CSP3 requires careful consideration, as Cu^+ readily undergoes disproportionation in aqueous solution. The addition of a Cu^+ chelating ligand that both stabilizes Cu^+ and provides competition with the protein for the Cu^+, ensuring the experimental binding affinities are within the accuracy range for the ITC. These stabilizing ligands, however, have different binding affinities with Cu^+, allowing for modification of the ITC experiments through the use of stronger or weaker competing ligands. Ligands utilized are acetonitrile (MeCN), hexamethyltrien (Me_6Trien), and reduced glutathione (GSH), which bind Cu^+ with increasing affinity. Similar considerations are required for the binding of Zn^{2+} and Hg^{2+}, although these metal ions do not require a stabilizing ligand to maintain their oxidation state. Competing ligands for Zn^{2+} and Hg^{2+} were determined from initial experiments of the metal titrated into the protein without the addition of a competing ligand.

7.3. Results and Analysis

7.3.1. Calorimetric Characterization of Copper(I) Binding to CSP1

Accurate determination of calorimetric data for Cu^+ binding to biomolecules requires appropriate and adequate stabilization of Cu^+ in aqueous solution under anaerobic conditions. This requires Cu^+ stabilizing ligands to be present in large excess (100 fold excess to copper), to minimize dipsoportionation.[28] The analysis must then account for the binding affinity of the stabilization ligand for the metal ion. Thus, careful consideration of the stabilizing ligand is required. Acetonitrile (MeCN), although a weakly-binding Cu^+ ligand, was selected as the primary competing Cu^+-stabilizing ligand for the calorimetric characterization of the Cu^+-CSP1 and Cu^+-CSP3 interaction.

Titrations of Cu^+ stabilized by acetonitrile into CSP1 show three exothermic inflections associated with three binding populations of Cu^+ (**Figure 7.3.1.1**). The first inflection occurs upon the addition of 7 ± 0.2 Cu^+, the second inflection occurs upon the continued addition of ~4 Cu^+, and the third inflection is found upon the addition of 2.8 ± 0.6 Cu^+. Both the first and second inflections have a binding affinity that is challenging to obtain, as the differentiation between the two exothermic events is minimal and these Cu^+ bind stronger than the third set. However, the stoichiometry can be approximated using Origin's two-site binding model and the enthalpy of the first inflection can be quantified in a similar manner. The enthalpy of the second binding event is determined by the enthalpy from a two-site binding model that includes the first and second binding events, where the enthalpy from the third event are masked out (**Figure 7.3.1.1, A**). The third binding inflection, which is the weakest binding population, however, is easily fit with a one-site binding model to quantify the apparent binding affinity and experimental enthalpy. This is done by masking (red data points) the first and second binding events (**Figure 7.3.1.1, B**) The lack of a difference between the enthalpy of the second and third binding populations events suggest that the latter enthalpy may by slightly underestimated, as this enthalpy includes both the final binding of the second inflection and the beginning binding of the third.

Fitting these inflections to establish the enthalpy or both then enthalpy and binding affinity is completed using the Origin software provided. Although a typical analysis requires multiple buffers to determine protein deprotonation, this was not possible for this system at this time. As such, assumptions from fundamental inorganic chemistry were

utilized, as will be discussed in detail. However, for the binding of Cu^+ to CSP1, a single experiment in another buffer, ACES, was obtained for qualitative visualization of similarities between two buffers (**Figure 7.3.1.1, C**). Thus, all ITC data reveal characterizable binding events, reflecting three populations of Cu^+ binding to CSP1 for a total of 13.8 ± 0.2 Cu^+ bound to CSP1 in HEPES.

The noticeable "beat pattern" that is observed in the raw experimental data in **Figure 7.3.1.1** is due to a visual artifact when a figure of the data contains a large number of injections from an ITC experiment. Close proximity of the injection peaks in the figure results in a peak-averaging effect, in which the drawing of the peaks blends together. This results in the "beat-pattern" but maintains the integrity of the data.

Titrations of a $Cu(MeCN)_3^+$ complex into CSP1 were carried out, primarily, in HEPES buffer, and show well-defined peaks that indicate a strongly exothermic interaction. Previous results report a strong binding interaction, which is associated with for the first and second populations of Cu^+ with data that fall well outside the quantifiable C-window. The average experimental, or apparent, thermodynamic values from the two-site fitting model are shown in **Table 7.3.1.1**, which defines the binding enthalpy of the first event. The enthalpy of the second binding event is masked by the enthalpy of the third binding event and is not quantified. A fit of the third binding event, with a one-site fitting model, defines the apparent binding affinity and enthalpy for this binding and the total number of Cu^+ that bind to CSP1. Since the stoichiometry of this third binding event is not the number of Cu^+ that bind in this population, but the total Cu^+ stoichiometry, the stoichiometries of the first and second binding events can be utilized, to find the stoichiometry of the third population where,

$$n_{Total} = n_1 + n_2 + n_3 \qquad \textbf{\textit{Equation}}\ \mathbf{7.3.1.1.}$$

and,

$$n_3 = n_{Total} - n_1 - n_2 \qquad \textbf{\textit{Equation}}\ \mathbf{7.3.1.2.}$$

By subtracting the stoichiometries of the first and second binding event from the total number of Cu^+ that bind, the stoichiometry of the third event can be estimated (**Table 7.3.1.1**).

Because these experiments were not done in multiple buffers, quantification of the cysteine deprotonation is based on the assumption that Cu^+ binds in a linear, two-coordinate

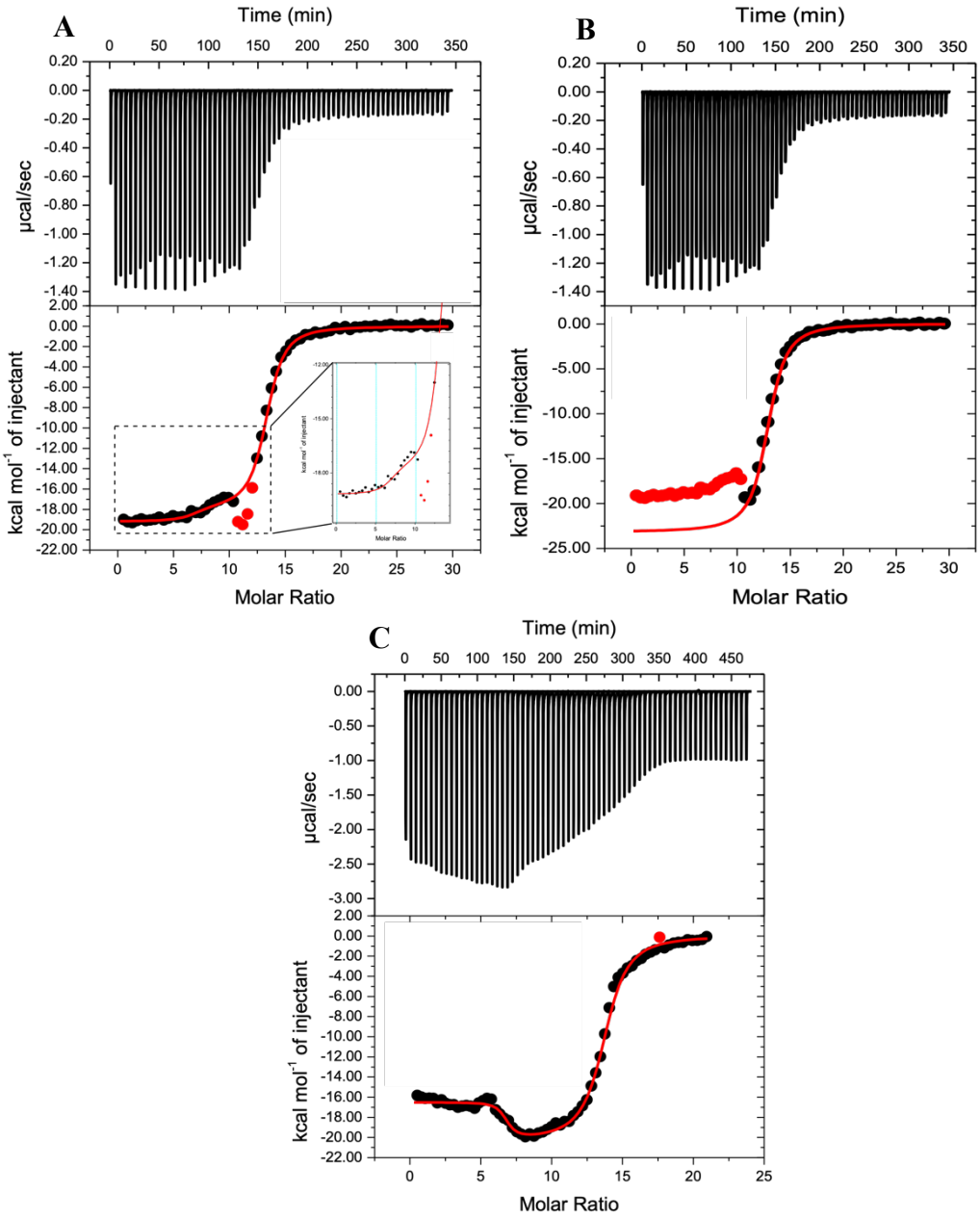

Figure 7.3.1.1. Representative isotherms of Cu^{+}, stabilized by excess acetonitrile (MeCN), titrated into *M. trichosporium OB3b* copper storage protein 1 (CSP1) in 20 mM buffer, 200 mM NaCl, pH 7.5. Experimental data considers CSP1 in the monomeric form, with each monomer of the tetramer being identical. (A) $Cu(MeCN)_3^{+}$ into CSP1 in HEPES (Two-Site Fit): (First Inflection) n_{ITC} = 6.8 ± 0.3, K_{ITC} = 2 (± 1)×10^8, ΔH^o_{ITC} = -19.19 ± 0.09 kcal/mol, and (Second Inflection): n_{ITC} = 6.4 ± 0.3, K_{ITC} = 4.2 (± 0.2)×10^6, ΔH^o_{ITC} = -17.8 ± 0.2 kcal/mol. Summation of these two binding populations indicates a total of 13.2 ± 0.4 Cu^{+} bind. (B) $Cu(MeCN)_3^{+}$ into CSP1 in HEPES (One-Site fit): n_{ITC} = 12.8 ± 0.04, K_{ITC} = 6.8 (± 0.4)×10^6, ΔH^o_{ITC} = -23.17 ± 0.03 kcal/mol. (C) $Cu(MeCN)_3^{+}$ into CSP1 in ACES: qualitative utilization of this data only, as this data was not replicated, however the best fit indicates n_1 = 6.7 ± 0.1, K_1 = 5 (± 3)×10^8, ΔH^o_1 = -16.5 ± 0.1 kcal/mol and n_2 = 7.0 ± 0.1, K_2 = 1 (± 1)×10^5, ΔH^o_2 = -20.4 ± 0.2 kcal/mol.

Table 7.3.1.1. Experimental thermodynamics for the binding of Cu^{+}, in excess acetonitrile, to CSP1. Values are the average from at least 3 independent experiments. Experimental data for the first and second inflections (Site 1 and Site 2, respectively) was fit using a two-site fitting model to establish estimated stoichiometries and enthalpy. The third inflection was fit using a one-site fitting model to establish the total stoichiometry, which gives the stoichiometry of this binding event, as well as the apparent binding affinity and enthalpy.

CSP1	Buffer	Protons Released	n_{ITC}	K_{ITC}	ΔH^{o}_{ITC} (kcal/mol)
			Site 1		
Two-Site Fit	**HEPES**	12	7 ± 0.2	>> 10^6	-20.2 ± 0.7
			Site 2		
	HEPES	0	~4	> 10^6	-17.7 ± 0.3
			Site 3		
One-Site Fit	**HEPES**	0	2.8 ± 0.6	4 (± 2)×10^6	-24 ± 2

geometry, and the number of protons released upon Cu^+ binding is determined *a priori*. Experimentally or computationally determining the pK_a values of each cysteine in CSP1 would be challenging due to the large number of cysteine residues. As such, the pK_a of a free cysteine ($pK_a \approx 8.6$) will be utilized as an approximation of the pK_a of each cysteine in CSP1. This assumption is supported by literature precedence that had shown that the binding affinity of Cu^+ was dependent on pH, suggesting that these cysteines become more protonated as the solution becomes more acidic.[29,30]

It is emphasized that this is an assumption of cysteine deprotonation and may not accurately represent the true nature of Cu^+ binding. Further experimentation to determine the number of protons that are released from CSP1 upon Cu^+ binding for each population would be required for the most accurate thermodynamic characterization. This assumption, however, is adequate for a preliminary quantification of the enthalpic contribution to Cu^+ binding for the first binding event, and both the binding affinity and enthalpy for the third Cu^+ binding event. Experimental thermodynamics associated with the second binding event is blurred between the first and third binding event and is difficult to quantify.

With these assumptions in mind, at the experimental pH of 7.5, each cysteine is assumed to be protonated by 0.92 protons, for a total of 12.0 protons that are proposed to be released upon Cu^+ binding to the 13 cysteine residues of CSP1. Expected deprotonation of these cysteines by Cu^+ binding takes the place of a proton inventory, which would typically be utilized. The competing equilibria in the titration of $Cu(MeCN)_3^+$ into CSP1 are found in (**Scheme 7.3.1.1** for the first binding event and **Scheme 7.3.1.2.** for the second and third binding events). With these contributing enthalpies from the competing equilibria, the buffer-independent, thermodynamics can be quantified for the first and third Cu^+ binding events at pH 7.5.

First, the enthalpy of the metal-protein interaction for the first binding event, which involves the binding of 7 Cu^+ and the release of 12 protons, fully deprotonating the CSP1, is determined by rearranging and substituting CSP1 deprotonation into **Equation 7.3.1.3** such that:

$$[(7\Delta H_{MP})] = [\Delta H_{ITC}] + \left(7\Delta H_{ML_1}\right) + \left(7\Delta H_{ML_2}\right) + \left(7\Delta H_{ML_3}\right) - (12.0\Delta H_{BH}) \quad \boldsymbol{Equation\ 7.3.1.4}$$

Scheme 7.3.1.1. Competing equilibria for the first binding event, in which 7 ± 0.2 Cu^+ bind to CSP1, fully deprotonating the protein upon binding. ΔH_{ML1}, $\Delta H_{M2,}$ and ΔH_{M3} are the enthalpies associated with each of the 3 stabilizing MeCN (L) ligands with Cu^+ (M); although these enthalpies are negligibly small and not necessary, they are included for completness. ΔH_{PH} is the enthalpy associated with deprotonation of the cysteine residues on the protein. ΔH_{BH} is the enthalpy associated with protonation of the buffer (B), and ΔH_{MP} is the desired enthalpy of the metal-protein interaction. ΔH_{ITC} is the experimental enthalpy, which is the summation of all competing equilibria that occur in solution (**Equation 7.3.1.3**).

Cu^+–$MeCN_1$	⇄	$Cu^+ + MeCN_1$	$-(nCu^+\Delta H_{ML1})$
Cu^+–$MeCN_2$	⇄	$Cu^+ + MeCN_2$	$-(nCu^+\Delta H_{ML2})$
Cu^+–$MeCN_3$	⇄	$Cu^+ + MeCN_3$	$-(nCu^+\Delta H_{ML3})$
CSP1–H_x	⇄	CSP1 + H^+_x	$n_{H+}\Delta H_{PH}$
H^+_x + Buffer	⇄	Buffer–H_x	$n_{H+}\Delta H_{BH}$
Cu^+ + CSP1	⇄	Cu^+–CSP1	$nCu^+\Delta H_{MP}$

$$\Delta H_{ITC} = -(nCu^+\Delta H_{ML1})-(nCu^+\Delta H_{ML2})-(nCu^+\Delta H_{ML3})+(n_{H+}\Delta H_{PH})+(n_{H+}\Delta H_{BH})+(nCu^+\Delta H_{MP})$$

Eq. 7.3.1.3

Scheme 7.3.1.2. Competing equilibria for the second binding event in which ~4 Cu^+ bind to CSP1, which has already been fully deprotonated. The titration involves Cu^+ stabilized with acetonitrile (MeCN) added to CSP1 in 20 mM HEPES, 200 mM NaCl, pH 7.5. ΔH_{ML1}, $\Delta H_{M2,}$ and ΔH_{M3} are the enthalpies associated with each of the 3 stabilizing MeCN (L) ligands with Cu^+ (M). ΔH_{MP} is the desired enthalpy of the metal-protein interaction. ΔH_{ITC} is the experimental enthalpy, which is the summation of all competing equilibria that occur in solution (**Equation 7.3.1.5**).

Cu^+–$MeCN_1$	⇄	$Cu^+ + MeCN_1$	$-(nCu^+\Delta H_{ML1})$
Cu^+–$MeCN_2$	⇄	$Cu^+ + MeCN_2$	$-(nCu^+\Delta H_{ML2})$
Cu^+–$MeCN_3$	⇄	$Cu^+ + MeCN_3$	$-(nCu^+\Delta H_{ML3})$
$Cu^+ + CSP1$	⇄	Cu^+–CSP1	$nCu^+\Delta H_{MP}$

$$\Delta H_{ITC} = -(nCu^+\Delta H_{ML1})-(nCu^+\Delta H_{ML2}) -(nCu^+\Delta H_{ML3})+(nCu^+\Delta H_{MP}) \quad \textbf{Eq.7.3.1.5}$$

Table 7.3.1.2. Condition-independent thermodynamics of Cu^{+} binding to CSP1 from at least 3 independent experiments. Post-hoc analysis provides the average buffer-independent, thermodynamics of the Cu^{+}-CSP1 interaction on a *per-metal* basis at pH 7.5 as determined by ITC, unless otherwise noted.

CSP1	Buffer	n_{ITC}	K	ΔH^{o} (kcal/mol)	$-T\Delta S^{o}$ (kcal/mol)	ΔG^{o} (kcal/mol)
Site 1	**HEPES**	7 ± 0.2	[a]1.3 (± 0.1)×10^{17}	+5.9 ± 0.3	[c]-29.2 ± 0.3	[b]-23.3 ± 0.1
Site 2	**HEPES**	~4	$10^{7} < K_a < 10^{17}$	-4.4 ± 0.3	-5.2 < -TΔS < -18.9	-9.6 < ΔG < -23.3
Site 3	**HEPES**	2.8 ± 0.6	1.2 (± 0.6)×10^{7}	-8.5 ± 0.7	-1.1 ± 0.8	-9.6 ± 0.4
Total		*13.8 ± 0.5*				

[a]Average Cu^{+}-CSP1 equilibrium constant from Dennison et al. (2015)[23].
[b]Quantification of Gibbs free energy from Dennison et al. (2015)[23].
[c]Quantification of –TΔS is combined literature and experimental data.

Quantification of the buffer-independent enthalpy associated with metal binding is calculated on a *per-monomer* basis at pH 7.5. Simply dividing this enthalpy by the number of Cu^+ gives the thermodynamics on a *per-metal* basis (**Table 7.3.1.2**).

Some assumptions are made for this *post-hoc* analysis. Of particular note is the enthalpy associated with protein deprotonation, ΔH_{PH}. This value, under typical circumstances, is unknown for most proteins. However, I am assuming that the binding of 7 Cu^+ results in the deprotonation of each cysteine, that is approximated as a free cysteine and protonated with 0.92 protons at pH 7.5. Continuing this general assumption that the cysteine residues in CSP1 are similar to free cysteines, the enthalpy of cysteine deprotonation ΔH_{PH} = -8.4 kcal/mol can be included. This enthalpy, however, is not included within the *post-hoc* analysis, as it quantifies the enthalpy associated with the Cu^+-thiolate interaction, not the condition-independent Cu^+-CSP1 interaction. Further simplifying **Equation 7.3.1.4,** the enthalpy associated with formation of the $Cu(MeCN)_3^+$ is negligibly small and its dissociation does not significantly contribute to the binding enthalpy, which is supported by the fact that a change in the concentration of MeCN did not alter the apparent thermodynamics.[31] With these assumptions, the average *post-hoc* binding enthalpy in HEPES buffer for the first binding event, in which ~7 Cu^+ binds to CSP1, is +5.9 ± 0.3 kcal/mol metal which, I propose, fully displaces the estimated 12.0 protons from the CSP1 cysteine residues.

A similar analysis could be utilized for the second binding event, if the experimental enthalpy was well-defined. This, however, is not the case. The enthalpy of the second population of Cu^+ binding to CSP1 is difficult to separate from the enthalpy of the third binding event, as these data are overlapping. However, some insight can still be gained. As we are assuming that all 12.0 Cys protons are displaced when the first population of Cu^+ binds, the second population is binding to Cu^+-bound thiolates, resulting in the initial formation of bridging cysteine coordination. Competing equilibria associated with the second binding event are shown in **scheme 7.3.1.2**. Thus, the enthalpic contribution of Cu^+ binding to CSP1 would be quantified by the rearrangement of **Equation 7.3.1.5** to give:

$$[(4\Delta H_{MP})] = [\Delta H_{ITC}] + (4\Delta H_{ML_1}) + (4\Delta H_{ML_2}) + (4\Delta H_{ML_3}) \quad \textbf{\textit{Equation}}\ \mathbf{7.3.1.6}$$

Because it is proposed that no protons are displaced from CSP1 with the addition of these ~4 Cu^+ ions, there is no enthalpic contribution from protein deprotonation. Similar to the binding of the first population, the enthalpy associated with the $Cu(MeCN)_3^+$ interaction is negligibly small, and does not contribute to the overall enthalpy. By substituting the experimental enthalpy for this second binding event into **Equation 7.3.1.6**, the enthalpy *per-metal* is calculated to be -4.4 ± 0.3 kcal/mol Cu^+.

Unfortunately, condition-independent binding affinities for both the first and second binding events cannot be quantified directly by ITC, as they likely fall outside the experimental range of the ITC. However, Dennison and coworkers have determined the average equilibrium constant for the binding of Cu^+ to CSP1 to be equal to 1.3 (±0.1)×10^{17}, from the competitive chelation of Cu^+ by BCA. This equilibrium constant is used as an approximation of the affinity of the strongest binding site observed by ITC. Utilizing this binding affinity also allows the Gibbs free energy and entropy for Cu^+ binding to CSP1 to be determined (**Table 7.3.1.2**). Given that the second Cu^+ population would bind weaker to CSP1 than the first, I can only establish a range of binding affinities for these Cu^+ of $10^{7}_{(\text{weakest binding})} < K_{(\text{second binding})} < 10^{17}_{(\text{strongest binding})}$.

Lastly, the condition-independent enthalpy and binding affinity for the most weakly bound Cu^+ (third inflection) can be quantified. The binding of these 2.8 ± 0.6 Cu^+ ions are assumed to not displace any protons and the competing equilibria shown in **Scheme 7.3.1.2** are identical to those of the second binding population. The enthalpic contribution for the binding of 2.8 ± 0.6 Cu^+ to CSP1 on a *per-metal* basis can be quantified by rearranging **Equation 7.3.1.5** to give,

$$[(2.8\Delta H_{MP})] = [\Delta H_{ITC}] + (2.8\Delta H_{ML_1}) + (2.8\Delta H_{ML_2}) \qquad \textbf{\textit{Equation}}\ \mathbf{7.3.1.7}$$

It is assumed that no protons are released upon Cu^+ binding, and the $Cu(MeCN)_3^+$ enthalpy is negligibly small, so neither are included in the analysis. The buffer-independent binding enthalpy for the weakest binding population of 2.8 ± 0.6 Cu^+ at pH 7.5 is –8.5 ± 0.7 kcal/mol Cu^+ on a *per-metal* basis (**Table 7.3.1.2.**). The more exothermic binding is from the Cu^+-thiolate bonding through bridging coordination. This enthalpy is proposed to be primarily the condition-independent binding enthalpy of the third population of Cu^+, but some of this enthalpy originates from the binding of Cu^+ in the second population.

Quantification of the binding affinity of the third population, in which 2.8 ± 0.6 Cu^+ bind to CSP1 is determined by:

$$K_{MP} = K_{ITC} * (1 + K_{ML1}[L] + \beta_{ML2}[L]^2 + \beta_{ML3}[L]^3) \quad \textbf{Equation 7.3.1.8}$$

It is assumed that there is no protein deprotonation associated with these Cu^+ binding, and only the $Cu(MeCN)_3^+$ formation equilibrium are included in the relationship. So, the average Cu^+ affinity on a *per-metal* basis for the 2.8 ± 0.6 Cu^+ that bind to CSP1 in the population point bind with an equilibrium constant of 1.2 (± 0.6)×10^7 M^{-1} on a *per-metal* basis. Average *post*-hoc analysis thermodynamics are summarized in **Table 7.3.1.2.**

7.3.2 Calorimetric Characterization of Cu^+ *Binding to CSP3*

Stabilization of Cu^+ by acetonitrile (MeCN) for the binding to CSP3 is required to prevent disproportionation while and allowing Cu^+ to bind to all available metal-binding sites. A large excess of acetonitrile (100X excess to Cu^+) satisfies both of these requirements for the binding of Cu^+ to CSP3.

A titration of $Cu(MeCN)_3^+$ into CSP3 reveals 2 to 3 distinct Cu^+ binding populations. Like $Cu(MeCN)_3^+$ titratd into CSP1, the first binding event occurs at a stoichiometry of approximately 4, the second binding event at a stoichiometry of 4.1 ± 0.4 and the third binding event at 10 ± 1. While there is no obvious inflection for the first binding event, the two-site fitting model for the whole isotherm consistently results in a poor fit for the initial data points. With this in mind, the total number of Cu^+ that bind to CSP3 is 18.4 ± 1. Fitting of these three binding sites utilizes the Origin two-site fitting model, in which only the enthalpy of the first binding event is quantified. Then the datapoints of this first binding event are masked out, and the second and third binding events are fit by a two-site fitting model. The fitting and masking of data points mimics those of CSP1, in which the binding of CSP3 may be expected to behave similarly. Large experimental heats are typically due to buffer-mismatch, but this explanation was excluded by the reproducibility of these large peaks in several experiments (**Figure 7.3.2.1**). A total of 6 independent experiments were completed, each of which showed these characteristic injection heats. The noticeable "beat pattern" is a visual artifact that is found with the display of a large number of injections. Close proximity of the injection peaks results in a

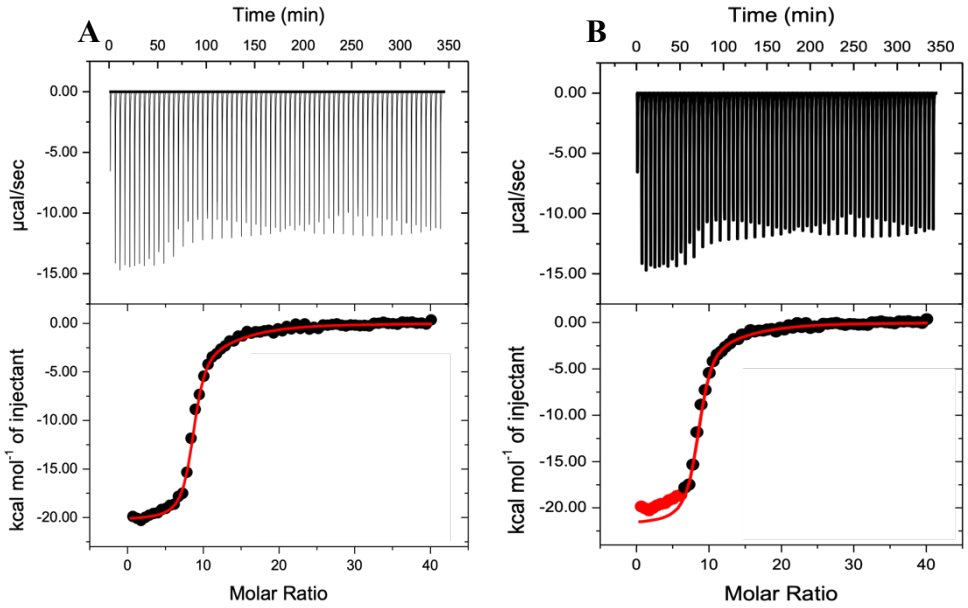

Figure 7.3.2.1. *A representative dataset for Cu^{+}, stabilized by excess acetonitrile (MeCN), titrated into* M. trichosporium OB3b *copper storage protein 3 (CSP3) in 20 mM HEPES, 200 mM NaCl, pH 7.5. Experimental data considers CSP3 in the monomeric form, with each monomer of the tetramer being identical. The first binding event (n ~ 4) is the formation of the 4 Cu^{+}-CSP1 copper-thiolate clusters. The second inflection (n = 4.1 ± 0.4) is the continued formation of the Cu^{+}-thiolate clusters, resulting in a total of ~8.1 Cu^{+} binding to the monomer of CSP3. The final inflection is the binding of a weak population of Cu^{+} (n = 10 ± 1) to bring the total of 18 ± 1 Cu^{+} binding to CSP3. Similar to the analysis of $Cu(MeCN)_3^{+}$ binding to CSP1, the first inflection is too strong for quantification of the equilibrium constant, thus only the enthalpy of this binding event can be established (A). The apparent thermodynamics of the second and third inflections (B) are measured by a two-site fit after masking out the first binding event. Titrations in HEPES: (Inflection 1, A) n_{ITC} = ~4, ΔH^{o}_{ITC} = -20.25 ± 0.01 kcal/mol; (Inflection 2, B) n_{ITC} = 4.34 ± 0.07, K_{ITC} = 9 (± 5)×10^{6}, ΔH^{o}_{ITC} = -21.8 ± 0.8 kcal/mol; (Inflection 3, B) n_{ITC} = 8 ± 2, K_{ITC} = 9 (± 5)×10^{4}, ΔH^{o}_{ITC} = -2.3 ± 1.2 kcal/mol.*

Table 7.3.2.1. *Experimental binding thermodynamics for the binding of Cu^{+}, in excess acetonitrile, to CSP3. Values are average thermodynamic values for at least 3 independent experiments. Experimental data were fit using a two-site fitting model, in which the first inflection is defined as Site 1 and the second inflection as Site 2.*

Protein Sample	Buffer	n_{ITC}	K_{ITC}	ΔH^{o}_{ITC} (kcal/mol)
Copper Storage Protein 3 (CSP3)			**Site 1**	
	HEPES	~4	—	-21.7 ± 0.7
			Site 2	
	HEPES	4.1 ± 0.4	6 (± 2)×10^{6}	-24 ± 3
			Site 3	
	HEPES	10 ± 1	8 (± 2)×10^{4}	-1.9 ± 0.6
Total		*18 ± 1*		

peak-averaging effect, in which the drawing of the peaks blends together. This results in the "beat-pattern" but maintains the integrity of the data.

These $Cu(MeCN)_3^+$ titrations were done in HEPES buffer with equivalent concentrations of MeCN in both the cell and the syringe. Average experimental thermodynamics from the two-site fitting model are shown in **Table 7.3.2.1**. Similar to CSP1, these titrations were only done in one buffer, and quantification of the protein protonation was estimated with the free predicted cysteine pK_a values. Thus, at pH 7.5, each cysteine is protonated by 0.92 protons. CSP3 has 18 cysteine residues that have been shown to bind a total of 19 Cu^+. Thus, full saturation of CSP3 with Cu^+ would displace 16.68 protons. With each Cu^+ binding to two cysteine residues, the first ~4 Cu^+ that bind to CSP3 are predicted to displace 7.36 protons. The competing equilibria for the binding of ~4 Cu^+ to CSP3 are shown in **Scheme 7.3.2.1**. With these competing equilibria, and their enthalpic contributions, established, the buffer-independent *post-hoc* thermodynamics at pH 7.5 can be quantified for the first inflection, corresponding to ~4 Cu^+ binding to CSP3. Rearranging **Equation 7.3.2.1.** to solve for the enthalpy associated with the Cu^+-CSP3 interaction on a *per-protein* basis results in:

$$[(4\Delta H_{MP})] = [\Delta H_{ITC}] + (4\Delta H_{ML_1}) + (4\Delta H_{ML_2}) + (4\Delta H_{ML_3}) - (7.36\Delta H_{BH}) \quad \boldsymbol{Equation\ 7.3.2.2}$$

Dividing this thermodynamics value by the total number of Cu^+ that bind results in the *post-hoc* enthalpy value on a *per-metal* basis (**Table 7.3.2.2**).

Like the binding of Cu^+ to CSP1, some assumptions must be addressed. The number of protons that are displaced upon metal binding, is estimated from the assumption that the cysteine have a pK_a to be similar to a free cysteine. Furthermore, the thermodynamics associated with the formation of $Cu(MeCN)_3^+$ is assumed to be negligible and has only been included in the competing equilibria for clarity. The enthalpic values for this complex contribute minimally, and are not included in the *post-hoc* analysis.

With these assumptions in mind, the buffer-independent thermodynamic values for the first ~4 Cu^+ that bind to CSP3 at pH 7.5, which displaces 7.36 protons, can be quantified. The enthalpic contribution is 4.0 ± 0.3 kcal/mol on a *per-metal* basis for these copper(I) ions.

Scheme 7.3.2.1. Generalized relevant competing equilibria for the first binding event in which ~4 Cu^+ bind to CSP3, which results in the release of 7.36 protons. ΔH_{ML1} and ΔH_{M2} are the enthalpies associated with each of the 3 stabilizing MeCN (L) ligands with Cu^+ (M), although these enthalpies are negligibly small and not necessary, it is included for clarity. ΔH_{PH} is the enthalpy associated with the deprotonation from the cysteine residues of the protein. ΔH_{BH} is the enthalpy associated with the protonation of the buffer (B), and ΔH_{MP} is the desired enthalpy of the metal-protein interaction. ΔH_{ITC} is the experimental enthalpy, which is the summation of all competing equilibria that occur in solution (**Equation 7.3.2.1**).

Cu^+–$MeCN_1$	⇄	$Cu^+ + MeCN_1$	$-(nCu^+\Delta H_{ML1})$
Cu^+–$MeCN_2$	⇄	$Cu^+ + MeCN_2$	$-(nCu^+\Delta H_{ML2})$
Cu^+–$MeCN_3$	⇄	$Cu^+ + MeCN_3$	$-(nCu^+\Delta H_{ML3})$
CSP3–H_x	⇄	CSP3 + H^+_x	$-n_{H+}\Delta H_{PH}$
H^+_x + Buffer	⇄	Buffer–H_x	$n_{H+}\Delta H_{BH}$
Cu^+ + CSP3	⇄	Cu^+–CSP3	$nCu^+\Delta H_{MP}$

$$\Delta H_{ITC} = -(nCu^+\Delta H_{ML1})-(nCu^+\Delta H_{ML2})-(nCu^+\Delta H_{ML3})-(n_{H+}\Delta H_{PH})+(n_{H+}\Delta H_{BH})+(nCu^+\Delta H_{MP}) \quad \textbf{Eq. 7.3.2.1}$$

Table 7.3.2.2. *Condition independent thermodynamics of Cu^{+} binding to CSP3. Values are the average from at least 3 independent experiments and are the average buffer-independent thermodynamics of the Cu^{+}-CSP3 interaction at pH 7.5 on a per-metal basis.*

CSP3	Buffer	Protons Released	n_{ITC}	K	ΔH^{o} (kcal/mol)	$-T\Delta S^{o}$ (kcal/mol)	ΔG^{o} (kcal/mol)
Site 1	**HEPES**	7.36	~4	[a]$2.0 (\pm 0.1)\times10^{17}$	+4.0 ± 0.3	[c]-27.6 ± 0.3	[b]-23.6 ± 0.1
Site 2	**HEPES**	9.2	4.1 ± 0.4	$1.9 (\pm 0.6)\times10^{7}$	+5.9 ± 0.3	-15.8 ± 1.0	-9.9 ± 0.1
Site 3	**HEPES**	0	10 ± 1	$2.2 (\pm 0.6)\times10^{5}$	-0.2 ± 0.1	-7.0 ± 0.2	-7.3 ± 0.2
Total		***16.56***	***18 ± 1***				

[a]Average Cu^{+}-CSP3 equilibrium constant from Dennison et al. (2016)[24].
[b]Quantification of Gibbs free energy from Dennison et al. (2016)[24].
[c]Quantification of $-T\Delta S$ is combined literature and experimental data.

Scheme 7.3.2.2. General relevant competing equilibria for the second binding event in which 4.1 ± 0.4 Cu^+ bind to CSP3, which results in the displacement of 9.2 protons. The titration of Cu^+, stabilized with acetonitrile (MeCN), into CSP3 in 20 mM HEPES and 200 mM NaCl, at pH 7.5. ΔH_{ML1}, $\Delta H_{M2,}$ and ΔH_{M3} are the enthalpies associated with each of the 3 stabilizing MeCN (L) ligands with Cu^+ (M). ΔH_{MP} is the desired enthalpy of the metal-protein interaction. ΔH_{ITC} is the experimental enthalpy which is the summation of all competing equilibria that occur in solution (**Equation 7.3.1.9**).

Cu^+–$MeCN_1$	⇄	$Cu^+ + MeCN_1$	$-(nCu^+\Delta H_{ML1})$
Cu^+–$MeCN_2$	⇄	$Cu^+ + MeCN_2$	$-(nCu^+\Delta H_{ML2})$
Cu^+–$MeCN_3$	⇄	$Cu^+ + MeCN_3$	$-(nCu^+\Delta H_{ML3})$
CSP3–H_x	⇄	CSP3 + H^+_x	$-n_{H+}\Delta H_{PH}$
H^+_x + Buffer	⇄	Buffer–H_x	$n_{H+}\Delta H_{BH}$
Cu^+ + CSP3	⇄	Cu^+–CSP3	$nCu^+\Delta H_{MP}$

$$\Delta H_{ITC} = -(nCu^+\Delta H_{ML1})-(nCu^+\Delta H_{ML2})-(nCu^+\Delta H_{ML3})-(n_{H+}\Delta H_{PH})+(n_{H+}\Delta H_{BH})+(nCu^+\Delta H_{MP})$$

Eq. 7.3.2.4

Quantification of the buffer-independent equilibrium constants on a *per-metal* basis for the first Cu^+-binding population is not possible with current experimental conditions. However, like CSP1, the initial data points correspond to the Cu^+ that bind most tightly. As such, I use the average equilibrium constant quantified by Dennison and coworkers as an approximation for the binding affinity for this first Cu^+ population. They determined this with BCA as a Cu^+-chelating ligand, and report an average binding affinity of 2 (± 0.1)×10^{17}. This value was utilized for the condition-independent affinity for the first binding event in these ITC experiments and allowed quantification of the Gibbs free energy and the entropic contribution to binding (**Table 7.3.2.2**).

Quantification of the enthalpic contribution of metal binding and the equilibrium constants for the second inflection in the titration of Cu^+ into CSP3 follows a similar *post-hoc* analysis. It was assumed that the initial population of Cu^+ displaces 7.36 protons from CSP3, and the second population of Cu^+ displaces the remainder of the protons that are still bound to Cys residues, which is approximately 9.2 protons. Likewise, the enthalpic contribution from the $Cu(MeCN)_3^+$ is negligibly small and not included in the *post-hoc* analysis, though it is included in the competing equilibria analysis for clarity (**Scheme 7.3.2.2**). Thus, rearranging **Equation 7.3.2.4**, the *post-hoc* analysis of the enthalpy associated with the second binding population in the titration of Cu^+ into CSP3 is found with:

$$[(4.1\Delta H_{MP})] = [\Delta H_{ITC}] + (4.1\Delta H_{ML_1}) + (4.1\Delta H_{ML_2}) + (4.1\Delta H_{ML_3}) - (9.2\Delta H_{BH}) \quad \textbf{Equation 7.3.2.5}$$

The buffer-independent binding enthalpy on a *per-metal* basis is 5.4 ± 0.3 kcal/mol Cu^+ at pH 7.5 (**Table 7.3.2.2**). Quantifying the equilibrium constant for this second population of Cu^+ binding to CSP3 on a *per-metal* basis also requires the competing equilibria analysis (**Scheme 7.3.2.2**). Taking these competing equilibria into account gives:

$$K_{MP} = K_{ITC} * (1 + K_{ML1}[L] + \beta_L[L]^2 + \beta_{ML3}[L]^3) \quad \textbf{Equation 7.3.2.6}$$

which quantifies the buffer-independent binding affinity of 1.9 (± 0.6)×10^7 at pH 7.5.

Finally, the average enthalpy for the third Cu^+ binding population is determined by,

$$[(10\Delta H_{MP})] = [\Delta H_{ITC}] + (10\Delta H_{ML_1}) + (10\Delta H_{ML_2}) \quad \textbf{Equation 7.3.2.7}$$

As with Cu^+ binding to CSP1, the resulting formation enthalpy is -0.2 ± 0.1 kcal/mol Cu^+ at pH 7.5.

Finally, the equilibrium constant can be solved similarly to Equation 7.3.2.6, which shows that the equilibrium constant for this third binding population is 2.2 (± 0.6)×10^5 on a *per-metal* basis (**Table 7.3.2.2**). Average *post-hoc* enthalpic and entropic contributions, as well as Gibbs free energy for the first and second Cu^+ populations binding to CSP3 are also shown in **Table 7.3.2.2**.

7.3.3 Binding of Zinc to CSP1

Unlike Cu^+, titrations involving Zn^{2+} are much less complicated. Due to the stability of Zn^{2+} in aqueous solution and its redox stability, experimental solutions with known metal concentrations can be prepared in buffer without the need for stabilizing or competing ligands, unless required for the desired experiment (i.e. competition or chelation experiments).

Isothermal titration calorimetry (ITC) experiments to quantify the thermodynamics of the Zn^{2+}–CSP1 interaction were undertaken. These titrations show two binding events, an initial exothermic binding population with an average stoichiometry of n = 0.9 ± 0.4, and a second endothermic binding population with an average stoichiometry of n = 7 ± 1 (**Figure 7.3.3.1**). Fitting these two events is done with a two-site binding model in the Origin data analysis software.

Titrations of Zn^{2+} into CSP1 were carried out in HEPES buffer and show well-defined peaks that indicate weak net exothermic and endothermic enthalpic events, when fit to a two-site binding model. The experimental binding affinities for both binding events fall well within the c-window range. Average experimental thermodynamic values from the two-site fitting model are shown in **Table 7.3.3.1**. Unlike the binding of Cu^+ to CSPs, which have known metal-bound structures, there are no known Zn^{2+}-CSP structures. As such, the post-hoc analysis is more difficult without knowledge of CSP1 deprotonation upon Zn^{2+} binding. However, there is a stoichiometry correlation of the dipositive Zn^{2+}, and the monopositive Cu^+ that reflects the total charge on the metal ions that bind: 7.5 ± 0.8 Zn^{2+} and 13.8 ± 0.5 Cu^+. The natural assumption that follows is that saturation of CSP1 with Zn^{2+} results in complete deprotonation of the CSP1 Cys residues, similar to the analysis of Cu^+ binding to CSP1. As with the Cu^+ analysis, each cysteine is protonated by

Scheme 7.3.3.1. Competing equilibria for the first binding event in which 0.9 ± 0.4 Zn^{2+} bind to CSP1, with an expected tetrahedral geometry, releasing an average of 0.92 H^+ per cysteine residue for a total of 3.31 H^+ released. ΔH_{MB} is the enthalpy of the Zn^{2+} (M) and the Buffer (B), HEPES. ΔH_{PH} is the enthalpy associated with the deprotonation of the cysteine residues on the protein. ΔH_{BH} is the enthalpy associated with the protonation of the buffer, and ΔH_{MP} is the desired enthalpy of the metal-protein (P) interaction. ΔH_{ITC} is the experimental enthalpy, which is the summation of all competing equilibria that occur in solution (**Equation 7.3.3.1**).

Zn^{2+}–Buffer	⇄	Zn^{2+} + Buffer	$-(nZn^{2+}\Delta H_{MB})$
CSP1–H_x	⇄	CSP1 + H^+_x	$-(n_{H+}\Delta H_{PH})$
H^+_x + Buffer	⇄	Buffer–H_x	$n_{H+}\Delta H_{BH}$
Zn^{2+} + CSP1	⇄	Zn^{2+}–CSP1	$nCu^{+}\Delta H_{MP}$

$$\Delta H_{ITC} = -(nZn^{2+}\Delta H_{MB})-(n_{H+}\Delta H_{PH})+(n_{H+}\Delta H_{BH})+(nZn^{2+}\Delta H_{MP}) \quad \textbf{Eq. 7.3.3.1}$$

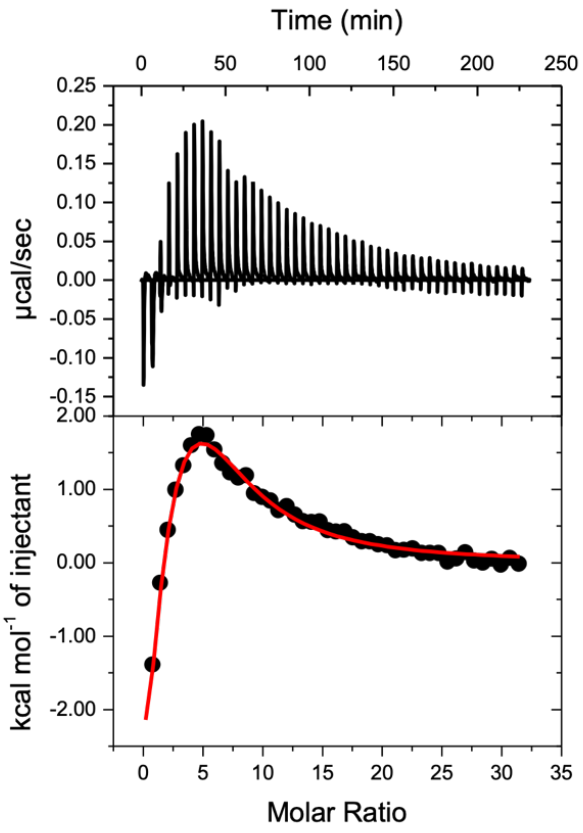

Figure 7.3.3.1. *Representative isotherm of* Zn^{2+} *titrated into* M. trichosporium OB3b *copper storage protein 1 (CSP1) in 20 mM HEPES, 200 mM NaCl, pH 7.5. Experimental data considers CSP1 in the monomeric form, with each monomer identical in the tetramer.* Zn^{2+} *into CSP1 in HEPES: (First Inflection)* $n_{ITC} = 1.4 \pm 0.3$, $K_{ITC} = 5\ (\pm 4)\times10^5$, $\Delta H^o_{ITC} = -8 \pm 6$ *kcal/mol and (Second Inflection):* $n_{ITC} = 5 \pm 1$, $K_{ITC} = 8\ (\pm 1)\times10^4$, $\Delta H^o_{ITC} = 5 \pm 3$ *kcal/mol.*

Table 7.3.3.1. *Average experimental thermodynamics for* Zn^{2+} *binding to* M. trichosporium OB3b copper storage protein 1 (CSP1) *from at least 3 independent measurements. and fit using a two-site binding model, in which the first inflection is defined as Site 1 and the second inflection as Site 2.*

Protein Sample	Buffer	n_{ITC}	K_{ITC}	ΔH^{o}_{ITC} (kcal/mol)
Copper Storage Protein 1 (CSP1)	**HEPES**		**Site 1**	
		0.9 ± 0.4	8 (± 2)×10^5	–9 ± 2
	HEPES		**Site 2**	
		7 ± 1	8 (± 2)×10^4	+4 ± 1

Table 7.3.3.2*. Average buffer-independent thermodynamics associated with* Zn^{2+} *binding to CSP1 at pH 7.5 on a* per-metal *basis from at least 3 independent experiments.*

CSP1	Buffer	n_{ITC}	K	ΔH° (kcal/mol)	–TΔS° (kcal/mol)	ΔG° (kcal/mol)
Site 1	**HEPES**	0.9 ± 0.4	9 (± 8)×10^6	+9 ± 2	-19 ± 2	-9.5 ± 0.1
Site 2	**HEPES**	7 ± 1	1.5 (± 0.4)×10^6	+7 ± 1	-16 ± 1	-8.4 ± 0.7

Scheme 7.3.3.2. Competing equilibria for the second binding event in which 6.6 ± 1.2 Zn^{2+} bind to CSP1, and displace an estimated total of 8.69 H^+. ΔH_{MB} is the enthalpy of the Zn^{2+} (M) and the Buffer (B), HEPES. ΔH_{PH} is the enthalpy associated with the deprotonation of the cysteine residues of the protein. ΔH_{BH} is the enthalpy associated with the protonation of the buffer, and ΔH_{MP} is the desired enthalpy of the metal-protein (P) interaction. ΔH_{ITC} is the experimental enthalpy which is the summation of all competing equilibria that occur in solution (**Equation 7.3.3.4**).

Zn^{2+}–Buffer	⇄	Zn^{2+} + Buffer	$-(nZn^{2+}\Delta H_{MB})$
CSP1–H_x	⇄	CSP1 + H^+_x	$-(n_{H+}\Delta H_{PH})$
H^+_x + Buffer	⇄	Buffer–H_x	$n_{H+}\Delta H_{BH}$
Zn^{2+} + CSP1	⇄	Zn^{2+}–CSP1	$nCu^+\Delta H_{MP}$

$$\Delta H_{ITC} = -(nZn^{2+}\Delta H_{MB})-(n_{H+}\Delta H_{PH})+(n_{H+}\Delta H_{BH})+(nZn^{2+}\Delta H_{MP}) \quad \textbf{Eq. 7.3.3.4}$$

an average of 0.92 protons at pH 7.5, resulting in the release of 12.0 protons upon the 7.5 ± 1.5 Zn^{2+} binding. This is, however, complicated by the two binding events, one with n = 0.9 ± 0.4, and the other with n = 6.6 ± 1.2, which should have different proton displacement associated with their binding. However, as discussed previously, Zn^{2+} generally prefers to bind with a tetrahedral geometry (See Chapter 1), which is likely to occur with four cysteine thiolates in the first binding event, with the displacement of 3.3 protons. Following that line of reasoning, the second binding event of 6.6 ± 1.2 Zn^{2+} would result in the loss of 8.7 protons. Using the free cysteine pK_a and the number of protons that would be displaced, the buffer-independent binding thermodynamics on both a *per-metal* and *per-protein* level can be determined for both Zn^{2+} binding events at pH 7.5.

With this estimation of the number of protons that are released upon Zn^{2+} binding, the binding enthalpy for the first binding event can be quantified. This requires the competing equilibria in **Scheme 7.3.3.1**. Taking the enthalpies associated with each equilibrium into account allows the rearrangement and substitution of known enthalpic values into **Equation 7.3.3.1** to solve for the desired ΔH_{MP} in which:

$$0.9\Delta H_{MP} = \Delta H_{ITC} + (0.9\Delta H_{MB}) - (3.31\Delta H_{BH}) \qquad \boldsymbol{Equation\ 7.3.3.2}$$

The buffer-independent binding enthalpy for the first binding event, where the Zn^{2+} is proposed to have a tetrahedral, tetrathiolate coordination, is 9 ± 2 kcal/mol on a *per-metal* basis at pH 7.5.

To determine the remaining thermodynamic values, the buffer-independent binding affinity, and thus Gibbs free energy, the competing equilibria must be considered. The calculation for the binding affinity is as follows:

$$K_{MP} = K_{ITC} * (1 + K_{MB}[B]_{Basic}) \qquad \textbf{Equation 7.3.3.3}$$

The first Zn^{2+} that binds to CSP1 has a buffer-independent equilibrium constant of 9 (± 8)×10^6 on a *per-metal* basis. Average condition-independent equilibrium constants for the Zn^{2+} binding to CSP1 at pH 7.5 are shown in **Table 7.3.3.2**.

With the thermodynamics of the first Zn^{2+} that binds to CSP1 quantified, the thermodynamics of the second binding event can be determined through a similar *post-hoc* analysis. Additional Zn^{2+} binding completes the deprotonation of the CSP1 Cys residues with 6.6 ± 1.2 more Zn^{2+} displacing the remaining 8.7 protons. The competing interactions and the enthalpic contributions from their equilibria must first be established (**Scheme**

7.3.3.2). Rearranging **Equation 7.3.3.4** to solve for the buffer-independent enthalpy of Zn^{2+} binding to CSP1, on a *per-protein* basis, for the second binding event, shows that:

$$6.6\Delta H_{MP} = \Delta H_{ITC} + (6.6\Delta H_{MB}) - (8.69\Delta H_{BH}) \qquad \boldsymbol{Equation\ 7.3.3.5}$$

Thus, buffer-independent enthalpic contribution to the binding of Zn^{2+} to CSP1 is 7 ± 1 kcal/mol on a *per-metal* basis at pH 7.5 (**Table 7.3.3.2**). The equilibrium constant for the second set of Zn^{2+} ions binding to CSP1 is then quantified by accounting for the competing equilibria. This buffer-independent Zn^{2+}-CSP1 binding affinity for the second population is calculated similar to that for the first Zn^{2+} population, by:

$$K_{MP} = K_{ITC} * (1 + K_{MB}[B]_{Basic}) \qquad \textbf{Equation 7.3.3.6}$$

This results in an equilibrium constant for this second inflection that is equal to 1.1 (± 0.4)×10^6 on a *per-metal* basis. The condition-independent thermodynamics for Zn^{2+} binding to CSP1 at pH 7.5 are found in **Table 7.3.3.2**.

7.3.4 Binding of Zinc to CSP3

The binding of Zn^{2+} to CSP3, like CSP1, shows two distinct binding events with two inflections. The first inflection occurs at a stoichiometry of 2.7 ± 0.8, and is weakly exothermic, followed by the binding of 5.3 ± 2.0 Zn^{2+} , which is weakly net endothermic (**Figure 7.3.4.1**). This results in a total of 9.2 ± 2.7 Zn^{2+} binding to CSP3. These two binding events were fit using the two-site binding model in Origin. Similar to Zn^{2+} binding to CSP1, quantifying the condition-independent thermodynamics of Zn^{2+} binding to CSP3 is complicated by the lack of experimental proton displacement data from measurements of Zn^{2+} binding in multiple buffers. This is compounded by the lack of structural information on Zn^{2+}-CSP3. However, by making a few logical assumptions, built upon a foundation of inorganic chemistry, the number of protons released upon the binding of Zn^{2+} for both the first and second events can be quantified, assuming that the pK_a of each cysteine on CSP3 is approximately the same as a free cysteine, pK_a = 8.6. Thus, at the experimental pH of 7.5, each cysteine is protonated by 0.92 protons. With CSP3, 18 cysteine residues are involved in the binding of metal ions. Furthermore, the total number of Zn^{2+} that are able to bind to CSP3, similar to CSP1, is approximately half the number of Cu^{+} that are able to bind, ~9. Like the binding of 18 Cu^{+}, which involves all 18 cysteine residues,

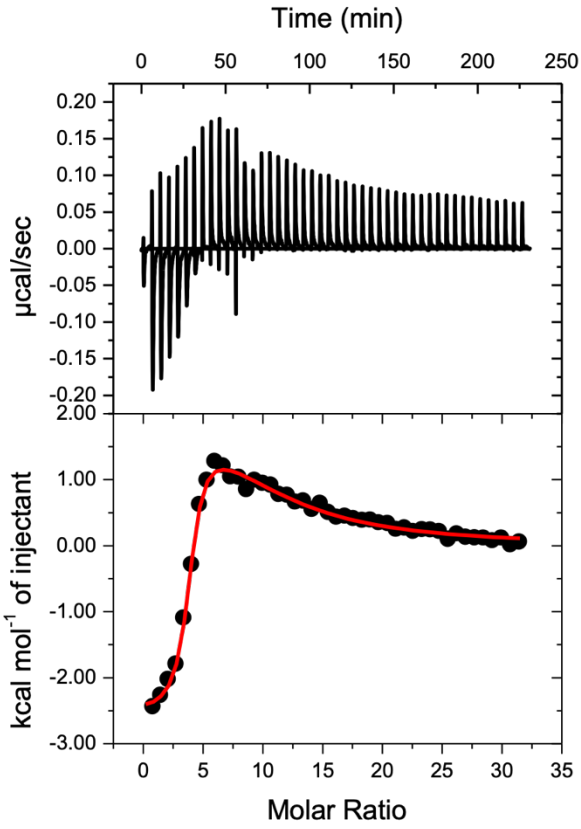

Figure 7.3.4.1. *Representative isotherm of* Zn^{2+} *titrated into* M. trichosporium OB3b *copper storage protein 3 (CSP3) in 20 mM HEPES, 200 mM NaCl, pH 7.5. Experimental data considers CSP3 in the monomeric form, with each monomer identical in the tetramer.* Zn^{2+} *into CSP3 in HEPES: (First Inflection)* $n_{ITC} = 3.66 \pm 0.06$, $K_{ITC} = 5\ (\pm 2) \times 10^6$, $\Delta H^o_{ITC} = -2.54 \pm 0.07$ *kcal/mol and (Second Inflection):* $n_{ITC} = 7 \pm 1$, $K_{ITC} = 5\ (\pm 1) \times 10^4$, $\Delta H^o_{ITC} = 2.6 \pm 0.5$ *kcal/mol.*

Table 7.3.4.1. *Average experimental thermodynamics for Zn^{2+} binding to* M. trichosporium OB3b *copper storage protein 3 (CSP3) from at least 3 independent experimentsanddata were fit using a two-site binding model, in which the first inflection is defined as Site 1 and the second inflection as Site 2.*

Protein Sample	Buffer	n_{ITC}	K_{ITC}	ΔH^{o}_{ITC} (kcal/mol)
Copper Storage Protein 3 (CSP3)	**HEPES**	**Site 1**		
		2.7 ± 0.8	5.3 (± 0.4)×10^6	-2.3 ± 0.2
	HEPES	**Site 2**		
		5.3 ± 2.0	5.5 (± 0.5)×10^4	+2.0 ± 0.5

Scheme 7.3.4.1. Competing equilibria for the first binding event in which 2.7 ± 0.8 Zn^{2+} bind to CSP3, with an expected tetrahedral geometry, displacing 0.92 H^+ per cysteine residue for a total of 9.9 H^+ released. ΔH_{MB} is the enthalpy of the Zn^{2+} (M) and the Buffer (B), HEPES. ΔH_{PH} is the enthalpy associated with the deprotonation of the cysteine residues of the protein. ΔH_{BH} is the enthalpy associated with the protonation of the buffer, and ΔH_{MP} is the desired enthalpy of the metal-protein (P) interaction. ΔH_{ITC} is the experimental enthalpy which is the summation of all competing equilibria that occur in solution (**Equation 7.3.4.1**).

Zn^{2+}–Buffer	⇄	Zn^{2+} + Buffer	$-(nZn^{2+}\Delta H_{MB})$
CSP3–H_x	⇄	CSP3 + H^+_x	$-(n_{H+}\Delta H_{PH})$
H^+_x + Buffer	⇄	Buffer–H_x	$n_{H+}\Delta H_{BH}$
Zn^{2+} + CSP3	⇄	Zn^{2+}–CSP3	$nCu^+\Delta H_{MP}$

$$\Delta H_{ITC} = -(nZn^{2+}\Delta H_{MB})-(n_{H+}\Delta H_{PH})+(n_{H+}\Delta H_{BH})+(nZn^{2+}\Delta H_{MP}) \quad \textbf{Eq. 7.3.4.1}$$

Scheme 7.3.4.2. Competing equilibria for the second binding event in which 5.3 ± 2 Zn^{2+} bind to CSP3, a total of 6.7 H^+. ΔH_{MB} is the enthalpy of the Zn^{2+} (M) and the Buffer (B), HEPES. ΔH_{PH} is the enthalpy associated with the deprotonation of the cysteine residues of the protein. ΔH_{BH} is the enthalpy associated with the protonation of the buffer, and ΔH_{MP} is the desired enthalpy of the metal-protein (P) interaction. ΔH_{ITC} is the experimental enthalpy, which is the summation of all competing equilibria that occur in solution (**Equation 7.3.4.4**).

Zn^{2+}–Buffer	⇄	Zn^{2+} + Buffer	$-(nZn^{2+}\Delta H_{MB})$
CSP3–H_x	⇄	CSP1 + H^+_x	$-(n_{H+}\Delta H_{PH})$
H^+_x + Buffer	⇄	Buffer–H_x	$n_{H+}\Delta H_{BH}$
Zn^{2+} + CSP3	⇄	Zn^{2+}–CSP3	$nCu^+\Delta H_{MP}$

$$\Delta H_{ITC} = -(nZn^{2+}\Delta H_{MB})-(n_{H+}\Delta H_{PH})+(n_{H+}\Delta H_{BH})+(nZn^{2+}\Delta H_{MP}) \quad \textbf{Eq. 7.3.4.4}$$

***Table 7.3.4.2**. Average buffer-independent thermodynamics for Zn^{2+} binding to CSP3 at pH 7.5 on a <u>per-metal</u> basis and obtained from the fit using the Origin two-site binding model. Average values were calculated from at least 3 independent experiments.*

CSP3	Buffer	n_{ITC}	K	ΔH^o (kcal/mol)	$-T\Delta S^o$ (kcal/mol)	ΔG^o (kcal/mol)
Site 1	**HEPES**	2.7 ± 0.8	1.0 (± 0.1)×10^8	18.4 ± 0.3	-29 ± 2	-11 ± 2
Site 2	**HEPES**	5.3 ± 2.0	1.0 (± 0.1)×10^6	6.8 ± 0.4	-15 ± 1	-8 ± 1

a total of 16.56 protons are displaced when all 9.2 ± 2.7 Zn^{2+} bind to CSP3. It is also logical to assume that the first binding event, in which 2.7 ± 0.8 Zn^{2+} bind to CSP3, would provide the preferred tetrahedral geometry for each Zn^{2+}, resulting in the release of 9.9 protons. Following that line of reasoning, the second binding event would result in 6.7 protons displaced when the remaining Zn^{2+} bind.

With these estimates for the number of protons released from CSP3, the remaining competing equilibria can be determined (**Scheme 7.3.4.1**). Taking these into account, the buffer-independent binding thermodynamics for the first binding event at pH 7.5 can be quantified. Beginning with the condition-independent binding enthalpies, **Equation 7.3.4.1** can be rearranged such that:

$$2.7\Delta H_{MP} = \Delta H_{ITC} + (2.7\Delta H_{MB}) - (9.9\Delta H_{BH}) \qquad \textbf{\textit{Equation}}\ \mathbf{7.3.4.2}$$

This condition-independent *post-hoc* analysis shows that, on a *per-metal* basis, the binding enthalpy is equal to 18.4 ± 0.3 kcal/mol.

Continuing to utilize the competing equilibria to determine the equilibrium constant for the first binding event upon titration of Zn^{2+} into CSP3 allows the Gibbs free energy, and thus the entropic contribution to binding, to be determined on a *per-metal* basis. This analysis takes the equilibrium constant for each competing equilibrium into account, which is shown in **Equation 7.3.4.3.**

$$K_{MP} = K_{ITC} * (1 + K_{MB}[B]_{Basic}) \qquad \textbf{Equation 7.3.4.3}$$

The condition-independent binding constant at pH 7.5, taking all competing equilibria into account, is equal to 1.0 (± 0.1)×10^8 on a *per-metal* basis. The buffer-independent thermodynamic values for the first Zn^{2+} binding event at pH 7.5 are shown in **Table 7.3.4.2**.

Lastly, the condition-independent binding thermodynamics for the second binding event where 5.3 ± 2 Zn^{2+} bind to CSP3, was determined. The binding of these Zn^{2+} ions displaces the remaining protons from CSP3, so 6.7 protons are released from the protein upon metal binding. The competing equilibria, which include protein deprotonation, metal-buffer interactions, and the metal-protein interactions, that are taken into account (**Scheme 7.3.4.2**) are identical to those for the first inflection.

Determining the condition-independent binding enthalpy for the second binding event on a *per-metal* and *per-protein* basis follows a *post-hoc* analysis similar to that for the first binding event. Rearranging **Equation 7.3.4.4** gives,

$$5.3\Delta H_{MP} = \Delta H_{ITC} + (5.3\Delta H_{MB}) - (6.7\Delta H_{BH}) \qquad \textbf{\textit{Equation}}\ \mathbf{7.3.4.5}$$

This results in a binding enthalpy of 6.8 ± 0.4 kcal/mol on a *per-metal* basis.

Finally, the binding constant, and Gibbs free energy and entropy, were quantified by taking the equilibrium constants of the competing equilibria into account. This results in **Equation 7.3.4.6**, which allows the CSP3 affinity for Zn^{2+} to be quantified on a *per-metal* and *per-protein* basis:

$$K_{MP} = K_{ITC} * (1 + K_{MB}[B]_{Basic}) \qquad \textbf{Equation}\ \mathbf{7.3.4.6}$$

The condition-independent equilibrium constant is equal to 1.0 (± 0.1)×10^6 M^{-1} on a *per-metal* basis for the second population of Zn^{2+} binding to CSP3.

These condition-independent binding thermodynamics include the sum of the metal-thiolate interaction and the deprotonation of the thiol. The condition-independent values for the second population of Zn^{2+} binding to CSP3 is found in **Table 7.3.4.2**.

7.3.5 Binding of Hg^{2+} *to CSP1 and CSP3*

Unlike the binding of Cu^+ and Zn^{2+}, the condition-independent thermodynamics for the binding of Hg^{2+} to CSPs are difficult to determine without further experimentation and quantification of the number of protons that are released upon metal binding. This is evident by the number of Hg^{2+} that are able to bind to CSP1 and CSP3, which does not correspond to the binding of Cu^+ or Zn^{2+}. This is further confounded by the dynamic coordination preferences of Hg^{2+}. These factors make a logical and inorganic-based determination of the number of protons that are released upon metal binding difficult. Nonetheless, experimental thermodynamics, and their comparisons to Cu^+ and Zn^{2+}, can still be made.

Mercury binding experiments were completed in HEPES buffer and are similar to those of Zn^{2+}, in which Hg^{2+} is initially bound to the buffer as a competing ligand. These experiments show three binding events with CSP1. The first inflection is highly exothermic and shows approximately 2 Hg^{2+} binding to the protein. This binding event appears to be much stronger than can be accurately determined by ITC, as the fit of these datapoints is poor. For this binding event, only the stoichiometry and enthalpy are quantifiable. The second inflection is also exothermic with a well-defined inflection. Lastly, the third population of Hg^{2+} that bind to CSP1 have weakly exothermic binding, and a high

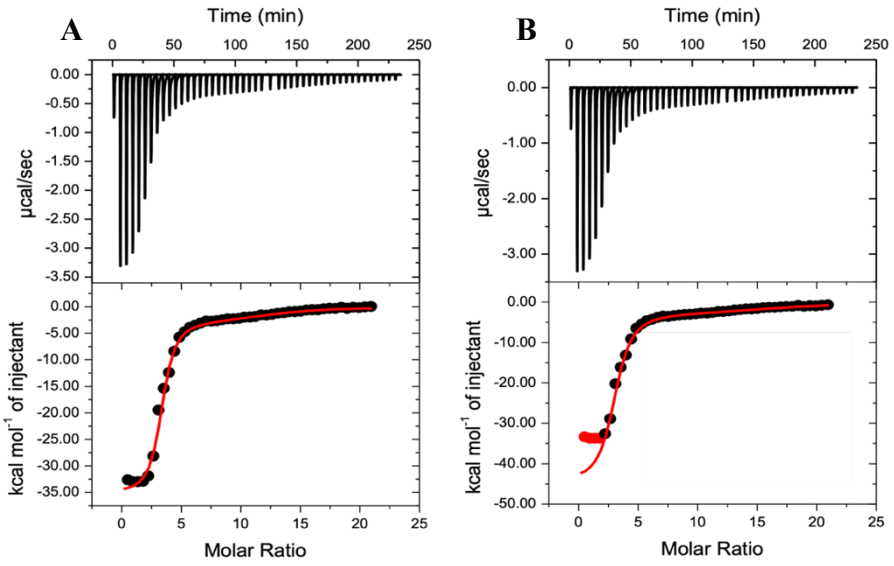

Figure 7.3.5.1. *Representative isotherms of* Hg^{2+} *titrated into* M. trichosporium OB3b *CSP1 in 20 mM HEPES, 200 mM NaCl, pH 7.5. (A, First Binding Event)* $n_{ITC} = \sim 2$ *and* $\Delta H^{o}_{ITC} = -35.3 \pm 0.5$ *kcal/mol; (B, Second Binding Event)* $n_{ITC} = 2.94 \pm 0.07$, $K_{ITC} = 1 (\pm 1) \times 10^{7}$, $\Delta H^{o}_{ITC} = -44.5 \pm 0.2$ *kcal/mol; (B, Third Binding Event)* $n_{ITC\,(Total)} = 14 \pm 1$, $K_{ITC} = 1 (\pm 1) \times 10^{5}$, $\Delta H^{o}_{ITC} = -3.1 \pm 0.7$ *kcal/mol.*

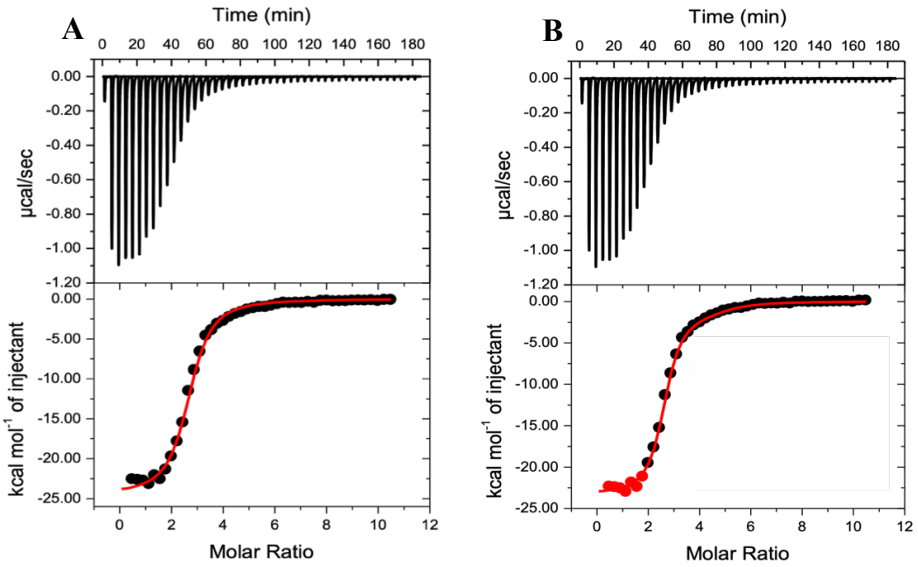

Figure 7.3.5.2. *Representative isotherms of Hg^{2+}, in buffer, titrated into* M. trichosporium OB3b *CSP3 in 20 mM HEPES, 200 mM NaCl, pH 7.5. Experimental data considers CSP3 in the monomeric form, with each monomer of the tetramer being identical. Hg^{2+} into CSP3 in HEPES): (A, First Binding Event) n_{ITC} = ~1 and ΔH^{o}_{ITC} = -24.5 ± 0.3 kcal/mol; (B, Second Binding Event): n_{ITC} = 2.52 ± 0.01, K_{ITC} = 5 (± 1)×10^{7}, ΔH^{o}_{ITC} = -23.3 ± 0.5 kcal/mol; (B, Third Binding Event): n_{ITC} = 2.4 ± 0.3, K_{ITC} = 8 (± 2)×10^{5}, ΔH^{o}_{ITC} = -1.9 ± 0.5 kcal/mol.*

Table 7.3.5.1. *Average experimental binding thermodynamics for Hg^{2+} binding to CSP1 and CSP3 in HEPES buffer at pH 7.5 from at least 2 independent experiments. Each isotherm shows three binding events, indicating 3 distinct populations of Hg^{2+} binding.*

Protein Sample	Buffer	n_{ITC}	K_{ITC}	ΔH^{o}_{ITC} (kcal/mol)
CSP1	HEPES	~2	**Site 1** >>10^7	-35.8 ± 0.6
	HEPES	3 ± 0.1	**Site 2** 3 (± 3)×10^7	-44 ± 1
	HEPES	13 ± 2	**Site 3** 5 (± 5)×10^5	-2.4 ± 1.0
CSP3	HEPES	~1	**Site 1** >>10^7	-25 ± 1
	HEPES	2.4 ± 0.1	**Site 2** 4.8 (± 0.3)×10^7	-23.6 ± 0.4
	HEPES	2 ± 0.6	**Site 3** 7.4 (± 0.9)×10^5	-3 ± 2

stoichiometry, suggesting adventitious binding (**Figure 7.4.5.1**). These binding events were fit and the first inflection has an experimental enthalpy of -35.8 ± 0.6 kcal/mol, the second inflection has an experimental enthalpy of -44 ± 1 kcal/mol and a binding constant of 3 (± 3)×10^7, and the third inflection shows an apparent binding enthalpy of -2.4 ± 1.0 kcal/mol and an apparent binding constant of 5 (± 5)×10^5. Average experimental thermodynamic values for the binding of Hg^{2+} to CSP1 are found in **Table 7.3.5.1** from the data from at least 2 independent experiments.

Similar to Hg^{2+} binding to CSP1, a *post-hoc* analysis for the binding of Hg^{2+} to CSP3 is currently not feasible due to the current lack of binding experiments in multiple buffers to quantify the number of protons that are released from CSP3 upon Hg^{2+} binding. However, a comparison of these experimental stoichiometries, enthalpies, and equilibria constants, to the best of my ability, can be utilized in a comparison to the binding of native Cu^+ and non-native Zn^{2+}.

The binding of Hg^{2+} to CSP3 results in three distinct binding events. The first event shows a binding of approximately 1 Hg^{2+} to CSP3 with an experimental binding enthalpy of –25 ± 1 kcal/mol. By masking the first four data points, a fit can quantify the second and third binding events. The second event has a binding stoichiometry of 2.4 ± 0.1 Hg^{2+} with an apparent binding enthalpy of -23.6 ± 0.4 kcal/mol, and an apparent binding constant of 4.8 (± 0.3)×10^7. Finally, the third inflection shows 2 ± 0.6 Hg^{2+} binding with an experimental enthalpy of -3 ± 2 kcal/mol and a binding constant of 7.4 (± 0.9)×10^5 (**Figure 7.3.5.2**). Average experimental thermodynamics are found in **Table 7.3.5.1**.

The experimental thermodynamics for Hg^{2+} binding to CSP1 and CSP3 is surprising, given the favorable mercury-cysteine interaction. Thus, a control experiment, in which a Hg-EDTA complex was titrated into CSP1, was performed. The stability constant for the Hg-EDTA complex is 3.2×10^{21}. CSP1 was not able to chelate Hg^{2+} from EDTA, indicating that, unlike Cu^+, CSPs are not able to bind and store a large number of Hg^{2+}.

7.4. Discussion

Characterization of the thermodynamics for CSP binding Cu^+, Zn^{2+}, and Hg^{2+} is challenging because of a number of unknown variables. Of particular importance is the

number of protons that are released upon metal binding. Therefore, the analysis to determine the thermodynamics had one key assumption: the cysteine residues that line the metal-storage channel in both CSP1 and CSP3 have a pK_a of 8.6, equivalent to that of a free cysteine. Although the individual pK_a's may not be the exact value, this provides a reasonable approximation for the number of protons that are released upon metal binding at pH 7.5. This information is complemented by structures of the Cu^+-CSP1 and Cu^+-CSP3 complexes, which provide information on Cu^+-cysteine coordination, and thus the number of protons that can be displaced at a given time. Taking these different competing equilibria into account results in the ability to quantify the buffer-independent binding thermodynamics on both a *per-metal* basis and a *per-monomer* basis at the experimental pH. However, it cannot be emphasized enough that further experimental work to determine the number of protons that are released upon Cu^+ binding will likely alter the condition-independent metal-binding thermodynamics, although I propose that general trends will hold true.

The binding of Cu^+ was studied using a large excess of the weakly chelating ligand, acetonitrile (MeCN), which stabilizes Cu^+ in aqueous solution under anaerobic conditions. Up to 4 acetonitrile molecules are capable of binding and stabilizing Cu^+; however, the first three provide the most significant complex with Cu^+ ($\log \beta_3 = 4.23$), and are the only ones included in the *post-hoc* analysis.

Unlike Cu^+, neither Zn^{2+} nor Hg^{2+} are readily oxidized or reduced under aqueous, anaerobic conditions. As such, these metal-binding experiments require only simple metal-in-buffer titrations, in which the buffer, at its high concentration, acts as a competing ligand.

In this study, isothermal titration calorimetry (ITC) was utilized to quantify the experimental thermodynamics of the metal-CSP interaction. By taking into account the different competing equilibria (metal-ligand, metal-buffer, buffer-protonation, protein-deprotonation, etc.), the buffer-independent metal-binding thermodynamics were quantified at the experimental pH. This provides the thermodynamic foundation for metal selectivity and specificity in the storage of Cu^+, relative to other d^{10} metals in both CSP1 and CSP3 and provides evidence for the interplay of thermodynamic and kinetic is important for the binding and release of Cu^+ from CSP1 and CSP3. Dissecting these

equilibrium constants to determine the enthalpic and entropic contributions to metal binding further expands our understanding of how *M. trichosporium* OB3b can store and regulate cellular Cu^+ without interference from other competing metals.

First, I focus the discussion on the thermodynamics of Cu^+ binding to CSP1 and CSP3. The enthalpic and entropic contributions to Cu^+ binding can be directly compared to other known Cu^+-protein systems to gain insight into the molecular differences and provides a valuable comparison with non-native metals binding to CSP1 and CSP3. Next, the condition-independent thermodynamics of Zn^{2+} binding to CSP1 and CSP3 are compared to Zn^{2+} binding to other cysteine-rich systems (i.e. metallothionein, cysteine-rich peptides, etc.), as well as to the Cu^+-CSP interactions. Lastly, I turn my attention to the binding of mercury. Of all physiologically- or environmentally-relevant metals, Hg^{2+} is most likely to outcompete Cu^+ for binding to cysteine-rich proteins. The molecular mechanism for the preference of CSP1 and CSP3 to bind to Cu^+, over Zn^{2+} or Hg^{2+} is discussed using these experimental thermodynamics.

7.4.1. Quantification of the Thermodynamics of each Copper(I) Population Binding to CSP1.

The binding of Cu^+ to CSP1 shows three distinct binding events, indicating that three separate populations are forming with different formation thermodynamics. The first population ($n_{Cu+} = 7 \pm 0.2$) is proposed to completely deprotonate the Cys residues upon binding. The subsequent binding population of ~4 Cu^+ forms copper-thiolate clusters without proton displacement, as all cysteine protons are proposed to have already been displaced in the first binding event. Lastly, the weakest binding population of 2.8 ± 0.6 Cu^+, bind to the fully deprotonated protein, likely near the entrance of the metal-binding channel.

Given that the CSP1 affinity for the first population of Cu^+ is too high for accurate quantification by ITC under these experimental conditions, the equilibrium constant from Dennison and coworkers was utilized for this first Cu^+ population. Although their equilibrium constant, $1.3\ (\pm\ 0.1)\times10^{17}$, is an average of the entire population of Cu^+ that binds to CSP1, I propose this is a good approximation for the binding affinity of the strongest bind event in these ITC experiments. I also propose that this binding affinity can

be used to provide approximate condition-independent thermodynamics for this Cu^+ population.

This equilibrium constant is used to, solve for Gibbs free energy by,

$$\Delta G = -RTln(K_a) \qquad \textbf{Equation 7.4.1.1.}$$

where R is the gas constant (0.001987 kcal/mol*K), T is the experimental temperature in kelvin (298.15 K), and K_a is the condition-independent binding constant. This shows that the first population of Cu^+ binds with a favorable change in free energy of ΔG = -23.3 ± 0.1 kcal/mol Cu^+. With this value, and the condition-independent enthalpy quantified by ITC (ΔH = +5.9 ± 0.3 kcal/mol Cu^+), the entropy of binding can then be determined by:

$$\Delta G = \Delta H - T\Delta S \qquad \textbf{Equation 7.4.1.2.}$$

Rearranging Equation 7.4.1.2:

$$-T\Delta S = \Delta G - \Delta H \qquad \textbf{Equation 7.4.1.3.}$$

Thus, the condition-independent entropic contribution is determined to be $-T\Delta S$ = -29.2 kcal/mol Cu^+ at 25 °C.

Unlike the binding of the first Cu^+ population, where the analysis used the average equilibrium constants determined by Dennison and coworkers, the binding affinity of the second population is more difficult to determine under these experimental conditions. Given that I propose that the CSP1 cysteines are fully deprotonated by the binding of the first Cu^+ population, the second population is binding without proton displacement and forms bridged Cu^+-thiolate bonds, which are inherently weaker that terminal Cu^+-thiolate bonds. However, as this binding event occurs between the binding of the first and third populations, it is only possible to determine a range for the binding constants of this population, $10^7 < K_2 < 10^{17}$. Although not inherently useful, this provides both the upper and lower limit of binding for this second Cu^+ population. By using this range for the binding constant, and subsequently the upper and lower limits of the binding Gibbs free energy, ΔG = -9.6 < ΔG <–23.3 kcal/mol, and combining this with the condition-independent binding enthalpy of ΔH = -4.4 ± 0.3 kcal/mol, the upper and lower limits of the binding entropy can then be established such that $-T\Delta S$ = -5.2 < $-T\Delta S$ < –18.9 kcal/mol Cu^+.

Unlike the first and second Cu^+ populations, where the complete binding thermodynamics are not well defined, the third binding event, in which 2.8 ± 0.6 Cu^+ bind

can be completely quantified by ITC. This Cu^+ population binds to CSP1 with K = 1.2 (± 0.6)×10^7, ΔG = -9.6 ± 0.4 kcal/mol Cu^+, ΔH = -8.5 ± 0.7 kcal/mol Cu^+, and –TΔS = -1.1 ± 0.8 kcal/mol Cu^+.

The thermodynamics of each Cu^+ population binding to CSP1 provide fundamental insight into protein structural contributions, metal specificity and selectivity, bond formation, and protein desolvation, thereby enhancing our understanding of the molecular contributions to copper storage and overall copper homeostasis.

The Cu^+ stoichiometries are in agreement with values that Dennison and coworkers had found, using a similar $Cu(MeCN)_3^+$ complex. Our data, along with literature data, indicate that ~14 Cu^+ are bound to CSP1 when a weak competing ligand is present in solution.[23] Although the cysteine pK_a values and deprotonation of CSP1 upon metal binding is unknown, it was noted that the binding affinity of Cu^+ depends on pH.[23] This indicates there is pH-dependent metal binding mechanism, which is important for the thermodynamic analysis. Thus, general agreement with the literature on the characteristics of the Cu^+-CSP1 interaction gives confidence to the data collected and analyzed herein.

7.4.2 Binding of Three Distinct Cu^+ *Populations to CSP1.*

Three distinct populations of Cu^+ bind to CSP1 at pH 7.5. This is significant, in that this had not been observed previously. Prior to this work, Dennison and coworkers had determined CSP3 structures with varying Cu^+ stoichiometries to determine Cu^+-thiolate cluster formation, which is also expected for similar CSP1.[26] I propose that each Cu^+ binding population is associated with a different Cu^+ coordination and metal-binding conditions.

Initially, the 13 CSP1 cysteines are protonated by 12 protons, 0.92 protons per cysteine residue at pH 7.5. Upon Cu^+ binding to CSP1, these protons are displaced to give Cu^+-thiolate bonds. The first population of 7 ± 0.2 Cu^+ bind to CSP1 with a binding enthalpy of +5.9 ± 0.3 kcal/mol Cu^+. Each proton that is displaced contributes an enthalpic penalty from breaking the S-H bond and an entropic benefit from loss of H^+. Subtracting the deprotonation enthalpy for each cysteine (–8.6 kcal/mol) results in an average change in enthalpy of -9.9 ± 0.3 kcal/mol Cu^+ for the Cu^+-thiolate bonding. Assuming that each

Cu^+ is binding in a linear geometry to two cysteine residues, this bond enthalpy is for terminal thiolate coordination.

The second population of ~4 Cu^+ that binds to Cu^+_7-CSP1 do not displace any protons since all 13 cysteine residues are already coordinated to Cu^+ in the Cu^+_7-CSP1 complex. I propose that this binding population do binds in a linear geometry to two cysteine residues, but through bridging-thiolate coordination.[23] Although no protons are displaced, the Cu^+-thiolate$_{(bridging)}$ interaction would be less enthalpically favorable and bind with a lower affinity. Compared to the first Cu^+ population, the second population binds with a Cu^+-thiolate formation enthalpy of –4.4 ± 0.3 kcal/mol. Indeed, this lower Cu^+-thiolate enthalpy for the proposed bridging coordination is lower than that of the terminal Cu^+-thiolate coordination. Unlike the enthalpy, the entropic contribution is not known for this binding event, a range for the change in free energy and entropy of this binding can be defined but is large. Overall, the energetics indicate that the binding of this population is both enthalpically and entropically favorable and likely entropically driven.

The third inflection, corresponding to the formation of the third Cu^+ population that binds to CSP1, is the weakest binding event, but most characterizable by ITC, which indicates that 2.8 ± 0.6 Cu^+ bind to Cu^+_{11}-CSP1. Condition-independent binding thermodynamics for this population show that each Cu^+ binds with an affinity of 2.2 (± 0.6)×10^6, which is lower than would typically be expected from the soft-soft Cu^+-cysteine interaction. Visual inspection of the Cu^+-bound CSP1 structure shows several methionine and histidine residues at the opening of the metal-binding channel **Figure 7.1.3.1**. In the crystal structure, 2 Cu^+ ions are found in this opening bound to these amino acids, and may correspond to this binding event. Unlike the Cu^+-cysteine interaction, Cu^+-methionine and Cu^+-histidine interactions are much weaker. I propose that this event correlates to the Cu^+ ions binding at the opening of the channel. Given the amino acid types, no protons are likely to be displaced at pH 7.5. This population of Cu^+ that binds to CSP1 shows a binding enthalpy of -8.5 ± 0.7 kcal/mol and entropy of -1.8 ± 0.8 kcal/mol Cu^+. Further insight on these thermodynamic data for the binding of each Cu^+ population can be achieved through comparisons with known Cu^+ binding systems (*vide infra).*

7.4.3 Thermodynamic Contributions of Copper(I) Binding in CSP1

There are no other copper storage proteins that have reported binding thermodynamics. However, metallothionein (MT), which has some metal-storage capabilities (See Chapter 6) provides a valuable comparison to better understand Cu^+ binding in CSP1. Like CSP1, MT binds a large number of metals using conserved cysteine residues. This includes the binding of up to 7 Zn^{2+} or Cd^{2+}, and 8 Cu^+ in excess GSH. Most importantly, however, MT is unstructured and metal-binding results in the stabilization of a well-defined protein structure. CSP1 on the other hand, has a stable 4-helix protine structure that shows little change upon Cu^+ binding to the protein scaffold. The neuronal isoform, MT3, has a Cu^+ binding affinity of ~4 (± 4)×10^{19}, a binding enthalpy of $\Delta H = -10 \pm 1$ kcal/mol, and a Cu^+ binding entropy of $-T\Delta S = -17 \pm 1$ kcal/mol, *per*-Cu^+. However, Cu^+ binds to MT with a mixed coordination, in which both Cu^+-$thiolate_{terminal}$ and Cu^+-$thiolate_{bridging}$ interactions are present, in contrast to Cu^+ binding to CSP1, with only Cu^+-$thiolate_{bridging}$ interactions.

To better understand the enthalpic (and entropic, *vide infra*) contribution of the Cu^+-thiolate interactions in CSP1, it is useful to consider the sources that can contribute to the binding enthalpy (**Figure 7.4.3.1**). Typical contributions are (1) (de)-protonation of the metal-binding site, (2) changes in the electrostatic and hydrogen bonding interactions within the protein, and (3) metal-bond formation.

Consider the first Cu^+ population that binds to CSP1. Assuming the change in enthalpy is mostly due to bonding, the average Cu^+-thiolate bond enthalpy, after subtracting the cysteine deprotonation enthalpy is –9.9 kcal/mol. The Cu^+-thiolate bond enthalpy of MT3 is –7 kcal/mol, so the Cu^+ bond enthalpy of CSP1 is ~2 kcal/mol more favorable than it is for MT3. The most impactful difference likely comes from the Cu^+-thiolate interaction itself. In MT3, the binding of 6 Cu^+ results in mixed bridging and terminal thiolate-coordination; however, for CSP1, the first Cu^+ population that binds to CSP1 only has terminal thiolate bonding. A comparison of the binding enthalpies ($\Delta HCu^+_{\text{-CSP1,1}} = +5.9$ kcal/mol and $\Delta HCu^+_{\text{-MT3}} = -10$ kcal/mol) show dramatic differences. Beyond deprotonation and metal-bond formation differences *per*-Cu^+ in CSP1 and MT3, electrostatic interactions in the protein scaffold can also contribute. For MT3, the binding of monovalent and divalent metals stabilizes conformational changes within the protein and interdomain interactions and enthalpically favorable metal clusters. This, however,

Binding Enthalpy	Binding Entropy
1. (De)–Protonation 2. Changes in Hydrogen Bonding 3. Metal Bond Formation	1. Metal Desolvation 2. Conformational Restraints 3. Metal Coordination 4. Water Displacement 5. Cratic Entropy

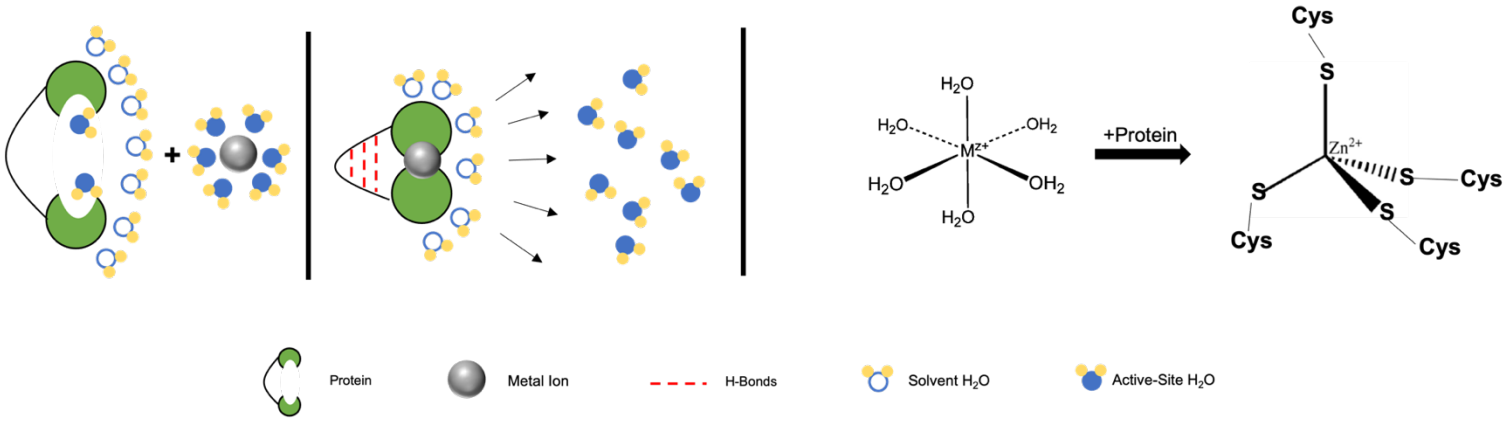

Figure 7.4.3.1. *Graphical representation of major components that make up the enthalpic and entropic contributions to metal binding in a protein in aqueous conditions.*

does not appear to be the case for CSP1, which shows little structural differences between apo- and Cu^+-bound CSP1, although this is only observed for the fully-metalated CSP1, and partial metalation could result in small conformational changes.

From an entropic perspective, the binding of Cu^+ to CSP1 is entropically favorable and entropically driven, with $-T\Delta S = -29.2 \pm 0.3$ kcal/mol Cu^+. The binding of Cu^+ to MT3 is also entropically favorable and entropically driven, with the entropic contribution equal to –11.3 kcal/mol per proton released when Cu^+ binds. Given the dynamic nature of MT3, much of this difference likely originates from Cu^+-stabilization of the MT3 protein scaffold, which would be more entropically disfavorable than Cu^+ binding to CSP1, which has less conformational differences. Other aspects may also play a role, including protein desolvation, water displacement, and cratic entropy, which may be more favorable for MT3, than CSP1.

A similar analysis, at least for known enthalpic contributions to Cu^+ binding, can be made for the binding of the second Cu^+ population. The bridging thiolate coordination for this population results in a lower overall binding enthalpy of –4.4 kcal/mol Cu^+ and assuming this is entirely due to Cu^+ bonding, an average Cu^+–thiolate bond enthalpy of –2.2 kcal/mol. This is 4.8 kcal/mol more enthalpically disfavorable than the Cu^+-thiolate interaction in MT3. However, as previously mentioned, this population of Cu^+ is likely binding to CSP1 through bridging thiolate bonds, which are expected to be weaker than the mixed terminal and bridging thiolate coordination in MT3. This decrease in Cu^+-thiolate bond enthalpy is also noticeable in comparison to the binding of the first Cu^+ population to CSP1, although changes in the electrostatics are also possible, even though this seems unlikely given the conformational stability of CSP1.

Unlike the first and second Cu^+ binding population, the third Cu^+ population is not likely to be binding solely to cysteine residues, but some combination of methionine, histidine, and cysteine residues. This makes direct comparisons difficult. However, the lower binding affinity, $\sim 1\times10^7$, supports this hypothesis. Likewise, this binding is both enthalpically and entropically favorable and enthalpically driven. I propose that there would still be no protein deprotonation, so much of this binding enthalpy is from Cu^+-amino acid bond formation. The weakly entropically favorable binding further supports the idea that there are minimal conformational changes upon metal binding, although

stabilization of this more dynamic region of the protein may result in a more disfavorable enthalpy of binding.

These three populations of Cu^+ ions, one that binds strongly to CSP1, one that binds with a moderate affinity, and one that binds weakly, may provide a mechanistic advantage for the uptake, storage, and management of Cu^+ by CSP1. The high affinity binding would favor the uptake of Cu^+, resulting in its storage properties. A lower affinity Cu^+ binding site would provide Cu^+ for by yet-unknown metallochaperones, and the moderate Cu^+ binding site would mediate interaction between the strong and weak sites, allowing for efficient transfer from one population to the other. Thus, both a stable and labile Cu^+ pool isas the hallmark of protein function. Curiously, it was noted by Dennison and coworkers that the binding of Cu^+ showed evidence of positive cooperativity, further supporting this interplay between distinct populations of Cu^+, leading to the uptake, storage, and release of Cu^+. Unfortunately, positive (or negative) cooperativity is difficult to discern by ITC; thus, more experimentation is required. Furthermore, the physiological function of positive cooperative in CSP1, but not CSP3, remains unknown.

7.4.4. CSP3 Binds Copper(I) in Three Distinct Thermodynamically Stable Populations

Unlike CSP1, CSP3 is not tagged for removal from the cytosol by the twin-arginine translocation pathway and it is not directly involved in providing Cu^+ to pMMO. As of yet, the function of CSP3, beyond a cytosolic Cu^+ storage protein, is not known, nor is the principal metalloprotein target for the stored Cu^+ known. However, a thermodynamic comparison between CSP3 and CSP1 can be made.

Titrations of $Cu(MeCN)_3^+$ into CSP3 also revealed three distinct binding populations. The first population of ~4 Cu^+, that bind to CSP3 is estimated to displace ~7.4 protons. Significantly fewer Cu^+ bind in this first population than bind initially to CSP1, although the average binding affinity is believed to be similar. With the average equilibrium constant determined by Dennison and coworkers, 2.0 ($\pm$ 0.1)$\times 10^{17}$, an approximation for the equilibrium constant for this first Cu^+ population of CSP3. Using this affinity, and the condition-independent binding enthalpy determined by ITC, in which $\Delta H = +4.0 \pm 0.3$ kcal/mol Cu^+, the binding entropy can be estimated as $-T\Delta S = -29.2 \pm 0.3$ kcal/mol Cu^+ at 25 °C. By subtracting the heat of cysteine protonation (–8.6 kcal/mol) for

each Cu^+ in this first population where it is estimated that 1.84 protons are displaced *per*-Cu^+, an average Cu^+-thiolate binding enthalpy of –11.8 ± 0.3 kcal/mol Cu^+ is obtained. Although protein protonation may be different in CSP3, than in CSP1, this average Cu^+-thiolate binding enthalpy is moderately different ($\Delta H_{Cu+thiolate,CSP1}$ = -9.9 ± 0.3 kcal/mol vs. $\Delta H_{Cu+thiolate,CSP3}$ = -11.8 ± 0.3 kcal/mol). However, these Cu^+-thiolate binding enthalpies are similar, supporting the idea that the initial Cu^+ binding is to both proteins through terminal cysteine bonds.

The second population of 4.1 ± 0.4 Cu^+ bind with an average buffer-independent binding constant of 1.9 (± 0.6)×10^7 at pH 7.5, displacing the remaining 9.2 protons from the Cys residues of CSP3. Through an analysis of the ITC data, the condition-independent binding entropy and enthalpy for this population were determined. Directly measured by ITC is the binding enthalpy, *per*-Cu^+, which is $\Delta H_{Cu+-CSP1,2}$ = +5.9 ± 0.3 kcal/mol. Again, by taking this cysteine deprotonation into account, each Cu^+ binds with a Cu^+-thiolate bond enthalpy for the complex of –13.4 ± 0.3 kcal/mol Cu^+. This enthalpy is consistent with terminal cystine coordination, given the large number of cysteine residues that are present in CSP3. Finally, each Cu^+ in this second population binds to CSP3 with a condition-independent change in entropy equal to $-T\Delta S$ = -15.8 ± 1.0 kcal/mol at 25 ºC.

Finally, there is a large, but weakly-bound population of 10 ± 1 Cu^+ that bind with an average condition-independent binding constant of 2.2 (± 0.6)×10^5. Taking the binding change in free energy and the condition-independent enthalpy (ΔH = -0.2 ± 0.1 kcal/mol) into account allows the quantification of the binding entropy ($-T\Delta S$ = -7.0 ± 0.2 kcal/mol). By this third population, I propose that all the CSP3 cysteines have been fully deprotonated. Unlike Cu^+ binding to CSP1, which has a few methionine and histidine residues at the entrance of the metal-binding channel that can bind ~3 Cu^+ weakly, the binding of ~10 Cu^+ to CSP3 is more difficult to understand. At the opening of CSP3 is only one histidine and it seems unlikely that this Cu^+ population binds at the opening of the metal-channel. These Cu^+ may be binding to CSP3 through bridging thiolate bonds, similar to the binding of the second population in CSP1. Curiously, the binding of this Cu^+ population is entropically driven, but the source of this contribution, particularly if the coordination is through bridging thiolate bonds is unknown. This unusual binding stoichiometry and thermodynamics may be affected by different Cu^+ binding kinetics, as Dennison and

coworkers previously found that the chelation of Cu^+ from CSP3 is very slow. Slow kinetics may prevent the accurate quantification of the Cu^+ thermodynamics under current experimental conditions.

These three Cu^+ populations are similar to those of CSP1, one Cu^+ population binds initially and strongly to CSP3, followed by one with a significantly weaker binding affinity, and finally one that binds even weaker. These differential binding affinities may provide a mechanistic advantage for the uptake, storage, and delivery of Cu^+ by CSP3. The strong binding event would favor the uptake of Cu^+, resulting in its storage properties. The weak Cu^+ binding site would allow delivery of Cu^+ to a physiologically relevant metallochaperone, and the intermediate Cu^+ binding site may be similar to that of CSP1. The difference in affinity between this second population, and most tightly bound Cu^+ population is unusual, at least compared to CSP1. It still may function as an intermediate Cu^+ binding population that aids in the uptake and storage of Cu^+, but without the cooperative binding of CSP1. The large differential in binding affinities may also shift the function of CSP3 to a more efficient storage protein with diminished Cu^+ lability. Differences in this second Cu^+ binding population of CSP1 and CSP3 may be the origin of cooperativity differences for the binding of Cu^+.

7.4.5. Thermodynamic Contributions to Copper(I) Binding in CSP3

Similar to the analysis of CSP1, the enthalpic and entropic contributions to the binding of Cu^+ to CSP3 can be compared to known Cu^+-protein thermodynamics (**Figure 7.4.3.1**). Again, given the similarities and differences between CSP3 and metallothionein (MT), this comparison is apt.

The first Cu^+ population of CSP3, binds with a condition-independent change in enthalpy of $+4.0 \pm 0.3$ kcal/mol and an average Cu^+-thiolate binding enthalpy equal to ΔH = -11.8 kcal/mol. This is moderately more favorable than the average Cu^+-thiolate formation enthalpy of MT3, which is ΔH = -7.0 kcal/mol. Considering expected contributions to binding, this difference may originate from different protein electrostatic interactions. This is supported by the similarities between CSP1 and CSP3, which are expected to have similar electrostatic contributions, unlike that of MT3. From an entropic perspective, in which the first Cu^+ population binds with a change in entropy of $-T\Delta S$ = -

27.6 ± 0.3 kcal/mol Cu^+ at 25 ºC, which is equivalent to –15 kcal/mol per proton released upon Cu^+ binding. Likewise, each proton in MT3 shows a change in entropy of approximately –11 kcal/mol, indicating that the binding of Cu^+, and subsequent proton displacement is more entropically disfavorable. These thermodynamic differences suggest that the primary difference between the binding of Cu^+ to MT3 and first Cu^+ population binding in CSP3 likely originates from the protein electrostatics in different metal-stabilized structures.

For the second Cu^+ population, the enthalpic contribution is nearly identical to that of the first population, but the overall protein affinity is much weaker, and quantifiable by ITC. This Cu^+ population binds with an equilibrium constant of 1.9 (± 0.6)×10^7 *per*-Cu^+. The condition-independent binding enthalpy for this population, is ΔH = +5.9 ± 0.3 kcal/mol Cu^+, which, if it assumed that Cu^+ coordinates to two terminal cysteine residues, results in a Cu^+-thiolate formation enthalpy of –13.4 kcal/mol Cu^+, after the enthalpy of cysteine deprotonation is considered. This results in a total entropic contribution of $-T\Delta S$ = -15.8 ± 1.0 kcal/mol per proton that is displaced when each Cu^+ binds. Comparing this to both CSP1 and MT3 suggests that this entropic contribution is more entropically disfavored than either protein. This is particularly surprising in the comparison with CSP1, as the proton displacement is similar and suggests that these Cu^+'s are binding through terminal cysteine bonds. Considering the reported cooperativity in the binding of Cu^+ to CSP1, but not CSP3, these differences in Cu^+ binding thermodynamics for this second Cu^+ binding population may be expected to be different. The mechanism for cooperative Cu^+-binding to CSP1 is currently unknown and these thermodynamics differences may provide some insight about the cooperative mechanism.

Lastly, the size of the third population of 10 ± 1 Cu^+ indicates a significant difference between CSP1 and CSP3. For CSP1, the last Cu^+ population only has ~3 Cu^+, which suggests that this population binds several methionine and histidine residues at the entrance of the metal-binding channel. However, this could not be the case for CSP3, suggesting that some other Cu^+ binding sites must be present. This binding is also very entropically favorable, with very little enthalpic contributions to metal binding. It may be that these Cu^+ are binding to the exterior of the helix bundle.

7.4.6. Comparative Analysis of CSP1 and CSP3 and their Copper(I)-Binding Properties

Although speculative, differences in the binding between CSP1 and CSP3 may originate from cooperativity differences between these systems. Much more work is necessary to uncover the molecular mechanisms of this kinetic and cooperativity differences in CSP1 and CSP3. Two distinct differences are noticed between CSP1 and CSP3. Dennison and coworkers previously determined that the binding of Cu^+ to CSP1 had shown positive cooperativity, whereas CSP3 did not.[22–24] Furthermore, the kinetics associated with Cu^+ chelation from CSP1 and CSP3 were vastly different, in which the chelation of Cu^+ from CSP1 was much more rapid than CSP3. As previously mentioned, the determination of cooperativity by ITC is very difficult to observe or quantify. Curiously, the titration of $Cu(MeCN)_3^+$ into CSP3, unlike CSP1, does not show the typical isotherm in the raw data, which was reproducible in independent ITC experiments. This may be suggestive of the cooperativity that has been observed by prior metal chelation experiments. This is supported by the similarity of the first binding event for both proteins, in which cooperativity and the kinetics may play less of a role, but the subsequent binding events are significantly different.

7.4.7. Evaluating the Zinc(II)-CSP1 Interaction

Earlier studies of CSP1 have shown that it binds Cu^+ tightly, but does not appear to bind Zn^{2+}, Mn^{2+}, or Fe^{2+} *in-vivo*.[22] Although this binding preference is not surprising, given hard-soft acid-base theory and the preference of Cu^+ over Zn^{2+} for thiols, thermodynamic data on the binding of other relevant metals to proteins provides important insight into metal selectivity, specificity, and fundamental principles that govern protein function within a cell.

I have shown by ITC that CSP1 is, in fact, able to bind Zn^{2+}, where CSP1 is able to bind half the number of Zn^{2+} (n_{total}= ~7) as Cu^+ (n_{total} = ~14) through two distinct binding events. Given their similar size, this suggests that the overall charge of the metal ion may play a role in the metal binding stoichiometry. As Zn^{2+} is dipositive and Cu^+ is monopositive, it seems that CSP1 binds enough metals to charge-balance the thiolates that are present in the core of the protein after cysteine deprotonation. This is particularly interesting when comparing the binding of Cu^+ and Zn^{2+} to metallothionein, which does

not show this charge-balancing. Mammalian MT3 binds 7 Zn^{2+} and, in the presence of excess glutathione, 8 Cu^{+} (See Chapter 6), suggesting that charge differences in the metal-bound protein may modify or modulate the metal binding properties of the protein.

Condition-independent binding affinities for both Zn^{2+} binding populations can be quantified. Like the binding of Cu^{+}, the primary limitation is a lack of experimental evidence for the protonation of each CSP1 cysteine residue. However, fundamental biochemical and inorganic principles can guide the *post-hoc* analysis, with some basic assumptions that make chemical sense. It is estimated that each cysteine residue is protonated with 0.92 protons, which is based on the pK_a of 8.6 for free cysteine at pH 7.5. So, for CSP1, which has 13 cysteine residues, a total of 12 protons would be displaced upon Zn^{2+} binding. It can also be assumed that the first Zn^{2+} (n = 0.9) would bind with the preferred tetrahedral, tetrathiolate coordination to CSP1. Thus, if 4 cysteine residues are binding to the 0.9 Zn^{2+}, then a total of ~3.3 protons would be released upon metal binding. This gives an approximation that 8.7 protons are still bound to $(Zn)_1$-CSP1. The second binding event would then displace the remainder of these protons, forming both bridging and terminal Zn^{2+}-thiolate bonds.

Using these estimated deprotonation events, the condition-independent affinity for the first Zn^{2+} and the subsequent Zn^{2+} ions can be quantified, followed by the determination of the entropic contribution to Zn^{2+} binding. These thermodynamics can then be compared to metallothionein to gain insight into metal binding.

7.4.8. Comparative Zinc(II)-Binding Thermodynamics in CSP1 and Metallothionein

Considering Zn^{2+} binding, the α-domain of MT3 is similar to CSP1, in that it relies on a large number of cysteines to bind the Zn^{2+} and other metal ions. The α-domain is preferred for this comparison as the thermodynamics of Zn^{2+} binding to the full-length MT3 are complicated by other protein interactions that are specific to metallothionein (i.e. interdomain interactions) but not present in the separated domain, which makes it a viable system for comparison. Although metallothionein and its domains are very conformationally dynamic, it binds Zn^{2+} with ~4 orders of magnitude higher affinity than CSP1. Nevertheless, Zn^{2+} binding to MT3 is both enthalpically disfavorable and entropically driven, which is similar for Zn^{2+} binding to CSP1.

The first Zn^{2+} that binds to CSP1 has a condition-independent binding enthalpy of $\Delta H = 9 \pm 2$ and a binding entropy is of $-T\Delta S = -19 \pm 2$ kcal/mol, whereas Zn^{2+} binds to αMT3 with a condition-independent binding enthalpy of $\Delta H = 4.26 \pm 0.05$ kcal/mol and a binding entropy of $-T\Delta S = -20 \pm 1$ kcal/mol. Subtracting the cysteine deprotonation enthalpy from the Zn^{2+} binding enthalpy for CSP1, in which 0.9 Zn^{2+} displaces 3.3 protons, suggest a total cysteine-thiolate enthalpy of –21.5 kcal/mol Zn^{2+}. This is compared to a similar Zn^{2+}-thiolate binding to MT3, which gives an average Zn^{2+}-thiolate bond enthalpy of –9.6 kcal/mol Zn^{2+}, although this includes both mixed bridging and terminal thiolate bonding, which would lower the change in the enthalpy. This may be the primary difference in the binding enthalpy between these two systems, but other possibilities may also exist, as Zn^{2+}-thiolate bonding in CSP1 is believed but not well characterized.

A less favorable Zn^{2+}-thiolate formation enthalpy in MT3 is suggestive of other contributions from the protein scaffold that lead to the endothermic interaction. This distinction may suggest that the CSP1 structural dynamics contributes minimally to the binding of Zn^{2+}, in comparison to MT3, where the protein structure is stabilized by the binding of Zn^{2+}. Likewise, the entropic contribution to Zn^{2+} binding to CSP1 is ~10 kcal/mol more favorable than it is for MT3. Considering the entropic contributions to metal binding, the binding of the first Zn^{2+} is likely driven by the deprotonation. Other entropic components also impact this to varying degrees. Protein desolvation, protein conformational dynamics, and cratic entropy all contribute to the entropy of the first population of Zn^{2+} binding to CSP1, although quantification of each of these is challenging. However, protein conformational dynamics are likely the major contributor in the difference, as Zn^{2+} stabilizes the conformationally dynamic MT protein, but the binding of Zn^{2+} to CSP1 likely results in minimal change in the protein structure and dynamics.

A similar analysis for the condition-independent thermodynamics of the second Zn^{2+} binding population can also include a comparison with MT3. The binding of this Zn^{2+} population should result in the complete deprotonation of CSP1 through the release of ~8.7 protons, giving a binding enthalpy of $\Delta H = +7$ kcal/mol $Zn^{2+}$and a binding entropy of $-T\Delta S = -16$ kcal/mol Zn^{2+}. In this population, where Zn^{2+} is proposed to bind with some bridging thiolate coordination, the Zn^{2+} ions would displace ~8.7 protons. By subtracting

the cysteine deprotonation enthalpy, this shows an average Zn^{2+}-thiolate bond formation enthalpy of $-\Delta H = 10 \pm 1$ kcal/mol Zn^{2+}.

First, consider the difference in the Zn^{2+}-binding thermodynamics between the first and second populations of Zn^{2+}. This second binding event is proposed to include bridged Zn^{2+}-thiolate bonds, which would, inherently, have a lower binding enthalpy than terminal Zn^{2+}-cysteine bonds. From an entropic perspective, more protons are released upon the second population of Zn^{2+} binding, but the number of protons released per Zn^{2+} is different, resulting in a moderate entropic difference between these two sites. Other entropic contributions should not provide much entropic favorability or disfavorability, as they are likely to be similar. This includes protein desolvation, metal desolvation, and protein conformational changes that should be very similar between the two Zn^{2+} binding populations. Cratic entropy would be different, but this contribution has been controversial and unlikely to provide a significant entropic difference.[32,33] This leaves protein deprotonation as the main difference in the entropic contribution to these two binding events.

A comparison of this binding site with αMT3, however, shows distinct similarities. The enthalpy associated with the Zn^{2+}-thiolate formation, for example, is –10 kcal/mol Zn^{2+} for CSP1 and –9.6 kcal/mol Zn^{2+} for αMT3. This suggests similar Zn^{2+}-thiolate coordination of Zn^{2+} to both proteins. αMT3 is known to have both terminal and bridging Zn^{2+} thiolate bonds and the binding of the second Zn^{2+} population to CSP1 may include both terminal Zn^{2+}-thiolate bonds, and bridging Zn^{2+}-thiolate coordination. Other factors including electrostatic interactions within the protein scaffold may also play a role.

7.4.9. CSP3 Binds Zinc(II) in Two Thermodynamically-Distinct Populations

Like CSP1, there is no known thermodynamic, structural, or biochemical characterization of the Zn^{2+}-CSP3 complex. Although it is unlikely that Zn^{2+} would compete with Cu^{+} for binding to a cysteine-rich protein, the thermodynamics of metal selectivity and specificity can still be useful in understanding physiological function. Thermodynamics of Zn^{2+} binding to CSP3 were determined with ITC measurements.

Similar to CSP1, the binding of two distinct Zn^{2+} populations were observed. Like CSP1, they show a similar charge-dependent stoichiometry, in which a total of 8 ± 2 Zn^{2+}

bind to the entire protein, which is half that number of monopositive Cu^{+} ions that bind. This suggests that, given the size similarities, CSP3 balances the negative charges of the deprotonated cysteine residues of the protein by the positive charge of the bound metal ions.

The buffer-independent equilibrium constants at pH 7.5 for each Zn^{2+} binding population are readily quantified by ITC through the inclusion of the coupled and competing equilibria that occur in solution. However, given the lack of knowledge about Zn^{2+} binding to CSP3, protein deprotonation is difficult to determine. Taking an approach similar to that of CSP1 for the determination of condition-independent Cu^{+} binding thermodynamics, metal binding to CSP3 is expected to displace 16.56 H^{+}, or 0.92 protons per cysteine residue. Although the exact number of protons that are displaced from CSP3 is unknown, this provides a reasonable approximation for the determination of protein deprotonation upon metal binding. For CSP3, the first Zn^{2+} population includes 2.7 ± 0.8 Zn^{2+}. As CSP3 has a total of 18 cysteine residues that line metal-binding channel, it can be expected that each of these Zn^{2+} would bind to terminal thiolates in a tetrahedral coordination. With this assumption in mind, I predict that this population of Zn^{2+} could displace 9.96 protons. Continuing these assumptions, the second Zn^{2+} binding population would bind to CSP3 with both terminal and bridging coordination, which would result in the complete deprotonation of CSP3. As I predict that the CSP3 cysteines have 16.56 protons, and the first Zn^{2+}-binding population displaces 9.96 protons, then this second Zn^{2+} population would displace the remaining 6.7 protons. Using this deprotonation, the condition-independent binding affinity and enthalpy, and subsequently the free energy and entropic contribution to metal binding, can be determined. An evaluation of the contributions from the enthalpic and entropic components can then be completed, with a comparison to known Zn^{2+} binding proteins like metallothionein.

7.4.10. Thermodynamic Contributions to Zn^{2+} Binding in CSP3

Considering the first Zn^{2+}-binding population, 2.7 ± 0.8 Zn^{2+} bind and displace 9.96 protons, with a condition-independent binding constant of 1.0 (±0.1)×10^{8}. The binding enthalpy is measured directly by ITC and, taking the competing equilibria into account, along with the free energy, the buffer-independent binding enthalpy is ΔH = 18.4 ± 0.3

kcal/mol Zn^{2+}, and the binding entropy is $-T\Delta S = -29 \pm 2$ kcal/mol Zn^{2+}. To compare these first Zn^{2+}'s that bind to CSP3 to Zn^{2+} binding to other proteins, the cysteine deprotonation enthalpy must be taken into account, as these thermodynamics are pH-dependent and vary, depending on the number of metal ions that bind in each population. Subtracting the cysteine deprotonation enthalpy, these first Zn^{2+} ions have an enthalpy of –24.8 kcal/mol for the Zn^{2+}-thiolate binding. This Zn^{2+}-thiolate enthalpy is similar to that of CSP1, –21.6 kcal/mol. Consider the various contributions to the enthalpic and entropic components (**Figure 7.4.3.1**). Binding of the first Zn^{2+} population in CSP3 is slightly more exothermic. As the metals are the same, and the protein deprotonation is subtracted from the binding enthalpy, his suggests that this small enthalpic difference may originate from differences in the protein electrostatic interactions. Like the comparison for CSP1, the enthalpy of the Zn^{2+}-thiolate binding to the α-domain of MT3 is $\Delta H = -9.6$ kcal/mol. Again, the difference between these enthalpies, after cysteine deprotonation, suggest that the more enthalpically favorable the binding of the first population of Zn^{2+} to CSP3 is due to protein scaffold electrostatic interactions.

A similar analysis of the entropic contribution can also be undertaken. The first Zn^{2+} population binds to CSP3 with a change in entropy of $-T\Delta S = -29 \pm 2$ kcal/mol. Zn^{2+} binding to CSP1, where $-T\Delta S = -19 \pm 2$ kcal/mol, which is much more entropically favorable. This is due, in part, to the differences in deprotonation. Considering that these two Zn^{2+} populations bind with a similar affinity and minimal differences in the Zn^{2+}-thiolate formation enthalpy, this entropic difference may come from differences in the protein structure.

The second Zn^{2+} binding population shows condition-independent binding thermodynamics with an average equilibrium constant for the 5.3 ± 2 Zn^{2+} of $K = 1.0 (\pm 0.1) \times 10^6$. With a condition-independent binding enthalpy of $\Delta H = -15 \pm 1$ kcal/mol Zn^{2+}, the entropic contribution is then calculated to be $-T\Delta S = -8 \pm 1$ kcal/mol. To compare this population of Zn^{2+} to those binding to CSP1, the Zn^{2+}-thiolate formation enthalpy can be utilized. For the second Zn^{2+} population, this is equal to $\Delta H = -9.6$ kcal/mol, which is very similar to the Zn^{2+}-thiolate binding enthalpy of CSP1, $\Delta H = -10.3$ kcal/mol Zn^{2+}. Overall, the Zn^{2+} binding thermodynamics of CSP1 and CSP3 are very similar, indicating that the protein contribution to the binding of this population is not significantly different between

these two proteins. Furthermore, this Zn^{2+}-thiolate binding enthalpy is identical to that of αMT3, ΔH = -9.6 kcal/mol Zn^{2+}.

Finally, there is a comparison of the entropic contributions to Zn^{2+} binding. This second Zn^{2+} population binds to CSP3 with a change in entropy of $-T\Delta S$ = -15 ± 1 kcal/mol whereas the second Zn^{2+} population binds to CSP1 with a change in entropy of $-T\Delta S$ = -16 ± 1 kcal/mol. This entropic contribution is not different, but the number of Zn^{2+} that bind are not the same.

7.4.11. Comparative Zinc(II)-Binding Thermodynamics in CSP1 and CSP3

The thermodynamics of the populations of Zn^{2+} ions binding to CSP1 and CSP3 are similar, with CSP3 having a slightly more enthalpically favorable first Zn^{2+} binding population. Given that the binding of Cu^{+} to CSP1 has been shown to have a positive cooperativity, and CSP3 does not, and that the binding of the Cu^{+} populations are distinctly different, it is curious that the Zn^{2+}-binding thermodynamics of CSP1 and CSP3 are similar. There is no evidence in the ITC data for cooperativity in the binding of Zn^{2+} but the similar Zn-binding thermodynamics of CSP1 and CSP3 may suggest there is no cooperativity in the binding of this metal ion. I would predict that the second Zn^{2+} binding population would have different thermodynamics if cooperativity was present. The source and mechanism of any metal-binding cooperativity is unknown, as this aspect of the copper storage proteins has not been explored. Future experimentation to understand the mechanism of cooperative Cu^{+} binding is necessary to connect to these thermodynamic differences. Lack of cooperativity in the binding of other metals could be a mechanism to ensure that Cu^{+} is the preferred metal, aiding in metal specificity and selectivity.

7.4.12. Binding of Mercury to CSP1 and CSP3

Of the metals encountered in nature, Hg^{2+} is the most likely to outcompeting Cu^{+} in the binding to cysteine residues. This is even more true when many cysteine residues are present. This is highlighted by the binding of Hg^{2+} and Cu^{+} to a metal-binding domain, WND4, of the Wilson's disease protein, which binds Cu^{+} with an affinity of $\sim 10^{16}$ and binds Hg^{2+} with an affinity of $\sim 10^{32}$ M^{-1}. How, then, could CSP1 and CSP3 preferentially bind Cu^{+} over Hg^{2+}?

Given current experimental limitations, the condition-independent Hg^{2+} binding thermodynamics of CSP1 and CSP3 are not known. Unlike Zn^{2+}, Hg^{2+} readily binds in 2-, 3-, and 4-coordinate geometries, so it is not possible to predict the deprotonation of CSP1 or CSP3. However, there are important qualitative differences that are apparent in the binding of Hg^{2+} to CSP1 and CSP3. From these ITC experiments, only a few Hg^{2+} bind tightly to the protein, which has an affinity for additional Hg^{2+} that is surprisingly low and occurs at a much lower stoichiometry than Cu^{+}. Both CSP1 and CSP3 bind three Hg^{2+} populations. For CSP1, the first population binds tightly ($K > 10^7$) with a stoichiometry of ~2, a second Hg^{2+} population includes 3 ± 0.1 Hg^{2+}, and a final Hg^{2+} population includes 13 ± 2 Hg^{2+} binding. For CSP3, only a single Hg^{2+} binds strongly and the second Hg^{2+} population binds weaker with a stoichiometry of 2.4 ± 0.1, and the final, most weakly bound Hg^{2+} population, has a stoichiometry of 2 ± 0.6.

Only the first Hg^{2+} population, in which 1-2 Hg^{2+} ions bind to CSP1 and CSP3, have a large binding affinity. The other two Hg^{2+} populations bind with weaker affinities. This population may be binding adventitiously to CSP1, which would explain the very weak interaction.

I propose that copper storage proteins are able to bind Cu^{+} over Hg^{2+} based on metal ion size. This is qualitatively supported by an examination of the structures of CSP1 and CSP3. In the crystal structures the distance between two cysteine residues with the greatest distance is ~1.4 Å. To calibrate the distance that is required for linear Hg^{2+}-cysteine coordination, the solution structure of Hg-bound MerP. Here, the distance between the two cysteine residues that bind Hg^{2+} is ~1.6 Å. Although not definitive, it appears that the distance required to bind Hg^{2+} in a linear geometry is not available in CSP1 or CSP3. Due to this size restriction, and Hg^{2+} being much larger than either Cu^{+} or Zn^{2+}, few, if any, Hg^{2+} would be predicted to enter the metal-binding channel of CSP1 or CSP3.

Thus, how does CSP1 and CSP3 selectively and specifically bind Cu^{+} and not Hg^{2+}? I hypothesize that these copper storage proteins prevent larger metal ions from entering the cysteine-lined protein core. Given the dipositive nature of Hg^{2+}, if size was not precluding the binding of Hg^{2+}, then a similar stoichiometry as Zn^{2+} would not be expected, given the charge similarities. This size dependency could be tested with the binding of Ag^{+} to CSP1 and CSP3, which is very similar to Cu^{+}, but larger. This would provide valuable insight on

how CSP1 and CSP3 modulate metal binding, preventing aberrant metal storage and subsequent cell damage.

7.4.13. Metal Selectivity, Specificity, and Cooperativity in CSP1 and CSP3

Metal selectivity and specificity in CSP1 and CSP3 appears to be modulated by size restrictions, in which these proteins are able to preclude the binding of Hg^{2+}, over Cu^{+}, because of the larger size of Hg^{2+}, which is unable to enter the metal-binding channel. Zn^{2+}, unlike Hg^{2+}, is approximately the same size as Cu^{2+}, and is able to enter the channel. However, the number of Zn^{2+} that are able to bind is then limited by the overall charge. Although Cu^{+} is expected to outcompete the Zn^{2+} binding due to the greater Cu^{+} thiophilicity, the similarities in Zn^{2+} binding to CSP1 and CSP3 suggest that Zn^{2+} does not bind cooperatively to these proteins. The presence of cooperativity in Cu^{+} binding may aid in the storage of Cu^{+} over Zn^{2+}.

I propose additional ITC and colorimetric experiments on the binding and chelation of Ag^{+}, which has a similar thiophilic nature as Cu^{+}, but is larger. These experiments would provide an intriguing counterpoint to Zn^{2+} and Hg^{2+} binding and can be compared to Cu^{+}. Furthermore, Co^{2+} could be used as a spectroscopic probe to investigate coordination and cooperativity in the binding of Zn^{2+} and thereby gain a more thorough understanding of Zn^{2+} interactions with both CSP1 and CSP3.

7.5. Conclusions

Much work still needs to be done to quantify and characterize the Cu^{+}-binding thermodynamics of *Methylosinus trichosporium* copper storage proteins. The interplay between thermodynamics, kinetics, and cooperativity in these samples is of particular interest, as their connections may provide information on the physiological function of CSPs and the circumstances when other thiophilic metals like Zn^{2+} and Hg^{2+} are present. Thermodynamic data provide insight about these interactions. This is the first time that distinct populations of metals that bind to copper storage proteins has been observed and characterized. Both CSP1 and CSP3 bind three Cu^{+} populations, with distinctly difference thermodynamics. It is illustrative to compare these thermodynamics to those of metallothionein, which binds metals similarly, but with vastly different protein

contributions to metal binding. For MT3, the binding of Cu^{+} and Zn^{2+} stabilize the metalloprotein structure, leading to more entropic disfavorability, which is not seen for the binding of these metals to CSP1 or CSP3. This suggests that both CSP1 and CSP3 have significantly less conformational changes upon metal binding.

These studies aim to establish a thermodynamic foundation for metal selectivity and specificity in CSP1 and CSP3. Although determining the metal-binding thermodynamics required certain assumptions, these thermodynamic results provide important insight for how copper storage proteins selectively bind Cu^{+} over other thiophilic metals through size exclusion and possibly metal-binding cooperativity.

7.6. References

(1) Stankus, T. Biochemistry and Molecular Biology. *Ser. Libr.* **1996**, *27* (2–3), 67–78. https://doi.org/10.1300/J123v27n02_05.

(2) Andrei, A.; Öztürk, Y.; Khalfaoui-Hassani, B.; Rauch, J.; Marckmann, D.; Trasnea, P. I.; Daldal, F.; Koch, H. G. Cu Homeostasis in Bacteria: The Ins and Outs. *Membranes*. MDPI AG September 1, 2020, pp 1–45. https://doi.org/10.3390/membranes10090242.

(3) Macomber, L.; Imlay, J. A. The Iron-Sulfur Clusters of Dehydratases Are Primary Intracellular Targets of Copper Toxicity. *Proc. Natl. Acad. Sci. U. S. A.* **2009**, *106* (20), 8344–8349. https://doi.org/10.1073/pnas.0812808106.

(4) Chillappagari, S.; Seubert, A.; Trip, H.; Kuipers, O. P.; Marahiel, M. A.; Miethke, M. Copper Stress Affects Iron Homeostasis by Destabilizing Iron-Sulfur Cluster Formation in Bacillus Subtilis. *J. Bacteriol.* **2010**, *192* (10), 2512–2524. https://doi.org/10.1128/JB.00058-10.

(5) Fung, D. K. C.; Lau, W. Y.; Chan, W. T.; Yan, A. Copper Efflux Is Induced during Anaerobic Amino Acid Limitation in Escherichia Coli to Protect Iron-Sulfur Cluster Enzymes and Biogenesis. *J. Bacteriol.* **2013**, *195* (20), 4556–4568. https://doi.org/10.1128/JB.00543-13.

(6) Banci, L.; Bertini, I.; Ciofi-Baffoni, S. Copper Trafficking in Biology: An NMR Approach. *HFSP J.* **2009**, *3* (3), 165–175. https://doi.org/10.2976/1.3078306.

(7) Wernimont, A. K.; Huffman, D. L.; Lamb, A. L.; O'Halloran, T. V.; Rosenzweig,

A. C. Structural Basis for Copper Transfer by the Metallochaperone for the Menkes/Wilson Disease Proteins. *Nat. Struct. Biol.* **2000**, *7* (9), 766–771. https://doi.org/10.1038/78999.

(8) Andrews, N. C. Metal Transporters and Disease. *Curr. Opin. Chem. Biol.* **2002**, *6* (2), 181–186. https://doi.org/10.1016/S1367-5931(02)00307-1.

(9) Mercer, J. F. B. The Molecular Basis of Copper-Transport Diseases. *Trends Mol. Med.* **2001**, *7* (2), 64–69. https://doi.org/10.1016/S1471-4914(01)01920-7.

(10) Pountney, D. L.; Schauwecker, I.; Zarn, J.; Vašák, M. Formation of Mammalian Cu8-Metallothionein in Vitro: Evidence for the Existence of Two Cu^{+}4-Thiolate Clusters. *Biochemistry* **1994**, *33* (32), 9699–9705. https://doi.org/10.1021/bi00198a040.

(11) Calderone, V.; Dolderer, B.; Hartmann, H. J.; Echner, H.; Luchinat, C.; Del Bianco, C.; Mangani, S.; Weser, U. The Crystal Structure of Yeast Copper Thionein: The Solution of a Long-Lasting Enigma. *Proc. Natl. Acad. Sci. U. S. A.* **2005**, *102* (1), 51–56. https://doi.org/10.1073/pnas.0408254101.

(12) Scheller, J. S.; Irvine, G. W.; Wong, D. L.; Hartwig, A.; Stillman, M. J. Stepwise Copper(i) Binding to Metallothionein a Mixed Cooperative and Non-Cooperative Mechanism for All 20 Copper Ions. *Metallomics* **2017**, *9* (5), 447–462. https://doi.org/10.1039/c7mt00041c.

(13) Gold, B., Deng, H., Bryk, R., Vargas, D., Eliezer, D., Roberts, J., Jiang, X., & Nathan, C. (2008). Identification of a copper-binding metallothionein in pathogenic mycobacteria. *Nature Chemical Biology*, *4*(10), 609–616. https://doi.org/10.1038/nchembio.109

(14) Huckle, J. W.; Morby, A. P.; Turner, J. S.; Robinson, N. J. Isolation of a Prokaryotic Metallothionein Locus and Analysis of Transcriptional Control by Trace Metal Ions. *Mol. Microbiol.* **1993**, *7* (2), 177–187. https://doi.org/10.1111/j.1365-2958.1993.tb01109.x.

(15) Ross, M. O.; MacMillan, F.; Wang, J.; Nisthal, A.; Lawton, T. J.; Olafson, B. D.; Mayo, S. L.; Rosenzweig, A. C.; Hoffman, B. M. Particulate Methane Monooxygenase Contains Only Mononuclear Copper Centers. *Science (80-.).* **2019**, *364* (6440), 566–570. https://doi.org/10.1126/science.aav2572.

(16) Hakemian, A. S.; Rosenzweig, A. C. The Biochemistry of Methane Oxidation. *Annual Review of Biochemistry*. 2007, pp 223–241. https://doi.org/10.1146/annurev.biochem.76.061505.175355.

(17) Cutsail, G. E.; Ross, M. O.; Rosenzweig, A. C.; Debeer, S. Towards a Unified Understanding of the Copper Sites in Particulate Methane Monooxygenase: An X-Ray Absorption Spectroscopic Investigation. *Chem. Sci.* **2021**, *12* (17), 6194–6209. https://doi.org/10.1039/d1sc00676b.

(18) Ross, M. O.; Rosenzweig, A. C. A Tale of Two Methane Monooxygenases. *Journal of Biological Inorganic Chemistry*. Springer Verlag April 1, 2017, pp 307–319. https://doi.org/10.1007/s00775-016-1419-y.

(19) DiSpirito, A. A.; Semrau, J. D.; Murrell, J. C.; Gallagher, W. H.; Dennison, C.; Vuilleumier, S. Methanobactin and the Link between Copper and Bacterial Methane Oxidation. *Microbiol. Mol. Biol. Rev.* **2016**, *80* (2), 387–409. https://doi.org/10.1128/mmbr.00058-15.

(20) El Ghazouani, A.; Baslé, A.; Gray, J.; Graham, D. W.; Firbank, S. J.; Dennison, C. Variations in Methanobactin Structure Influences Copper Utilization by Methane-Oxidizing Bacteria. *Proc. Natl. Acad. Sci. U. S. A.* **2012**, *109* (22), 8400–8404. https://doi.org/10.1073/pnas.1112921109.

(21) Baslé, A.; El Ghazouani, A.; Lee, J.; Dennison, C. Insight into Metal Removal from Peptides That Sequester Copper for Methane Oxidation. *Chem. - A Eur. J.* **2018**, *24* (18), 4515–4518. https://doi.org/10.1002/chem.201706035.

(22) Dennison, C.; David, S.; Lee, J. Bacterial Copper Storage Proteins. *J. Biol. Chem.* **2018**, *293* (13), 4616–4627. https://doi.org/10.1074/jbc.TM117.000180.

(23) Vita, N.; Platsaki, S.; Baslé, A.; Allen, S. J.; Paterson, N. G.; Crombie, A. T.; Murrell, J. C.; Waldron, K. J.; Dennison, C. A Four-Helix Bundle Stores Copper for Methane Oxidation. *Nature* **2015**, *525* (7567), 140–143. https://doi.org/10.1038/nature14854.

(24) Vita, N.; Landolfi, G.; Baslé, A.; Platsaki, S.; Lee, J.; Waldron, K. J.; Dennison, C. Bacterial Cytosolic Proteins with a High Capacity for Cu^{+} That Protect against Copper Toxicity. *Sci. Rep.* **2016**, *6* (39065), 1–11. https://doi.org/10.1038/srep39065.

(25) Mehlenbacher, M.; Poli, M.; Arosio, P.; Santambrogio, P.; Levi, S.; Chasteen, N. D.; Bou-Abdallah, F. Iron Oxidation and Core Formation in Recombinant Heteropolymeric Human Ferritins. *Biochemistry* **2017**, *56* (30), 3900–3912. https://doi.org/10.1021/acs.biochem.7b00024.

(26) Baslé, A.; Platsaki, S.; Dennison, C. Visualizing Biological Copper Storage: The Importance of Thiolate-Coordinated Tetranuclear Clusters. *Angew. Chemie* **2017**, *129* (30), 8823–8826. https://doi.org/10.1002/anie.201703107.

(27) Lee, J.; Dennison, C. Cytosolic Copper Binding by a Bacterial Storage Protein and Interplay with Copper Efflux. *Int. J. Mol. Sci.* **2019**, *20* (17). https://doi.org/10.3390/ijms20174144.

(28) Johnson, D. K.; Stevenson, M. J.; Almadidy, Z. A.; Jenkins, S. E.; Wilcox, D. E.; Grossoehme, N. E. Stabilization of Cu^{+} for Binding and Calorimetric Measurements in Aqueous Solution. *Dalt. Trans.* **2015**, *44* (37), 16494–16505. https://doi.org/10.1039/c5dt02689j.

(29) Awoonor-Williams, E.; Rowley, C. N. Evaluation of Methods for the Calculation of the PKa of Cysteine Residues in Proteins. *J. Chem. Theory Comput.* **2016**, *12* (9), 4662–4673. https://doi.org/10.1021/acs.jctc.6b00631.

(30) Tajc, S. G.; Tolbert, B. S.; Basavappa, R.; Miller, B. L. Direct Determination of Thiol PKa by Isothermal Titration Microcalorimetry. *J. Am. Chem. Soc.* **2004**, *126* (34), 10508–10509. https://doi.org/10.1021/ja047929u.

(31) Stevenson, M. J. Thermodynamic Studies of Cu^{+} and Other d 10 Metal Ions Binding to Proteins in the Copper Homeostasis Pathway and the Organomercurial Detoxification Pathway, 2016.

(32) Gilson, M. K.; Given, J. A.; Bush, B. L.; McCammon, J. A. The Statistical-Thermodynamic Basis for Computation of Binding Affinities: A Critical Review. *Biophys. J.* **1997**, *72* (3), 1047–1069. https://doi.org/10.1016/S0006-3495(97)78756-3.

(33) Tamura, A.; Privalov, P. L. *The Entropy Cost of Protein Association*; 1997; Vol. 273. https://doi.org/10.1006/jmbi.1997.1368.

Chapter 8:

Reflections of Cysteine Metallobiochemistry Thermodynamics and the Implications in Biological Systems

What ties these thesis chapters together? Cysteines, of course. Each metalloprotein that was studied utilizes cysteines in the metal-binding site, which leads to the proteins function. This may be through gene regulation, metal transport, metal storage, or cellular protection but each of these use cysteines differently. Oftentimes, their function is to bind a metal tightly, preventing metal-mediated cell damage, as in MerP or CSP, or these cysteines are used to modulate protein structure, as within MerR and MT-3. These diverse set of functions are possible through the unique chemistry of cysteine residues. The thermodynamic foundation of the metal-cysteine interactions in these proteins are readily quantified by isothermal titration calorimetry (ITC), and can provide valuable insight into the ruleset that governs these protein functions. This thesis aimed to understand how these proteins bind metals, providing a thermodynamic foundation for their function and establish the structure-function relationship through metal-mediated conformational dynamics. A secondary objective was to establish the enthalpic and entropic contributions that occur in the formation of metal-cysteine bonds, thereby allowing the protein to function correctly.

Cysteine is an unusual amino acid. With the exception of histidine, it's pK_a is closest to physiological pH which leads to the functionalization of both the protonated thiol, as a hydrogen-bond donor, and the deprotonated thiolate, as a hydrogen-bond acceptor. This thiol-thiolate interplay is both sensitive and reactive to the surrounding environment. Both the thiol and thiolate can be readily stabilized by other amino acids in proximity to the cysteine. Thus second-sphere interactions greatly impact the functional role of cysteines in these metalloproteins. Beyond this sensitivity to the second-sphere coordinating environment, cysteines also provide a viable foundation in the function of metalloprotein with non-native metals, with their capability of binding a wide range of transition metals. If cysteines are so prevalent in biology and they have a strong propensity to bind a wide range of transition metals, what is gained by the understanding of absolute or relative metal-binding thermodynamics as characterized by ITC?

Absolute thermodynamics, as compared to relative thermodynamics, provide a basic understanding of how the protein binds each metal, however this is of limited value. Relative, or comparative, thermodynamics, however, are effectively the difference in the absolute metal-binding thermodynamics from two comparative protein systems. This could

be differences between two different ligands binding to the same ligand-binding site or wild-type proteins vs. variant proteins. These differences provide insight into how each change in the system impacts metal binding. Of course, none of this applies only to cysteines, but it does illustration how thermodynamics, at a basic level, can provide insight into metal binding and how this can be modulated by protein structural changes.

Cysteines generally bind metals following hard-soft acid base (HSAB) theory, with softer metals, like mercury, binding much stronger than relatively harder metals, like zinc or iron. This was readily predicted from foundational inorganic chemistry and was shown experimentally by ITC throughout this thesis. However, this explanation is only supported through the binding affinity. However, the individual components of the binding affinity, binding enthalpy and entropy, are much more nuanced as they are far more dependent on the conditions and environment surrounding the metal binding.

This modulation of the binding of transition metals to cysteine containing proteins may be from protein deprotonation, buffer protonation, metal-chelator thermodynamics, protein conformational dynamics, and (de)-solvation, to name a few. Although the magnitude of the enthalpy associated with metal-cysteine bond formation could be approximately predicted, the entropic contribution is much less defined, as these principles do not strictly adhere to HSAB theory, although they are connected.[1,2] Many of the individual components that define the binding enthalpy and entropy are not directly quantified, but relative thermodynamic differences provide an approximation for these contributions. The strength of using ITC lies within the quantification of these individual thermodynamic components and the factors that lead to these thermodynamic components. Although this type of analysis can be achieved using other techniques that quantify binding affinity, spectroscopy for example; ITC is capable of these measurements without the need to change the experimental temperature and minimizes sample use as all primary thermodynamic components can, theoretically, be quantified in a single experiment.

Throughout this thesis, ITC was used to quantify the buffer-independent, pH-dependent absolute and relative binding thermodynamics, providing a thermodynamics foundation for metals and their interactions with cysteines in proteins. But these direct metal-binding thermodynamics are only part of the insight gained. The qualitative determination of the surrounding factors that impact metal-binding thermodynamics are

far more important. Protein dynamics or inter-protein interactions can grossly modulate metal binding and, likewise, metal binding can modulate these functions as well, leading to dynamic metal-protein interplay. This thesis highlights this importance, leading to valuable insight on how each protein system modulates metal binding or how the binding of a metal ion can modulate protein structure and function.

Of all protein systems explored in this thesis, quantifying the energetics of mercury-mediated allosteric interactions in MerR is of greatest importance that shows the thermodynamic foundation of the metal-protein interplay. The binding of mercury alters the MerR-*merO* interaction, which changes the RNA polymerase binding site thereby leading to transcription and translation of the mer-pathway proteins. From a fundamental inorganic chemistry perspective, it is expected that MerR would bind mercury very strongly, but prediction of the allosteric interactions or the thermodynamic components of metal binding is not possible from fundamental inorganic principals alone. This is because mercury binding leads to a conformational change in MerR, bringing the RNA polymerase binding sites on *merO* closer together. Cysteines mediate this protein change. This property is not unique to cysteines, but is vital for the function of MerR. Initially, the three cysteines are not in close proximity, but they are brought closer together when mercury binds. It is predicted that this change in this metal binding site propagates molecular changes throughout MerR, which leads to conformational differences. The quantification of this change is not readily possible with most techniques, which highlights the importance of ITC in determining metal-binding thermodynamics.

Each chapter in this thesis quantifies the thermodynamics of metal-cysteine bond formation when the metal binds to the metal-binding site on each protein. Yet, the fundamental thermodynamics appear to be similar, while providing different functions, illustrating how cysteines are sensitive to changes in their protein environment. Metal binding is dependent on the surrounding protein system, which is aided by cysteines reactivity. This reactivity and sensitivity are what dominate the function of the protein, not necessarily the cysteine-metal bonding. From a thermodynamics perspective, this is gives greater weight on the quantification of comparative thermodynamics, not absolute thermodynamics. A comparison of two similar systems can provide a thermodynamic foundation for the enthalpic and entropic contributions, without the addition of the metal-

cysteine bond formation thermodynamics being different. This is seemingly underwhelming, but it gives greater confidence in comparative thermodynamics in understanding what is occurring within the protein at a molecular level. Without knowing that cysteine-metal bond formation thermodynamics are similar, general comparative thermodynamics would have lesser impact, thereby the findings within these chapters strengthen the use of ITC to quantify the thermodynamic foundation of the protein function.

8.4. References

(1) Drago, R. S.; Kabler, R. A. A Quantitative Evaluation of the HSAB Concept. *Inorg. Chem.* **1972**, *11* (12), 3144–3145. https://doi.org/10.1021/ic50118a064.

(2) Pearson, R. G. Hard and Soft Acids and Bases, HSAB, Part II: Underlying Theories. *J. Chem. Educ.* **1968**, *45* (10), 643–648. https://doi.org/10.1021/ed045p643.